

Development of a Flying Wind Measurement System for Collective Operation

Von der Fakultät für Luft- und Raumfahrttechnik und Geodäsie der
Universität Stuttgart zur Erlangung der Würde eines Doktors der
Ingenieurwissenschaften (Dr.-Ing.) genehmigte Abhandlung

vorgelegt von
Christian Molter
aus Stuttgart

Hauptberichter: Prof. Dr. Po Wen Cheng
Mitberichter: Prof. Dr. Simon Watkins
Tag der mündlichen Prüfung: 03/07/2020

Institut für Flugzeugbau
Universität Stuttgart

2020

Abstract

While the field of wind energy evolved to a mature technology during the last 30 years and the annual energy production volume in Germany has been doubled from 51 TWh in 2013, when this project started, to 103 TWh in 2017, there are still some fundamental research questions to answer. Flow over complex terrain, the decay rate of tip vortices and the wind evolution from one turbine to another in a wind park, to name only some of them. All of those topics are mostly related to the fields of fluid dynamics and acoustics. With state of the art flow measurement technology it is sometimes not possible to support this type of research. A met mast is expensive to install and can only measure at one fixed location in space. Remote measurements with LIDARs have a low temporal resolution and therefore cannot capture small scale turbulence.

Inspired by an ongoing project at the Institute of Aircraft Design at the University of Stuttgart the idea developed to utilize remotely piloted rotary wing aircraft for in-situ wind measurements. Additionally, a swarm of aircraft should be used for a high spatial resolution. This results in a novel add-on to conventional measurement technologies because outdoor measurements at several arbitrary locations in three-dimensional space at high temporal and spatial resolution have not been possible before.

If such a swarm measurement is to be realized with a group of conventional multirotor aircraft, a number of potential problems exist:

- The flow field of the rotors will disturb the free stream measurement. Consequently, a long boom is necessary to gain distance to the rotors.
- To hold its position in space the aircraft has to "lean" against the wind. If the wind speed and elevation changes this pitch angle of the aircraft has to change which results in a fast rotational movement to cope with the wind. A fast rotation of the aircraft combined with a long measurement boom induces a velocity on the flow measurement probe mounted at the tip of the boom.
- The long measurement boom causes disturbances in form of large yawing moments in cross-winds but the maximum yaw control moment, for a multirotor produced by different rotor speeds and rotor torques, is very limited.
- Because conventional multirotor aircrafts are designed to hover in a windless environment the flight time will be significantly reduced at higher windspeeds.
- Due to the different dynamic pressure at the advancing and retreating rotor blade, every helicopter and multirotor aircraft is a potential source of vibrations. Consequently, it can be expected that the flow measurement probe will be influenced by these vibrations.
- The measurement equipment has to be connected to the autopilot to make live-readings on the ground possible and to align the aircraft heading with the wind direction. If the heading is not aligned the angular measurement range of the flow measurement probe might be exceeded.

- For the desired swarm application the rotor wake of an aircraft might disturb the measurement taken by another aircraft flying behind. The far wake behaviour of multirotor aircraft has not been explored yet.

To cope with these problems, the present work has been divided into two parts. On the one hand, the underlying effects have been investigated by analytical calculations, simulations and experiments to gain a deeper understanding and derive guidelines and procedures regarding flying wind measurements, as well as multirotor design in general. On the other hand a purpose designed aircraft has been developed most suited for the measurement task.

The proposed solution is a multirotor aircraft with tilting rotors. This solves most of the problems described above. The tilting rotors, in combination with a special control algorithm, can keep the airframe and the measurement boom, attached to it, always horizontal. This reduces not only the airframe drag but also eliminates rotations of the aircraft and hence induced velocities on the flow measurement probe. Because it takes less time to tilt only the rotors instead of the entire aircraft, wind speed changes can be counteracted faster and the position keeping capabilities in windy environments are improved. When the rotors are tiled differentially (e.g. left hand side forward and right hand side backwards) a large yaw control moment, by magnitudes larger than that of a conventional multirotor, can be achieved. Furthermore, with the help of tilting rotors an additional degree of freedom is created which allows the entire aircraft to be tilted towards a nose-up attitude without changing its position. This feature will be used during take-off and landing to increase the distance between flow measurement probe and ground and hereby protect the probe.

By detailed rotor flow field investigations at different levels of fidelity an optimal probe placement was derived and the wind speed range for which flying measurements are feasible was identified. In addition, the behaviour of the rotor wake could be characterized in order to predict possible flying patterns for swarm measurements.

Together with a probe manufacturer a custom flow measurement probe was developed. This design combines the robustness of a Prandtl tube with the high temporal resolution and directional sensitivity of a triple hot wire probe. The data acquisition system for the probe was also customized and connected to the autopilot in order to make live-readings and automatic alignments of the aircraft with the wind direction possible. Finally, to address the problem of vibrations a modal analysis and frequency tuning of the measurement boom has been conducted.

The flight and measurement performance of the first prototype aircraft could be demonstrated with great success. To characterize the lower end of the measurable wind speed range free flights in a gust wind tunnel have been undertaken, while the "real life" measurement performance was shown in a field test next to a met mast at wind speeds up to 13 *m/s*.

Zusammenfassung

Während sich die Windenergie in den letzten 30 Jahren zu einer ausgereiften Technologie entwickelt hat und sich die jährliche Energieproduktion in Deutschland von 51 TWh im Jahr 2013, als dieses Projekt begann, auf 103 TWh im Jahr 2017 verdoppelt hat, gibt es immer noch grundlegende wissenschaftliche Fragestellungen zu beantworten. Die Strömung im komplexen Gelände, die Zerfallsrate von Blattspitzenwirbeln und die Windevolution von einer Anlage zur nächsten Anlage in einem Windpark sind nur einige davon. All diese Themen stehen hauptsächlich im Bezug zu den Gebieten der Strömungsmechanik und Akustik. Mit Strömungsmesstechnik auf aktuellem Stand der Technik ist es manchmal nicht möglich, diese Art der Forschung zu unterstützen. Die Installation eines Messmastes ist teuer und er kann nur an einer festen Stelle im Raum messen. Fernmessungen mit LIDAR besitzen eine niedrige zeitliche Auflösung und können deshalb kleinskalige Turbulenz nicht erfassen.

Inspiziert von einem laufenden Projekt am Institut für Flugzeugbau an der Universität Stuttgart, entwickelte sich die Idee, ferngesteuerte Drehflügler für ortsfeste Windmessungen einzusetzen. Zusätzlich soll ein Schwarm von Fluggeräten für eine hohe räumliche Auflösung verwendet werden. Dies führt zu einer neuartigen Ergänzung zu konventionellen Messsystemen, denn Freifeldmessungen an verschiedenen beliebigen Orten im dreidimensionalen Raum mit hoher zeitlicher und räumlicher Auflösung waren bisher nicht möglich.

Wenn eine solche Schwarmmessung mit einer Staffel konventioneller Multikopter realisiert wird, entstehen eine Reihe von potentiellen Problemen:

- Das Strömungsfeld der Rotoren beeinflusst die Messung der freien Anströmung. Deshalb ist ein langer Ausleger nötig um Abstand zu den Rotoren zu gewinnen.
- Um seine Position im Raum zu halten, muss das Fluggerät sich gegen den Wind "lehnen". Wenn Windgeschwindigkeit und vertikale Windrichtung sich ändern, muss sich auch der Anstellwinkel des Fluggerätes ändern, was wiederum zu einer schnellen, rotatorischen Bewegung führt, um gegen den Wind anzukommen. Eine schnelle Rotation des Fluggerätes in Kombination mit einem langen Messausleger induziert eine Geschwindigkeit an der Sonde zur Strömungsmessung, die an der Spitze des Auslegers montiert ist.
- Der lange Messausleger ruft Störungen in Form von großen Giermomenten bei Seitenwind hervor. Jedoch ist das maximale Giersteuermoment eines Multikopters stark begrenzt, sofern es durch unterschiedliche Drehzahlen und Drehmomente der Rotoren erzeugt wird.
- Da konventionelle Multikopter für einen Schwebeflug bei Windstille ausgelegt sind, reduziert sich die Flugzeit bei höheren Windgeschwindigkeiten deutlich.
- Durch den unterschiedlichen Staudruck am vorlaufenden und rückangeströmten Rotorblatt ist jeder Hubschrauber und Multikopter eine potentielle Vibrationsquelle. Deshalb ist zu erwarten, dass die Sonde zur Strömungsmessung durch diese Vibrationen beeinflusst wird.
- Die Messtechnik muss mit dem Autopiloten verbunden sein, um eine Echtzeitdarstellung der Messwerte am Boden zu ermöglichen und das Fluggerät in Windrichtung auszurichten.

Wenn die Ausrichtung mit der Windrichtung nicht übereinstimmt, könnte der Messbereich der Sonde überschritten werden.

- Bei der angestrebten Schwarmanwendung könnte der Nachlauf eines Fluggerätes die Messung eines der nachfolgenden Fluggeräte stören. Das Verhalten des Rotornachlaufs eines Multikopters ist nicht genau erforscht.

Um diese Probleme zu behandeln, ist die vorliegende Arbeit in zwei Teile gegliedert. Einerseits wurden die grundlegenden Effekte durch analytische Berechnungen, Simulationen und Experimente erforscht, um ein tieferes Verständnis zu erlangen und Richtlinien sowie Prozeduren bezüglich fliegender Windmessungen und ganz allgemein des Entwurfs von Multikoptern abzuleiten. Andererseits wurde ein Fluggerät speziell entwickelt um der Aufgabe der fliegenden Windmessung gewachsen zu sein.

Die vorgeschlagene Lösung ist ein Multikopter mit schwenkbaren Rotoren. Dadurch werden die meisten der oben beschriebenen Probleme gelöst. Die schwenkbaren Rotoren können in Kombination mit einem speziellen Regelalgorithmus das Chassis des Fluggerätes und den daran befestigten Messausleger stets horizontal halten. Dies reduziert nicht nur den Luftwiderstand des Fluggerätes, sondern beseitigt auch die Rotationen und somit induzierte Strömungen auf die Sonde zur Strömungsmessung. Da es weniger Zeit benötigt, nur die Rotoren anstatt des ganzen Fluggerätes zu schwenken, können Änderungen der Windgeschwindigkeit schneller ausgeglichen werden und die Fähigkeit, eine feste Position im Raum zu halten, wird verbessert. Wenn die Rotoren gegensinnig geschwenkt werden (z.B. links nach vorne und rechts nach hinten), können große Giersteuermomente erreicht werden, die um eine Größenordnung höher sind als bei konventionellen Multikoptern. Des weiteren wird mit Hilfe der Schwenkrotoren ein weiterer Freiheitsgrad geschaffen, der es dem Fluggerät erlaubt, mit einem höheren Anstellwinkel zu schweben, ohne seine Position zu verändern. Diese Eigenschaft wird während Start und Landung genutzt, um den Abstand zwischen der Sonde zur Strömungsmessung und dem Boden zu erhöhen und somit die Sonde zu schützen.

Durch detaillierte Untersuchungen zum Strömungsfeld der Rotoren mit verschiedenem Modellierungsgrad wurde eine optimale Platzierung der Sonde hergeleitet und der zulässige Bereich der Windgeschwindigkeit, für den fliegende Windmessungen möglich sind, ermittelt. Zusätzlich wurde das Verhalten des Rotornachlaufs beschrieben, um mögliche Flugformationen für Schwarmmessungen zu erarbeiten.

Zusammen mit einem Hersteller für Strömungsmesssonden wurde eine angepasste Sonde entwickelt. Das Design kombiniert die Robustheit einer Prandtl Sonde mit der hohen zeitlichen Auflösung und Richtungsempfindlichkeit einer Dreifach-Hitzdraht-Sonde. Das Datenerfassungssystem für die Sonde wurde angepasst und mit dem Autopiloten verbunden, um eine Echtzeitvorschau und eine automatische Ausrichtung des Fluggerätes im Wind zu ermöglichen. Zuletzt wurde eine Modalanalyse und dynamische Anpassung des Messauslegers durchgeführt, um das Problem von möglichen Vibrationen zu vermeiden.

Die Flugleistung und Messleistung des ersten Prototyps konnte mit großem Erfolg demonstriert werden. Um das untere Ende des Messbereichs zu charakterisieren, wurden ungefesselte Flüge in einem Böenwindkanal durchgeführt, während die "real life" Leistungsfähigkeit des Gesamtsystems in einem Freifeldtest neben einem Messmast bei Geschwindigkeiten bis zu 13 m/s gezeigt wurde.

Acknowledgments

First of all, I would like to thank Po Wen Cheng, who made this work possible and offered me the unique possibility to pick this interesting research as PhD topic. When I first came to his office and applied for a completely different position and also a completely different PhD topic he came up with the spontaneous idea of unmanned wind measurements in a swarm. While this idea and wind measurements with multirotors in general seem to be quite "trendy" today, almost six years ago this idea was revolutionary and no other research group worked in this area. Furthermore he always supported me and gave me the creative freedom I needed to discover the right path.

I am also highly thankful for the support of my family, even if I had very little time for them during important stages of this work.

I have to admit that I sometimes had my difficulties to fit in at SWE, because I am the only one not directly doing research regarding wind energy or even renewable energy at all. However there are many colleagues for whose I am thankful, because they always supported me. First of all Stefan Baehr, who I had the pleasure to share an office with for the first four years. He warmly welcomed me and taught me so many new things. His explanations regarding fundamentals of wind energy, which was completely new to me when I started, have been very beneficial. But also his broad knowledge about electronics, mechanics and almost every other aspect in life was always of high value for me and my project and I highly appreciate this.

I am also very thankful for the support of Holger Fürst and Florian Haizmann whose excellent project management for the ANWIND project prevented administrative chaos many times and who always supported me and my crazy experiments. With the greek "newbie" Vasilis Pettas I had many interesting and inspiring discussions about aerodynamics and other topics. For this inspiration and support I am also very thankful.

An interesting side-show project started in the end of 2015 with my colleague Matthias Arnold - the folding mobile wind turbine. Together with a group of students we worked hard but also had a lot of fun designing and building this device for a competition. In addition Matthias greatly supported me when it came to the actuator disc simulation which has been very important for my studies. Many thanks for this.

When writing about direct colleagues, last but not least, I would like to express my appreciation for the support from the secretary's office first and foremost Sabine Mitchell. Without your kind and calm nature and your positive attitude during many administrative tasks the fast progress in this project wouldn't have been possible.

I do not only have to thank my direct colleagues from SWE for their support but also my colleagues from IFB. Whenever I needed a briefing for a machine, I haven't used before, Heiko Sommer but also many other people have been there for me. With Gerd Falk and Markus Blandl I had a most productive cooperation during another sideshow project. The "spider copter" which was built to lay out carbon fiber rovings. Many thanks for this inspiring project and also for all the support you showed me.

Furthermore I am most grateful for the support and kindness with whom I was met by Bernd Peters from IAG during the extensive wind tunnel tests of my propellers and the final measurement probe. Even if we are working at the same university, the IAG was not officially involved in the project and it cannot be taken for granted that another institute is allowed to use the facilities

and is supported with so much advice. Bernd took always time to help me out and explain the equipment to me with his kind and patient nature. The wind tunnel experiments have been a tremendous asset to my studies and without Bernd they wouldn't have been possible.

I am also very thankful for my student assistants. Especially Svetozar Karaivanov was always working hard to manufacture parts for me and the project. He can be considered a human 3D printer. One day you design a part in CAD and the other day Svetlio has finished it. This often took a lot of burden off me. Thank you very much for the good work.

Also my bachelor and master students greatly supported the project with their good work. I would like to name Marc Aurel Frankenbach, Jakob Maier, Marco Bienek and Ruben Gleiter.

I would also like to thank Uwe Kaiser and Detlef Bergmann from SVMTec for the kind and professional cooperation during the project. Without your close support we wouldn't have a flow measurement probe and what would a wind measurement aircraft be without a probe? It was always exciting to see how your small, but fine company works and to learn something new from you.

The ANWIND project (Förderkennzeichen 0324014A) was founded by the German Federal Ministry for Economic Affairs and Energy (Bundesministerium für Wirtschaft und Energie - BMWi). I am thankful for this founding which made the development of ANDroMeDA possible.

Contents

Abstract	iii
Zusammenfassung	v
Acknowledgments	vii
Abbreviations	xv
List of Main Symbols	xix
1 Introduction	1
1.1 Motivation	1
1.2 Requirements	2
1.3 State of the Art	2
1.3.1 Met Mast	2
1.3.2 LIDAR	4
1.3.3 Tethered Airborne Measurements	4
1.3.4 Untethered Airborne Measurements	5
1.4 Proposed Solution	6
1.5 Legal Limitations	6
1.6 Research Objectives	7
2 Extreme Wind Conditions	9
2.1 Influence of Changes in Wind Speed and Wind Direction on an Aircraft	9
2.2 IEC Standard	9
2.3 Offshore Measurements	10
2.4 Onshore Measurements	12
2.5 Conclusions	12
3 Comparison between Fixed Wing and Rotary Wing Aircraft	15
3.1 Flight Performance	15
3.2 Influence of Quickly Changing Wind Direction on Flight Mechanics	16
3.3 Experiences Regarding a Steady Flight with Fixed Wing Aircraft	17
3.3.1 Wind Tunnel Tests with Tethered Aircraft	17
3.3.2 UAV Research at RMIT University	17
3.4 Conclusions	18
4 Comparison of Flow Measurement Equipment	19
4.1 Constraints of Airborne Flow Measurements	19
4.2 Ultrasonic Anemometer	19
4.3 Pitot/Prandtl Tube	21
4.4 Multi Hole Probe	22

4.5	Hot Wire Probe	24
4.6	Indirect Measurement Using Aircraft Attitude and Movements	25
4.7	Conclusions	26
5	Conceptual Design of ANDroMeDA	27
5.1	Introduction to the ANDroMeDA Philosophy	27
5.2	Definitions	29
5.2.1	Phrases "Propeller" and "Rotor"	29
5.2.2	Angle of Attack of the Rotor Disc	29
5.2.3	Flight Mechanical Quantities	29
5.3	Constraints and Design Point	30
5.3.1	Design Point	30
5.3.2	Forces Acting on the Aircraft in Forward Flight	30
5.3.3	Drag Estimations Based on Conventional Multirotor Aircraft	32
5.3.4	Disturbances from the Rotor Flow Field	33
5.3.5	Velocities Induced on the Measurement Probe by Vehicle Rotations	34
5.3.6	Solutions to Alleviate Velocities Induced by Aircraft Rotations	35
5.4	Methodology in Conceptual Design	37
5.5	Approaches to Reduce Control Response Time	39
5.5.1	Possible Multirotor Configurations	39
5.5.2	Example Case	40
5.5.3	Actuator Response Times	40
5.5.4	Maximum Control Moment	41
5.5.5	Time needed to Tilt the Aircraft	43
5.5.6	Conclusions	45
5.6	Approaches to Alleviate Induced Velocities	47
5.6.1	Gimbal	47
5.6.2	Tilting Propellers	48
5.6.3	Conclusion	49
5.7	Rotor Flow Field Investigations	50
5.7.1	Problem Description	50
5.7.2	Simulation Description	51
5.7.3	Wind Tunnel Setup	56
5.7.4	Oblique Inflow Rotor	57
5.7.5	Dimensional Analysis of the Results	67
5.7.6	Modeling Approaches	67
5.7.7	Conclusions	70
5.8	Aerodynamic Considerations on Rotor Sizing	71
5.8.1	Problem Description	71
5.8.2	Blade Geometry Scaling	71
5.8.3	Induced Power	74
5.8.4	Conclusions and Maximal Propeller Size	75
5.9	Possible Rotor Layouts	78
5.9.1	Configuration 1: H-4	79
5.9.2	Configuration 2: Y-6	82
5.9.3	Configuration 3: H-6	86
5.9.4	Configuration 4: H-8	89
5.9.5	Configuration 5: H-8 Parallel	91

5.10	Overall Aerodynamic Simulation	93
5.10.1	Simulation Description	93
5.10.2	Interference Between Front and Rear Rotors	97
5.10.3	Maximum Yawing Moment	100
5.10.4	Aerodynamically Shaped Cover	102
5.10.5	Drag of Different Configurations	105
5.10.6	Modeling Approach	106
5.10.7	Conclusions	107
5.11	Flight Time Analysis	108
5.12	Complete Comparison of the Remaining Configurations	110
5.12.1	H-4	110
5.12.2	Y-6	112
5.12.3	H-8	113
5.13	Decision Matrix	115
5.14	Remaining Parameters	116
5.14.1	Rotor Distances	116
5.14.2	Maximum Rotor Diameter	121
5.14.3	Maximum Weight of an Useful Aerodynamic Cover	122
6	Prototyping of AnDroMeDA	123
6.1	Detailed Design	123
6.1.1	Frame Design	123
6.1.2	Tilt Mechanism	127
6.1.3	Landing Gear	129
6.1.4	Battery Mount	131
6.1.5	Measurement Boom	132
6.1.6	Aerodynamic Cover	132
6.1.7	Wiring	135
6.2	Fabrication	136
6.2.1	Pre-Testing	136
6.2.2	Frame Assembly	136
6.2.3	Wiring	137
6.2.4	Fabrication Time	137
6.3	Flow Measurement Probe	141
6.3.1	Fundamental Principles of Triple Hot Wire Probes	141
6.3.2	Integration of the Measurement Equipment	143
6.3.3	Advanced Methods of Hot Wire Calibration and Data Reduction	145
6.3.4	Testing and Characterization of the Measurement Probe	151
6.3.5	Applying Advanced Calibration Methods to the Measurement Probe	160
6.3.6	Conclusions	163
7	Flight Control	165
7.1	Problem Description	165
7.2	Hardware Used for ANDroMeDA-1	166
7.3	Flight Mechanical Considerations	167
7.4	Control Strategy for Tilting Propellers	167
7.5	Modifications to the PX4 Flight Control Software	169
7.5.1	Yaw Controller	169

7.5.2	Position Controller	169
7.5.3	Notch Filter	170
7.5.4	Data Acquisition	171
7.5.5	Custom MAVLINK Package	171
7.6	Modifications to the QGroundControl Software	171
7.6.1	Custom MAVLink Package	171
7.6.2	Data Preview	172
8	Flight Tests and Evaluation of the Overall Wind Measurement System	173
8.1	Flight Tests	173
8.1.1	Software Test Platform Baby ANDroMeDA	173
8.1.2	Observations during Flight Testing of ANDroMeDA-1	173
8.1.3	Drag Coefficient	174
8.1.4	Flight Envelope	174
8.1.5	Conclusions	175
8.2	Validation of ANDroMeDA-1 as a Wind Measurement System	177
8.2.1	Forward Flight in Calm Air	177
8.2.2	Gust Wind Tunnel	177
8.2.3	Field Validation at a Met Mast	178
8.3	Multi-Aircraft Measurements	179
8.4	Conclusions	180
9	Conclusions and Outlook	183
9.1	Conclusions	183
9.1.1	Design of ANDroMeDA	183
9.1.2	General Conclusions	184
9.1.3	Component Tests	185
9.1.4	Flow Measurement Probe Development	186
9.2	Outlook	186
9.2.1	Detailed Improvements of the Measurement Aircraft	186
9.2.2	Flight Tests	186
9.2.3	Advanced Simulations	187
9.2.4	Measuring Wind Turbine Tip Vortices	187
9.2.5	Multi Aircraft Measurements	188
A	Selection and Evaluation of Aircraft Components	189
A.1	Propeller Tests and Simulations	189
A.1.1	Test Rigs	190
A.1.2	Simulations	193
A.1.3	Propeller Overview and Static Tests	201
A.1.4	Wind Tunnel Tests of Propellers at Forward Flight Conditions	203
A.1.5	Conclusions	207
A.2	Modeling Motor/Propeller Dynamics	208
A.2.1	General Approach	208
A.2.2	Dimensional Analysis	209
A.3	Motor Comparison	212
A.4	ESC Comparison	214
A.4.1	Background	214

A.4.2	Test Program	215
A.4.3	Tested ESCs	216
A.4.4	Additional Features	216
A.4.5	Test Results	218
A.4.6	Additional Observations	223
A.4.7	Conclusions	223
A.5	Tiltrotor Actuator Testing	224
A.5.1	Physical Description	224
A.5.2	Analytical Approach	227
A.5.3	MBS Simulations	229
A.5.4	Test Rig	232
A.5.5	Measurements and Conclusions	236
A.6	Vibration Isolation of Flow Measurement Equipment	238
A.6.1	Sources of Vibrations	238
A.6.2	Influence of Vibrations on the Flow Measurement	238
A.6.3	Testing Procedure	238
A.6.4	Approaches to Isolate the Measurement Probe	239
A.6.5	Test Results and Conclusions	240
A.7	Battery Choice	243
B	Mass Estimation	245
B.1	Propulsion System	245
B.1.1	Propeller	245
B.1.2	Motor	246
B.1.3	ESCs	248
B.1.4	Wiring	248
B.1.5	Conclusion	249
B.2	Structure	249
B.2.1	Airframe	249
B.2.2	Motor Arms	249
B.2.3	Tilt Mechanism	250
B.3	Aerodynamic Cover	250
B.4	Payload	251
B.5	Other Components	251
B.5.1	Flight Control Systems	251
B.5.2	Miscellaneous	252
B.6	Conclusions	252
C	Flight Mechanical Simulation Model	255
C.1	Inertia	255
C.2	Aerodynamics	255
C.3	Propeller Thrust and Torque	256
C.4	Simulation Results with Changing Wind Speed and Wind Direction	257
D	Notch Filter Class	259
	Bibliography	261

Abbreviations

ACD Actuator Disc

ADC Analog Digital Converter

ANDroMeDA ANWIND Drone for Measurement and Data Acquisition

ANWIND Anwendungsorientierte Windfeldforschung (applied wind field research)

BE Blade Element Theory

BEC Battery Eliminating Circuit

BEM Blade Element Momentum Theory

BLDC Brushless DC

CAD Computer Aided Design

CAN Controller Area Network

CCA Constant Current Temperature Anemometry

CCW Counterclockwise

CFD Computational Fluid Dynamics

CFRP Carbon Fiber Reinforced Plastics

CG Center of Gravity

CTA Constant Temperature Anemometry

CW Clockwise

D.L. Disc Loading

DAC Digital Analog Converter

DC Direct Current

DCM Direct Cosine Matrix

DOF Degrees of Freedom

DSLR Digital Single-Lens Camera

EKF Extended Kalman Filter

EMF Electromagnetic Field

EOG	Extreme Operating Gust
EPROM	Erasable Programmable Read-Only Memory
ESC	Electronic Speed Controller
FEA	Finite Element Analysis
FEM	Finite Element Method
FET	Field-Effect Transistor
FINO	Forschung in Nord- und Ostsee (Research in North Sea and Baltic Sea)
FPGA	Field-Programmable Gate Array
GFRP	Glas Fiber Reinforced Plastics
GmbH	Gesellschaft mit beschränkter Haftung (Legal Form of a Company in Germany)
GPS	Global Positioning System
HIL	Hardware in the Loop
HW	Hot Wire
I2C	Inter-Integrated Circuit
IAG	Institute of Aerodynamics and Gas Dynamics
IC	Integrated Circuit
IEC	International Electrotechnical Commission
IFR	Flight Mechanics and Controls Lab at the University of Stuttgart
IMU	Inertial Measurement Unit
LBA	Luftfahrtbundesamt - German Federal Aviation Authority
LDA	Laser Doppler Anemometry
LES	Large Eddy Simulation
LiPo	Lithium Polymer
LOS	Line of Sight
LTA	Lighter than Air Vehicle
MBS	Multi Body Simulation
MCU	Micro Controller Unit
MOSFET	Metal-Oxide-Semiconductor Field-Effect Transistor
MTOW	Maximum Take-Off Weight

PID Proportional-Integral-Derivative

PIV Particle Image Velocimetry

POM Polyoxymethylen

PSD Position Sensitive Detector / Power Spectral Density

PWM Pulse Width Modulation

RAM Random Access Memory

RANS Reynolds Averaged Navier Stokes Equations

RMIT Royal Melbourne Institute of Technology

RPAS Remotely piloted Aircraft System

RPM Revolutions per Minute

SAS Stability Augmentation System

SD Secure Digital

SLS Selective Laser Sintering

SPI Serial Peripheral Interface

SPS Samples per Second

SST Shear Stress Transport

STL Stereolithography

SWE Stuttgart Wind Energy Research Group at the Institute of Aircraft Design

T.I. Turbulence Intensity

TKE Turbulent Kinetic Energy

TOW Take-Off Weight

UART Universal Asynchronous Receiver Transmitter

UAV Unmanned Aerial Vehicle

USB Universal Serial Bus

WindForS Wind Energy Research Cluster

List of Main Symbols

Greek Letters

α	°	angle of attack of an airfoil/aircraft/measurement probe etc.
	°	angle between velocity vector and first wire of a triple hot wire probe
	°	yaw angle of single hot wire probe
α_R	°	angle of attack at rotor blade tip
β	°	rotor blade flapping angle
	°	angle between velocity vector and second wire of tripel hot wire probe
γ	°	angle between velocity vector and third wire of tripel hot wire probe
γ_a	°	angle between aerodynamic frame of reference and geodetic frame of reference
μ	—	advance ratio of a rotor/propeller, $\mu = v_{flight}/(\Omega R)$
Ω	rad/s	rotational speed
ω	rad/s	rotation vector
ψ	°	rotor azimuth angle
ρ	kg/m ³	air density
ρ_A	kg/m ²	areal weight
σ	—	standard deviation
	°	rotor/propeller tilt angle
	—	rotor solidity
θ	°	aircraft pitch angle (between body frame of reference and geodetic frame of reference)

	°	opening angle of free jet
	°	rotor blade pitch angle
	°	pitch angle of single hot wire probe
θ_{AE}	°	wind vector azimuth
θ_E	°	wind vector elevation
φ	°	sweep angle of motor arms for Y-6 multirotor configuration

Latin Letters

A	m^2	area
	—	calibration factor for hot wire probe
$a_{i,j}$	$1/N; 1/Nm$	coefficients of calibration matrix
AR	—	aspect ratio
b	m	wing span
B	—	calibration factor for hot wire probe
$b_{chassis}$	m	width of a multirotor airframe
c	m	blade chord
\mathbf{C}	$1/N; 1/Nm$	calibration matrix
$c_{a\alpha}$	$1/rad$	airfoil lift curve slope
c_D	—	drag coefficient for entire wing/aircraft
c_d	—	airfoil drag coefficient
c_L	—	lift coefficient for entire wing/aircraft
c_l	—	airfoil lift coefficient
C_Q	—	torque coefficient of helicopter rotor: $C_Q = Q(\rho AR(\Omega R)^2)$
C_T	—	thrust coefficient of helicopter rotor: $C_T = T(\rho A(\Omega R)^2)$

D	m	diameter of turbine, rotor or propeller
D	N	drag force
d	m	inner diameter or diameter of small objects
	m	deflection
$D.L.$	N/m^2	disc loading
$d_{aircraft}$	m	distance between two consecutive aircraft in a measurement group
E	N/mm^2	Young's modulus
	–	calibration factor for hot wire probe
E_{batt}	Wh	energy of a battery
e_{batt}	Wh/kg	specific energy of a battery
f	Hz	frequency
F	N	force in general
\mathbf{F}	N, Nm	vector with forces and/or moments
$F.o.M.$	–	figure of merit
h	m	height
	m	distance of two coaxial rotors
	–	pitch factor of hot wire probe
I	mm^4	second moment of area
I	A	electrical current
I_{prop}	kgm^2	moment of inertia of a propeller about its rotational axis
I_{xx}	$kg m^2$	moment of inertia about x-axis
I_{yy}	$kg m^2$	moment of inertia about y-axis
I_{zz}	$kg m^2$	moment of inertia about z-axis

List of Main Symbols

k	–	coefficient of proportionality
	–	yaw factor of hot wire probe
k_v	min^{-1}/V	speed coefficient of brushless DC motor
L	N	aerodynamic lift
l	m	length
L	Nm	aircraft rolling moment
\mathbf{L}	kgm^2/s	angular momentum vector
$l_{chassis}$	m	length of a multirotor airframe
m	kg	mass
M	Nm	moment of force in general
	Nm	aircraft pitching moment
\mathbf{M}	Nm	moment vector
Mx_{rotor}	N	x-component of rotor torque
Mz_{rotor}	N	z-component of rotor torque
n	g	load factor
	–	number of rotor blades
	min^{-1}	rotational speed of propeller/motor
N	Nm	aircraft yawing moment
	–	number of rotors
\mathbf{O}	–	origin straight vector
P	W	power
p	N/m^2	pressure
	rad/s	aircraft roll rate

$P_{i_{vor}}$	W	induced power of a propeller in forward flight
$P_{propulsive}$	W	propulsive power needed for forward flight
q	N/m^2	dynamic pressure
	rad/s	aircraft pitch rate
Q	Nm	helicopter rotor torque
\mathbf{q}	N/m^2	vector of dynamic pressure, $\mathbf{q} = [u^2 v^2 w^2]^T$
r	rad/s	aircraft yaw rate
R	m	rotor/propeller radius
Re	–	Reynolds number
$\mathbf{R}_{HW-aero}$	–	rotation matrix from hot wire axis system to aerodynamic axis system
\mathbf{R}_{HW-i}	–	transformation matrix from i-th hot wire probe to hot wire axis system
t	s	time
	m	thickness
T	N	thrust force of rotor or propeller
	s	period of time
$T.I.$	%	turbulence intensity
T_{fluid}	$^{\circ}C$	fluid temperature
\mathbf{T}_{p-i}	–	transformation matrix from propeller to inertial frame of reference
$T_{wire,corr}$	$^{\circ}C$	corrected hot wire temperature
Tx_{rotor}	N	x-component of rotor thrust
Tz_{rotor}	N	z-component of rotor thrust
u	m/s	longitudinal component of wind vector
\mathbf{U}	–	vector with measured raw data

List of Main Symbols

U_b	V	voltage measured by hot wire probe
	m/s	normal velocity component on hot wire probe, perpendicular to probe shaft
U_{batt}	V	battery voltage
U_n	m/s	normal velocity component on hot wire probe, tangential to probe shaft
U_t	m/s	tangential velocity component on hot wire probe
v	m/s	lateral component of wind vector
V_{hub}	m/s	wind speed at wind turbine hub height
v_{wire}	m/s	velocity measured by hot wire probe
w	m/s	vertical component of wind vector
W	N	weight force
W_E	kg	empty weight
X	N	aircraft longitudinal force
$x d_{rotor}$	m	longitudinal rotor distance of a multirotor configuration
Y	N	aircraft lateral force
$y+$	$-$	dimensionless wall distance
$y d_{rotor}$	m	lateral rotor distance of a multirotor configuration
Z	N	aircraft vertical force
z_{hub}	m	hub height
z_d	m	vertical rotor wake displacement

Subscripts

$(\cdot)_a$	aerodynamic frame of reference
$(\cdot)_{ACD}$	actuator disc
$(\cdot)_{arm}$	motor arm of multirotor aircraft

$(\cdot)_b$	body frame of reference
$(\cdot)_{blade}$	propeller/rotor blade
$(\cdot)_{disc}$	quantity taken at rotor or actuator disc
$(\cdot)_{frame}$	quantities referred to the aircraft frame
$(\cdot)_g$	geodetic frame of reference
$(\cdot)_H$	in-plane rotor forces and moments
$(\cdot)_{HW}$	hot wire
$(\cdot)_i$	induced
$(\cdot)_\infty$	free stream quantity without any disturbances
$(\cdot)_{i/rev}$	i-th multiple of rotor rotational speed
$(\cdot)_p$	probe
$(\cdot)_{res}$	quantity resulting from superposition of several components
$(\cdot)_{rotor}$	rotor of a multirotor aircraft
$(\cdot)_s$	static
$(\cdot)_t$	total
$(\cdot)_\perp$	component perpendicular to a reference plane

Superscripts

$(\cdot)^i$	i-th rotor of a multirotor vehicle
$(\cdot)^i$	i-th probe of a triple hot wire probe
$(\cdot)'$	rotor frame of reference on a tiltrotor
$(\cdot)''$	motor arm frame of reference on a tiltrotor

Operators

$(\cdot)^{\mathbf{T}}$	transposed matrix
------------------------	-------------------

$\hat{(\cdot)}$	amplitude of a periodic quantity
$(\cdot)^{-1}$	inverted matrix
$(\cdot)_{\mathbf{xy}}$	projection of a vector to xy-plane
$(\cdot)_{\mathbf{xz}}$	projection of a vector to xz-plane
$(\cdot)_{\mathbf{yz}}$	projection of a vector to yz-plane
$\dot{(\cdot)}$	time derivative

1 Introduction

1.1 Motivation

The idea of a rotary wing aircraft built with four individual rotors is now almost one hundred years old. In 1922, before "conventional" helicopters with a tail rotor existed, Étienne Oemichen flew his quadrotor, the Oemichen No.2. Even if the Keyence GyroSaucer, a model aircraft working quite well after the same principle, existed already in 1991 it did not happen until the past decade that small, unmanned multirotor aircraft became highly popular and characterized the term "drone" so that nowadays children speak of a "drone" whenever they see something consisting of four rotors. The reason for this development is that, besides the success of lithium polymer batteries, the sensors necessary to operate such a vehicle in a stable flight became very reliable and highly affordable because they are mass produced today and can be found in almost every mobile phone and tablet as well as in many entertainment devices.

Another fact that motivated this work is the fast development of flight control hard- and software during the past years. This makes it possible to operate an unmanned aerial vehicle (UAV) automatically without pilot input and even operate multiple aircraft at a time. A swarm flight with 49 illuminated quadrotors has been successfully demonstrated already in 2012 by the Austrian company Ars Electronica Linz GmbH resulting in a very impressive light show. In the mean time they have increased their record to 100 quadcopters flying simultaneously in a pre-defined pattern.

These two advances in aerospace technology motivated this thesis in 2013. The initial vision, later also referred to as "multiscalar UAV measurements", was to use several unmanned aircraft hovering simultaneously at fixed locations in space to measure wind and hereby gather new information about the flow around wind turbines that couldn't be measured with previous methods. Additionally the aircraft should be very light weight to avoid any complicated authorization procedure.

One could also describe the general idea as "wind measurements with a swarm of drones" but the terms "drone" and "swarm" will be avoided here because, other than the recent reference to quadrotor aircraft, a "drone" is normally used for military operations and meant to operate on its own, which is not needed for wind measurements. Also the term "swarm" implies some intelligent, autonomous behaviour where the swarm members have to communicate with each other. Again this is not needed for wind measurements and instead the term "a group of aircraft" will be used.

In 2016 the work was included into work package B2 of the ANWIND project, founded by the German Federal Ministry for Economic Affairs and Energy. This was a very good fit because the ANWIND project has the general purpose of "application oriented wind field research" and a better understanding of wind fields.

The motivation for this work from the authors personal point of view was not only or not necessarily to carry out a final measurement campaign but also to explore the problems to overcome making such a campaign possible. From the start on the project could be considered as very ambiguous and included many open questions to answer. This made it exciting to figure out the limits of what is possible and to gather some fundamental research findings first.

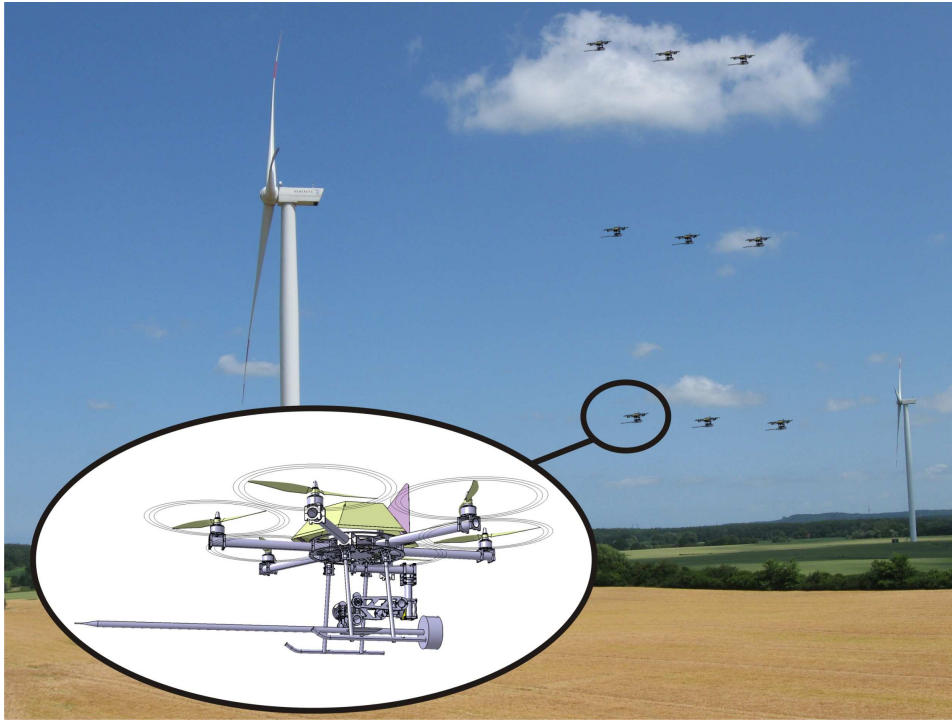


Figure 1.1: The vision: Multi-aircraft wind measurements.

1.2 Requirements

To realize the benefits from airborne multi-aircraft measurements the following requirements should be met:

- The position of aircraft inside the group should be as flexible as possible to enable a reaction to changing wind directions during the measurement period and to investigate different phenomena.
- A measurement flight should last longer than 10 minutes.
- Aircraft positions should be fixed in space.
- The aircraft must meet regulations from aviation authorities to avoid complicated special permits for its operation.
- A high temporal and high spatial resolution are necessary to enable the use of measurement data directly as an input for large eddy simulations (LES).

1.3 State of the Art

1.3.1 Met Mast

A measurement tower, in wind energy usually called a met mast, which stands for meteorological mast, is the most common technology to measure wind speeds at relevant heights. The mast consists generally of vertical steel truss segments that are braced to the ground with steel cables. For site assessment a measurement has to be carried out at hub height which results in a mast

slightly higher than the turbine's hub height. For research purposes also higher masts exist like the 200 meter high met mast in Rödeser Berg in the region of Kassel. The highest met mast, even if it is not used particularly for wind energy research, is the Amazon Tall Tower Observatory (ATTO) in the Amazon rainforest of Brazil with a height of 325 meters.

For site assessments met masts are equipped with cup anemometers and wind vanes. If a met mast is used for research purposes it does often carry sonic anemometers which are able to measure the wind velocity in three dimensions at frequencies up to 100 Hz. A met mast enables a reliable measurement at a fixed location for many months or even years.

On the contrary it is also the most expensive way to measure wind speeds because a high infrastructural effort is necessary to built it (compare Figure 1.2). Another disadvantage is that the measurement location is fixed and usually only one met mast is present. Consequently no wind speed correlations at different spots can be investigated and the position cannot be changed if it turns out that another location would be also worth investigating during the measurement campaign.

Exceptions are research location like the wind energy test site near the village of Stötten which will be equipped with four met masts or the danish test site in Østerlid.



Figure 1.2: Met mast assembly at the WindForS test site. The small crane is necessary to assemble the larger crane. A mobile temporary road has to be layed out with panels.

1.3.2 LIDAR

With a LIDAR (light detection and ranging) device it is possible to sense wind speeds remotely with a laser beam using the backscattered light, which is phase shifted due to the Doppler effect. Experiments with this technology began in the 1970s and the first wind LIDAR was mounted on a wind turbine in 2003 ([1]). In the last 15 years several companies introduced LIDAR devices especially for the wind industry that can be ground based or mounted on the nacelle of a wind turbine. Most devices are so called "staring" models that can only deploy a laser beam in a fixed direction. Less common are scanning LIDARs that can point with the laser beam in different directions. At SWE a very fast scanning head for a leosphere LIDAR was developed in the past. Also included in the ANWIND project is the development of an entirely new LIDAR scanner model in cooperation with the OpticSense GmbH. The design of the new device is driven by requirements of robustness and light weight construction to improve the handling.

The biggest advantage of a wind LIDAR is its flexibility and that it can be deployed without high infrastructural effort. Especially if it is a ground based device it is very easy to install but also the effort and cost to install a nacelle based LIDAR are a lot lower than the installation of a met mast. However the measurement availability depends strongly on the environmental conditions (number of aerosols, humidity, clouds). Furthermore a LIDAR cannot replace a met mast completely because the technology has several limitations compared to the measurement devices that can be installed on a met mast.

First of all a LIDAR measurement is a volumetric measurement and not a point measurement. This means that the measured wind speed is averaged over a measurement volume and thus it is not possible to detect small scale turbulent structures for example. Further more for a LIDAR device it is not possible to sense other components of the wind speed than the one in the line of sight (LOS) direction of the laser. Consequently it is not possible to determine a 3D wind vector at any arbitrary location in space. However this disadvantage can be overcome if three LIDAR devices are used pointing to the same target from different locations. Such a procedure is still subject of ongoing research but first results look promising ([2]).

When a scanning LIDAR on a nacelle is used, it is possible to reconstruct the three dimensional wind field only with the measured line of sight wind speeds if some assumptions are made ([3]). Such an assumption is for example a mathematical wind shear model. The computation of a three dimensional wind field from line of sight LIDAR data is called "wind field reconstruction". The resulting wind fields are very important for wind energy research as for example as input for CFD simulations. By using the proposed multi aircraft measurements simultaneously with a scanning LIDAR a valuable combination of measurement techniques is available that can improve the current wind field reconstruction algorithms.

A last disadvantage of scanning LIDAR measurements is the low temporal resolution of the LIDAR device of only one Hertz. While staring LIDARs have a higher temporal resolution, a scanning LIDAR needs even more time to move the beam to the next location in addition to the pure measurement period when the sampled values are averaged which results in an even lower temporal resolution.

1.3.3 Tethered Airborne Measurements

In the 1970s the idea of using the aerodynamic forces acting on a kite to measure wind speed and direction has been patented (see [4]). Hereby the kite line is attached to an anchor in a way that it can rotate freely about the vertical axis. An angle sensor and force sensor are used to measure angle and tension of the kite line which can be transformed to wind speed and direction if

the aerodynamic properties of the attached kite are known.

If additional measurement equipment is used a balloon, airship or kite can be used to carry this equipment. A good overview on all kind of airborne measurement vehicles and results of a comparative measurement campaign are given in [5].

The biggest advantage of tethered airborne measurements is that the measurement duration is almost not limited. If the deployed vehicle is a lighter than air vehicle (LTA) like a hot air balloon or an airship it can be operated also at very low wind conditions or even if the wind speed decreases to zero during the measurement period. For kites this means that they have to be relaunched manually. Considering the wind speeds worth measuring for useful turbine operation this is not expected to be a problem.

The biggest disadvantage of all tethered vehicles is the little flexibility regarding the measurement location. Depending on the drag of the vehicle and the tether line an angle will form between ground and tether line. Especially for vehicles with high drag forces like a balloon this angle can be very shallow. Consequently no operation in close proximity to a wind turbine is possible because a change of the wind direction might result in a collision. Also the measurement location can change if the wind direction changes during the measurement duration and it is not possible to change the location on purpose during flight unless the anchor point or winch of the tether line is set up on a strong ground vehicle.

One configuration that hasn't been explored yet, according to the author's knowledge, is a powered tethered aircraft. If for example a multirotor aircraft is tethered to ground all power can be transmitted through the tether cable and this would result in an unlimited measurement duration. However preliminary calculations revealed that for measurement altitudes above 100 meters the weight of the necessary power cable is quite high so that with the legal weight limit for the aircraft of five kilograms only very little payload can be carried. Another question that hasn't been answered is of course the legal role of such a configuration. Maybe it is possible to receive a permanent permission for tethered flights with a ground powered aircraft heavier than five kilograms because a fly away is not possible without a power source on board. In this case longer measurements would be possible. Because the outcome of this legal issues is hard to predict and even if longer measurements are possible the limitation of the measurement location with a tether always remains the idea hasn't been pursued further. However, recently a company demonstrated the feasibility of a ground powered configuration with an impressive aircraft that is able to clean wind turbine blades ([6]). The aircraft can lift up to 200 kg of payload.

1.3.4 Untethered Airborne Measurements

Untethered airborne wind speed measurements can be divided into two categories: Non-stationary fixed wing measurements and stationary rotary wing measurements. The former ones make wind field research more difficult because the wind speed has to be averaged over a certain amount of time and space.

A good overview on untethered airborne measurements is given in [5]. A newer overview with more emphasis on the measurement equipment is given in [7]. Most of the flying wind measurements are done with fixed wing aircraft flying in straight legs. When this work started in 2013 the only two exceptions have been the Vario XLC helicopter (described in [5]) and the AMPAIR helicopter at the institute of aircraft design at the University of Stuttgart. The two helicopters follow different design approaches. Both helicopters use sonic anemometers for wind measurements. While the Vario XLC carries a slung load that hangs five meters below the helicopter the AMPAIR uses a boom attached to the fuselage as described in [8].

In the meantime a few other rotary wing concepts developed. At the University of Applied

Sciences Ostwestfalen-Lippe a quadrotor was equipped with a measurement boom (see [9] and [10]). For flow measurements a custom made probe is used which is basically a multi hole probe but with a hot wire element inside the probe instead of conventional pressure transducers. Since during the last years a new, more lightweight type of ultrasonic anemometer was introduced by FT technologies some research groups also started using quadrotor aircraft with such a sensor mounted on a vertical or horizontal boom (see [11]).

At the RMIT University in Melbourne a small quadrotor was developed for wind measurements. It uses as multihole flow sensor mounted at the tip of a long horizontal measurement boom pointing in the direction of flight ([12]). Unfortunately regulations in Australia only allow to fly an unmanned aerial vehicle commercially at a take-off weight below two kilograms without a special pilot license. Below two kilograms the aircraft falls into the so called 'excluded category'. Consequently the quadrotor from RMIT is quite small which reduced the flight time to only 11 minutes ([12]) but gained promising measurement results.

Just recently at the École Polytechnique Fédérale de Lausanne (EPFL) in Switzerland another multirotor aircraft was equipped with a multi hole fast response probe for wind measurements which is described in [13]. Also for this campaign the results are quite promising however clearly noticeable deviations between the wind speeds measured by the aircraft and a met mast exist especially if short term periods are compared instead of longer periods or average wind speeds. It is assumed that this fact is based on uncertainties introduced by motions of the aircraft and the post-processing procedure to compensate those motions with IMU measurements.

1.4 Proposed Solution

The proposed solution is the development of an aircraft especially for wind measurements where the measurement system is fully integrated into the autopilot. Most of the other systems described above consist of a regular multirotor aircraft which is equipped with additional sensors or a measurement boom as payload. This leads to severe limitations regarding the measurement accuracy and flight times of the system. With the proposed solution, a purpose designed vehicle, such limitations can be overcome and the flight and measurement envelope can be extended.

Furthermore the idea of measurements with a group of aircraft will be pursued from the beginning of the project so that the mutual interference of group members will also be subject of this research.

1.5 Legal Limitations

The legal framework for UAV operations in Germany has changed during the project. Before April 2017 every remotely piloted aircraft, including multirotor aircraft, was considered as model aircraft, but after April 2017 the law for approval of air vehicles (Luftverkehrs-Zulassungs-Ordnung) was slightly changed. A separate altitude limitation for multirotor vehicles has been introduced to cope with the public "fear" of "drone flight". But in general most limitations existed also before this change but they have been made more visible now. The current regulations are summarized especially for model airplane pilots and hobbyists in [14].

In addition to the altitude limitation for multirotor aircraft another important change is that operators of remotely piloted aircraft with a take-off weight above 2 kilograms need a proof of knowledge and if a remotely piloted aircraft is operated for a commercial purpose an extended proof of knowledge is necessary. All other legal demands that are of importance for the project are listed below:

- All unmanned air vehicles (UAV) are only allowed to be operated as remotely piloted aircraft system (RPAS) with uninterrupted visual contact to the aircraft. An automated mission behind obstacles without visual contact is not permitted. Consequently this means that for the intended group of aircraft as many safety pilots as aircraft are needed to meet the legal requirements.
- To avoid a special permission for every particular flight the take-off weight of a remotely piloted vehicle has to be below five kilograms.
- It is not allowed to fly closer than 100 meters to a facility that generates energy, which also includes wind turbines, unless the operator gives its explicit permission. Since most measurement campaigns are intended to be conducted in cooperation with a turbine manufacturer or a wind park operator this limitation is not expected to cause problems.
- A distance greater than one and a half kilometers to urban areas and airfields has to be maintained. Because wind turbines usually have to keep similar distances this is also not expected to be a problem but has to be checked for every individual mission.
- If the purpose of a flight is commercial, which is usually also considered to be the case for research flights, a special permit is required. If the take-off weight of an aircraft is below five kilograms a permanent permit can be requested for one federal state of Germany. Unfortunately no permanent permit throughout entire Germany can be given because the authority to grant a permission lies with the regional council of the corresponding federal state instead of German Federal Aviation Authority (LBA).
However if the other requirements are met and safety pilots for each aircraft are available it is expected that a local permanent permit can be obtained without complications.

In summary it can be noted that the most important requirement is to keep the take-off weight below five kilograms. A heavier aircraft would increase the effort of a measurement campaign severely because a special permit for every flight would be necessary.

1.6 Research Objectives

In the beginning of the project the following research objectives have been defined:

- A concept has to be developed for in situ wind speed measurements at a fixed point in space.
- A flying measurement device has to be designed in detail and fabricated following this concept.
- The measurement performance of this device has to be proven and compared to other measurement techniques.
- The feasibility of a small series production and multi aircraft measurement with this device has to be investigated.
- Design specifications with the performance requirements have to be formulated.

Further research objectives include:

- Answering the question: "What is the difference in measurement performance between a fixed, motion compensated, measurement boom and a physically stabilized measurement boom?".

- Quantification of the benefit in holding its position in space during extreme wind conditions for a tilting propeller aircraft configuration.

2 Extreme Wind Conditions

For the development of an aircraft that is able to fly at extreme wind conditions it is necessary to quantify these conditions at first. For this quantification three different approaches will be considered.

The most simple approach is an analytical description of an extreme gust according to the IEC 61400-1 standard. For the second approach offshore measurement data from the FINO (Forschungsplattformen in Nord- und Ostsee - research platforms in North Sea and Baltic Sea) met mast will be analyzed. From this met mast wind speed measurements acquired with a sonic anemometer at $f_{FINO} = 35 \text{ Hz}$ are available and hence a high resolution analysis is possible.

For the third approach measurements from a met mast close to the village of Stötten on the Swabian Alb has been used. Unfortunately only wind speed measurements from cup anemometers at $f_{Stötten} = 20 \text{ Hz}$ and wind vane measurements are available. But as described below the most significant changes in the vertical direction occur mostly at low wind speeds and hence the largest effect on an aircrafts flight mechanics is expected at higher wind speeds. Since Stötten is a good example of complex terrain and flow in complex terrain is expected to be highly turbulent these measurements are a valuable addition.

One benefit of using wind measurements instead of the analytical approach from IEC 61400 is that a high frequency time series can be taken directly as an input for a flight simulation of the designed aircraft to see how well a fixed position in space will be maintained during perturbations.

2.1 Influence of Changes in Wind Speed and Wind Direction on an Aircraft

To assess the impact of a wind speed and wind direction change its effect on the flight mechanics of an aircraft, whether rotary wing or fixed wing aircraft, has to be derived. All aerodynamic lift forces regardless if produced by a wing, a fin or a rotor blade can be written as:

$$L_{aero} = c_a \cdot q \cdot S = \alpha \cdot c_{a\alpha} \cdot \rho/2 \cdot v_\infty^2 \cdot S \quad (2.1.1)$$

Where $c_{a\alpha}$ is the lift curve slope, assuming linear aerodynamics, α is the angle of attack, S is the reference area and q is the dynamic pressure consisting of $q = \rho/2 \cdot v_\infty^2$.

If the air density is assumed to be constant it follows that the forces which are influenced by external conditions change by:

$$\frac{dL}{dt} \propto \frac{d}{dt}(\alpha \cdot v_\infty^2) \quad (2.1.2)$$

2.2 IEC Standard

A generic wind speed variation, referred to as an extreme operating gust (EOG) is defined in the IEC 61400-1 standard and is usually an important criteria for the design of wind turbines. The exact time series of the EOG is influenced by a set of parameters. As a worst case scenario for a hovering aircraft the following parameters have been chosen:

- N=1: The gust shall correspond to an extreme event that occurs once a year. The other case is N=50 which corresponds to an even more severe extreme event that only occurs every 50 years but it is not planned to fly during a 50-year storm.
- Flight at hub height $z_{hub} = 100 \text{ m}$.
- Gust modeled for a turbine with a rotor diameter of $D = 100 \text{ m}$.
- Wind speed at hub height $V_{hub} = 25 \text{ m/s}$. This is the typical cut-off speed.
- Turbulence class A: Category for higher turbulence characteristics.

The resulting gust modeled with these parameters is shown in Figure 2.1. The maximum time derivative is less than $dv_{wind}/dt = 8 \text{ m/s/s}$.

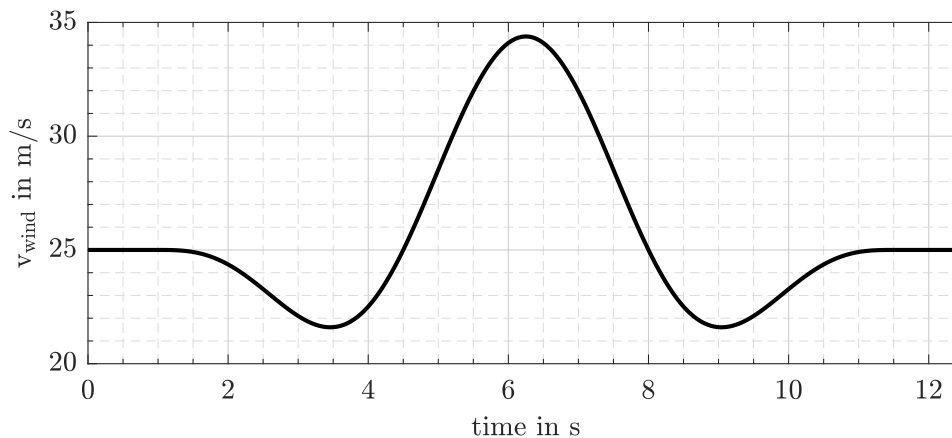


Figure 2.1: Extreme operating gust modeled according to IEC 6400-1.

2.3 Offshore Measurements

Since measurements from the FINO met mast are available in components u , v , w of the wind vector from a sonic anemometer they have to be transformed to spherical coordinates in order to obtain the magnitude and two angles of the wind velocity:

$$v_{wind} = \sqrt{u^2 + v^2 + w^2} \quad (2.3.1)$$

$$\theta_E = \arccos\left(\frac{w}{v_{wind}}\right) \quad (2.3.2)$$

$$\theta_A = \arctan\left(\frac{v}{u}\right) \quad (2.3.3)$$

Where θ_A is the wind direction (in the horizontal plane) and θ_E is the elevation (direction in the vertical plane). Only if the wind speed is expressed in this notation the effect of changes in wind speed and direction on an aircraft can be evaluated.

For the FINO measurement data a period of 16 days from 22.12.2011 to 06.01.2012 has been investigated. For a worst case scenario the highest sonic anemometer, mounted at a height of $h_{fino} = 52.5 \text{ m}$, was considered. In order to find situations with the highest impact on an aircraft, several quantities have been considered as search criteria:

- \bar{v}_{wind}

- $\sigma(v_{wind}) \cdot \bar{v}_{wind}$
- $\sigma(v_{wind})$
- $\sigma(\theta_E) \cdot \bar{v}_{wind}^2$
- $\sigma(\theta_A) \cdot \bar{v}_{wind}^2$

Where \bar{v}_{wind} is the mean wind velocity and σ is the standard deviation. These quantities have been computed for a time period of $t_{seed} = 10 \text{ min}$ which is common in wind energy and usually referred to as a "seed".

A direct search for the quantities $\sigma(\theta_E)$ and $\sigma(\theta_A)$ revealed that the derivatives of azimuth and elevation can become as high as $d\theta_A/dt = 315^\circ/s$ and $d\theta_E/dt = 700^\circ/s$ but these high values occur at wind speeds far below $v_{wind} = 1 \text{ m/s}$. This general experience is also well illustrated in [15]. Consequently seeds with the highest standard deviation of θ_A and θ_E are not relevant for a hovering aircraft because the dynamic pressure is so low that even the largely inclined inflow will not produce significant disturbing forces.

The worst case wind seeds found by these criteria have been investigated for the highest time derivatives to find the largest changes in direction and wind speed. This results in the following numbers:

- $\theta_{A,max} = \theta_{E,max} = \pm 45^\circ$ if $v_{wind} < 10 \text{ m/s}$
- $\theta_{A,max} = \theta_{E,max} = \pm 20^\circ$ if $v_{wind} > 10 \text{ m/s}$
- $\frac{d\theta_E}{dt} = 125^\circ/s$
- $\frac{d\theta_A}{dt} = 135^\circ/s$
- $\frac{dv_{wind}}{dt} = 30.5 \frac{\text{m/s}}{\text{s}}$

Especially the derivative dv_{wind}/dt is difficult to evaluate because it can become very high just for a fraction of a second which is assumed to only have a minor effect on the aircraft because short term disturbances are expected to be damped by the aircraft's inertia (compare Section 4.6). In addition it is also relevant for the influence on an aircraft if a very high value of dv_{wind}/dt is caused by just a small increase or decrease of v_{wind} or a rather large change.

To gain a better understanding of those two effects a filter was implemented to neglect any derivatives caused by changes shorter than $t_{min} = 0.15 \text{ s}$. To see how big the wind speed changes are the derivative dv_{wind}/dt was divided into different classes of Δv_{wind} . The results are shown in Figure 2.2.

For analytical calculations during the conceptual design of the aircraft the numbers above will be considered but after the conceptual aircraft design has been completed and all parameters are fixed a complete time series of measurement data will be used as an input for a simulation also including the flight controller to see how the aircraft can cope with rough wind conditions.

Because a simulation of the entire $t_{seed} = 10 \text{ min}$ is not necessary and needs too much computational power the corresponding seeds have been split into $t_{seed} = 20 \text{ s}$ and searched again by the criteria above to find the most challenging disturbance for the aircraft. The final simulation results can be found in Section C.

2.4 Onshore Measurements

In addition onshore measurement data was also used to define an extreme wind situation because changes in wind speed and wind direction are in generally expected to be higher at an onshore location and especially for complex terrain. Onshore measurement data was available from a site northwest of the village of Stötten on the Swabian Jura. This site was equipped with a met mast till the end of 2015 that was initially installed for a certification campaign of a Schuler prototype wind turbine. Since the company Schuler retired from the wind energy business the met mast was removed in the end of 2015. However at almost the same location a wind energy test field initiated by the research cluster WindFors will be build. The location, illustrated in Figure 2.2, is defined as complex terrain because it is a high plateau with steep slopes at three sides: South, west and north. Since the prevailing wind direction is west to northwest the inflow is highly influenced by the steep slope. The met mast was equipped with several cup anemometers of type "First



Figure 2.2: Left: View from above the met mast to the west. Right: Two cup anemometers mounted on top of the met mast.

Class" from Thies Clima. For an extreme wind condition estimation the two highest anemometers mounted at $h_{Stötten} = 100\text{ m}$ above ground have been used as shown in Figure 2.2.

Similar to the FINO measurements seeds with the highest average wind speed and the highest standard deviation have been searched hand has been found for the period between 10:30 and 10:40 on 31st of March in 2015. For this particular time frame the highest time derivatives have been computed and categorized to different speed range classes. The results are shown in Figure 2.3. It can be seen that even larger changes of wind speeds can occur at higher time derivatives. The largest change found in Stötten is $\Delta v_{wind} = 11.9\text{ m/s}$ at a change rate of $dv_{wind}/dt = 26.4\text{ m/s/s}$ which means that the wind speed changes by $\Delta v_{wind} = 11.9\text{ m/s}$ in only $\Delta t = 0.45\text{ s}$. The time series of this incident is depicted in Figure 2.4

2.5 Conclusions

From Figure 2.3 it is obvious that the wind speed does not change faster in Stötten than at the FINO site but this result has to be considered carefully because the cup anemometers add a certain amount of inertia so that very fast changes might not be captured.

Measurements from both locations are very valuable for the conceptual design of an aircraft that is supposed to hover at windy conditions. The calculated time derivatives will be used analytically

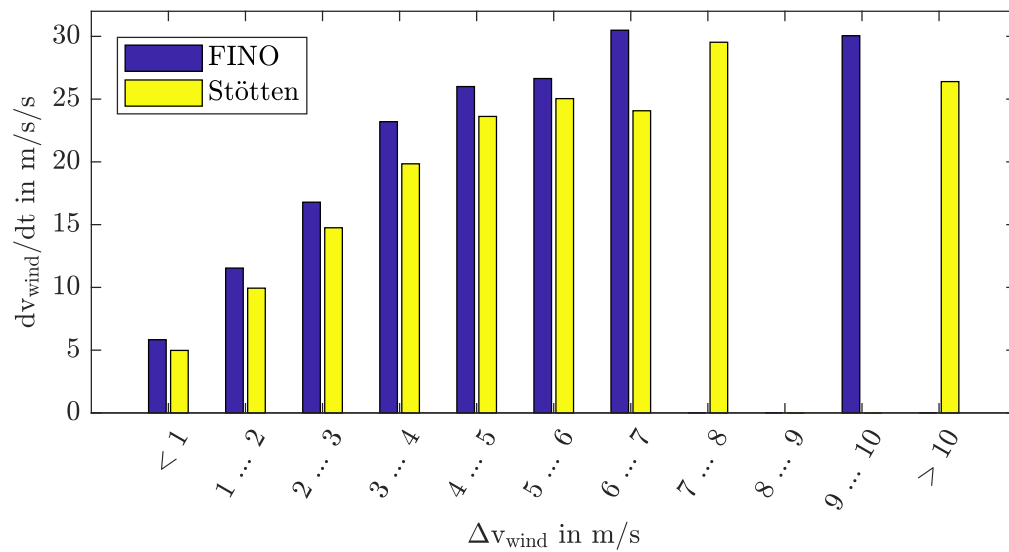


Figure 2.3: Different classes of wind speed jumps.

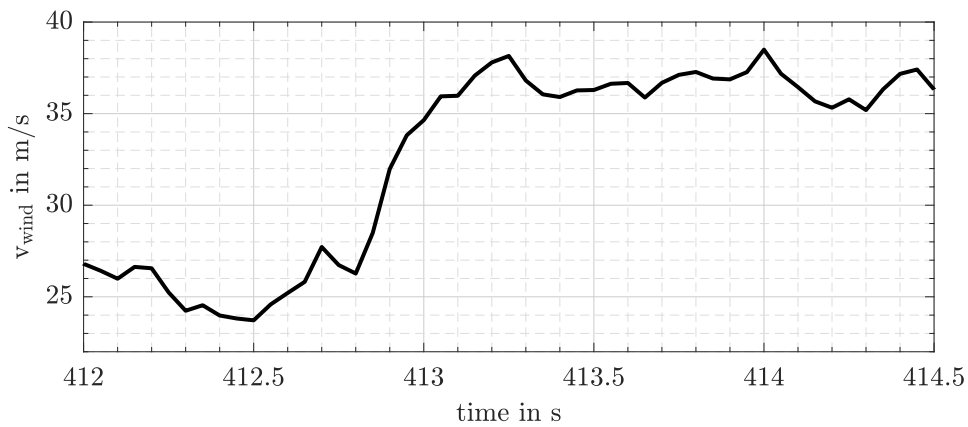


Figure 2.4: Largest wind speed change found in Stötten.

and the relevant time series will be used to simulate a flight with the final aircraft.

The extreme operating gust according to IEC standards seems to be a lot less severe for an aircraft compared to wind speed changes from actual measurements. Nevertheless the EOG will also be used for simulations with the final aircraft configuration.

3 Comparison between Fixed Wing and Rotary Wing Aircraft

With aerobatic model airplanes a hovering flight has been successfully demonstrated ([16]). This becomes possible if the thrust to weight ratio is greater than one and the airplane has large control surfaces which are immersed in the propeller slipstream.

If a fixed wing airplane is operated in a headwind an equilibrium of thrust, lift, drag and weight forces can be also achieved with a thrust to weight ratio less than one. Because a fixed wing aircraft can accomplish a much longer flight duration compared to a rotary wing aircraft the possibility to use a fixed wing aircraft combined with a sophisticated flight controller was investigated before a final decision about the aircraft configuration was made.

3.1 Flight Performance

If a steady wind speed of v_{wind} is assumed a hovering aircraft will experience the same wind speed as free stream inflow: $v_{\infty} = v_{wind}$. This in turn means that from the perspective of the aircraft it makes no difference if it is flying at v_{flight} in calm air or if it is holding its position over ground at a steady windspeed v_{wind} as long as the two speeds are the same: $v_{wind} = v_{flight} = v_{\infty}$.

In [17] a basic comparison between a helicopter rotor and a fixed wing in forward flight is derived based on momentum theory for the helicopter rotor and Prandtl's lifting-line theory for the wing. The induced velocity of a wing can be expressed as:

$$v_i = v_{\infty} \cdot \frac{D_i}{L} \quad (3.1.1)$$

Where D_i is the induced drag of the wing and L is the wings lift. For an elliptically loaded wing, which is the optimal case, the non-dimensional drag coefficient becomes:

$$c_{Di} = \frac{c_L^2}{\pi \cdot AR} \quad (3.1.2)$$

It can be seen that the induced drag depends on the aspect ratio AR . When substituting lift and drag by non-dimensional coefficients the induced velocity can be restated as a function of wing area, inflow velocity and lift:

$$v_i = \frac{2 \cdot L}{v_{\infty} \cdot \pi \cdot AR \cdot \rho \cdot A} = \frac{2 \cdot L}{v_{\infty} \cdot \pi \cdot \rho \cdot b^2} \quad (3.1.3)$$

For the helicopter rotor a similar relation can be derived if Glauerts empirical formulation of the induced velocity, given in [18], is used (compare Eq. (5.7.2)) and the angle of attack α of the rotor disc is assumed to be small:

$$v_i \approx \frac{T}{2 \cdot v_{\infty} \cdot \rho \cdot A} \quad (3.1.4)$$

Consequently for a given take off-weight $W = T = L$ and a given forward flight speed v_{∞} the induced velocity of a helicopter rotor is equal to the induced velocity of a circular wing with an aspect ratio of $AR = 1$ and a wing area of $A = (\pi \cdot b^2)/4$.

If the two aircraft have the same induced velocities at the same thrust / lift they are also consuming the same induced power. Considering that at an equal take-off weight most fixed wing aircraft have a much larger wing area than a corresponding rotary wing aircraft and further more considering that a wing aspect ratio of $AR = 1$ is quite low even this basic comparison reveals that a fixed wing aircraft clearly exceeds the flight duration of a rotary wing aircraft. Additionally the parasitic drag of a rotary wing aircraft is expected to be much higher because of the changing inflow conditions at the retreating and advancing blade. Hence it is very tempting to use a fixed wing aircraft for wind measurements to make longer measurement durations possible.

3.2 Influence of Quickly Changing Wind Direction on Flight Mechanics

The biggest difference between a fixed wing aircraft and a rotary wing aircraft when they experience a sudden change in inflow direction is illustrated in Figure 3.1. The thrust vector of a rotary wing aircraft points in the vertical direction while the thrust vector of the fixed wing aircraft points in the horizontal direction.

For lower wind speeds a large portion of the resulting force counteracting the aircraft's weight has to be the thrust force from its propeller because the wing can produce only little lift at low inflow speeds and hence low dynamic pressures. For a sudden change of the vertical inflow direction or a sudden decrease of the wind speed the angle of attack of the aircraft has to be changed to obtain a new equilibrium state. This angle of attack change is larger for a fixed wing aircraft than for a rotary wing aircraft. In the same manner the fixed wing aircraft has to be yawed by a large

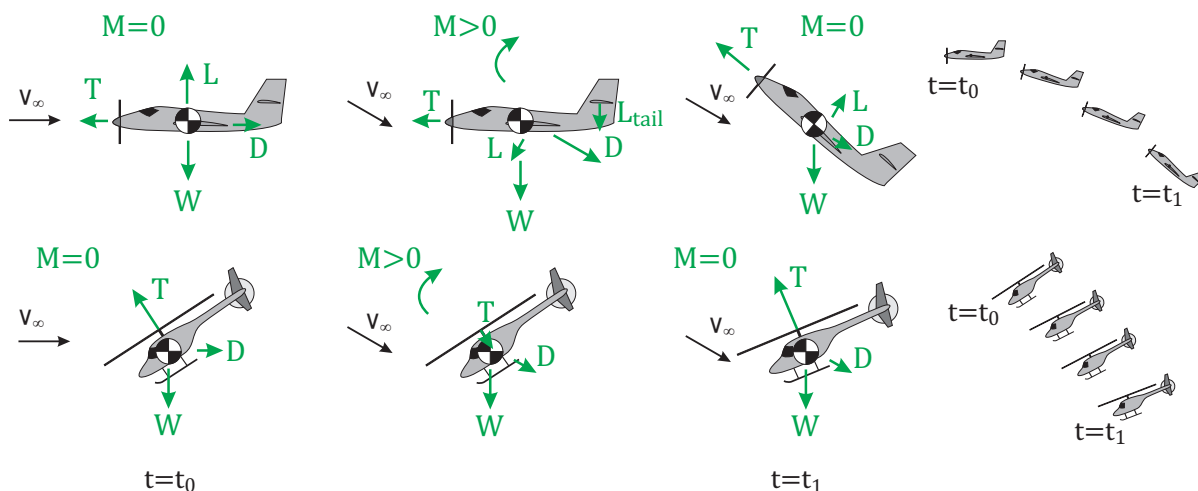


Figure 3.1: Influence of fast changing inflow direction on a fixed wing and rotary wing aircraft.

amount if the wind direction changes in the horizontal plane because the thrust vector has to be re-aligned with the wind direction. In contrast a rotary aircraft is can tilt it's thrust vector in any horizontal direction by utilizing cyclic blade pitch at a helicopter or differential thrust of the particular propellers at a multirotor aircraft.

The larger angular change that is necessary for a fixed wing aircraft automatically leads to a slower response time. This fact will be derived in detail with the angular conservation of momentum in Section 5.5.

Another advantage of a rotary wing aircraft in strong winds is that the tip speed of the rotor is

usually much higher than the wind speed itself and thus it is less sensitive to wind speed changes. In addition, the large surfaces of a fixed wing aircraft can be a disadvantage because they produce large forces at large inflow angles whereas a rotary wing aircraft only has a small projected area.

Consequently a rotary wing aircraft is capable of hovering in windy conditions much better. Nevertheless with a highly adaptive wing it is not impossible to stay at a fixed location in space without rotating wings, as it can be seen at birds hovering in an headwind.

3.3 Experiences Regarding a Steady Flight with Fixed Wing Aircraft

This section describes experiences at other research groups and state of the art technology to use a fixed wing aircraft for a steady flight in a headwind.

3.3.1 Wind Tunnel Tests with Tethered Aircraft

The probably earliest desire to hold a fixed wing aircraft at a steady location in a headwind can be traced back to wind tunnel tests for stability analysis. An example has been illustrated in [19]. The wind tunnel model is fully equipped with control actuators and a motor. Motor and actuators are driven via cables and controlled manually to achieve a stable flight in the wind tunnel. Although an additional safety cable is attached to the model the flight can be considered as a free-flight in a headwind.

A more modern approach to fly a fixed wing aircraft in a wind tunnel can be found in [20]. Here a custom made flight controller was used, including a full physical model of the airplane combined with an external 3D camera system instead of an internal IMU, with the purpose to achieve a steady hover. This goal could only be reached partially since not all maneuvers succeeded. A specific source of problem could not be identified and it was concluded that several uncertainties in the physical model of the aircraft, the camera system and the launch mechanism lead to the not entirely satisfying results.

3.3.2 UAV Research at RMIT University

Since 2005 the Royal Melbourne Institute of Technology (RMIT University) works on methods to improve the capability of fixed wing aircraft to hover in turbulent flows. A major difference is that the goal of the experiments at RMIT is a fixed wing aircraft that is able to hover outdoor in turbulent winds while the experiments described above are meant to characterize the flight mechanical characteristics of an airplane and the hovering flight in a wind tunnel is used to simulate a free flight (e.g. fast forward flight) in calm air.

As a first step atmospheric turbulence has been investigated and methods to replicate that turbulence in a wind tunnel have been presented in [21] and [22]. Several successful flight tests could than be conducted inside a turbulent wind tunnel during the past years. Starting with radio controlled model airplanes proceeding to an automated flight controller and airplanes designed to fly in turbulent environments.

To improve the recognition of an incoming gust two multi hole probes have been used, protruding from the leading edges of the left and right wing and hereby allowing a predictive control. As an improvement for the control, actuated leading edge flaps have been investigated ([23]) and a tandem wing configuration has been identified to offer significant improvements in gust alleviation compared to a conventional aircraft configuration ([24]).

3.4 Conclusions

As proven by experiments in different wind tunnels during the past century and especially by the research conducted at RMIT University during the past years it is in general possible to use a fixed wing aircraft and make it hover at a fixed location over ground in a turbulent headwind. However such an approach still has to be considered subject of ongoing research and not state of the art as hovering with a rotary wing aircraft.

Consequently the rotary wing aircraft was chosen for wind measurements in the present work. However that research subject should be observed for the next couple of years. For future projects it might be possible to use a fixed wing aircraft with sophisticated sensors and special actuators instead of a rotary wing aircraft to achieve longer measurement durations, but further research would be necessary to prove the viability of such a concept for wind measurements.

4 Comparison of Flow Measurement Equipment

In general a large number of flow measurement equipment exists for various applications from research in the lab to outdoor measurement campaigns. For flying wind measurements only a few flow measurement techniques are suitable.

This chapter lists only the technologies that are currently used by other research groups for flying wind measurements or that are suitable for those.

4.1 Constraints of Airborne Flow Measurements

One additional task for a successful measurement procedure is the exact acquisition of the aircraft's movements and attitude. Without that knowledge the inflow vector, measured in the aircraft coordinate system, cannot be transformed to the fixed earth coordinate system. It cannot be expected that any aircraft, even if it is a rotary wing aircraft, can just be "parked" in the air absolutely motionless.

With the help of the autopilot's IMU (inertial measurement unit) or an additional external IMU it is possible to measure the roll and pitch attitude quite accurately. This is normally done with the help of a Kalman filter that combines the measured raw values of translational and angular acceleration. In a modern autopilots usually the Kalman filter also includes the GPS, barometer and magnetometer values.

The most difficult navigational parameter to calculate is the heading. During forward flight with a relative speed to the ground a heading information can be gained from GPS coordinates. For a hovering aircraft however the only heading information comes from the magnetometer. This instrument is not very precise and also subjected to disturbances from electromagnetic fields caused by the motors of a multicopter aircraft. For a regular mission, as for example taking pictures automatically, a heading discrepancy of a few degrees has no impact in most cases. For an accurate flow measurement, especially if the wind direction is of interest, it is however important to determine the exact heading of the aircraft.

Another factor of great practical importance is the possibility to have a live preview of the flow measurement on the ground station. Without this possibility it will be difficult or even impossible to fly a complete mission because most probes have a limited inflow angle range and in addition if the wind direction changes so that the aircraft experiences an inflow from the rear the measurements of this flight will have no value.

4.2 Ultrasonic Anemometer

The ultrasonic anemometer, or sometimes also called sonic anemometer, was developed in the 1950s and uses ultrasonic sound waves to measure wind speeds. The speed at which sound waves propagate through air is well known and easy to calculate because the only unknown variable is the air temperature which is also easy to measure. All other quantities necessary to calculate the

speed of sound in air are constants of nature. A sonic anemometer utilizes this fact and measures the time needed for an ultrasonic pulse to travel from a transmitter to a receiver over a known distance. If there is wind present this time increases or decreases depending if the wind blows in the direction of the sound pulse or against it.

By the use of several of those sound paths the wind velocity can be measured in two or even all three dimensions. During the last decades ultrasonic anemometers have become quite common in wind energy research because they are easy to use and very robust. Unless the transducers are iced up or there is heavy rain or fog in the air an ultrasonic anemometer is always capable of measuring the wind speed adequately. Figure 4.1 pictures a generic ultrasonic anemometer. The mathematics of the measurement principle is described in detail in [25].

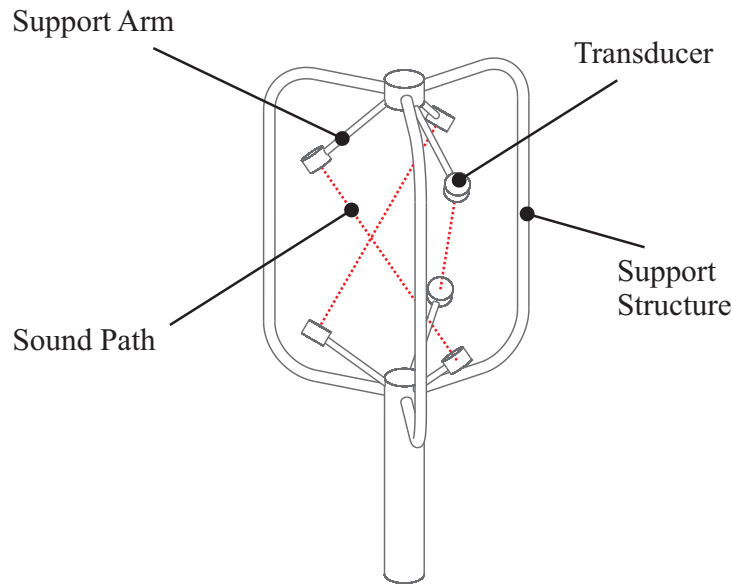


Figure 4.1: Example of three dimensional ultrasonic anemometer design.

Two sources of measurement error can occur when using an ultrasonic anemometer. Because the transducers have to be supported in some way it is necessary to use a support structure which in turn can cause a distortion for the sound path. A description of this problem together with advanced calibration methods is given in [26]. Another source of error is a non-uniform flow field. For the algorithms used to calculate wind speeds from an ultrasonic anemometer it is assumed that the inflow is uniform over the sound path. If this is not the case errors can occur as described in [27] in detail.

Most ultrasonic anemometers are quite large and heavy which makes it impossible to use them on a small unmanned aircraft. A Windmaster 3D sonic anemometer from Gill Instruments Limited for example weighs $m_{Gill} = 1.0 \text{ kg}$ and a 3D sonic anemometer from Adolf Thies GmbH & Co. KG even weighs $m_{Thies} = 3.4 \text{ kg}$. One exception that appeared on the market just recently in 2017 is the TriSonica Mini from Anemoment LLC in Colorado. It weighs only $m_{TriSonica} = 50 \text{ g}$ and can measure wind speeds in three dimensions. However while its larger counterparts are able to measure at sampling rates up to $f_{sonic} = 100 \text{ Hz}$ (e.g. Gill R3-100 and Thies sonic anemometer) its sampling rate is limited to $f_{TriSonica} = 10 \text{ Hz}$. If robust low speed measurements are of interest this device could be a good choice for flying anemometry but since it was not available for the concept phase of the project it hasn't been considered yet.

Another type of ultrasonic anemometers are acoustic resonance anemometers as they have

been patented in 2000 by FT Technologies. The working principle, as described in [28], utilizes an acoustic resonance and measures the phase shift, caused by an airflow perpendicular to this resonance. Unfortunately it is only possible to measure flow in two dimensions so that two of such devices have to be used together to capture three dimensional flow. However FT Technologies recently started advertising their newest products especially for UAV applications and they already have been used by some research groups. The FT205 weighs $m_{FT205} = 100 \text{ g}$ and can measure at a maximum sampling rate of $f_{FT205} = 10 \text{ Hz}$ and a very low power consumption of $P_{FT205} = 0.3 \text{ W}$ according to the manufacturer. Similar to the TriSonica if a low speed measurement is satisfactory this device could be an interesting choice but hasn't been available during the conceptional project phase.

One last type of sonic anemometer that is often used for marine applications but recently also being advertised explicitly for UAV operations is the CV7 from LCJ Capteurs in France. The working principle is also slightly different to regular ultrasonic anemometers. Four transducers are used that can either transmit or receive. All transducers are mounted on the bottom of the cylindrical device and the sound wave is reflected on the upper part of the device. Similar devices are also available from Gill Instruments Limited with a higher weight. The CV7 head weighs $m_{CV7} = 100 \text{ g}$ and its fastest sampling rate is $f_{CV7} = 4 \text{ Hz}$. With this working principle only flow measurements in two dimensions are possible.

4.3 Pitot/Prandtl Tube

Especially in aviation it is common to measure the flow velocity with a small tube pointing directly into the flow direction. As the tube is connected to a pressure transducer on the other side and is hereby completely enclosed the flow comes to a rest inside the tube and the pressure increases to the so called total pressure or stagnation pressure. According to Bernoulli's equation the flow velocity can be calculated if the total pressure is compared to the static pressure of the fluid:

$$u = \sqrt{\frac{2(p_t - p_s)}{\rho}} \quad (4.3.1)$$

Where p_t is the total pressure measured by the pitot tube and p_s is the static pressure. The static pressure could be measured separately with pressure holes perpendicular to the flow for example at the aircraft hull. It is however more practicable to combine both pressure measurements on one tube. Such a tube is also called a Prandtl tube if the difference between total pressure and static pressure is measured directly with only one single pressure transducer.

Prandtl tubes are meanwhile also available at low cost for UAV applications. Models developed especially for UAV applications often include the possibility to connect a light weight data acquisition unit or offer compatibility to a bus system that can be read by common UAV autopilot systems like I2C, UART, SPI or CAN. If a custom electronics is developed and combined with a high end commercial Prandtl tube any pressure transducer with the desired resolution and accuracy can be used. Since the working principle is quite simple no individual calibration for each probe is needed as long as a high quality factory-calibrated transducer is used. In order to calculate an exact airspeed a measurement of the air density is also needed. This can be done either with a ground station or in the optimal case by measuring temperature and humidity on board the aircraft.

Most Prandtl tubes are directional sensitive which means that the exact wind speed can only be measured if they are aligned directly with the inflow. However some models exist that are insensitive to a directional misalignment to some extent. An insensitivity up to $\alpha = \pm 20^\circ$ has

been observed by the author (compare Section 6.3.4). It is assumed that this is achieved by a sophisticated choice of tip diameter and bore diameter.

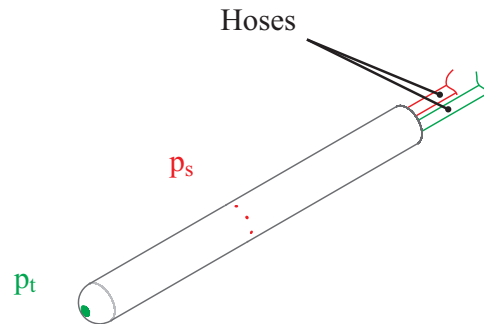


Figure 4.2: Example of a Prandtl tube.

A Prandtl tube or to be more precise the entire measurement system using a Prandtl tube has a limited frequency range of several hundred Hertz because the tube is usually connected to the pressure transducer with two hoses. High frequency fluctuations in the inflow speed cannot be transmitted through a long hose because of the acoustic resonance frequency of the air inside this hose.

Depending on the length a small Prandtl tube weighs approximately between $m_{Prandtl} = 10\text{ g}$ and $m_{Prandtl} = 20\text{ g}$. Some weight is also added by the pressure hoses. The pressure transducer usually is a very small integrated circuit (IC) just big enough to carry two connectors for the hoses and consequently also only weighs a few grams. In conclusion it can be stated that a Prandtl tube is a simple, low cost and well developed instrument suitable for airborne operation but it can only measure flow in one direction.

4.4 Multi Hole Probe

An extension of the Prandtl tube is the multi hole probe. It also consists of a tube often with a round tip, similar to a Prandtl tube, but instead of only one hole for the total pressure the tip includes several holes. The number of holes differs between three and 14. The holes are connected to individual pressure transducers which allow to measure pressure differences between the individual holes and therefore derive information about the magnitude and direction of the inflow vector. These individual transducers are either located outside of the tube and connected with hoses or they are located inside the tube close the bores. The latter solution is able to provide high frequency readings because standing waves inside the hoses are avoided. This is also referred to as fast response probe. A fast response probe is usually more expensive than a system with external pressure transducers because the small transducers are more expensive and difficult to assemble inside the tube.

Even if the flow measurement procedure with a multi hole probe sounds quite simple it is in no way comparable to the simple nature of a Prandtl tube. The equations to solve are quite complicated and include many calibration factors because the behaviour of the pressure readings is highly non-linear at inclined inflow. In addition hysteresis effects exist so that a dynamic calibration might be necessary besides the static calibration. Unfortunately the flow around these probes, usually made from metal, is so sensitive to geometrical differences that even small manufacturing tolerances can have a severe impact on the measurement and an individual calibration of every particular probe is mandatory. Hence it is no exaggeration to say that the biggest challenge of

a multi hole probe lies in its calibration procedure and the proper data reduction scheme. Until

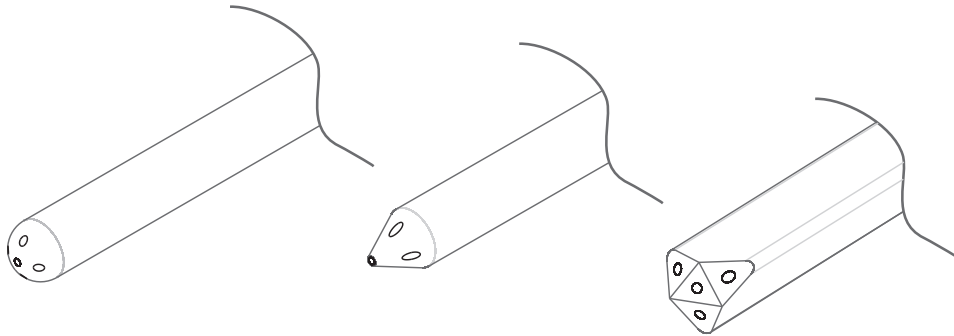


Figure 4.3: Possible tip geometries of MHP probes.

2017 only two commercial manufacturers of multi hole probes existed: The American Aeroprobe corporation and the Australian Turbulent Flow Instrumentation Pty Ltd or short TFI. In 2018 the German Vectroflow GmbH entered the market. While Aeroprobe and Vectroflow probes have round or conical tips TFI usually manufactures the probes with sharp polygons (see Figure 4.3). It is assumed that this is done to avoid laminar flow separations and force a turbulent flow around the probe head.

As only manufacturer in this segment Aeroprobe offers a small, light weight electronics for real time data reduction called Micro Air Data Computer or short μ ADC. A μ ADC device weighs between $m_{\mu ADC} = 135\text{ g}$ and $m_{\mu ADC} = 170\text{ g}$ depending on the exact model.

For commercial products the data reduction scheme is usually not published and works as a black box. For probes from Aeroprobe for example, a calibration file is provided when a fully pre-calibrated probe is purchased. This calibration file can be used with the proprietary software AeroFlow which calculates flow velocity and inflow angles from raw data provided by the probe. Fortunately it is also possible to obtain dll files for the calibration procedure to run the data reduction of a pre-calibrated probe with Matlab, LabView, C++ or Python. Hence it should be possible to build a custom data acquisition system, for example with a raspberry pi microcomputer, and use it with pre-calibrated probes. However, the calibration algorithm is still a black-box because it is implemented in the dll files.

A commercial multi hole probe system is quite expensive which is also an important factor regarding multi aircraft operation. If operated with μ ADC the following costs have to be considered:

- μ ADC device with data logging: 11 195 € (with GPS: 18 825 €)
- Straight five hole probe with tip diameter $d_{tip} = 3.18\text{ mm}$: 3 200 €
- Probe calibration for speeds below and above $v_{\infty} = 10\text{ m/s}$: 2 920 €

The prices are dated to November 2017. The items listed above are all necessary which means that for one particular aircraft of a measurement group the price of the measurement equipment is approx 17 315 €. Unfortunately the angular measurement range is limited to $\alpha = \pm 20^\circ$ if a μ ADC device is used for data reduction even if the probes themselves are specified up to $\alpha = \pm 45^\circ$

Fast response probes are significantly higher priced and cannot be operated with the μ ADC device and a custom data acquisition system has to be designed.

Prices from TFI have not been requested and are not available online but it is assumed that they are in a similar range. Furthermore TFI does not offer the possibility to build a light weight system suitable for flying operation because a large electronic interface is mandatory.

Because of this relatively high amount that has to be spent for a pre-calibrated multi hole probe system most research groups using multi hole probes tend to do their own calibration or even manufacture their own probes. At the University of Braunschweig a custom made five hole probe has been developed ([29]) which is used by several fixed wing UAV research groups (compare [30]). In [30] and [31] the calibration procedures and data reduction schemes are presented for multi hole probes. This process is very labor-intensive and can only be performed with regular access to a wind tunnel of satisfactory flow quality. An interesting approach that greatly reduces the effort during a calibration is presented in [32]. Therefore a fully automated calibration rig with stepper motors was built that sweeps through the entire range of inflow angles very quickly.

Another interesting advancement in [32] is the development of a 3D printed probe manufactured with stereolithography (STL). This technique promises lower manufacturing tolerances and can possibly work without an individual calibration of every particular probe. As stated in [32] such a general calibration already works to some extent. The Vectoflow GmbH advertises their probes as all metal 3D printed and also Aeroprobe announced a patented additive manufacturing process, thus 3D printed probes without the need for individual calibration could be expected in the future.

At the ETH Zurich a new piezorestrictive miniature silicon sensor has been developed and implemented in a custom fast response probe ([33]). This probe has already been operated in a fixed wing UAV for wind energy research ([34]).

In conclusion multi hole probes have been excluded for the current project because they are either very expensive or need a high effort and regular access to a wind tunnel for calibration. The main focus of the present study is the development of an aircraft for wind measurements.

It can be noted, however, that multi hole probes have been proven to be a reliable and robust measurement device for UAV applications.

4.5 Hot Wire Probe

A hot wire probe uses the cooling effect of an airflow on a very thin heated wire. Because this wire is so thin even short term changes of the wind speed up to several kilohertz can be detected. A hot wire probe as depicted in Figure 4.4 is well established for wind tunnel measurements and laboratory experiments but rather rare for outdoor measurements. Because only the flow velocity

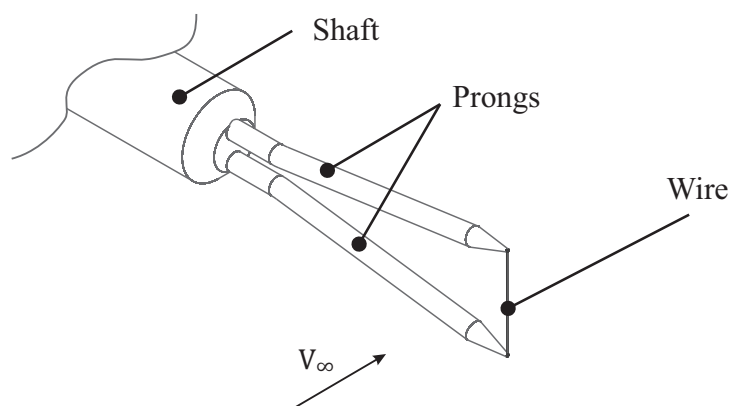


Figure 4.4: Components of a hot wire probe.

perpendicular to the wire can be measured it is not possible to measure flow in several directions with a single hot wire probe.

Because the relation between wire voltage and the flow speed is highly non-linear, calibration of

hot wire probes is very challenging. Often they are calibrated shortly before an experiment with a small calibration wind tunnel directly in the the lab.

The biggest disadvantage of a hot wire probe is that a wire can easily break when it gets hit by debris, insects or even rain drops. In addition it has a limited life-span because of contamination during the measurement periods by burnt dust particles etc.

In general the use of hot wire probes for a wind measurement aircraft is a significant challenge. However, the probe manufacturer SVMTec GmbH offers hot wire probes with a wire diameter of $d_{wire} = 10 \mu m$ which is thicker than the wire of any other hot wire probe and hence slightly more robust. SVMTec offered a customized light weight electronics including support during the project and pre-calibrated hot wire probes with replacement probes for all aircraft of the planned measurement group.

4.6 Indirect Measurement Using Aircraft Attitude and Movements

Another approach to measure wind speeds with a multicopter aircraft is not to use any instrumentation at all but the multicopter itself. Depending on the wind speed and the aerodynamic forces acting on the aircraft it will need to "lean against the wind" at a different angle. This angle can be measured with the IMU that every flight controller hardware has built in to control the aircraft.

That this concept can work under real life conditions for low wind speeds has been demonstrated several times ([35], [36], [37]). However in all these results serious short term discrepancies can be observed between external measurements and the "flying anemometer" which is why this method can only be seen as a rough wind estimate.

The main reason for the observed uncertainty is that any hovering rotary wing aircraft is a complex system which cannot be described easily. To compute wind speed and heading from IMU measurements a complete mathematical description of the system is needed including the flight mechanics of the aircraft and the control algorithm. For a regular flight simulation the wind speed is entered as an external disturbance and the simulation outputs the aircraft motion as a result. In order to calculate the wind speed from the measured motion this complete simulation chain has to be inverted. When such a simulation model is set up usually many simplifications are made:

- The propeller aerodynamics is simplified to a high extent and oblique propeller inflow or flapping of larger propellers are ignored. For most cases it is even assumed that the resulting thrust force is always aligned perpendicular to the propeller disc.
- The bluff body aerodynamics of the airframe is usually also highly simplified. Non-linearities, vortex shedding and unsteady aerodynamics are completely ignored in most cases.
- The response to changes of the commanded thrust, depending on the dynamics of motors, behaviour of motor controllers (ESCs) and inertia of the propellers is usually also simplified.
- In many cases, for example if no exact CAD model is present or if not all components have been weighed, the inertia tensor of the aircraft has to be simplified.
- Sensor noise is usually not included in the simulation.
- Only if a second flight controller unit is operated as hardware in the loop (HIL) the behaviour of the real flight controller is known. Otherwise the control loops have to be modeled with simplifications.

All these uncertainties introduced by the above listed simplifications add up and make the wind measurement very uncertain. An example how the aircraft developed in this work is modeled for a simulation with simplifications can be seen in Section C. A complete model with special regard to indirect wind measurements is presented in [38].

Even if considering a perfect model of the reality without any simplifications there is still one serious disadvantage of the indirect wind speed measurement. Because each aircraft has a certain inertia the attitude will not change immediately if the wind speed changes very fast. In Section 5.5 a sudden wind speed change from $v_\infty = 10 \text{ m/s}$ to $v_\infty = 15 \text{ m/s}$ is assumed and the time that an aircraft needs to reach a new equilibrium state is estimated. For a large fixed pitch multicopter aircraft this time constant is $\Delta t = 0.19 \text{ s}$ which in turn means that wind speed changes faster than $f_{wind} = 1/\Delta t = 5.3 \text{ Hz}$ cannot be measured indirectly by the aircraft's attitude because it acts as a low pass filter.

In conclusion, it can be noted that computing wind speeds indirectly from a rotary wing aircraft's attitude is a low cost method because no additional hardware is needed. However the necessary calculations are complex and the result depends strongly on the quality of the aircraft parameter identification. Furthermore it is not expected that high frequency turbulence can ever be measured with this method.

4.7 Conclusions

It has been shown that almost no flow measurement equipment exists that can be bought "off the shelf" and directly mounted at an UAV without further modification or adaptation. In most cases at least a customized data acquisition system with an interface to the autopilot has to be developed in order to receive live readings on the ground station. The only exception is the μ ADC system from Aeroprobe or the recently introduced small sized sonic anemometers.

In addition the choice might significantly alter depending if one has unlimited access to a wind tunnel with good flow quality. In the beginning of the project this was not the case. In 2014 the author built a small mobile wind tunnel for teaching. This tunnel was utilized for preliminary test of the used probe but showed a very poor flow quality which means it is not suited for probe calibrations. Some of the presented probes like the small ultrasonic anemometers do not need an individual calibration at all while others, like the multi hole probes, make such a calibration mandatory if they shall be used at affordable costs.

Because of the unique opportunity to work together closely with a manufacturer and to fill the gap of high frequency measurements, which is not done by many research groups, the development of a customized triple hot wire probe was initiated at SVMTec. In addition a Prandtl tube will be used as a more conventional technology and to compensate a possible drift of the hot wire probes. Each of the three probes forming the triple will be delivered pre-calibrated at different ambient temperatures so that no individual calibration of every particular measurement boom is necessary.

5 Conceptual Design of ANDroMeDA

5.1 Introduction to the ANDroMeDA Philosophy

As described in Section 3.4 a rotary wing aircraft will be used because it can hover in a windy environment more easily than a fixed wing aircraft which is normally not able to hover at all.

For the sake of mechanical simplicity and low maintenance effort a multirotor will be used. Conventional helicopters in main and tail rotor configuration as well as in a coaxial rotor configuration, consisting of two main rotors, contain many mechanical parts that will wear off over the aircraft's lifespan like bearings, gears, connection rods, tail shaft or tail belt etc. A multirotor aircraft on the other hand does not have any of those elements.

The multirotor will be designed especially for the purpose of wind measurements. It was decided not to use a commercially available multirotor as a platform and attach the measurement equipment as payload.

As previously described the rather simple approach of using an off-the-shelf multirotor aircraft would result in many difficulties. First of all commercially available multirotor designs are mostly symmetric in the horizontal plane. Therefore it is difficult to achieve distance between the propellers and the measurement probe. If a long boom is used in the front the required center of gravity (CG) cannot be achieved anymore.

In addition commercially available multirotors are not designed for fast forward flight or to hover at higher wind speeds. They are mostly designed to hover for a long duration in a calm environment e.g. in surveillance missions with a camera.

Another important issue is the measurement data acquisition and connection to the autopilot system which is also difficult with a pure platform/payload concept. It is mandatory for the autopilot to know the wind direction because it can change during the flight.

Consequently a multirotor will be designed especially for wind measurements at higher wind speeds and in gusty environments. This will affect the frame geometry, aerodynamics and integration of the measurement system to the autopilot system.

The purpose designed aircraft / measurement probe unit, also called a "wind measurement system", developed during the ANWIND project was named ANDroMeDA = ANWIND Drone for Measurement and Data Acquisition.

The phrase "drone" was used for the sake of a good acronym. Even if the word "drone" was strongly related to military operations in the past the usage of this phrase has changed a lot during the past decade. It is also used to describe multirotors in general or even children's toys in the present day.

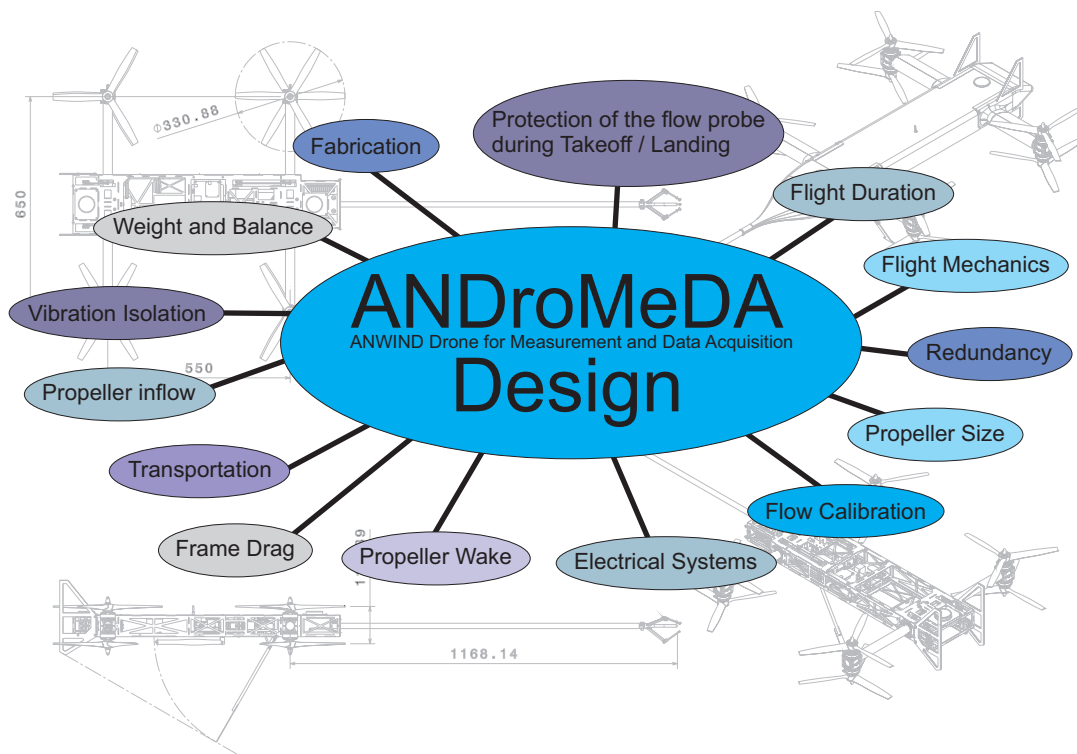


Figure 5.1: Design considerations for the development of ANDroMeDA

5.2 Definitions

5.2.1 Phrases "Propeller" and "Rotor"

Typically when speaking of an airplane "propeller" one thinks of the propulsion system of an aircraft at an axial, steady state, rotationally symmetric inflow condition. For a helicopter on the other hand the phrase "rotor" is common. Aerodynamically a helicopter rotor in climb is exactly the same as a propeller in forward flight. In forward flight of a helicopter when its rotor is tilted forward, towards the inflow, the aerodynamic behaviour is different.

In addition from a more practical point of view one might also speak of "propellers" referring to the propulsion system for a multirotor UAV because most often regular model airplane propellers without any adjustable blade pitch are used here.

In order to avoid confusion for the reader and to take advantage of a straight forward definition the two terms will be distinguished in the following manner:

- For an axial, rotationally symmetric inflow condition (e.g. airplane propeller at zero angle of attack in forward flight) the term "propeller" will be used.
- For a hovering condition with only the induced velocity v_i present (e.g. a helicopter in hover) the term "rotor" will be used.
- For the operation at an angle of attack (e.g. helicopter in forward flight) the term "rotor" will also be used.

5.2.2 Angle of Attack of the Rotor Disc

The angle of attack of the rotor disc, α_{disc} will be defined as follows:

- A helicopter rotor in hover is described by $\alpha_{disc} = 0^\circ$.
- An axial inflow propeller is described by $\alpha_{disc} = 90^\circ$.
- If an equation in the original reference is denoted otherwise (e.g. $\alpha_{disc} = 0^\circ$ for the propeller) it will be transformed to the notation described above to keep up consistency.

5.2.3 Flight Mechanical Quantities

Flight mechanical quantities will be described according to the standard LN 9300 whenever possible. The used quantities are also described in the list of symbols.

5.3 Constraints and Design Point

5.3.1 Design Point

The following parameters have been chosen for the design point of ANDroMeDA:

- $MTOW = 5 \text{ kg}$
- $v_{design} = 10..12 \text{ m/s}$
- $v_{max} = 25 \text{ m/s}$

According to legal regulations it is not allowed to fly an aircraft heavier than 5 kg (TOW) without a special permission outside a designated model airplane flying field (compare Section 1.5). To avoid the effort of a special permission for each mission $MTOW = 5 \text{ kg}$ was chosen.

The design wind speed range was chosen to be $10 \text{ m/s} .. 12 \text{ m/s}$ since this is the rated wind speed of typical onshore wind turbines.

Instead of a fixed value for the design wind speed a speed range has been chosen to cope with different requirements. To calculate the flight time it's reasonable to use the upper end of this range while it makes sense to use the lower value to evaluate flow measurement quality because the propeller influence is stronger at lower inflow speeds (compare Section 5.7).

The maximum flight speed / wind speed in hover was selected to be $v_{\infty} = 25 \text{ m/s}$ because this is the cut-off wind speed for most wind turbines.

A collective measurement with up to nine aircraft is planned and hence the cost for one aircraft should be lower than 3200 € without flight batteries to keep the total cost low.

5.3.2 Forces Acting on the Aircraft in Forward Flight

In general the forces acting on a multirotor aircraft are quite complex. Figure 5.2 shows all forces and moments from a pure mechanical point of view. Each individual rotor and the airframe can produce three forces and three moments about the center of gravity. Figure 5.3 illustrates the relevant forces acting on a multirotor aircraft hovering in a headwind with the velocity v_{∞} , inclined by an angle γ_a . For $\gamma_a = 0 \text{ deg}$ this scenario is the same as flying at a forward flight speed of $v_{cruise} = v_{\infty}$ in a calm environment. The following simplifications are made:

- No aerodynamic moments result from the aircraft's frame ($M_{frame} = L_{frame} = N_{frame} = 0$) since the geometry of a conventional multirotor is symmetric. In reality the flow around the frame will be different at front and rear due to the propeller wakes and hence develop some aerodynamic moment.
- As a result of the former simplification all rotors develop the same thrust ($T^I = T^{II} = T^{III} = T^{IV}$) because they don't need to compensate for aerodynamic moments in steady flight.
- The propeller moments (M_{Hx}, M_{Hy}) at a forward flight condition are not considered. Every propeller will develop a strong rolling moment and also some pitching moment in forward flight because of the asymmetric inflow. Since the multirotor configuration consists of the same number of counter-clockwise and clockwise rotating propellers the resulting moments will cancel each other out and it is assumed that this simplification is valid.

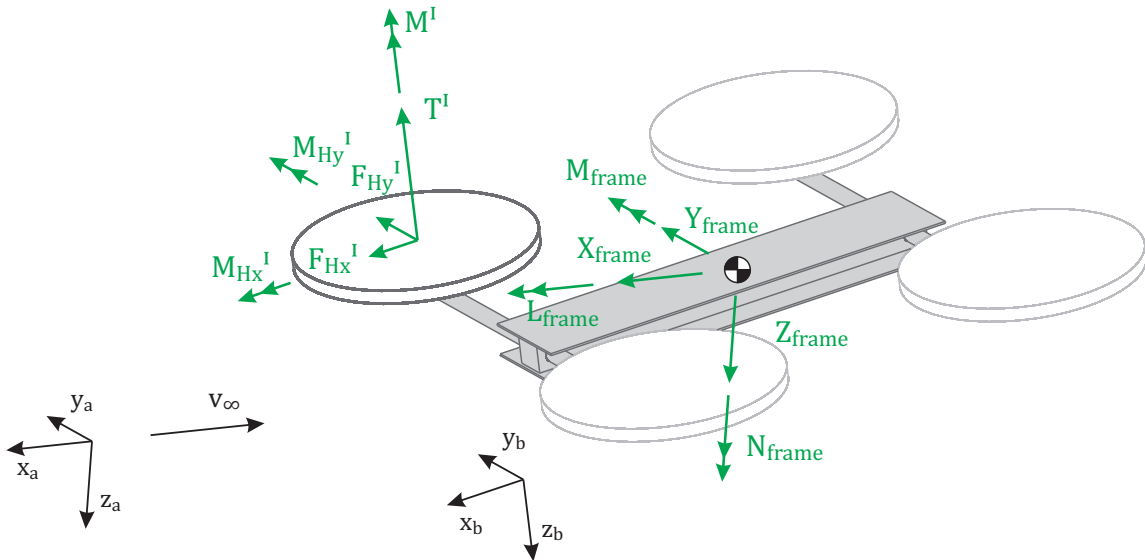


Figure 5.2: All forces and moments acting on multirotor aircraft in forward flight / hovering in a headwind. Rotor forces and moments are expressed in the rotor/body frame of reference (x_b, y_b, z_b) . Forces and moments on the airframe are expressed in the aerodynamic frame of reference (x_a, y_a, z_a) .

- The propeller in-plane forces (F_{Hx}, F_{Hy}) in forward flight are neglected. Mostly due to airfoil drag every inclined propeller will develop also a drag force in forward flight. It is assumed that this force is small compared to the propeller's thrust and the drag of the multirotor frame. This assumption could be confirmed by BEM simulations of inclined rotors (compare Section A.1.2).

Fortunately not all forces and moments have to be considered for every flight condition. At

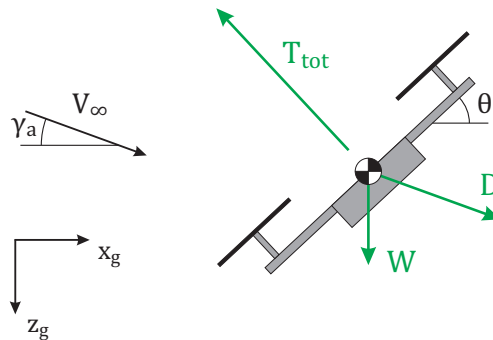


Figure 5.3: Simplified forces acting on a multirotor aircraft hovering in a headwind.

$\gamma_a = 0^\circ$ the balance of forces results in two basic equations:

$$\cos(\theta) \cdot T = W \quad (5.3.1)$$

$$\sin(\theta) \cdot T = D \quad (5.3.2)$$

Analyzing those simplified equations reveals that the aircraft's pitch angle in forward flight (or hovering in a headwind) is only determined by the weight to drag ratio of the aircraft:

$$\tan(\theta) = \frac{D}{W} \quad (5.3.3)$$

While the thrust necessary to obtain a certain angle is only determined by the weight of the aircraft:

$$T(\theta) = \frac{W}{\cos(\theta)} \quad (5.3.4)$$

The speed of the aircraft at a given pitch angle is:

$$v_{\infty}(\theta) = \sqrt{\frac{2 \cdot W \cdot \tan(\theta)}{c_D \cdot \rho \cdot A}} \quad (5.3.5)$$

Where A is the reference area e.g. the footprint area or the frontal area of the airframe. The highest uncertainty in this equation is attributed to the drag coefficient of the airframe (c_D). When the maximum thrust is known from the manufacturer's data or propeller measurements it is easy to predict the pitch angle at which the aircraft will fly at its maximum speed with the help of Eq. (5.3.4). But the prediction of the maximum speed / maximum headwind is not possible without the aircraft's drag coefficient. Unfortunately only few measurements are available on multirotor drag coefficients in general.

5.3.3 Drag Estimations Based on Conventional Multirotor Aircraft

Based on test flights with the already available hexrotor aircraft (see Figure 5.4) a value for $c_D \cdot A$ could be estimated. For the test flights the SWE hexrotor was flown at high speeds on a calm day to determine the maximum flight speed. High speed flights have been repeated in both directions to cope with the influence of wind. The maximum speed has been analyzed by GPS log files. From static thrust measurements it is known that the SWE hexrotor has a thrust to weight ratio between $T/G = 1.7$ and $T/G = 2.0$. The takeoff weight is $TOW = 4.2 \text{ kg}$. During flight tests a maximum flight speed between $v_{max} = 17 \text{ m/s}$ and $v_{max} = 18 \text{ m/s}$ was reached. Uncertainties remain because the thrust to weight ratio was measured with only one motor and a full battery. In flight the battery voltage will drop further due to the power needed for take-off and the higher current demand of all six motors. Furthermore the test flights were piloted manually and flying at a steady altitude manually is difficult. Additionally at full speed the aircraft leaves the pilot's field of view soon.

Nevertheless this data can be used with the help of Eq. (5.3.1) and Eq. (5.3.5) to achieve at least a rough estimate of the hexrotor's drag which results in $c_D \cdot A = 0.29 \text{ m}^2 \dots 0.43 \text{ m}^2$. The drag coefficient c_D is a function of the angle of attack α of a multirotor's airframe which was neglected for this simple drag estimation which is why the value of $c_D \cdot A$ can only be seen as a maximum value at highest flight speed. How strong the drag coefficient c_D depends on the angle of attack is very much related to the geometry of the investigated aircraft. For a nearly spherical shaped airframe like the SWE hexrotor with its large camera at the bottom, this dependency is supposed to be less strong than for a very slim, aerodynamically shaped airframe.

In general the value of $c_D \cdot A = 0.3 \text{ m}^2 \dots 0.4 \text{ m}^2$ has to be seen as an upper constraint. Because ANDroMeDA is designed to fly at very high wind speeds and its airframe is shaped more aerodynamically. Further estimations on multirotor airframe drag for different configurations is presented in Section 5.10. Fig. 5.5 shows the resulting flight conditions for a fixed value of $c_D \cdot A = 0.3 \text{ m}^2$.

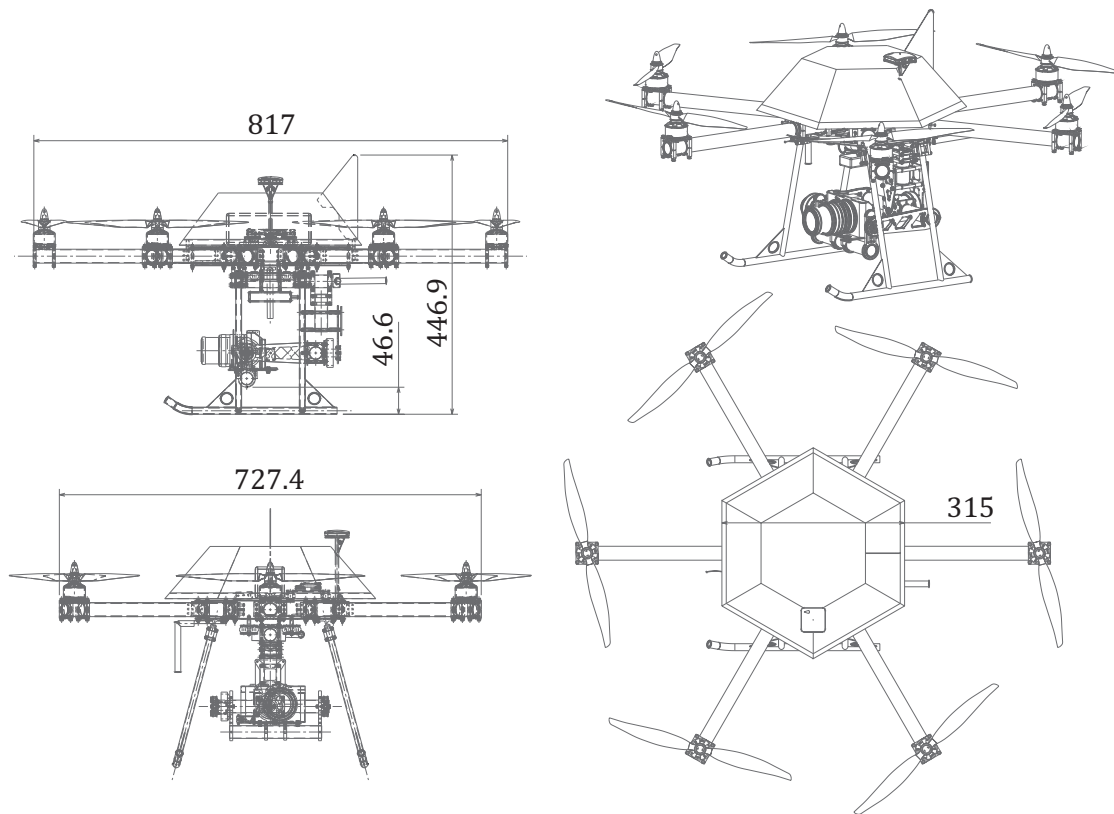


Figure 5.4: Hexrotor built at SWE.

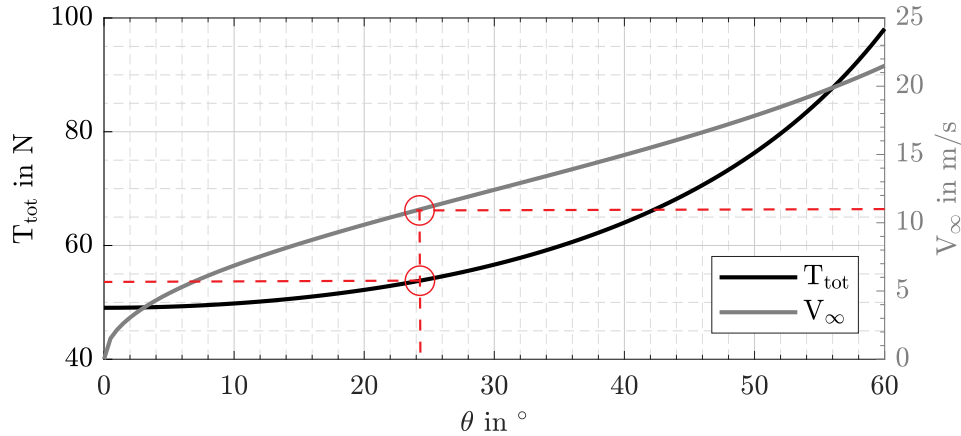


Figure 5.5: Inclination angle and thrust at different wind speeds for a multirotor with a drag coefficient of $c_D \cdot A = 0.3 \text{ m}^2$ hovering in a headwind. The design point is marked in red.

5.3.4 Disturbances from the Rotor Flow Field

One of the most important questions to answer during the development of a wind measuring multirotor aircraft is: "How much will the airflow of the aircraft's rotors influence the measurement of ambient winds?".

While the general qualitative answer to the problem is easy, "One has to keep as much distance to the rotors as possible.", the quantitative answer to the questions "Where to place the

measurement probe?" and "How far does it need to be from the rotors at least?" is not easy to give. For the rotor wake of manned helicopters there are many references available based as on numerical analysis as well as on experiments. However, these references are not applicable in general because mostly only one operating condition of interest was investigated. Furthermore, Reynolds number, Mach number, advance ratio of the rotor and the dynamic properties (Lock number) are very different from small unmanned multirotor designs. For the inflow region in front of a rotor no references could be found because this region is normally of no interest.

From a performance point of view it is not desirable to place the probe on top, bottom or sideways of the airframe because the necessary structure to mount the probe would cause a lot of additional drag and decrease the flight time.

When multiple aircraft are deployed another question raises besides the placement of the flow measurement probe: "How big will the influence of the entire wake of all rotors of one particular aircraft be on the other aircraft following?".

These key questions have a significant influence on the entire design of ANDroMeDA and are treated in detail in Section 5.7.

5.3.5 Velocities Induced on the Measurement Probe by Vehicle Rotations

As stated in the previous section some distance to the rotors has to be maintained if wind measurements are carried out with a multirotor aircraft or in general with a rotary wing aircraft. Because from a flight mechanical point of view there is no other option than placing the rotors around the center of gravity, this fact will automatically result in a probe placement far off the C.G. Thus rotations of the aircraft will result in movements and therefore also induced velocities at the probe. From Figure 5.6 the following relations can be derived:

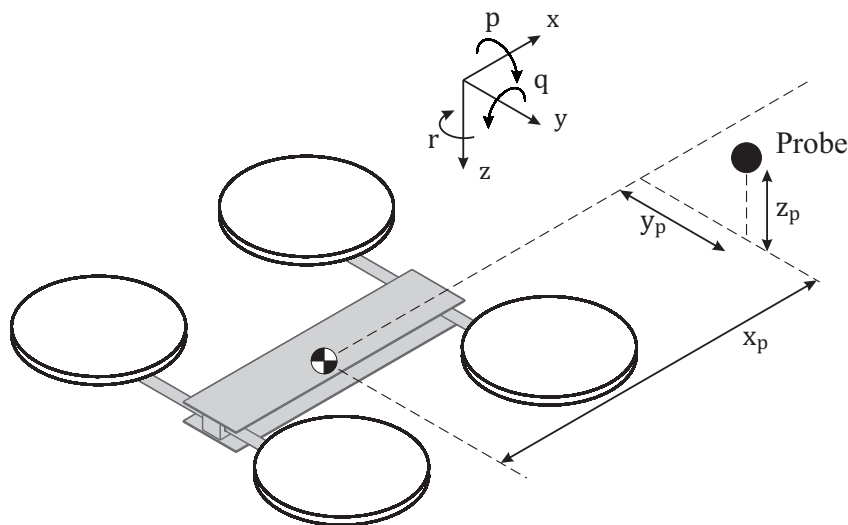


Figure 5.6: Probe mounted at an offset x_P, y_P, z_P to the center of gravity.

$$\dot{x}_p = \dot{x}_s - z_p \cdot q - y_p \cdot r \quad (5.3.6)$$

$$\dot{y}_p = \dot{y}_s + x_p \cdot r + z_p \cdot p \quad (5.3.7)$$

$$\dot{z}_p = \dot{z}_s + x_p \cdot q - y_p \cdot p \quad (5.3.8)$$

The coordinate system was chosen according to DIN 9300. Hence p, q, r are the rotational rates about the x, y, z Axes (e.g. $p = \dot{\theta}$).

Considering the changes of wind direction and speed derived in Chapter 2 from offshore and onshore measurements the maximum rotational rates of the aircraft can be estimated.

Taking the forces acting on a multirotor aircraft sketched in Figure 5.3 into account again, but this time without the simplification of $\gamma = 0^\circ$, the inclination angle of the aircraft, θ in the geodetic coordinate system can be related to the free stream velocity v_∞ and inclination angle γ_a of the wind speed vector. Eq. (5.3.1) becomes:

$$\cos(\theta) \cdot T - W + \sin(\gamma_a) \cdot D = 0 \quad (5.3.9)$$

Equation 5.3.2 changes to:

$$-\sin(\theta) \cdot T + \cos(\gamma_a) \cdot D = 0 \quad (5.3.10)$$

From these two equations the inclination angle of the aircraft can be determined:

$$\tan(\theta) = \frac{\cos(\gamma_a) \cdot D}{W - \sin(\gamma_a) \cdot D} \quad (5.3.11)$$

Substituting D with $D = c_D \cdot A \cdot \frac{\rho}{2} \cdot v_\infty^2$ together with the simplification of a fixed value for $c_D \cdot A = 0.3 \text{ m}^2$ leads to the desired relation between v_∞ , γ_a and θ .

Two scenarios, derived from Section 2, have been considered:

- Scenario 1: γ_a changes from $\gamma_a = -20^\circ$ to $\gamma_a = 20^\circ$ at a rate of $\dot{\gamma} = 124.5^\circ/s$ at a fixed wind speed of $v_\infty = 12 \text{ m/s}$.
- Scenario 2: Inflow angle stays constant at $\gamma_a = 0^\circ$ while the wind speed is changing from $v_\infty = 10 \text{ m/s}$ to $v_\infty = 15 \text{ m/s}$ at a rate of $\dot{v}_\infty = 30.5 \text{ m/s/s}$.

Scenario 1 results in a necessary pitch rate of $\dot{\theta} = 19^\circ/s$ while scenario 2 has a more severe impact on $\dot{\theta}$ because the entire aircraft has to be tilted quickly to compensate for the higher drag. Consequently scenario 2 results in $\dot{\theta} = 118^\circ/s$. This means that the pitch angle has to be changed from $\theta = 20.2^\circ$ to $\theta = 39.6^\circ$ in only $T = 0.164 \text{ s}$ to compensate for the higher wind speed.

Assuming a 1.2 m long measurement boom to achieve a reasonable distance to the rotor airflow ($x_p = 1.2 \text{ m}$, $y_p = 0 \text{ m}$, $z_p = 0 \text{ m}$) scenario 1 induces a vertical velocity of $w = 0.41 \text{ m/s}$ and an error in the measured inflow angle of $\alpha_{error} = 2.3 \text{ deg}$ while scenario 2 will result in a vertical induced velocity of $w = 2.48 \text{ m/s}$ and an error in the measured inflow angle of $\alpha_{error} = 13.9 \text{ deg}$. This rough estimate assumes a perfect flight controller without any delays as well as no delay (no inertia) when tilting the aircraft. It is expected that an actual flight controller with delays in the sensor readings and delay in the control loop and real flight mechanics will lead to much higher angular rates for the aircraft to keep its position in space.

With this rough estimation it can be clearly seen that velocities induced on the measurement probe by the fast rotations of the aircraft can become critical at extreme wind conditions. Of course this effect could be canceled out completely by mounting the probe directly at the center of gravity. This is however contradicting the goal of a clean measurement without rotor inflow and rotor wake disturbances.

5.3.6 Solutions to Alleviate Velocities Induced by Aircraft Rotations

There are two possible solutions to this problem: The induced velocities can be avoided by physically stabilizing the measurement boom. The other possibility is a digital compensation of the induced velocities while processing the data.

The second approach has some serious difficulties to overcome. First of all, further measurement errors are introduced when measuring the boom's angle. An angle measurement is performed either with the autopilot's IMU or a separate IMU at the tip of the boom. An IMU, however, does not measure its attitude directly but measures angular and lateral accelerations. The attitude is then calculated with a DCM method ([39]) or nowadays more likely with a Kalman Filter ([40], [41]). The accuracy of these methods is limited by sensor noise and numerical errors. All errors introduced by the calculation of the boom's angle will add up to the flow measurement errors.

Furthermore, even with a perfect angle measurement the risk remains that during fast rotations of the aircraft the inflow angle will exceed the measurement range of the probe.

Another source of problem that needs to be investigated are aerodynamic errors. Fast movements of the boom could for example result in flow separations at the probe. Such dynamic effects, possibly comparable to the dynamic stall of an airfoil, can theoretically result in a difference between the measurement of a fixed boom and the measurement of fast moving boom even with an ideal motion compensation.

Because the uncertainties with a fixed boom and the advantages regarding flight performance described in the following sections, a stabilized boom was chosen for ANDroMeDA.

5.4 Methodology in Conceptual Design

In Section 5.1 it was stated that a multirotor design will be used because of its lower mechanical complexity and its small maintenance effort. In general there is no straight forward procedure for aircraft design, which is an iterative process. Almost every design decision influences another one so that there is no way of making them one after another. Figure 5.7 and Table 5.1 illustrate how the design considerations are interconnected to each other. In the beginning of the conceptual

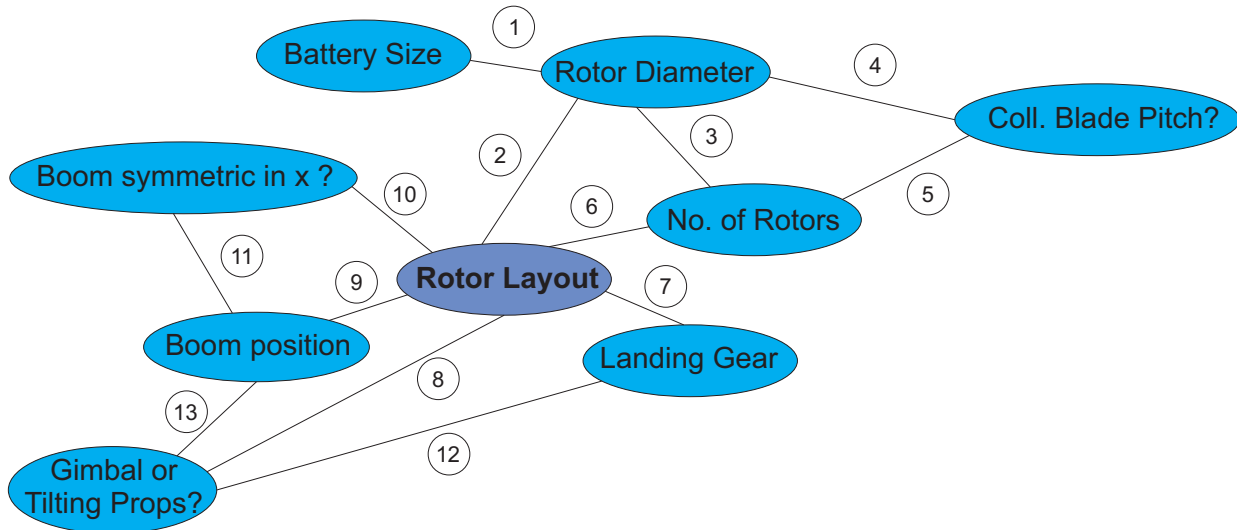


Figure 5.7: Relations between the ANDroMeDA design decisions.

design phase some basic knowledge has to be gained to be able to deal with the most important decisions. This fundamental understanding is treated in the following sections. An analytical description of the involved relations is of course always the most efficient way to be able to compare different conceptual solutions. For more complex issues like the airframe drag or propeller inflow simulations are carried out followed by an analytical description of the simulation results.

As an initial step in Section 5.5 different concepts are investigated to design an aircraft that is capable of better position keeping in high wind environments.

In Section 5.6 the previously described problem of velocities induced on the probe by aircraft rotations is addressed and the two possible approaches to overcome this problem, a gimbaled measurement boom and tilting rotors, are compared.

The rotor flow field is studied in Section 5.7. The results are essential for probe placement and an important step towards the final aircraft configuration.

Because the number of rotors of the aircraft is still undefined at this point in Section 5.8 analytical relations are derived to size the rotor diameter and blade geometry according to the number of rotors.

As pictured in Figure 5.7 the decision with the highest impact is the one about the number of rotors and rotor layout. Therefore after all relevant relations have been derived possible rotor layouts are described and their flight mechanical behaviour is compared in Section 5.9. To be able to compare them the resulting airframe drag of these different configurations is determined with the help of an aerodynamic simulation which is presented in Section 5.10. Finally all configurations are compared in a decision matrix in Section 5.13.

Connection	Explanation
①	Larger propellers will result in stronger motors that may only work with higher cell numbers.
②	Larger or smaller rotors may not allow the same layout.
③	Diameter has to be scaled to for the same induced power.
④	Availability of stock blades for different rotor diameters?
⑤	Effort for collective pitch is too high for more than four rotors.
⑥	Not all rotor layouts are possible with an arbitrary no. of rotors.
⑦	Space needed for landing gear.
⑧	Space for gimbal.
⑨	Space for boom.
⑩	Space for boom differs between symmetrical and non-symmetric boom.
⑪	Symmetric boom designed to be placed in C.G., asymmetric boom can also placed forward.
⑫	Landing gear with a gimbal needs more space.
⑬	For a gimbal the boom has to be mounted in C.G.

Table 5.1: Description of the design relations shown in Figure 5.7.

5.5 Approaches to Reduce Control Response Time

5.5.1 Possible Multirotor Configurations

One key aspect for the development of an aircraft that has to hover in extreme wind conditions is the reduction of the aircraft's actuation response time. The faster a new equilibrium state can be obtained the better a fixed position in space can be maintained.

Three possible aircraft configurations will be compared in this section:

- Conventional multirotor configuration: To accomplish an equilibrium state the entire vehicle has to be tilted. The control moment for this rotation is realized by different rotational speeds of the rotors.
- Multirotor configuration with collective rotor blade pitch: To accomplish an equilibrium state also the entire aircraft has to be tilted but it is expected that the rotation can be finished much faster because there is a smaller delay to change the thrust compared to fixed pitch rotors. Furthermore, negative thrust can be produced at each rotor.
- Multirotor configuration with tilting fixed pitch rotors: To reach an equilibrium state the airframe remains horizontal and only the motor arms are tilted. Due to the lower inertia of the moving parts it is expected that this requires significantly less time than tilting the entire aircraft.

A combination of the last two concepts is possible but will lead to a much higher mechanical system complexity and higher weight. Therefore this approach is not pursued any further.

As well as for the estimation of the induced velocity on the probe (Section 5.3.5) a complete flight simulation model of the aircraft and time series of an extreme wind situation would be the most exact way to compare the three different configurations. For the conceptual design no complete simulation model was developed for every configuration, instead a simple analytical approach was chosen.

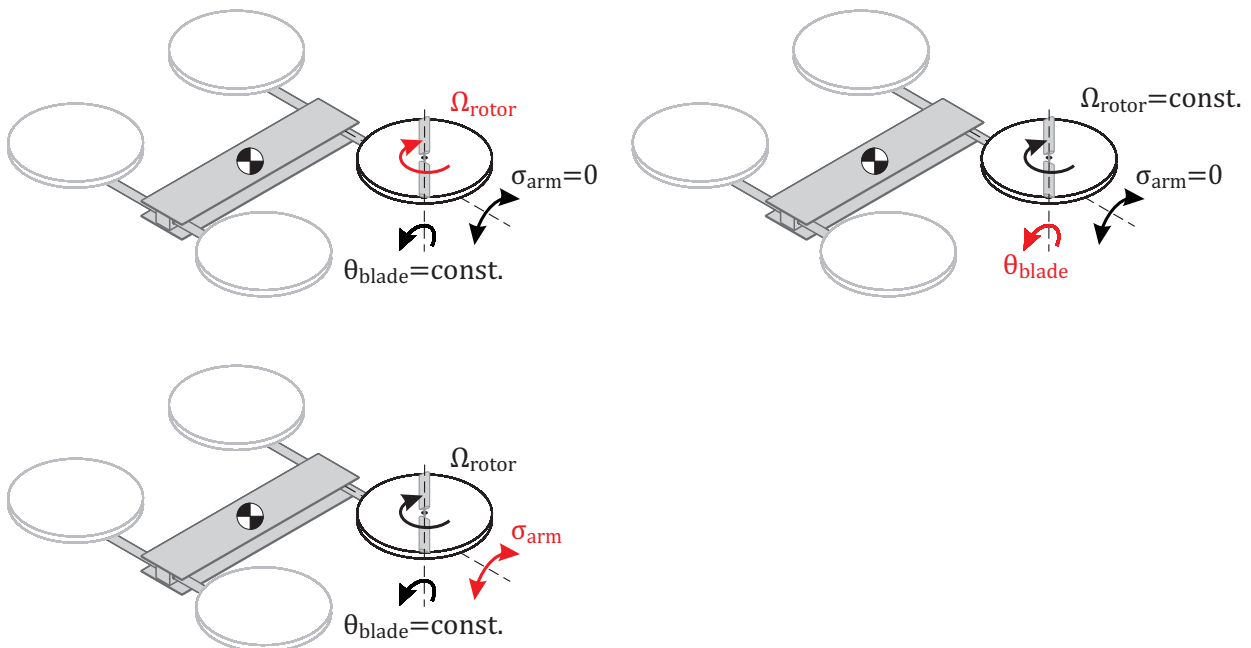


Figure 5.8: Different actuator configurations. The primary actuator is shown in red.

5.5.2 Example Case

For an analytical comparison between the three configurations a sudden wind speed change from $V_\infty = 10 \text{ m/s}$ to $V_\infty = 15 \text{ m/s}$ at a constant inflow angle of $\gamma_a = 0 \text{ deg}$ is considered. This was derived from the analysis of extreme wind conditions in Section 2.3.

With the help of Eq. (5.3.11) in combination with the assumption of a fixed value for $c_D \cdot A = 0.3 \text{ m}^2$ the necessary change of the aircraft's attitude angle can be calculated to $\Delta\theta = 19.4^\circ$. Since the drag coefficient c_D is assumed to be constant over the entire range of angle of attack the same amount of tilting can be used for the tilting propeller configuration ($\Delta\theta = \Delta\sigma$). Figure 5.9 illustrates the difference between the configurations. For the tilting rotor configuration the aircraft's attitude remains always level while the non-tilting configurations need to adjust their airframe attitude to the current wind speed to achieve an equilibrium state.

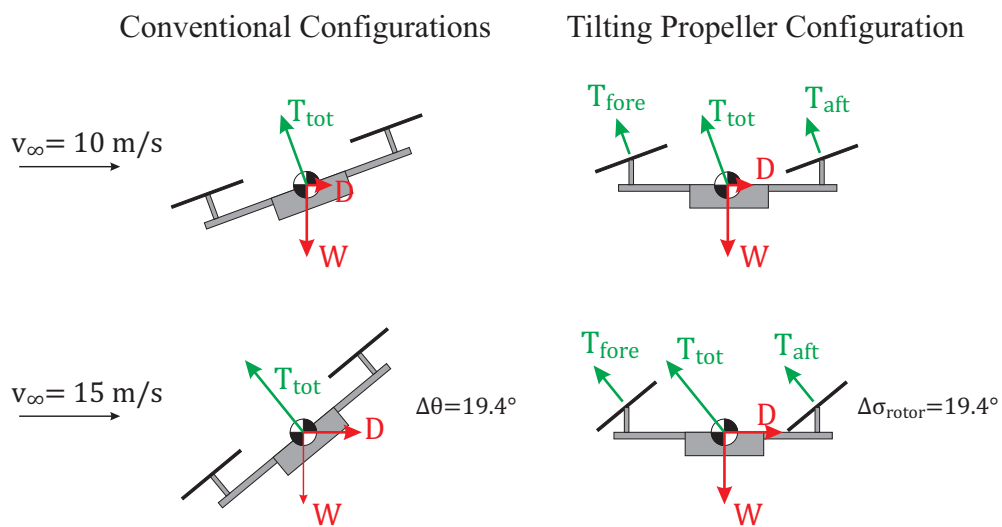


Figure 5.9: Comparison between conventional configurations (left) and tilting propeller configuration (right).

5.5.3 Actuator Response Times

An interesting comparison between a fixed blade configuration and a collective blade pitch configuration can be found in [42]. According to this comparison a fixed pitch rotor needs about 0.2 s to 0.3 s to speed up from hover thrust to double hover thrust. This number matches well with the component test that have been conducted for the detailed design of ANDroMeDA (see also Section A.4). The Motor/Propeller/Battery combination finally used for ANDroMeDA-1 has a rise time of $t_{rise,motor} = 0.2 \text{ s}$. In Section A.4 it is shown that the fall time has a similar value because all modern multirotor ESCs support active braking.

According to [42] this rise time can be reduced considerably by the use of a collective pitch propeller. For a collective pitch configuration the rotor's rotational speed is held constant by the motor's speed controller (ESC) while the thrust is changed only by the blade pitch. Consequently the rise time depends only on the speed of the pitch servo actuator. Fast modern servos of suitable size e.g. the MKS HV9780, usually used for helicopter tail rotors, have an actuation time between $0.03 \text{ s}/60^\circ$ and $0.04 \text{ s}/60^\circ$.

This actuation time, specified by servo manufacturers, is usually the no-load speed. According to experiences with the tilt-rotor test stand (see Section A.5) this value has to be roughly doubled

under load conditions. Since servo actuators usually have a travel range of 120° and the usable blade pitch range will be much smaller some mechanical transmission, realized by different lengths of the servo lever and the blade grip lever, has to be used.

Assuming a linear relation between thrust and the blade angle of attack ($T \propto \theta_{blade}$) and assuming that one third of the blade pitch range is used for a change from hover thrust to double hover thrust, this leads to a corresponding actuator travel of 20° (see Figure 5.10). If the actuation time under operational load conditions is $0.06 \text{ s}/60^\circ$ a rise time of $t_{rise,pitch} = 0.02 \text{ s}$ can be realized. The MKS HV9780 servo is faster than the servo used in [42]. For the actuation time from hover thrust to double hover thrust Cutler ([42]) has determined a rise time of $t_{rise,pitch} = 0.04 \text{ s}$ in experiments. As a conventional assumptions a rise time of $t_{rise,pitch} = 0.03 \text{ s}$ was used for the comparisons in this chapter. Similar to the collective blade pitch concept the rise time of tilting

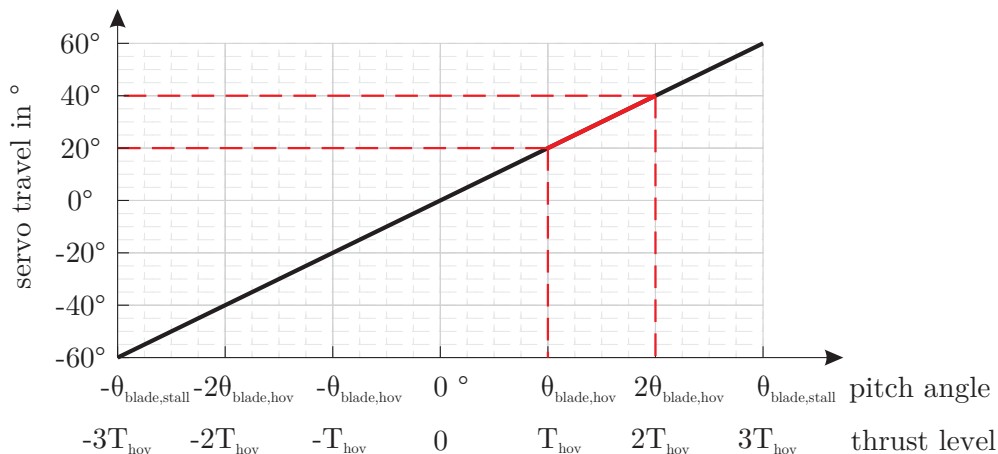


Figure 5.10: Servo travel used for a thrust change from hover to double hover thrust.

propellers depends only on the behavior of the servo actuator. For high maneuverability a 1 to 1 ratio between servo angle and motor arm angle is considered. Therefore the change of $\Delta\sigma = 19.4^\circ$ will need about one third of the time needed for $\Delta\sigma = 60^\circ$. Figure 5.11 shows that the time needed for the acceleration and deceleration is negligible compared to the overall response time. Unfortunately the temporal resolution of the tilt rotor test stand is only $f_{tilt} = 50 \text{ Hz}$, which makes it difficult to demonstrate this fact. However, a Sony RX100 IV camera with 1000 fps was used to confirm this hypothesis. To tilt the entire motor arm, which has a much higher inertia than the rotor blades, a stronger and therefore slower servo actuator is needed than the one used for the collective pitch configuration. For the tests in Figure 5.11 a HBS 860 servo actuator has been used (compare Section A.5). Also visible in Figure 5.11 is that a higher rotor thrust will not influence the tilt actuator speed. The actuation time needed to tilt a motor arm in the final ANDroMeDA configuration by $\Delta\sigma = 19.4^\circ$ is less than $t_{rise,tilt} = 0.07 \text{ s}$.

In summary the rise times for the different configurations have been determined as:

- $t_{rise,motor} = 0.2 \text{ s}$
- $t_{rise,pitch} = 0.03 \text{ s}$
- $t_{rise,tilt} = 0.07 \text{ s}$

5.5.4 Maximum Control Moment

The maximum control moment used for the comparison of the three different concepts is estimated using the geometry of the SWE hexrotor as a baseline configuration. In general, a larger distance

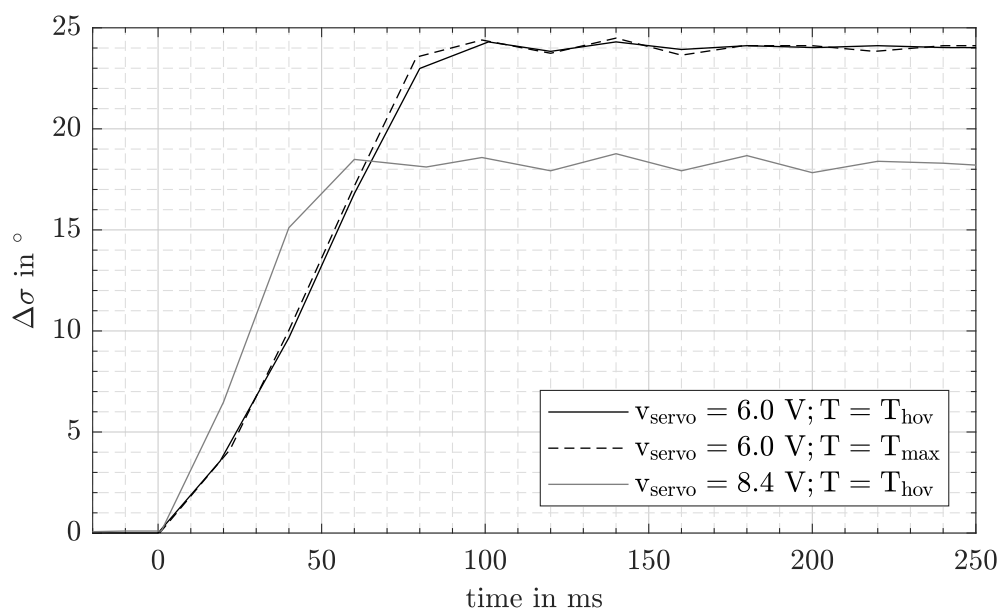


Figure 5.11: Step response of a HBS860 servo actuator measured on tilt rotor test rig (compare Section A.5).

between the motors and the aircraft's center of gravity will result in a larger control moment but will also result in a higher aircraft inertia.

The maximum control moment differs between the fixed pitch and collective blade pitch configuration. For the fixed pitch configuration it is usually not possible to produce negative thrust. If no negative thrust can be produced the thrust on one side of the aircraft cannot be higher than the double hover thrust. Otherwise this would not only result in a pitch/roll moment but also in a vertical force, hence a climb maneuver (see Figure 5.12).

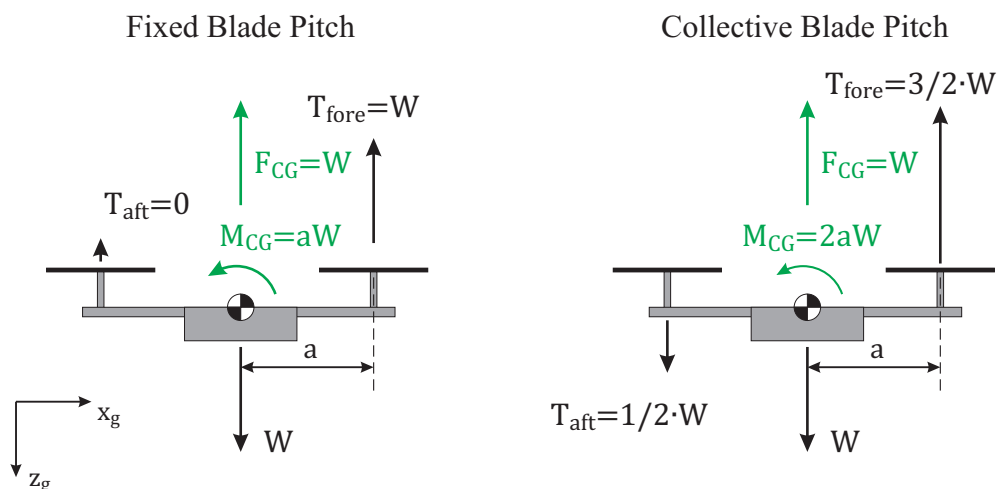


Figure 5.12: Maximum control moment for fixed blade pitch and collective blade pitch configuration.

If enough power is available a higher control moment can be reached with collective blade pitch using negative thrust on one side and a thrust value higher than double hover thrust on the other side. For most multicopter configurations a thrust higher than three times of hover thrust is not feasible.

5.5.5 Time needed to Tilt the Aircraft

To determine the time that is needed to reach the new state of equilibrium the conservation of angular momentum is used:

$$M = I_{yy} \cdot \ddot{\theta} \quad (5.5.1)$$

Where M is the pitching moment and I_{yy} is the aircraft's moment of inertia about the y-axis. The moment of inertia of the SWE hexrotor is estimated as $I_{yy} = 0.1162 \text{ kg} \cdot \text{m}^2$. Solving Eq. (5.5.1) analytically by considering the first half of rotation with a constant pitching moment M and performing a double time integration leads to:

$$t_{Rotation} = \sqrt{\frac{2 \cdot \Delta\theta}{M \cdot I_{yy}}} \quad (5.5.2)$$

Hence, it can be seen that a lower moment of inertia ($I_{yy,2} < I_{yy,1}$) as well as a higher control moment ($M_2 > M_1$) will not affect the time needed to rotate the aircraft linearly but by the factor of $\sqrt{M_2/M_1}$ respectively $\sqrt{I_{yy,1}/I_{yy,2}}$. Therefore the doubled control moment when using negative thrust with collective pitch control will only decrease $T_{Rotation}$ by 30 %.

The differential equation Eq. (5.5.1) was solved numerically to implement different actuator models as shown in Figure 5.13. This results in a time needed to tilt the aircraft of $t_{ideal,1} = 0.1287 \text{ s}$ without negative thrust and $t_{ideal,2} = 0.091 \text{ s}$ with negative thrust. For these calculations the non-delayed control moments shown in Figure 5.13 have been used.

These ideal cases demonstrate the physical limits due to the aircraft's inertia. Even with infinitely short actuator response times a considerable amount of time is needed to tilt the aircraft into the new state of equilibrium when the wind speed changes.

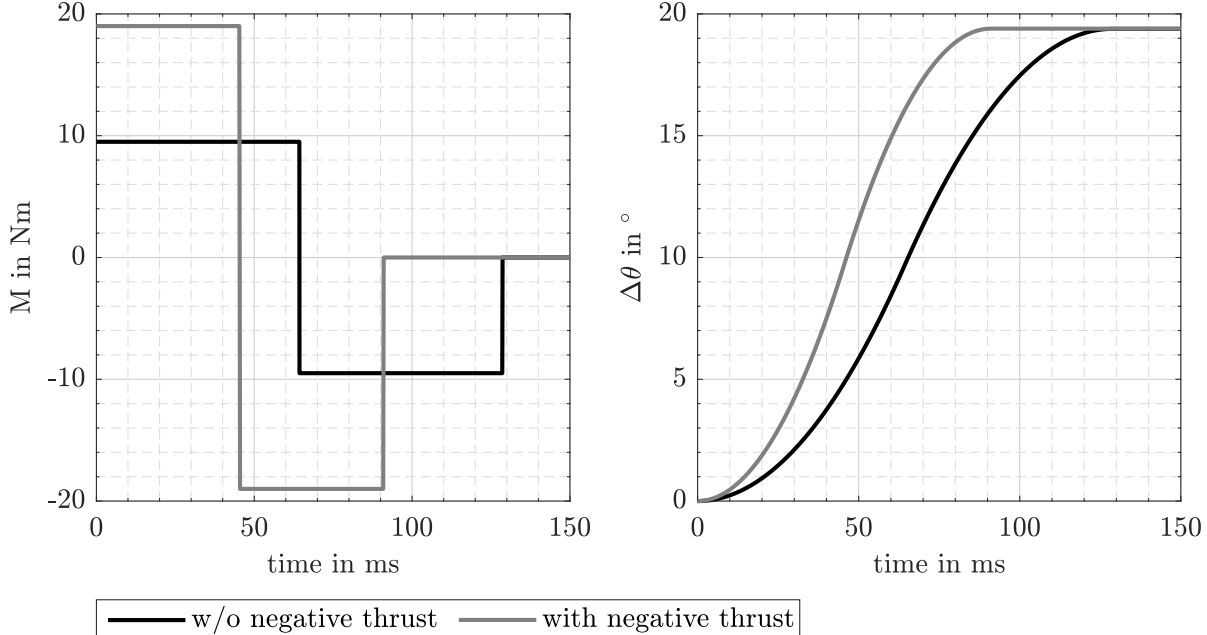


Figure 5.13: Ideal cases without any delays.

Figure 5.14 introduces an actuator delay for the collective pitch aircraft configuration. The control moment is modeled with a linear increase and decrease. As illustrated previously in Figure 5.11 this is valid for the tested tilt servo actuators which are very similar to suitable

blade pitch servo actuators. For a change from hover thrust to double hover thrust a rise time of $t_{rise,pitch} = 0.03 s$ was set. This linear thrust increase and decrease results in a time needed to tilt the aircraft of $t_{tilt,coll1} = 0.1622 s$ without negative thrust and $t_{tilt,coll2} = 0.1584 s$ using negative thrust. The reason for this small difference is that the full control moment cannot be utilized for the current case because the actuation time is too slow. Hence the angular rotation has to be stopped before the full control moment can develop. Consequently for aircraft with higher inertia or larger rotation angles the difference will be larger.

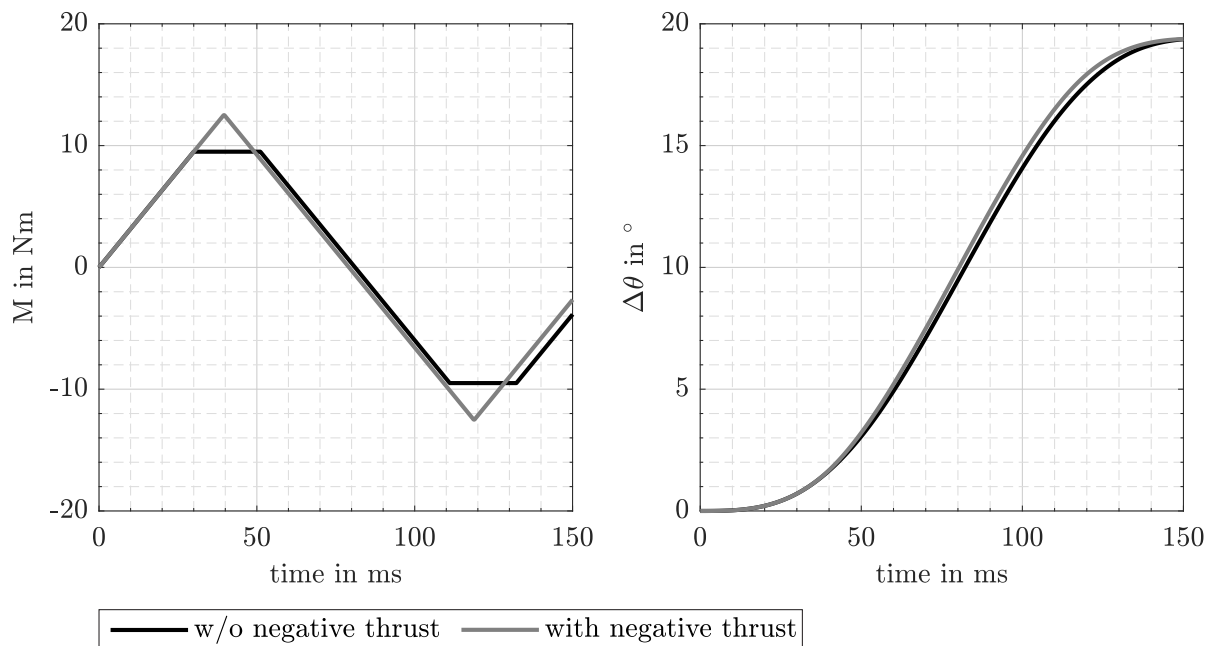


Figure 5.14: Collective blade pitch aircraft.

Modeling the control moment hence the propeller thrust of the fixed pitch configuration is more challenging since it involves the behavior of the motor controller (ESC). Figure 5.15 demonstrates that there is a severe difference whether a low thrust increase or a high thrust increase is commanded. For small changes in the commanded thrust the ESC will use a much lower motor torque and take a lot more time to realize this small thrust changes. As a result the measured rise time of $t_{rise,motor} = 0.2 s$ to increase the thrust from $T = T_{hov}$ to $T = 2 \cdot T_{hov}$ will remain almost unchanged even for small thrust changes.

If the maximum thrust is commanded the increase rate will be linear ($dT/dt = const.$) until the double hover thrust is reached. After that point the change rate will be smaller which can be explained by the rising aerodynamic propeller torque (see Section A.2.1).

If however, a smaller thrust increase is commanded, as shown by the blue dashed line in Figure 5.15, the response time is by magnitudes slower. Assuming that the flight controller will command a higher thrust than the target thrust, which is shown by the dashed black line in Figure 5.15, the maximum measured control moment can be used for the fixed pitch model. This corresponds to a very aggressive flight controller using a full thrust command for the first half of the rotation and a minimum thrust command for the second half of the rotation. It is assumed that this can be achieved by a proper tuning of PID values in the angular rate control loop (compare Section 7). In addition limits due to the propeller inertia and aerodynamics according to Section A.2.1 have been included in the simulations.

A more realistic estimation of the response of the fixed pitch aircraft could be achieved in the future with a hardware in the loop experiment. Therefore equation (5.5.1) has to be solved by numerical integration using a given aircraft inertia while measuring the propeller thrust on the whirl tower (see Section A.1) and controlling the ESC with a PID loop emulating a virtual aircraft attitude θ .

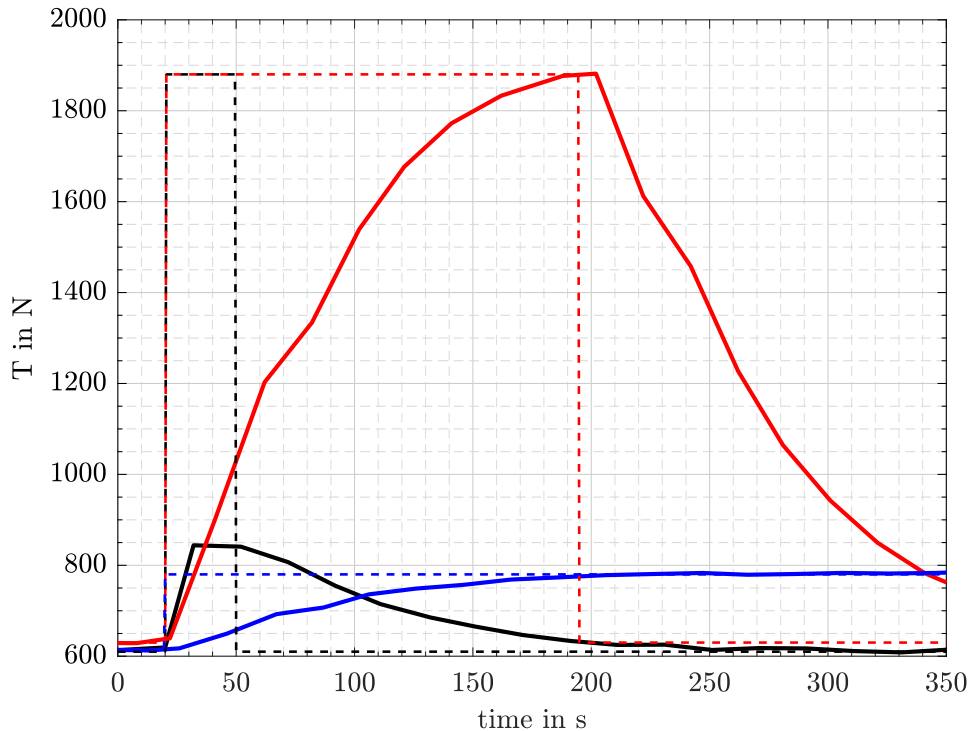


Figure 5.15: Thrust response of a propulsion system similar to the one finally used in ANDroMeDA-1: BLHeli ESC, Arris MT4010 Pro motor and Fiala 13x8 propeller. Measured thrust is plotted in solid lines and commanded thrust is shown in dashed lines.

Figure 5.16 shows the rotation of the fixed pitch aircraft configuration. After the maximum control moment has been reached a small amount of time is given for the ESC to adopt the new command (also compare to measurements in Figure 5.15). With the previously mentioned aggressive flight control strategy, the time needed to tilt the aircraft is approx. $t_{fixed-pitch} = 0.190 s$.

5.5.6 Conclusions

It has been shown that the tilting propeller configuration has a considerable advantage over the other configurations resulting in less than half of the time needed to obtain a new state of equilibrium after a wind speed change because it is not necessary to tilt the entire aircraft. Even a multicopter aircraft with fast collective pitch propellers and a maximum thrust capacity of three times hover thrust ($T_{max} = 3 \cdot T_{hov}$) needs more than twice the time to gain a new equilibrium state. Figure 5.17 compares the aircraft tilting times for the relevant cases.

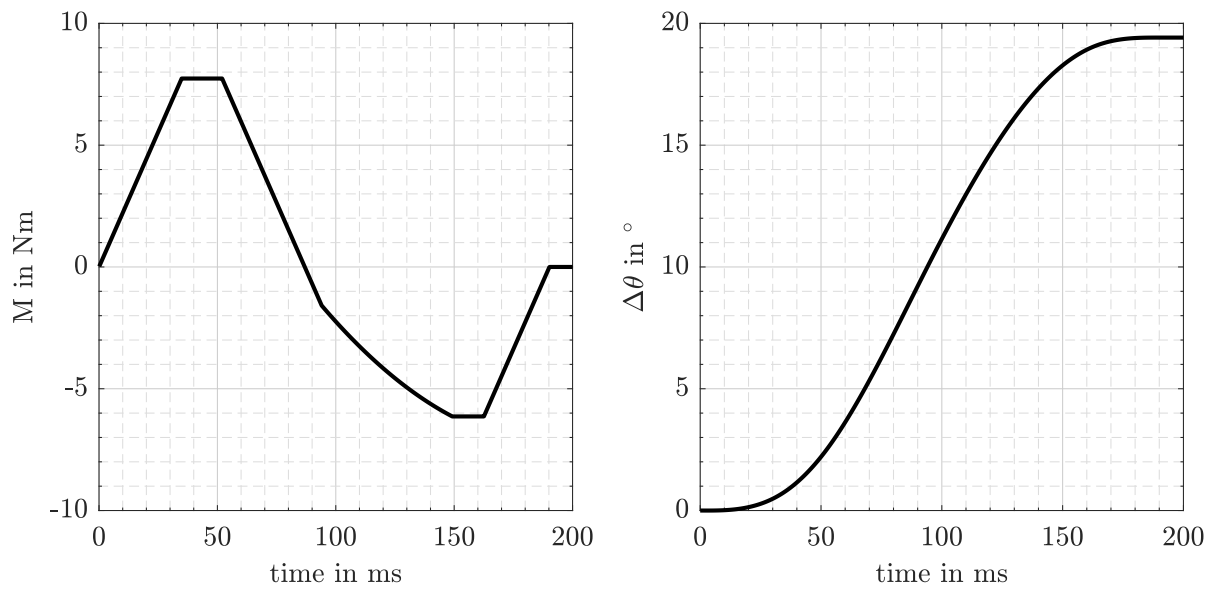


Figure 5.16: Fixed pitch aircraft with very aggressive attitude controller.

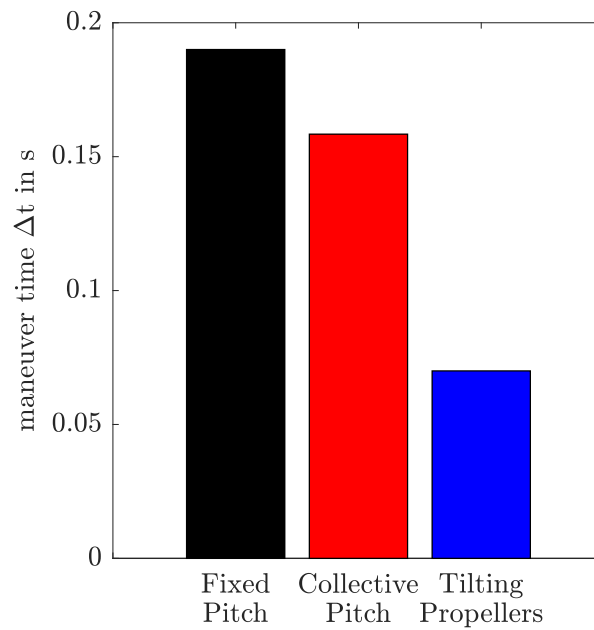


Figure 5.17: Comparison of time needed to tilt an aircraft by $\Delta\theta = 19.4^\circ$ for different actuator concepts.

5.6 Approaches to Alleviate Induced Velocities

As it has been derived in Section 5.6 every rotation of the aircraft about its center of gravity will induce a motion and hence a velocity on the measurement probe. Two solutions are considered to alleviate this effect. One solution is the tilting propeller configuration that has been presented in the previous section. The other solution is an active gimbal to suspend the measurement boom below the center of gravity.

5.6.1 Gimbal

Active gimbals driven by servo actuators or brushless motors are successfully used on UAVs to operate cameras during their mission. With the help of those gimbals the camera always points in the same direction and is not disturbed by aircraft motions. Figure 5.18 shows a gimbaled camera configuration mounted at the SWE hexrotor. Brushless motors with a high torque and a low rotational speed are used as drive units for the gimbal. These motors are often modified versions of propulsion drives using a thinner wire and a higher number of windings.

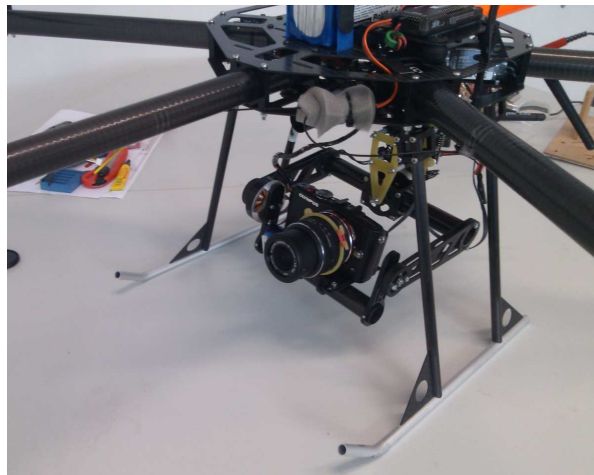


Figure 5.18: Example of a gimbaled camera mount at the SWE hexrotor.

Figure 5.19 illustrates the idea of a measurement boom connected to the measurement aircraft with a gimbal. To investigate the feasibility of this concept the moment of inertia of two preliminary measurement booms was compared to the moment of inertia of a heavy DSLR camera. Figure 5.20 explains the basic dimensions of the considered measurement booms and the simple model used to gain a rough estimate of the camera's moment of inertia.

The Canon EOS 5D Mark III camera was used as an example for a heavy DSLR camera that has been successfully used with multirotor gimbals. Camera body and camera lens have been modeled by simple homogenous bodies. The lens used for this estimation is the model EF-S f/2.8 17-55mm. Two different measurement booms have been modeled. One very light version with a CFRP tube with an outer diameter of $D_{boom} = 11 \text{ mm}$ and an inner diameter of $d_{boom} = 10 \text{ mm}$. This light version includes measurement equipment with a weight of $m_{probe} = 20 \text{ g}$ as well as the necessary counter weight of $m_{counterweight} = 183.3 \text{ g}$.

The heavy version consists of a CFRP tube with an outer diameter of $D_{boom} = 20 \text{ mm}$ and an inner diameter of $d_{boom} = 18 \text{ mm}$. The measurement equipment for this version has a mass of $m_{probe} = 50 \text{ g}$ and consequently a larger counter weight of $m_{counterweight} = 548.6 \text{ g}$. A comparison between the three models yields in:



Figure 5.19: Concept sketch of an aircraft with a measurement boom mounted on an active gimbal.

- $I_{yy,DSL R} = 5.6 \cdot 10^6 \text{ gmm}^2$
- $I_{yy,boom1} = 6.2 \cdot 10^7 \text{ gmm}^2$
- $I_{yy,boom2} = 1.81 \cdot 10^8 \text{ gmm}^2$

Because the moment of inertia even for a light measurement boom is ten times higher than the moment of inertia of a heavy DSLR camera it is highly unlikely that a standard off the shelf gimbal solution can be used. Special actuators with a higher torque have to be developed.

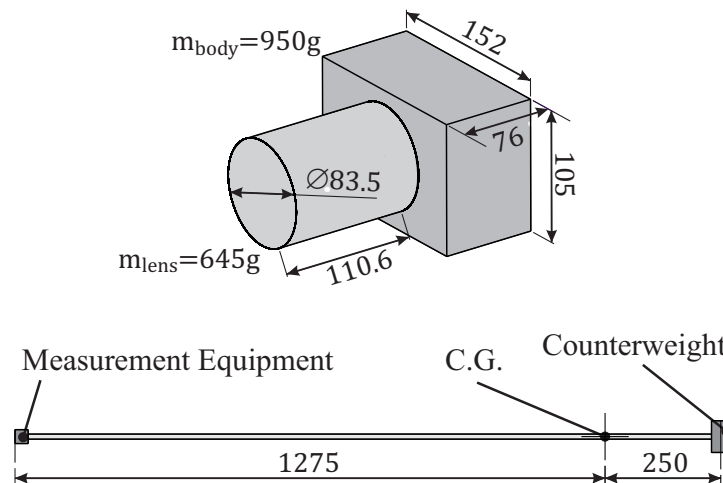


Figure 5.20: Dimensions of the modeled DSLR camera and measurement boom.

5.6.2 Tilting Propellers

With the help of tilting propellers an additional degree of freedom is introduced to the system and it becomes possible to control the aircraft's attitude without producing translational movements (see Figure 5.9). This additional degree of freedom can be used to implement a control loop

to keep the aircraft's frame, as well as the measurement boom mounted to it rigidly, always level. Unlike the gimbal solution this stabilization is only possible in one axis. However, if the measurement boom is mounted symmetrically about the y-axis this will be enough to avoid any induced velocities on its tip.

Compared to a conventional multirotor, the control strategy for tilting propellers has to be different which means more effort on the software development while the hardware to tilt the propellers with a servo actuator is expected to be less complex.

5.6.3 Conclusion

The gimbal approach is expected to be heavier. Even if the counter weight can be realized with flight batteries or a battery for the measurement equipment the gimbal motors are an additional mass and do not offer other functionalities like the actuators of the tilting propeller configuration do.

The tilting propeller configuration also offers some advantages in terms of flight performance (lower drag) and flight mechanics (better position keeping). In addition, the gimbal concept was rated as a higher development risk because of the much higher moment of inertia of a measurement boom compared to a camera and was discarded already in an early phase of the conceptual design. A suitable control strategy to drive the tilting propellers will be implemented in the autopilot as described in Section 7.

5.7 Rotor Flow Field Investigations

5.7.1 Problem Description

A very important part of the conceptual design of ANDroMeDA is to gain a well founded knowledge about the flow field in the vicinity of the rotors of a multirotor aircraft. First of all this understanding is essential for the measurement probe placement. Additionally, it is also relevant to know the behavior of the rotor wake if several ANDroMeDA aircraft are supposed to measure wind speed in a group. Only if it can be made sure that one aircraft is not influenced by another aircraft flying ahead this multi aircraft measurement will yield in satisfying results.

With analytical formulations little insight can be gained about the rotor wake. For an aircraft propeller in forward flight (corresponds to a multirotor aircraft in climb) the propeller thrust is related to the induced velocity in the rotor disc by:

$$T = 2\rho A(v_\infty + v_i)v_i \quad (5.7.1)$$

For a rotor inclined by an angle α the induced velocity cannot be determined analytically because the exact shape of the stream tube is not known. Glauert derived an empirical relation in [18]:

$$T = 2\rho A \cdot v_{res} \cdot v_i \quad (5.7.2)$$

$$= 2\rho A \cdot \sqrt{(v_\infty \cdot \sin(\alpha) + v_i)^2 + (v_\infty \cdot \cos(\alpha))^2} \cdot v_i$$

The velocity in the rotor disc v_{res} is hereby calculated by the vector addition of the free-stream velocity v_∞ and the induced velocity v_i as shown in Figure 5.21. This empirical relation is widely (compare [43] and [44]).

Such a simplified analytical approach can only calculate the velocity directly in the rotor disc. Upstream and downstream of the rotor disc no quantitative velocity can be determined. Using simple momentum theory, it can be derived that the induced velocity "far away from the rotor disc", as often stated in literature, is twice of the induced velocity inside the rotor disc. How far from the disc this maximum is reached cannot be derived using analytical equations.

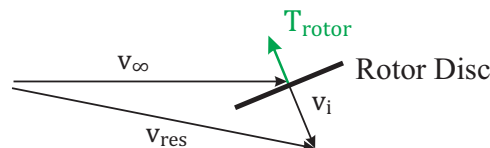


Figure 5.21: Velocities in the rotor disc according to simple momentum theory.

To obtain a better understanding of the rotor wake a number of two dimensional CFD simulations with an actuator disc model as well as one three dimensional CFD simulation with a rotating rotor have been conducted. The results of this simulations have been validated with wind tunnel tests, wherever possible. The two dimensional simulations only need limited computational resources while the three dimensional simulation is very computational intensive so that it was used to validate the two dimensional simulations.

With the help of the simulations on inclined rotors the following questions can be evaluated:

- How accurate is the afore mentioned superposition of the velocity vectors of the free stream velocity and the induced velocity? Can it be used to predict the resulting direction of the rotor wake?

- How does the flow pattern in front of the rotor disc look like?
Since for most applications the flow field in front of a rotor is not relevant, only limited information can be found in the literature.
- At which position should the flow measurement probe be placed to minimize the influence by the rotors?
- How far behind the rotor disc will the ambient air flow still be disturbed?

The last question of interest is the dimensional analysis of the simulations: Can the results be adopted to other rotor sizes?

5.7.2 Simulation Description

The simulations have been conducted with the software ANSYS CFX which is a finite volume flow simulation software used to solve the Reynolds Averaged Navier Stokes Equations (RANS). Because of the finite volume method the two-dimensional simulations are only quasi two dimensional using a mesh with only one element in third dimension.

Investigated Flight Conditions

To ensure that the simulations match the operating conditions of ANDroMeDa, the corresponding inflow speeds, inclination angles and rotor thrusts have to be selected.

The rotor disc loading (D.L.) of ANDroMeDA is not known at this stage and a general understanding of the rotor wake is the target of the simulations. To select the range of disc loadings for the simulation, different multirotor configurations have been considered: A minimum disc loading

Aircraft Name	No. of rotors	TOW in g	$D_{rotor}[m]$	D.L. in N/m^2
JXD Airbus	4	12.2	0.03	42
Hubsan X4	4	35	0.055	36
3D Robotics DIY Kit	4	1900	0.254	92
SWE hexrotor	6	4000	0.3302	76

Table 5.2: Disc loadings for different multirotor configurations and sizes.

of $D.L._{min} = 20 N/m^2$ and a maximum disc loading of $D.L._{max} = 125 N/m^2$ has been chosen to cover the range of possible applications and flight conditions.

For a hovering flight in a head wind the rotor inflow speed v_∞ will be the ambient wind speed. Since wind speeds below $4 m/s$ are not relevant in the field of wind energy and the typical rated wind speed of an onshore wind turbine is $12 m/s$, a range between $v_\infty = 4 m/s$ and $v_\infty = 12 m/s$ has been chosen for the studies. It can be demonstrated by these studies that for wind speeds above this range, the rotor inflow and rotor wake direction can be easily predicted. The rotor inclination angle and rotor inflow speed are related to each other by the flight mechanics of the aircraft. This has been derived in Section 5.3.2. With the help of Eq. (5.3.4) for each inclination angle α_{disc} a corresponding thrust T_{rotor} can be calculated. With Eq. (5.3.5) for each inclination angle α_{disc} a corresponding inflow speed v_∞ can be calculated. These values are only valid for a steady hover. In dynamic maneuvers, for example, a combination of a very high thrust and a small inclination angle is possible. But it is useful to keep those relations in mind for the parameter

choice of the wake studies since it is not meaningful to investigate combinations that will only occur briefly in highly dynamic maneuvers. In general, a possible disc inclination between $\alpha_{disc} = 5^\circ$ and $\alpha_{disc} = 45^\circ$ is considered to be representative.

Meshes

The two dimensional simulations have been conducted with structured hexhedral meshes with only one element in the third dimension. The thickness of the actuator disc is $0.1D$ for all meshes. The disc consists of 60 elements in diameter and 15 elements in thickness. Figure 5.22 pictures the refinements close to the actuator disc following a parabolic law.

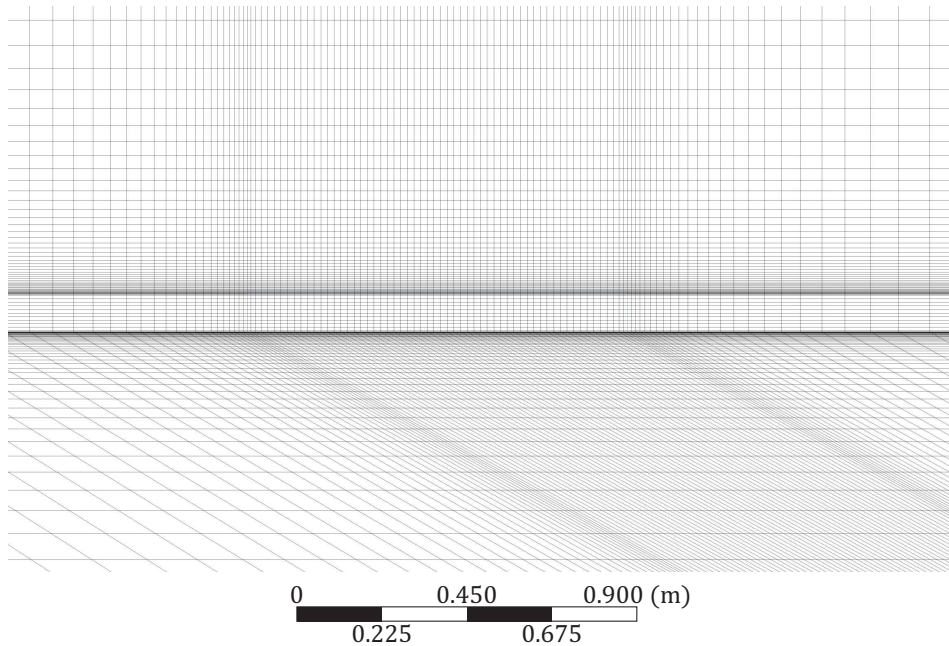


Figure 5.22: Mesh refinements close to the actuator disc.

Two different mesh geometries are used. While the actuator disc is always located horizontally the inflow direction is set according to the inclination angle. To place the mesh refinements as close as possible to the rotor wake, meshes with a designated wake angle of 45° and a designated wake angle of 22.5° have been created. The smallest in-plane element dimension of the actuator disc is $0.01D$ while the smallest element dimension perpendicular to the actuator disc is $0.001D$. As result of this topology some non-orthogonal, highly skewed elements exist at the lower left corner. The flow in this region is, however, considered not to be relevant to the problem. The meshes consist of 46 096 elements.

To ensure that the meshes are not too coarse for the problem some simulations were performed with 105 820 elements. With the use of a source term to model the ambient turbulence no significant differences could be detected, therefore the meshes with the lower element number have been used. Without the source term non negligible differences in the wake have been registered. However, these differences only apply for the far wake and are not relevant for the flow region in front of the rotor or the wake direction. The estimation of the wake decay without any artificial turbulence is not possible, even with finer meshes, because the dissipation of energy in the wake is a very sensitive process.

While all meshes described until here have been set up with a rotor diameter of $D = 1.0 m$

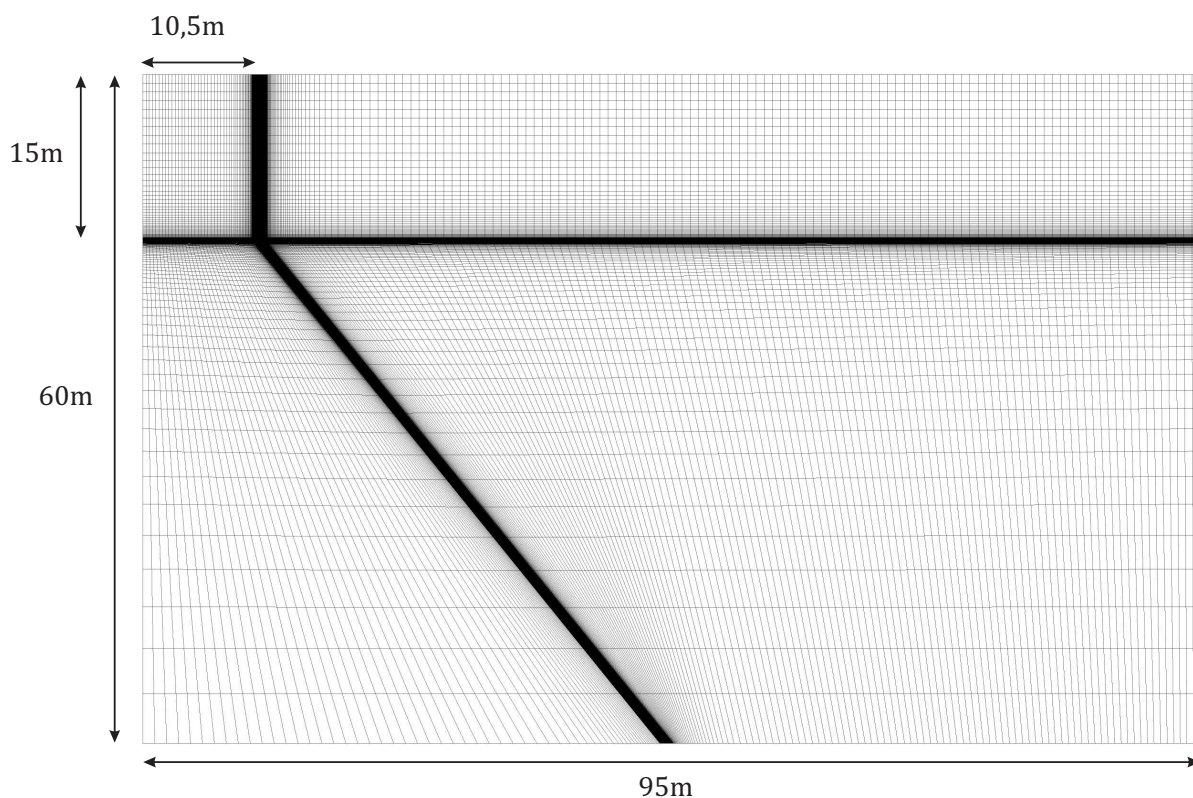


Figure 5.23: Mesh_45N.

all meshes have also been set up again with a rotor diameter of 0.5 m and 0.25 m to investigate the effects of different rotor sizes. The number of elements and control volume size remained unchanged for these meshes. Table 5.3 gives an overview of the used meshes. If not specified otherwise in the description, the meshes with $D = 1.0\text{ m}$ have been used for all simulations.

Mesh Name	Designated Inflow Direction	$D_{rotor}[m]$	No. of elements
Mesh_22N	22.5°	1.0	46 096
Mesh_22F	22.5°	1.0	105 820
Mesh_45N	45°	1.0	46 096
Mesh_45F	45°	1.0	105 820
Mesh_22N_025	22.5°	0.25	46 096
Mesh_22N_05	22.5°	0.5	46 096
Mesh_45N_025	45°	0.25	46 096
Mesh_45N_05	45°	0.5	46 096

Table 5.3: Mesh overview for the 2D simulations.

For the three dimensional simulation an unstructured mesh has been used and a three-bladed propeller of the type Master Airscrew 13x6 (13 inch diameter) was modeled. The complete mesh,

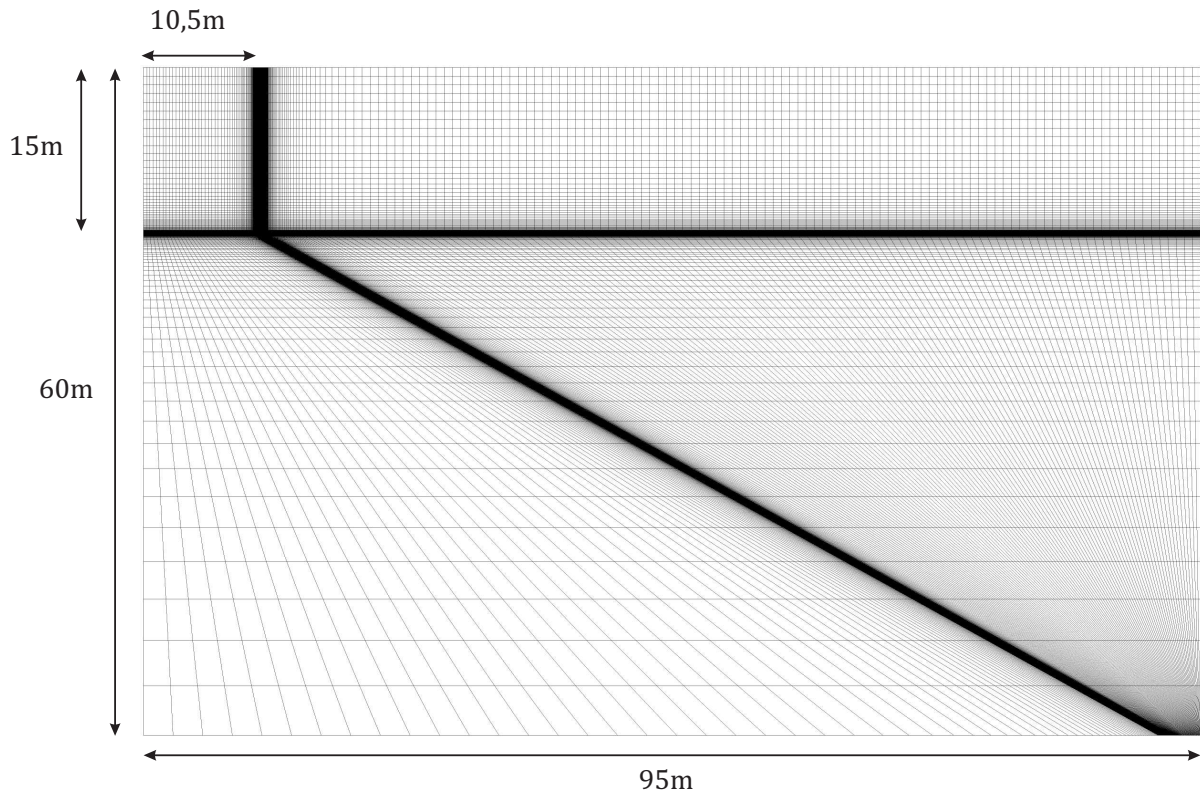


Figure 5.24: Mesh_22N.

shown in Figure 5.27, consists of 5.95 million elements. As pictured in Figure 5.25 and Figure 5.26 the rotor blades implement a finer mesh on their surface while the boundary layer is resolved to some degree by prism layers. Around the rotating mesh in form of a cylinder another cylindrical area is defined as mesh refinement region. Also the entire region where the wake is expected to develop was also refined.

Actuator Disc and Momentum Source

The actuator disc was realized with a region called a subdomain. For this subdomain a volume based momentum source term called "general momentum source" can be set up. This scalar value has the unit $Force/Length^3$. Hence, the thrust of the actuator disc calculates to:

$$T = source_{momentum} \cdot A_{rotor} \cdot t_{disc} \quad (5.7.3)$$

For the two dimensional simulations the rotor area is $A_{rotor} = D_{rotor} \cdot h_{disc}$ with $h_{disc} = 1\ m$ which is the width of the one element in the third dimension. If $source_{momentum}$ is set to a fixed value the disc loading becomes:

$$D.L. = source_{momentum} \cdot t_{disc} \quad (5.7.4)$$

The term $source_{momentum}$ can also be defined based on local coordinates. This opens the possibility to model a load distribution of the actuator disc. For most cases a uniform disc loading was used since no rotor data has been defined yet and the purpose of the actuator disc simulations is to provide a general understanding.

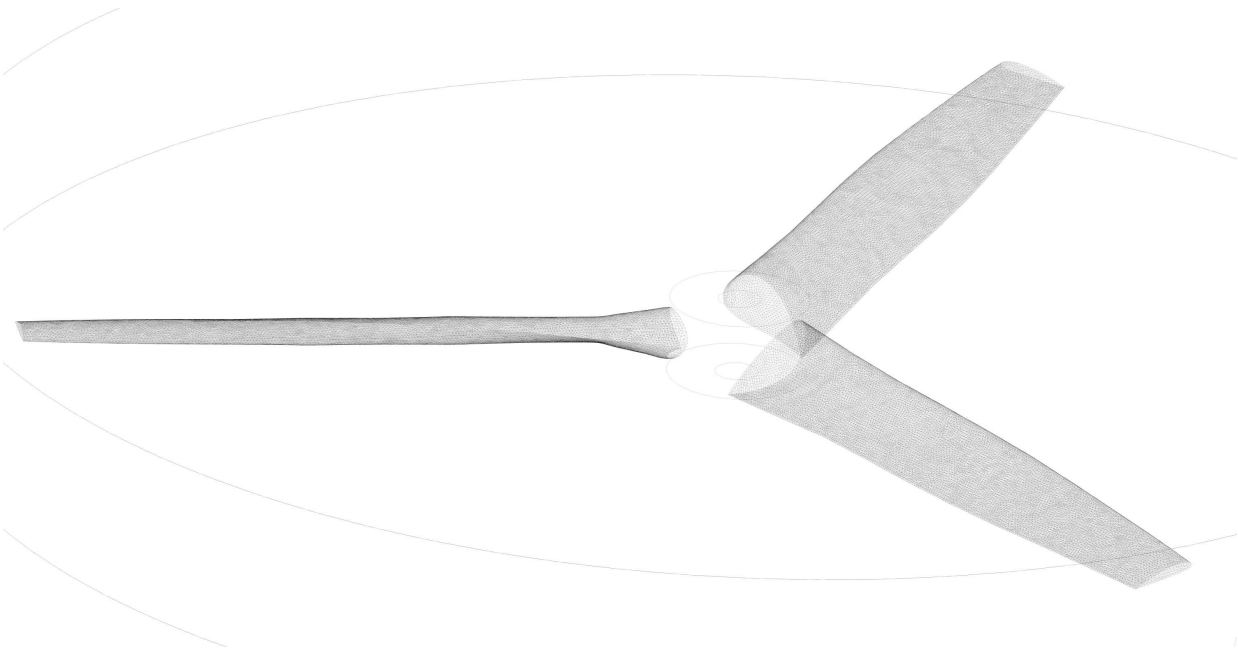


Figure 5.25: Modeled three bladed propeller with surface mesh.

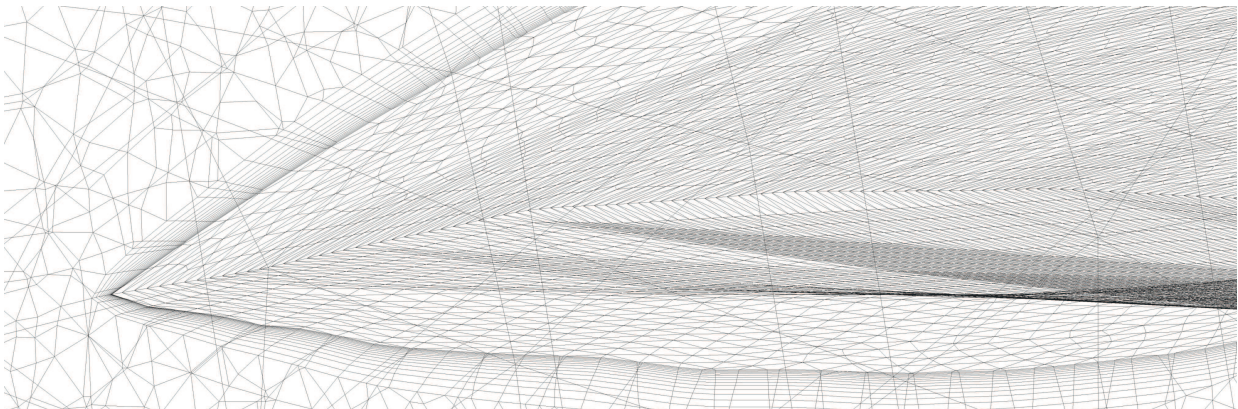


Figure 5.26: Mesh refinements at the propeller surface and prism layers.

Ambient Turbulence Modeling

Modeling turbulence in CFD should always be done with great care because of the numerical dissipation of the turbulence defined for a given region.

Because the ambient turbulence is assumed to have a strong impact on the rotor wake decay an artificial turbulence source was implemented. This procedure is described for CFX in [45]. In CFX a scalar quantity with the unit of $Power/Length^3$ can be defined as a source term for the turbulent kinetic energy (TKE). Because it is not possible to define a TKE or turbulence intensity (T.I.) target value in the control volume with this method the actual local source term is set for each time step as:

$$TKE_{source} = p \cdot (TKE_{desired} - TKE_{actual}) \quad (5.7.5)$$

The desired TKE can be related to the desired ambient turbulence intensity by:

$$TKE_{desired} = 3/2 \cdot (T.I._{desired} \cdot u)^2 \quad (5.7.6)$$

Unfortunately this does not result in a constant T.I. and the parameter p has to be readjusted

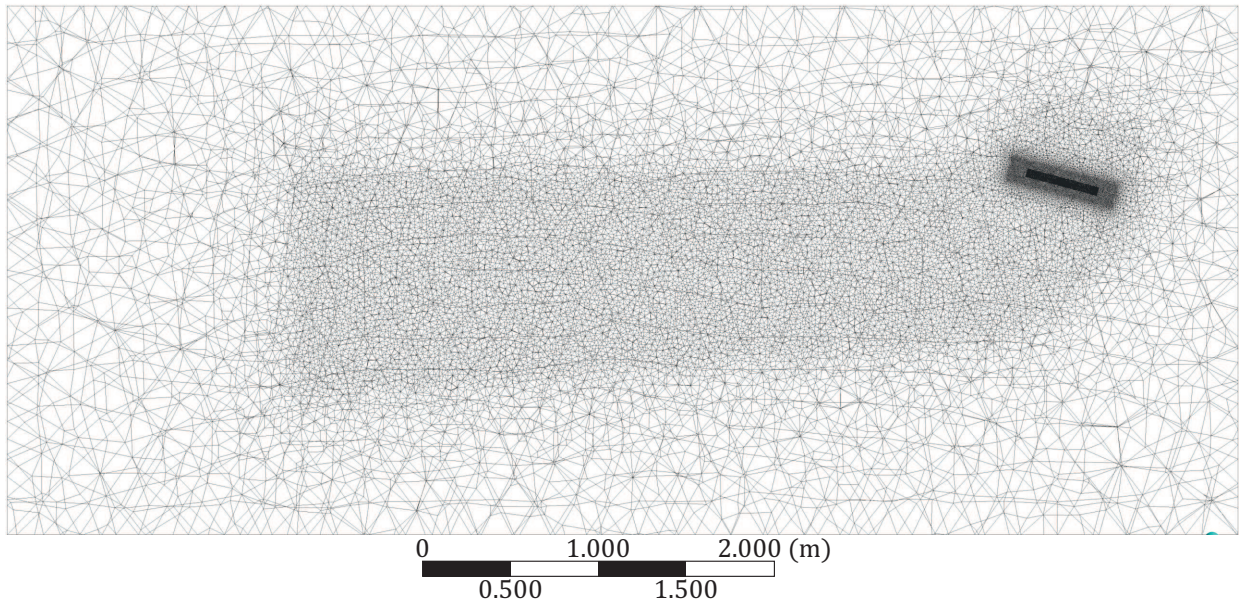


Figure 5.27: Overall view of the unstructured mesh for rotating rotor simulation.

for each simulation case.

One has to be careful about the physical meaning of this source term. To avoid overestimating its effect all simulations have been performed with and without this artificial turbulence. Some discrepancies with the method described in [45] which are assumed to lead to a non-physical result have been discovered at preliminary straight inflow propeller simulations. After all modeling ambient turbulence in further detail is beyond the scope of this project. For a more realistic model of the ambient turbulence, field measurements of straight and inclined rotors at different ambient turbulence levels have to be conducted.

General Settings

The time step was set automatically and the shear stress transport model (SST) was set. To avoid numerical instabilities the momentum source of the actuator disc was slowly increased during the first ten time steps. The inflow speed was set to a fixed value using the inlet property for the left face of the control volume.

5.7.3 Wind Tunnel Setup

To validate the different simulations with respect to the inflow field and wake of an inclined rotor, wind tunnel experiments have been conducted. The whirl tower described in Section A.1.4 has been mounted in a wind tunnel. The experiments have been conducted in the medium sized wind tunnel at the Institute of Aerodynamics and Gas Dynamics (IAG) at the University of Stuttgart. The tunnel is a Göttinger type tunnel with an open test section and a nozzle diameter of 1m.

The thrust was measured with the whirl tower to ensure that the disc loading in the experiments matches the disc loading in the simulations. Other measurements such as motor current, motor voltage, torque and RPM were not necessary for the investigations in this section. To visualize the rotor wake a laser sheet visualization technique has been used.

To determine the influence of a spinning rotor on the free-stream velocities, a one dimensional hot wire probe was used. The wire has a diameter of $d_{wire} = 10 \mu m$ and a length of $l_{wire} = 4 mm$. It was used in a constant temperature mode (CTA). The CTA electronics module has a built

in low pass filter of $f_{filter} = 5 \text{ kHz}$ while all measurements have been sampled with $f_{sample} = 10\,000 \text{ samples/s}$. The probe position could be precisely adjusted with the help of an electronic traverse system. Figure 5.28 depicts the wind tunnel setup with the hot wire probe while Figure 5.29 gives an overview of the different measurement locations.

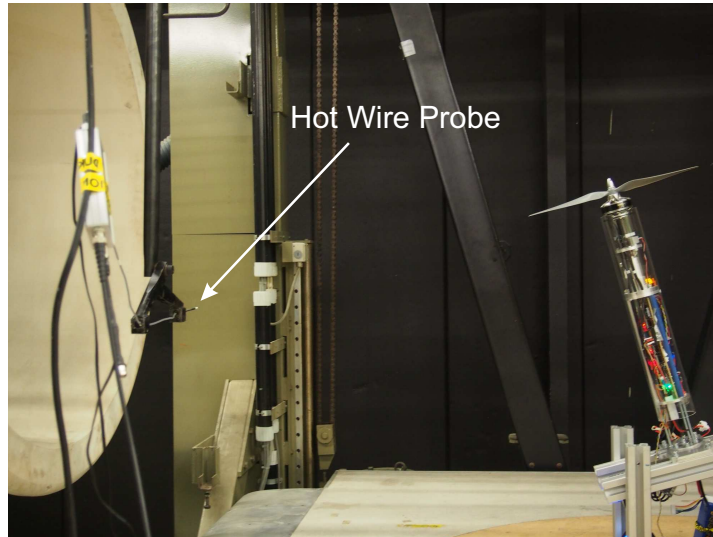


Figure 5.28: Wind tunnel setup with hot wire probe.

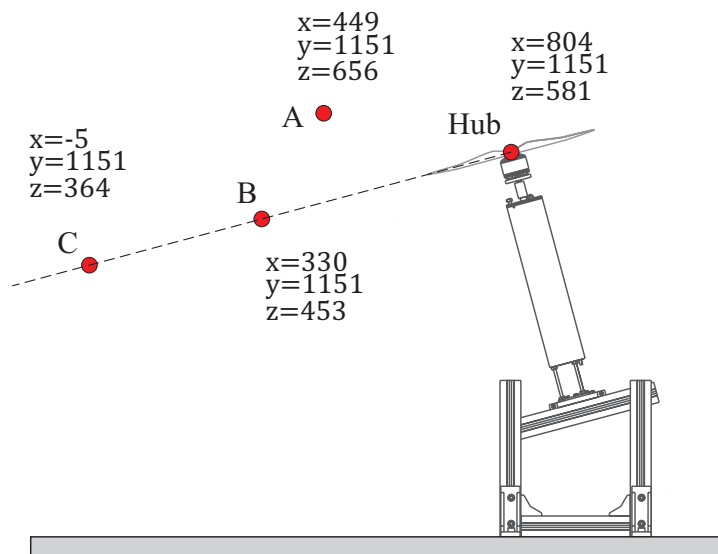


Figure 5.29: Hot wire probe locations. Drawing true to scale.

5.7.4 Oblique Inflow Rotor

Operating Conditions

The most relevant case for ANDroMeDA is the wake of a rotor in oblique inflow. For this setup three parameters can be varied:

- Rotor inclination / inflow angle.
- Inflow speed.
- Rotor thrust / disc loading.

To work with a reasonable parameter set, realistic flight conditions according to Eqs. (5.3.4 and 5.3.5) have to be considered. For example it would make no sense to use a very high thrust combined with a very low rotor inclination angle. Because this would represent the beginning of a climb maneuver but not a steady measurement flight.

Because the drag of the aircraft is still an estimate and the simulations are meant to be a general parametric study, the parameters have been chosen in a relatively wide range.

Wake

Parameter studies conducted with the simple 2D actuator disc model show that the induced velocity calculated with Eq. (5.7.2) and the vector addition of the free stream velocity and the induced velocity as shown in Figure 5.21 agrees well with simulation results. Because the maximum induced velocity is reached close to the rotor disc, the rotor wake realigns with the free stream direction after less than a couple of rotor diameters. This leads to a rotor wake displaced parallel to the free stream direction by the length z_d as shown in Figure 5.30. The parameter z_d depends on the ratio between the inflow speed and induced velocity. It becomes largest at low inflow speeds and large thrust. In all simulated cases z_d is less than $4D$.

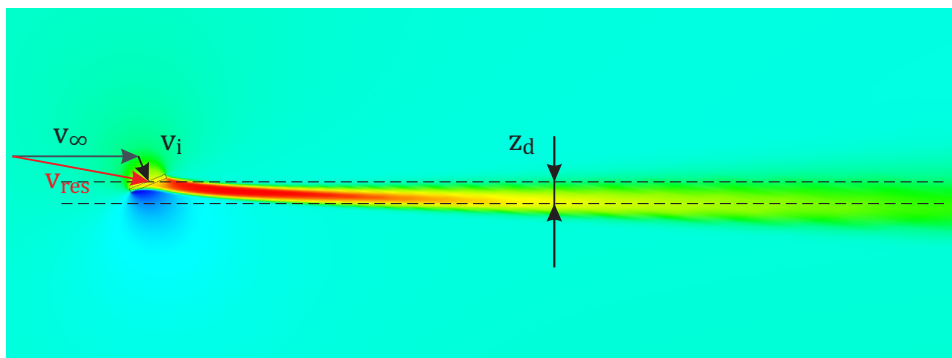


Figure 5.30: Realignment of the rotor wake with the free stream direction. Arrows v_i , v_∞ and v_{res} are drawn to scale. Parameters: $\alpha_{disc} = 22.5^\circ$; $v_\infty = 10 \text{ m/s}$; $D.L. = 125 \text{ N/m}^2$.

The wake decay of an inclined rotor is influenced by the ambient turbulence level. Fortunately this effect is much smaller than for an axial inflow propeller because the free stream introduces additional energy to dissolve the wake. Figure 5.32 shows the difference between axial inflow propeller and inclined rotor operating at different ambient turbulence levels. Nevertheless the distance for the wake to dissolve completely is the most difficult parameter to determine and still needs further investigations in form of field measurements. According to the 2D actuator disc simulations, a general recommendation would be to keep a distance of $50D$ for multi aircraft measurements. This recommendation is based on the assumption that the rotor wake can be considered as completely dissolved if the free stream velocity has recovered within a threshold of 2 %. Figure 5.33 depicts the wake speed for different simulation cases.

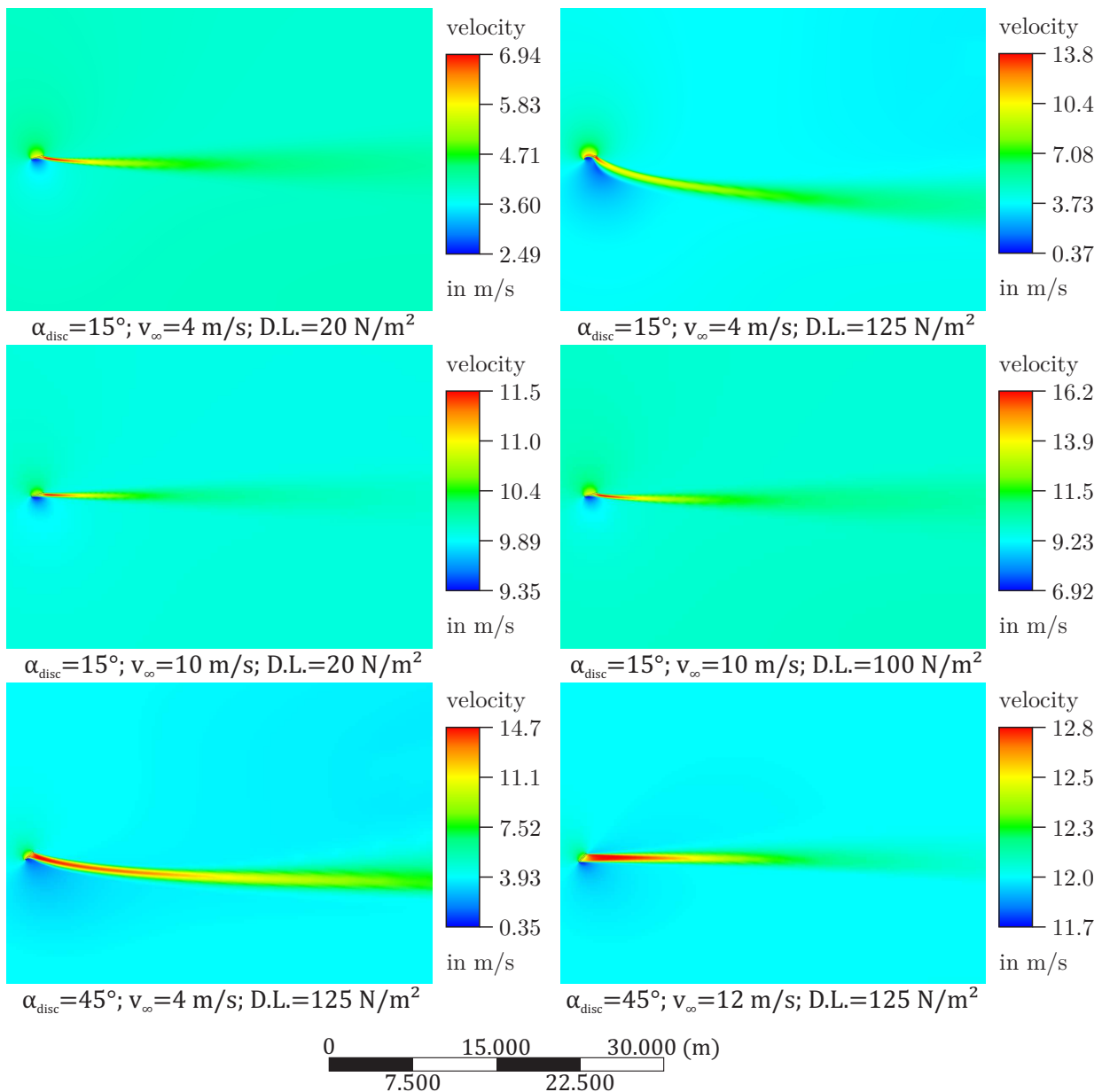


Figure 5.31: Overview of some simulation cases carried out with the standard meshes ($D_{rotor} = 1.0 m$.)

Inflow Region

The inflow region of an inclined rotor varies in strength depending on the free stream velocity. Its pattern is however always similar to a dipole singularity in potential flow theory. Above the rotor disc a low pressure region with an over-speed builds up while below the disc a high pressure, low speed region is formed. Figure 5.34 demonstrates how the inflow field changes with different free stream velocities for the same disc loading.

Hence, the best place for a measurement probe without too much disturbance from the rotor is sideways in the rotor disc plane as shown in Figure 5.35. It should be mentioned however that plotting only the velocities might result in underestimating the rotor influence. Figure 5.36 shows the vector field in the inflow region and thereby reveals a change in flow direction also at distances

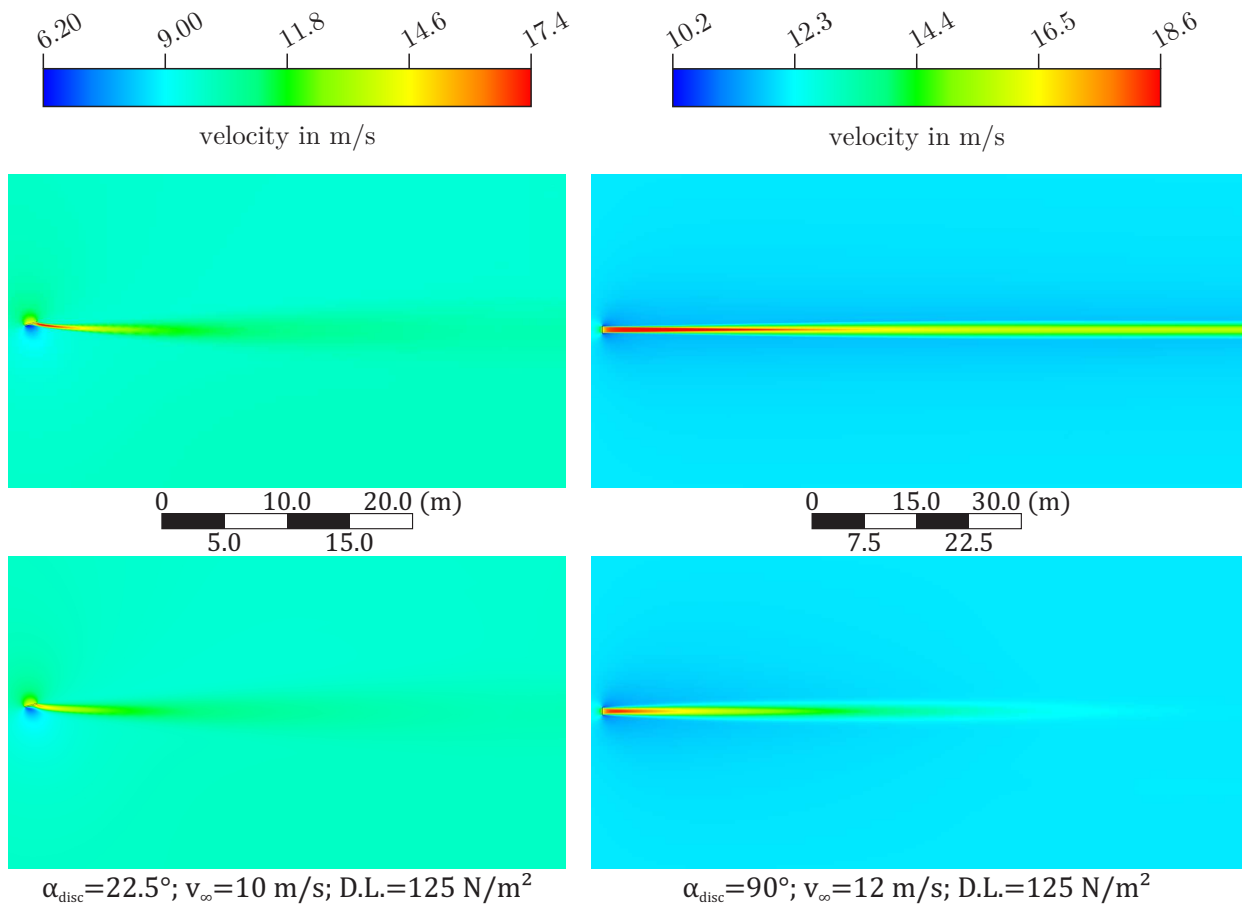


Figure 5.32: Influence of ambient turbulence on axial inflow propeller and inclined rotor. Top: Without artificial turbulence. Bottom: $T.I. = 10\%$.

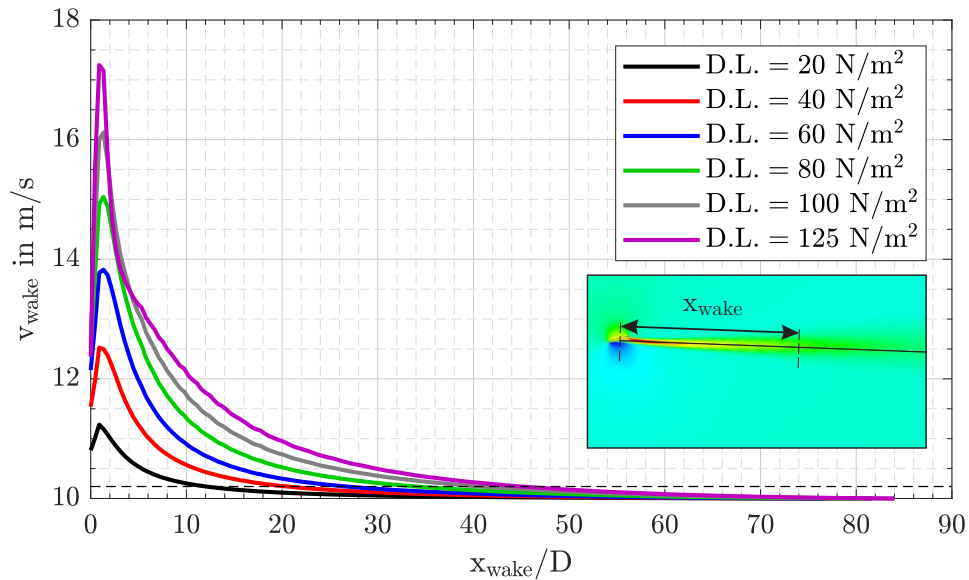


Figure 5.33: Velocities in the wake center line at $\alpha_{disc} = 15^\circ; v_\infty = 10 \text{ m/s}$. The horizontal line expresses the 2% threshold.

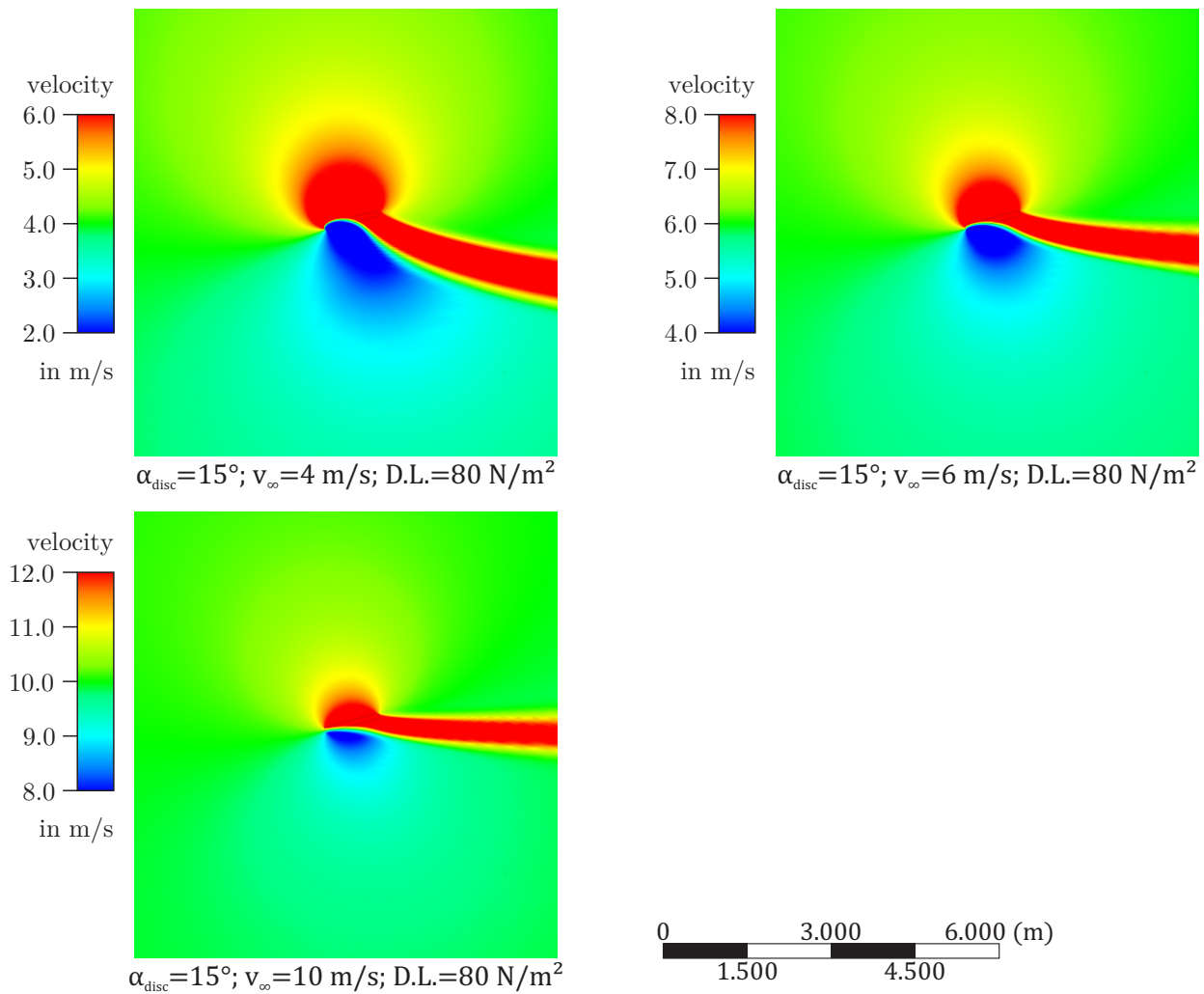


Figure 5.34: Inflow regions of a an inclined rotor with the same disc loading at different inflow speeds. To illustrate the disturbing effect on a wind measurement the color range was set to $v_\infty \pm 2 \text{ m/s}$ for all cases.

further away from the rotor where the magnitude of inflow speed is not much influenced by the rotor anymore. This fact was also observed in [12] in wind tunnel tests with a quadrotor.

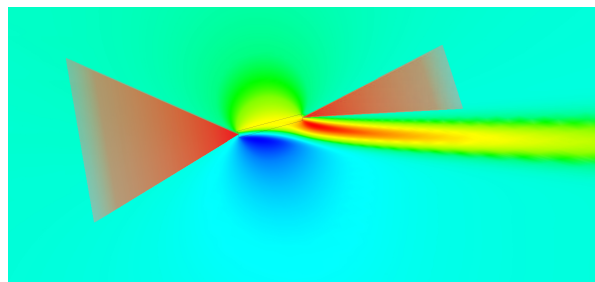


Figure 5.35: Possible regions for the placement of a flow measurement probe in the vicinity of an inclined rotor.

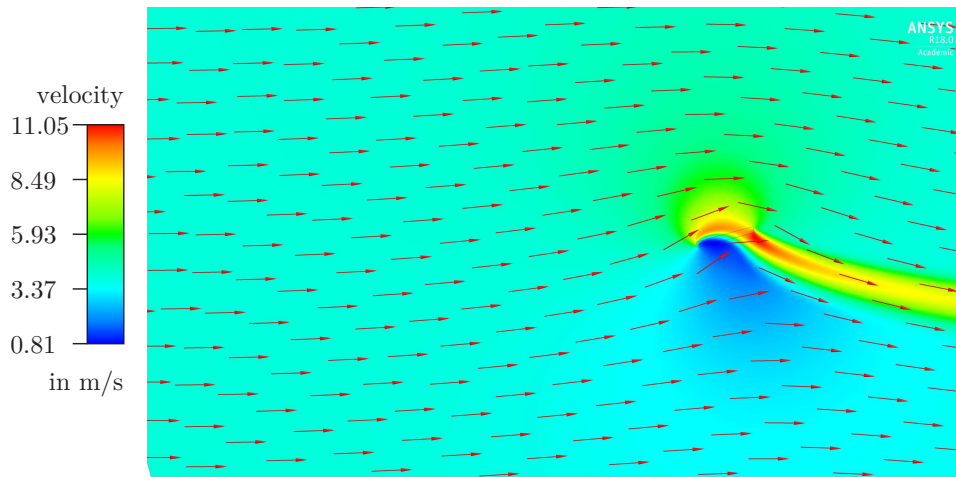


Figure 5.36: Vector field in the inflow region of an inclined rotor at $\alpha_{disc} = 15^\circ$, $v_\infty = 4 \text{ m/s}$, $D.L. = 80 \text{ N/m}^2$.

Comparison of Different Simulation Methods and Wind Tunnel Experiments

In addition to the low fidelity two dimensional actuator disc simulations, a high fidelity three dimensional simulation with a rotating rotor was carried out for the design point of ANDroMeDA. This simulation could confirm the relatively simple structure of the inflow region similar to a dipole in potential flow as well as the fast wake realignment with the free stream direction. But it also revealed that the high pressure, low speed region in the inflow below the rotor disc is slightly over-predicted while the wake displacement z_d is underestimated by the simple two dimensional simulations.

The underestimation of the wake displacement could also be confirmed by the wind tunnel tests. To investigate the reason of this underestimation, an additional simulation with a three dimensional actuator disc, as used for the drag estimation in Section 5.10, was conducted. This three dimensional actuator disc simulation shows two vortices, similar to the tip vortices of a lifting wing (Figure 5.38). It is assumed that those vortices are responsible for the most significant differences between the three dimensional and two dimensional simulations.

Considering the inflow region, wake direction and wake realignment the three dimensional actuator disc simulation proved to be completely sufficient to cover all the effects observed in the rotating rotor simulation and wind tunnel tests. The computational effort is still by magnitudes lower than for the rotating rotor simulation. The two dimensional actuator disc simulation is considered to be sufficient enough to demonstrate general tendencies and is very useful for parametric studies.

To confirm the simulation results regarding the flow measurements in front of a rotor, wind tunnel experiments with a hot wire probe have been conducted. A single, two bladed propeller of the type APC 13x6.5 has been operated at a fixed disc loading of $D.L. = 75 \text{ N/m}^2$. The measurement locations are shown in Figure 5.29. Inflow speeds of $v_\infty = 4 \text{ m/s}$ and $v_\infty = 10 \text{ m/s}$ have been studied.

A sampling rate of 10 000 samples/s has been used and therefore the turbulence intensity could also be determined. However no difference in turbulence intensity could be observed with and without the propeller running.

The wind tunnel speed is always fluctuating slightly and therefore it is difficult to tell if a change in the measured speed is the result of the propeller operation or a fluctuation of the wind tunnel

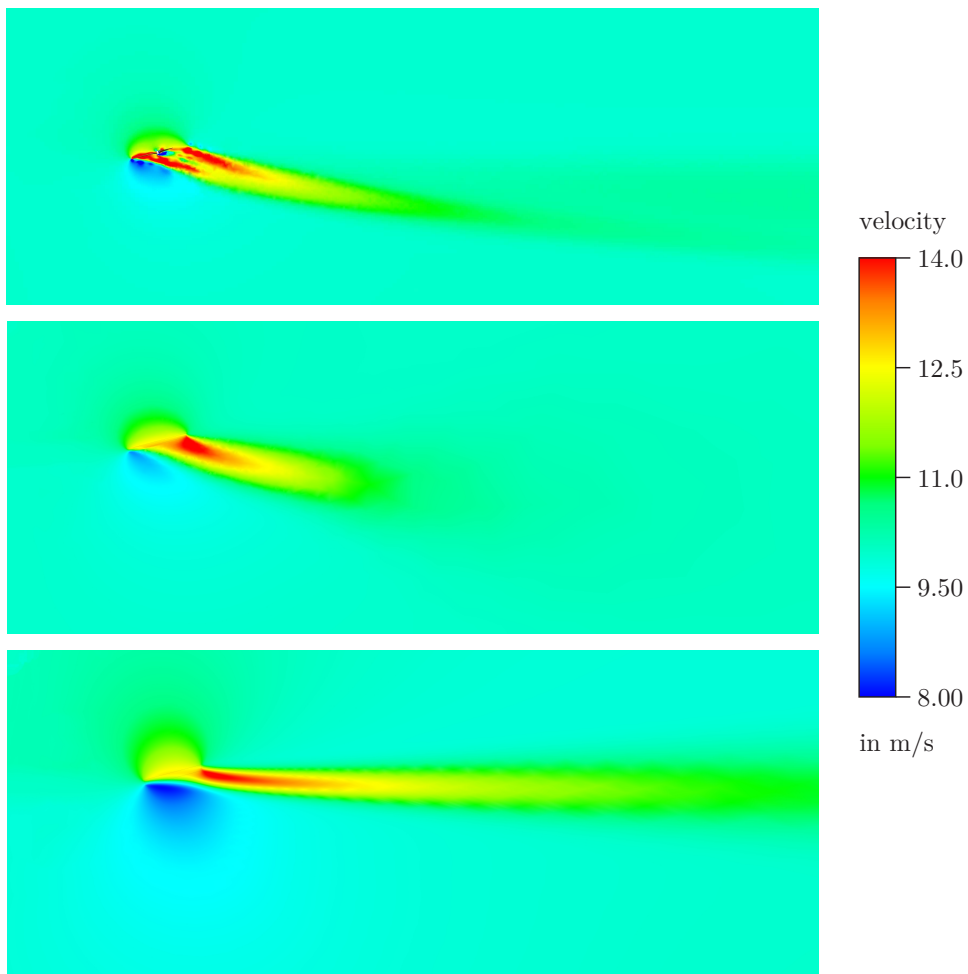


Figure 5.37: Comparison of different simulation techniques at ANDroMeDA design point ($\alpha_{disc} = 15^\circ$; $v_\infty = 10 \text{ m/s}$; $D.L. = 70 \text{ N/m}^2$). Top: Rotating rotor. Center: 3D actuator disc. Bottom: 2D actuator disc.

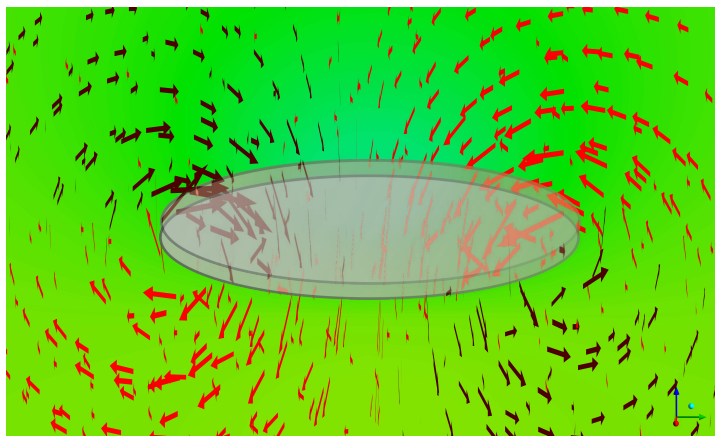


Figure 5.38: Vector field behind a 3D actuator disc reveals two vortices.

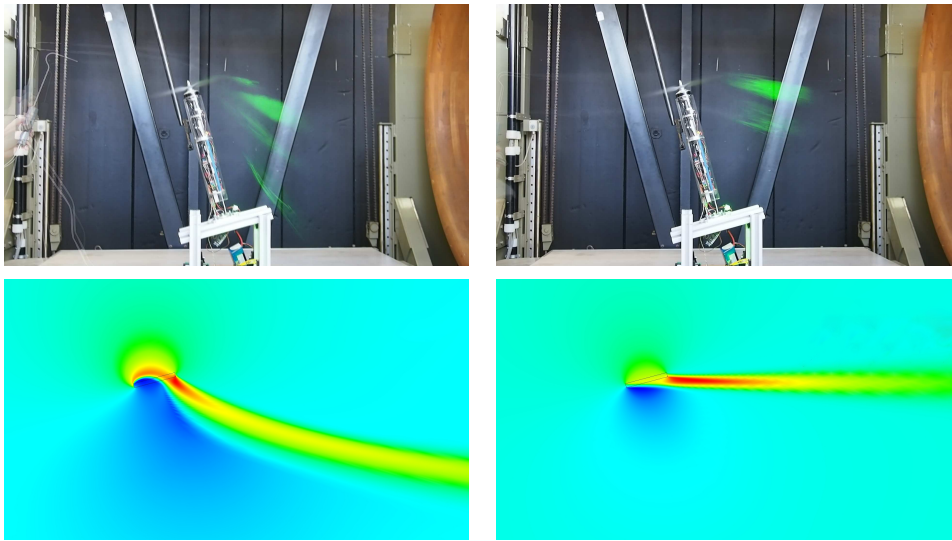


Figure 5.39: Comparison of 2D actuator disc simulation with wind tunnel experiment; Left: $\alpha_{disc} = 15^\circ$, $v_\infty = 4 \text{ m/s}$, $D.L. = 125 \text{ N/m}^2$. Right: $\alpha_{disc} = 15^\circ$, $v_\infty = 10 \text{ m/s}$, $D.L. = 20 \text{ N/m}^2$.

speed. To make it easier to observe the propeller influence the propeller was either started up or shut down during the measurement duration of $t = 10 \text{ s}$. Figure 5.40 shows the measurement results at points A, B and C. At point A the propeller operation increases the measured velocity while in point B the propeller operation decreases the measured velocity. This matches with the inflow region according to the simple actuator disc simulation shown in Figure 5.41. Interestingly the velocity change in point C can be larger than in point B even if it is farther away from the rotor disc. This behaviour is also shown in the simulations (see Table 5.4) but to a less significant extent.

At the design point of ANDroMeDA at $v_\infty = 10 \text{ m/s}$ only a slight influence of the propeller operation can be observed. Even at point A, very close to the rotor disc, the error is only about 1 % to 2 %. At the lower speed of $v_\infty = 4 \text{ m/s}$ the error is larger but still acceptable for field measurements.

	Point A	Point B	Point C
Δu at $v_\infty = 4 \text{ m/s}$	+1.18	+0.028	-0.06
Δu at $v_\infty = 10 \text{ m/s}$	+0.46	-0.042	-0.043

Table 5.4: Velocity changes according to 2D simulation.

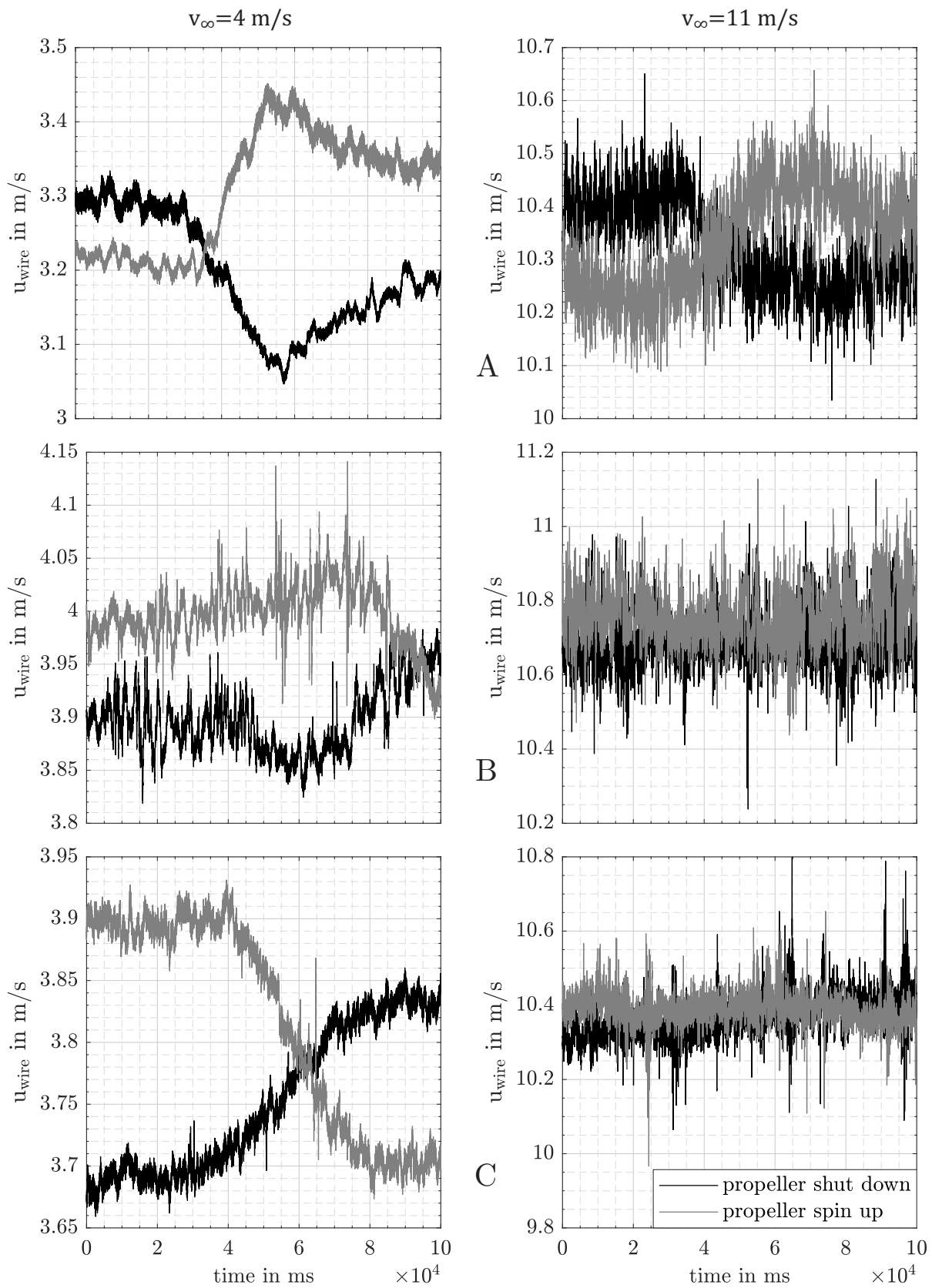


Figure 5.40: Hot wire measurements in the wind tunnel close to a rotor operated at $\alpha_{disc} = 15^\circ$; $D.L. = 75 \text{ N/m}^2$.

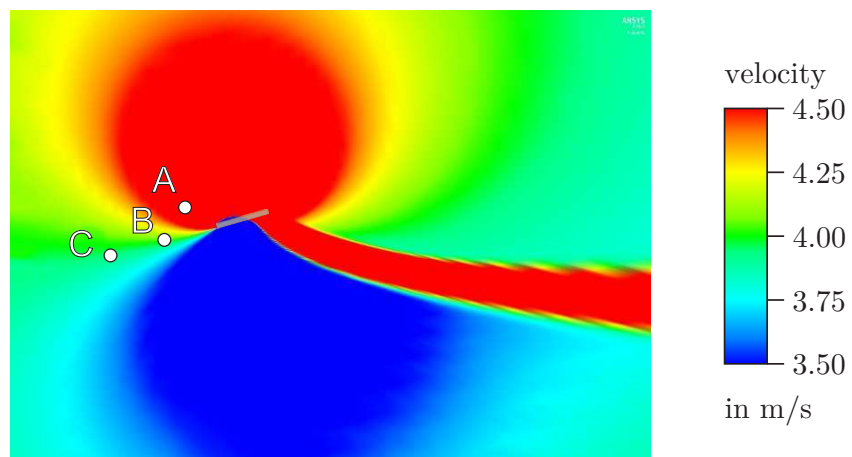


Figure 5.41: Hot wire measurement points shown in 2D actuator disc simulation with extensively drawn velocity ranges.

5.7.5 Dimensional Analysis of the Results

Since the rotor diameter for the final ANDroMeDA aircraft is not fixed yet, and since it is of general interest to know how different rotor diameters will influence the flow field, parameter studies have been conducted. Therefore the previously described meshes for a rotor diameter of $D_{rotor} = 0.5 \text{ m}$ and $D_{rotor} = 0.25 \text{ m}$ have been used.

Disc Loading

It can be observed that with a constant disc loading the inflow region and wake structure of an inclined rotor stays absolutely unchanged if the length scales are also adjusted to $x/D = const.$. Figure 5.42 demonstrates this. Rotor diameters and also element sizes of the mesh are changed but the picture size has been adjusted accordingly (compare scale at the bottom of the pictures).

This is a very favorable outcome since recommendations about the distance of the measurement probe to the rotor disc and distance of following aircraft are valid for all rotor diameters if expressed by multiples of rotor diameters instead of meters.

Advance ratio

Additionally, it could be observed that a constant advance ratio μ will result in the same wake displacement z_d and the same shape of the wake although the wake speeds are different as shown in Figure 5.43. This fact could be beneficial for the previously mentioned simplified modeling of the rotor wake by potential flow theory because it eliminates one parameter. Instead of a matching inflow speed and a matching disc loading / induced velocity these two parameters could be combined by a matching advance ratio. Consequently with only two sets of parameters: μ, α_{disc} the wake direction could be determined in real time with potential flow equations or interpolated from a lookup table. Because the actuator disc simulations do not include any rotational speed the advance ratio $\mu = v_\infty / (\Omega \cdot r)$ has to be expressed as a function of disc loading $D.L.$. Since the thrust is a function of the square of the rotational speed a constant advance ratio results in the following equation:

$$\frac{D.L.2}{D.L.1} = \left(\frac{v_{\infty,2}}{v_{\infty,1}} \right)^2 \quad (5.7.7)$$

5.7.6 Modeling Approaches

A simple approach to model the inflow field and wake direction of an inclined rotor is the use of potential flow theory. Figure 5.44 gives an example of the flow field created by the superposition of a uniform stream potential function with a potential vortex. Because the flow field is similar to the flow around an inclined rotor, it is assumed that it is possible to adjust the parameters to achieve a close fit for different operating conditions of the rotor. This approach has not been pursued any further yet but could result in the possibility of real-time modeling the wake direction and therefore improved measurements in a group of several ANDroMeDA aircraft. The ground control station could automatically adjust the flight path to fly in a close formation and still avoid the rotor wake of other group members.

An even less computational intensive approach to predict the rotor wake is a look-up table according to the dimensional analysis results in the previous section. If the velocity of the wake is also of interest, a look-up table with three dimensions, v_∞, α_{disc} and $D.L.$, would be necessary. If the knowledge of the wake direction is sufficient a look-up table with two dimensions, α_{disc} and μ would be sufficient.

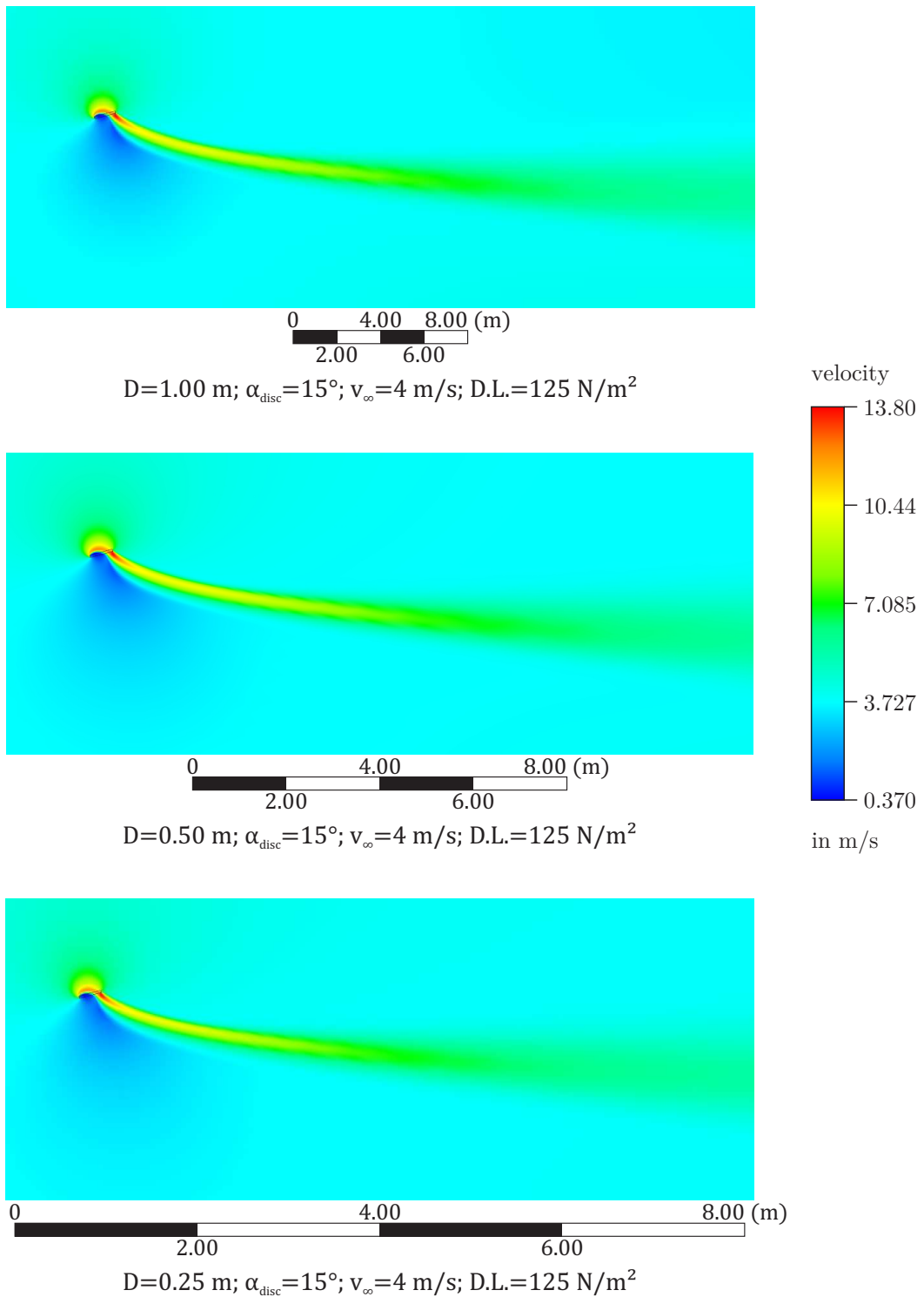


Figure 5.42: Wake of an inclined rotor at different rotor diameters.

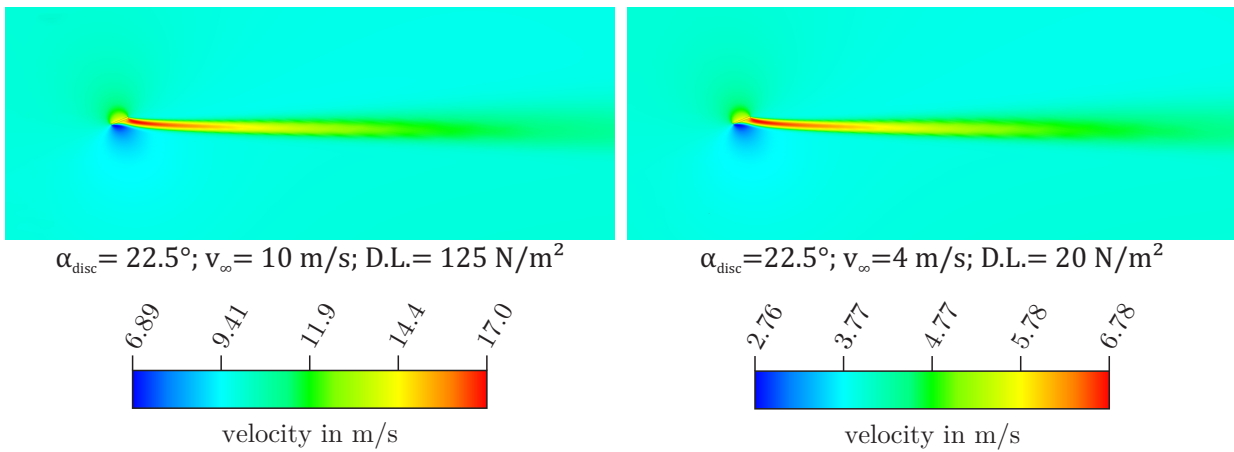


Figure 5.43: Wake of an inclined rotor at two different operating conditions which both result in the same advance ratio μ . Turbulence intensity $T.I. = 5\%$.

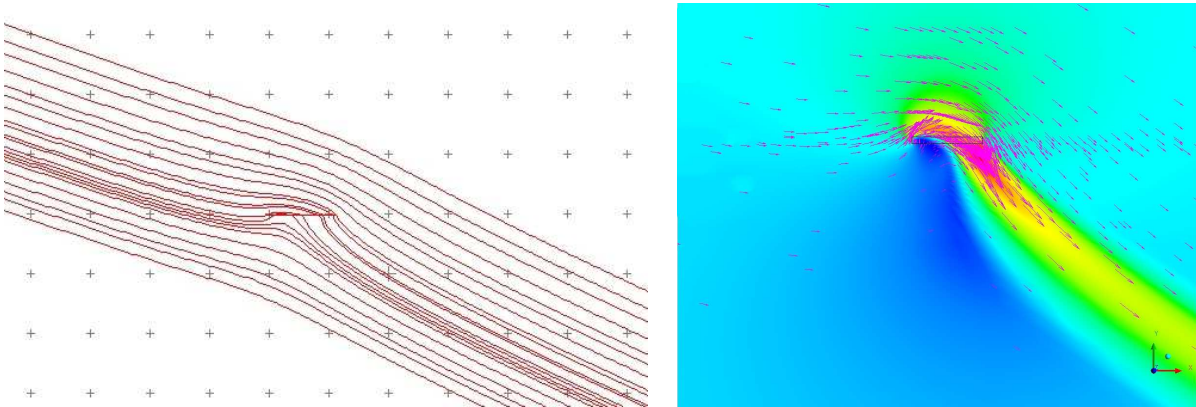


Figure 5.44: Similarity of a flow field created by superposition of singularities in potential flow and an inclined rotor simulated with a 2D actuator disc.

5.7.7 Conclusions

After several simulations and wind tunnel experiments regarding the inflow region and wake of an inclined rotor it could be ensured that measurements of the ambient flow in the vicinity of a rotor are feasible. The following recommendations can be made:

- Measurements at $v_\infty < 4m/s$ should be avoided.
- If an aircraft is flown directly in the wake of another aircraft a distance of $d_{aircraft} > 50 D$ should be maintained.
- The best possibility to avoid flying in the wake of another aircraft is to stagger the aircraft horizontally or vertically by at least $4 D$. In general the wake direction is very easy to predict since the wake will always realign with the initial inflow direction within only a couple of rotor diameters.
- 2D actuator disc simulations with a very low computational effort are sufficient for general parameter investigations but due to the lack of three-dimensional effects in the wake a 3D actuator disc simulation provides better results. A rotating rotor simulation with its very high computational effort is not necessary to characterize the inflow region of the rotor or the wake direction.

The work done in this section was focused on the investigation of a single rotor / propeller. It is also conceivable that other effects come into play when several rotors are combined. Therefore the flow field of an entire multirotor aircraft could be investigated by a simulation with several actuator discs or by further wind tunnel experiments in the future.

5.8 Aerodynamic Considerations on Rotor Sizing

5.8.1 Problem Description

From simple momentum theory it is known that a larger rotor will always result in a lower induced power and hence in a lower power needed to hover. A very good demonstration for that principle are the large human powered helicopters that have been built in the last decades [46]. However, the ANDroMeDA aircraft will not be designed to hover in calm air but to hover in headwinds of $v_\infty = 11 \text{ m/s}$ and above.

Consequently, the question of aerodynamic sizing of an inclined rotor arises. If an optimal rotor size for the design point exists, it should be determined.

The phrase "optimal rotor size" in this chapter is solely focused on rotor aerodynamics. Clearly, other parameters like motor mass, resulting motor arm length, rotor dynamics etc. also have to be taken into account. In addition to the maximum rotor size the scalability of rotor geometry and rotational speed will be investigated.

5.8.2 Blade Geometry Scaling

Rotor in Hover

As already mentioned, the induced power of a hovering rotor decreases when the rotor size is increased. Consequently, the power needed to hover will converge to zero as the rotor diameter is increased to infinity. But even with that knowledge one might ask: "How can the blade chord and rotational speed be scaled? Can a very large rotor be built for a very low thrust or will the blade's airfoils be operated below their design points on such a large rotor?"

The scaling laws for a hovering rotor will be derived with the help of an optimal rotor according to [47]. An optimal rotor has a hyperbolic blade chord distribution and a hyperbolic blade pitch angle distribution:

$$c(r) = c_R \cdot \frac{R}{r} \quad (5.8.1)$$

$$\theta(r) = \alpha_R + \frac{v_{i,0}}{\Omega \cdot r} \quad (5.8.2)$$

This will result in a constant angle of attack for all blade positions of $\alpha_R = \text{const.}$ and a constant induced velocity along the blade radius of $v_i = v_{i,0} = \text{const.}$ The following degrees of freedom remain to be scaled for an optimal rotor:

- Scaling of the rotational speed Ω .
- Scaling of the blade chord / the chord c_R at the blade tip.

These two parameters have to be chosen such that the thrust remains constant. Furthermore, the objective of rotor scaling is to preserve the aerodynamic properties of the rotor such as the figure of merit or the airfoil lift and drag coefficients at all blade sections for different rotor sizes.

According to [48] the figure of merit of a rotor can be expressed purely by the rotor solidity σ and airfoil coefficients:

$$F.o.M. = \frac{1}{1 + \frac{\frac{2}{3} \cdot \sqrt{3}}{\sqrt{\sigma} \cdot \frac{c_l}{c_d}}^{3/2}} \quad (5.8.3)$$

Since the airfoil coefficients should not change, once the optimal rotor has been derived for one rotor diameter, the only way to leave the figure of merit unchanged is to keep the solidity σ constant when changing the rotor diameter:

$$\sigma_1 = \sigma_2 \rightarrow \frac{c_{R,2}}{c_{R,1}} = \frac{R_2}{R_1} \quad (5.8.4)$$

This means the blade chord is scaled linearly with the rotor diameter. The rotational speed can then be calculated from the requirement of equal thrust for both rotor sizes:

$$T = n \cdot \frac{\rho}{2} \cdot \Omega^2 \cdot c_{a\alpha} \cdot \alpha_R \cdot R \cdot \int_0^R c_R \cdot r dr = n \cdot \rho \cdot \Omega^2 \cdot c_{a\alpha} \cdot \alpha_R \cdot \frac{R^3}{4} \cdot c_R \quad (5.8.5)$$

With $T_1 = T_2$ it follows:

$$\frac{\Omega_2^2}{\Omega_1^2} = \frac{c_{R,1}}{c_{R,2}} \cdot \frac{R_1^3}{R_2^3} \quad (5.8.6)$$

In combination with Eq. (5.8.4) this leads to the relation:

$$\frac{\Omega_2}{\Omega_1} = \left(\frac{R_1}{R_2}\right)^2 \quad (5.8.7)$$

BEM simulations confirmed that this scaling law is not only valid for an optimal rotor but for any hovering rotor (compare Section A.1.2). For two different rotors that have been scaled according to the derived rules the following statements can be made:

- The thrust of the two rotors will be exactly the same without any need to adjust the blade pitch.
- The figure of merit will remain exactly the same. Accordingly, a well working geometry (plan-shape, twist, airfoils etc.), designed for one rotor diameter, will be applicable for other rotor diameters.
- The effective angle of attack for all blade sections will remain unchanged.
- The induced velocity along the rotor radius will change in quantity but will not change its distribution. E.g. an optimal rotor with $v_i = v_{i,0} = \text{const.}$ will remain an optimal rotor.

Therefore the derived rules can be taken as general scaling laws for a rotor in hover:

$$\frac{\Omega_2}{\Omega_1} = \left(\frac{R_1}{R_2}\right)^2 \quad (5.8.8)$$

$$\frac{c(r/R)_2}{c(r/R)_1} = \frac{R_2}{R_1} \quad (5.8.9)$$

With the help of this laws it is possible to upscale a rotor to an arbitrary size for a fixed thrust and hence it is possible to design a very large rotor, operating at a low thrust and low disc loading.

Propeller in Forward Flight

For a propeller in forward flight the induced velocity only has a minor influence, compared to a rotor in hover because the inflow velocity is a few magnitudes higher than the induced velocity ($V_\infty \gg v_i$). Hence the inflow angle ϕ can be determined as:

$$\phi(r) = \frac{v_\infty + v_i(r)}{\Omega \cdot r} \approx \frac{v_\infty}{\Omega \cdot r} \quad (5.8.10)$$

The inflow angle ϕ needs to remain unchanged when scaling the propeller in forward flight. Otherwise the lift distribution and the aerodynamic properties of the propeller will change. Therefore, the first approach to scale a propeller in forward flight is:

$$R \cdot \Omega = \text{const.} \quad (5.8.11)$$

The second approach is obtained from a fixed thrust value for two different rotor sizes. As a simplification, the thrust of a propeller blade with rectangular planform is considered. The thrust of a propeller, optimized to achieve the same lift coefficient $c_l(r) = \text{const.} = c_{l_{opt}}$ for all blade sections, is:

$$T = n \cdot \int_0^R c_{l_{opt}} \cdot \frac{\rho}{2} (\Omega \cdot r)^2 \cdot c \cdot dr = n \cdot \rho \cdot \frac{c_{l_{opt}}}{6} \cdot \Omega^2 \cdot R^3 \cdot c \quad (5.8.12)$$

From $T_1 = T_2$ follows:

$$\frac{c_2}{c_1} = \left(\frac{\Omega_1}{\Omega_2}\right)^2 \cdot \left(\frac{R_1}{R_2}\right)^3 \quad (5.8.13)$$

With the help of the first approach $\Omega_1 \cdot R_1 = \Omega_2 \cdot R_2$ the following relation can be derived:

$$\frac{c_2}{c_1} = \frac{R_1}{R_2} \quad (5.8.14)$$

This means that with an increasing propeller diameter the blade chord has to decrease. The limits are of course defined by Reynolds number effects (Reynolds number decreases linearly with the propeller diameter) and the static design of the propeller blade.

BEM simulations show that this scaling approach also works for propellers with arbitrary planforms. For two propellers, scaled according to these scaling laws, the following observations can be made:

- The thrust of the two propellers remains the same without a significant adjustment of blade pitch (adjustment less than 1.5°).
- The inflow angle and its distribution remain exactly the same.
- Angle of attack and lift coefficients for the blade sections remain nearly the same.

Consequently, the general scaling laws applicable for all propellers in forward flight are:

$$\frac{\Omega_2}{\Omega_1} = \frac{R_1}{R_2} \quad (5.8.15)$$

$$\frac{c(r/R)_2}{c(r/R)_1} = \frac{R_1}{R_2} \quad (5.8.16)$$

Conclusions

It can be shown that every rotor in hover and every propeller in forward flight can be aerodynamically scaled and there is no maximum propeller size per se. Limits are dictated by the Reynolds number and the static design of the blades, which have to become very slender for a large propeller. These two parameters should always be considered carefully.

For the inclined rotor no scaling law has been derived. It is assumed that the inclined rotor has to be scaled with a rule between a rotor in hover and a propeller in forward flight. This has to be done iteratively with BEM simulations.

From the other two operating conditions it can be concluded, that the inclined rotor has also no maximum rotor size and every propeller / rotor can be scaled to a reasonable extent without introducing airfoil losses. BEM simulations for inclined rotors confirmed this hypothesis and an almost constant figure of merit could be achieved for different rotor sizes. Because the design point of ANDroMeDA is much closer to a hovering flight, than to a propeller in forward flight, the scaling law for a hovering rotor can be applied. Since ANDroMeDA will be equipped with commercially available, fixed pitch propellers and therefore it is not feasible to design a custom made propeller no further generic BEM simulations have been conducted.

5.8.3 Induced Power

Even with a constant figure of merit for varying rotor diameters, the overall power can vary if the induced power changes. For this reason, the induced power for different operating conditions will be compared analytically.

Induced Power of a Rotor in Hover

The induced power of a rotor in hover will always decrease if the rotor diameter is increased:

$$P_i = \sqrt{\frac{T^3}{2 \cdot \rho \cdot A}} \quad (5.8.17)$$

For instance doubling the rotor diameter will always result in halving the induced power.

Induced Power of Propeller in Forward Flight

The induced power of a propeller in forward flight is given by:

$$P_{i_{vor}} = T \cdot \left(\frac{v_\infty}{2} + \sqrt{\left(\frac{v_\infty}{2}\right)^2 + \frac{T}{2 \cdot \rho \cdot A}} \right) \quad (5.8.18)$$

For an infinite propeller area ($A \rightarrow \infty$) the induced power will converge to the propulsive power $P_{propulsive} = T \cdot v_\infty$. Increasing the propeller size only makes sense up to a certain degree. Compared to a rotor in hover the absolute benefit becomes smaller with increasing propeller diameters. Therefore, it is useful to define a threshold, e.g. $P_{i_{vor}}/P_{propulsive} = 1.05 \dots 1.1$, to limit the propeller diameter to a reasonable value.

Induced Power of an Inclined Rotor

As already mentioned in Section 5.7, the induced velocity of an inclined rotor cannot be calculated from the classical momentum theory. Glauert introduced an empirical relation in [18], shown in

Eq. (5.7.2). This relation has to be solved for v_i numerically. With the induced velocity the induced power of an inclined rotor is given by:

$$P_i = T \cdot (v_\infty \cdot \sin(\alpha) + v_i) \quad (5.8.19)$$

Similar to the propeller in forward flight with increasing rotor diameter (for a fixed thrust, inflow velocity and inclination angle) the induced power converges to a finite value.

5.8.4 Conclusions and Maximal Propeller Size

As demonstrated in Figure 5.45 and Table 5.5, the induced power of a propeller in forward flight or a rotor at an angle of attack converges to a fixed value, while for a rotor in hover there is always potential to reduce the induced velocity by increasing the rotor diameter. This means that with respect to the induced power, without considering any power losses, the inclined rotor has a maximum useful diameter. The maximum useful size of an inclined rotor depends also on the

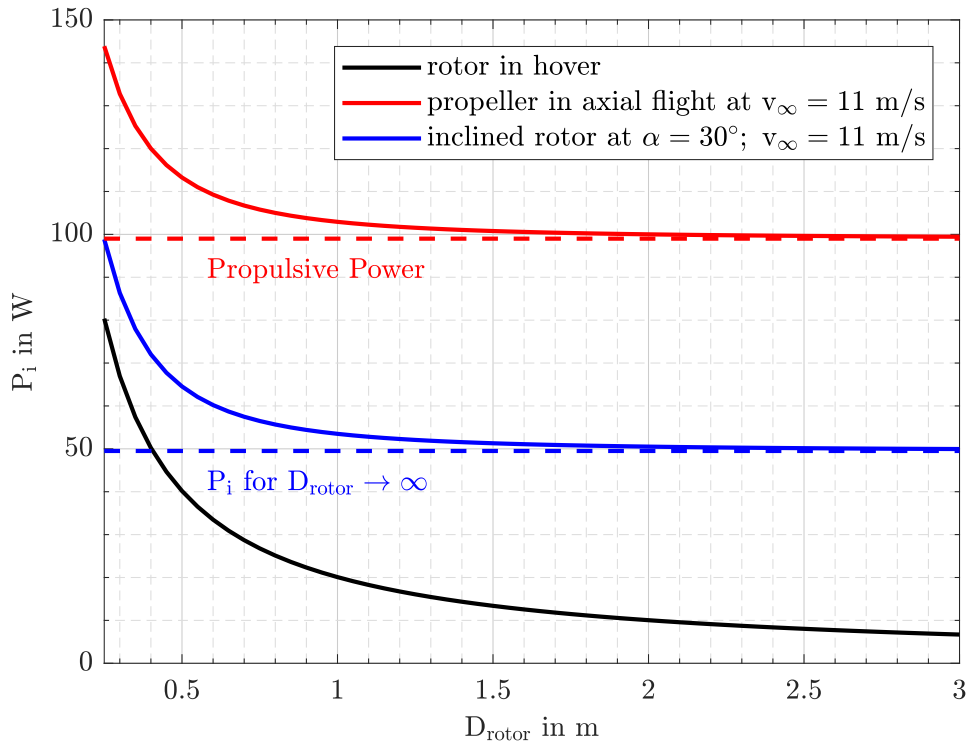


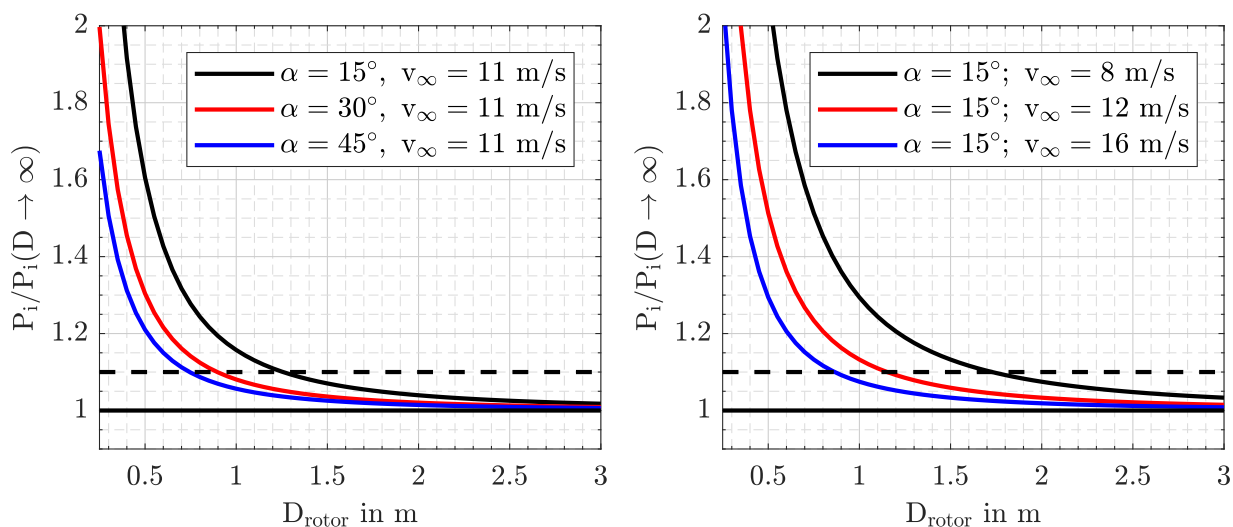
Figure 5.45: Induced power for different types of rotor operation at $T = 9 \text{ N}$; $\rho = 1.15 \text{ kg/m}^3$.

inclination angle and the inflow speed as shown in Figure 5.46. Because the number of rotors has not been defined yet, it is not possible to derive the thrust per rotor. Fortunately if the induced power is normalized with the induced power for a rotor of infinite size ($P_i/P_i(D \rightarrow \infty)$) the same disc loading will result in the same normalized induced power. Consequently, it is possible to derive a minimum disc loading if a limit value for the induced power is set. In case of ANDroMeDA this limit was set to 10 %:

$$\left(\frac{P_i}{P_i(D \rightarrow \infty)} \right)_{min} = 1.1 \quad (5.8.20)$$

With this minimal disc loading a maximal rotor diameter for the corresponding quad-rotor, hex-rotor and octo-rotor configurations can be determined. According to Section 5.3 the design wind

D in m	$P_{i_{hov}}$ in W	$P_{i_{prop}}$ in W	$P_{i_{rotor}}$ in W; $\alpha = 30^\circ$
		$v_\infty = 11 \text{ m/s}$	$v_\infty = 11 \text{ m/s}$
0.25	80.36	143.89	98.85
0.5	40.18	113.25	64.54
1.0	20.09	102.92	53.49
2.0	10.05	100.01	50.51
$\rightarrow \infty$	0	99.0	49.5

Table 5.5: Induced power for different rotor operating conditions.

Figure 5.46: Induced power at different angles of attack and different inflow speeds at $T = 9 \text{ N}$; $\rho = 1.15 \text{ kg/m}^3$.

speed is $v_\infty = 12 \text{ m/s}$ and according to Figure 5.5 the rotor angle of attack is $\alpha = 28^\circ$. Figure 5.5 was derived with the assumption of an aircraft drag of $c_D \cdot A = 0.3 \text{ m}^2$. Since this conventional approximation expresses a rather large drag, it is expected that the angle of attack for the final aircraft will be smaller. Figure 5.47 gives an overview of the normalized induced power over disc loadings for different angles of attack at the design inflow speed. The assumption of $\alpha = 28^\circ$ results in a minimal disc loading of $(D.L.)_{min} = 15.9 \text{ N/m}^2$ (see Figure 5.47). This results in the maximal rotor diameters shown in Table 5.6. It should be emphasized, that these maximal diameters derived here are only based on aerodynamics. When considering the actual benefit in flight time, the additional weight due to the larger rotors has to be considered. In most cases it will

No. of Rotors	D_{max}
4	1.06 m
6	0.86 m
8	0.75 m

Table 5.6: Maximal rotor diameters for different configurations at $T_{total} = 55.6 \text{ N}$; $v_\infty = 12 \text{ m/s}$; $\alpha = 28^\circ$.

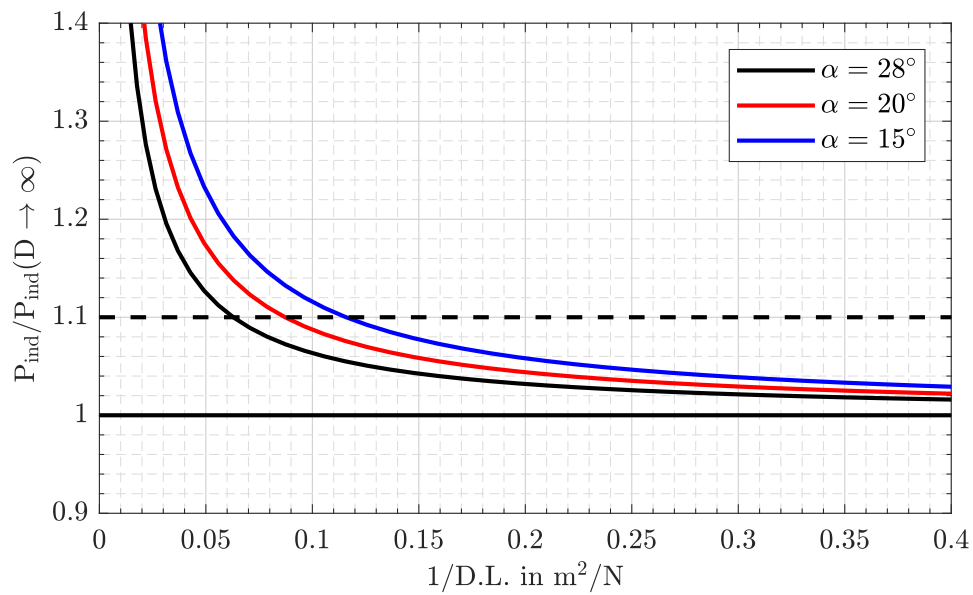


Figure 5.47: Induced power for different angles of attack at the ANDroMeDA design point ($v_\infty = 12 \text{ m/s}$; $\rho = 1.15 \text{ kg/m}^3$).

be necessary to use a larger and heavier motor to drive larger rotors. The only other option is to use a gear, which has been excluded because of the reduced lifetime and higher maintenance effort. For a fair comparison a configuration with larger rotors has to be compared to a configuration with the original rotor size, equipped with a heavier battery, which yields most often in a very similar flight time.

Also the lower rotational speed of the rotors could result in a slower response time and hence, a reduced flight control authority. All those aspects will be investigated in detail in the following sections.

5.9 Possible Rotor Layouts

In order to decide for a number of rotors and a rotor layout, different layouts have to be compared and their effects on all disciplines have to be analyzed. Before carrying out a detailed comparison between the possible configurations in Section 5.12, all rotor layouts will be shortly described and their flight mechanical properties will be derived analytically. In the following sections their aerodynamic characteristics will be described. A mass estimation of all configurations can be found in Section B.

To make sure to that the configurations are comparable to each other, the rotors are sized for a constant disc loading of $D.L. = 70 \text{ N/m}^2$. As previously derived, this results in the identical induced power for all configurations. The disc loading of $D.L. = 70 \text{ N/m}^2$ corresponds to a rotor diameter of $D_{rotor} = 0.4 \text{ m}$ for a hexrotor configuration. According to the experiences with the SWE hexrotor, this is a reasonable choice and not too far from a conventional design. As stated in the last section, the rotor diameter can be increased further with aerodynamic benefits but also with disadvantages regarding the mass of the propulsion system. A detailed approach to size the rotors for the final configuration will be presented in Section 5.14.

The distances between the rotors in x and y direction will be chosen relatively close to each other for the H-4 configuration and will then be flight mechanically scaled for the other configurations, so that every configuration is able to produce the same control moments. This ensures an objective comparison between the configurations regarding weight and drag.

No. of Rotors	D_{scaled}
4	0.49 m
6	0.40 m
8	0.35 m

Table 5.7: Rotor diameters for the different configurations with $D.L. = 70 \text{ N/m}^2$.

5.9.1 Configuration 1: H-4

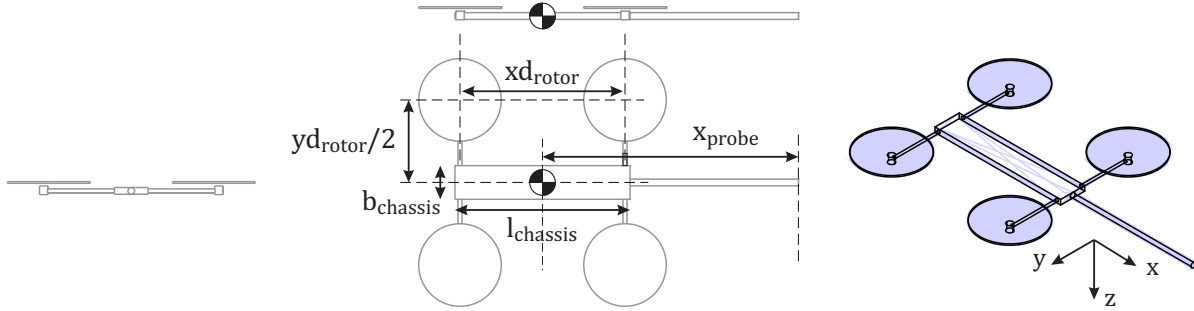


Figure 5.48: H-4 Rotor Layout.

The quadrotor configuration is the most common multirotor configuration. It is also possible to arrange the motor arms as a cross (so called X4 or +4 configuration) but this does not allow the motor arms to be tilted. Due to the use of a tilting rotor configuration (see Section 5.6), the H-4 configuration is the only possible quadrotor configuration.

Flight Mechanics

To produce plain control moments without introducing a climb maneuver, the rotors on one side of the frame can only use a maximum thrust of $T_{max} = 2 \cdot T_{hover}$, while the thrust on the other side is reduced to zero (compare Figure 5.12). For a hover without wind and consequently zero tilt angle ($\sigma_{rotor} = 0^\circ$) this results in a pitching moment of:

$$M_{max} = 2 \cdot \frac{x_{d_{rotor}}}{2} \cdot (2 \cdot T_{hover}) \quad (5.9.1)$$

and a rolling moment of:

$$L_{max} = 2 \cdot \frac{y_{d_{rotor}}}{2} \cdot (2 \cdot T_{hover}) \quad (5.9.2)$$

To calculate the maximum yawing moment the rotor torque has to be known. Thrust and torque are both proportional to the square of the rotational speed of the rotor:

$$T = C_T \cdot \rho A (\Omega R)^2 \quad (5.9.3)$$

$$Q = C_Q \cdot \rho A R (\Omega R)^2 \quad (5.9.4)$$

Hence, a rotor at double hover thrust ($T = 2 \cdot T_{hover}$) produces also twice the hover torque ($Q = 2 \cdot Q_{hover}$). With two diagonal rotors spinning at $T = 2 \cdot T_{hover}$ and two rotors completely standing still this results in:

$$N_{max} = 4 \cdot Q_{hover} \quad (5.9.5)$$

According to BEM simulation data of the propeller manufacturer APC (see [49]) a propeller of type APC 19x8E, operated at $T = 13 \text{ N}$, results in a torque of $Q = 0.33 \text{ Nm}$. A propeller with a higher blade pitch of type APC 19x16 will result in a torque of $Q = 0.45 \text{ Nm}$ for the same operating condition. This estimation results in a maximum overall yawing moment of $N_{max} = 1.8 \text{ Nm}$ for the latter propeller.

During an actual hovering flight with a headwind the rotors are tilted forward and the control moment calculation becomes more complex. Figure 5.49 shows the control moments with the

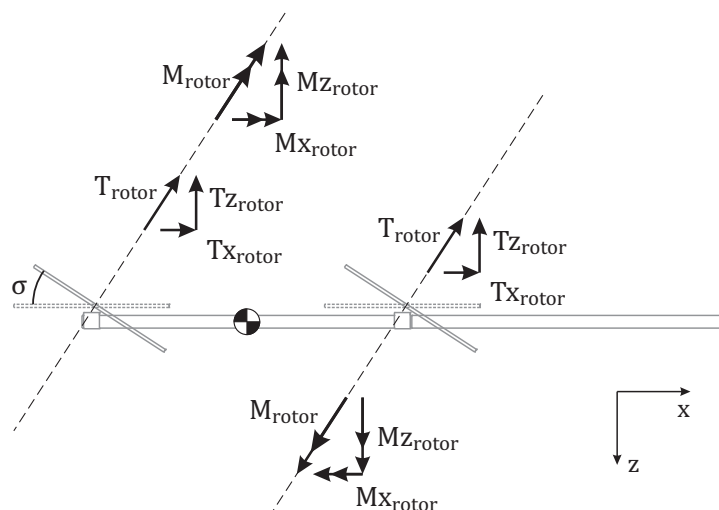


Figure 5.49: Rotor forces and moments for the H-4 configuration with rotors tilted forward. Figure shows the two right rotors (positive y-axis).

rotors tilted by an angle of σ_{rotor} . When tilting the rotors forward, the maximum pitching and rolling moments are:

$$M_{max} = 2 \cdot \frac{x d_{rotor}}{2} \cdot T_Z = 2 \cdot \frac{x d_{rotor}}{2} \cdot (2 \cdot T_0 \cdot \cos(\sigma)) \quad (5.9.6)$$

$$L_{max} = 2 \cdot \frac{y d_{rotor}}{2} \cdot T_Z = 2 \cdot \frac{y d_{rotor}}{2} \cdot (2 \cdot T_0 \cdot \cos(\sigma)) \quad (5.9.7)$$

The thrust in a steady state flight condition, without a roll or pitch maneuver, is denoted T_0 . Because the forces in z-direction have to be balanced in the steady state flight condition, T_0 calculates to $T_0 = W/(4 \cdot \cos(\sigma))$ and consequently the pitching and rolling moments remain unchanged compared to the hovering state without headwind.

As a consequence of the forward tilted rotors a coupling between rolling and yawing moments and vice versa is created. Figure 5.50 shows a roll maneuver to the right. Due to the increased thrust on the left side of the aircraft the thrust component in the x-direction is increased asymmetrically, resulting in a yawing moment to the right.

Figure 5.51 shows a yaw maneuver to the right. The unbalanced rotor torque in x-direction ($M_{x_{rotor}}$) results in a rolling moment to the left. These couplings have to be compensated for by the flight controller.

Another possibility to produce yawing moments can be achieved by differential tilting of the motor arms. This would produce a higher yawing moment and less roll-yaw / yaw-roll coupling.

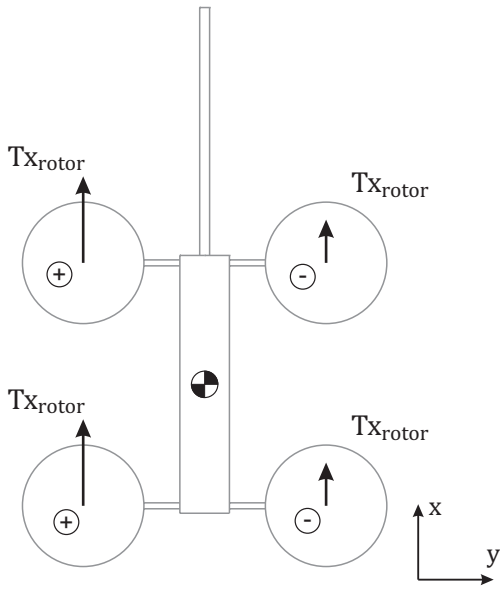


Figure 5.50: Yawing moment resulting from a roll maneuver.

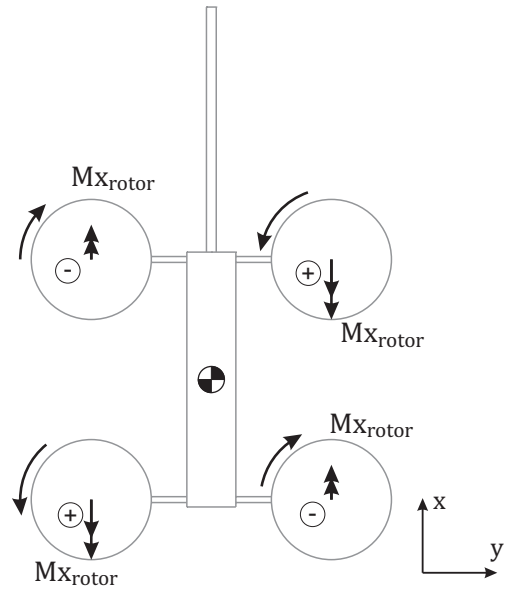


Figure 5.51: Rolling moment resulting from a yaw maneuver.

5.9.2 Configuration 2: Y-6

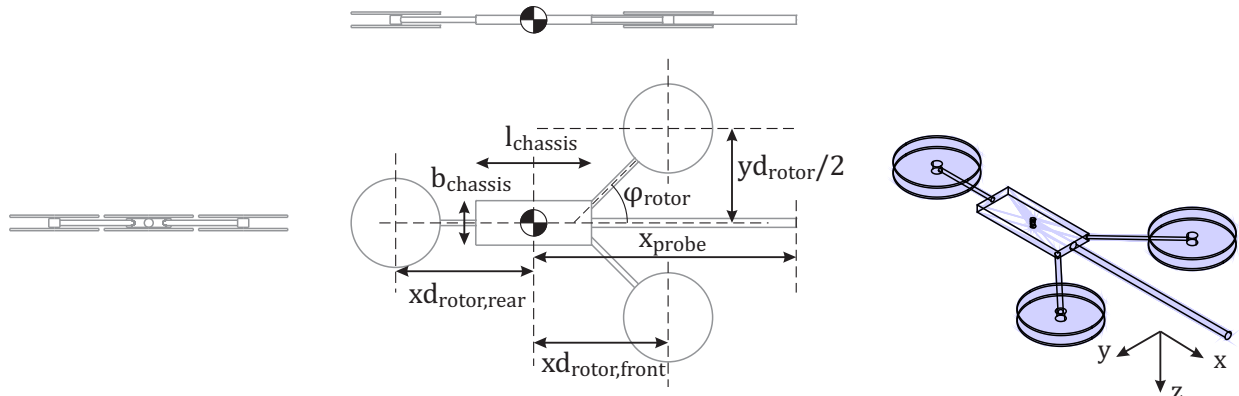


Figure 5.52: Y-6 Rotor Layout.

The asymmetric Y-6 configuration consists of two coaxial pairs of rotors at the front and one coaxial pair of rotors at the rear end of the airframe. The biggest difference between the Y-6 configuration and other configurations is, that rotor tilting is only possible for the front rotors, unless the rear rotors are connected by a fork-shaped frame instead of a conventional motor arm (see Figure 5.53).

In general, different designs are possible for the rear rotors. These designs are listed as the following sub variants:

- Variant A: Rear rotors can be tilted about the x-axis to enhance yawing moment.
- Variant B: Rear rotors can be tilted about the y-axis using a fork-shaped frame (Figure 5.53).
- Variant C: Rear rotors can be tilted about x-axis and y-axis using a gimbal support.
- Variant D: Rear rotors are fixed at a pre-tilt angle.

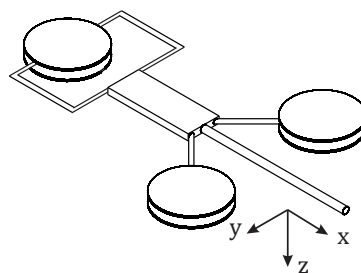


Figure 5.53: Attachment of the rear rotors with fork-shaped frame.

Flight Mechanics

To achieve a balanced thrust distribution, the distance between the rear and the front rotors must be:

$$x_{d_{rotor, rear}} = 2 \cdot x_{d_{rotor, front}} \quad (5.9.8)$$

Since the forces in the z-direction should remain balanced in hover, the maximum nose-up pitching moment is:

$$M_{max} = W \cdot x_{d_{rotor,front}} = x_{d_{rotor,front}} \cdot 4 \cdot \left(\frac{3}{2} T_{hover} \right) \quad (5.9.9)$$

The nose-up pitching moment is limited by the overall force in z-direction. If the four front rotors produce more than $1.5 \cdot T_{hover}$ of thrust, it will result not only a nose-up pitching moment but also a vertical force leading to a climb maneuver. For the nose-down pitching moment, on the other hand, it is possible to achieve a higher value:

$$M_{max} = -W \cdot x_{d_{rotor,rear}} = -2 \cdot W \cdot x_{d_{rotor,front}} = x_{d_{rotor,rear}} \cdot 2 \cdot (3 \cdot T_{hover}) \quad (5.9.10)$$

Hence, the nose-down pitching moment can be twice as high as the nose-up pitching moment, if the rear rotors are capable of producing a thrust of $T = 3 \cdot T_{hover}$, because the rotors are farther away from the center of gravity. For the comparison with other configurations only the nose-up pitching moment was considered, resulting in:

$$x_{d_{rotor,rear}}(Y6) = 2 \cdot x_{d_{rotor,front}}(Y6) = x_{d_{rotor}}(H4 \text{ or } H8) \quad (5.9.11)$$

The maximum rolling moment in a hovering flight without headwind ($\sigma = 0^\circ$) is then:

$$L_{max} = 2 \cdot y_{d_{rotor}}/2 \cdot (2 \cdot T_{hover}) \quad (5.9.12)$$

Because the rear rotors do not contribute to the rolling moment, the distance $y_{d_{rotor}}$ has to be larger than for other configurations, where half of the rotors are contributing to the rolling moment:

$$y_{d_{rotor}}(Y6) = \frac{3}{2} \cdot y_{d_{rotor}}(H4 \text{ or } H8) \quad (5.9.13)$$

If the rear rotors are not tilted about the x-axis to enhance the yawing moment, and the yawing moment is purely produced by differential speed of the 6 rotors (3 rotors running at $T = 2 \cdot T_{hover}$ and 3 rotors at $T = 0$) it is:

$$N_{max} = 6 \cdot Q_{hover} \quad (5.9.14)$$

An APC 16x55MR propeller results in a rotor torque of $Q_{hover} = 0.19 \text{ Nm}$, when running at $T_{hover} = 8.7 \text{ N}$, according to the manufacturers BEM simulation (see [49]). The maximum yawing moment produced conventionally is $N_{max} = 1.14 \text{ Nm}$. This yawing moment can be enhanced either by tilting the rear rotors about the x-axis or differential tilting of the front rotors. If the rear rotors are tilted about the x-axis by $\delta_{tail} = 45^\circ$, the thrust of each of the rear rotors has to be increased to $T = \sqrt{2} \cdot T_{hover}$ to keep the same vertical forces. In this case the yawing moment increases to:

$$N_{max} = x_{d_{rotor,rear}} \cdot 2 \cdot T_{rear} \cdot \sin(\delta_{tail}) = x_{d_{rotor,rear}} \cdot 2 \cdot (\sqrt{2} \cdot T_{hover}) \cdot \sin(45^\circ) \quad (5.9.15)$$

Assuming a rear rotor distance of $x_{d_{rotor,rear}} = 0.6 \text{ m}$ results in a maximum yawing moment of $N_{max} = 10.44 \text{ Nm}$ and therefore increases the yawing moment capabilities by a factor larger than nine.

Figure 5.54 shows the forces and moments in forward flight / hovering flight in a headwind, when the rotors are tilted forward ($\sigma > 0$). The biggest difference between the Y-6 configuration and the other configurations is, that the tilt angle σ has to be readjusted whenever a pitching moment is produced. If the rear rotors are mounted horizontally (without pre-tilt angle) the horizontal thrust force Tx_{rotor} is not in balance with the aircraft's drag force D (see Figure 5.3) anymore,

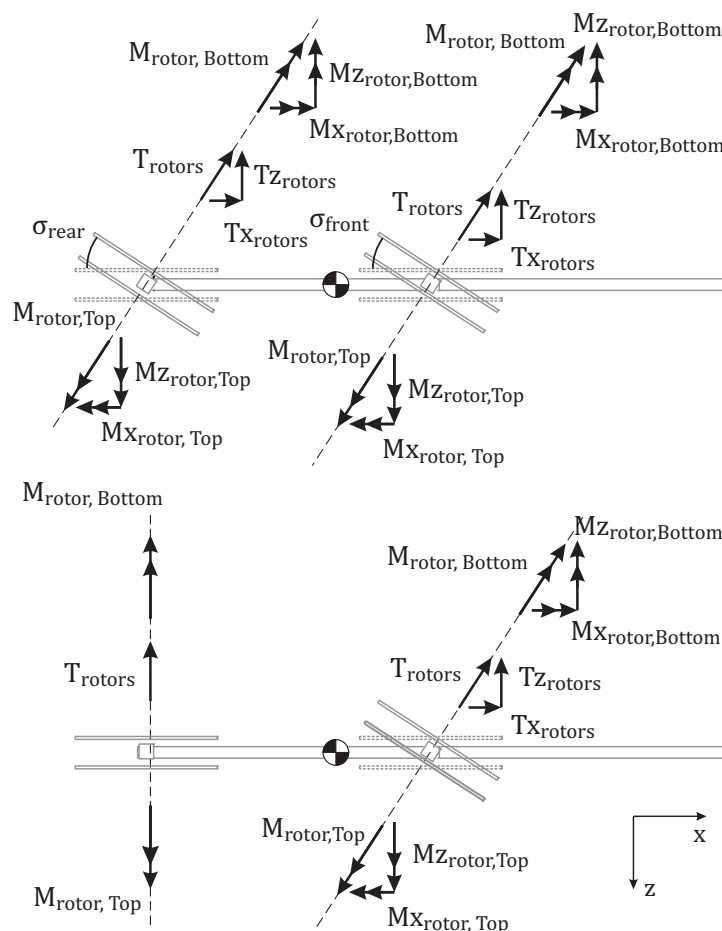


Figure 5.54: Rotor forces and moments for the Y-6 configuration with rotors tilted forward. The figure shows the two front right rotors (positive y-axis). In the top picture the rear rotors are attached at a pre-tilt angle or tiltable. In the bottom picture the rear rotors are rigidly attached in the horizontal plane.

whenever the thrust on the front rotors is altered. For all other rotor layouts (symmetric about the yz-plane) the total horizontal rotor forces Tx_{rotors} will remain constant during a pitching maneuver, because the front and rear rotor tilt angle σ is equal. Consequently, the rotor thrust force increase on one side (front or rear) equals the rotor thrust force decrease on the opposite side.

If the rear rotors are mounted at a pre-tilt angle or if they are also tiltable like the front rotors this effect is weaker but still present, because the distance from the C.G. to the front and rear rotors is different (see Eq. (5.9.8)).

Similar to the H-4 configuration, there is a yaw-roll coupling and vice versa. This is depicted in Figure 5.55 and Figure 5.55.

If the sweep angle of the front rotors is smaller than $\varphi_{rotors} = 90^\circ$, and if the front rotors are tilted directly about the motor arms, it is possible to use the rotor tilting for lateral position control. However, this adds further complexity to the flight mechanics and control system.

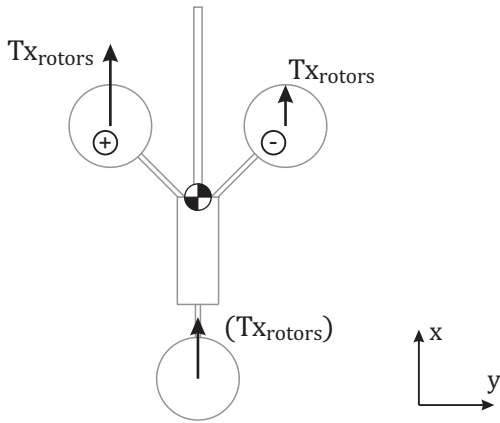


Figure 5.55: Yawing moment resulting from a roll maneuver.

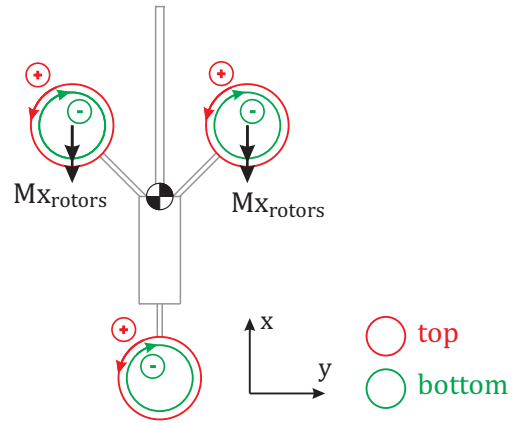


Figure 5.56: Rolling moment resulting from a yaw maneuver.

5.9.3 Configuration 3: H-6

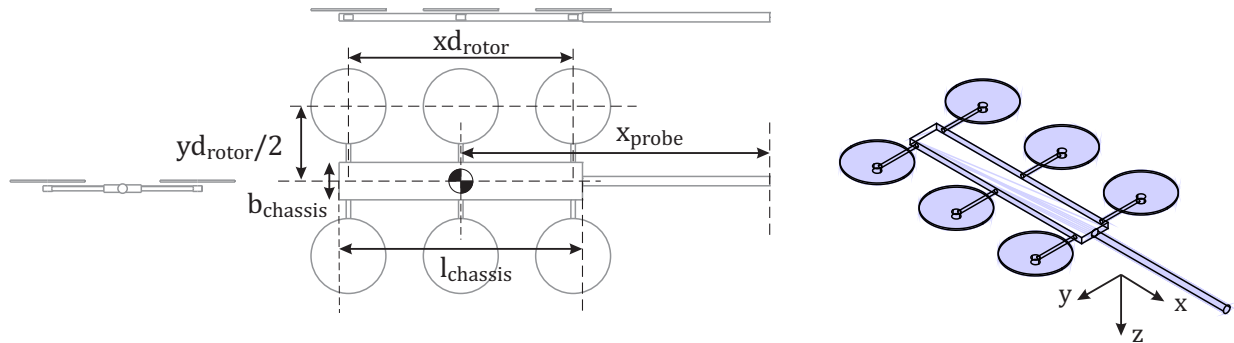


Figure 5.57: H-6 Rotor Layout.

A conventional X-6 or +6 hexarotor configuration is not feasible with tilt-able rotors, because the motor arms are in the way. The H-6 configuration addresses the need for a hexarotor with tilt-able rotors without using a coaxial rotors.

Flight Mechanics

The biggest difference between the H-6 configuration and the other configurations is that the center rotors will not contribute to the pitching moment. At zero tilt angle ($\sigma_{rotor} = 0^\circ$) the maximum pitching moment is:

$$M_{max} = 2 \cdot \frac{x_{d_{rotor}}}{2} \cdot (3 \cdot T_{hover}) \quad (5.9.16)$$

This maximum pitching moment can only be reached if the propulsion system is capable of producing a maximum thrust of three times hover thrust. In that case, for a nose down pitching moment the thrust of the front and middle rotors can be reduced to zero and the entire weight of the aircraft is carried by the rear rotors. This corresponds to a significantly higher pitching moment compared to a H-4 configuration with the same dimension $x_{d_{rotor}}$.

If the maximum thrust of the propulsion system is less than three times hover thrust, the thrust of the front rotors can still be reduced to zero, while the thrust of the middle rotors can be used to compensate for the difference between the maximum thrust of the rear rotors and $T = 3 \cdot T_{hover}$. The resulting pitching moment is consequently lower.

All six rotors are involved, when producing a rolling moment:

$$L_{max} = 3 \cdot \frac{y_{d_{rotor}}}{2} \cdot (2 \cdot T_{hover}) \quad (5.9.17)$$

The H-6 configuration also differs from the other configurations when producing a yawing moment. For a H-4 configuration, for example, the yawing moment is achieved by a lower RPM of the corresponding diagonal rotors. For the H-6 configuration, with directions of rotation according to Figure 5.58, it is not possible to simply reduce the thrust of three rotors and increase the thrust of the other three rotors by the same amount. This would result in a rolling moment, because the rotors 2 and 6 on the right hand side produce more thrust together than rotor 4 on the left hand side.

The solution for a pure yawing moment is:

$$T_2 = T_6 = \frac{3}{2} \cdot T_{hover} \quad (5.9.18)$$

$$T_4 = 3 \cdot T_{hover} \quad (5.9.19)$$

$$T_1 = T_3 = T_5 = 0 \quad (5.9.20)$$

This solution with $T_{hover} = W/6$ results in a maximum yawing moment, without introducing a rolling or pitching moment and a balanced vertical thrust force, opposed to the aircraft's weight W . If the propulsion system is incapable of producing a maximum thrust of $T_{max} = 3 \cdot T_{hover}$, the yawing moment would be lower and rotors 1,3,5 cannot be shut down completely. The thrust of the rotors 2,4 and 6 can still be increased with the same ratio.

Assuming the same APC 16x5.5MR propeller as for the Y-6 configuration with a torque of $Q_{hover} = 0.16 \text{ Nm}$ the maximum yawing moment can be determined as:

$$N_{max} = 2 \cdot \frac{3}{2} Q_{hover} + 3 \cdot Q_{hover} = 6 \cdot Q_{hover} = 1.14 \text{ Nm} \quad (5.9.21)$$

Figure 5.59 illustrates forces and moments in forward flight / hovering in a headwind. Similar to

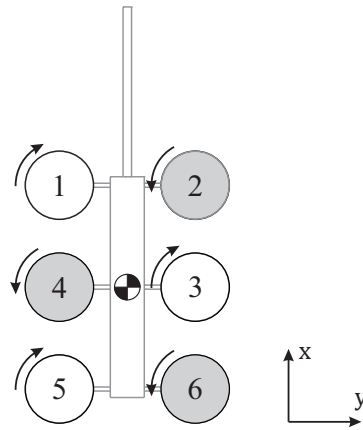


Figure 5.58: RPM change during a yaw maneuver.

the H-4 configuration a roll-yaw coupling and vice versa exists. These effects are shown in Figure 5.60 and Figure 5.61.

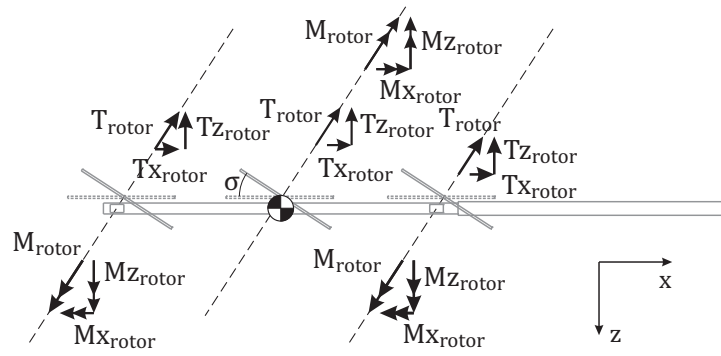


Figure 5.59: Rotor forces and moments for the H-6 configuration with rotors tilted forward. The figure shows the three right rotors (positive y-axis).

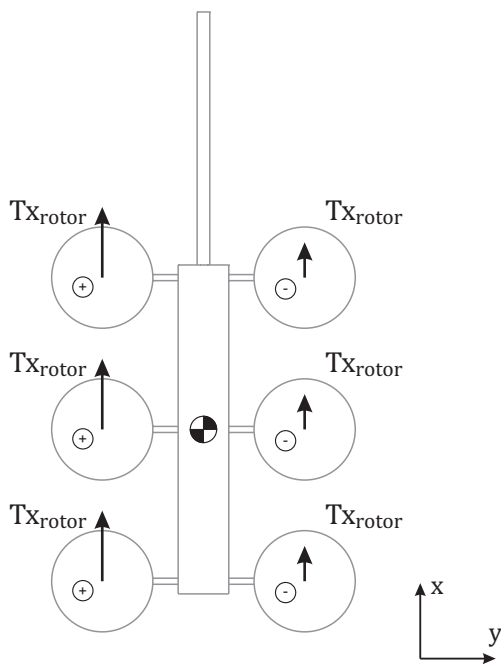


Figure 5.60: Yawing moment resulting from a roll maneuver.

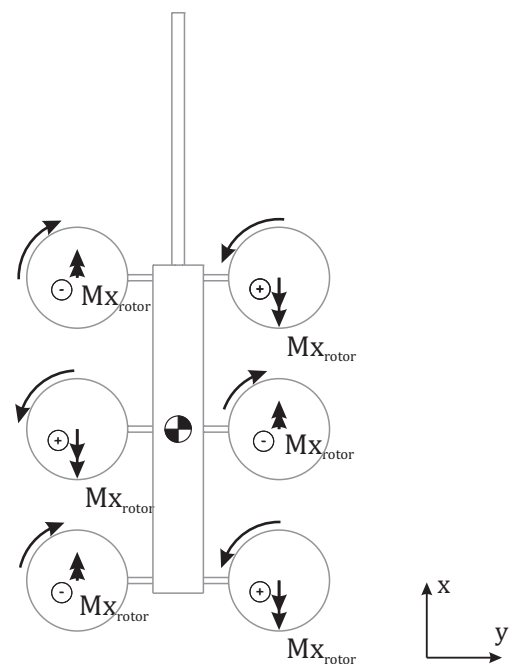


Figure 5.61: Rolling moment resulting from a yaw maneuver.

5.9.4 Configuration 4: H-8

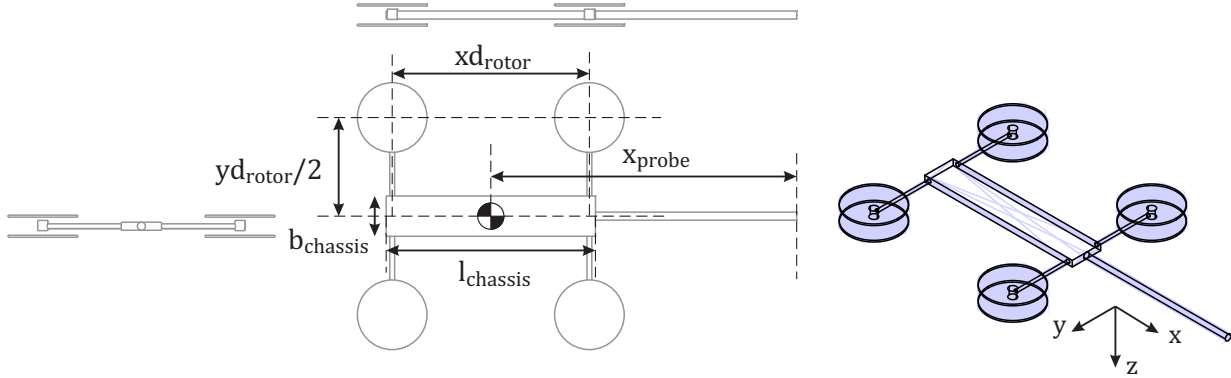


Figure 5.62: H-8 Rotor Layout.

The H-8 configuration is very similar to the H-4 configuration, except that the four motor arms are arranged in a coaxial rotor setup instead of a single rotor.

Flight Mechanics

The maximum pitching moment in hover without headwind is:

$$M_{max} = 4 \cdot \frac{xd_{rotor}}{2} \cdot (2 \cdot T_{hover}) \quad (5.9.22)$$

While the maximum rolling moment in hover without wind is:

$$L_{max} = 4 \cdot \frac{yd_{rotor}}{2} \cdot (2 \cdot T_{hover}) \quad (5.9.23)$$

Again each rotor can only use a maximum thrust of $T_{max} = 2 \cdot T_{hover}$ without introducing a climb maneuver. According to the manufacturer's data (see [49]) an APC 13.5x9 propeller at hover thrust has a torque of $Q_{hover} = 0.15 \text{ Nm}$ while an APC 14x55MR propeller has a hover torque of $Q_{hover} = 0.13 \text{ Nm}$. Hence, the maximum yawing moment with the higher torque propeller in hover is:

$$N_{max} = 4 \cdot (2 \cdot Q_{hover}) = 1.2 \text{ Nm} \quad (5.9.24)$$

Similar to most of the other configurations, the maximum yawing moment can be enhanced by differential tilting of the motor arms or an additional vertical tail fin to increase directional stability in headwind.

Forces and moments with the rotors tilted forward are shown in Figure 5.63.

Similar to the H-4 configuration, a positive yaw-roll coupling and a negative roll-yaw coupling are introduced, when the rotors are tilted forward as illustrated in Figure 5.64 and Figure 5.65.

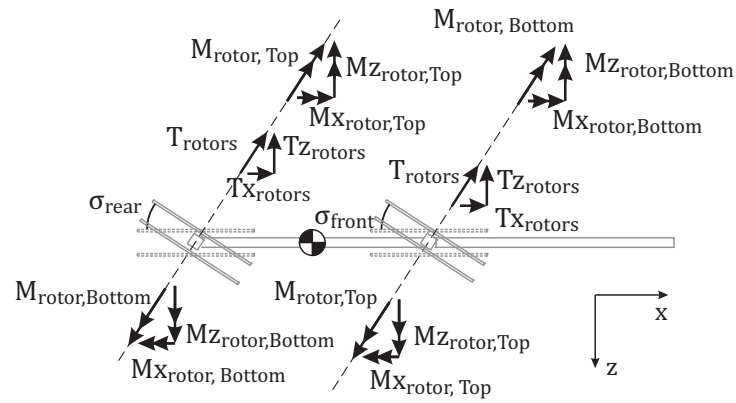


Figure 5.63: Rotor forces and moments for the H-8 configuration with rotors tilted forward. The four right rotors (positive y-axis) are shown.

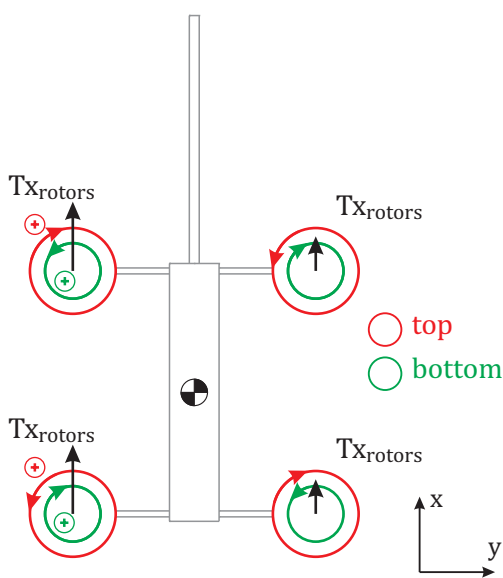


Figure 5.64: Yawing moment resulting from a roll maneuver.

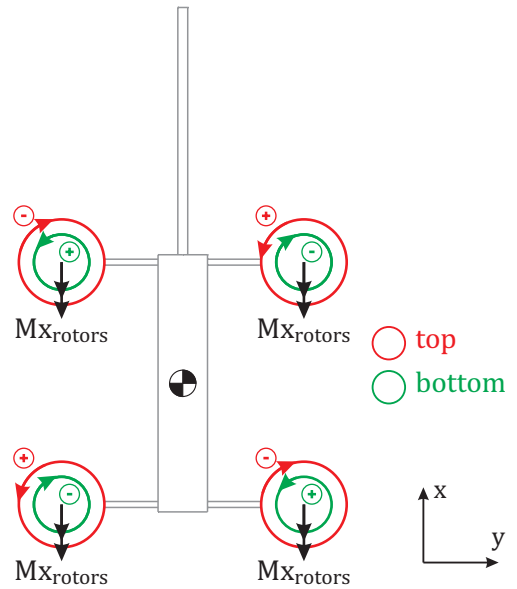


Figure 5.65: Rolling moment resulting from a yaw maneuver.

5.9.5 Configuration 5: H-8 Parallel

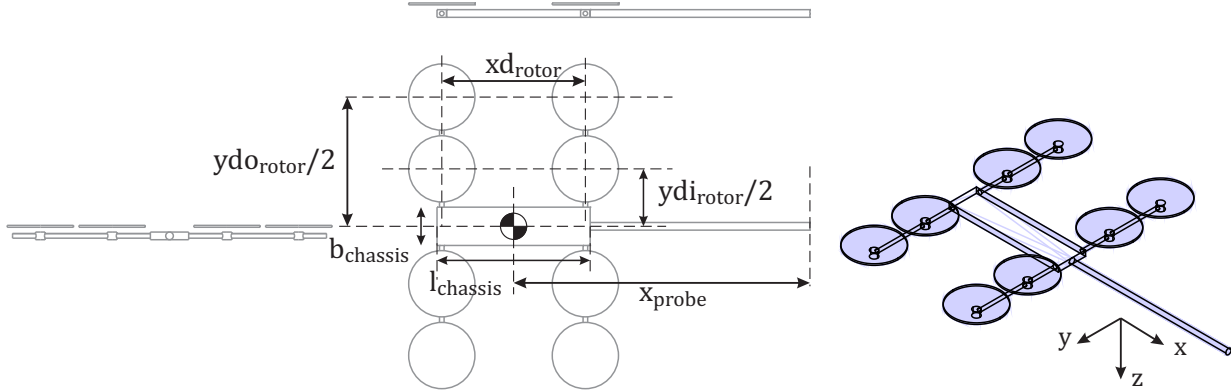


Figure 5.66: H-8 parallel configuration.

If a coaxial rotor is to be avoided but eight rotors shall be used, for reasons of redundancy or a short response time (compare Section A.2.2), the rotors can also be arranged in parallel, here referred to as "H-8 parallel" configuration and illustrated in Figure 5.66.

Flight Mechanics

To accomplish a rolling or pitching moment all the front/rear or left/right rotors can be reduced to zero thrust while the thrust of the other half of rotors has to be increased to $T = 2 \cdot T_{hover}$. If the rotors are not tilted forward ($\sigma_{rotor} = 0^\circ$) this will result in a balanced vertical force and in a maximum pitching moment of:

$$M_{max} = 4 \cdot \frac{x_{d_{rotor}}}{2} \cdot (2 \cdot T_{hover}) \quad (5.9.25)$$

The corresponding maximum rolling moment consequently becomes:

$$L_{max} = 2 \cdot \frac{y_{d_{rotor}}}{2} \cdot (2 \cdot T_{hover}) + 2 \cdot \frac{y_{d_{rotor}}}{2} \cdot (2 \cdot T_{hover}) \quad (5.9.26)$$

If the smallest possible distance in x direction of $x_{d_{rotor}} = D_{rotor}$ and the smallest possible distances in y-direction of $y_{d_{rotor}} = D_{rotor}$ and $y_{d_{rotor}} = 3 \cdot D_{rotor}$ are considered, it can be seen that the rolling moment is always bigger than the pitching moment by a factor of at least 2. When compared to other configurations, an effective distance in the y-direction of $y_{d_{rotor}} = (y_{d_{rotor}} + y_{d_{rotor}})/2$ has to be used.

If the same propeller size is used and the aerodynamic interference effects of the coaxial rotor setup are neglected, the yawing moment can be calculated in accordance to the H-8 coaxial configuration, resulting in a maximum yawing moment of $N_{max} = 1.2 \text{ Nm}$. Forces and moments with the propellers tilted forward are shown in Figure 5.67. Similar to the other configurations, a positive roll-yaw and a negative yaw-roll coupling also exist for the H-8 parallel configuration as illustrated in Figure 5.68 and Figure 5.69.

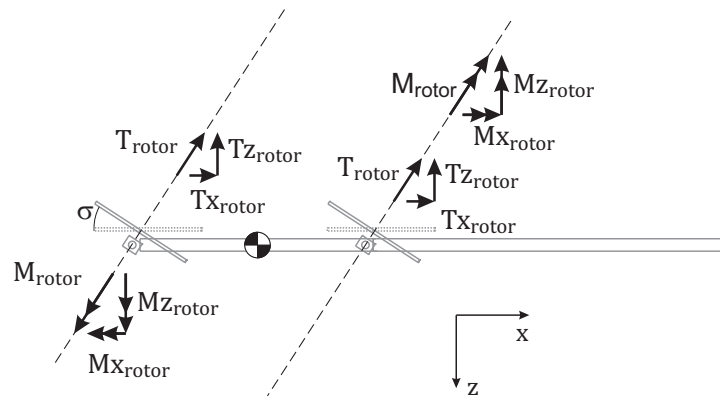


Figure 5.67: Rotor forces and moments for the H-8 parallel configuration with rotors tilted forward. The figure shows the four most right rotors (positive y-axis).

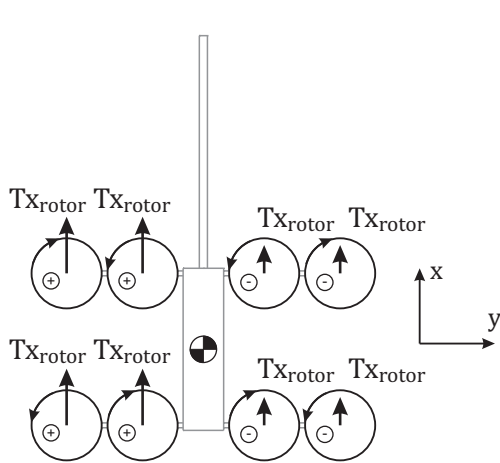


Figure 5.68: Yawing moment resulting from a roll maneuver.

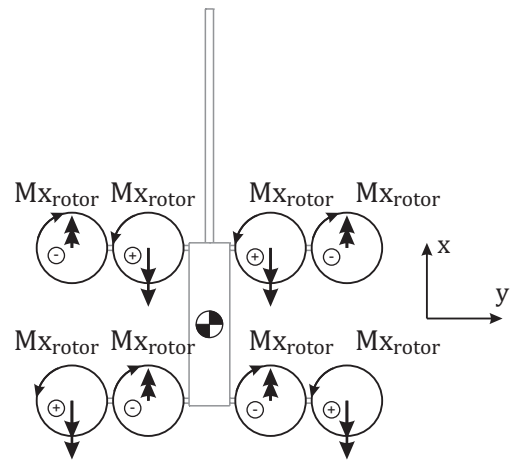


Figure 5.69: Rolling moment resulting from a yaw maneuver.

5.10 Overall Aerodynamic Simulation

A very important parameter for the conceptual design of ANDroMeDA, as already derived in Section 5.3.2, is the aircraft's aerodynamic drag. Drag and weight of the aircraft are responsible for flight performance, respectively the maximum flight speed / maximum headwind and the duration of a measurement mission. An estimation of the aircraft's drag coefficient is difficult, because not many references exist and the few existing references are focused on a particular design case (e.g. airframe shape, number of rotors etc.).

To be able to make a prediction of the aircraft's drag and to draw a valid comparison between the different configurations, presented above, several aerodynamic simulations were carried out. For this simulations the frames of the different aircraft configurations were modeled in a simplified way. In addition, the rotors were modeled as 3D actuator discs. This is necessary to model the effect of the rotor wakes on the drag. Because large portions of the motor arms are immersed in the rotor slipstreams it was assumed and later confirmed, that this effect cannot be neglected.

For the H-4 configuration a smooth aerodynamic cover was also modeled to see its effect on the aircraft's drag. Using a smooth aerodynamically shaped cover is a trade-off between additional mass, added by the design, and the power saved due to reduced drag. Other points of interest investigated by the overall aerodynamic simulation are the mutual interference of front and rear rotors and the estimation of the maximum aerodynamic yawing moment.

Another very important result of the overall aerodynamic simulation is the estimation of all forces and moments at different angles of attack α and different sideslip angles β . These numbers will be used for the complete flight mechanical simulation, used to design the aircraft's controller as described in Section C.

5.10.1 Simulation Description

All configurations were modeled in parametric CAD files. Rotor diameters were set according to Table 5.7. To achieve a fair comparison, the rotor distances for the different configurations, as introduced in the previous section, have been scaled in a way that rolling and pitching moments in hover are equal for all configurations. As a starting point, the H-4 configuration was set up with small distances xd_{rotor} and yd_{rotor} leaving a reasonable amount of clearance between rotors and frame. The results are presented in Table 5.8.

The tilt angle was set to $\sigma_{rotor} = 33^\circ$, according to a preliminary drag estimation in Section 5.3. To avoid any disturbance from the control volume boundaries, the control volume size for the H-4 basic configuration was set to 100 *m* in all dimensions, while the aircraft mesh was placed at 25 *m* downstream of the inlet. From the results of the H-4 simulations it could be seen that the control volume dimensions can be reduced to 50 *m* without problems. This distance was then used for the other configurations. The thickness of the actuator disc cylinders was set to $t_{disc} = 20 \text{ mm}$

The H-8 (coaxial) configuration was not simulated, because the airframe is the same as for the H-4 configuration. The application points of forces and moments at the frame are the same and the rotor distances xd_{rotor} and yd_{rotor} are also the same. The portion of motor arms immersed in the rotor slipstream is smaller for the H-8 configuration. On the other hand the slipstream speed is higher because of the smaller rotor diameter and the coaxial rotor setup. This effects have been neglected here. To investigate the mutual rotor interference a mesh with four single actuator discs without any frame was set up.

The parametric CAD models were imported in the ANSYS workbench meshing module and an automatic unstructured tetrahedral mesh was created. For the rotor wake a mesh refinement region was defined. The boundaries of the actuator disc cylinders were refined with prism layers

as well as the surface of the frame, as shown in Figure 5.70 and Figure 5.72.

The non-dimensional wall distance, y^+ , is a measure for how well the flow past a wall is resolved. The mesh refinement at the airframe surface resulted in a maximum y^+ value of 5.6 for the basic H-4 configuration (see Figure 5.71). According to [50], due to the automatic near-wall treatment of CFX, this is an acceptable range, if the boundary layer is covered by at least 10 elements. The maximum y^+ value occurs at the rear motor arms, where the flow separates.

The flow separation point of cylindrical objects is in general very difficult to predict with CFD. Because the same modeling accuracy is used for all cases and therefore a higher y^+ value results in the same relative error for all cases, the maximum y^+ value of 5.6 was accepted. A finer mesh and a lower y^+ value would also increase the simulation time.

Because the y^+ value and the number of elements inside the boundary layer was verified, no mesh refinement studies have been conducted. The focus of the overall aerodynamic simulations is a simplified drag estimation and the comparison between different possible configurations at a conceptual design stage, which is more important than computing more precise values for $c_D A$.

The basic H-4 configuration case needs a computation time of approx. 2 hours on Windows server machine with Intel E5645 2.4 Ghz six core CPU and 48 GB of RAM. Therefore, it is possible to compare different cases (e.g. different tilt angles) in a short period of time due to the reasonable computational effort.

All simulations have been carried out at the design point, $\sigma_{rotor} = 33^\circ; v_\infty = 11 \text{ m/s}$ which corresponds to a relatively high frame drag.

Configuration	D_{scaled}	xd_{rotor}	yd_{rotor}	No. of Elements
4 rotors	0.49 m	0.59 m	0.69 m	$6.08 \cdot 10^6$
H4	0.49 m	0.59 m	0.69 m	$8.75 \cdot 10^6$
H4 smooth	0.49 m	0.59 m	0.69 m	$8.79 \cdot 10^6$
H6	0.40 m	0.89 m	0.69 m	$11.3 \cdot 10^6$
Y6	0.40 m	0.66 m	1.03 m	$8.9 \cdot 10^6$
H8 parallel	0.35 m	0.59 m	0.86 m	$10.9 \cdot 10^6$

Table 5.8: Mesh parameters for the simulations.

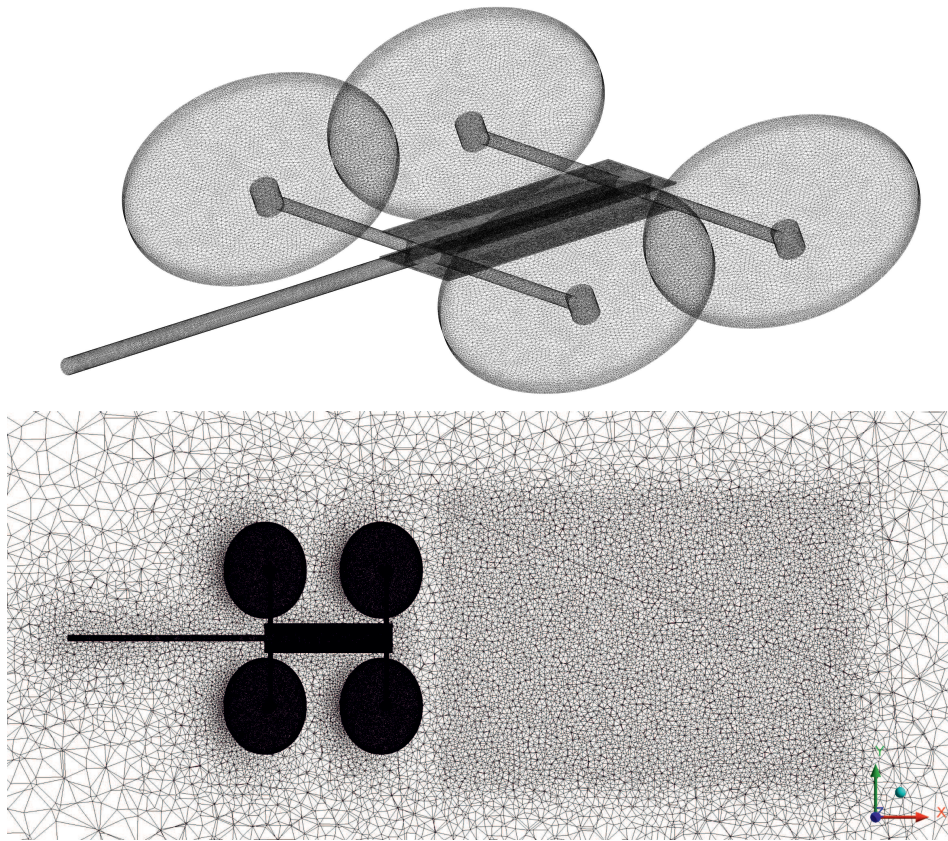


Figure 5.70: Top: Surface mesh of the H-4 configuration. Bottom: Mesh refinement at the rotor wake region.

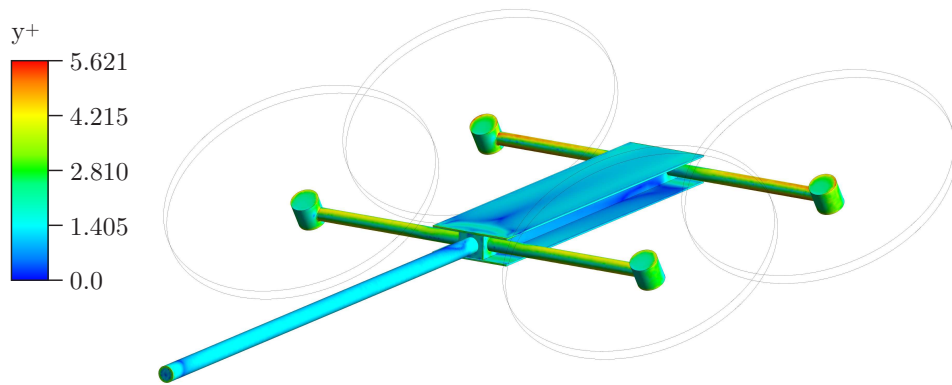


Figure 5.71: y^+ value at the surface of the H-4 frame.

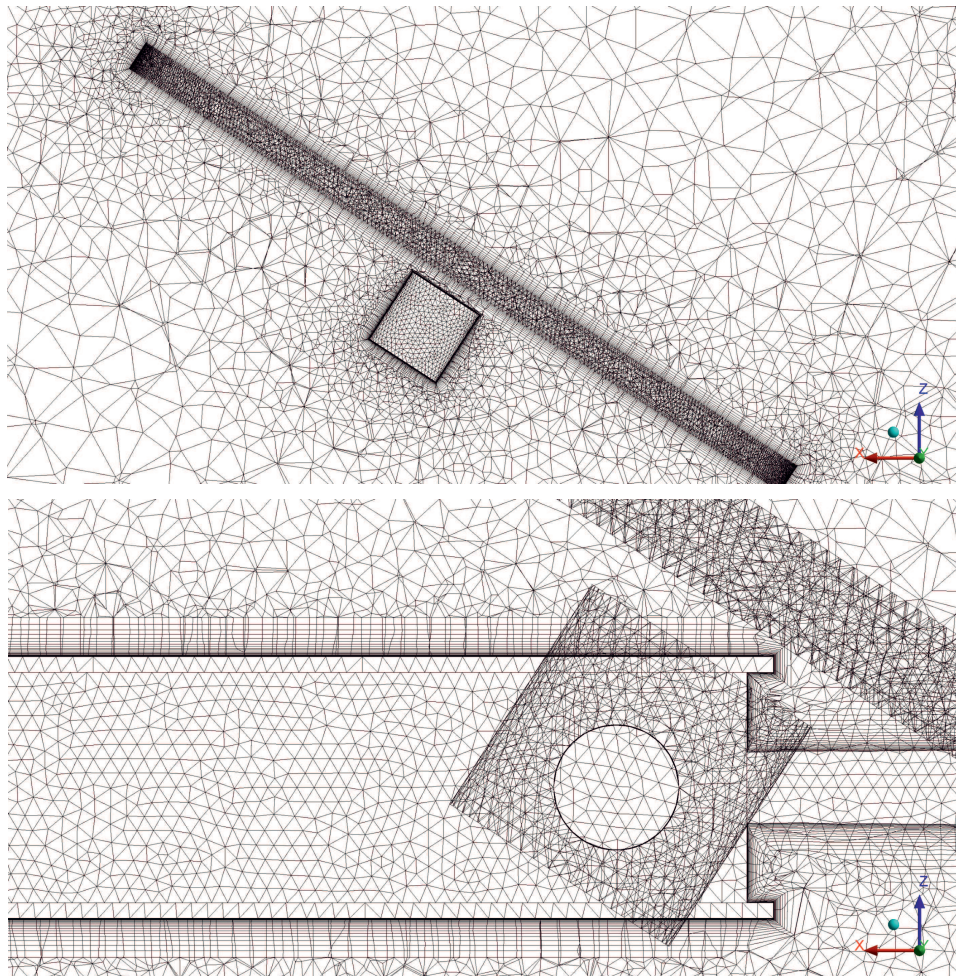


Figure 5.72: Prism layers used for boundaries of the actuator discs and the surface of the frame.

5.10.2 Interference Between Front and Rear Rotors

One interesting question that developed during the conceptual design process is: "How much are the rear rotors influenced by the front rotors if they are operated in their wake?". For a conventional design, especially at a high drag coefficient, the entire aircraft has to be tilted forward. This, on the other hand, moves the rear rotors above the front rotors. For the ANDroMeDA concept, with tilting rotors, the rear rotors are always located exactly behind the front rotors.

To investigate the consequences of this rotor arrangement a simple mesh with four isolated actuator discs was set up. The actuator discs have been set to a constant thrust (constant momentum source) and the induced power, necessary to obtain this thrust, was calculated from the simulation results by the following equation:

$$dP = dp \cdot v_{\perp} \quad (5.10.1)$$

Where dP is the power on one single face of the mesh, dp is the pressure on this face and v_{\perp} is the velocity normal to this face. By summing up dP over the top and bottom surface of each actuator disc, the power applied to the discs can be calculated.

For the isolated actuator disc model, four different operating conditions have been investigated:

- $T = \frac{1}{4} \cdot T_{hover}$
- $T = \frac{1}{2} \cdot T_{hover}$
- $T = T_{hover}$

For $T = 1/2 \cdot T_{hover}$ and $T = T_{hover}$ a constant power increase of $P_{rear}/P_{front} = 1.123$ could be observed. For the lowest thrust level of $T = 1/4 \cdot T_{hover}$ this slightly decreased to $P_{rear}/P_{front} = 1.092$. Thus, it can be assumed, that for the relevant thrust range, a rear rotor in the wake of a front rotor will need about 12.3 % more power.

According to [43] the induced power of a rotor for a given angle of attack can be calculated as:

$$P_i = T \cdot (v_{\perp} + v_i) \quad (5.10.2)$$

The inflow velocity component, perpendicular to the rotor disc, is denoted as v_{\perp} . For a higher mass flow through the rotor disc by a higher v_{\perp} , the induced velocity v_i will always decrease. At lower flight speeds and a small angle of attack, this effect can dominate Eq. (5.10.2), so that the induced power is reduced even if the inflow speed increases (see Section A.1.4). However, for most operating conditions, a higher inflow speed will result in an increased induced power. This explains, that a rear rotor, operated in the wake of a front rotor, needs a higher induced power.

Another observation that can be explained by simple momentum theory, is that for the H-6 configuration, with three rotors in a row, the power increase from the second to the third row is relatively small with $P_{rear}/P_{mid} = 1.02$, while the power increase from the first row to the second row is $P_{mid}/P_{front} = 1.109$. A rotor operating in the wake of another rotor experiences an inflow speed increased by the induced velocity of this other rotor.

For the inclined rotor the induced velocity can be calculated numerically by solving Eq. (5.7.2). Figure 5.73 shows the induced velocity v_i and induced power P_i at a given thrust, given rotor size and given angle of attack for different inflow speeds. Figure 5.74 shows the wake speeds of an H-4 configuration. To compute these wake speeds two straight lines behind the rotor discs, aligned with the rotor wake, have been determined from the simulation. These two lines are shown in Figure 5.75. As shown in Figure 5.74 the front rotor has to accelerate the air from 11 m/s to

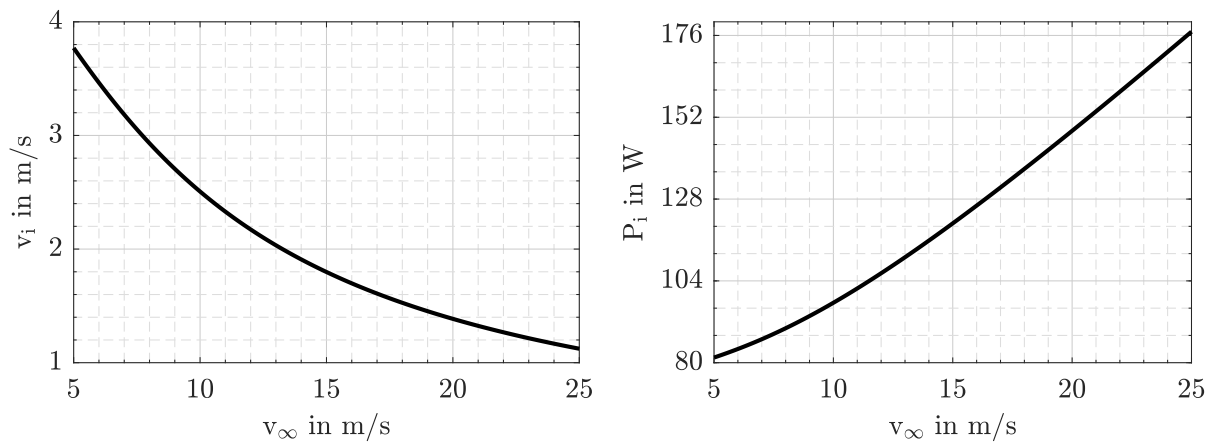


Figure 5.73: Induced velocity and induced power with changing rotor inflow speed v_i at $T = 13 \text{ N}$; $\alpha_{disc} = 33^\circ$; $D = 0.49 \text{ m}$; $\rho = 1.185 \text{ kg/m}^3$ according to Equation 5.7.2 and Equation 5.10.2

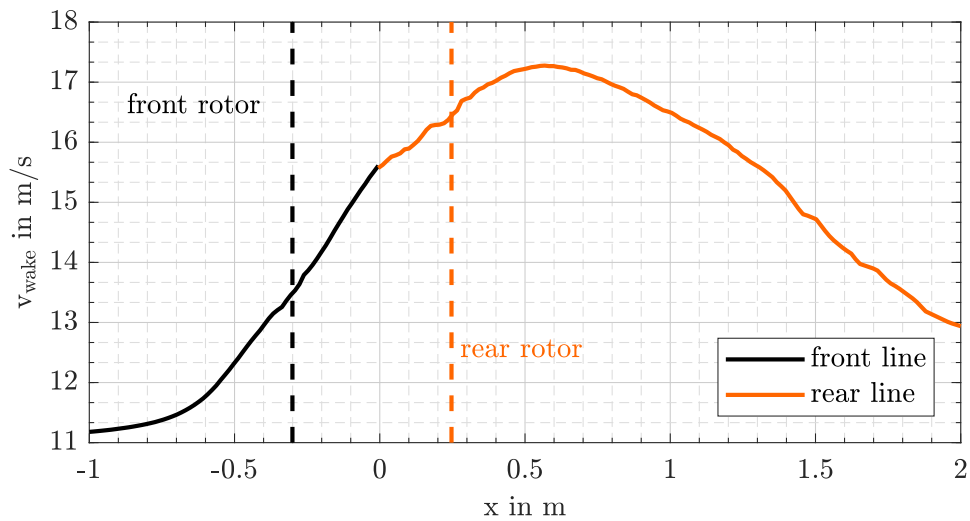


Figure 5.74: Wake speeds behind two successive rotors in the isolated rotor simulation with $\alpha_{disc} = 33^\circ$; $T = 13 \text{ N}$; $D = 0.49 \text{ m}$; $\rho = 1.185 \text{ kg/m}^3$

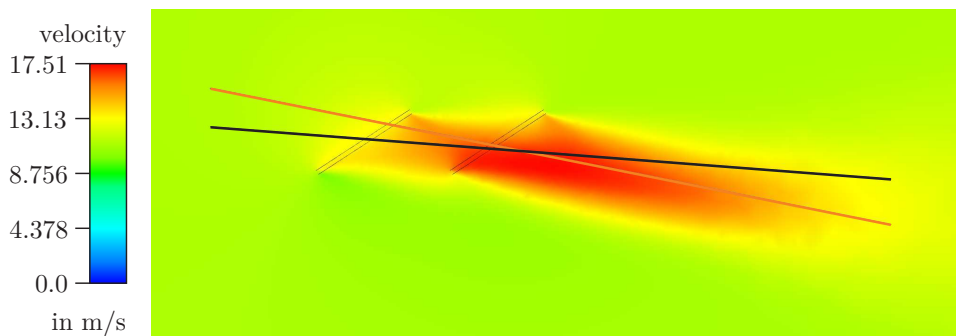


Figure 5.75: Wake lines used to determine the speeds in Figure 5.74

15.5 m/s to produce a thrust of $T = 13 N$. The rear rotor only has to accelerate the air by less than $\Delta v = 2 \cdot v_i = 2 m/s$ to 17.3 m/s to achieve the same thrust. Because for each following rotor this speed increase becomes smaller, the additional induced power also reduces.

Another effect of a lower induced velocity at higher inflow speeds is shown in Figure 5.76. The airflow redirection also reduces for each following rotor and the difference in wake speed and wake direction between the middle rotors and rear rotors is rather small, for this reason.

When the full simulation, including the multirotor's frame, is used to determine the power increase of the rear rotors, a thrust dependency can be observed. While for the isolated four rotor model, the thrust increase of the rear rotors appeared to be independent of the rotor thrust over a wide range from $T = 1/2 \cdot T_{hover}$ to $T = \cdot T_{hover}$, this changes when the influence of the frame is taken into account. Figure 5.77 illustrates this fact for the basic H-4 model as well as for the H-4 model with a smooth aerodynamic cover. It is assumed that this thrust dependency is caused by the wake of the motor arms.

In [51] a complete quadrotor configuration was simulated with the rotating rotors. When operated as an X-4 layout, with the rear rotors operating in the wake of the front rotors, at a constant RPM of the four rotors, the thrust of the rear rotors was found to be about 15 % lower than the thrust of the front rotors. This confirms the findings made with the actuator disc simulations here.

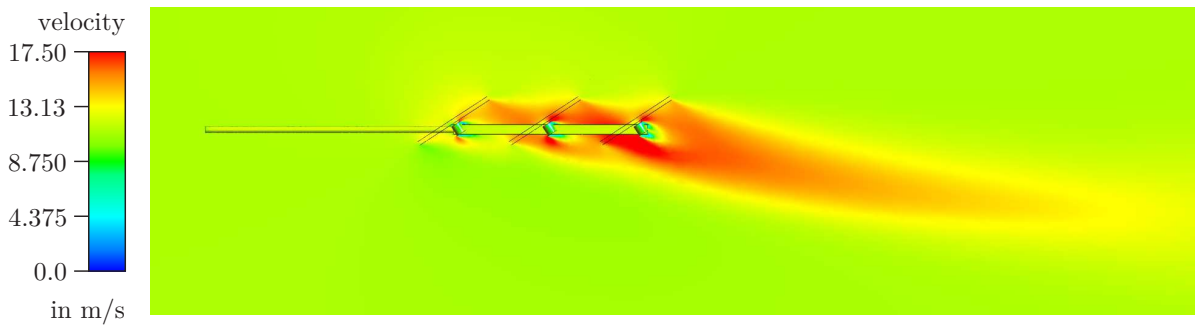


Figure 5.76: Rotor flow patterns of the H-6 configuration at $\sigma_{rotor} = 33^\circ$; $v_\infty = 11 m/s$; $T_{rotor} = 7.5 N$.

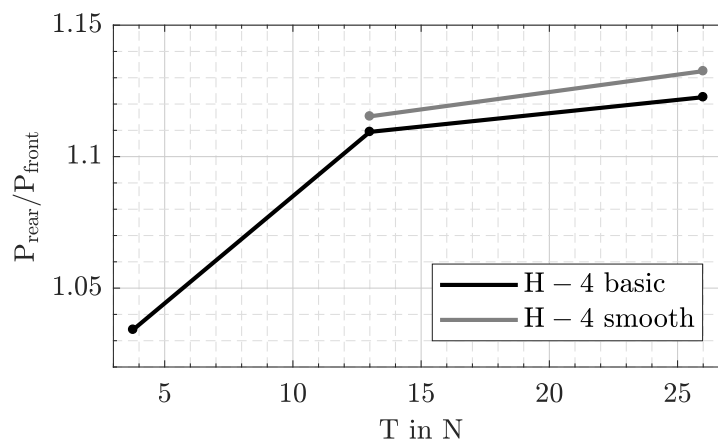


Figure 5.77: Dependency of rotor power ratio on rotor thrust at $v_\infty = 11 m/s$; $\sigma_{rotor} = 33^\circ$; $\rho = 1.185 kg/m^3$.

5.10.3 Maximum Yawing Moment

To estimate the aerodynamic moment, caused by the long measurement boom in front of the aircraft, simulations with the basic H-4 configuration at several sideslip angles β have been carried out. Figure 5.79 shows the flow pattern in the middle plane for two different sideslip angles. Figure 5.78 presents the results in numbers.

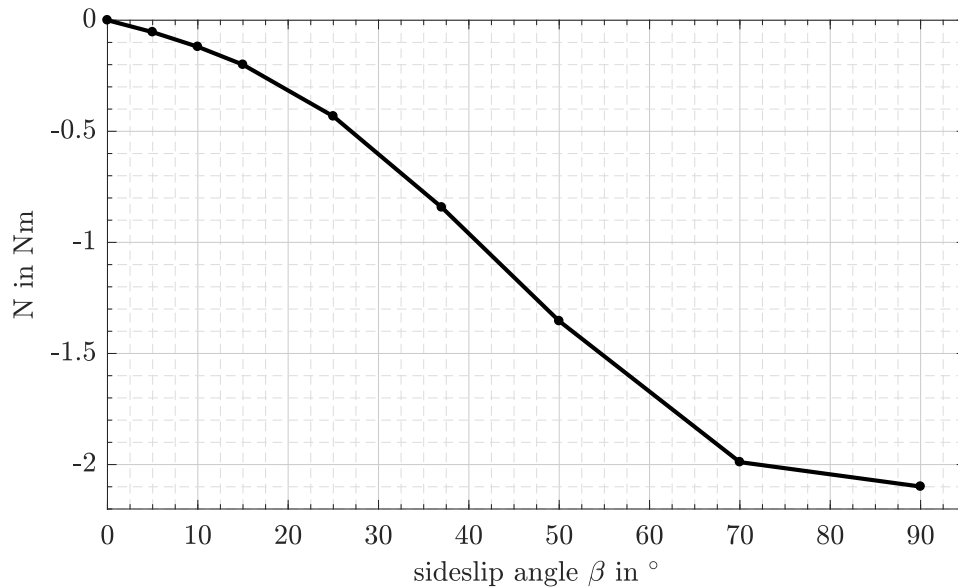


Figure 5.78: Yawing moments for the H-4 basic configuration at $\sigma_{rotor} = 33^\circ$; $v_\infty = 11 \text{ m/s}$; $T_{rotor} = 13 \text{ N}$; $\rho = 1.185 \text{ kg/m}^3$.

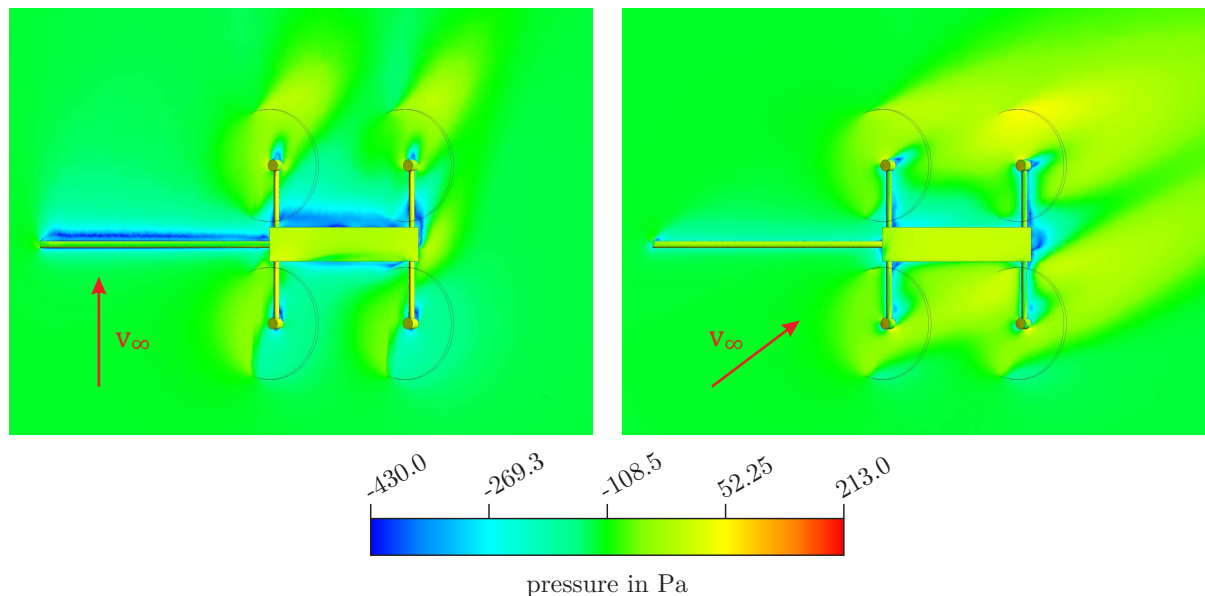


Figure 5.79: Flow visualization of the basic H-4 configuration at two different sideslip angles at $\sigma_{rotor} = 33^\circ$; $v_\infty = 11 \text{ m/s}$; $T_{rotor} = 13 \text{ N}$. Left: $\beta = 90^\circ$. Right: $\beta = 37^\circ$

Because the flow at the airframe itself appears to be almost symmetrical, the main source of

yawing moment is assumed to be the measurement boom and it is concluded, that the maximum yawing moment must be similar for all configurations.

5.10.4 Aerodynamically Shaped Cover

To investigate the use of an aerodynamically shaped airframe or an aerodynamically shaped cover mounted around the multirotor frame, the H-4 configuration was also modeled with such a smooth geometry. This study is, however, not aimed at a design optimization of a smooth airframe but meant to determine its impact in general.

The transition between measurement boom and main body was modeled in a smooth way, the main body was smoothed with a radius of $R = 16 \text{ mm}$ at the longitudinal edges and the rear end was closed with a wedge-like geometry.

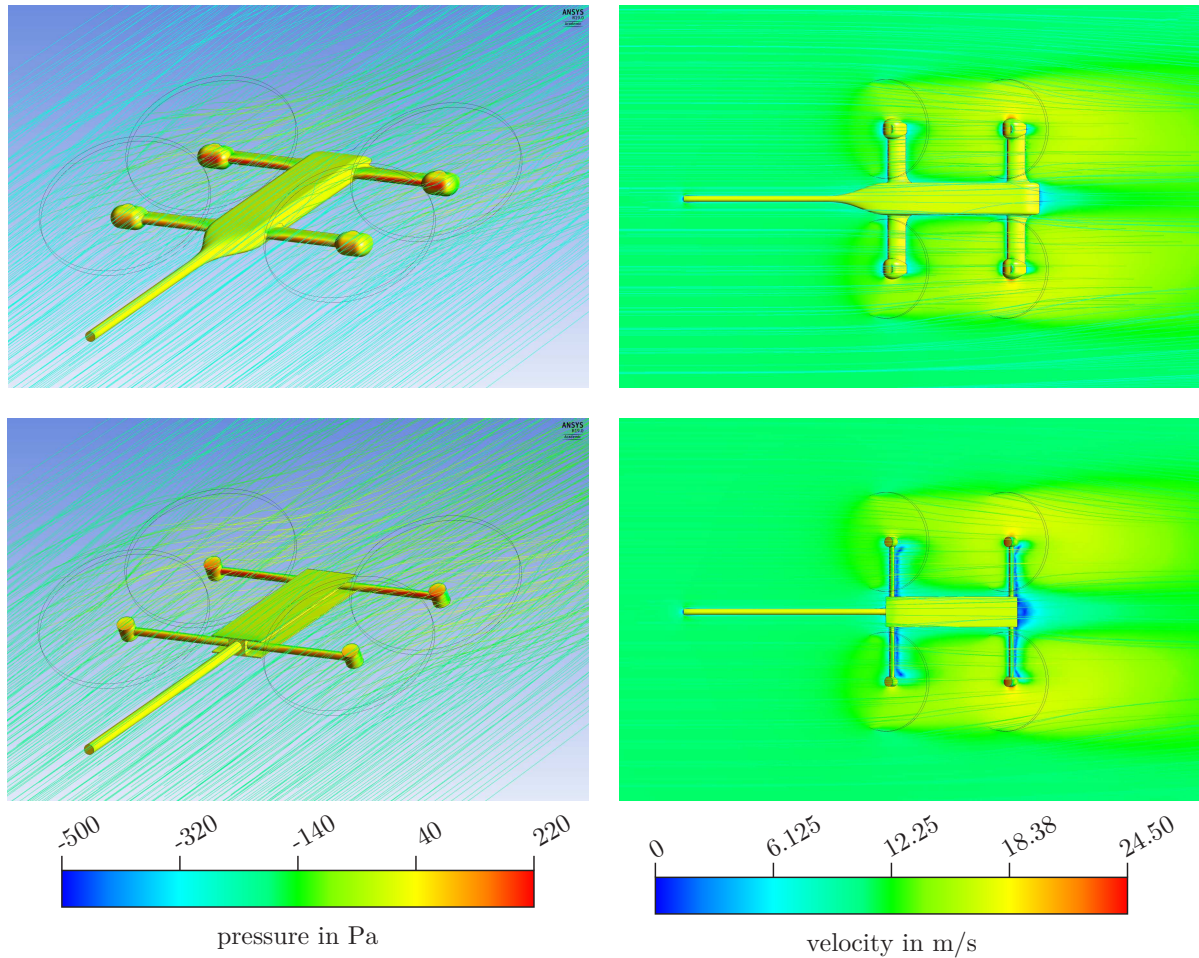


Figure 5.80: Flow around the basic H-4 and the smooth H-4 configuration at design point: $\sigma_{rotor} = 33^\circ$; $v_\infty = 11 \text{ m/s}$; $T_{rotor} = 13 \text{ N}$.

The motor arms have been surrounded by a symmetric, airfoil shaped profile with a chord of $c_{arm} = 89 \text{ mm}$ and a thickness of $t_{arm} = 16.6 \text{ mm}$. A smooth transition between the motor arms and the main body has been created and the motor cylinders at the end of the motor arms have also been covered with a thicker, symmetric, airfoil shaped extrusion.

Figure 5.80 demonstrates the differences between the basic H-4 configuration and the smoothed version. The biggest difference can be observed in the wake of the motor arms and the main body which is essentially larger for the basic H-4 configuration. This indicates a large source of pressure drag at the basic H-4 configuration. A comparison of overall drag for both configurations is given

in Figure 5.81. At zero thrust the smooth version has 45 % less drag and at $T = T_{hover}$ this value slightly increases to 50 % less drag.

Comparing the contribution of different airframe parts to the total drag, it can be shown that for both configurations more than 90 % drag is caused by the motor arms. At the basic H-4 configuration the drag force at the rear motor arms is 28 % higher than at the front motor arms. For the smooth configuration the drag at the rear motor arms is 50 % higher than at the front motor arms. A comparison of the wall shear forces of both configurations confirms the assumption,

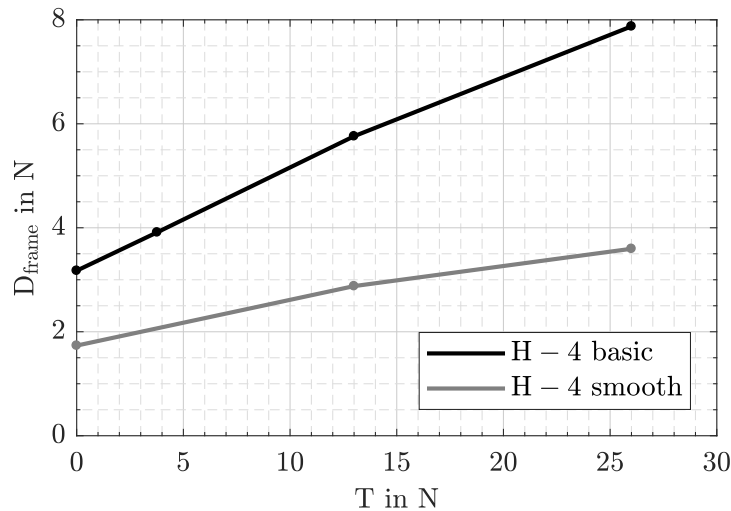


Figure 5.81: Drag force of the H-4 basic and the H-4 smooth configuration airframe at $v_\infty = 11 \text{ m/s}$; $\sigma_{rotor} = 33^\circ$; $\rho = 1.185 \text{ kg/m}^3$.

that the higher drag of the basic H-4 configuration is caused mostly by the stronger wakes of its motor arms. Because the flow around a circular object is a complicated phenomena, it should be noted once again, that the drag obtained from the aerodynamic simulations is only a rough estimate and the purpose of these simulations is a relative comparison between different rotor layouts and an understanding of the general effects.

Figure 5.82 illustrates the pressure distribution around the rear motor arms at two different lateral positions. The pressure has been plotted over a polar coordinate ϕ . The main source of drag is the negative pressure in the wake at the rear end of the motors arms ($0^\circ < \phi < 180^\circ$). The resulting drag force is sensitive to the position of the flow separation point, which is in turn sensitive to the Reynolds number and surface roughness and can only be simulated with a very fine mesh or a sophisticated wall function.

The SST turbulence model, used here, simulates a fully turbulent flow and cannot predict the transition from laminar to turbulent flow. The drag of a circular body is not determined by the surface friction but by the pressure drag of the wake whose size is determined by the boundary layer properties and consequently the flow separation point (D'Alembert's paradox). More details on this subject can be found in [52].

This on the other hand means, that a better estimation of the drag of circular motor arms can only be achieved with higher simulation effort. Hence, the total drag of the final vehicle has still to be validated in flight tests, especially if circular motor arms are used.

Figure 5.83 illustrates the improved flow and consequently lower drag at the transition region between measurement boom and main body.

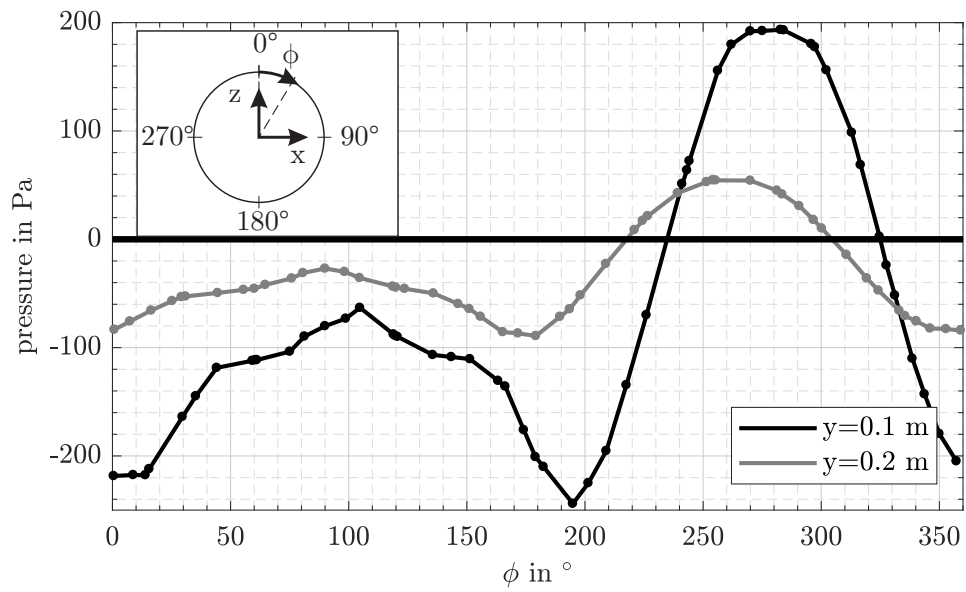


Figure 5.82: Pressure distribution on the rear motor arm surface of the H-4 basic configuration at design point: $\sigma_{rotor} = 33^\circ$; $v_\infty = 11$ m/s; $T_{rotor} = 13$ N.

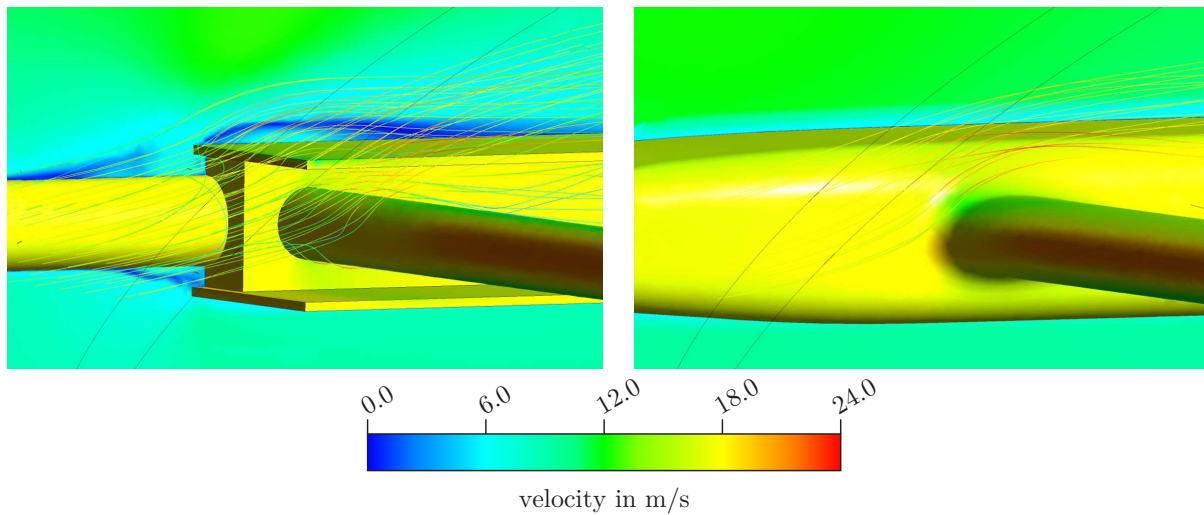


Figure 5.83: Flow around the transition region between measurement boom and main body for the basic H-4 and the smooth H-4 configuration at design point: $\sigma_{rotor} = 33^\circ$; $v_\infty = 11$ m/s; $T_{rotor} = 13$ N.

5.10.5 Drag of Different Configurations

Figure 5.84 gives an overview over the different configurations and the corresponding drag values. To be compare airframes with different reference areas, instead of c_D , $c_D \cdot A$ is compared, which is a direct measure for the resulting drag force.

It can be seen that the Y-6 configuration is the one with the lowest drag. This can be explained by the small motor arm frontal area. Another aerodynamic advantage of the Y-6 frame is the low influence of the front rotors on the rear rotors. The wake of the front rotors completely passes by the rear rotors without hitting them.

It should be mentioned however, that the Y-6 configuration was not trimmed and the front rotors have been set to $\sigma_{rotor} = 30^\circ$. To achieve a correct trim, the tilt angle of the front rotors as well as thrust of front and rear rotors have to be iteratively adjusted to achieve a balance of forces and moments. In general, the effect of different trim conditions on the drag value has been neglected for all configurations, but the biggest effect is expected for the Y-6 configuration.

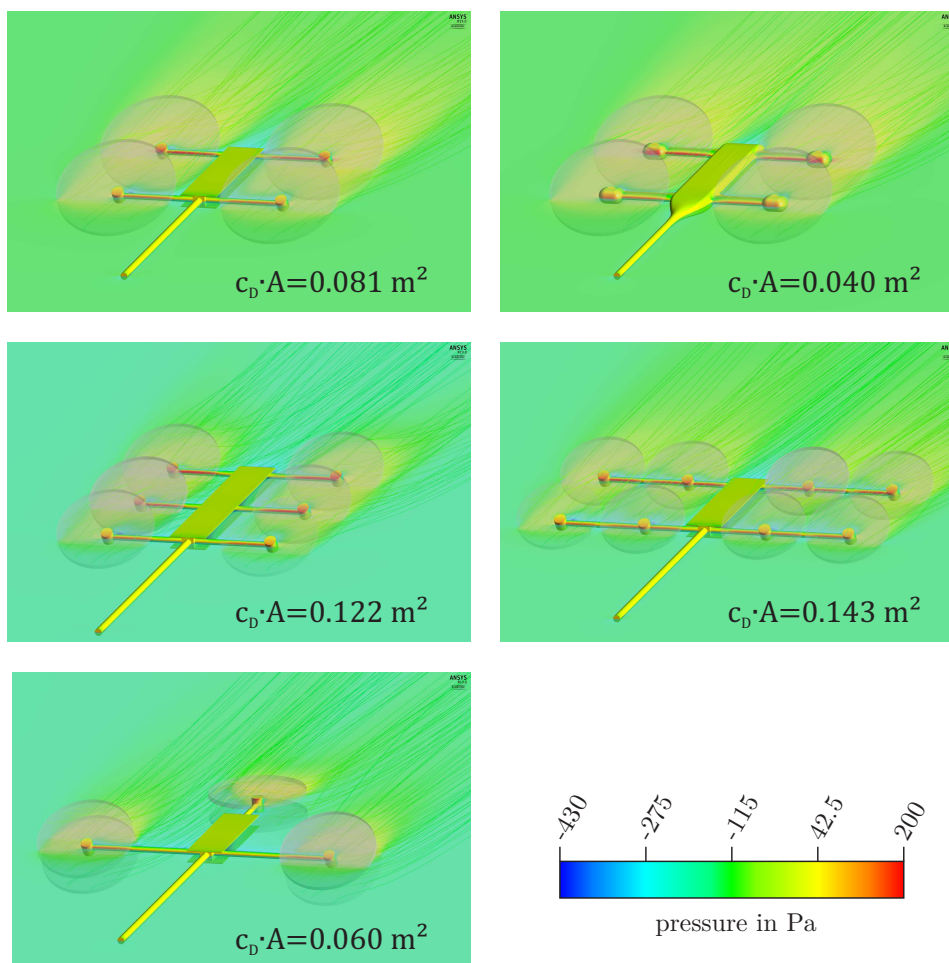


Figure 5.84: Flow patterns and drag values of the different configurations at the design point: $\sigma_{rotor} = 33^\circ$; $v_\infty = 11 \text{ m/s}$; $T_{total} = 52 \text{ N}$.

5.10.6 Modeling Approach

For a simple drag estimation during the conceptual design phase, it is always beneficial to have an analytical approach for different configurations instead of using a time consuming simulation process. It can be observed from the simulations, that the main sources of drag are the motor arms and the rear motor arms produce about 30 % more drag, because the rear rotors are operated in the wake of the front rotors and consequently need a higher induced velocity v_i . The following empirical simplification can be derived:

$$D = \frac{l_{eff}}{l_{0_{eff}}} \cdot D_0 \quad (5.10.3)$$

Where D_0 and $l_{0_{eff}}$ are the drag force and the effective boom length of the baseline configuration and l_{eff} is the effective boom length of the investigated configuration determined by:

$$l_{eff} = l_{front} + 1.3 \cdot l_{rear} \quad (5.10.4)$$

For the H-6 configuration the center and rear motor arms were both weighted with 1.3. Table 5.9 shows the result of this simplification, using D_0 from the H-4 configuration.

Configuration	H-4	Y-6	H-6	H-8 parallel
l_{front}	640 mm	985 mm	640 mm	1170 mm
l_{rear}	640 mm	0 mm	1280 mm	1170 mm
l_{eff}	1472 mm	985 mm	2304 m	2691 mm
D_{sim}	5.76 N	4.27 N	8.68 N	10.23 N
D_{est}	5.76 N	3.86 N	9.02 N	10.53 N
Error	0 %	-9.7 %	3.9 %	3.0 %

Table 5.9: Comparison of the frame drag modeled by Eq. (5.10.3) and the simulations.

5.10.7 Conclusions

The parametric CAD models in combination with automatic meshing and the actuator disc method have been proven as a powerful tool for the aerodynamic analysis in the conceptual design phase. Several rotor configurations were analyzed and compared. The following conclusions can be drawn:

- The maximum power increase for a rear rotor running in the wake of a front rotor was shown to be less than 15 % at the design point.
- The H-6 configuration with even three rotors operated in a row does not suffer from a much higher power penalty for the third row because the power increase from the second to the third row is much smaller than the power increase from first to the second row. This can be explained with momentum theory and the induced velocity which decreases if the inflow speed is increased.
- The wakes of the rotors have to be taken into account when determining the frame drag. A simulation of an isolated frame without rotor wakes will result in significantly less drag. The rotor thrust should be adjusted to a realistic range if the frame drag has to be determined accurately. A superposition of rotor forces and forces on an isolated frame is not recommended for flight performance evaluation.
- The maximum yawing moment with a measurement boom was identified to be approx. $N = 2 Nm$ for the basic H-4 configuration.
- The resulting drag for all configurations was significantly less than expected.
- Even with some safety margin for the real drag value the tilt angle is expected to be in the range between $\sigma_{rotor} = 15^\circ$ to $\sigma_{rotor} = 20^\circ$ instead of $\sigma_{rotor} = 30^\circ$ as calculated from the previous empirical drag estimation.
- For more detailed simulations in the future design processes, a balanced trim condition has to be derived by iterating tilt angle and thrust.
- A smooth aerodynamically shaped frame or an aerodynamically shaped cover mounted on top of the frame can reduce up to 50 % drag.
- The results are a simplified drag estimate, because the flow past circular objects is a phenomena sensitive to many parameters and difficult to predict without experiments. The drag of a multirotor frame with cylindrical motor arms has to be verified in flight tests or wind tunnel experiments.
- A simple empirical approach to model the frame drag by taking the motor arm length into account showed good agreement for the H-shaped configurations. In conclusion, it is possible to compensate for other motor arm lengths accurately, if a baseline simulation or experiment has been carried out.

5.11 Flight Time Analysis

The estimations regarding weight and drag for every configuration can be used to predict the flight time. The following input parameters are assumed:

- A take-off weight of $TOW = 4.8 \text{ kg}$ to maintain some reserve for additional equipment.
- A wind speed of $v_{wind} = v_{\infty} = 11 \text{ m/s}$.
- The drag value $c_D \cdot A$ determined from the overall aerodynamic simulations (see Section 5.10).
- The empty weights W_E from the mass estimation (Section B).

To calculate the flight times the resulting aircraft pitch angle θ is determined with the help of Eq. (5.3.5). This leads to the necessary total thrust using Eq. (5.3.4) which in turn can be used to determine the induced velocity by numerically solving Glauerts empirical approach given by Eq. (5.7.2). The result can be used to calculate the induced power with Eq. (5.10.2).

Preliminary BEM simulations (compare Section A.1.4) showed that the ratio between total power and induced power is approx. $P_{rotor,total}/P_{rotor,ind} = 1.5$. After the total power for each rotor has been calculated, the power of the rear rotors, operating in the wake of the front rotors, is increased by $P_{rotor,rear}/P_{rotor,front} = 1.12$, according to the overall aerodynamic simulations.

After the total mechanical power has been determined with the introduced correction factors, the total electrical power is computed with the assumption of an efficiency of $\eta_{electric} = 70 \%$ including motor losses, ESC losses and wiring losses.

The energy in the flight battery is estimated with the following generic equation:

$$E_{batt} = e_{batt} \cdot m_{batt} = \frac{5.0 \text{ Ah} \cdot 18 \text{ V}}{0.59 \text{ kg}} \cdot m_{batt} \quad (5.11.1)$$

The value for the specific energy of the flight battery, e_{batt} , has been taken from ([53]). This type of battery has been successfully used for the SWE hexrotor and as shown in Section A.7 the specific energy does not change much with different batteries.

Finally, the weight remaining for the flight battery is calculated by subtraction of the aircraft's empty weight W_E from the targeted take-off weight TOW and the flight time can be calculated as:

$$t_{flight} = \frac{E_{batt}}{P_{tot,electric}} \quad (5.11.2)$$

For the H-8 and Y-6 configuration, equipped with coaxial rotors, an additional loss by the coaxial rotor setup of $P_{coaxial}/P_{single} = 1.20$ is introduced. Performance measurements for the operation of coaxial propellers for multirotor aircraft in hover can be found in [55] and [56]. However, no reference is available for the operation of coaxial rotors in a multirotor aircraft in forward flight. It is assumed that these losses are smaller in forward flight (compare Section A.1.4).

Table 5.10 lists the resulting flight times for the different aircraft configurations. Because the H-6 and H-8 parallel configuration have a crucial deficiency regarding flight time, they have not been investigated any further.

Configuration	Resulting flight time
H-4	29.9 <i>min</i>
Y-6	30.0 <i>min</i>
H-6	15.2 <i>min</i>
H-8	24.8 <i>min</i>
H-8 parallel	19.2 <i>min</i>

Table 5.10: Resulting flight times for the different configurations.

5.12 Complete Comparison of the Remaining Configurations

After the most important parameters of all configurations have been identified and the H-6 and H-8 configuration could be ruled out, this section gives a short overview of all remaining configurations including additional aspects that haven't been considered yet. In addition, the previously estimated parameters are listed.

5.12.1 H-4

Weight and Balance

The H-4 configuration has an empty weight of $W_E = 3512 \text{ g}$ and the C.G. is easy to adjust because there is enough space for the flight batteries at the rear half of the airframe.

Flight Time

The Flight Time has been estimated to $t_{flight} = 29.9 \text{ min}$.

Vibration

If the RPM of the large rotors for the H-4 configuration is scaled according to Eq. (5.8.9) the advance ratio μ will be higher than it is for smaller rotors by the factor of $\mu_2/\mu_1 = R_2/R_1$. If the RPM is scaled according to Eq. (5.8.16) the advance ratio μ will be exactly the same as it is for the smaller rotors.

The advance ratio can be seen as a direct measure for the amplitude of the vibratory excitation forces in forward flight. If the advance ratio is kept constant, the amplitude of aerodynamic forces and moments, changing periodically once per revolution, caused by the different inflow conditions of the advancing and retreating blade, will be exactly the same for different rotor sizes. On the other hand, the excitation frequency is lower for larger rotors spinning at a lower RPM and hence farther away from the resonance frequency of the airframe and the motor arms, which are higher.

Since the design point of ANDroMeDA is closer to a hovering flight condition than it is to a forward flight condition (see Section 5.8), the advance ratio is expected to be higher for the larger rotors but still quite low in the range of $\mu = 0.15$.

The small number of rotors is also considered as a positive factor because less beat frequencies can occur.

In general vibrations are difficult to characterize without additional simulations and experiments. Therefore no negative effects are taken into account by the larger rotors regarding vibrations.

Flight Mechanics

As derived in detail in Section A.2.2, a larger propeller / motor combination is expected to result in a lower response time constant and hence in a reduced maneuverability and a reduced capability to hover in headwind at extreme wind conditions. According to the calculations in Section A.2.2 the response time of the H-4 configuration will be raised by a factor of 2 to 2.5, compared to an octorotor configuration.

Maximum Tilt Angle

The tilt angle of the H-4 configuration is not limited.

Redundancy

If one rotor fails the remaining three rotors are not able to keep the aircraft in a stable hovering flight. The only option for a safe landing is the periodic thrust change of the remaining rotors as demonstrated in [57] resulting in an aircraft spinning around the vertical axis. Since this method is still characterized as experimental and will most likely not be implemented in the flight controller, the H-4 configuration is classified as "non-redundant".

Transportation

The H-4 frame offers two different possibilities to fold the frame for transportation as pictured in Figure 5.85.

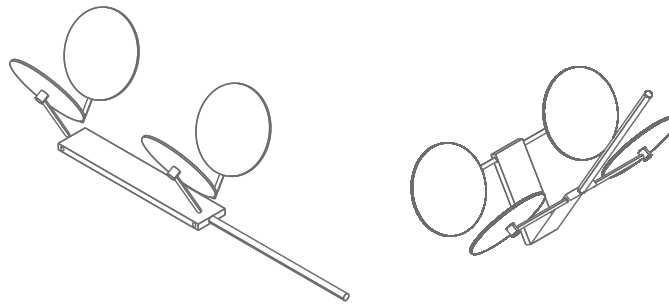


Figure 5.85: Possible folding patterns for transportation of the H-4 configuration.

Take-Off and Landing

Besides a complete retractable landing gear, another alternative is possible for the H-4 frame due to the tiltrotor concept. The tilting rotors offer an additional degree of freedom that can be utilized for take-off and landing. By tilting the entire frame towards a nose-up attitude it is possible to use only one single retractable landing strut. Another advantage of this concept is the increased distance between the tip of the measurement boom and the ground during take-off and landing.

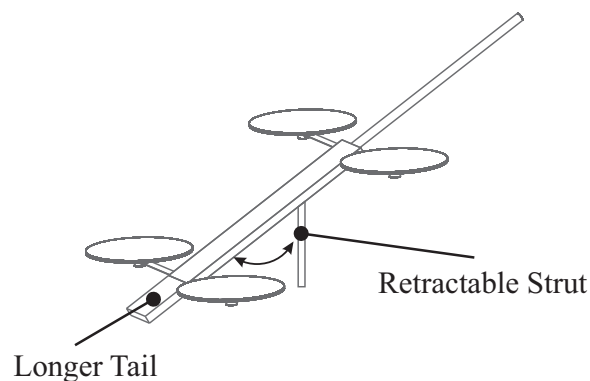


Figure 5.86: Landing configuration for the H-4 concept.

5.12.2 Y-6

Weight and Balance

The Y-6 configuration has an empty weight of $W_E = 3525 \text{ g}$, according to the preliminary mass estimation. The fact that the C.G. has to be closer to the front rotors than to the rear rotors could be beneficial and compensate for the C.G. shift caused by the long measurement boom, up to some extent. Because of the smaller frame with less space to move the flight battery, there is less flexibility to attain the C.G. position, compared to the other configurations.

Flight Time

The projected flight time for the Y-6 configuration is $t_{flight} = 30.0 \text{ min}$.

Vibration

The same considerations regarding rotor size, as noted for the H-4 configuration, are also valid for the Y-6 configuration. It could be beneficial that the rotors have a smaller diameter than the H-4 rotors because the advance ratio and hence the amplitude of vibratory loads is expected to be slightly lower. On the other hand the excitation frequency of aerodynamically induced excitations is higher and closer to the resonance frequency of the airframe if an under-critical operation is considered.

Another effect regarding vibrations that comes into play with the Y-6 configuration is the coaxial rotor configuration. This setup introduces an additional vibration source because the bottom rotors are immersed in the asymmetric wake of the upper rotors during forward flight / in headwinds.

In general, vibration characteristics are difficult to predict without dynamic simulations and experiments.

Flight Mechanics

According to Eq. (A.2.13), derived in Section A.2.2, the response time for the Y-6 configuration will be increased by a factor of 1.28 compared to an octorotor configuration. This result is based on a constant disc loading D.L.

Maximum Tilt Angle

If the front motor arms are not attached to the frame at an angle of $\varphi = 90^\circ$ (compare Figure 5.52), the maximum tilt angle is limited. The rear rotors are difficult to tilt and it is possible that, even if they are tilt-able, the rear tilt angle will be limited by the frame geometry.

Redundancy

If one of the front motors fails it is possible to shut down the one with the same direction of rotation on the opposite side. This results for example in two counter clockwise spinning front rotors and one clockwise spinning rear rotor. The one clockwise spinning rotor in the rear has to produce twice the thrust of the front rotors and hence the same torque than the two front rotors. This equilibrium state can only be achieved, if the rotors are capable of creating significantly more than $T = 2 \cdot T_{hover}$.

According to this considerations the Y-6 configuration is characterized as redundant to motor failures.

Transportation

For the Y-6 configuration possible folding patterns are given by folding the front motor arms forward or rearward. If three-bladed propellers are used it is not possible to fold the arms completely because the propellers will touch.

Take-Off and Landing

Take-off and landing with the Y-6 configuration is only possible with a fixed or completely retractable landing gear. It is not possible to point the entire frame upwards because of the rear rotor.

5.12.3 H-8

Weight and Balance

The H-8 configuration has an empty weight of $W_E = 3516\text{ g}$ and the C.G. is easy to adjust because there is enough space for the flight batteries at the rear half of the frame.

Flight Time

The projected flight time for the H-8 configuration is $t_{flight} = 24.8\text{ min}$

Vibration

Because of the smallest propellers, the H-8 configuration is operated at the lowest advance ratio, which reduces the amplitude of vibratory loads. On the contrary, the excitation frequency will be the highest and hence, closer to the natural frequencies of the frame, and due to the large number of rotors the most beat frequencies are expected. In addition, the aerodynamics of the coaxial rotor configuration is another possible source of vibrations. As for the other configurations, an exact quantification of vibrations is not possible during the conceptual design stage.

Flight Mechanics

As derived in Section A.2.2 the H-8 configuration is the one with the fastest thrust response.

Maximum Tilt Angle

The maximum tilt angle is not limited in the H-8 configuration.

Redundancy

If a motor fails, three other motors can be shut down and the H-8 configuration can be flown as a quadrotor. A general requirement is that the motors are capable of producing significantly more than $T = 2 \cdot T_{hover}$. Consequently, the H-8 configuration has a redundancy against motor failures.

Transportation

Folding patterns for the H-8 configuration are equivalent to the H-4 configuration, as illustrated in Figure 5.85.

Take-Off and Landing

The same take-off and landing concept, as introduced for the H-4 configuration in Figure 5.86, can be applied to the H-8 configuration.

5.13 Decision Matrix

After all features, advantages and disadvantages of the different configurations have been identified, a decision matrix is set up (Table 5.11). Because it is difficult to quantify the different aspects only three possible options are used. The option "1" is used if a negative impact is expected from this parameter. The option "2" is used if no clear statement can be made about this parameter and neither positive nor negative impacts are expected. If a parameter is expected to have positive impact a "3" is used. The H-8 configuration was chosen for ANDroMeDA, because of the highest

Parameter	Weight	H-4	Y-6	H-8
Flight Time	1	2	3	1
Vibrations	1	2	2	2
Response Time	2	1	2	3
Maximum Tilt Angle	1	3	1	3
Redundancy	1	1	3	3
Transportation	1	2	2	2
Take-Off and Landing	1	3	1	3
C.G. attainability	1	3	1	3
Score	-	18	17	23

Table 5.11: Decision Matrix.

score in the decision matrix. Another advantage of this configuration is that, if the coaxial rotor configuration causes strong vibrations, the H-8 configuration can be changed to a H-4 configuration during the flight evaluation stage.

5.14 Remaining Parameters

After rotor diameter, number of rotors and rotor layout have been fixed, several parameters still need to be defined:

- Width, length and height of the main body.
- Rotor distances xd_{rotor} and yd_{rotor} .
- Number of battery cells.
- Exact length of the measurement boom.
- Maximum rotor diameter.
- Maximum weight of an useful aerodynamic cover.

Width, length and height of the main body have been adjusted to reasonable values during the overall aerodynamic simulation. The final design values should be as small as possible.

The number of battery cells will be chosen during the aircraft component evaluation because it depends on the used motor and ESC. In general, a higher voltage leads to a lower current and thus lower electrical losses.

The exact length of the measurement boom can still be adjusted. The cable length between hot wires and hot wire electronics has to be exactly $l_{HW} = 0.9\text{ m}$. Depending on the needed space and placement of the hot wire electronics the length of the measurement boom slightly varies. During the estimation of the inertia tensor (see below), mass and dimensions of the hot wire electronics will be estimated and the measurement boom length will be adjusted.

5.14.1 Rotor Distances

The rotor distances have been previously scaled to achieve an equivalent flight mechanical behaviour of all configurations (see Section 5.9), but they have not been optimized for one particular configuration.

The rotor distances do have a significant influence on the maneuverability of the aircraft and there are two opposing effects:

On the one hand, a larger rotor distance will increase the maximum control moment because of the longer leverage. On the other hand, the moment of inertia increases, if the motor and propeller masses are moved farther away from the center.

The optimum rotor distances depend on the component weights and component placement. They are determined with the help of a more detailed CAD model than the one used during the overall aerodynamic simulation. Every component listed in the mass estimation (Section B) is modeled by a block and the blocks are placed according to their functions. During three iterations, each one supported by an analytical extrapolation, the control authority coefficients $M_{control}/I_{yy}$ and $L_{control}/I_{xx}$ have been optimized.

To evaluate the resulting control authority coefficients, they have been also calculated for the SWE hexrotor with a detailed CAD model (see Figure 5.4), which resulted in a value of $M_{control}/I_{yy} = 10.5 \cdot 10^{-8}\text{ Nm}/(g\text{ mm}^2)$ without payload and $M_{control}/I_{yy} = 8.1 \cdot 10^{-8}\text{ Nm}/(g\text{ mm}^2)$ with payload for the pitch control authority. The roll control authority was calculated as $L_{control}/I_{xx} = 9.06 \cdot 10^{-8}\text{ Nm}/(g\text{ mm}^2)$ without payload and $L_{control}/I_{xx} = 7.0 \cdot 10^{-8}\text{ Nm}/(g\text{ mm}^2)$ with payload.

Roll and pitch control authorities slightly differ even if payload and airframe of the SWE hexrotor are symmetric because of the asymmetric rotor layout. The SWE hexrotor is considered as an agile aircraft, therefore similar values are targeted for ANDroMeDA.

The three iteration steps are shown in Figure 5.87. Figure 5.88 describes the different components implemented in the model.

The first iteration with a distance of $x_{d_{rotor}} = 0.59 \text{ m}$ resulted in a pitch control authority of $M_{control}/I_{yy} = 2.9 \cdot 10^{-8} \text{ Nm}/(g \text{ mm}^2)$ while the second iteration with a distance of $x_{d_{rotor}} = 0.80 \text{ m}$ could reach a pitch control authority of $M_{control}/I_{yy} = 4.13 \cdot 10^{-8} \text{ Nm}/(g \text{ mm}^2)$. For the third iteration the distance was reduced again to $x_{d_{rotor}} = 0.55 \text{ m}$ but with a different component placement and corrected assumptions for the mass estimation. The pitch control authority could hereby be further increased to $M_{control}/I_{yy} = 4.52 \cdot 10^{-8} \text{ Nm}/(g \text{ mm}^2)$.

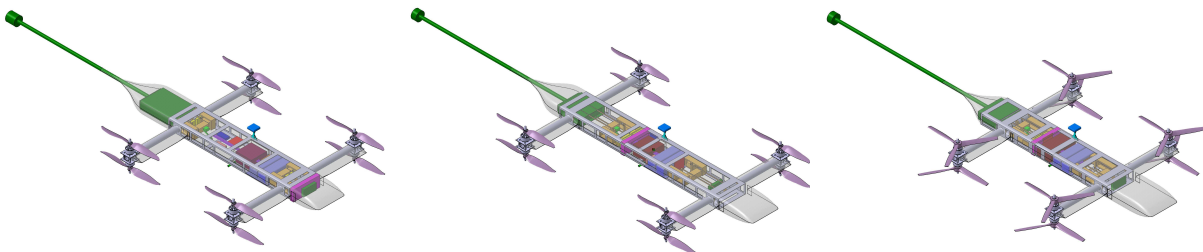


Figure 5.87: Left: First iteration. Center: Second iteration. Right: Third iteration.

Regarding the roll control authority, ANDroMeDA's long and slender design has a big advantage. Therefore, it was decided to use a lateral rotor distance of $y_{d_{rotor}} = 0.65 \text{ m}$ without any further optimization. A higher value will increase the airframe drag. It is likely that a lower value exists that will result in a better roll control authority but with the chosen value it is possible to mount propellers up to $D_{prop} = 0.47 \text{ m}$ and consequently the H-8 configuration can be transformed into a H-4 configuration without any modifications to the frame and motor arms, if vibration problems occur, caused by the coaxial rotors.

The roll control authority for the final configuration is $L_{control}/I_{xx} = 11.9 \cdot 10^{-8} \text{ Nm}/(g \text{ mm}^2)$, which is higher than the target value.

It has to be noted that the same value of pitch control authority as for the SWE hexrotor could not be reached but a value of the same magnitude could be achieved. The reason for that is mostly the measurement equipment with its large distance to the C.G., as well as the needed counterweight to attain the C.G. Also the H-topology instead of a X-topology, as used for the SWE hexrotor, comes into play. This demonstrates, that a purpose-designed aircraft makes much more sense for airborne wind measurements, compared to the use of an existing multirotor aircraft equipped with a probe.

Regarding the lower pitch control authority, one should also keep in mind, that due to the tilting rotor concept it is not necessary to tilt the entire aircraft in order to hold its position in space. To get an impression of the different masses involved and their contribution to the overall moment of inertia the pie chart in Figure 5.89 illustrates how the moment of inertia is mostly driven by components that change their position with $x_{d_{rotor}}$, but also by the measurement equipment, while the fixed components only have a minor influence.

The shares of the non-fixed components are segmented in further detail in Figure 5.90.

During the component placement a general question arose: "Is it better to adjust the C.G. by moving smaller masses or the larger ones?". This question can easily be answered if two bodies are considered, one with the mass m and a second heavier one with a mass of m' , scaled by a

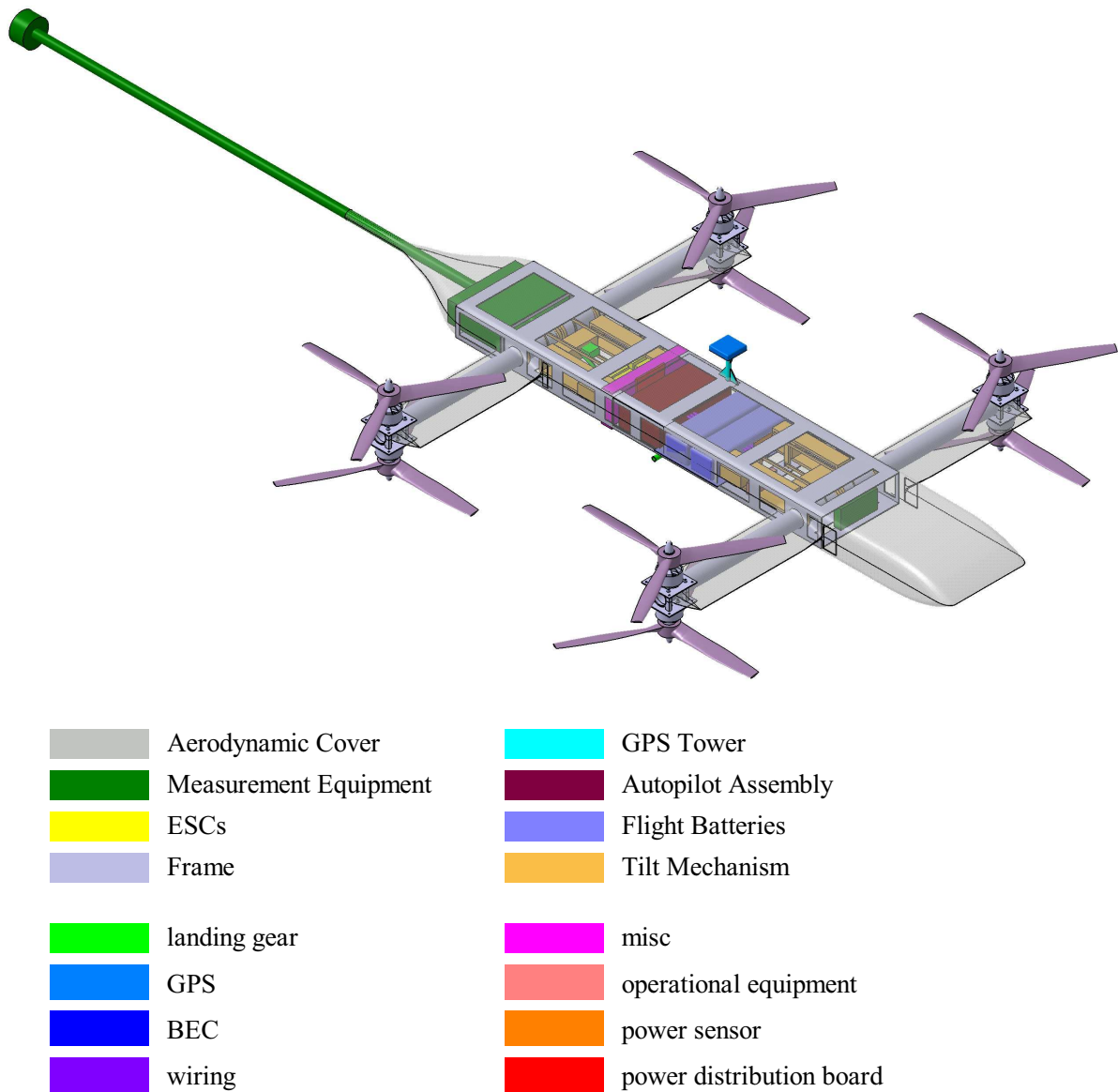


Figure 5.88: Components used for the model.

factor a so that $m' = a \cdot m$. The resulting mass moment will be:

$$ms = d \cdot m \quad (5.14.1)$$

Where d is the distance to the C.G. At the same time the additional contribution to the overall moment of inertia about the y-axis is:

$$I_{yy} = m \cdot d^2 \quad (5.14.2)$$

For the considerations here, only the second term of the parallel axis theorem is of interest, because the examined objects will be present anyway and they are just moved fore or aft so the first term for both objects remains unchanged.

If one assumes a fixed imbalance ms , that has to be compensated for by moving either m or m'

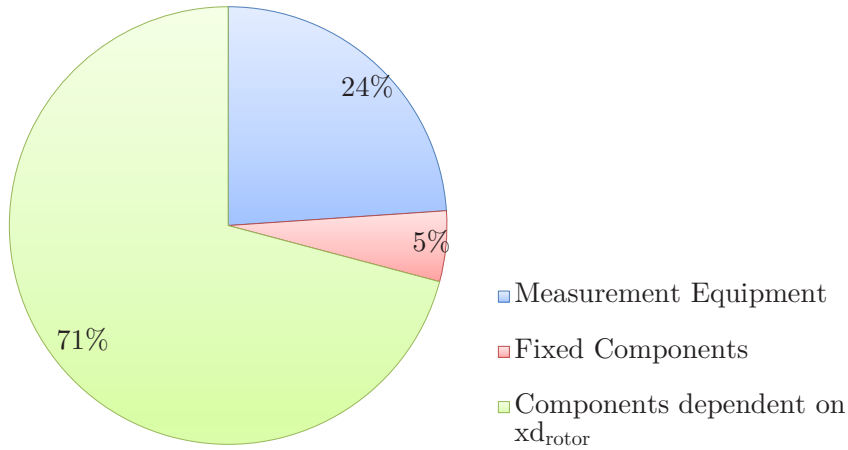


Figure 5.89: Contribution from different categories to the moment of inertia about the y-axis I_{yy} .

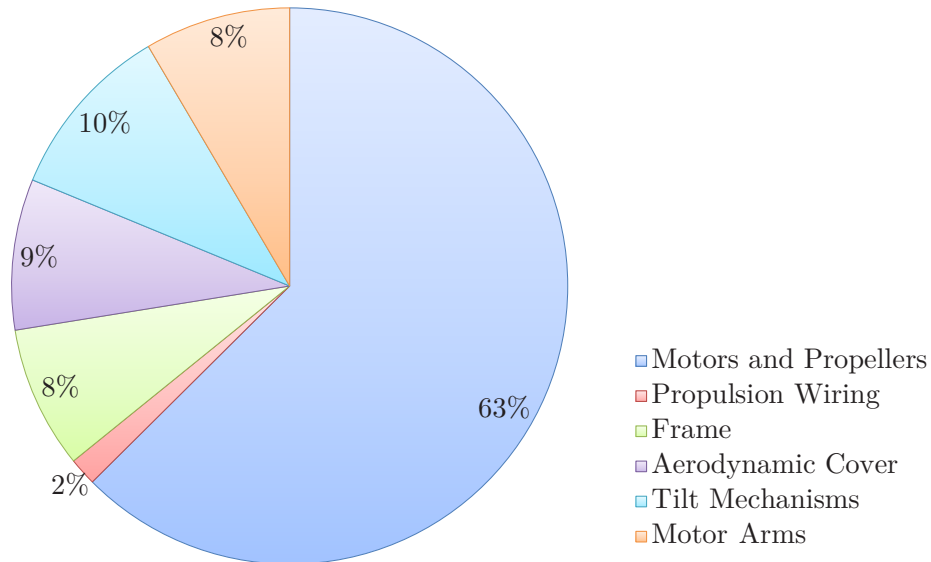


Figure 5.90: Contribution to the moment of inertia about the y-axis I_{yy} from components changing their position if $x_{d_{rotor}}$ is changed.

away from the C.G., the resulting distances to achieve ms are related by:

$$\frac{d'}{d} = \frac{1}{a} \quad (5.14.3)$$

This means that the heavier mass has to be moved less outward by a factor inversely proportional to a . At the same time this results in a smaller contribution to the moment of inertia by the same factor:

$$\frac{I'_{yy}}{I_{yy}} = \frac{1}{a} \quad (5.14.4)$$

Hence, a lower moment of inertia can be achieved if heavy components are used to adjust the C.G. because they have only to be moved away from the C.G. very little while lighter components have to be moved further away. These relations have been used as a general guideline during the detailed design and component placement.

To check how close the third iteration is to the optimal control authority the additional contribution to the moment of inertia about the y-axis has been calculated by Eq. (5.14.2) for all non-fixed components. To evaluate the pitch control authority for other rotor distances, the baseline moment of inertia was scaled by $(xd'_{rotor}/xd_{rotor})^2$. The results are shown in Figure 5.91. Consequently, with a smaller distance xd_{rotor} the pitch authority could be increased by 10 % but a smaller rotor distance would mean that the H-8 configuration cannot be changed to the H-4 configuration. Since the space for components inside the frame is limited, the rotor distance from the third iteration of $xd_{rotor} = 0.55 \text{ m}$ was used as final value.

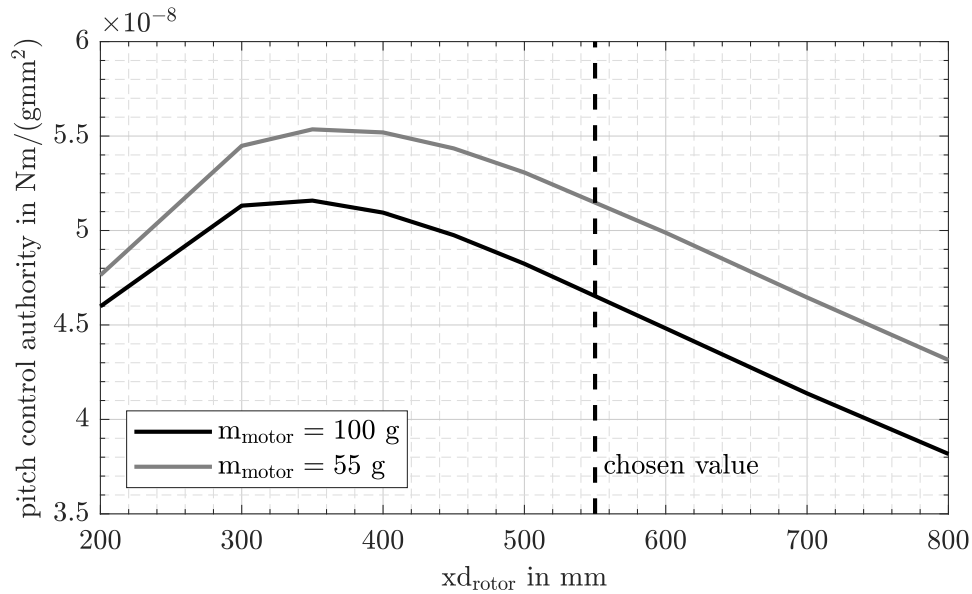


Figure 5.91: Resulting pitch control authority for different rotor distances xd_{rotor} .

5.14.2 Maximum Rotor Diameter

For the previous comparison of all configurations the rotor diameters have been scaled for a constant disc loading, which has been chosen according to experiences with existing multirotor aircraft. For the final design of ANDroMeDA it is important to know which maximum rotor size is beneficial.

As derived in Section 5.8, considering only aerodynamics, rotors of much larger diameters, than the ones shown in Table 5.7, will still result in a lower induced power. On the contrary, it is shown in Section A.2.2 that a larger propeller will also result in a slower response time of the propulsion system.

One aspect that has not been investigated yet, is the effect of additional weight, introduced by larger propellers and larger motors, on the flight time. Only if that effect is considered, an optimal propeller size can be derived.

As stated in Section 1.5 the take-off weight is a fixed value because of legal limitations. This on the other hand means, that all weight saved by lighter propellers and lighter motors can be used for a larger flight battery. Following the procedure from Section 5.11 the induced power is calculated as a function of rotor diameter and then multiplied by different factors accounting for the power losses caused by rotor aerodynamics, rotor interferences and the electrical losses. In the end the overall electrical power is obtained.

While the flight time t_{flight} is kept constant at a baseline value, the necessary battery weight is calculated for different values of induced power and hence different rotor diameters:

$$m_{batt}(D_{rotor}) = \frac{E_{batt}}{e_{batt}} = \frac{t_{flight} \cdot P_{tot,electric}(D_{rotor})}{e_{batt}} \quad (5.14.5)$$

By subtracting this battery weight from the baseline battery weight, a maximum additional weight for the propulsion system can be calculated, which is shown in Figure 5.92. If the additional weight of larger propellers and motors is less than this value the flight time will increase. Figure 5.92 will

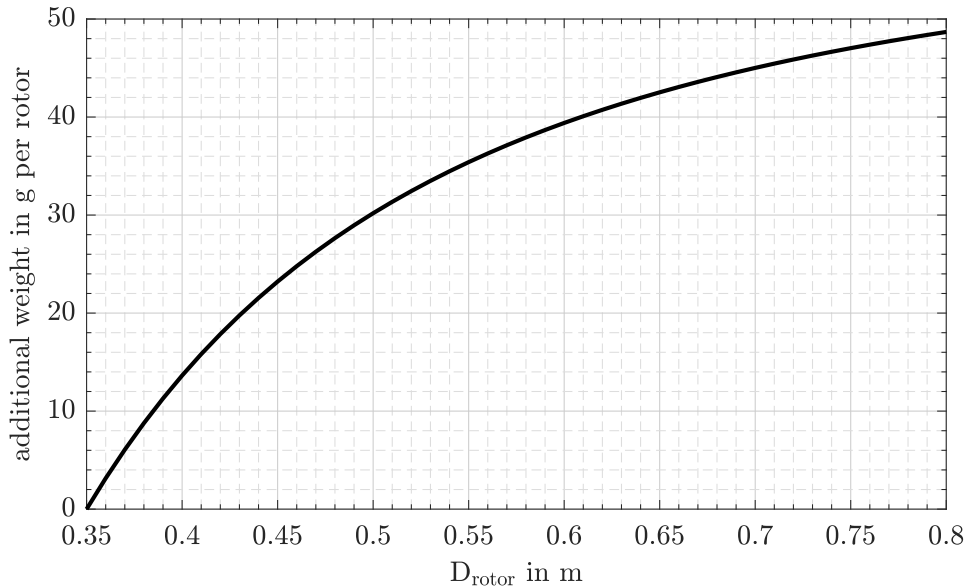


Figure 5.92: Maximum allowable weight increase due to larger propellers at design point: $v_{\infty} = 11 \text{ m/s}$; $c_D \cdot A = 0.081 \text{ m}^2$; $TOW = 4.8 \text{ kg}$ (with reserve); $\rho = 1.18 \text{ kg/m}^3$; $t_{flight} = 18 \text{ min}$; $e_{batt} = 0.151 \text{ Wh/g}$.

be used during the aircraft component evaluation and detailed design of ANDroMeDA. Compared to the pure reduction of induced power, caused by the larger rotors only a small increase of rotor diameter is useful when the additional weight is considered (see motor and propeller weights in Section B.1).

5.14.3 Maximum Weight of an Useful Aerodynamic Cover

In a similar manner as the maximum additional weight for larger propellers the maximum weight of an useful aerodynamic cover can be estimated. The reduced drag resulting from an aerodynamic cover will result in a smaller tilt angle σ_{rotor} and thus in a lower rotor thrust. This can be computed with Eq. (5.3.3). For the basic H-4 configuration, with a drag coefficient of $c_D \cdot A = 0.081$, an equilibrium condition is reached at $\sigma_{rotor} = 7^\circ$ and $v_\infty = 11 \text{ m/s}$. With the smooth H-4 configuration and a drag coefficient of $c_D \cdot A = 0.040$ an equilibrium will be reached at a tilt angle of $\sigma_{rotor} = 3.47^\circ$.

If the weight remains unchanged, the new inflow condition for the rotors would result in a flight time of $t_{flight} = 30.47 \text{ min}$ instead of $t_{flight} = 24.8 \text{ min}$. The more interesting question is, how much the aerodynamic cover can weigh, without reducing the flight time.

This question can be answered by calculating the battery weight that will result in the same flight time at the lower total power $m_{batt}(P_{total}(\sigma_{rotor} = 3.47^\circ, t_{flight} = 24.8 \text{ min}))$. This battery mass is then subtracted from the initial battery mass used for the H-4 frame without an aerodynamic cover to reach the same flight time $m_{batt}(P_{total}(\sigma_{rotor} = 7^\circ, t_{flight} = 24.8 \text{ min}))$.

The result is a maximum weight for the cover of $m_{cover} = 239 \text{ g}$. An aerodynamic cover that is heavier than that value will result in a shorter flight time, in spite of the reduced drag. The reason for the relatively low increase in flight time and the low value of m_{cover} is that the design point of ANDroMeDA is close to a hovering flight condition. At higher speeds the lower drag of an aerodynamically shaped cover will have a much larger effect. During the detailed design stage, when a more precise estimation of the cover weight is available, the use of an aerodynamic cover will be reevaluated.

6 Prototyping of AnDroMeDA

6.1 Detailed Design

The detailed design of ANDroMeDA can be divided into the following main assembly groups:

- Frame
- Tilt mechanism
- Landing gear
- Battery mount
- Measurement boom / measurement probe
- Aerodynamic cover

When the necessary interfaces are considered, it can be seen, that each of the above listed assembly groups has an interface with the frame assembly, but no other interfaces are present between the different assemblies. Furthermore, no hard interface exists between tilt mechanism and frame because the two are highly integrated.

Consequently, the design concepts for the frame and the tilt mechanism will be defined first and after that, every assembly group can be designed more or less independently.

6.1.1 Frame Design

For the ANDroMeDA frame five different methods of construction have been considered as sketched in Figure 6.1.

Method A is the most common one to build a multicopter aircraft at the present time. Two baseplates are connected by several screws and clamps or screws and distance tubes. However, for a larger number of screws is necessary to build a H-configuration and the weight is expected to be quite high, compared to an usual X-configuration, where the center plate is small and can be connected with only a few screws. Even for the SWE hexrotor frame with a small center and a total frame weight of $m_{total} = 352 \text{ g}$, a weight of $m_{screws} = 159 \text{ g}$ accounts for the screws.

Method B eliminates the need for many of the screws. It uses a single center plate and several other boards that are glued to the center plate, ideally with the help of a tongue and groove design. This design offers a very good accessibility of all components. On the other hand, the components are not well protected and the bending and torsional stiffness of the frame is expected to be low.

Method C makes use of the tongue and groove technique. Several bulkheads, a front and a rear part, side parts and top and bottom boards are glued together. This design offers good protection for the components with good accessibility through openings, in combination with a very stiff frame, made from CFRP material. A disadvantage is the relatively high fabrication effort to achieve the necessary tolerances for the tongues and grooves and to glue all the parts together by hand.

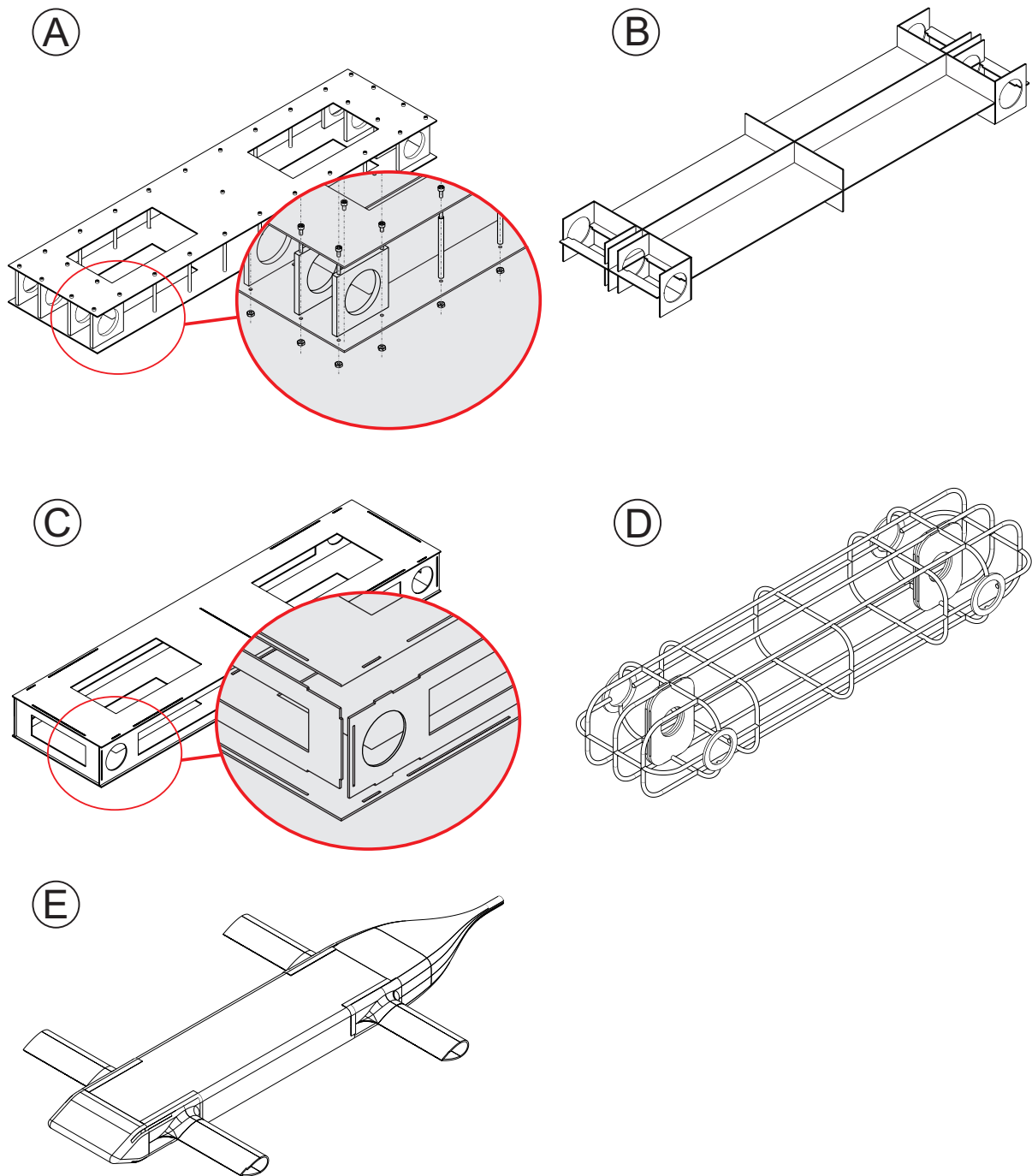


Figure 6.1: Construction methods considered for the ANDroMeDA frame.

Method D builds the frame from carbon fiber rovings, laid out in several particular molds or one mold with a disposable core, for the entire frame. This results in a very lightweight frame with an optimal placement of all carbon fibers according to the current load directions. The design can be optimized with the help of a genetic algorithm and FEA. On the downside the fabrication effort is extremely high, because even after the molds have been fabricated the carbon fiber lay out is done by hand. Furthermore, the optimized design might result in a low accessibility of the components because only few openings remain.

Method E uses a shell and several bulkheads, similar to a regular composite airplane fuselage, and hereby eliminates the need for an additional aerodynamic cover. It is however not expected, that this results in a lighter construction than a frame built with method A to D, combined with a light weight aerodynamic cover. In addition, the accessibility of the components is poor, unless large, weakening openings are included. The manufacturing effort is expected to be quite high, because similar to method D, molds have to be fabricated and the build up process is done by hand.

Parameter	A	B	C	D	E
Frame weight	1	1	3	3	1
Fabrication effort	3	2	1	1	1
Accessibility of components	2	3	3	1	1
Score	6	6	7	5	3

Table 6.1: Decision Matrix for the frame construction method.

All the considerations are concluded in a decision matrix shown in Table 6.1. Based on the evaluation, method C was chosen for ANDroMeDA. To increase the torsional stiffness of the frame, diagonal struts have been used (not shown in Figure 6.1). Material thickness and all dimensions such as the width of the struts e.g. have been chosen empirically according to previous building experiences. No particular load case driven design has been chosen for the frame but

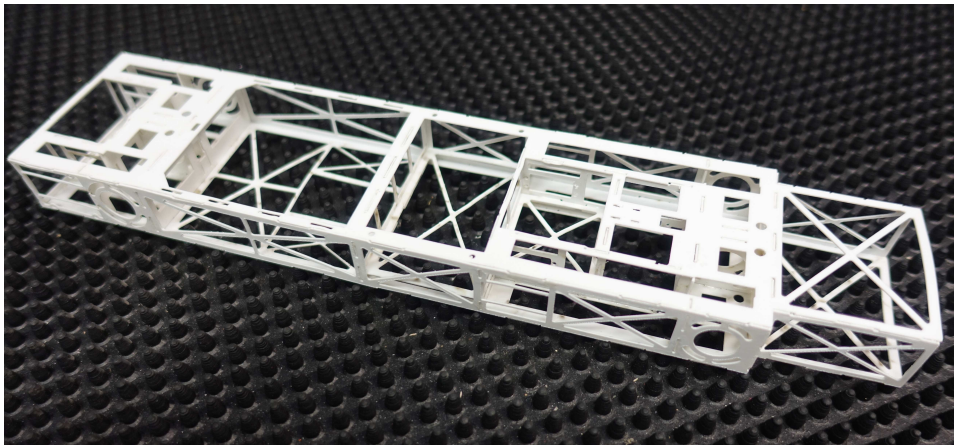


Figure 6.2: Test model of the ANDroMeDA frame in scale 1/3.

some improvements could be made after the CAD model was finished in the first iteration. The frame was scaled down to a 1/3 scale and was test-built from a polystyrene sheet with $t = 0.5 \text{ mm}$ instead of CFRP boards with $t = 1.5 \text{ mm}$. The polystyrene sheet was cut with an epilog laser cutter and engraver and could be assembled in a couple of hours. Figure 6.2 shows the result and it was possible to ensure that all the connections have been drawn properly in the CAD model. Furthermore, by applying loads to the small scale model, several structural weaknesses could be identified and improved, as shown in Figure 6.3.

For components that have to be screwed to the frame press-in steel nuts have been chosen as shown in Figure 6.4. Some slightly loaded components, as for example the GPS antennas or the light weight aerodynamic cover, are mounted with nylon screws and M2 threads are cut directly

into the CFRP boards.

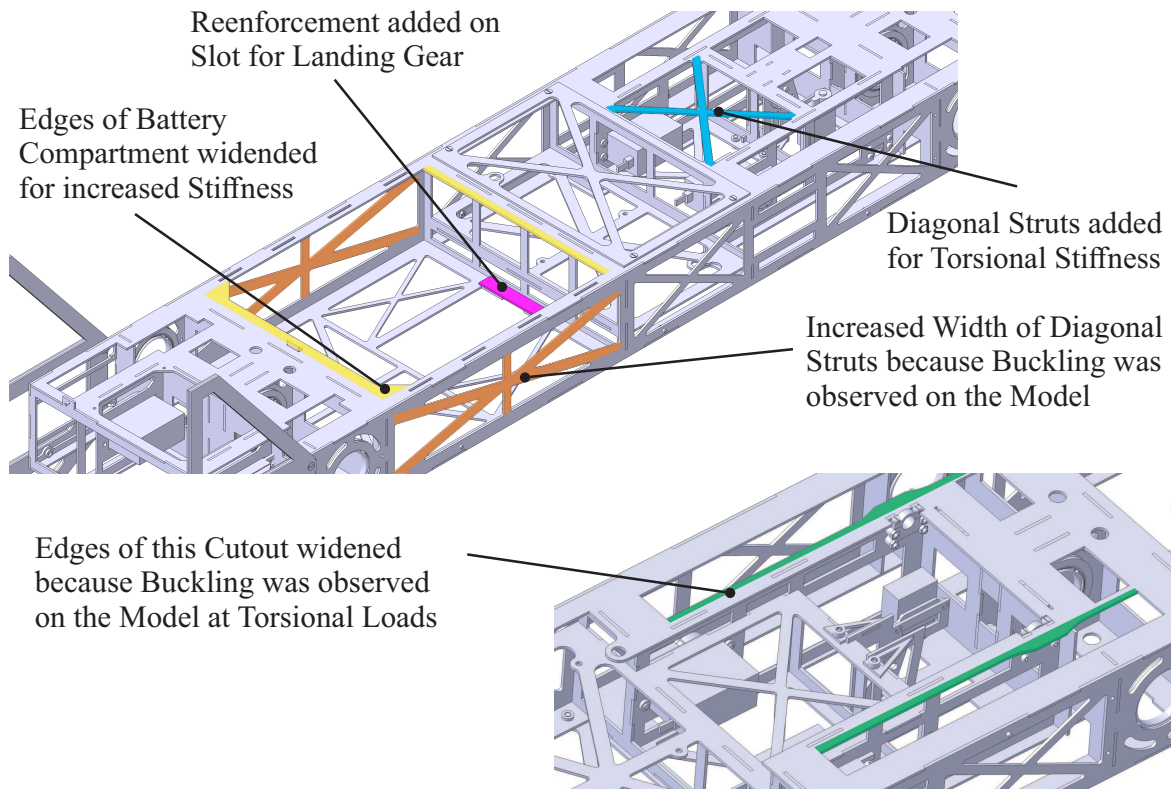


Figure 6.3: Structural improvements derived from the 1/3 scale model.

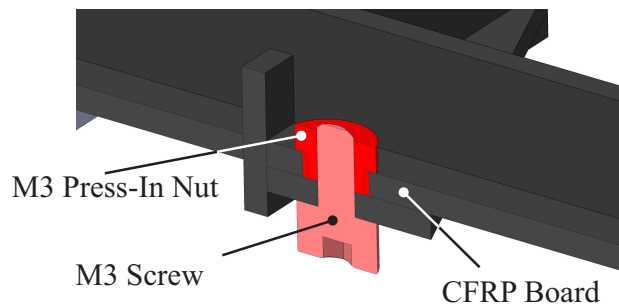


Figure 6.4: Assembly with M3 press-in nut at the landing gear module.

6.1.2 Tilt Mechanism

Working principle

For the design of the tilt mechanism different working principles have been considered as shown in Figure 6.5. The features of each solution are:

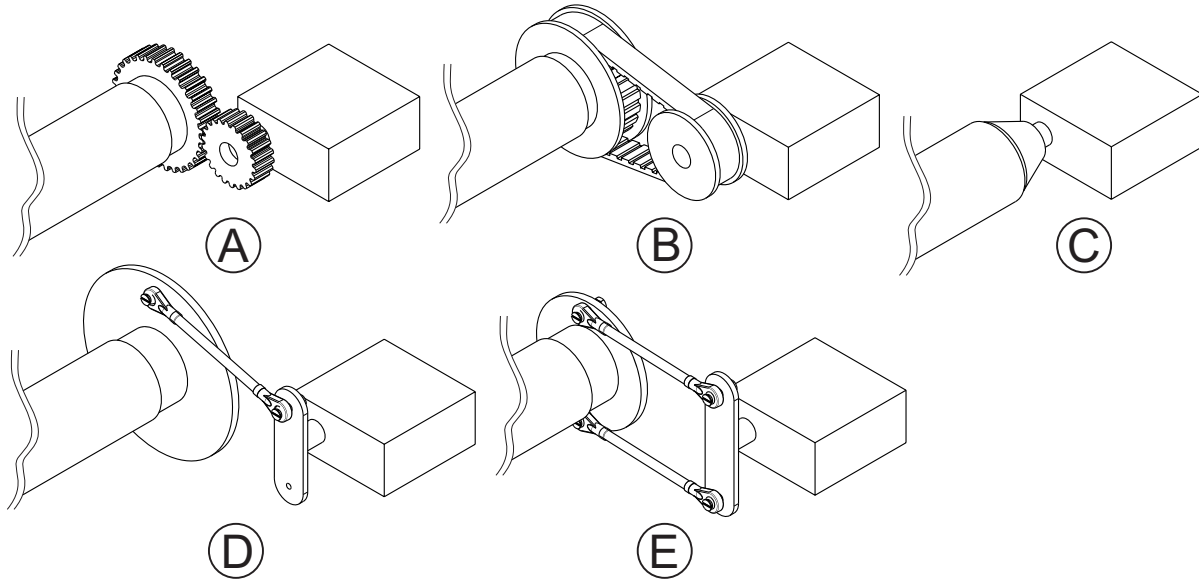


Figure 6.5: Working principles of a propeller tilting mechanism.

- Principle A - Actuator and motor arm are connected with gears:
Continuous rotation is possible and a reduction of the actuator speed is possible. For operation with low friction a minimal amount of play is necessary.
- Principle B - Actuator and motor arm are connected with a toothed belt:
Continuous rotation is possible and a reduction of the actuator speed is possible. Play in the connection can be almost eliminated by a proper belt tension. The belt might wear off and might need replacement after a certain maintenance interval.
- Principle C - Actuator axis of rotation and motor arm axis of rotation coincide:
Continuous rotation is possible. A reduction of the actuator speed is not possible. The connection is free of play. Additional space is needed along the arm axis which increases the necessary frame width.
- Principle D - Actuator and motor arm are connected with a single rod:
Continuous rotation is not possible. A reduction of the actuator speed is possible. The connection has some play in the spherical bearings and due to deflection of the rod.
- Principle E - Actuator and motor arm are connected by two push-pull rods:
Continuous rotation is not possible. A reduction of the actuator speed is not possible. The connection has very little play because one rod is always pulled and thereby the opposite rod cannot deflect.

For the operation of ANDroMeDA a continuous rotation of the tilting propellers is not needed. Considering the nose up attitude of $\theta = 30^\circ$, that the aircraft will take during take-off and landing,

a maximum propeller tilt angle of $\sigma = \pm 60^\circ$ is foreseen. This range is exactly the angular travel of most servo actuators. Consequently, no travel/speed reduction is needed. After good experiences on the tilt rotor test rig (see Section A.5.4) with working principle E, this principle was chosen for the ANDroMeDA tilting mechanism.

Bearing of the Motor Arms

After identification of the eigenfrequencies of several CFRP tubes, a tube with an outer diameter of $D_{arm} = 28 \text{ mm}$ has been selected for the motor arms. Other than the smaller tubes, this tube, combined with the mass of motors and propellers, has a first natural bending frequency higher than the second harmonic of the propeller's rotational frequency. Because bearings of this diameter are usually quite heavy, thin section bearings with $D = 37 \text{ mm}$, $d = 30 \text{ mm}$, $w = 4 \text{ mm}$ and a weight of $m_{bearing} = 8 \text{ g}$ have been selected. With eight bearings, two for each motor arm, a weight of $m_{bearing,total} = 64 \text{ g}$ is needed for a proper bearing solution. Because CFRP tubes usually are not available with precise diameter tolerances, additional aluminum tubes with $d = 28 \text{ mm}$ and $D = 30 \text{ mm}$ have to be machined.

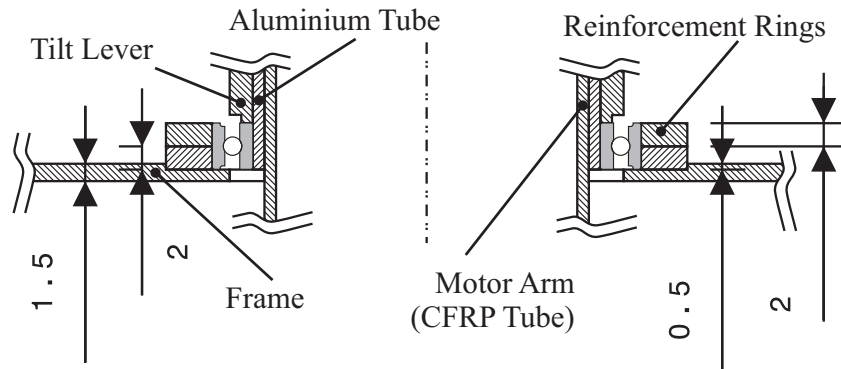


Figure 6.6: Pockets in the side CFRP boards of the chassis ensure a positive connection.

To keep the weight as low as possible, the bearings are directly inserted to the CFRP side parts of the frame, which are thickened by glued on reinforcement rings around the bearings, as illustrated in Figure 6.6. To ensure that the reinforcement rings are positively connected to the side parts of the frame, and the connection is not only relying on the bonding, pockets of $t = 0.50 \text{ mm}$ depth are milled in the CFRP frame side parts.

Two plastic parts, milled from POM have been designed to serve as axial stops. The outer stop also fulfills the function of a lever for the push-pull connections. Due to the limited space, the stops are equipped with a press-in nut. To enable access to both sides, screw head and press-in nut, holes on top and bottom of the frame have been added. The entire design is shown in Figure 6.7.

Servo Mounts

The tilt servo actuators will be mounted to the frame using the same M3 press-in nuts as depicted in Figure 6.4. To be able to insert the servos, cutouts in the side CFRP boards of the frame are added as shown in Figure 6.8.

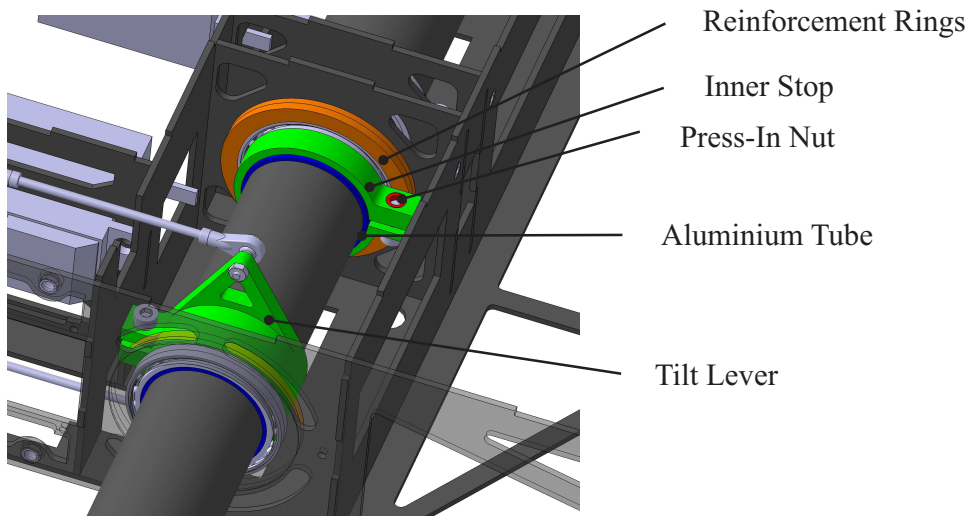


Figure 6.7: Final tilting mechanism design.

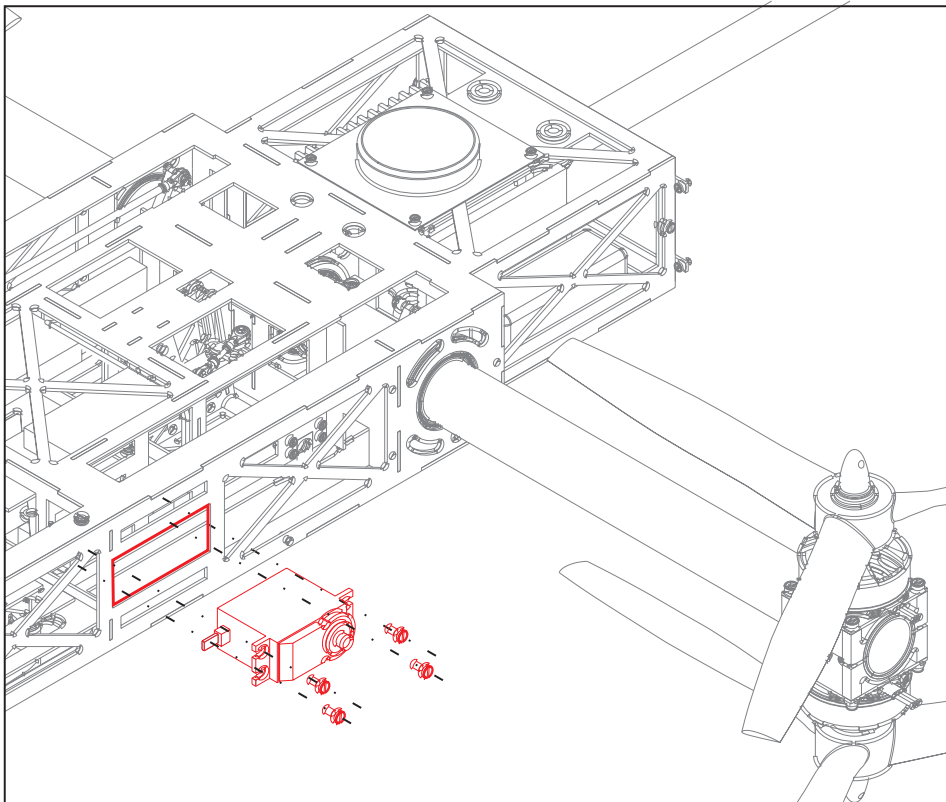


Figure 6.8: Servo assembly.

6.1.3 Landing Gear

The landing gear consists of a large lever, glued to the landing strut, and a second L-shaped lever. In both positions, retracted and lowered, the L-shaped lever takes a 90° angle with the first lever (see Figure 6.9). This design ensures that the landing gear is locked in both positions and hence,

even if the servo actuator is not powered, it will remain in its position. Furthermore, no forces will be transmitted to the actuator due to landing shocks.

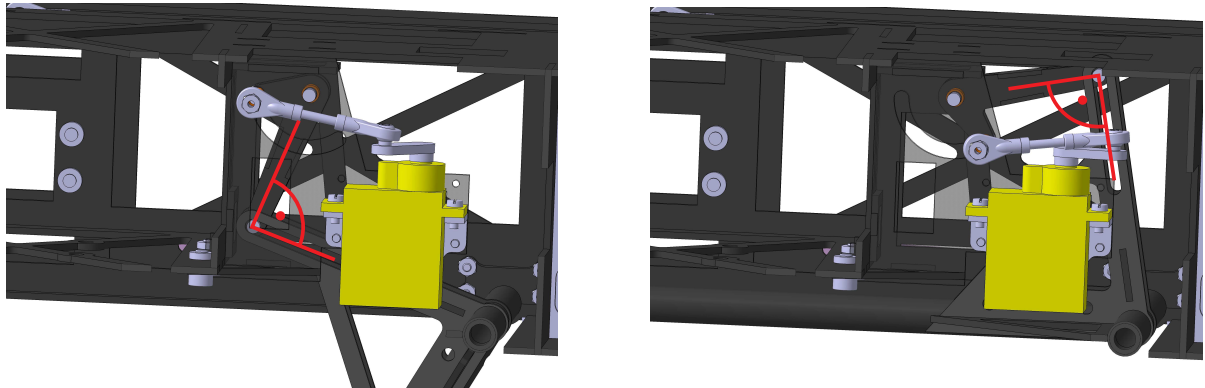


Figure 6.9: Landing gear locked in both positions.

The entire landing gear unit is designed modular and can be removed with only six screws (see Figure 6.10). Consequently, in case of a rough landing the unit can be replaced quickly on the field. Additionally, it is possible to redesign and reinforce the landing gear unit at a later stage, if necessary. As illustrated on the right side of Figure 6.10, the main strut is mounted with bearings milled from POM. These bearings are divided into two parts, so that the lower part of the bearing, formed as a clamp, can be removed to disassemble the unit. The upper half of the bearing is screwed to a CFRP board of the frame. However, strong loads during hard landings are not carried by the four small screws but are directly transmitted to the frame by load bearing surfaces.

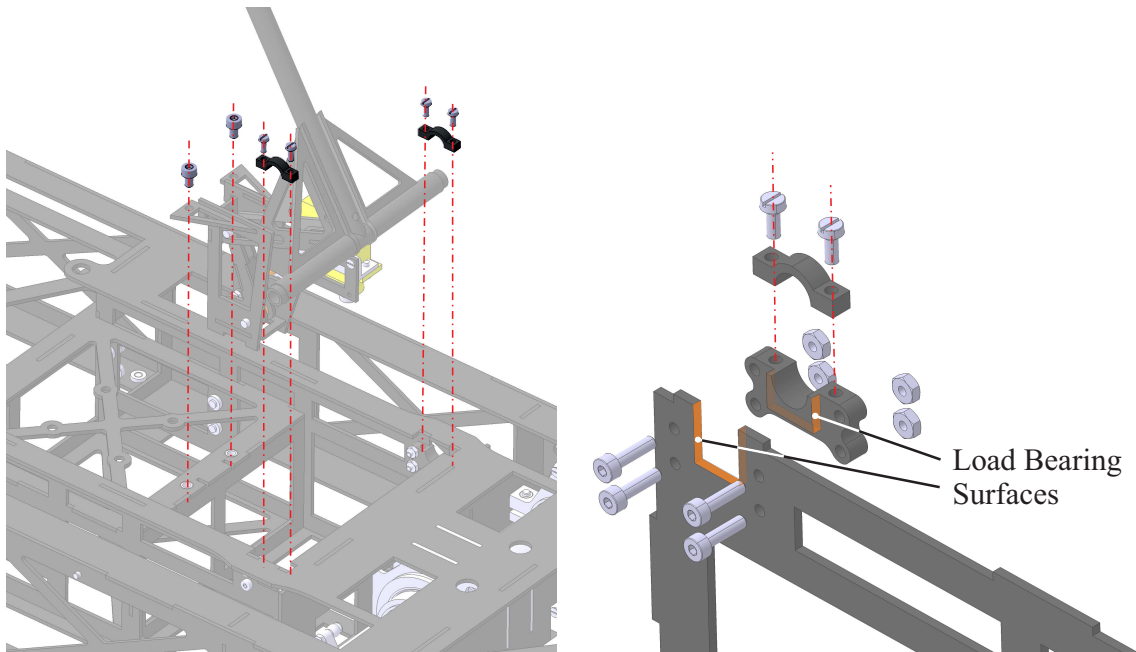


Figure 6.10: Modular landing gear unit.

While the entire landing gear was supposed to only weigh $m_{\text{landing-gear}} = 50 \text{ g}$, according to the

early mass estimations, the detailed design results in $m_{\text{landing-gear}} = 60 \text{ g}$, according to the CAD model. This is, nevertheless a light design, compared to other multirotor landing gear designs. As an actuator a KST X08 servo with a weight of only $m_{\text{servo}} = 8 \text{ g}$ was chosen, because of a relatively high torque and it can be driven directly from the tilt actuator BEC at a supply voltage of $U_{\text{servo}} = 8.4 \text{ V}$, which is quite rare for such a tiny servo actuator.

6.1.4 Battery Mount

The battery bay of ANDroMeDA is quite large - larger than it would possibly be needed for the biggest flight battery used. However, extensive weight and balance tests with the fully detailed CAD model showed, that this range will be needed to achieve the desired flexibility. The rearmost position is needed for a very light battery in combination with heavy measurement equipment, while the foremost position is needed with very heavy batteries (e.g. 10 000 mAh or more) in combination with very light measurement equipment.

To achieve the desired flexibility, a cover board for the battery bay was designed. This cover board has several slots that allow the battery to be attached to the cover with velcro straps at different positions. The cover is slid into the frame quickly, with the help of four hooks on both sides, as shown in Figure 6.11. The hooks slide into slots milled into the top of the frame. An expected additional benefit is a stiffening effect, because the cover can counteract movements of the frame in the horizontal plane due to torsional loads. The battery mount is equipped with a

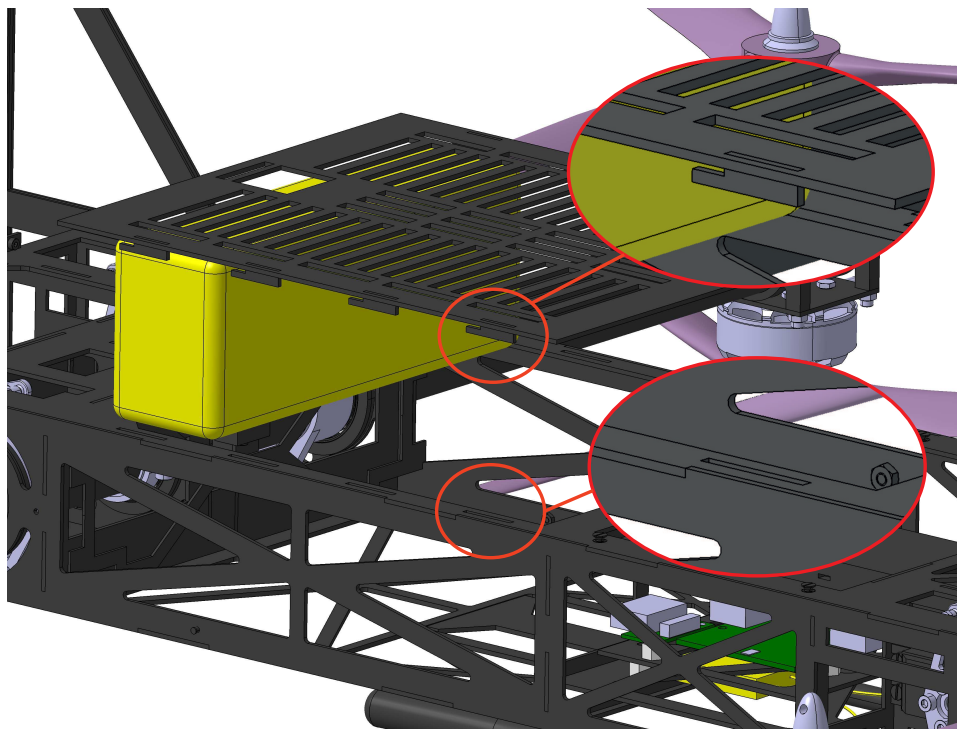


Figure 6.11: Modular landing gear unit.

quick release system. A spring loaded latch is screwed to the frame, as illustrated in Figure 6.12. When a new battery is loaded, the cover will be slid into the frame and the latch will snap into a gap in the lid and hereby lock the battery. To release the battery, the operator pushes the latch down and moves the cover to the front. All parts of the latch are 3D printed.

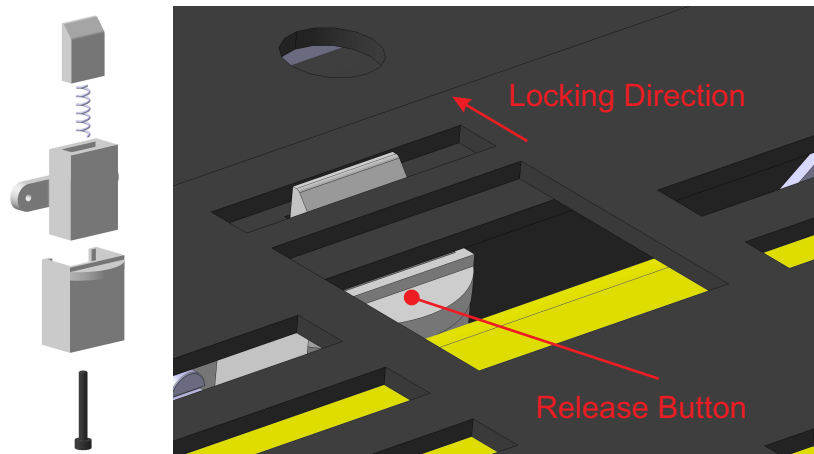


Figure 6.12: Battery quick release system with spring loaded latch.

Another advantage of a separate cover for each battery, is that for each battery unit a fuel gage chip can be used. Such a chip, e.g. the Maxim MAX17205 or Texas Instruments bq78350, is included in almost every battery pack today. It monitors voltage and current for every discharging and charging cycle. While the battery ages, the chip saves information on its EPROM and learns about the battery's health condition. Special algorithms allow accurate readings of the charging condition and remaining capacity. For UAV applications however, they are barely used, especially if the aircraft is custom made.

If such a chip will be used on a custom made circuit board, this circuit board can be mounted to the cover assembly and hereby integrated with the battery. Considering the intended operation of multiple aircraft at the same time, this can be a very valuable safety feature for the future.

6.1.5 Measurement Boom

The measurement unit, as presented in Section 6.3, includes a box that serves as a case for the measurement electronics and a separate measurement battery. This box is slid into a drawer at the front of the frame and will be secured with two screws. A quick release mechanism, as used for the battery assembly, was also considered but changing the sensitive hot wire equipment should work as smooth as possible without components snapping into place.

Because of the modular system, the measurement equipment could also be replaced by other equipment as for example a multi hole probe. As a result of the unique arrangement with a long boom, ANDroMeDA cannot be flown without that boom, because a balanced C.G. cannot be achieved without. Consequently, for test flights without measurement equipment, a dummy boom was designed that weighs the same as the real measurement boom and has a similar inertia tensor.

As a first approach, an attachment of the measurement boom to the measurement box has been designed using rubber dampers as used for camera gimbals. Further tests on this design and the final changes to the boom attachment are presented in Section A.6.

6.1.6 Aerodynamic Cover

A very lightweight aerodynamic cover has been designed from styrene sheets with a thickness of $t_{styrene} = 0.3 \text{ mm}$ and foamed styrene sheets, known as Depron ([58]), with a thickness of $t_{Depron} = 3 \text{ mm}$. Depron has a lower weight per unit area of only $\rho_A = 115 \text{ g/m}^2$, compared to the styrene sheets ($\rho_A = 315 \text{ g/m}^2$) despite the fact it is thicker. Since Depron is more difficult

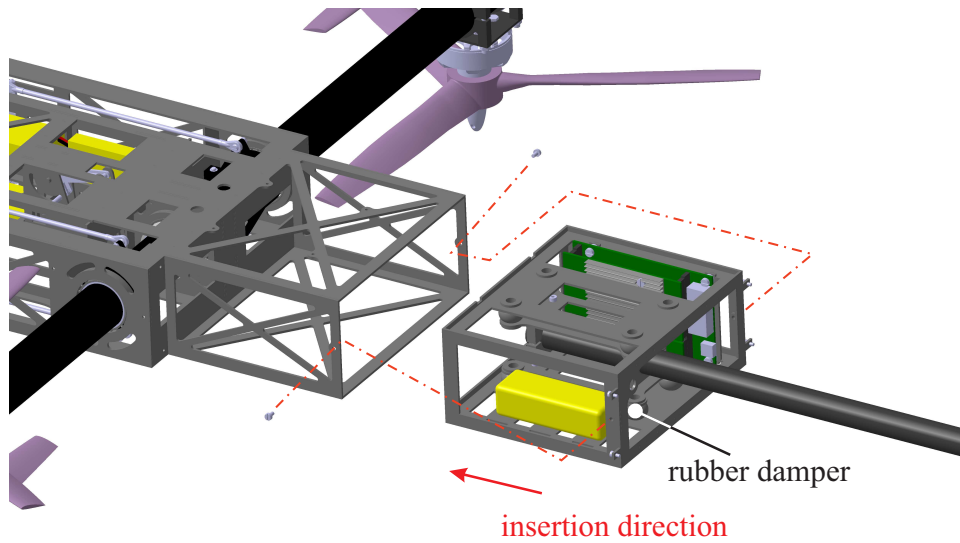


Figure 6.13: Measurement boom and frame drawer.

to vacuum form it will be only used for straight parts or single curved parts. Parts that are more complex will be manufactured from vacuum formed styrene sheets. The vacuum forming process needs less manual labor compared to hand laminated GFRP parts. Figure 6.14 shows the used materials for the aerodynamic cover.

To allow easy access to all components the cover will be open on the bottom and the middle section, which is secured with 3D printed clips on the bottom, can be quickly detached and lifted up as illustrated in Figure 6.15.

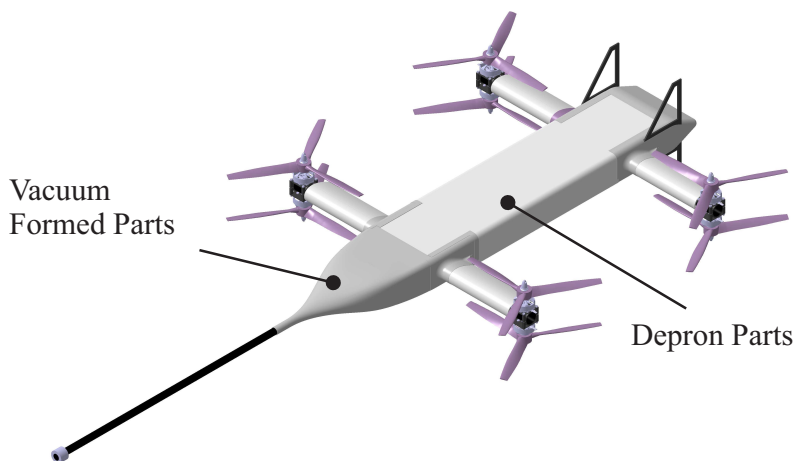


Figure 6.14: Materials used for the cover.

The front part, which forms a soft transition between the measurement boom and the frame, will be mounted directly at the measurement boom with the help of small M2 nylon screws, that will be screwed into CFRP parts. To save weight, the necessary threads will be cut directly into the CFRP parts. If nylon screws instead of steel screws are used, this is possible without the risk of over-tightening the screw and damaging the CFRP. A bulkhead made from thin GFRP with a

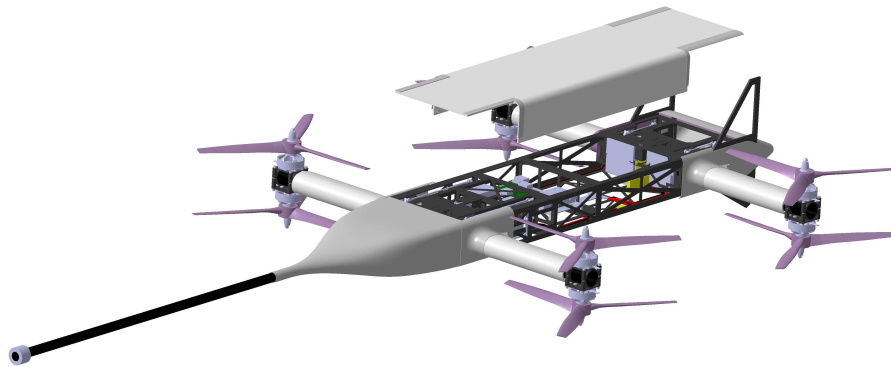


Figure 6.15: Cover mid section detached.

thickness of $t = 0.5 \text{ mm}$ is glued to the vacuum formed part to take the M2 screws as shown in Figure 6.16.

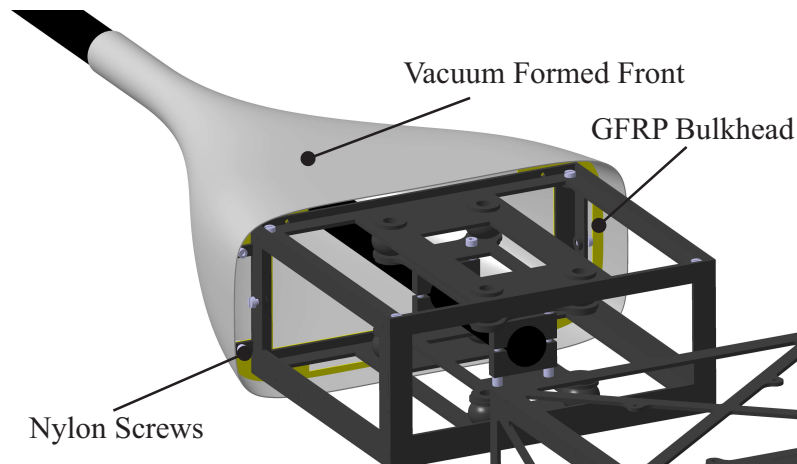


Figure 6.16: Front cover mounted at the measurement boom.

The arm covers consist of two halves, as shown in Figure 6.17, in order to assemble the cover without having to remove the entire motor arms or motors. Tabs made from GFRP with a thickness of $t = 0.5 \text{ mm}$ are used to screw both halves to the frame. To ensure a good alignment a small brass tube will be glued to the front half and a steel pin will be glued to the rear half. In addition tape will be used over the entire length.

According to the CAD model this cover will have a total weight of $m_{cover} = 175 \text{ g}$, which is still below the limit of $m_{cover,max} = 239 \text{ g}$, derived in Section 5.14.3, but it offers only a small benefit. Consequently, it is not clear if whether the cover is really necessary, because of the fabrication effort and the low component accessibility. ANDroMeDA-1 will be built with the necessary interfaces to mount the cover but will be flown without a cover at the beginning. The benefit is expected to be much higher for operation at higher wind speeds.

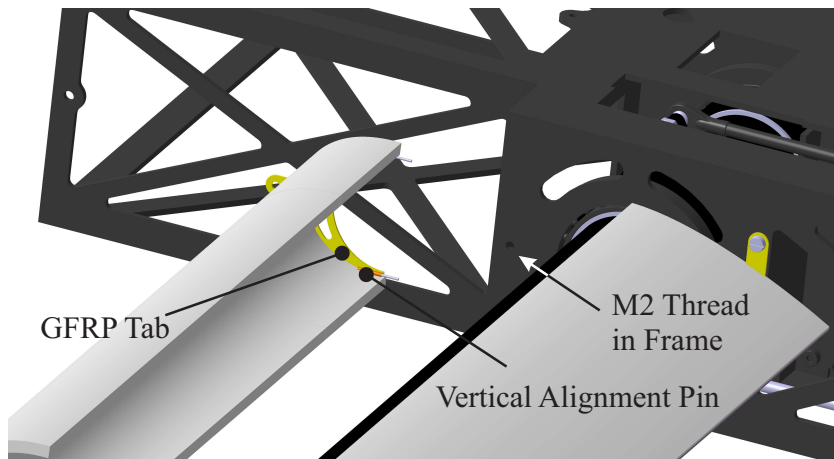


Figure 6.17: Wing cover assembly.

6.1.7 Wiring

Wires have been modeled in CAD partly, as shown in Figure 6.18. The exact wire locations and type of wire fastening will be devised during the build of ANDroMeDA-1.

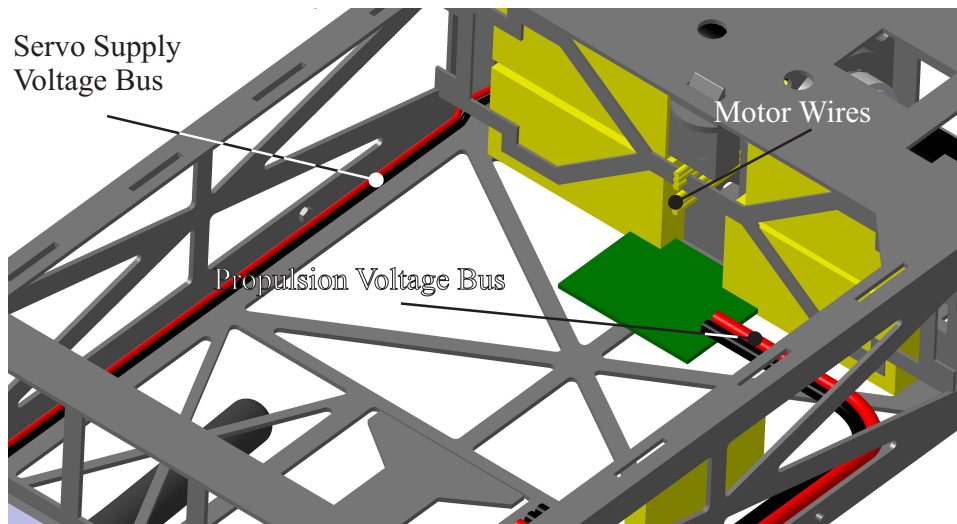


Figure 6.18: Wire planning in the CAD model.

Because of its highly three-dimensional nature, drawing every single wire in a CAD model is a time consuming task, but on the other hand a clean and reproducible wiring is an important factor for safe and reliable UAV operation and reproducible measurement results. More advanced wiring details will be determined during the build and operation of ANDroMeDA-1, so that for the following aircraft a well documented wiring plan is available.

6.2 Fabrication

6.2.1 Pre-Testing

ANDroMeDA-1 has been fabricated entirely in workshops at the University of Stuttgart. This ensured a flexible work-flow without the need to wait for suppliers, in case of design changes. With the experiences made during the fabrication of ANDroMeDA-1, several parts will be ordered from suppliers for the following aircraft.

At the beginning of the fabrication process, several tasks need prior testing:

- Inserts in tilt lever and tilt clamp: Worked well but the manufacturer had to be changed, because the one chosen during the design phase refused to deliver low quantities.
- Fit of the tilt bearings in the CFRP frame side boards: This has to be adjusted on the fly at the milling machine, because not every milling bit is the same. That could be a problem for the series production with the CFRP frame parts, manufactured by a supplier. If the supplier is not able to adjust the fit, the bearing pockets have to be milled in-house after the parts have been prepared by the supplier.
- Bonding of the chassis side boards and the reinforcement rings: This particular step is critical, because if the bonding fails, the entire motor arm comes loose (compare Figure 6.6). However, the connection seems to work properly after it was manufactured.
- As mentioned above, press-in nuts are used to mount the tilt servos and several other parts in the frame. Prior tests showed, that the press-in nuts will only work on CFRP boards with a lot of material around the nut. On the slender design of the ANDroMeDA frame the CFRP will break if the nuts are pressed in. Consequently, all nuts have been glued to the frame. Notches have been cut to the nuts, to increase the torque carrying capability of the bonding as shown in Figure 6.19.

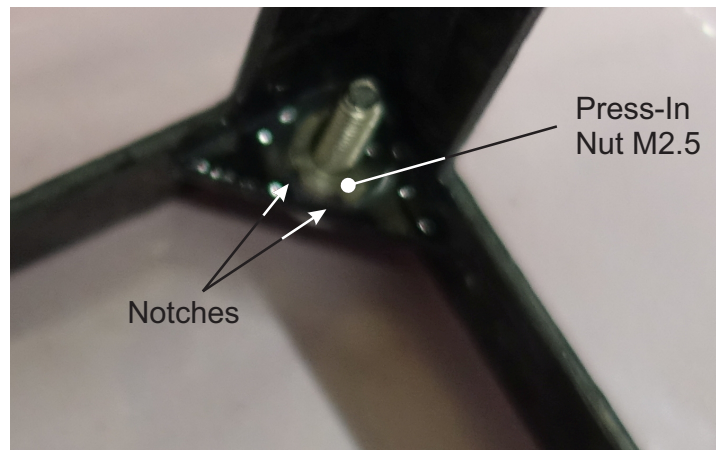


Figure 6.19: Press-in nut glued in.

6.2.2 Frame Assembly

No further problems have been experienced during the manufacturing process and only minor changes to the CAD design had to be made. The finished frame weighs $m_{frame} = 622 \text{ g}$ compared

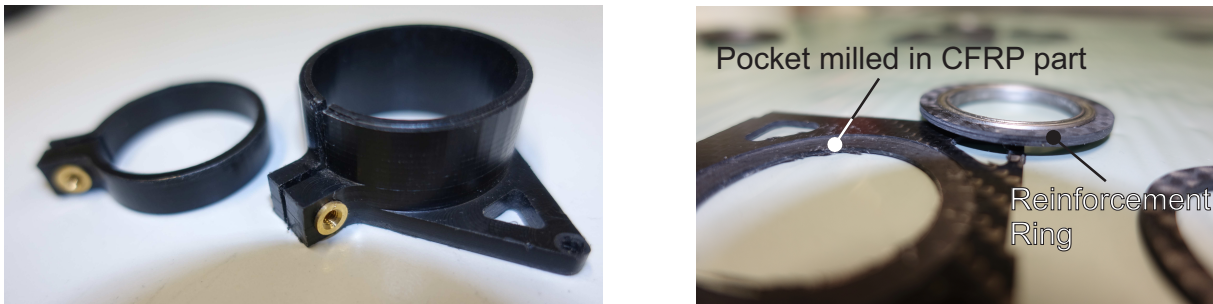


Figure 6.20: Fabrication of the tilt mechanism.

to the estimated weight in the CAD model of $m_{frame,CAD} = 662.5 \text{ g}$. The main reason for that is, that the CFRP boards have been delivered with a thickness between $t = 1.3 \text{ mm}$ and $t = 1.4 \text{ mm}$ instead of $t_{nominal} = 1.5 \text{ mm}$. Only about $m_{glue} = 5 \text{ g}$ to $m_{glue} = 10 \text{ g}$ of the frame weight can be attributed to the glue. This has not been accounted for in the CAD model and was a source of uncertainty in the weight estimation. No problems have been experienced with weak bondings and the frame is very stiff. It is assumed, that CFRP boards with $t = 1.0 \text{ mm}$ would also work and save weight, but to avoid further experiments, the design will not be altered.

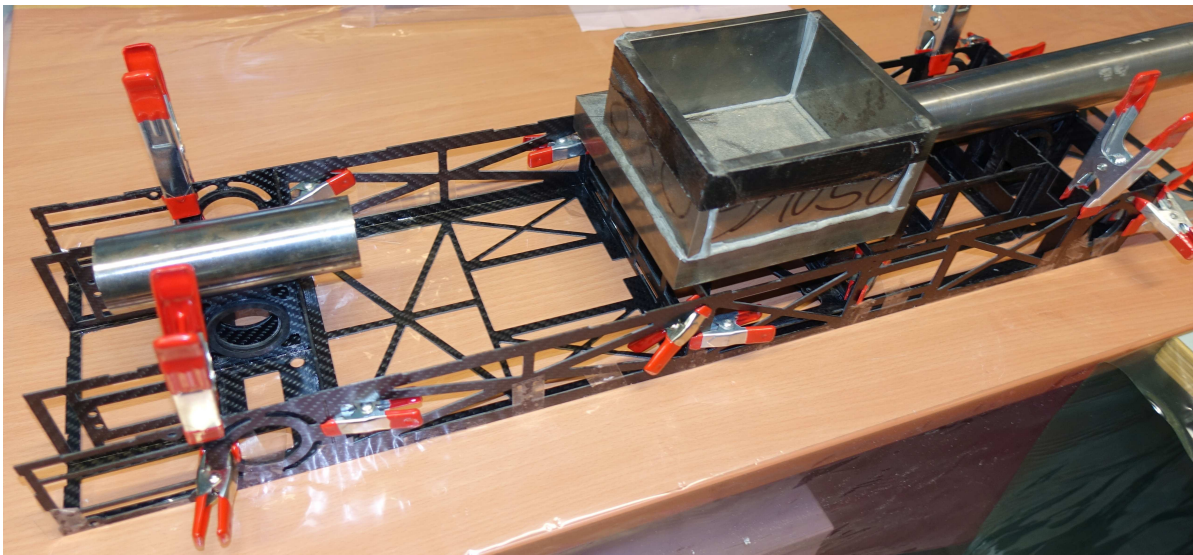


Figure 6.21: Frame assembly step 5.

6.2.3 Wiring

As already stated in Section A.4 the wiring process could be simplified considerably, if a "4in1" ESCs will be used. For the following aircraft the wiring process will be improved by the use of more connectors, so that wiring harnesses can be prepared at once on the workbench. The wiring schematics of ANDroMeDA-1 is shown in Figure 6.22.

6.2.4 Fabrication Time

The fabrication of ANDroMeDA-1 took approximately 325 man hours. This includes also the milling of all parts and all the wiring which needed about 70 hours. For a small series production

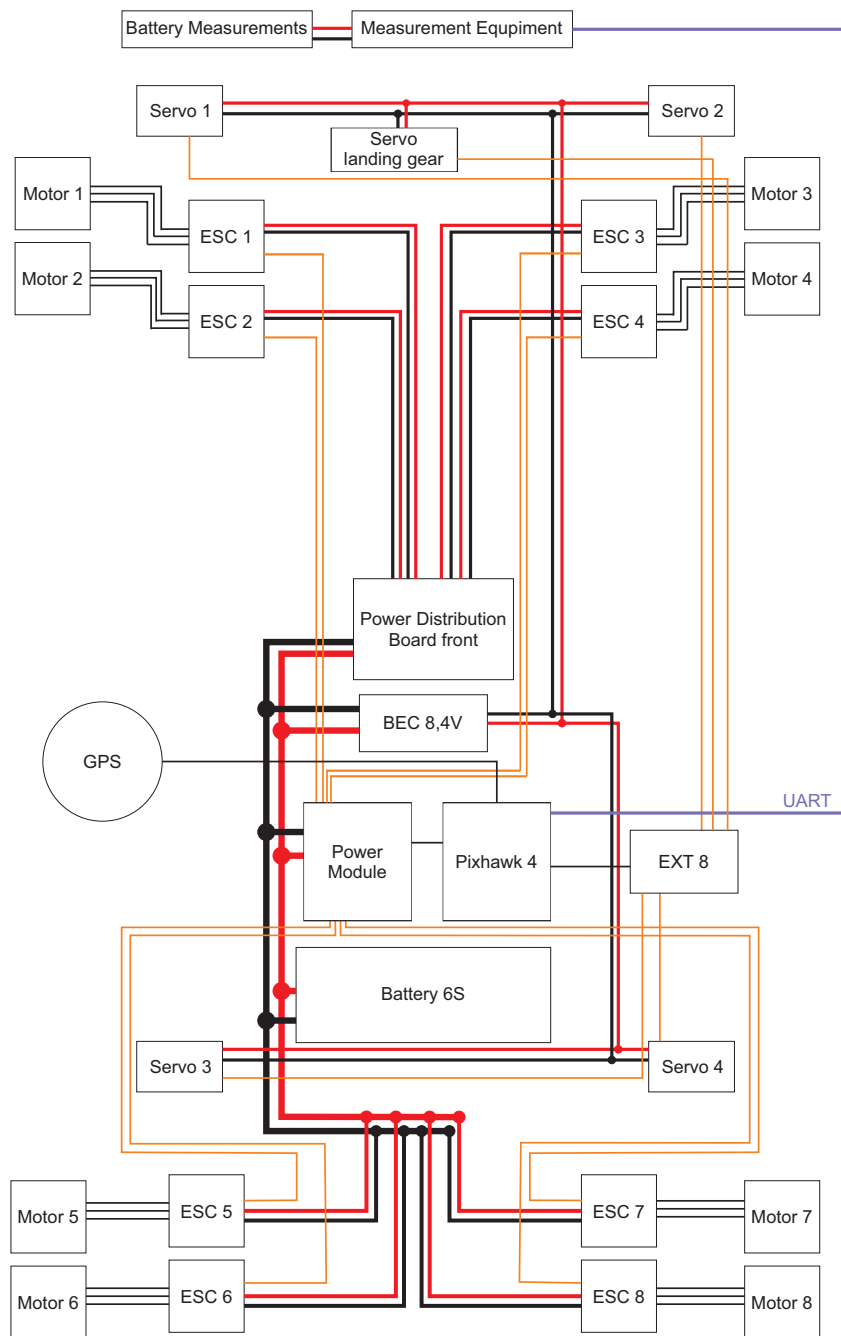


Figure 6.22: AnDroMeDA-1 wiring schematics.

of ANDroMeDA, about 50h to 70h will be saved, because the parts milled from CFRP board will be ordered from a supplier.

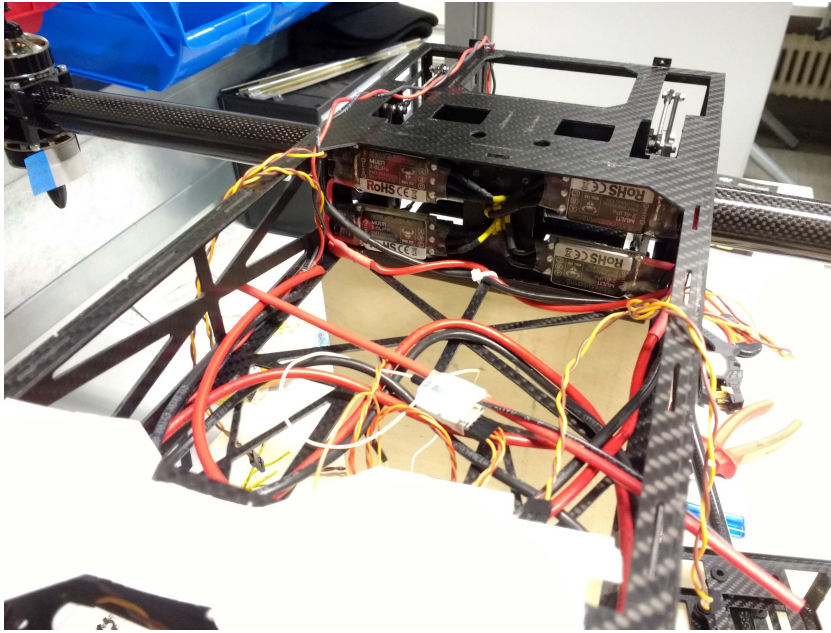


Figure 6.23: Many wiring tasks cannot be prepared on the bench and have to be done inside the frame.

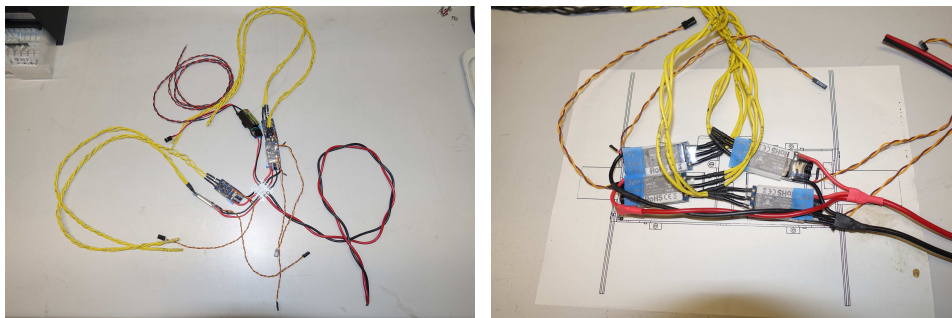


Figure 6.24: Left: Front ESC wiring. Right: Rear ESCs wiring.

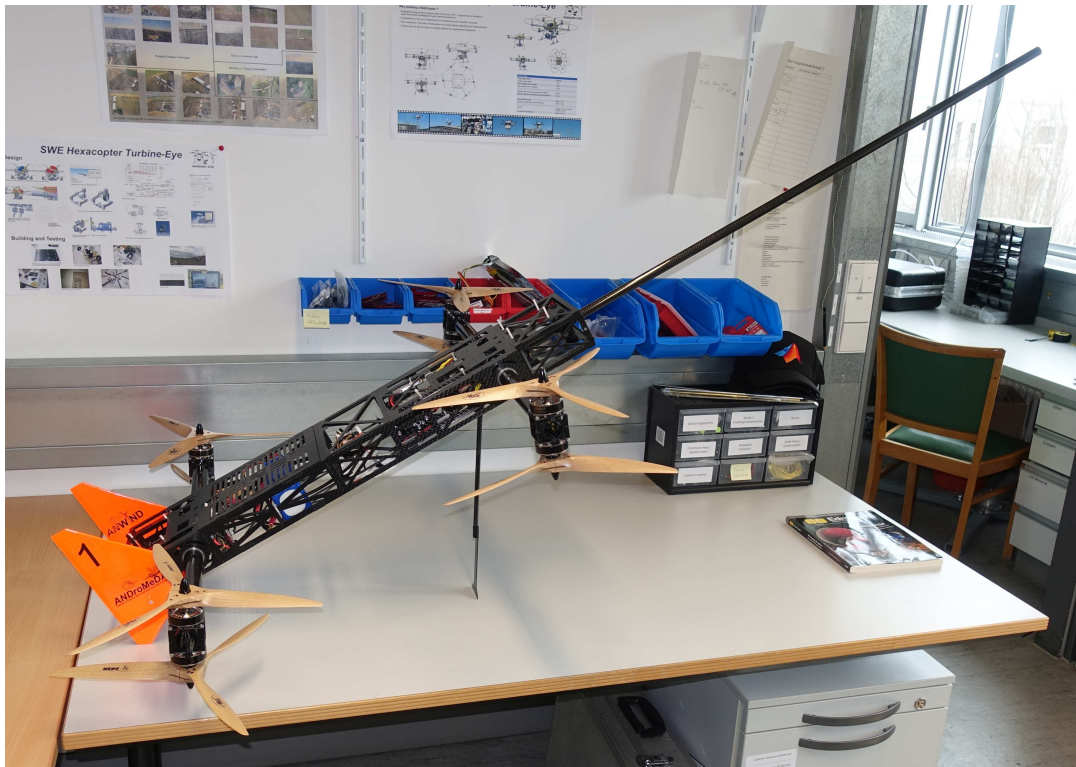


Figure 6.25: Finished ANDroMeDA-1 prototype in take-off / landing position.

6.3 Flow Measurement Probe

6.3.1 Fundamental Principles of Triple Hot Wire Probes

The principle of hot wire anemometry is based on the cooling effect of a flow past a very thin wire, usually between $5 \mu\text{m}$ and $10 \mu\text{m}$ in diameter, and thus about 10 times thinner than a human hair. This cooling effect is a measure for the fluid velocity and since the thermal inertia of a very thin wire is quite low, velocity changes up to several kHz can be detected.

Two implementations of the necessary electrical circuit exist: The constant current anemometer (CCA), where the current to heat the wire is kept constant and the constant temperature anemometer (CTA), where the temperature of the wire is kept constant. The latter one is the most common method today. More details about hot wire anemometry can be found in [59]. A model to calculate the fluid velocity from the heat convection of the wire was introduced by King [60] in 1914 and is still used today, commonly known as "King's Law".

The velocity measured by a single hot wire can be expressed with the help of "King's Law" in the form of:

$$v_{\text{wire}} = \left(A + B \cdot \frac{U_b^2}{T_{\text{wire,corr}} - T_{\text{fluid}}} \right)^E \quad (6.3.1)$$

Where U_b is the measured voltage at the CTA bridge and A , B and E are calibration factors that have to be determined for every individual probe by calibration. The corrected wire temperature $T_{\text{wire,corr}}$ also differs for every individual probe and has to be identified during the calibration. It can be seen, that a measurement of the ambient temperature T_{fluid} is mandatory to obtain the fluid velocity past a hot wire probe.

In the most basic modeling approach for a triple hot wire probe, it is assumed that only the velocity component perpendicular to a wire will have a cooling effect and that a velocity component parallel to the wire will not have any effect at all. In other words, this implies that each wire only "sees" the perpendicular velocity. This is also referred to as "cosine law".

The velocity components u , v , w cannot be measured directly, if each wire only "sees" the velocity component perpendicular to it. In other words, it is not possible to use three wires in a way that $v_{1\perp} = u$, $v_{2\perp} = v$, $v_{3\perp} = w$. But it is possible to use the information of all three wires together to calculate u , v and w . This procedure is called "data reduction". The most simple data reduction scheme, the application of the cosine law, is derived and explained in this section. More sophisticated, but also more complex data reduction schemes, will be presented in Section 6.3.3.

In Figure 6.26 the geometrical relations between the three hot wire probes aligned along the x,y and z-axis and an inflow vector \mathbf{v}_∞ are presented. The velocity component perpendicular to the x-axis is gained by projecting \mathbf{v}_∞ into the yz plane. Accordingly, the velocity perpendicular to the y-axis is gained by projecting \mathbf{v}_∞ into the zx plane and the velocity perpendicular to the z-axis by projecting \mathbf{v}_∞ into the xy plane. As usual, the vector \mathbf{v}_∞ can be expressed by the components u , v , w :

$$\mathbf{v}_\infty = \mathbf{u} + \mathbf{v} + \mathbf{w} = u \cdot [1 \ 0 \ 0]^T + v \cdot [0 \ 1 \ 0]^T + w \cdot [0 \ 0 \ 1]^T = [u \ v \ w]^T \quad (6.3.2)$$

But it is also possible to express \mathbf{v}_∞ in terms of $v_{x\perp}$, $v_{y\perp}$ and $v_{z\perp}$:

$$2 \cdot \mathbf{v}_\infty = \mathbf{v}_{x\perp} + \mathbf{v}_{y\perp} + \mathbf{v}_{z\perp} \quad (6.3.3)$$

Consequently, it is possible to write the magnitude of v_∞ directly as function of the measured speeds:

$$|\mathbf{v}_\infty| = \sqrt{\frac{v_{x\perp}^2 + v_{y\perp}^2 + v_{z\perp}^2}{2}} \quad (6.3.4)$$

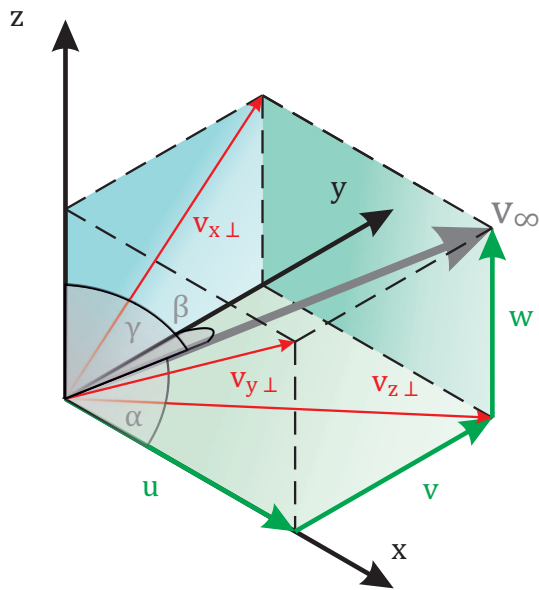


Figure 6.26: Principle of directional flow measurements with three orthogonally oriented hot wires.

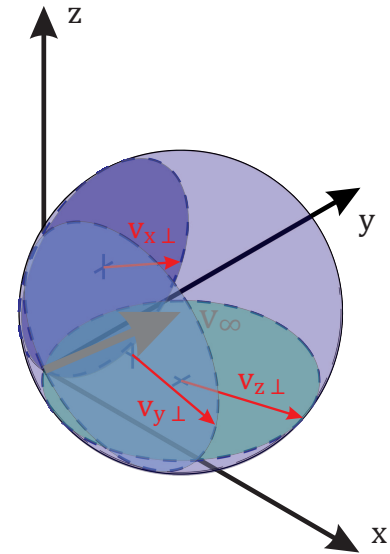


Figure 6.27: Alternative way of illustrating flow measurements with three orthogonal hot wires.

The components u , v , w can be derived from the measured speeds $v_{x\perp}$, $v_{y\perp}$ and $v_{z\perp}$ using the following three relations:

$$v^2 + w^2 = v_{x\perp}^2 \quad (6.3.5)$$

$$u^2 + w^2 = v_{y\perp}^2 \quad (6.3.6)$$

$$u^2 + v^2 = v_{z\perp}^2 \quad (6.3.7)$$

This system of linear equations yields in:

$$u = \sqrt{\frac{v_{y\perp} + v_{z\perp} - v_{x\perp}}{2}} \quad (6.3.8)$$

$$v = \sqrt{\frac{v_{x\perp} + v_{z\perp} - v_{y\perp}}{2}} \quad (6.3.9)$$

$$w = \sqrt{\frac{v_{x\perp} + v_{y\perp} - v_{z\perp}}{2}} \quad (6.3.10)$$

Another way of deriving the desired velocity components u , v , w is given by the angles α , β , γ between the vector \mathbf{v}_∞ and the corresponding axes. After calculating the magnitude of \mathbf{v}_∞ by Eq. (6.3.4) these angles can be computed by:

$$\sin \alpha = \frac{v_{x\perp}}{v_\infty} \quad (6.3.11)$$

$$\sin \beta = \frac{v_{y\perp}}{v_\infty} \quad (6.3.12)$$

$$\sin \gamma = \frac{v_{z\perp}}{v_\infty} \quad (6.3.13)$$

And consequently, the components u , v , w are given by:

$$u = \cos \alpha \cdot v_{\infty} \quad (6.3.14)$$

$$v = \cos \beta \cdot v_{\infty} \quad (6.3.15)$$

$$w = \cos \gamma \cdot v_{\infty} \quad (6.3.16)$$

This method is completely equivalent to Eqs. (6.3.8 to 6.3.10).

From the fact that in order to derive Eqs. (6.3.8 to 6.3.10) the root of u^2 , v^2 , w^2 had to be taken, it is obvious that the solution is not unique. This can also be seen by the fact that the angles α , β and γ are not limited to the first octant of the three dimensional space, as sketched in Figure 6.26. Only if \mathbf{v}_{∞} lies in the first octant ($u > 0$, $v > 0$, $w > 0$) a unique solution by Eqs. (6.3.8 to 6.3.10) is given. This limits the measurement range of a triple hot wire probe, from a pure mathematical point of view, to one eighth of a sphere. This limitation can be overcome by the use of four instead of three wires.

Another way of illustrating the relations between perpendicular velocities for each wire and the free-stream velocity is shown in Figure 6.27. If the vector \mathbf{v}_{∞} is used to describe a sphere, where the tip of the vector arrow is the center of this sphere, and the bottom of this arrow lies on the surface of the sphere, the intersections with the xy , zx , yz planes will define three circles.

The radii of these three circles are also the velocity components of \mathbf{v}_{∞} perpendicular to the axes $v_{x\perp}$, $v_{y\perp}$, $v_{z\perp}$. With the help of this illustration another aspect of Eqs. (6.3.8 to 6.3.10) can be addressed. If for example $v_{x\perp} > v_{y\perp} + v_{z\perp}$ no real solution exists. In Figure 6.27 it can be seen, that this also is a non-physical or simply non-geometrical solution. If for example $u \rightarrow 0$ and $v \rightarrow 0$, that means that the radius of the intersection with the xy plane converges to zero and the remaining two circles are equally sized. One circle cannot be larger than the other one if they are described by the intersection of a sphere with the zx and yz plane.

This scenario is equivalent to the description of an inertia tensor by an ellipsoid, where likewise one moment of inertia cannot be larger than the sum of the other two. The limit is given by two moments of inertia being of the same size and consequently the third one converging to zero (e.g. $I_{xx} = I_{yy}; I_{zz} \rightarrow 0$), which corresponds to a plate being infinitely thin in one dimension.

At real life conditions, including measurement errors and measurement noise, it cannot be ensured that one measured velocity is never larger than the sum of the other two, and thus measures have to be taken when solving Eqs. (6.3.8 to 6.3.10). One possible approach is to simply take the absolute value of the expression under the radical. Another approach is a conditional statement correcting only the measured component that is too large.

Since the measurement equipment for ANDroMeDA is not designed for a specific measurement campaign the orthogonal wire orientation, as described here, was used for the triple hot wire probe. It should be mentioned however that for specific purposes other wire orientations might be beneficial. In [61], for example, it is explained that a 45° orientation is advantageous for the measurement of Reynolds stresses when not only the components u , v , w are of interest, but the combined values of uv , vw , uw are of importance.

6.3.2 Integration of the Measurement Equipment

Commercially available triple hot wire probes are normally expensive and the replacement of a broken wire is complicated, can normally done only by the manufacturer and is not possible in the field. On the other hand those commercial triple hot wire probes are of very small size and the wires are close together. This makes it possible to measure very small turbulence structures in the lab.

Since atmospheric turbulences are expected to be significantly larger and a larger wire spacing is possible for ANDroMeDA, another approach was taken. A hot wire adapter was designed to mount each of the three wires, including prongs and shafts, individually. This adapter is also used to mount a prandtl probe, which is used as a reference measurement. To avoid a labor-intensive individual calibration of each particular ANDroMeDA measurement boom, the single hot wire probes will be provided pre-calibrated by the manufacturer SVMtec.

This might result in a less accurate measurement, compared to an individually calibrated triple hot wire unit, but is expected to be sufficient for atmospheric measurements and, since AN-DroMeDA is intended for the operation in a group of nine aircraft, an individual calibration of every single aircraft would not be efficient. Additionally, with an individually calibrated triple hot wire probe a broken wire results in the need to change the entire unit.

Due to production tolerances of electronic and electromechanical parts, every particular hot wire probe has to be calibrated together with the corresponding CTA bridge, wires and connectors. For ANDroMeDA the topology, shown in Figure 6.28, has been developed, which means that three components are used for each probe position. For example for position I: CTA bridge I, wiring I including connectors CONN IA and CONN IB and probe I. These components are also calibrated

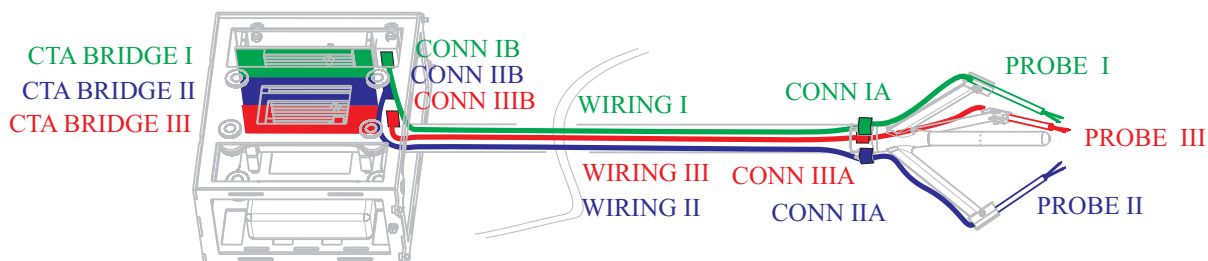


Figure 6.28: Toplogy of the ANDroMeDA measurement boom.

together, as one unit, at SVMtec including several spare probes for each position. The additional connectors at the hot wire adapter (e.g. CONN IA in Figure 6.28) allow a quick replacement of a particular probe in the field, if a wire breaks.

Figure 6.29 shows the hot wire adapter design. The probes can be clipped into the hot wire adapter and before they are secured with a M1.6 screw. Because the screw does not need to be removed completely and because the probe shaft holds in place also without the screw, the assembly of the sensitive hot wire probes is uncritical. The probes can be snapped in with both hands while the screw can be tightened later to adjust the remaining degree of freedom. To secure the connectors in place another clip is used.

The hot wire adapter was rapid prototyped using the selective laser sintering (SLS) technology. Figure 6.30 shows the assembled hot wire adapter with the three hot wire probes and the Prandtl probe.

The CTA bridges are a proven design from SVMtec, normally used in an aluminum case. In addition to the three CTA bridges, a customized electronics mainboard, design especially for ANDroMeDA is used. This mainboard, with a built in AD converter, reads in the analog voltages from the CTA bridges and processes the gained values with calibration factors which are stored in its EPROM. Applying the basic method, described in the previous section, the u, v, w velocity components are computed from the measured individual wire speeds.

Furthermore, the mainboard includes a pressure transducer to measure the Prandtl tube differential pressure and a connector for a temperature sensor, which is needed to compute the wire velocities. A barometric sensor was not built in because it is already included in the autopilot.

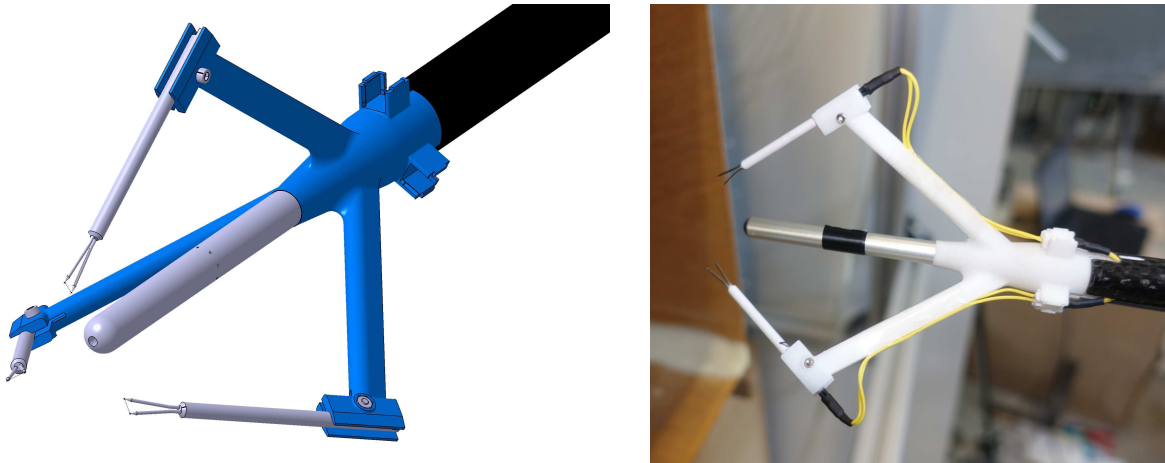


Figure 6.29: Design of the hot wire adapter. **Figure 6.30:** Assembled triple hot wire probe.

For ground testing purposes the mainboard is equipped with a mini usb connector. This interface can also be used for firmware updates and to set the calibration factors after a wire was replaced. A connection between the measurement mainboard and the autopilot is established with an UART interface.

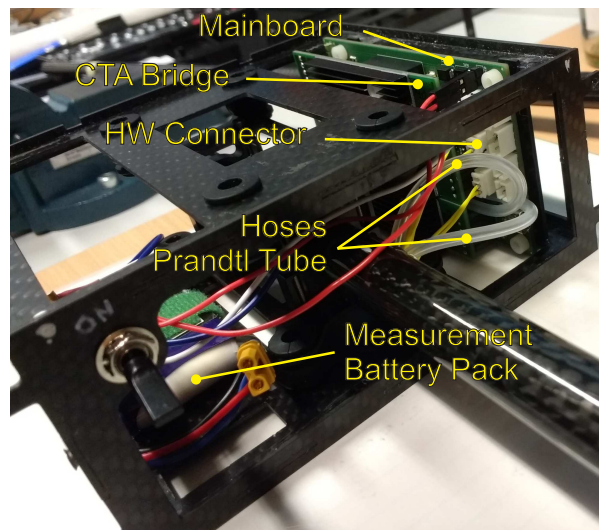


Figure 6.31: Assembled measurement drawer.

The mainboard will be supplied with power from a separate battery to avoid possible interference with the propulsion system. Figure 6.31 shows the mainboard with attached CTA bridges, assembled inside the measurement drawer. The entire measurement boom, including all equipment and the measurement battery, weighs 338 g.

In order to protect the sensitive hot wire probes during storage and transportation a special case for the entire measurement boom has been built (Figure 6.32).

6.3.3 Advanced Methods of Hot Wire Calibration and Data Reduction

In reality, a hot wire probe cannot be treated as an isolated wire, because the presence of the wire supports, called prongs, and the probe shaft, which will affect the airflow past the wire.

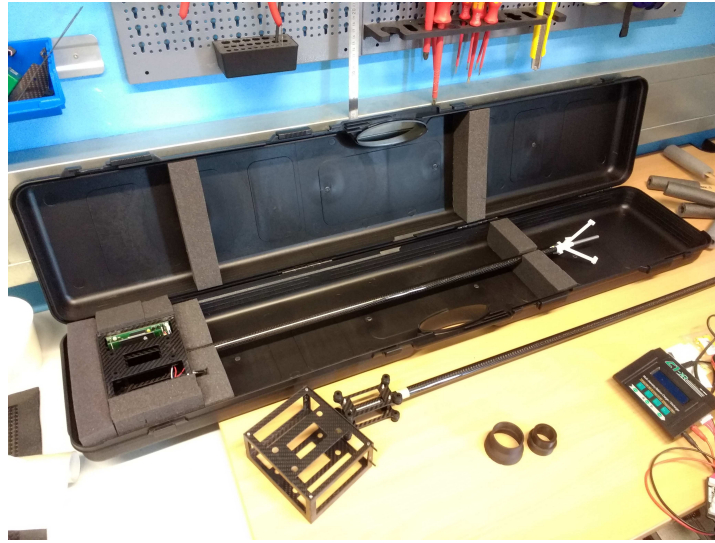


Figure 6.32: Case for the measurement boom.

Furthermore, a hot wire that is exposed to a pure parallel flow will also experience some cooling effect up to a certain degree.

To take these effects into account, another coordinate system is introduced in Figure 6.33. The velocity normal to the wire, pointing in the direction of the probe's shaft is denoted U_n . While the velocity normal to the wire pointing in a direction perpendicular to the shaft is denoted U_b and the velocity parallel to the wire is denoted U_t .

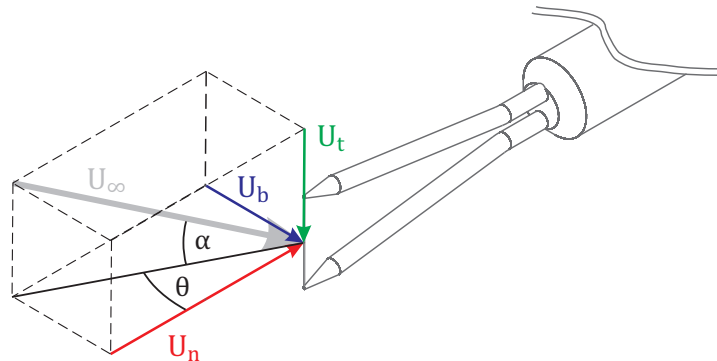


Figure 6.33: Coordinate system of a single hot wire probe.

One of the earliest approaches to model the effects described above was proposed by Hinze in 1959 ([62]):

$$U_{eff}^2 = U_n^2 + k^2 \cdot U_t^2 \quad (6.3.17)$$

Where U_{eff} is defined as the effective velocity, actually measured by the probe, and k is a correction factor that is usually between $k = 0.1$ and $k = 0.3$, according to Hinze. If the effective wire velocity is expressed by the magnitude of U_∞ and the angles α , commonly referred to as yaw angle, and θ , commonly referred to as pitch angle, Eq. (6.3.17) becomes:

$$U_{eff}^2 = U_\infty^2 \cdot (\cos^2(\alpha) + k^2 \cdot \sin^2(\alpha)) \quad (6.3.18)$$

For $k = 0$, Eq. (6.3.18) becomes the well known cosine law, where only the component perpen-

dicular to the wire is taken into account. Figure 6.34 shows the effect of different k values.

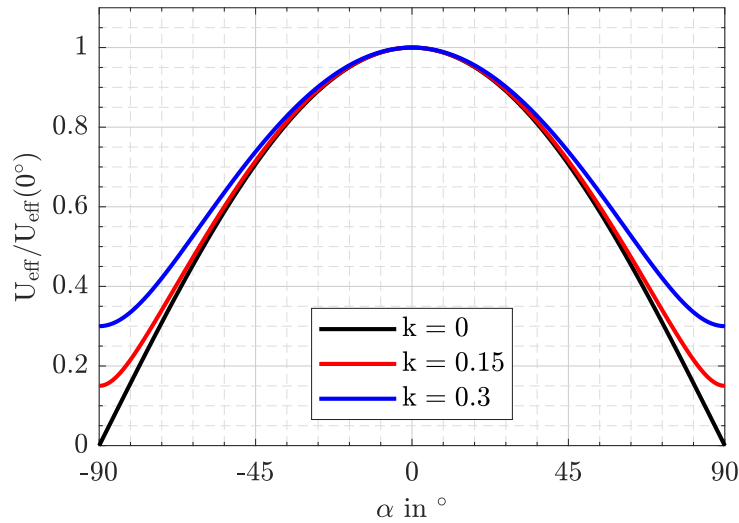


Figure 6.34: Influence of k factor in Eq. (6.3.18).

1971 Jorgensen ([63]) extended Hinze's model to account for the influence of the probe shaft and thus for different pitch angles θ :

$$U_{eff}^2 = U_n^2 + k^2 \cdot U_t^2 + h^2 \cdot U_b^2 \quad (6.3.19)$$

The pitch coefficient h is usually greater than 1. If the pitch factor is one and the k factor is zero, the general equation simplifies to the cosine law again. For other values of pitch and yaw factor Eq. (6.3.19) can be also written as:

$$U_{eff}^2 = U_\infty^2 \cdot (\cos^2\theta \cdot \cos^2\alpha + k^2 \cdot \sin^2\alpha + h^2 \cdot \sin^2\theta \cdot \cos^2\alpha) \quad (6.3.20)$$

During the following decades, several other correction models have been introduced by various authors. A good overview is given in [64] and in addition in [64] a new method, derived from potential flow theory, is presented.

If the coefficients of a correction model (e.g. k and h for the Jorgensen model) are determined for each wire of a triple hot wire probe during a calibration process, this is called an indirect calibration method. A calibration is referred to as a direct calibration, on the other hand, if no physical model is used at all, and the data reduction is done directly from a large number of calibration points at different inflow angles and inflow speeds.

This can be realized for example with a look up table including linear interpolation between the measured points during calibration. Over the last decades some authors also proposed highly sophisticated and fully automated calibration procedures. In [65] even a neural network approach was used. In [66] a four-wire probe was used without former calibration in an outdoor field test at the coastal region of Doha, Qatar together with a sonic anemometer. The four-wire probe was calibrated after the campaign using the data from the sonic anemometer with good results.

In general, a direct calibration method is not favorable for ANDroMeDA. On the one hand, the effort for a direct calibration is very high and needs regular access to a wind tunnel, as well as an automated calibration rig (e.g. with stepper motors) to sweep over all yaw and pitch angles and all speeds in a reasonable amount of time. On the other hand it is not possible to replace a broken wire in the field, if the entire triple hot wire unit was calibrated at once.

An indirect calibration method could resolve the latter issue, but would still need a lot of calibration points to perform a least square fit to determine the pitch and yaw factors of all three wires. A wire replacement in the field would be possible, if the pitch and yaw factors for all replacement wires have been already determined by prior calibration.

Another method is presented in [67], combining a physical model and a look-up table, which reduces the calibration complexity compared to a direct calibration.

Because of these disadvantages the simple model from Section 6.3.1 was chosen to be used for ANDroMeDA, combined with a precise factory calibration of the individual hot-wire probes at SVMTec. Especially for group measurements in an array of nine aircraft, a complex calibration is not feasible. Furthermore, the average wind speed is also available from the Prandtl probe as a reference value.

Even if no individual calibration of each ANDroMeDA measurement boom is intended, the question arises if the measurement results can be improved by taking into account general effects, e.g. choosing a general pitch and yaw factor for the Jorgensen model (Eq. (6.3.19)). In some references, e.g. [68] and [69], it is stated that pitch and yaw factor in Eq. (6.3.20) depend on the yaw and pitch angles themselves and hence, the function deviates from the pure sinusoidal form. However, in [68] it is explained that this behaviour originates in aerodynamic interference effects, caused by the close proximity of the three wires to each other and the close proximity of the prongs supporting the neighboring wires. Consequently, it could be assumed that these effects are less severe for the present configuration with a much wider wire spacing.

If a general pitch and yaw factor, applying to all three particular hot wire probes, is supposed to be introduced for the ANDroMeDA measurement boom it is important to understand the application of the Jorgenson correction model (Eqs. (6.3.19) 6.3.20)) in the data reduction scheme for a triple hot wire probe. Eq. (6.3.19) only gives the effective velocity for one particular hot wire probe. To combine the measurements of all three probes, the axis systems for all three probes as well as the general hot wire axis system (compare Figure 6.26) and an aerodynamic axis system are introduced in Figure 6.35.

It should be mentioned, that the directions are swapped compared to Figure 6.33. This only has an effect on the signs of the resulting velocity components and was done to achieve consistency with the flight mechanical axis system according to DIN LN 9300: If ANDroMeDA is hovering in a headwind of velocity v_∞ , the value u will be positive as well as if ANDroMeDA is flying forward in calm air at the speed v_∞ , even if the wind vector is pointing in the opposite direction of u .

The velocity components u_{HW} , v_{HW} , w_{HW} in the hot wire axis system can be easily transformed to the velocity components u , v , w in the aerodynamic axis system by a rotation: $[u, v, w]^T = \mathbf{R}_{\mathbf{HW}-\mathbf{aero}} \cdot [u_{HW}, v_{HW}, w_{HW}]^T$. The corresponding rotation matrix is:

$$\mathbf{R}_{\mathbf{HW}-\mathbf{aero}} = \begin{bmatrix} 1/\sqrt{3} & 1/\sqrt{3} & 1/\sqrt{3} \\ 0 & 1/\sqrt{2} & -1/\sqrt{2} \\ -2/\sqrt{6} & 1/\sqrt{6} & 1/\sqrt{6} \end{bmatrix} \quad (6.3.21)$$

If a given wind speed or flight speed is expressed in the aerodynamic axis system and needs to be converted to the hot wire axis system (e.g. to calculate the theoretical velocity that a wire would experience), this can be done by inverting $\mathbf{R}_{\mathbf{HW}-\mathbf{aero}}$. Because all axis systems in Figure 6.35 and hence all corresponding rotation matrices are orthogonal it is $\mathbf{R}_{\mathbf{aero}-\mathbf{HW}} = \mathbf{R}_{\mathbf{HW}-\mathbf{aero}}^{-1} = \mathbf{R}_{\mathbf{HW}-\mathbf{aero}}^T$.

In the same manner, it is possible to express the velocity components U_n , U_t , U_b of every particular hot wire probe in terms of the inflow vector: $[U_n^i \ U_t^i \ U_b^i]^T = \mathbf{R}_{\mathbf{HW}-i} \cdot [u_{HW} \ v_{HW} \ w_{HW}]^T$.

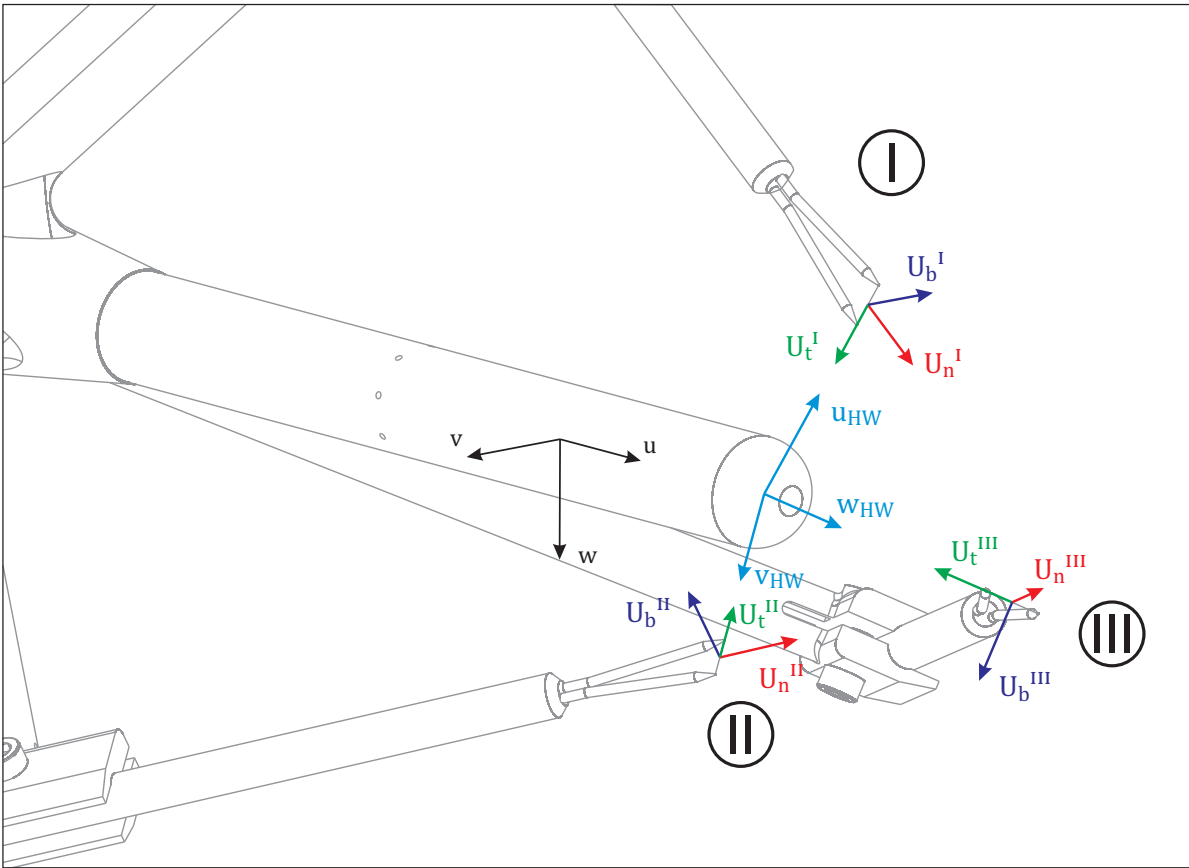


Figure 6.35: Coordinate systems of a all three hot wire probes.

The corresponding rotation matrices for the current wire orientation at the ANDroMeDA-1 measurement boom are:

$$\mathbf{R}_{\text{HW-I}} = \begin{bmatrix} 0 & \sqrt{2}/2 & \sqrt{2}/2 \\ -1 & 0 & 0 \\ 0 & -\sqrt{2}/2 & \sqrt{2}/2 \end{bmatrix} \quad (6.3.22)$$

$$\mathbf{R}_{\text{HW-II}} = \begin{bmatrix} \sqrt{2}/2 & 0 & \sqrt{2}/2 \\ 0 & -1 & 0 \\ \sqrt{2}/2 & 0 & -\sqrt{2}/2 \end{bmatrix} \quad (6.3.23)$$

$$\mathbf{R}_{\text{HW-III}} = \begin{bmatrix} \sqrt{2}/2 & \sqrt{2}/2 & 0 \\ 0 & 0 & -1 \\ -\sqrt{2}/2 & \sqrt{2}/2 & 0 \end{bmatrix} \quad (6.3.24)$$

If these rotations are combined with a correction model in form of $U_{eff} = f(U_n, U_t, U_b)$, as for example the Jorgensen model (Eq. (6.3.19)), it is possible to calculate the speeds $U_{eff}^I, U_{eff}^{II}, U_{eff}^{III}$, measured by the three particular hot wire probes for any inflow vector: $[U_{eff}^I \ U_{eff}^{II} \ U_{eff}^{III}]^T =$

$f([u_{HW} \ v_{HW} \ w_{HW}]^T)$. The Jorgenson correction model can be written as:

$$(U_{eff}^i)^2 = [1 \ k_i^2 \ h_i^2] \cdot \mathbf{R}_{\mathbf{HW}-i} \cdot [u_{HW} \ v_{HW} \ w_{HW}]^T \quad (6.3.25)$$

This yields in the following effective probe velocities:

$$\begin{bmatrix} (U_{eff}^I)^2 \\ (U_{eff}^{II})^2 \\ (U_{eff}^{III})^2 \end{bmatrix} = \begin{bmatrix} \left(\frac{\sqrt{2}}{2} \cdot v_{HW} + \frac{\sqrt{2}}{2} \cdot w_{HW} \right)^2 + k_1^2 \cdot u_{HW}^2 + h_1^2 \cdot \left(\frac{\sqrt{2}}{2} \cdot w_{HW} - \frac{\sqrt{2}}{2} \cdot v_{HW} \right)^2 \\ \left(\frac{\sqrt{2}}{2} \cdot u_{HW} + \frac{\sqrt{2}}{2} \cdot w_{HW} \right)^2 + k_2^2 \cdot v_{HW}^2 + h_2^2 \cdot \left(\frac{\sqrt{2}}{2} \cdot u_{HW} - \frac{\sqrt{2}}{2} \cdot w_{HW} \right)^2 \\ \left(\frac{\sqrt{2}}{2} \cdot u_{HW} + \frac{\sqrt{2}}{2} \cdot v_{HW} \right)^2 + k_3^2 \cdot w_{HW}^2 + h_3^2 \cdot \left(\frac{\sqrt{2}}{2} \cdot v_{HW} - \frac{\sqrt{2}}{2} \cdot u_{HW} \right)^2 \end{bmatrix} \quad (6.3.26)$$

The described procedure is possible for any arbitrary orientation of the three hot wire probes given by $\mathbf{R}_{\mathbf{HW}-I}$, $\mathbf{R}_{\mathbf{HW}-II}$, $\mathbf{R}_{\mathbf{HW}-III}$.

A data reduction is achieved by inverting this procedure, to be able to calculate the inflow vector from the three measured velocities U_{eff}^I , U_{eff}^{II} , U_{eff}^{III} . In case of the Jorgenson correction model combined with the current ANDroMeDA wire orientation, this is not possible analytically because if Eq. (6.3.26) is expanded it includes quadratic and coupled terms (e.g. u^2 or uv) and hence, the system of equations is non-linear. A solution can only be obtained with numerical algorithms and consequently the model can only be applied during post-processing.

If the pitch factor of all three hot wire probes is set to $h_1 = h_2 = h_3 = 1$ Eq. (6.3.26) simplifies to:

$$\begin{bmatrix} (U_{eff}^I)^2 \\ (U_{eff}^{II})^2 \\ (U_{eff}^{III})^2 \end{bmatrix} = \begin{bmatrix} v_{HW}^2 + k_1^2 \cdot u_{HW}^2 + w_{HW}^2 \\ u_{HW}^2 + k_2^2 \cdot v_{HW}^2 + w_{HW}^2 \\ u_{HW}^2 + k_3^2 \cdot w_{HW}^2 + v_{HW}^2 \end{bmatrix} = \mathbf{A} \cdot \begin{bmatrix} u_{HW}^2 \\ v_{HW}^2 \\ w_{HW}^2 \end{bmatrix} \quad (6.3.27)$$

This is now a system of linear equations and the solution can be obtained by inverting the matrix \mathbf{A} . In conclusion this means that the Hinze correction model can be applied analytically in real-time with the current wire orientation. If the yaw factor is set to $k = 0$ the solution simplifies once more. Inverting the matrix \mathbf{A} yields in:

$$\begin{bmatrix} u_{HW}^2 \\ v_{HW}^2 \\ w_{HW}^2 \end{bmatrix} = \mathbf{A}^{-1} \cdot \begin{bmatrix} (U_{eff}^I)^2 \\ (U_{eff}^{II})^2 \\ (U_{eff}^{III})^2 \end{bmatrix} = \begin{bmatrix} -1/2 & 1/2 & 1/2 \\ 1/2 & -1/2 & 1/2 \\ 1/2 & 1/2 & -1/2 \end{bmatrix} \cdot \begin{bmatrix} (U_{eff}^I)^2 \\ (U_{eff}^{II})^2 \\ (U_{eff}^{III})^2 \end{bmatrix} \quad (6.3.28)$$

This is equivalent to Eqs. (6.3.8 to 6.3.10), which were derived from the simple model. If the full Jorgenson correction model shall be applied in real-time with an analytical solution, another wire orientation is needed to eliminate the coupled terms in Eq. (6.3.26). Such an orientation is illustrated in Figure 6.36.

Here, each of the three hot wire probes is oriented in a way that the probe shaft of each probe points in the wire direction of one of the other two probes. Hereby Eq. (6.3.26) simplifies to:

$$\begin{bmatrix} (U_{eff}^I)^2 \\ (U_{eff}^{II})^2 \\ (U_{eff}^{III})^2 \end{bmatrix} = \begin{bmatrix} -k_1^2 & 1 & h_1^2 \\ h_2^2 & -k_2^2 & 1 \\ 1 & h_3^2 & -k_3^2 \end{bmatrix} \cdot \begin{bmatrix} u_{HW}^2 \\ v_{HW}^2 \\ w_{HW}^2 \end{bmatrix} \quad (6.3.29)$$

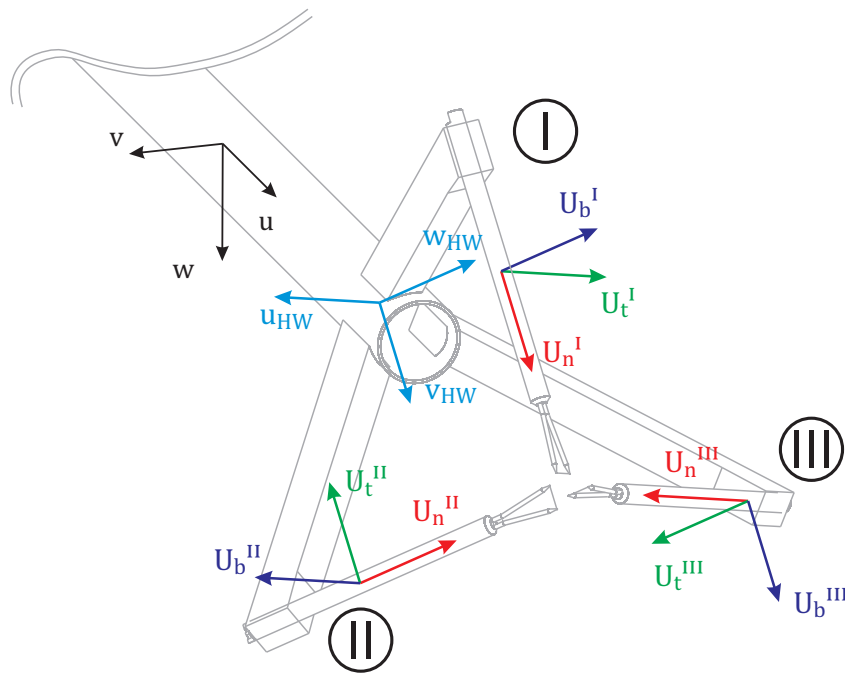


Figure 6.36: Alternative orientation of the three hot wire probes.

Consequently with another wire orientation it is possible to solve the full Jorgenson model analytically and thus to obtain a solution in real-time on the measurement mainboard. The question if it is beneficial to use this probe orientation will be discussed in Section 6.3.5.

6.3.4 Testing and Characterization of the Measurement Probe

As described earlier, the measurement mainboard has a mini USB port for testing purposes, which together with the separate measurement battery, allows the entire measurement boom to be used as an independent airflow probe connected to any laptop or tablet. To be able to "see" the inflow velocity and direction on screen, instead of receiving only numbers, a visualization software was written in Qt (Figure 6.37).

First qualitative tests have been conducted in a mobile wind tunnel (Figure 6.38), which is normally used at SWE to teach basic aerodynamic principles in the wind energy lecture. This open wind tunnel has a maximum wind speed of $v_\infty = 8 \text{ m/s}$. The ANDroMeDA measurement boom was used as a handheld airflow probe without any accurate adjustment of pitch and yaw angle of the boom. In this test it could be observed already that changes in the inflow direction are well covered and captured without delays. However, large fluctuations in the inflow direction could be observed which can be addressed to the low flow quality of the mobile wind tunnel.

To be able to conduct measurements at steady flow conditions, the measurement boom was mounted on a trolley and moved through still air. Because the trolley used for that test is equipped with rather small wheels and the floor was tiled, severe vibrations have been introduced to the measurement boom. These vibrations induce movements of the measurement boom mostly in the v and w direction of the aerodynamic axis system, while the u direction is not affected. Interestingly, as shown in Figure 6.39, in the hot wire axis system all velocity components are oscillating while in the aerodynamic axis system the u component keeps steady.

Since the vibration level during the test was significantly larger than the level expected in flight,

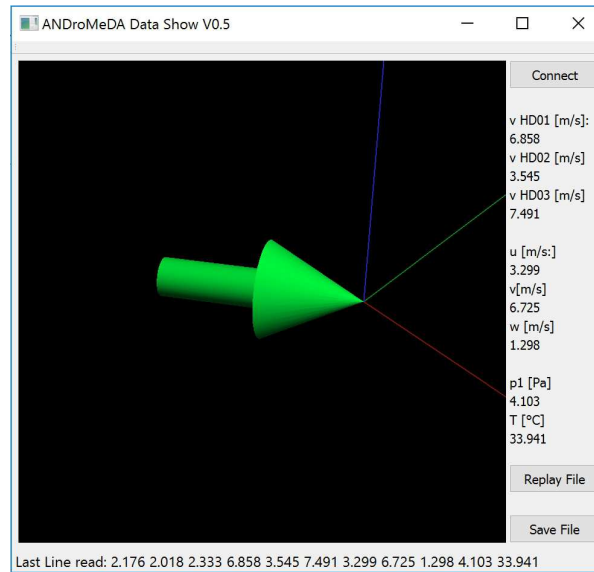


Figure 6.37: Visualization software ANDroMeDA DataShow.

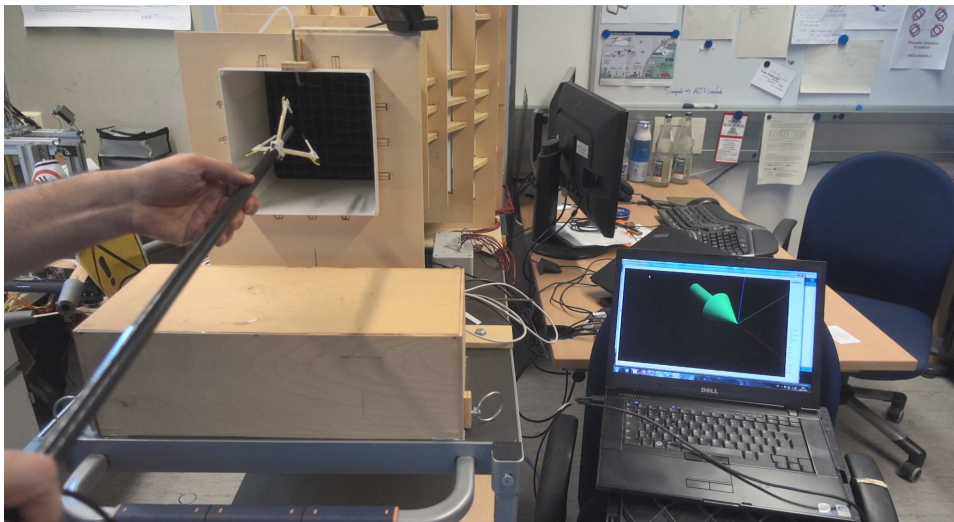


Figure 6.38: First test in the mobile wind tunnel.

this demonstrates that vibrations themselves do not affect the hot wire probes. However, every movement of the tip of the measurement boom will induce a velocity, which is captured correctly by the probes.

As illustrated in Figure 6.40 the Prandtl probe measurements during this trolley test are also oscillating at a high level. According to experiences at SVMTec the used pressure transducer itself is not sensitive to vibrations at all and it is assumed that the oscillations are a consequence of the silicon hoses fluttering inside the CFRP tube as a result of the vibrations. Therefore, the pressure hoses will be attached outside the boom, which is also beneficial for low vibrations (compare Section A.6).

After the general operation of the entire measurement boom has been ensured, another test at a laboratory wind tunnel at the Institute of Aerodynamics and Gasdynamics (IAG) has been

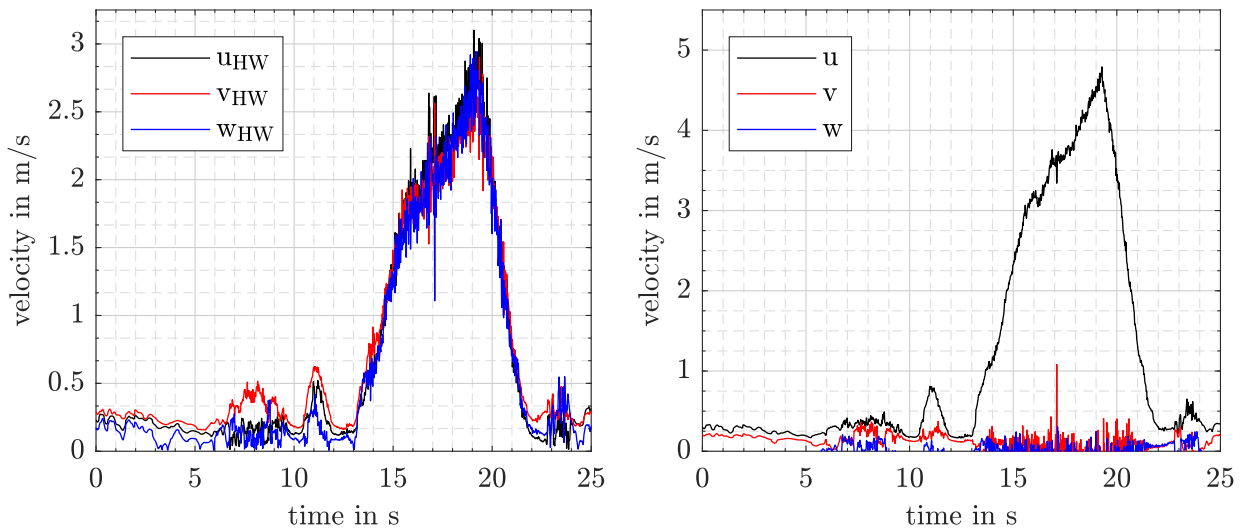


Figure 6.39: Velocities measured by the hot wire probes during the trolley run. Left: u_{HW}, v_{HW}, w_{HW} calculated with Eqs. (6.3.8 to 6.3.10). Right: After transformation to aerodynamic axis system by $\mathbf{R}_{HW-aero}$ (Eq. (6.3.21))

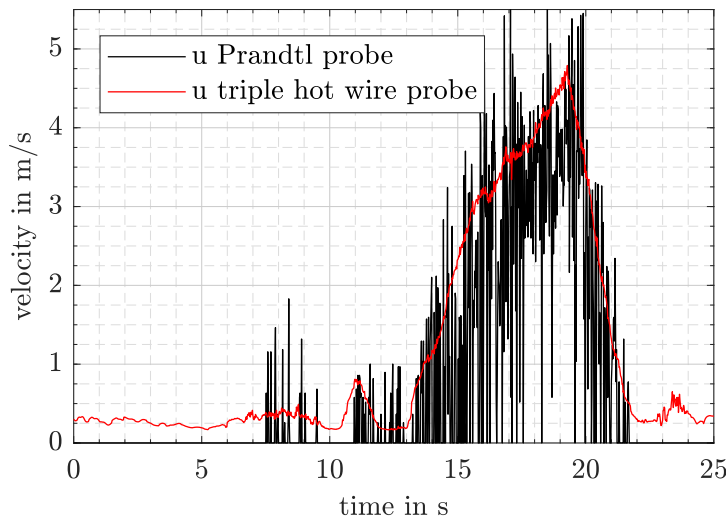


Figure 6.40: Fluctuating dynamic pressure during the trolley run yields in an oscillating velocity measurement from the Prandtl probe.

conducted. This wind tunnel is also an open wind tunnel and is also used for teaching purposes, but due to the larger distance between nozzle and fan, finer flow rectifiers and a larger contraction ratio it has a much higher flow quality than the mobile wind tunnel at SWE. The maximum flow speed is $v_\infty = 12.5 \text{ m/s}$. Figure 6.41 shows a test rig which was used to adjust exact angles about one axis (yellow circle). By turning the measurement boom around it's own axis (red circle) pitch and yaw angles α and β of the measurement boom can be set.

Because angle templates have been used to adjust the rig, the accuracy of the geometrical adjustment is assumed to be below $\Delta\alpha < 1^\circ$ and $\Delta\beta < 1^\circ$. With the help of this rig the angle of attack was varied from $\alpha = -45^\circ$ to $\alpha = +45^\circ$ with zero side-slip angle ($\beta = 0^\circ$) and vice versa. Combinations of angle of attack and side-slip angle could not be realized. An α -sweep and β -sweep has been recorded at $v_\infty = 13 \text{ m/s}$ and $v_\infty = 6.5 \text{ m/s}$.

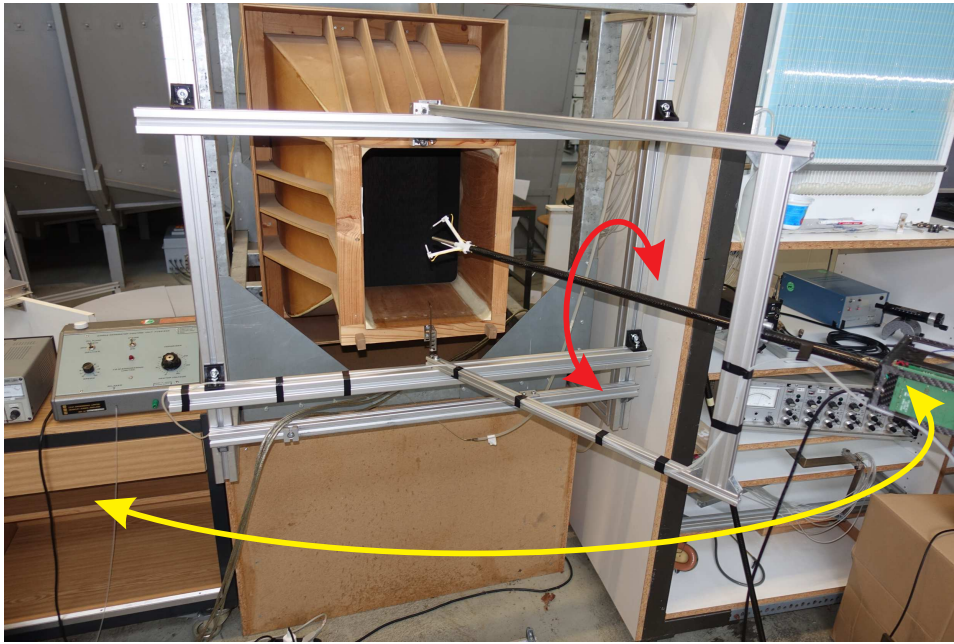


Figure 6.41: ANDroMeDA measurement boom mounted in the laboratory wind tunnel at IAG.

The lab wind tunnel is equipped with a pitot tube and a precise pressure transducer, which can be used to obtain a reference value for the tunnel speed. This reference speed showed that the Prandtl probe measurements are consistently lower. It is assumed that this is caused by a dam effect induced by the hot wire adapter arms and the probe shafts (compare Figure 6.29). Usually the static pressure holes are free of obstacles. The assumption could be confirmed when the static pressure holes were bypassed and the static pressure was taken externally.

To compensate this effect a correction factor was introduced:

$$u_{corr} = u_{Prandtl} + \Delta u_{corr} \quad (6.3.30)$$

Using a correction factor of $\Delta u_{corr} = 0.39 \text{ m/s}$, a good agreement with the tests and an error of less than 1 % can be achieved (see Figure 6.42). The used Prandtl probe from esa-systems, Berlin has a low directional sensitivity which could be confirmed during the tests (see Figure 6.43). Up to angles of $\beta = 20^\circ$ or $\alpha = 20^\circ$ the error is below 3% and therefore, the Prandtl probe measurements can be used as a reference value for the amount of v_∞ , measured by the triple hot wire unit.

Figure 6.44 illustrates the measured side-slip angle β of the measurement boom compared to the actually set side-slip angle. Between $\beta = -30^\circ$ and $\beta = +30^\circ$ the error remains below 5° .

In the same manner, the angle of attack measurement is compared to the actually set angle of attack in Figure 6.45. Between $\alpha = -45^\circ$ and $\alpha = +20^\circ$ the error is below 5° but surprisingly the measurement range is not symmetrically distributed around $\alpha = 0^\circ$.

To investigate this behaviour, the theoretical yaw angles of all three particular hot wire probes during an alpha sweep have been calculated. To calculate the wire yaw angles, the components $[U_n^i \ U_t^i \ U_b^i]^T$ for the i -th probe can be computed with the help of Eqs. (6.3.22 to 6.3.24) and the yaw angle can be derived from the trigonometric relations shown in Figure 6.33.

The result is presented in Figure 6.46 and it can be seen that the yaw angle of probe I varies linearly during an α -sweep. Probe II and probe III, whose yaw angles are identical, suffer from an asymmetric behaviour with a very small slope above $\alpha = 20^\circ$. The reason for the low slope is that

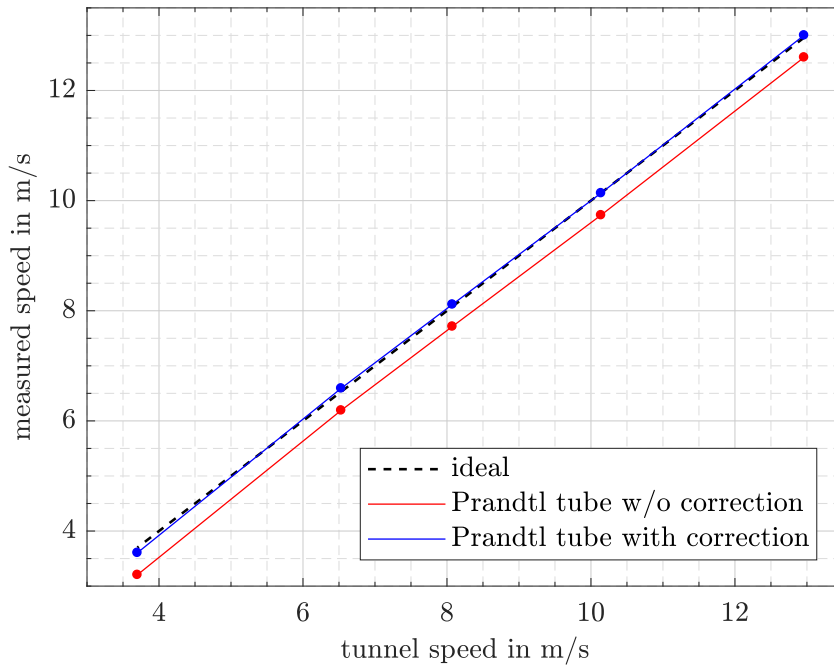


Figure 6.42: Speed measured with Prandtl tube.

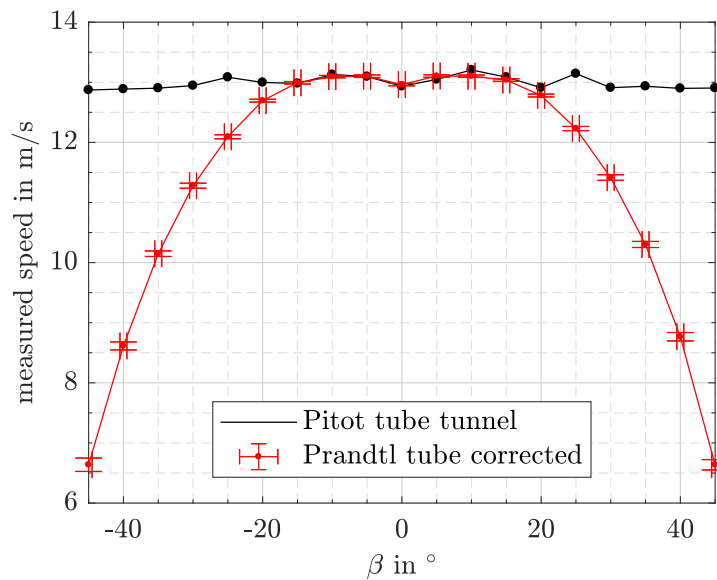


Figure 6.43: Directional response of the used Prandtl probe during β sweep.

the yaw angle of probes II and III does not change much for angles of attack higher than $\alpha = 20^\circ$. This means that, even if the yaw angles of probes II and III are still way below the point, where the effective cooling velocity stops following the cosine law (compare Figure 6.26), it is difficult to detect a change of angle of attack.

To understand why this effect is not symmetrical, the general orthogonal wire orientation of the three probes is illustrated in Figure 6.47. The orientation of the aircraft's x-axis in the current hot wire adapter design (Figure 6.29) is shown as an origin straight denoted "O" in Figure 6.47.

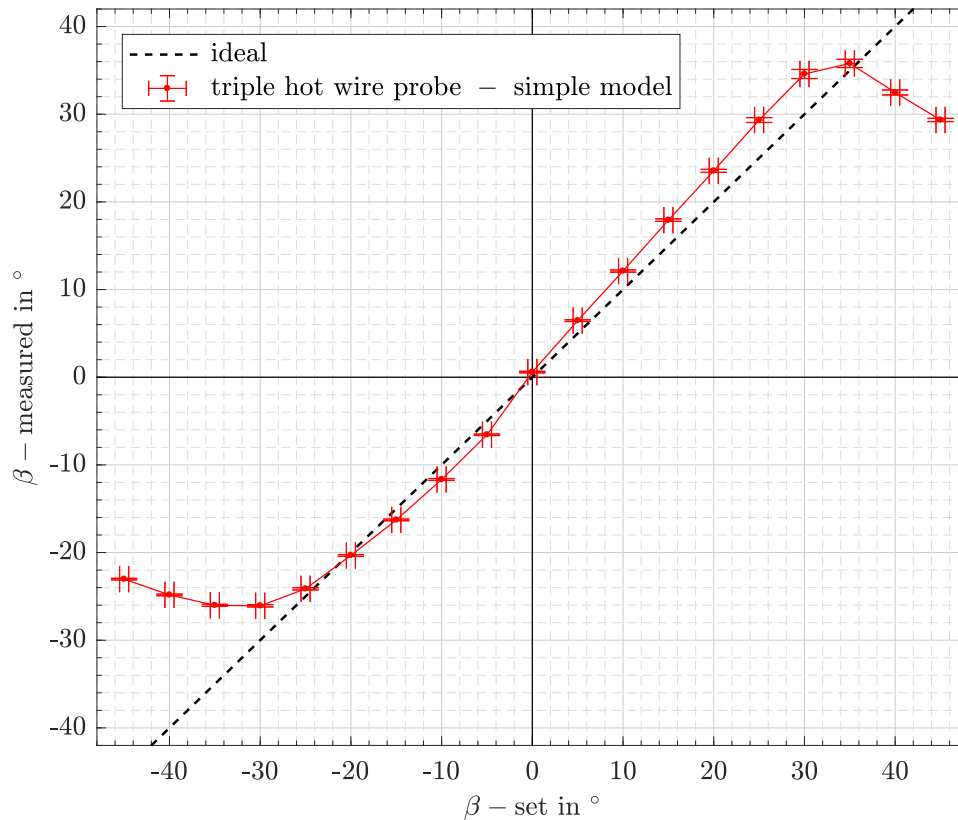


Figure 6.44: Side-slip angle measured with the triple hot wire unit during β sweep at $v_\infty = 13 \text{ m/s}$.

This origin straight could be also expressed as unit vector of $\mathbf{O} = [1/\sqrt{3} \ 1/\sqrt{3} \ 1/\sqrt{3}]^T$ or simply as $\mathbf{O} = [1 \ 1 \ 1]^T$ which means that $\mathbf{O}_x = \mathbf{O}_y = \mathbf{O}_z$. This orientation of the aircraft's x-axis (or in other words the longitudinal axis of the measurement boom) is clearly the most symmetrical solution because an inflow vector of zero side-slip angle and zero angle of attack will induce the same velocity component on all of the three wires ($\mathbf{O}_{xy} = \mathbf{O}_{yz} = \mathbf{O}_{zx}$). Also the yaw angles of all three wires will be identical for an inflow with zero side-slip angle and zero angle of attack. Using the notation in Figure 6.26 this is $\alpha = \beta = \gamma = \tan^{-1}(1/\sqrt{2}) = 35.26^\circ$.

However, this identical yaw angle for all three wires is not 45° . The angle of 45° only occurs between lines projected from \mathbf{O} in the xy-plane, yz-plane and zx-plane (shown as $\mathbf{O}_{xy}, \mathbf{O}_{yz}, \mathbf{O}_{zx}$ in Figure 6.47) and the wires (x,y,z axis). It might be seen as a geometrical paradox that the vector $[1 \ 1 \ 1]^T$ seems to be the most symmetric one but does not lie exactly in the middle of the measurement range.

To investigate the acceptable measurement range, a wire yaw angle limit of $\alpha_{max} = 70^\circ$ and a wire pitch angle limit of $\theta_{max} = 40^\circ$ was defined. In addition, a maximum angle of attack derivative of $(\Delta\alpha_{yaw}/\Delta\alpha)_{max} = 0.2$ and a maximum side-slip angle derivative of $(\Delta\alpha_{yaw}/\Delta\beta)_{max} = 0.4$ was set as limit of acceptance. The measurement range was discretized from an angle of attack of $\alpha = -45^\circ$ to $\alpha = +45^\circ$ and from a side-slip angle of $\beta = -45^\circ$ to $\beta = +45^\circ$ in steps of $\Delta\alpha = \Delta\beta = 1^\circ$.

If one of the three wires does not meet the criteria, the state (α, β) is defined as outside the acceptable measurement range. The results, shown in Figures 6.48 and 6.49, confirm that a shift of the zero angle of attack orientation of the measurement boom about 10° leads to a more uniform

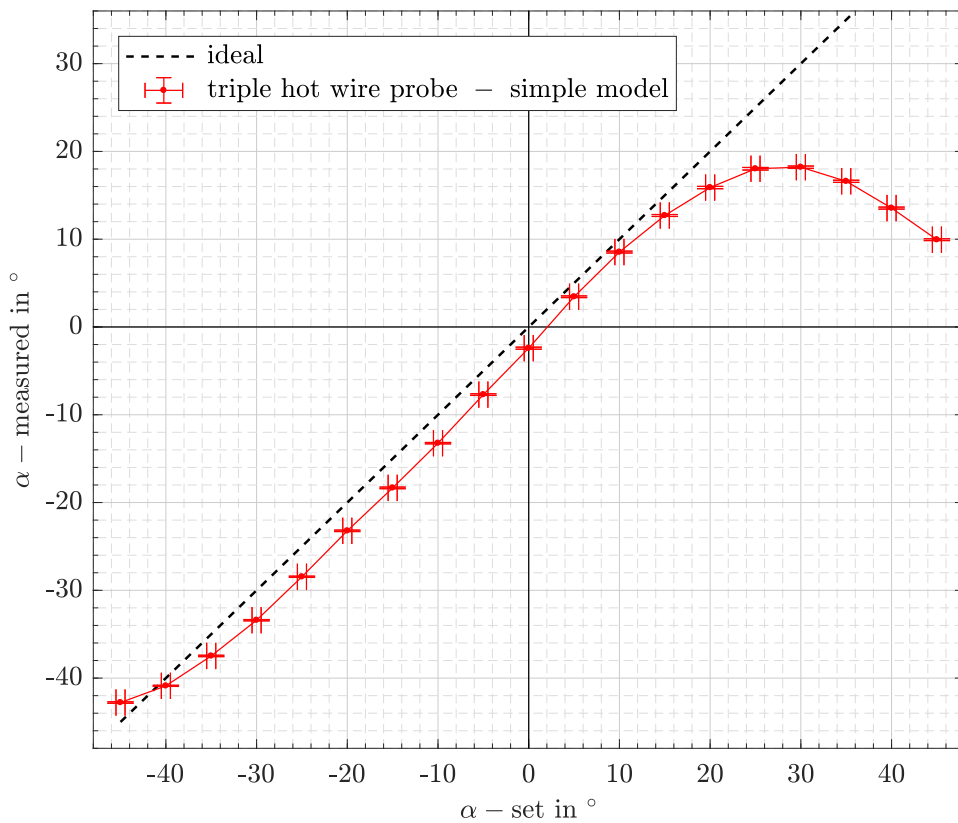


Figure 6.45: Angle of attack measured with the triple hot wire unit during α sweep.

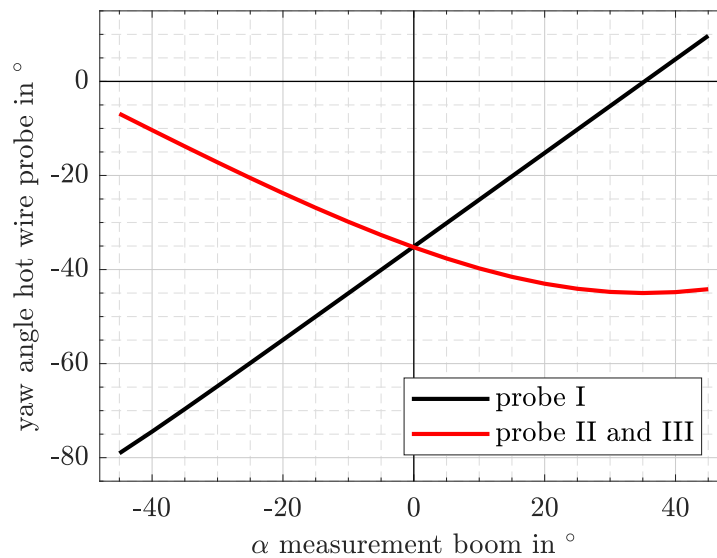


Figure 6.46: Theoretical yaw angles for the three hot wire probes during an α sweep.

distribution of the measurement range. However, a negative angle of attack α combined with larger sideslip angles β will then exceed the measurement range sooner (compare right side of Figure 6.49).

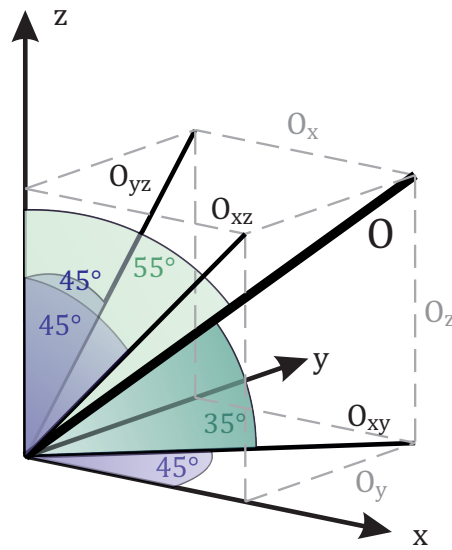


Figure 6.47: Orthogonal wire orientation with neutral inflow vector \mathbf{O} .

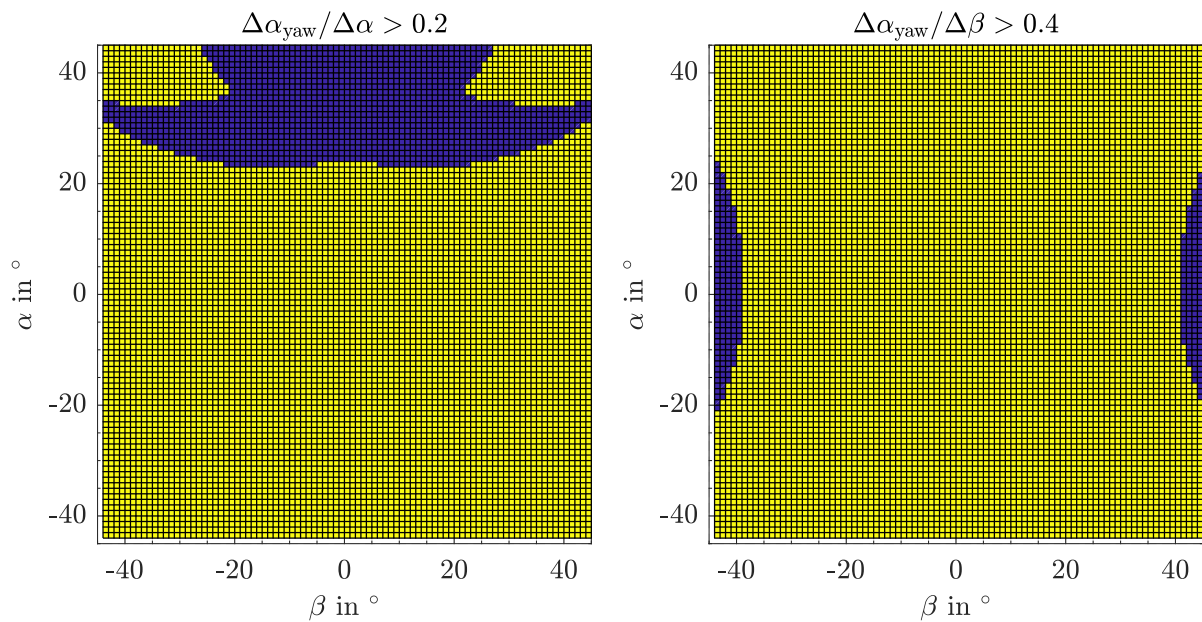


Figure 6.48: Acceptable range of sensitivity. Areas with $(\Delta\alpha_{yaw}/\Delta\alpha)_{max} < 0.2$ and $(\Delta\alpha_{yaw}/\Delta\beta)_{max} < 0.4$ shown in blue.

A remaining aspect, that is relevant for the characterization of the triple hot wire probe unit, is the magnitude of the inflow vector \mathbf{v}_∞ , measured at a non-zero angle of attack or non-zero side-slip angle. In Figure 6.50 this quantity is plotted for an α -sweep. The result for a β -sweep looks very similar.

The increasing speed measured at non-zero angles of attack can be explained by the fact, that no pitch-angle correction is carried out with the simple data reduction model (Eqs. (6.3.8 to 6.3.10)). It can be seen from the Jorgenson model (Eq. (6.3.19)) that non-zero pitch angles result in a higher effective cooling velocity.

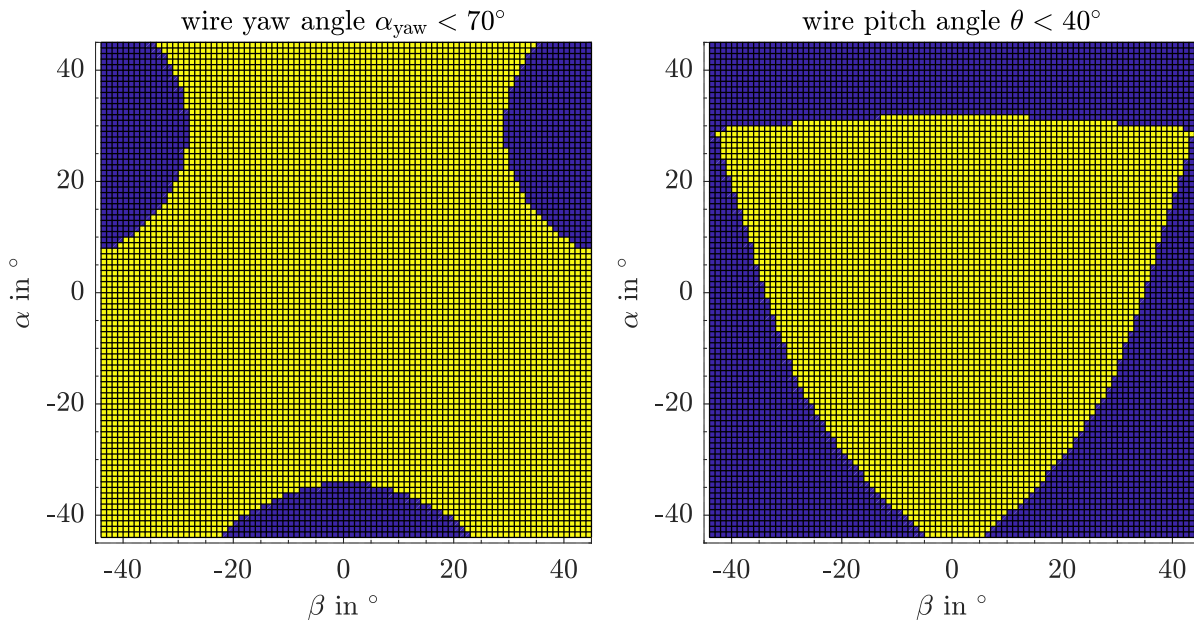


Figure 6.49: Acceptable measurement range. Areas with yaw angle $\alpha_{yaw} > 70^\circ$ and pitch angle $\theta > 40^\circ$ are shown in blue.

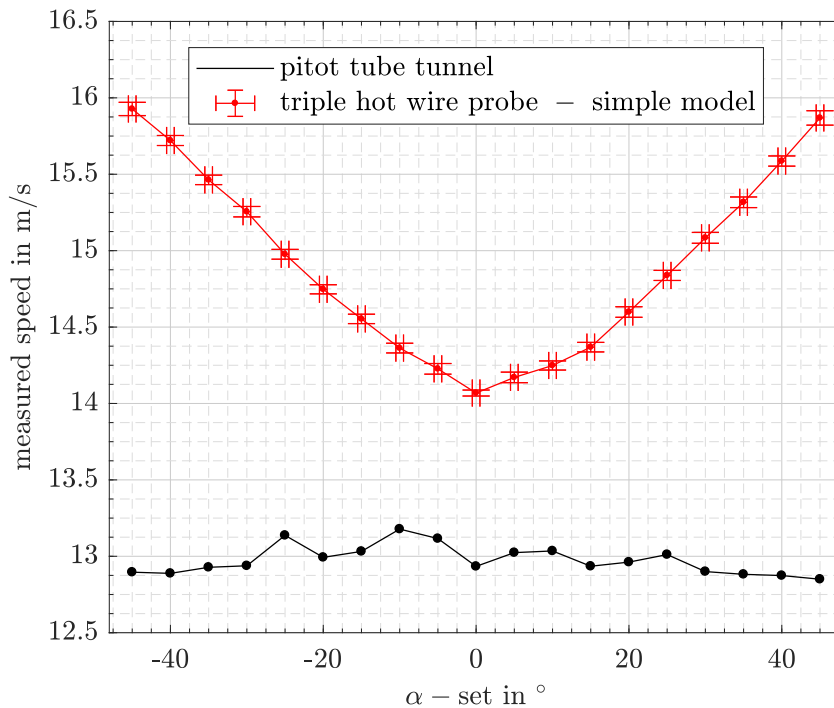


Figure 6.50: Inflow velocity v_∞ measured with the triple hot wire probe during an α -sweep.

The particular hot wire probes have been factory calibrated at SVMTec at a yaw angle of $\alpha_{yaw} = 45^\circ$. At zero angle of attack and zero side-slip angle all three probes will experience a yaw angle of $\alpha = 35.26^\circ$ (compare Figure 6.47). This explains the offset of 1 m/s at zero angle of attack.

6.3.5 Applying Advanced Calibration Methods to the Measurement Probe

In Figure 6.51 the normalized velocity, measured during an α -sweep by probe I, is shown. During an α -sweep, probe I has a zero pitch angle ($\theta = \text{const.} = 0^\circ$) and hence, it serves as a reference for adjusting the yaw angle model. At $\alpha_{yaw} = 0^\circ$ and $\alpha_{yaw} = 60^\circ$ there is a good agreement between the measured velocity and the theoretical velocity, according to the cosine law. For angles larger than $\alpha_{yaw} = 60^\circ$ the k factor in the Hinze model (Eq. (6.3.17)) or Jorgenson model (Eq. (6.3.19)) can be used to achieve a good fit between model and measurement.

It is assumed, that the discrepancy between $\alpha_{yaw} = 0^\circ$ and $\alpha_{yaw} = 60^\circ$ is originated in the aforementioned factory calibration of the hot wire probes at $\alpha_{yaw} = 45^\circ$, which causes an over-speed at $\alpha_{yaw} = 0^\circ$. To compensate for this effect another model, similar to the Jorgenson model,

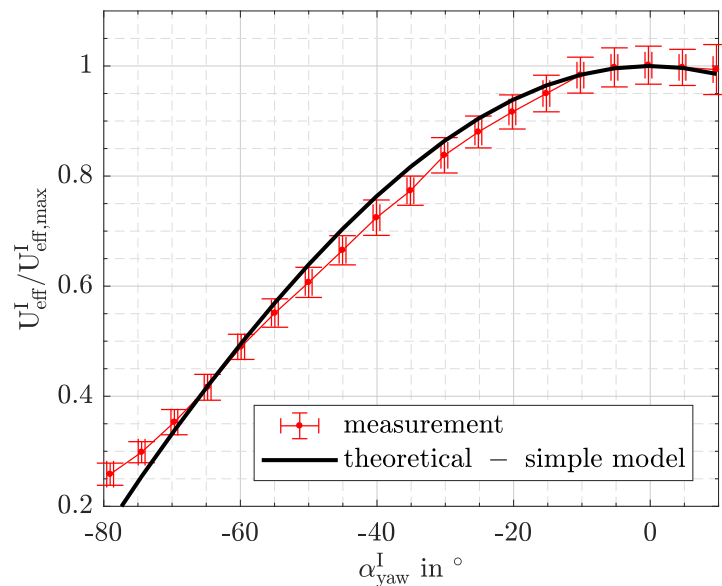


Figure 6.51: Normalized measured velocity of probe I during an α -sweep.

is introduced:

$$U_{eff}^2 = n^2 \cdot U_n^2 + k^2 \cdot U_t^2 + h^2 \cdot U_b^2 \quad (6.3.31)$$

With the factor n an over-speed at $\alpha_{yaw} = 0^\circ$ can be compensated. The model parameters were adjusted by hand. For future calibrations an automated least square method can be applied. To adjust n_1 a measurement point with $\alpha_{yaw} = 0^\circ$ and $\theta = 0^\circ$ during an α -sweep can be used. In a similar manner, k_1 can be adjusted with data available from the α -sweep. The parameter h_1 was adjusted with a plot from a β -sweep, where yaw angle changes are minor and the pitch angle is affected the most.

For the probes II and III the parameters n , k and h had to be adjusted during a β -sweep, while it was taken into consideration that there is a cross coupling effect between n and h . The first approach was to find a best compromise by setting the same factors $n_1 = n_2 = n_3$, $k_1 = k_2 = k_3$ and h_1, h_2, h_3 for all three probes. This approach did results in a poor agreement between the measured wire speeds and the theoretical wire speeds. The measured angle of attack α and side-slip angle β becomes less accurate compared to the simple model.

Only the magnitude of the measured inflow speed v_∞ agrees better with the measured wind tunnel speed and the v-shaped curve (compare Figure 6.50) gets flattened out. In general, applying the same model parameters for all three probes is not recommended.

A second approach with different parameters for each of the three probes resulted in the parameters shown in Table 6.2. In addition, during the parameter adjustment process it became

Probe No.	n	k	h
I	1.06	0.2	1.4
II	1.12	0.05	1.5
III	1.14	0.05	1.7

Table 6.2: Correction factors according to Eq. (6.3.31).

apparent that probe I might be mounted with an angle misalignment. To investigate this effect the matrix $\mathbf{R}_{\text{HW-I}}$ (Eq. (6.3.22)) was modified in a way that probe I is rotated at different small angles about the probe shaft (compare Figure 6.35). An angle of $+5^\circ$ (positive along vector \mathbf{U}_n^I) resulted in the best agreement between measurement and model. This wire orientation could be confirmed by a visual inspection of the measurement boom.

The effect of the detected misalignment can be seen in Figure 6.52. If probe I had been mounted without any misalignment, there would be only one line instead of two lines in Figure 6.52. The different probe velocities at the same yaw angle are caused by different pitch angles due to this misalignment.

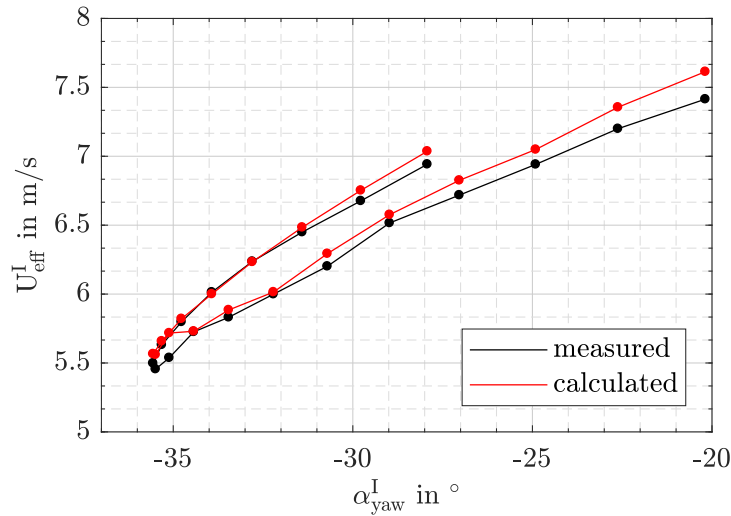


Figure 6.52: An angle misalignment of probe I expresses in different measured probe velocities at the same wire yaw angle during a β -sweep.

It should be mentioned however, that probe I was mounted less accurately compared to the other two probes because it was replaced after initial problems, without checking the precise angle alignment again. Since it is possible to aim for alignment of a wire along the corresponding arm of the hot wire adapter, it is expected that under normal circumstances an accuracy below 2° can be reached.

Figure 6.53 demonstrates that the advanced model (Eq. (6.3.31)) with individual parameters for each probe (Table 6.2) can achieve an improvement in the angle measurement accuracy. Also the inflow velocity v_∞ can be acquired more accurate as shown in Figure 6.54.

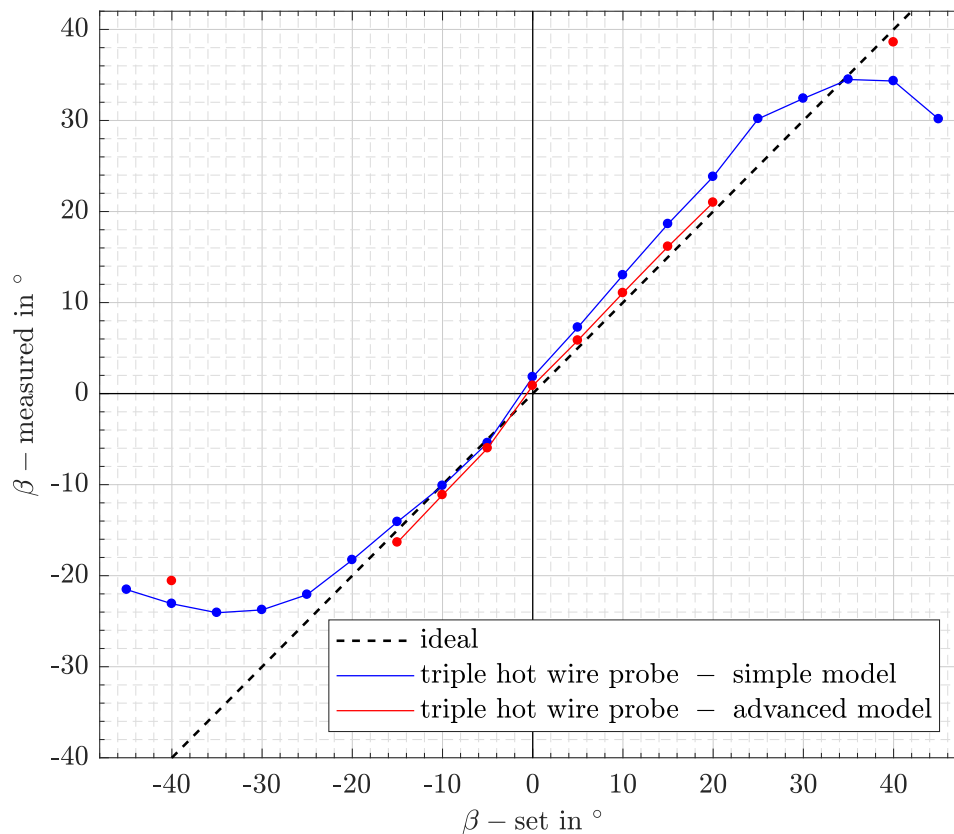


Figure 6.53: Measurement of side-slip angle during a β -sweep acquired with the simple and advanced data reduction model at $v_\infty = 6 \text{ m/s}$.

The biggest issue when the advanced model is used, is the fact, that an exact numerical solution cannot always be found. To solve the model, the MATLAB `fsolve` command was used, incorporating a "trust-region-dogleg" algorithm. While this method always provided a solution, this solution was not always an exact solution.

Another serious disadvantage of the advanced model is, that the parameters seem to depend on the inflow speed v_∞ . The parameters in Table 6.2 have been adjusted for an inflow speed of $v_\infty = 6 \text{ m/s}$ and did not lead to an improvement over the simple model at $v_\infty = 13 \text{ m/s}$.

In addition, as described earlier, an individual adjustment of n , k and h for each of the three hot wire probes is not feasible for the ANDroMeDA measurement boom. Since acceptable results with the advanced model could only be achieved with such individual correction factors, the robust simple model will be used instead.

However, for future probe designs some concluding remarks are given. A closer look at Table 6.2 shows that very similar parameters have been set for probe II and probe III, which are mounted symmetrically and differ from the orientation of probe I (compare Figure 6.35). This on the other hand, could mean that the parameters differ because of the geometrical probe placement. With the number of experiments conducted till now this cannot be confirmed. Under the following conditions it might be possible to improve the triple hot wire measurements without the necessity for an individual calibration of each measurement boom:

- A new hot wire adapter with an alternative probe orientation according to Figure 6.36 has to be designed.

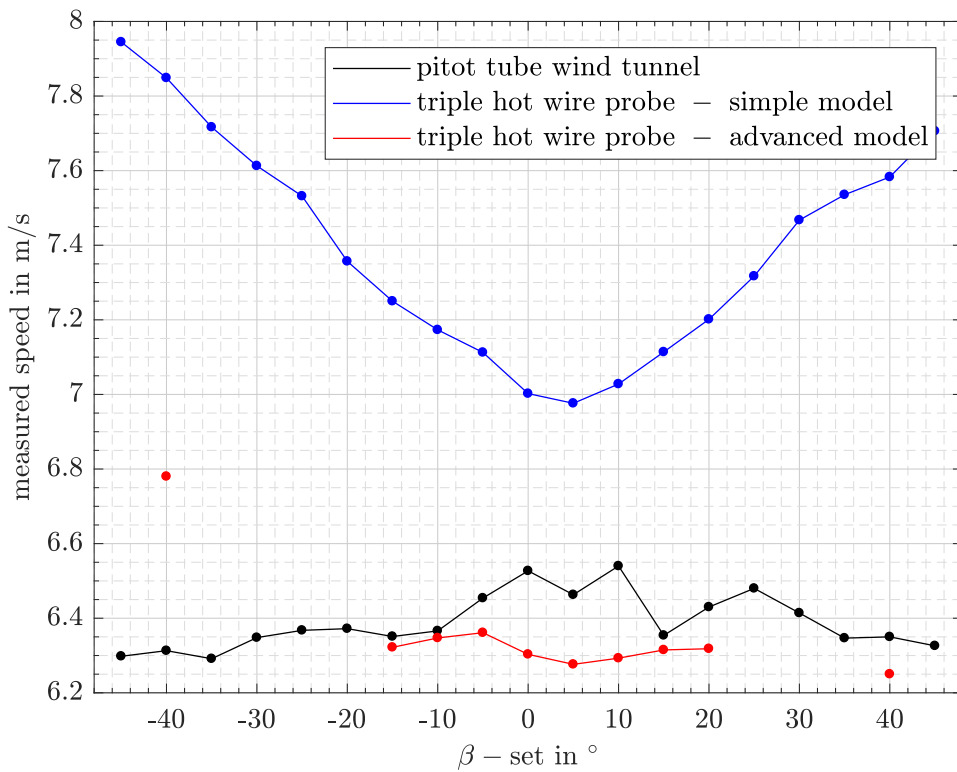


Figure 6.54: Measurement of inflow speed v_∞ during a β -sweep acquired with the simple and advanced data reduction model at $v_\infty = 6$ m/s.

- Consequently the advanced model (Eq. (6.3.31)) can be solved analytically.
- The three probes have to be mounted precisely in the new adapter. It should be mentioned, that for the alternative wire orientation the wires are aligned at 45° to the corresponding arm (compare Figure 6.36), which makes this task harder than it is for the current hot wire adapter.
- Because the arms of the new hot wire adapter will be closer to the static pressure holes of the Prandtl tube the correction introduced in Figure 6.42 has to be re-adjusted.
- Further experiments have to be conducted with several replacement hot wire probes to investigate if the correction factors n , k and h depend on the probe itself or on the position in the hot wire adapter. If these factors are not depending on the probes themselves, it should be possible to adjust the same factors for all three probe positions since the new design is completely symmetric.
- The factors n , k and h have to be determined for several inflow speeds.

6.3.6 Conclusions

A combined Prandtl tube / triple hot wire probe has been designed and successfully tested. A simple data reduction scheme has been derived to gain inflow speed and inflow direction from the three separate hot wire probes. More advanced data reduction schemes have also been described and one particular method has been derived especially for the pre-calibrated SVMTEC hot wire

probes. This method could be applied to the existing triple hot wire probe but did not succeed in general to improve the results.

A further improvement over the simple model might be possible with an alternative triple hot wire probe geometry and further investigations on general correction factors. However, the present probe demonstrated a reasonable performance with the simple model. The biggest improvement is expected by moving the zero angle of attack to $\alpha = -10^\circ$ in the current wire orientation.

7 Flight Control

7.1 Problem Description

While a conventional helicopter, even a small one, can be flown remotely without any artificial stabilization, a multirotor aircraft introduces another challenge. As it can be seen from Eq. (5.9.1) the thrust of a propeller is proportional to the square of its rotational speed. Consequently, a non-linear behaviour will develop if a multirotor aircraft is flown without a control loop.

It is not possible to manually fly a multirotor aircraft without additional electronic aid, using gyroscope sensors to support the pilot. For manned helicopters, such a system is referred to as stability augmentation system (SAS). In model helicopters it is referred to as "flybarless system" and for multirotor aircraft it is simply called a flight controller.

The flight controller of a multirotor aircraft usually has different flight modes, resulting in different levels of autonomy. In the most basic flight mode, the pilot is just slightly supported by the flight controller and the pilot input is used as a setpoint for the angular rates, which are measured by gyroscopic sensors. Thus, if all sticks are centered, zero angular acceleration is commanded.

If the aircraft is disturbed and takes a non-level attitude, this attitude will remain and the aircraft will "slip" to one side. This behaviour corresponds to the flying characteristics of a conventional helicopter and hence, the angular rate controller is crucial to make a multirotor aircraft flyable by overcoming the aforementioned nonlinearity of the propeller thrusts. Usually, the rate controller is implemented as a PID controller.

The more advanced flight modes of a multirotor flight controller are implemented by cascading different controllers after the basic rate controller. The next level controller is the angle controller. In addition to the gyroscopic sensors, acceleration sensors are used to measure the attitude of the aircraft, and the pilot input serves as a setpoint for this attitude. This means, that if the stick is released the aircraft will remain level, which makes it much easier to fly a multirotor aircraft in this flight mode than to fly a conventional helicopter.

The output of the angle controller is used as an input for the rate controller. In the same manner, a speed controller can be added after the angle controller, which uses its output, that can be seen as a desired translational velocity, as an input for the angle controller. The highest level of control and also the highest level of autonomy can be achieved using a position controller, usually realized with GPS measurements, whose output is a desired speed as an input for the speed controller. The entire control scheme is sketched in a simplified way for the longitudinal axis in Figure 7.4.

While the most basic rate controller only needs angular rates, measured by the gyroscope sensors, implemented in the IMU directly, the more advanced flight modes need also measurements of the aircraft's attitude, flight speed, heading and position which introduces a lot more complexity to the flight control, sometimes also referred to as "sensor fusion". A basic approach to combine gyroscope and acceleration sensors, also working with less powerful microprocessors, is the direct cosine method (DCM) explained in [39]. With the more powerful ARM processors, introduced over the last decade, the use of a Kalman filter, as described in [40] and [41], to combine the different sensor inputs, became common.

Besides the basic flight control, multirotor flight controllers most often include the abilities to fly to predefined way-points, return to launch and also take-off and landing functions. The automatic recognition of obstacles with cameras has been demonstrated by some universities, and also at a well developed stage on some commercial products like the DJI Mavic, but is still not standard for all autopilot systems at the present time.

For measurements with ANDroMeDA-1 and also for the operation of several aircraft in a group, those advanced functions are not needed, if the coordination and collision avoidance of all aircraft is done, in a centralized manner, from the ground control station. It is more important for the autopilot, to be able to read in wind measurement data, align the aircraft with the wind vector and send the measurement data to the ground in real-time. Also, as described below, a special control algorithm is necessary for the tilting propeller configuration. These requirements make an open source flight controller software, where the code can be modified, mandatory.

7.2 Hardware Used for ANDroMeDA-1

Because of the good experiences with the first generation of the Pixhawk flight controller the Pixhawk 4 (see [70]), is used for ANDroMeDA-1. The flight control compartment is shown in Figure 7.1. Because initially another hardware arrangement was planned, an adapter-board was used.

The Pixhawk 4 features a more powerful processor than it's predecessors, running at 168 Mhz, as well as a larger RAM and more peripheral connections. However, it is not able to log the measurement data at a high sampling rate and hence, an additional Raspberry Pi Zero MCU is used to log the measurement data on a micro SD card.

Because the UART bus, used to connect to the measurement electronics, is not limited to a single receiver, the Pixhawk and Raspberry Pi Zero can both receive measurement data and the Pixhawk can use this data to align the aircraft and its measurement boom with the wind as well as send measurement data to the ground control station, while the Raspberry Pi Zero can log the data at a higher sampling rate on the sd card. In addition the Rapsberry Pi Zero can log measurements from an additional IMU at the tip of the measurement boom to monitor vibrations.

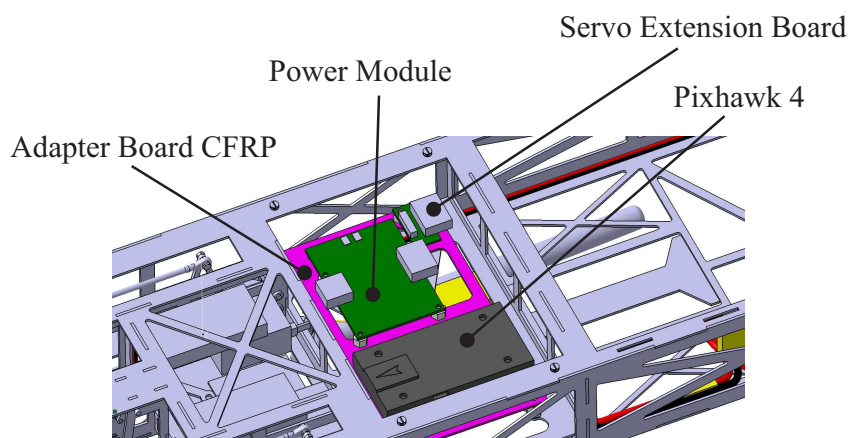


Figure 7.1: Installation of the Pixhawk 4 and corresponding Power Module (PM-07) in ANDroMeDA-1 on an adapter board.

7.3 Flight Mechanical Considerations

As already shown in Figure 5.64 and Figure 5.65 a roll-yaw and yaw-roll coupling exists if the propellers are tilted forward and the aircraft is conventionally actuated by differential propeller RPMs. Figure 7.2 and Figure describe that phenomena in more detail. For the illustrated param-

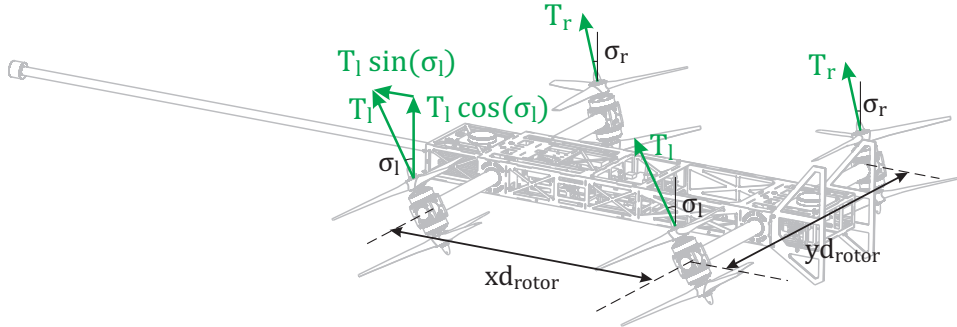


Figure 7.2: Rotor thrust forces with propellers tilted forward.

eters the resulting rolling and yawing moment are:

$$L = y d_{rotor} \cdot (\cos(\sigma_l) \cdot T_l - \cos(\sigma_r) \cdot T_r) \quad (7.3.1)$$

$$N = y d_{rotor} \cdot (\sin(\sigma_l) \cdot T_l - \sin(\sigma_r) \cdot T_r) \quad (7.3.2)$$

If the actual thrust level T_0 is known or estimated, it is possible to achieve a clean allocation of roll and yaw functions, so that, for example, a roll input results in a pure roll maneuver without a yawing moment:

$$\begin{bmatrix} T_1 \\ T_2 \\ T_3 \\ T_4 \\ \sigma_1 \\ \sigma_2 \\ \sigma_3 \\ \sigma_4 \end{bmatrix} = \begin{bmatrix} 1 & 0 & -\cos(\sigma_0)/(2 \cdot y d_{rotor}) & 1/(2 \cdot x d_{rotor}) & -\sin(\sigma_0)/(2 \cdot y d_{rotor}) \\ 1 & 0 & \cos(\sigma_0)/(2 \cdot y d_{rotor}) & -1/(2 \cdot x d_{rotor}) & \sin(\sigma_0)/(2 \cdot y d_{rotor}) \\ 1 & 0 & \cos(\sigma_0)/(2 \cdot y d_{rotor}) & 1/(2 \cdot x d_{rotor}) & \sin(\sigma_0)/(2 \cdot y d_{rotor}) \\ 1 & 0 & -\cos(\sigma_0)/(2 \cdot y d_{rotor}) & -1/(2 \cdot x d_{rotor}) & -\sin(\sigma_0)/(2 \cdot y d_{rotor}) \\ 0 & 1 & \sin(\sigma_0)/(T_0 \cdot 2 \cdot y d_{rotor}) & 0 & -\cos(\sigma_0)/(2 \cdot y d_{rotor} \cdot T_0) \\ 0 & 1 & -\sin(\sigma_0)/(T_0 \cdot 2 \cdot y d_{rotor}) & 0 & \cos(\sigma_0)/(2 \cdot y d_{rotor} \cdot T_0) \\ 0 & 1 & -\sin(\sigma_0)/(T_0 \cdot 2 \cdot y d_{rotor}) & 0 & \cos(\sigma_0)/(2 \cdot y d_{rotor} \cdot T_0) \\ 0 & 1 & \sin(\sigma_0)/(T_0 \cdot 2 \cdot y d_{rotor}) & 0 & -\cos(\sigma_0)/(2 \cdot y d_{rotor} \cdot T_0) \end{bmatrix} \cdot \begin{bmatrix} T_0 \\ \sigma_0 \\ L \\ M \\ N \end{bmatrix} \quad (7.3.3)$$

As an approximation, it can be assumed that the torque of each coaxial pair of propellers is zero. However, this allocation is also expected to work for a quadrotor configuration, because the rotor torques are in most cases balanced, as shown in Figure 7.3. The allocation matrix above has been tested with a flight mechanical model of a quadcopter, which includes the rotor torques.

7.4 Control Strategy for Tilting Propellers

As mentioned above the tilting propeller configuration needs another control algorithm to take full advantage their abilities. With tilting propellers an additional degree of freedom (DOF) is

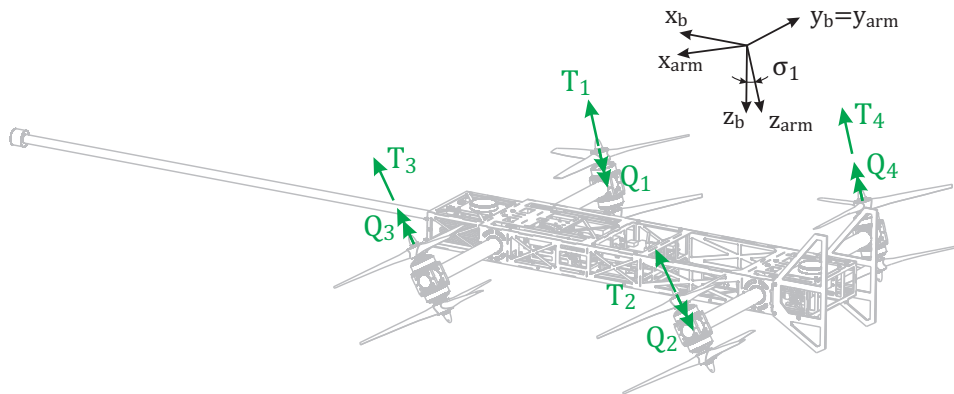


Figure 7.3: Thrust and torque of all four motor arms if no coaxial propellers are used or the torque of the coaxial propellers does not cancel out.

introduced. The corresponding control algorithm is sketched in Figure 7.4 for the longitudinal axis. The additional DOF, in form of the separately controllable aircraft pitch attitude, is only adjusted for take-off and landing (compare Figure 5.86). For the measurement phase of the flight, the controller tries to keep the aircraft's frame and the measurement boom, at zero angle of attack. With the tilt-able propellers the flight speed and thus the position is controlled. In addition, differential tilting is be used to produce large yawing moments.

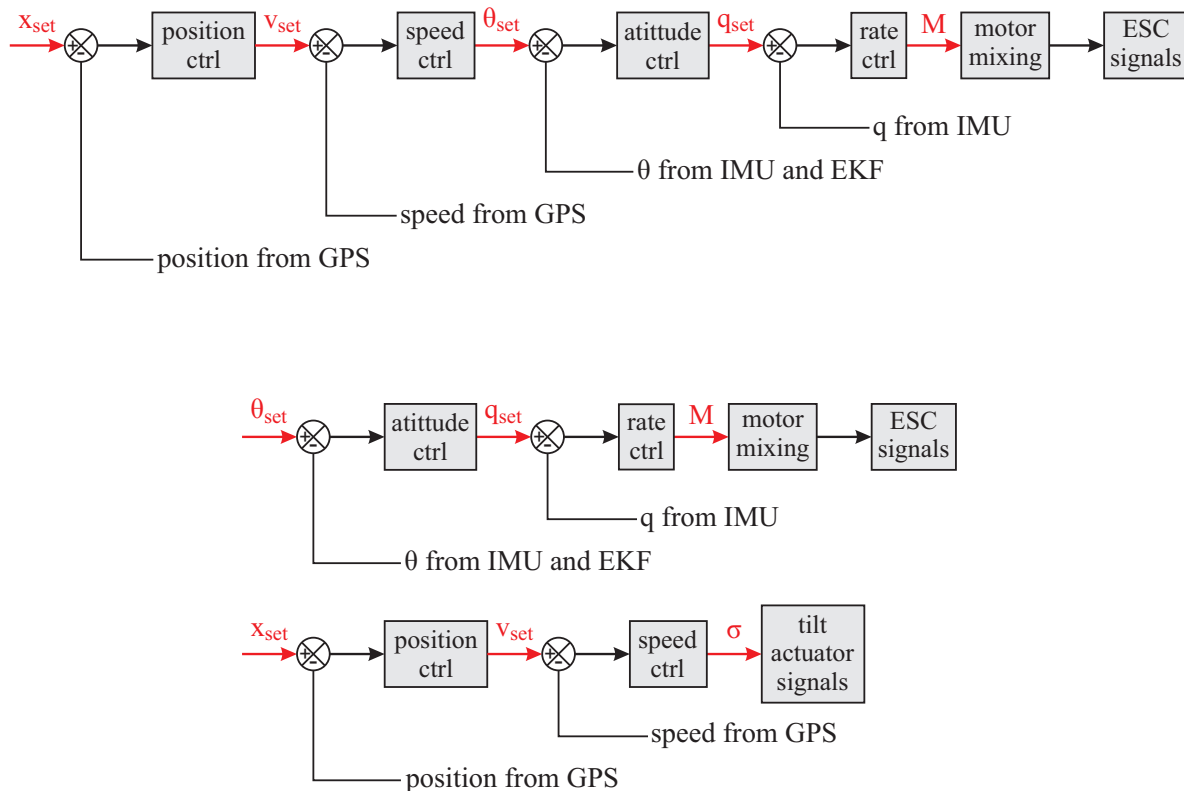


Figure 7.4: Control scheme for ANDroMeDA (bottom) compared to control scheme of a conventional multirotor aircraft (top).

7.5 Modifications to the PX4 Flight Control Software

7.5.1 Yaw Controller

As described in Section 7.3, for a clean allocation of rolling and yawing moments, the actual thrust of the propellers has to be estimated. This can only be done if a new mixer class for the ANDroMeDA aircraft is implemented in the PX4 firmware (block "motor mixing" in Figure 7.4).

Because the mixer classes in PX4 are quite complex, no new mixer class has been implemented yet. Instead, a conventional octrotor motor mixer is used and the conventional yaw output (differential RPM of diagonal rotors) has been disabled. In addition, a PX4 "Simple Mixer" line is used to forward the output of the yaw controller directly to the tilt servos.

Consequently, with the propellers tilted forward, a roll controller output will introduce a yawing moment, which is then counteracted by the yaw controller using differential tilting of the motor arms.

Likewise, with the propellers tilted forward, a yaw controller output will introduce a rolling moment, which is then counteracted by the roll controller by changing the propeller RPMs.

Even without a clean allocation of control moments, no problems could be observed in flight tests so far.

However, one modification was made to the original yaw controller: At different thrust levels the same amount of differential rotor tilting causes different yawing moments. As shown in Section 7.3, at a specific thrust level $T = T_0$ the yawing moment is proportional to this thrust level:

$$N = yd_{rotor} \cdot T_0 \cdot (\sin(\sigma_l) - \sin(\sigma_r)) \quad (7.5.1)$$

Therefore, a function was implemented to scale the yaw controller output according to the actual thrust level:

```
float thrust_sp_limited=math::constrain(_thrust_sp, 0.3f, 1.0f);
float yaw_reduced=0.3f/thrust_sp_limited * _att_control(2);
_actuators.control[2] = (PX4_ISFINITE(yaw_reduced)) ? yaw_reduced : 0.0f;
```

With this code the regular yaw controller output is reduced if the thrust is larger than 30 % of full thrust. Below 30 % the full yaw controller output, hence, the full actuator travel is used.

Without this function, the PID values for the yaw controller have to be adjusted at full thrust to avoid oscillations of the yaw controller. Consequently, without this function the PID values are much lower and the yaw axis is softer.

7.5.2 Position Controller

As described in [71], the attitude controller implemented in PX4 is completely quaternion based. This means, roll and pitch axis are not decoupled until the motor mixing takes place. For the attitude controller there is only an attitude setpoint quaternion. Consequently, it is not possible to control the roll axis independently and use the pitch output to control the tilt servos.

Instead, a new target attitude quaternion has to be determined, where the airframe is always in the x-y plane of the NED coordinate system. The difference between the new and old attitude quaternion has to be used, to determine how much the tilt servos have to move.

This is done in the following way:

- A rotation matrix is derived from the current attitude setpoint quaternion:

```
_R_setpoint=matrix::Quatf(_v_att_sp.q_d);
```

- The new x-axis of the aircraft is determined by creating a vector in the x-y plane with the current yaw angle:

```
Vector3f body_x_new(cosf(_v_att_sp.yaw_body),sinf(_v_att_sp.yaw_body),0.0f)
```

- The old z-axis of the aircraft is read from the third column of the attitude setpoint matrix:

```
Vector3f body_z_old(_R_setpoint(0,2),_R_setpoint(1,2),_R_setpoint(2,2));
```
- The new y-axis is constructed with the help of the cross-product between the old z-axis and the new x-axis:

```
body_y_new=body_z_old % body_x_new;
```

- The new z-axis is then calculated by the cross-product between new x-axis and new y-axis:

```
body_z_new=body_x_new % body_y_new;
```
- All axis vectors are normalized and combined to a new rotation matrix, which is then transformed into the new attitude setpoint quaternion.

- To determine the necessary motor arm tilt angle σ_0 , it has to be distinguished between a forward and backward tilted old z-axis:

```
if (_R_setpoint(2,0)>=0){  
  _servo_tilt_posctrl=-acosf(math::constrain(body_z_new.dot(body_z_old),-1.0f,  
  1.0f));  
}  
else {  
  _servo_tilt_posctrl=acosf(math::constrain(body_z_new.dot(body_z_old),-1.0f,  
  1.0f));  
}
```

- The value of `_servo_tilt_posctrl` is then normalized with the maximum tilt angle of the aircraft and published to `_actuators.control[4]` in control group 0 (usually used for flaps) and forwarded directly to the tilt servo actuators as a collective command. The latter step is done in the custom mixer input file by a "Simple Mixer" line.

7.5.3 Notch Filter

To avoid an excitation of the measurement boom's natural frequencies by the flight controller a notch filter was implemented. Because the PX4 firmware does not include a notch filter class, it was converted from the Arducopter firmware and can be found in ...

To tune this filter a new parameter set has been introduced with the attenuation as `MC_NOTCH_ATT`, the bandwidth as `MC_NOTCH_BW` and the center frequency as `MC_NOTCH_CENTER`. These new parameters can be adjusted from a ground control station without the need to recompile the entire firmware.

The notch filter is applied directly to the roll, pitch and yaw outputs of the attitude controller:

```
_att_control_filtered(0) = _notch_filters_boom[0].apply(_att_control(0));  
_att_control_filtered(1) = _notch_filters_boom[1].apply(_att_control(1));  
_att_control_filtered(2) = _notch_filters_boom[2].apply(_att_control(2));  
  
_att_control=_att_control_filtered;
```

7.5.4 Data Acquisition

The UART communication of hot wire electronics is received by the Pixhawk 4 with a new software module called `anwind_parser`. To be able to work with the data and send it to the ground a new uORB called `anwind_probe` is created (compare [72]).

7.5.5 Custom MAVLINK Package

The `anwind_probe` uORB is send to ground with a custom MAVLink message (compare [72]), called `ANWIND_AIRDATA`. Therefore the MAVLink library has to be recompiled. The definition of the `ANWIND_AIRDATA` message is:

```
<message id="410" name="ANWIND_AIRDATA">
<description>Air data probe for ANWIND project.</description>
<field type="uint64_t" name="time_usec" units="us">Timestamp when data was received
from the probe</field>
<field type="float[3]" name="airspeed" units="m/s">Airspeed from the three hot wire
probes</field>
<field type="float" name="p_diff" units="Pa">Differential pressure</field>
<field type="float" name="temp" units="degC">Temperature</field>
</message>
```

7.6 Modifications to the QGroundControl Software

As ground control software, QGroundControl is used. QGroundControl is open source and can be compiled for many different platforms. To be able to fulfill the special requirements needed for wind measurements, some modifications are needed.

7.6.1 Custom MAVLink Package

The same recompiled MAVLink library, as used on the aircraft's firmware, has to be used for QGroundControl. Otherwise the custom message cannot be decoded and will not be shown, because unknown message IDs are ignored. To be able to work with the received data a new FactGroup has to be created and the variables from the custom message have to be read:

```
void Vehicle::_handleAnwindAirdata(mavlink_message_t& message)
{
mavlink_anwind_airdata_t airdata;
mavlink_msg_anwind_airdata_decode(&message, &airdata);

_airdataFactGroup.airspeed1()->setRawValue(airdata.airspeed[0]);
_airdataFactGroup.airspeed2()->setRawValue(airdata.airspeed[1]);
_airdataFactGroup.airspeed3()->setRawValue(airdata.airspeed[2]);

_airdataFactGroup.pdiff()->setRawValue(airdata.p_diff);
_airdataFactGroup.temp()->setRawValue(airdata.temp);
}
```

7.6.2 Data Preview

For quick checks during the measurement flights or for a manual alignment of the aircraft's measurement boom with the wind direction, a precise and easy way of previewing the received data is crucial. For the purpose of customized widgets QGroundControl takes advantage of QML (Qt Meta-object Language) files.

With the help of a QML file a customized window is created that can include any of Qt's widgets. Elements consisting of 3D graphics (Qt3D) have been implemented successfully as a preliminary test. With this feature a visualization with a 3D arrow, similar to the software ANDroMeDA-DataShow (compare Figure 6.37), is possible.

However, at the present stage, gauge instruments are used. These gauge widgets, called CircularGauge, can be freely customized by using different tick marks for the outer and inner scale, custom angle ranges, etc. In addition to different widgets in the customized window, also math functions can be applied in a QML file. Therefore, it is possible to do most of the data reduction calculations in QGroundControl and to apply a plausibility check to show a warning, whenever the hot wire speeds are non-plausible and the resulting inflow vector is not trustworthy (compare Section 6.3.1). This usually happens if the inflow angle range is exceeded or a wire is broken.

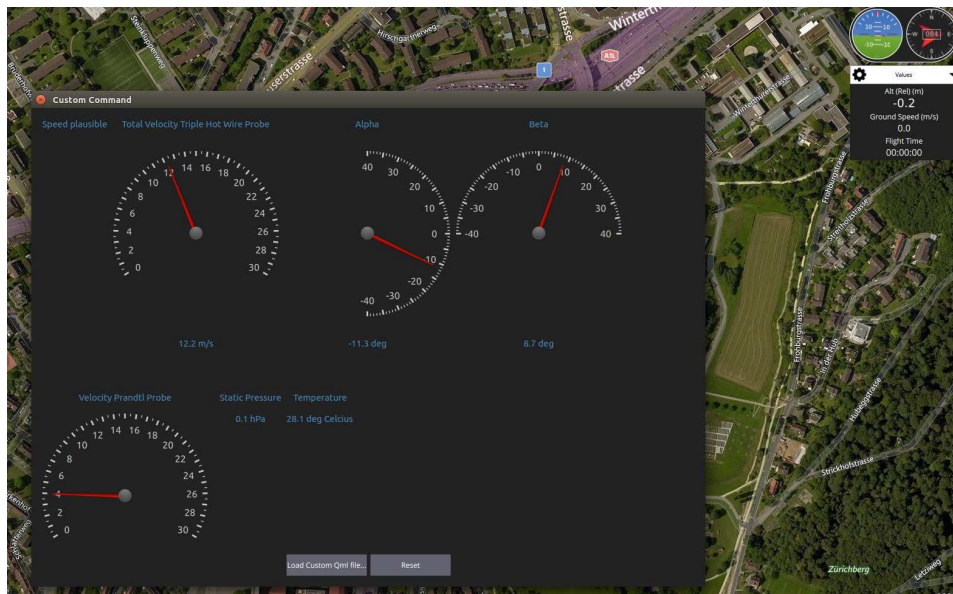


Figure 7.5: Live preview of wind measurements with QGroundControl.

8 Flight Tests and Evaluation of the Overall Wind Measurement System

8.1 Flight Tests

8.1.1 Software Test Platform Baby ANDroMeDA

To test the Firmware changes to the original PX4 firmware thoroughly, before applying them to ANDroMeDA-1, a smaller version of it, called Baby ANDroMeDA was built. Baby ANDroMeDA was relatively easy to design and can be built quickly, since most parts are used from a tilt-rotor kit. This kit originally includes only two tilt mechanisms and two tilt servo actuators, but from two kits one aircraft with four tilt actuators was built.

Because the same Pixhawk 4 is used for Baby ANDroMeDA, the same firmware can be uploaded and tested. Figure 8.1 shows Baby ANDroMeDA. First tests have been undertaken with a conventional quadrotor controller and the changes, described in Section 7.5, have been implemented successively, to make sure everything works as expected. In addition to flight tests, every minor software change, e.g. upgrades to newer firmware versions, changes regarding data acquisition etc., can be tested on Baby ANDroMeDA first. This makes it a very valuable "hardware in the loop" tool, because Baby ANDroMeDA is less critical to incidents during test flights, it's hardware is significantly less expensive and it does not need the extensive labor, as ANDroMeDA-1, to build it.



Figure 8.1: Small sized hardware in the loop platform, called Baby ANDroMeDA.

8.1.2 Observations during Flight Testing of ANDroMeDA-1

ANDroMeDA-1 was first set up as a conventional Octocopter and the PID values for the rate and attitude controllers of the roll and pitch axis have been tuned carefully. During that phase of the flight test program the retractable landing gear has not been used but a temporary fixed landing gear.

When the final yaw controller, using differential motor arm tilt, was tested it could be observed, that the first natural frequency of the long measurement boom (approx. $\omega_0 = 12.5 \text{ Hz}$), although it is far from the rotor frequencies, is excited by the flight controller. This behaviour can be mitigated

with "soft" PID values, but the situation is still critical. The oscillation of the measurement boom starts with small amplitudes but due to the constant excitation the amplitude increases slowly to a critical level during flight. It can only be stopped by a quick landing and shut down of the system.

This makes a notch filter for the flight controller absolutely mandatory. The notch filter, as described in Section 7.5.3, is quite effective and after its implementation, the measurement boom has a very low vibration level, as confirmed by onboard videos. The notch filter moves the frequency responses of the flight controller outputs towards lower and higher frequencies, where they are not exciting the measurement boom. This effect can be seen very well in an FFT of the actuator outputs, as shown in Figure 8.2.

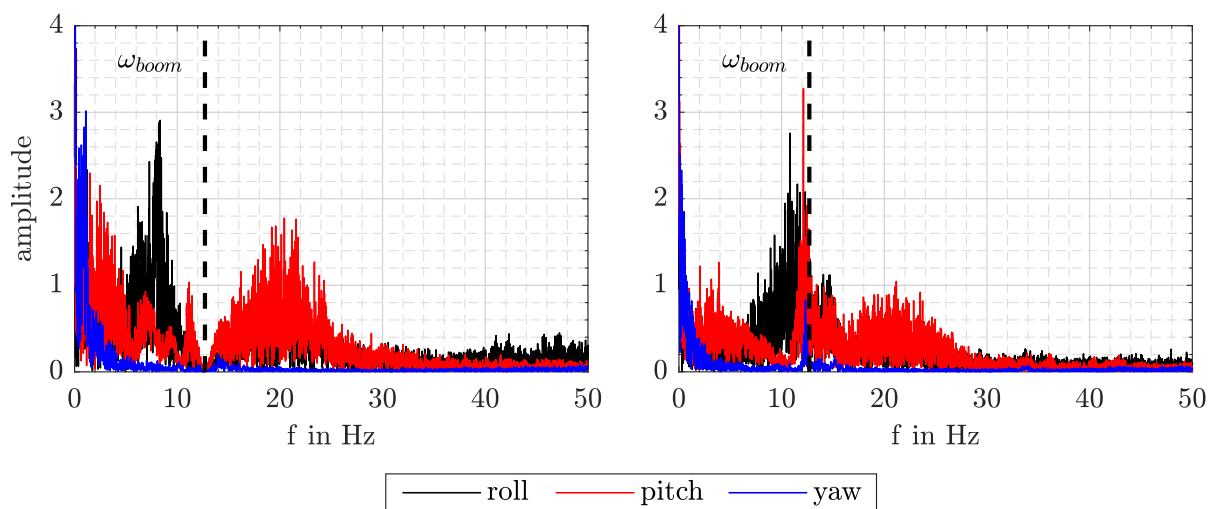


Figure 8.2: FFT of the actuator control outputs. Left: With notch filter. Right: Without notch filter.

8.1.3 Drag Coefficient

During the flight test program the drag value of ANDroMeDA-1 was identified as $c_D \cdot A = 0.174 \text{ m}^2$. This is more than twice the value determined by CFD Simulations (compare Section 5.10). However, the simulations have been conducted with many simplifications and the geometry does not match that of ANDroMeDA-1 exactly. For example, the motor arms have been modeled with an outer diameter of $D_{arm} = 24 \text{ mm}$ instead of $D_{arm} = 28 \text{ mm}$. Compared to a conventional multirotor design (e.g. SWE hexacopter with $c_D \cdot A = 0.29 \text{ m}^2 \dots 0.43 \text{ m}^2$) the value is still very low.

8.1.4 Flight Envelope

The flight envelope of ANDroMeDA-1 could be characterized:

- At a tilt angle of $\sigma_0 = 30^\circ$ the maximum horizontal speed is $v_{x_{max}} = 16.3 \text{ m/s}$.
- The maximum climb speed is $v_{z_{max}} = 10.5 \text{ m/s}$.
- The needed battery capacity per second of flight time is 9.8 mAh/s . This means, that the maximum flight time with two 6000 mAh batteries in parallel is approximately $t_{flight} = 20 \text{ min}$.

The maximum tilt angle was limited to $\sigma_0 = 30^\circ$, because higher values have not been tested yet. Without a clean control function allocation (compare Section 7.5.1 and Section 7.3) higher values could cause a critical flight behaviour. The maximum mechanical tilt angle of ANDroMeDA-1 is however higher at $\sigma_0 = 55^\circ$. Consequently, much higher flight speeds / wind speeds are possible. An extrapolation of the current flight test values is given in Figure 8.3. This leads to the conclusion that the theoretically possible flight speed is approximately $v_{xmax} = 25 \text{ m/s}$. However, this has to be confirmed by careful flight testing.

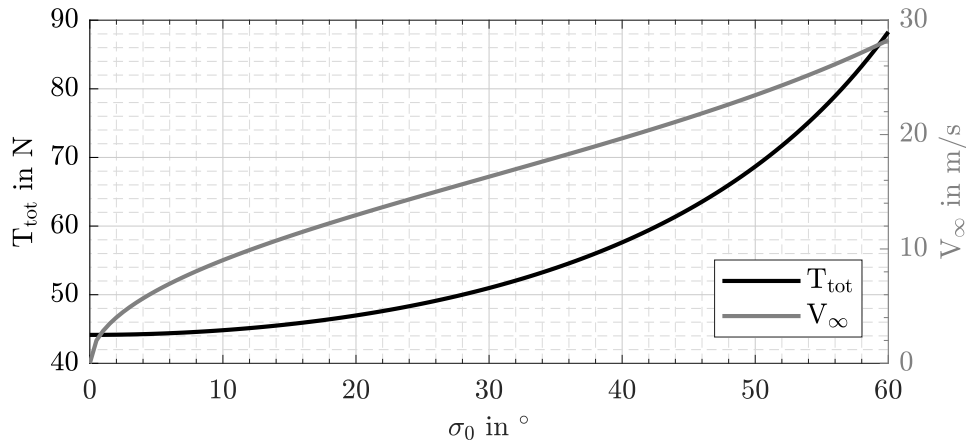


Figure 8.3: Extrapolated flight speeds of ANDroMeDA-1.

8.1.5 Conclusions

Even if the flight envelope is not exactly as predicted by the conceptual design and by the initial simulations, the results are nevertheless very satisfying. No significant problems occurred in the different stages of flight testing, except the oscillating measurement boom, which could be overcome by a notch filter.

A minor glitch could be observed during early indoor flight tests but could be attributed to a faulty reading of the magnetometer due to iron in the building and was an isolated incidence. Consequently, for future indoor tests, as for example the flights in the gust wind tunnel, magnetometer and GPS have been switched off. For outdoor wind measurement flights without the presence of surrounding buildings this is not relevant.

So far ANDroMeDA-1 can be seen as a reliable aircraft with more than 3 hours of flight time and over 50 flights.



Figure 8.4: ANDroMeDA-1 during outdoor flight tests.

8.2 Validation of ANDroMeDA-1 as a Wind Measurement System

8.2.1 Forward Flight in Calm Air

A first "real life" test was conducted in form of an outdoor flight during a calm day with almost no wind. The purpose of this test was to confirm that measurement the equipment works as expected, live-data are sent to the ground station and to verify, if the GPS ground speed agrees with the measured inflow speed.

To protect the sensitive hot wires from swirled debris and grass, a 4m x 5m tarp was laid out on the field and secured with tent pegs. This procedure worked well and no hot wires have been damaged.

The results from this flight are shown in Figure 8.5. The outliers can be explained with the strong turns in the flight path that exceeded the measurement range of the probe.

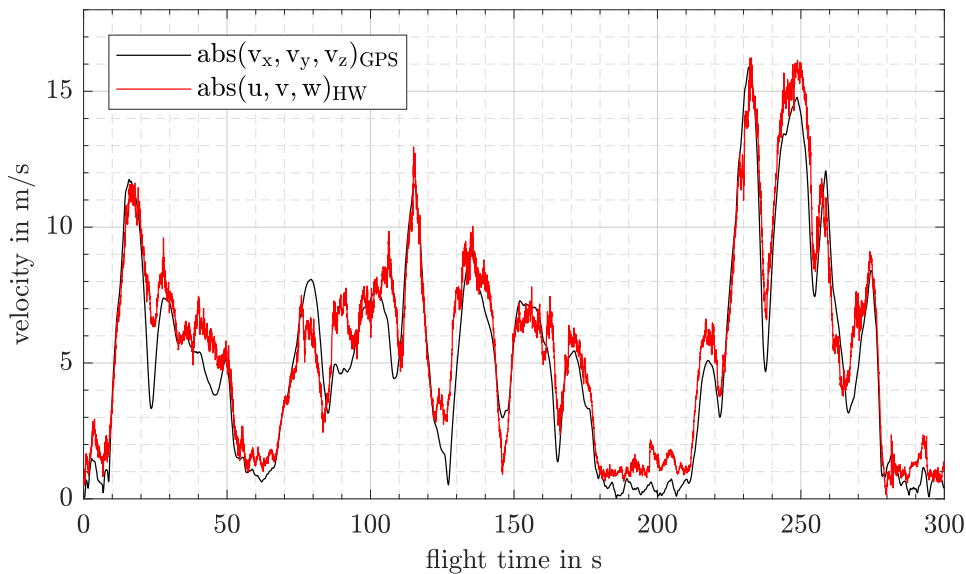


Figure 8.5: GPS ground speed compared to measured flight speed.

8.2.2 Gust Wind Tunnel

Another important step in the validation of the overall system was performed in the large gust wind tunnel of the Institute of Aerodynamics and Gasdynamics (IAG). This wind tunnel has a diameter of 6.3 m, which makes it possible to fly ANDroMeDA inside with a controlled wind speed for testing. As a reference measurement a sonic anemometer was mounted at a height of $h_{sonic} = 2.5$ m.

The purpose of this test was to quantify the lower end of the measurement range. From experiments with a single propeller (Section 5.7) it is known that at $v_{\infty} = 4$ m/s a slight influence of the propeller is noticeable in wind speed measurements in front of it.

To investigate how much the entire aircraft, with all propellers running at a realistic trim condition, will influence the flow field at the probe location, the experiment was designed as a free-flight. It would be safer to mount ANDroMeDA with a tripod and start the propeller, it is, however, almost impossible to find a valid trim condition with such a setup. With a free flight

experiment there is no doubt regarding realistic propeller RPMs.

Because the flow of the gust wind tunnel is turbulent and unsteady the flights have been divided into alternating phases of $t = 20$ s. In one phase ANDroMeDA was flown with the tip of the measurement boom very close to the sonic anemometer and in the other phase ANDroMeDA was flown approx 3 m behind the sonic anemometer at a lower altitude. At a tunnel speed of $v_\infty = 3.5$ m/s and below this flight pattern are visible in the readings of the sonic anemometer. Wind direction and vertical wind speed do change significantly when ANDroMeDA is operated close to the sonic. At tunnel speeds of $v_\infty = 4.0$ m/s and above no influence is visible.

The wind tunnel was operated between $v_\infty = 2.0$ m/s and $v_\infty = 6.0$ m/s. One flight was also carried out with the mounted triple hot wire probe to compare the measurements of the on-board probe with the sonic. The agreement is good, however, a constant offset of $\Delta v = 0.5$ m/s can be observed. It is assumed that this can be addressed to the fact that ANDroMeDA and the sonic hat a distance of approx. $\Delta y = 0.5$ m and the tunnel speed gets lower towards the walls.

Because the enclosed environment does not allow the use of GPS and magnetometer all flights had to be done manually, which leads to stronger aircraft movements than with an automated flight.



Figure 8.6: ANDroMeDA hovering inside the gust wind tunnel in close proximity to a sonic anemometer.

8.2.3 Field Validation at a Met Mast

The last validation stage is the comparison of ANDroMeDA's measurements with a sonic anemometer mounted on a met mast. The North-West met mast at the WINSSENT test site of the WindForS research cluster was chosen to conduct this experiment (compare Section 1.3.1).

To enable a comparison between in-flight measurements with ground measurements, a transfor-

mation is necessary:

$$\mathbf{v}_{\text{global}} = \mathbf{R}^T (u \ v \ w)^T - (v_x \ v_y \ v_z)^T - (q \ p \ r)^T \times (L \ 0 \ 0)^T \quad (8.2.1)$$

Where \mathbf{R} is a rotation matrix calculated from the current attitude quaternion, which is logged by the Pixhawk. The vector $(u \ v \ w)^T$ is the inflow vector, measured from the triple hot wire probe. The aircraft translational speeds are v_x , v_y , v_z and the roll-, pitch- and yaw rate are q , p and r .

Because of the actively stabilized measurement boom, the second and third part of Eq. (8.2.1) do not alter the results significantly. For most cases it would be sufficient to use only the rotation matrix. The rotation matrix, however, is absolutely mandatory to account for the current heading of the aircraft. The agreement between ANDroMeDA and the sonic anemometer is very good,

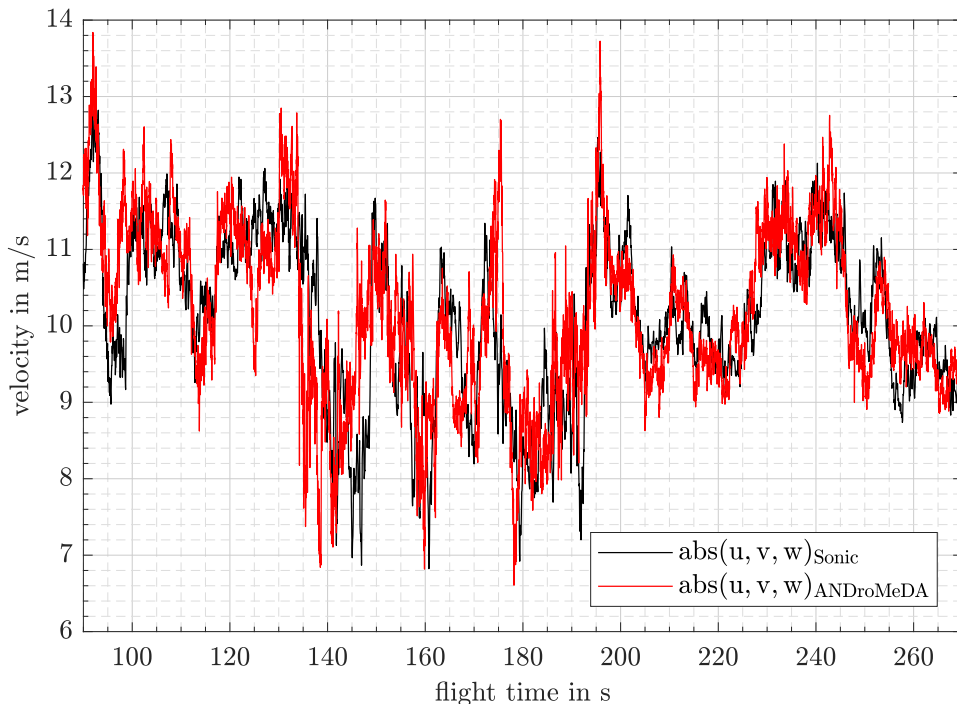


Figure 8.7: Wind speed measured with met mast and ANDroMeDA-1.

as shown in Figure 8.7 and Figure 8.8. The heading of the aircraft was corrected manually several times to keep the wind direction in the measurement range of the probe. This worked well with the help of the live data shown at the ground control station (compare Figure 7.5).

8.3 Multi-Aircraft Measurements

Because the only existing ANDroMeDA aircraft so far is ANDroMeDA-1, no multi-aircraft measurements could be completed yet. Because of legal limitations as many safety pilots as aircraft are needed for a multi-aircraft measurement. This means that, in the most simple case, several ANDroMeDAs will be operated independently with several pilots and several laptops. Therefore, no complications are expected, because ANDroMeDA-1 works well, when operated alone. However, the guidelines, derived in Section 5.7, should be taken into consideration to avoid any mutual influence.

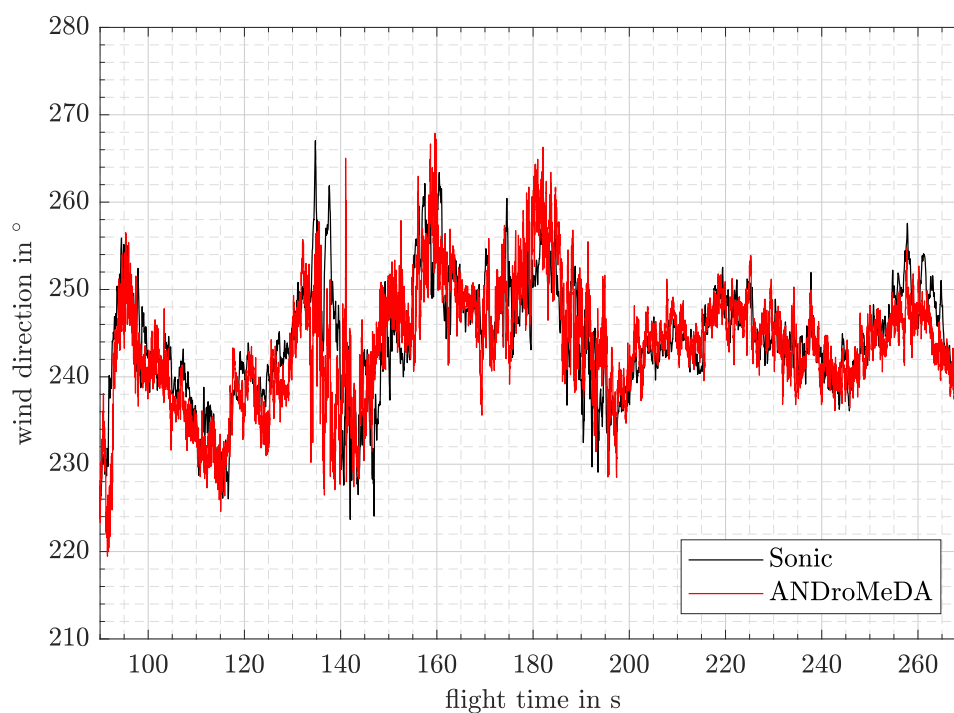


Figure 8.8: Wind direction measured with met mast and ANDroMeDA-1.



Figure 8.9: Automated hover next to a met mast.

To test automated multi-aircraft measurements and the "multi-vehicle" functionality of QGroundControl three Baby ANDroMeDA test platforms have been built. Flight tests with multiple aircraft have not been performed yet.

8.4 Conclusions

It could be demonstrated that the first prototype of the novel flying wind measurement system, ANDroMeDA-1, performs well at wind speeds above $v_{wind} = 4 \text{ m/s}$ and up to $v_{wind} = 13 \text{ m/s}$. According to the extrapolated flight speed of the aircraft, it is assumed that wind speeds up to $v_{wind} = 20 \text{ m/s}$ can be measured. So far, during several validation measurement flights and one flight after the validation campaign, none of the three hot wires of the probe had to be replaced.

In the future multiple aircraft will be used for group measurements, to investigate the nature of



Figure 8.10: Take-Off and landing area for measurement flights.



Figure 8.11: Automated group measurement control features can be tested with the three Baby ANDroMeDAs.

all kinds of flow phenomena, which can be explored by short duration measurements with a high spatial and temporal resolution.

9 Conclusions and Outlook

9.1 Conclusions

The research objectives, defined in Section 1.6, have been met. An aircraft concept, purpose-designed for wind measurements, has been realized and a prototype of this aircraft, named AN-DroMeDA - ANWIND Drone for Measurement and Data Acquisition - has been built. The feasibility of a small series production has been investigated and improvements in the manufacturing process have been formulated.

The measurement performance evaluation of ANDroMeDA-1, the first prototype, has been finished with great success. It could be shown that the measurement boom is well stabilized, so that a more detailed motion compensation does not provide any advantages.

The benefits when hovering in a windy condition, using tilting propellers, have been investigated analytically and also demonstrated in flight tests.

During this work a number of important findings to advance the airborne wind measurements with multirotor aircraft have been found. It is, however, difficult to keep track of all findings because of the number of different topics that has been investigated. Consequently, the most important findings will be listed here and sorted into different categories.

9.1.1 Design of ANDroMeDA

The tilting rotor concept offers a number of advantages compared to conventional designs for airborne wind measurements:

- When the wind speed or vertical wind direction changes an aircraft with tilting propellers needs only half of the time to adjust to the new state.
- The long measurement boom, necessary for flow measurements in the vicinity of running propellers, results in a high yawing moment if the wind direction changes in the horizontal plane. With the help of differential propeller tilting it is possible to produce control moments about the yaw axis that are one magnitude larger than the control moments of conventional multirotors. Thus the long measurement boom can be compensated with an active control instead of a large vertical tail fin.
- With tilting propellers an additional degree of freedom is introduced to the system which can be used to keep the airframe and measurement boom always level during wind speed changes. This improves the flow measurement because no velocities will be induced by aircraft rotations at the tip of the measurement boom.
- In addition, the drag of the entire aircraft will be lower with a level airframe which results in longer flights.
- The additional degree of freedom, which results from the tilting propeller configuration, can also be used to tilt the entire aircraft, including the measurement boom, in a nose-up attitude to protect the probe during take-off and landing.

A flight mechanical analysis has been conducted for different tilting rotor configurations with a different number of rotors and rotor layouts. For all configurations a yaw-roll coupling and vice versa exists. However, this coupling is expected to have only a minor effect on the overall flight mechanics because the tilt angle is small for most wind speeds. The maximum yawing moment with a long measurement boom is approximately $N_{max} = 2 Nm$ at a wind speed of $v_{wind} = 11 m/s$ and a 90° side slip angle, according to CFD simulations. This exceeds the maximum yaw control moment of most configurations by a factor of two, if different rotor speeds and hence rotor torques are used. The maximum yaw control moment produced by differential tilting is nevertheless sufficient.

Finally an H-8 configuration with eight coaxial rotors has been selected because the high number of small rotors offers redundancy against motor failures and a fast response when the rotor speed is changed. The longitudinal and lateral distance between the rotors has been determined iteratively to achieve a maximum maneuverability and the best position keeping performance in windy conditions. An optimal propeller size has been derived based on the aerodynamic performance of the propeller but also the weight of the propeller and the corresponding motor size.

It has been shown that the nominal wind speed of $v_{wind} = 11 m/s$, chosen for the design of ANDroMeDA, is relatively close to a hovering flight condition in terms of propeller performance and airframe drag. At higher wind speeds, the propeller thrust, at an equal power, drops significantly and the influence of the airframe drag coefficient on the flight time increases. The airframe drag coefficients of different configurations were identified and they are much lower than for conventional multirotors because ANDroMeDA has a slim design with a small frontal area. Exact numbers have been determined for the maximum weight of a useful smooth, aerodynamic cover to lower the drag of the airframe.

The eigenfrequencies and corresponding mode shapes of the CFRP tube used as measurement boom have been analyzed and tuned so that the nominal rotor frequency does not excite the measurement boom to oscillate.

The weight of ANDroMeDA predicted during the detailed design could be met during fabrication. One of the most time consuming procedures during the fabrication of ANDroMeDA-1 was the wiring of the entire propulsion and control system. Improvements for the future design have been proposed.

9.1.2 General Conclusions

Several simulations with different levels of fidelity have been performed to characterize the inflow region and wake of axial propellers and inclined rotors. The following observations could be made:

- The inflow region of a rotor/propeller is small compared to its wake and extends only a couple of diameters up-stream.
- The wake decay rate of a rotor/propeller is in general difficult to predict with simulations. However, the wake decay of an inclined rotor, relevant for multirotor operations, is a much more stable process than the wake decay of an axial propeller because the cross flow from the environment introduces additional energy to the wake and increases the dissipation.
- The wake direction of an inclined rotor is easy to predict because the wake will realign with the free stream direction in less than a few rotor diameters.
- The inflow region of an inclined rotor is always of similar form, which is comparable to a dipole singularity in potential flow theory, and its size depends only on the inflow velocity, angle of attack and the induced velocity.

- Simulations and wind tunnel experiments showed that it is possible to measure atmospheric wind speeds in close proximity to a propulsion system if a proper distance is kept and the inflow speed is higher than approximately 4 m/s.
- The results are perfectly scalable with the disc loading of the rotor. This, in consequence, means that recommendations about the probe placement can be made for an arbitrary rotor size if they are normalized with the rotor diameter.
- The best location for a flow measurement probe is directly in the rotor plane and at least several rotor diameters up-stream. The disturbances are larger above or below the rotor disc plane. Regarding the distance of several aircraft during a multi-aircraft measurement the aircraft should be staggered by at least four rotor diameters or a distance of at least 50 rotor diameters has to be kept for two successive aircraft.
- Two-dimensional actuator disc simulations have been found to be sufficient for parametric studies but tend to underestimate the wake displacement. Three-dimensional actuator disc simulations can predict inflow region and wake displacement / wake redirection.

If an inclined rotor in forward flight has to be scaled for constant aerodynamic coefficients, no upper limit of the diameter exists. But other than for a hovering helicopter rotor, an upper size limit exists in terms of induced power because the induced power will converge towards a fixed value, similar to the propulsive power for an axial propeller in forward flight.

CFD simulations with automatic meshing and actuator discs are a valuable tool for the preliminary design of a multirotor aircraft. Different than simulations with rotating rotors each case can be simulated in a few hours, which enables extensive parameter studies. For conventional multirotor airframes, the biggest sources of drag are the circular motor arms. An analytical approach has been proposed to estimate the airframe drag from effective motor arm lengths if a baseline configuration has been already investigated. For the simulated cases, this analytical model showed a good agreement. If the drag of a multirotor airframe has to be quantified, it is important to adjust a proper thrust level. A significant influence between rotor thrust and frame drag has been observed, which means they have to be considered in one combined simulation.

A universal procedure has been proposed to predict the aerodynamic performance of an inclined multirotor propeller in forward flight with the help of blade element simulations and static measurements without the need for a wind tunnel. This procedure showed a good agreement with wind tunnel validation measurements.

A detailed dimensional analysis has been presented to make a statement on the response times of multirotor propulsion systems at different motor sizes and propeller diameters. Because the moment of inertia of a two-bladed propeller depends on its azimuth angle, a three-bladed propeller is necessary for a tilting propeller aircraft, if the loads on the tilt actuators and bearings shall be kept low.

9.1.3 Component Tests

A large variety of commercially available propellers for multirotor operation has been tested on a whirl tower. It could be observed that the performance of all propellers is similar. If, however, a propeller reaches its maximum efficiency at a different thrust level than the design thrust level, differences of 20 %, compared to a well suited propeller, can occur due to the improper propeller choice. Wooden propellers have demonstrated a slightly worse performance in general. It is concluded that this results from the thicker airfoils that have to be used to meet the static requirements of the propeller blades.

During component tests it could be shown that all tested electronic speed controllers (ESCs) work after the same principle and hence the response time and flight performance does not change with different models.

9.1.4 Flow Measurement Probe Development

A combined Prandtl- triple hot wire probe has been developed in cooperation with SVMTec GmbH during this work. Because the particular hot wire probes are purchased pre-calibrated from SVMTec and a special topology has been chosen for the measurement boom it is possible to replace a single hot wire probe on the field, during a measurement campaign, without the need to recalibrate the entire measurement boom.

The probe worked well during preliminary tests in a wind tunnel. The accuracy can be improved, however, by an individual calibration of each particular measurement boom.

9.2 Outlook

Because this project, or to be more specific, the entire development of ANDroMeDA is a multi-disciplinary effort on many topics, it has to be decided which areas should be the subject of further improvements.

9.2.1 Detailed Improvements of the Measurement Aircraft

To further improve the series production and operation of ANDroMeDA component tests regarding a suitable "4-in-1" motor controller (ESC) are highly recommended. As described in Section A.4, if a "4-in-1" ESC is used, the wiring effort can be reduced. If, in addition, the autopilot is able to read telemetry data from this ESC, it can send warnings to the ground control station, which is an important enhancement of operational safety.

Another way to increase the operational safety is the use of a "fuel gauge" chip. While this is standard for most products with lithium polymer batteries, from cellphones to e-bikes, it is not yet common in custom built UAVs.

The custom flow measurement probe, developed in this project, also has potential for further improvements. As described in Section 6.3.4, the measurement range is currently shifted by $\Delta\alpha = 10^\circ$ which can be corrected for by a redesign of the hot wire adapter. In addition, with an alternative wire orientation, advanced data reduction models could be solved analytically instead of solving them numerically during the post-processing step. It is however recommended that this effort is only taken if a higher accuracy combined with the typical high frequency measurements of hot wire probes is needed for a specific measurement campaign. Furthermore, it has to be considered that calibration and life time of hot wire probes are limited.

Depending on the mission requirements of future projects, different measurement equipment can also be tested with ANDroMeDA. The modular concept with a detachable measurement boom makes such experiments easy. However, the acceptable center of gravity range and hence acceptable probe weight has to be kept in mind.

9.2.2 Flight Tests

Tilt angles higher than $\sigma_0 = 30^\circ$ have not been tested yet. This has to be done in the future to enlarge the flight envelope of ANDroMeDA.

9.2.3 Advanced Simulations

While several simulations in different disciplines have been already conducted, there is still a lot of potential for further improvements using a higher fidelity in these simulations.

Regarding the vibration isolation of the measurement equipment, an additional simulation with a tuned mass damper offers the prospect of damping the second eigenmode of the measurement boom, should it become a problem during measurement flights.

The highest potential for improvement in the flight mechanical simulation is clearly the implementation of aerodynamic moments. All necessary CFD simulations of the airframe to obtain the needed matrix have already been conducted but the matrix has not been implemented in the Simulink model. Because of the long measurement boom ANDroMeDA is different than conventional multirotor configurations where, due to the symmetric geometry, the aerodynamic moments only play a minor role. It is highly recommended for future investigations to implement a moment matrix.

If necessary the response time of the ANDroMeDA propulsion system with fixed pitch propellers can be characterized in more detail by a hardware in the loop (HIL) test with an emulated flight controller as described in Section 5.5. Such a test can show the interaction of the flight controller, respectively a control loop, and the propulsion system.

Until now, a complete aerodynamic simulation has only been performed for the H-4 airframe and not for the finally used H-8 airframe. Additional simulations with eight actuator discs, and ideally also swirl in the rotor wakes, can help to gain further knowledge about the flow field around ANDroMeDA, the airframe drag and also the inflow field in front of the combined eight rotors. To make the simulations more realistic, a trim point has to be determined iteratively by adjusting the tilt angle and rotor thrust.

The coaxial rotor setup in forward flight itself is also subject of further studies. The propeller aerodynamics can be studied at many levels of detail: BEM simulations, CFD with actuator discs, CFD with rotating propellers, more advanced wind tunnel measurements, etc. If the actual setup is sufficient in terms of flight time and vibrations, and if the focus of future research is on the measurements and measurement probe development, then advanced simulations may not be necessary.

9.2.4 Measuring Wind Turbine Tip Vortices

One very interesting but also challenging mission for ANDroMeDA is the exploration of wind turbine tip vortices. What makes this mission so interesting is the fact that there are not many measurements of full scale turbine vortices available and that in a group of aircraft the wake of a turbine could be "scanned" for the vortices. For example, with four ANDroMeDA aircraft, two aircraft could be moved vertically and two could be moved horizontally building a circle with increasing diameter. Because of the numerical dissipation it is difficult to predict the turbine wake with CFD simulations. However, detailed knowledge about turbine wakes is important for wind park operation in general and flight safety of manned aircraft in the proximity of wind parks.

Nevertheless, the quickly changing high velocities in a vortex make it difficult to maintain a steady hover. As found by Watkins et al. ([24]) the strongest impact on a UAV by a vortex is expected to be on the roll axis. The roll axis of ANDroMeDA is influenced mainly by two parameters: The rotor distance in the span wise direction and the response time of the rotors. Because ANDroMeDA uses eight smaller propellers the response time is faster, compared to a quadrotor configuration (compare Section A.2.2). The span wise rotor distance has not been optimized for the highest roll control authority, because in the preliminary design phase it was not

decided yet, if eight or four propellers should be used. Consequently, the span wise rotor distance was chosen in a way that larger propellers can also be mounted (compare Section 5.14). However, due to the long, slender design of ANDroMeDA, the roll performance is expected to be superior to conventional multirotor configurations. In addition, the span wise rotor distance could still be fine-tuned to some extent, without much mechanical effort, by the use of shorter or longer motor arms. Of course, the roll axis PID values of the flight controller have to be re-adjusted after the change.

As suggested in [21], atmospheric turbulence can be simulated in a wind tunnel experiment by the use of turbulence panels. Before using ANDroMeDA in a full scale experiment, another flight in the gust wind tunnel could therefore be beneficial to gain some data on the real flight performance when flying in a vortex.

9.2.5 Multi Aircraft Measurements

First multi aircraft measurements will be made in a simple form with fixed GPS positions for each aircraft and manual take-off and landing for each aircraft. Thus, collision avoidance lies within the responsibility of pilots. However, also the multi-vehicle control feature of QGroundControl will be tested and modified, if necessary.

Another responsibility of the ground control station, not having been considered so far, is the coordination of all aircraft during a measurement mission. In the simplest form, they just have to hover on a straight line and during the measurement they will realign with the wind vector. If a new formation is needed during the mission, the software complexity will increase.

As described in Section 5.7 the shape and direction of the rotor wakes can be determined reliably and most possibly a real-time prediction using a simplified simulation or a look-up table can be done. Together with live-data from every aircraft in the group, e.g. in form of the current tilt angle and current inflow vector, a "smart ground control station" could be realized which is able to predict the wake of each aircraft and automatically stagger the aircraft close to each other without wake-disturbed measurements.

A Selection and Evaluation of Aircraft Components

A.1 Propeller Tests and Simulations

While there is a large number of propellers available on the market, suitable for multirotor operation (available in clockwise and counterclockwise direction of rotation), usually no performance data is available for those propellers. The propeller manufacturer APC is the only manufacturer, who offers detailed data on their propellers ([49]). However, this data was created by numerical simulations using a blade element momentum theory (BEM). APC claims to apply a batch calculation system to update data files, whenever improvements are implemented in their simulation code ([49]). All other manufacturers do not supply performance data of any kind. Some measurements are available in [73] but unfortunately not for the propeller size needed for ANDroMeDA.

Besides own propeller measurements, a BEM based simulation software called "RotoCalc" was used to obtain knowledge about additional operating points. RotoCalc was developed earlier and could be improved during the ANWIND project. The objective of using measurements and simulations at the same time, was on one hand, a validation of the simulation software with measurements, which hasn't been done before at forward flight conditions, and on the other hand the following question should be answered: "Is it possible to evaluate the performance of a propeller at forward flight conditions, without wind tunnel testing, if static case measurements and simulations are combined?".

Figure A.1 shows the proposed procedure of propeller performance evaluation by a combined use of measurements and simulations.

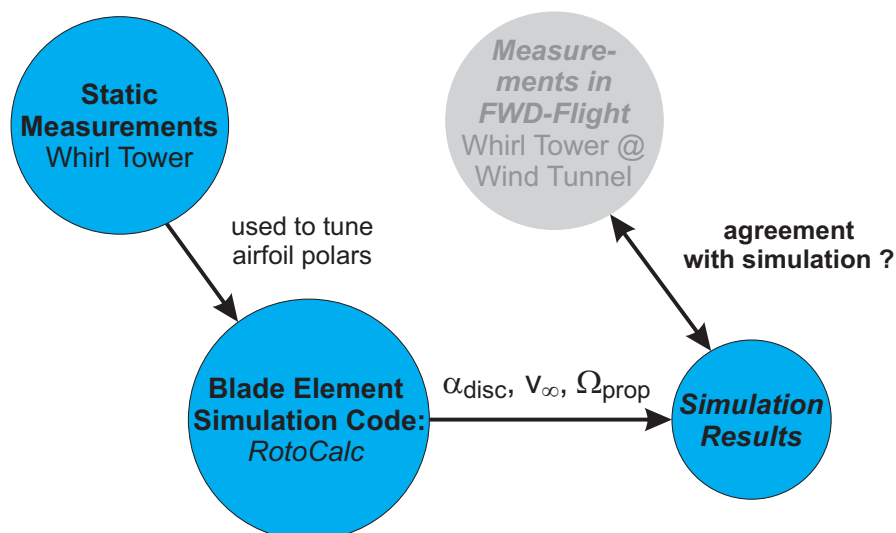


Figure A.1: Workflow to evaluate the propeller performance in forward flight.

A.1.1 Test Rigs

Consequently, it is crucial to build a test rig that is able to measure the propeller performance. Not only is the propeller performance an important factor for the flight performance of ANDroMeDA, but it is impossible to select a certain propeller without the ability to compare its performance to other propellers. In addition, the test rig can be used to characterize motor and ESC performance, for which the availability of measurements is also very limited.

Whirl Tower

The propeller test rig was designed as a whirl tower. The long cylindrical case of a whirl tower offers enough space for all the necessary measurement equipment without disturbing the propeller flow and the height of the whirl tower helps keeping a reasonable distance from the floor to avoid the ground effect. The following quantities can be measured by the whirl tower:

- Propeller thrust
- Propeller torque
- Propeller RPM
- Motor voltage
- Motor current
- ESC input signal

At the low cost whirl tower three "Arduino Pro Mini" MCUs are used to perform various tasks. One of the MCUs is the "Communication Master", receiving commands from a windows computer, collecting data from the other MCUs and sending it to the windows computer at a rate of $f_{data} = 50 \text{ Hz}$. The second MCU is controlling the motor ESC and the third one measures the RPM using the induced voltage at one phase of the motor. The three MCUs are connected via an I2C bus. The battery voltage is measured with a simple voltage divider circuit, while the motor current is measured with a hall sensor of type ACS758LCB-100U-PFF-T. Since the ADC of the Atmega 328p microcontroller, used in the Arduino Pro Mini, has a resolution of only 10 Bits an external ADS1115 ADC with a resolution of 16 Bits is connected to the I2C bus to read voltage and current signals. A detailed description of the whirl tower electronics can be found in [74]

Thrust and torque measurements are performed with low-cost load cells ([75]) and load cell amplifiers ([76]). Because components are mass produced and widely used for kitchen or letter scales, the accuracy is sufficient despite the low price. Figure A.2 illustrates the mechanical arrangement. To minimize the influence of torque, rolling and pitching moments on the thrust measurement, a 20 kg thrust load cell was used. In preliminary tests it could be confirmed, that the used load cells are insensitive to forces and moments outside the primary load direction. With the 20 kg load cell no influence of other forces and moments could be measured and in addition it also allows the use of larger propellers. For the torque measurement a 5 kg load cell was used, which limits the maximum torque measurement range to $M_{max} = 1.3 \text{ Nm}$. To keep aerodynamic loads from the load cells, a clear plastic cover is mounted around the whirl tower.

A proper calibration is crucial for precise measurements and consequently a calibration rig was designed, that can be mounted on the whirl tower to apply the thrust and torque loads with calibration weights. Figure A.3 shows the calibration rig and the base of the whirl tower, which enables the entire tower to be tilted forward for wind tunnel measurements. The friction of the

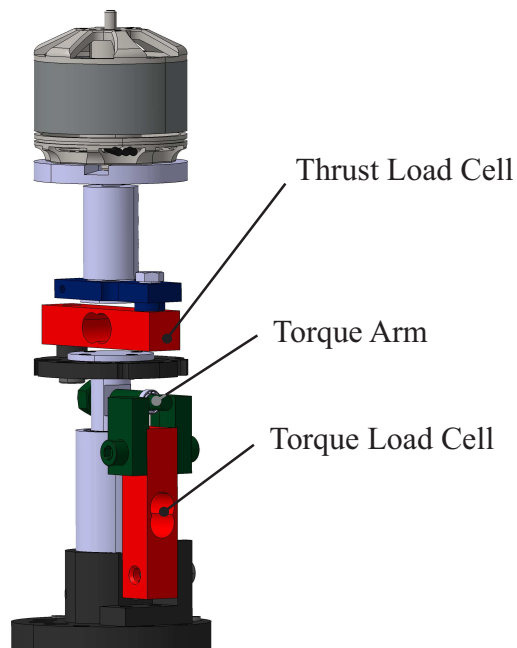


Figure A.2: Load cell arrangement inside the whirl tower.

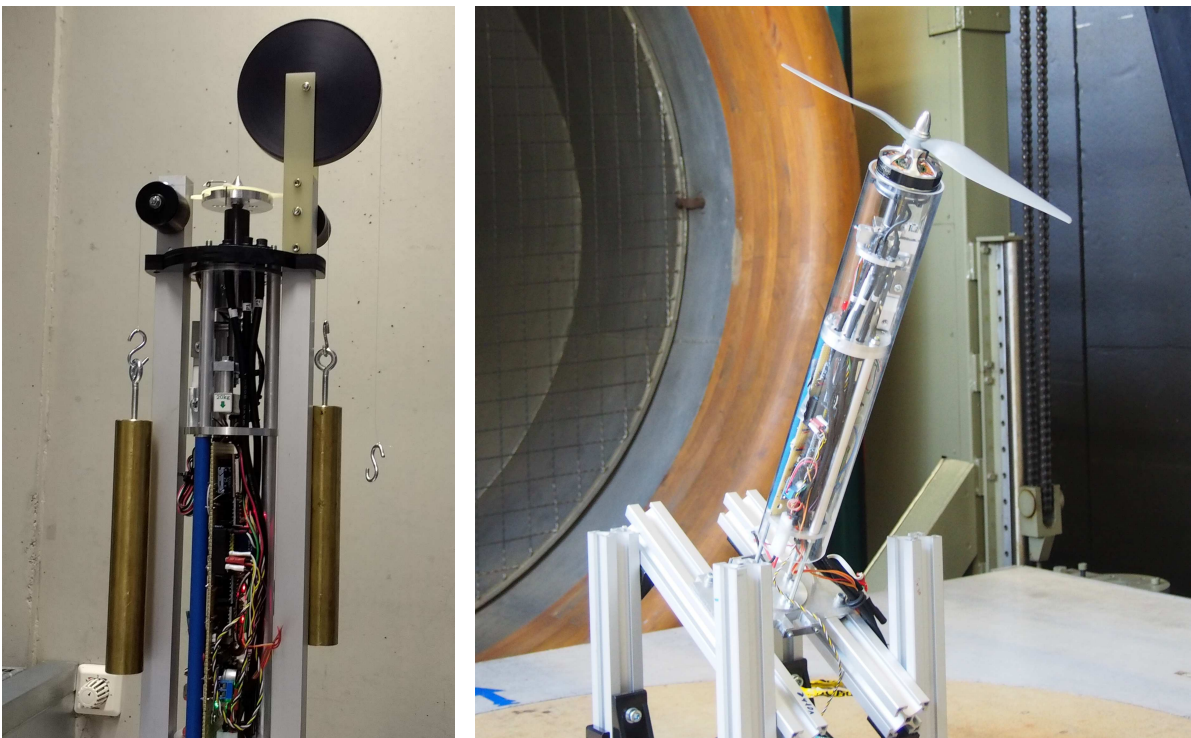


Figure A.3: Left: calibration rig with a pair of torque calibration weights applied. Right: Whirl tower tilted forward in the wind tunnel.

pulleys, at loaded condition, was identified to be lower than the torque, caused by a change of the calibration weight of $\Delta m_{calibration} = 3 \text{ g}$. During calibration the maximum relative error in thrust

was 0.6 % and the maximum relative error in torque was 1.6 %. For most cases, these errors were much smaller.

RPM changes during the measurement can be caused by a measurement error or can be actual fluctuations caused by motor and ESC. Therefore, a comparison with a strobe lamp was carried out and a maximal deviation of ± 10 RPM, compared to the internal whirl tower measurement, was determined.

The whirl tower is connected to a windows computer via bluetooth, which ensures a galvanic isolation. A special software was written with the Qt toolkit (Figure A.4) to control the whirl tower, display measurement data in real-time and save the measurements to a file. Furthermore, the stored files can be reviewed with the possibility to select several time intervals to calculate the mean values and standard deviations of the measured quantities.

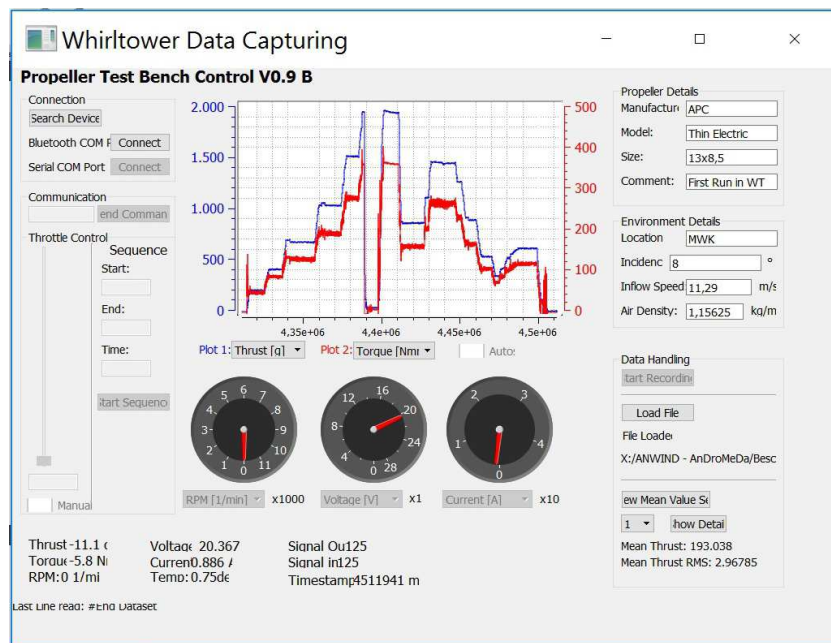


Figure A.4: Whirl tower control software.

Coaxial Propeller Test Rig

After it was decided, that a coaxial rotor configuration will be used for ANDroMeDA (compare Section 5.13), a special test rig was designed to investigate the behaviour of two propellers operating in a coaxial setup. For a complete comprehension of the underlying effects and a comparison with a corresponding simulation, it would be necessary to gather the same data as on the whirl tower (thrust, torque and RPM) for both propellers simultaneously.

Because in the given budget and time frame this was not possible, only the thrust of top and bottom propeller was measured independently, as shown in Figure A.5. The entire motor arm of

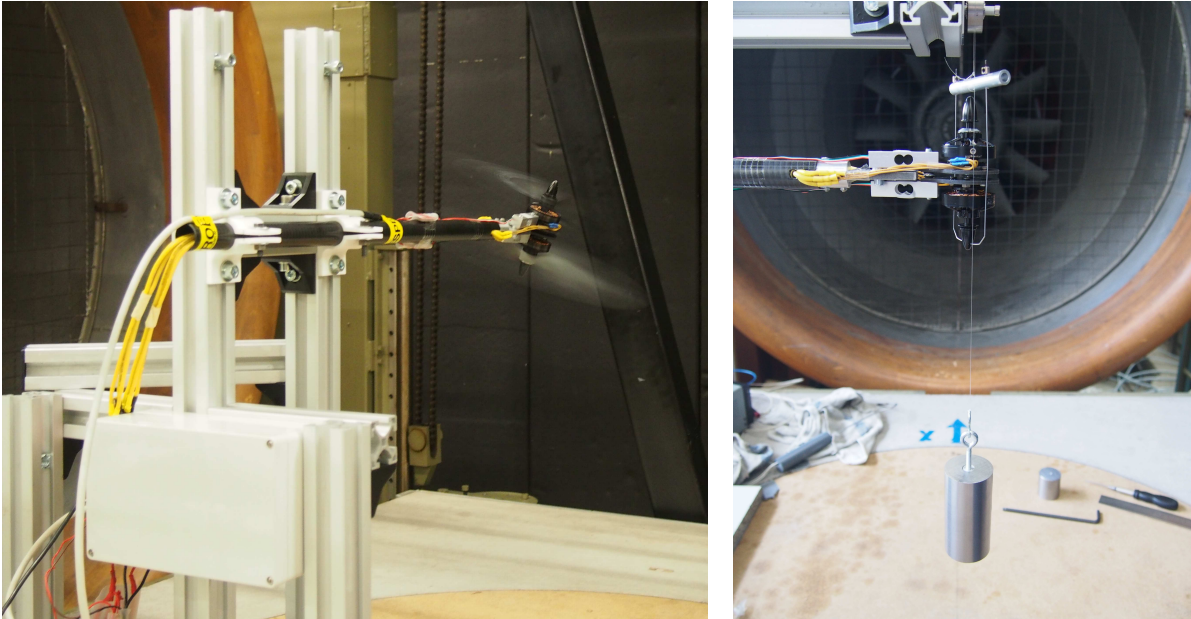


Figure A.5: Coaxial test rig with two thrust load cells.

the coaxial propeller test stand is mounted with an adjustable tilt angle at a vertical frame. The thrust measurement is realized with two low cost 20 kg load cells and the same HX711 load cell amplifiers as used for the whirl tower. The Qt Software to control the whirl tower (Figure A.4) was extended to two motors for the coax test stand control. More detailed information on the electronics of the coaxial test test stand is given in [78].

A.1.2 Simulations

Simulation Software RotoCalc

Several propeller simulation tools are available as open source license, or free to use, which are able to compute thrust and power of a propeller in axial flight or a helicopter rotor in hover. These tools are QProp ([79]) and XRotor ([80]), both developed by MIT professor Mark Drela, JavaProp from Martin Hepperle ([81]) and JBlade from the university of Beira in portugal ([82]). All those software tools are based on the blade element momentum theory (short BEM or BEMT) and for all those tools only one loop over the blade radius was implemented, because they are meant to solve only rotationally symmetric problems (axial inflow).

Even if the basic principles are the same (BET or BEMT), it is not possible to simulate an inclined rotor, because another loop over the rotor azimuth and the corresponding coordinate

system needs to be implemented. For the development of manned helicopters, either in-house tools are used or commercial tools with extensive capabilities. One of the most common commercial tools is CAMRAD ([83]). Those commercial codes are too expensive for UAV research at universities and the advanced features, including flexible rotorblades and complex rotor systems, are usually not needed for UAV development, because small scale rotors and propellers are very stiff compared to manned rotary wing aircraft rotors.

Because of this gap in the availability of simulation software, the blade element code RotoCalc was developed during past projects and improved for the development of ANDroMeDA. The code can simulate a rotor at arbitrary inflow angles and is capable of computing the flapping motion of a rigid rotor blade, which is attached to the hub with a flapping hinge at a flap hinge offset.

Because the ANDroMeDA propellers are modeled rigidly without any flapping motion, the numerical schemes to solve the flapping equation of motion are not described any further here. Much of the theory can be found in [84]. With the solution of the flapping motion in RotoCalc switched off, blade flapping can be prescribed by the following equation:

$$\beta(\psi) = \beta_0 + \beta_{1S} \cdot \sin(\psi) + \beta_{1C} \cdot \cos(\psi) \quad (\text{A.1.1})$$

For a rigid propeller without flapping and without coning angle this simply means: $\beta_0 = \beta_{1C} = \beta_{1S} = 0$. In the same manner, the blade pitch is prescribed by:

$$\theta(\psi) = \theta_0 + \theta_{1S} \cdot \sin(\psi) + \theta_{1C} \cdot \cos(\psi) \quad (\text{A.1.2})$$

For the rigid propeller again the coefficients are $\theta_{1C} = \theta_{1S} = 0$. The coefficient θ_0 can be used to adjust the fixed part of blade pitch to match a given propeller.

While the rest of the blade element approach is straight forward and described in several sources ([84], [85], [86]) special attention has to be paid to induced velocity modeling. For the classical blade element momentum scheme (BEM) the thrust received from two dimensional airfoil theory $dT_{Airfoil}$ is equated to the thrust computed from momentum theory $dT_{Momentum}$. To be able to compare the two quantities, the rotor disc is divided into annuli of width dr , which in turn form small circular stream tubes.

This procedure is not entirely correct, regarding the involved fluid mechanics (see [87]), but has proven to achieve acceptable results from a practical point of view and is hence widely used for hovering rotors or propellers in axial flight.

For an inclined rotor in forward flight this procedure is not directly applicable, because the exact shape of the stream tube is not known. As described in Section 5.7 the earliest approach to determine the induced velocity of an inclined rotor was proposed by Glauert (Eq. (5.7.2)). Eq. (5.7.2) was implemented in RotoCalc to gain a constant induced velocity over the entire rotor disc, which represents the simplest simulation method and is illustrated in Figure A.7.

If Eq. (5.7.2) is written in infinitesimal form, which according to [88] is "applicable", it results in:

$$dT_{Momentum} = 2 \cdot \rho \cdot dA(r, \psi) \cdot v_{res}(r, \psi) \cdot v_i(r, \psi) \quad (\text{A.1.3})$$

To use this equation, the resulting velocity component v_{res} has to be known as a function of rotor radius position r and rotor azimuth position ψ which can be done by vector addition of induced velocity and inflow velocity:

$$v_{res}(r, \psi) = \sqrt{(\sin(\alpha_{disc}) \cdot v_\infty + v_i(r, \psi))^2 + (\cos(\alpha_{disc}) \cdot v_\infty)^2} \quad (\text{A.1.4})$$

The local area $dA(r, \psi)$ for each position on the rotor disc calculates to:

$$dA(r, \psi) = r \, d\psi \, dr \quad (\text{A.1.5})$$

Using these relations, the combined momentum blade element theory (BEM) can be applied for a an inclined rotor in forward flight as illustrated in Figure A.8.

Recently in the field of multicopter aircraft another method was proposed by Gill ([89]). Gill proposes to calculate the induced velocity only as a function of the rotor radius ($v_i = v_i(r)$) and he derives a function for that approach from a stream tube model. However, a closer look at the equations shows, that the result is totally equivalent to the equation derived from Glauert's approach (Eq. (5.7.2)) with the area of an annulus of $dA(r) = 2\pi r dr$, instead of the total disc area.

Because Glauert's approach is usually considered empirical, the stream tube model derived in [89] is considered with a certain amount of scientific skepticism. Also the induced velocity gained from a CFD simulation of a rotating three-bladed rotor, presented in Section 5.7, shows a strong dependency of v_i on the the rotor azimuth (see Figure A.6). From Figure A.6 it can be seen, that

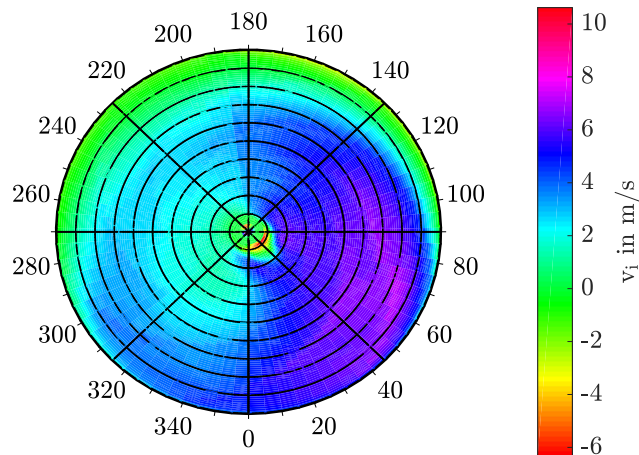


Figure A.6: Induced velocity at $\alpha_{disc} = 15^\circ$, $D.L. = 70 N/m^2$, $v_\infty = 10 m/s$ gained from a CFD simulation described in Section 5.7. The speed $\Delta v = v_\perp - v_{\infty,\perp}$ was averaged over one third of a rotor revolution (three bladed rotor).

the induced velocity on the right hand side of the rotor disc is significantly higher, because the advancing blades produce a higher lift due to the increased dynamic pressure.

However, the method proposed in [89] was implemented in RotoCalc, to compare it to the two other methods and to see its impact on rotor thrust and power from a practical point of view. The corresponding algorithm is illustrated in Figure A.9.

For all three simulation patterns a regula falsi scheme is used to gain the solution of Eq. (5.7.2) either for the complete rotor disc, in infinitesimal form or for a single annulus. This scheme is used because it is more robust than the newton method that was initially used in RotoCalc.

Another model implemented in RotoCalc is a prescribed induced velocity, proposed by Mangler and Squire in 1953 ([90]). Hereby the induced velocity field over the rotor disc is modeled using a Fourier series. This model is often quoted in literature but according to [90] it is only valid for high speed flight or low disc loadings were $v_\infty \gg v_i$.

One of the most important subroutines in the algorithms, described in Figure A.7 to Figure A.9, is "CalcForcesBE". Inside this subroutine the effective velocity components relative to a particular blade element (depending on ψ , r/R , θ , β and $\dot{\beta}$) are evaluated. With the effective angle of attack aerodynamic lift and drag forces can be computed, using two dimensional airfoil theory, and transformed into an in-plane and out-of-plane component. Additionally, the inertial force resulting from $\ddot{\beta}$ and centrifugal force is calculated. Hence, many different physical principles

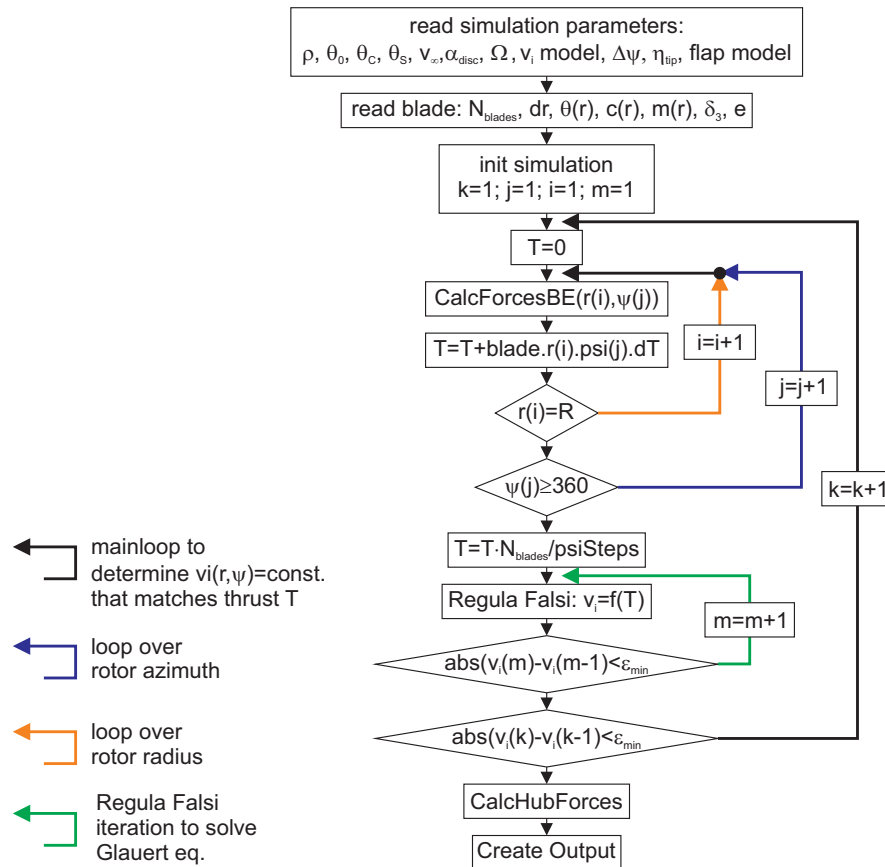


Figure A.7: Flow chart of RotoCalc forward flight setup with $v_i(r, \psi) = \text{const}$.

and coordinate transformations are included into this subroutine, which makes the validation of RotoCalc with wind tunnel experiments important.

For the application of two dimensional airfoil theory, every blade element software needs the capability of entering airfoil polars and assigning them to particular radius positions of the rotor blade. RotoCalc is quite flexible regarding this capability: The polars can be stored as tables of an arbitrary number of angles of attacks and arbitrary number of Reynolds number sets. Between angles of attack and between Reynolds numbers a linear interpolation is used. If an angle of attack or a Reynolds number exceeds the given range extrapolations are done with a warning in the output. For one rotor blade up to 10 different airfoils can be used.

A rotor blade can have an arbitrary number of key positions at which chord, twist, mass properties and airfoils are defined. In addition, the number of discretization steps to the next key position is entered and thus the number of key positions is not necessarily equal to the number of blade elements. If the airfoil is changed from one key position to the next key position lift and drag coefficient will be evaluated for both airfoils and the results will be interpolated linearly for all blade elements in between, which enables a smooth blend along the rotor radius.

Propeller Modeling

To compare measurements to simulations and to validate the general procedure, given in Figure A.1, two different two-bladed propellers were modeled in RotoCalc: The APC 13x6.5E and the Aeronaut CAM Carbon Light 13x6. The geometrical investigation was done manually without a

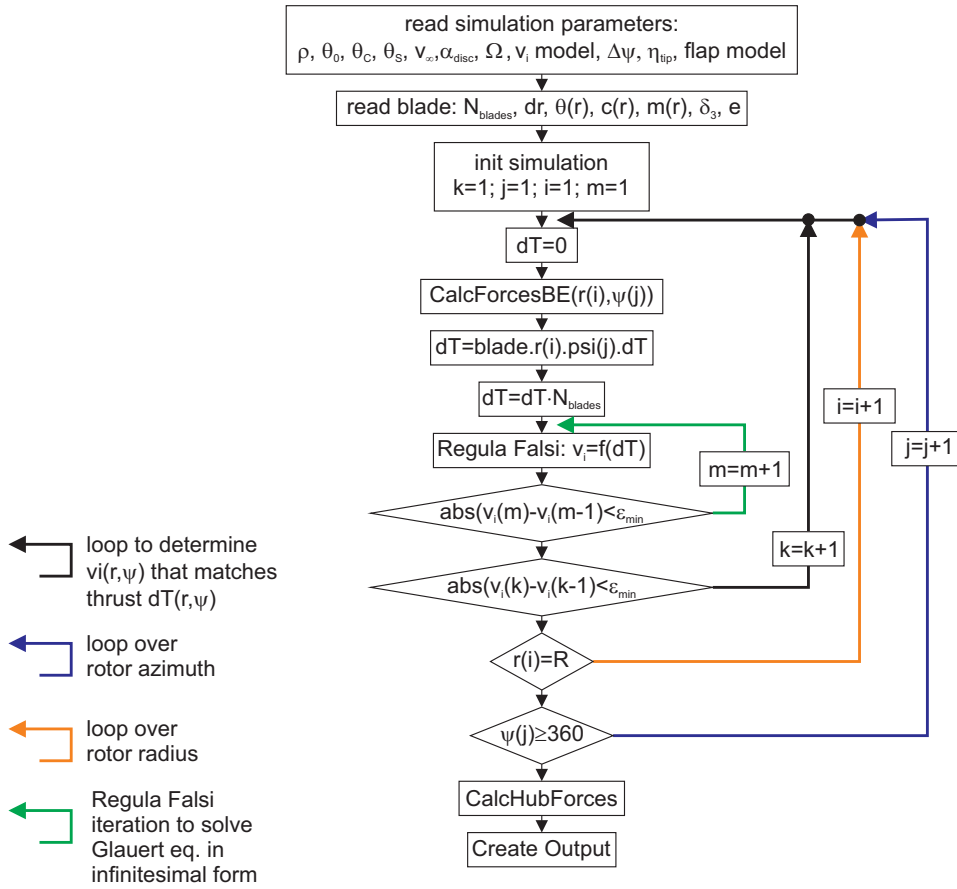


Figure A.8: Flow chart of RotoCalc forward flight setup with $v_i = v_i(r, \psi)$.

3D scanner or a comparable device. Therefore the chord c and airfoil thickness t was measured with a caliper at ten different radial positions ($r/R = 0.1, 0.2 \dots 1$). Furthermore the twist ($\theta(r/R)$) was determined at the same 10 radial positions using angle templates.

To choose a suitable airfoil to model the propeller aerodynamics, on one hand the relative thickness (t/c) was considered and additionally the propeller was cut at some positions to draw the contour line with a thin pen and scan it. Those scans could be used to choose a similar shaped airfoil.

For the APC propeller several NACA44XX airfoils with a thickness of 34 % at $r/R = 0.1$ and a thickness of 11 % at the blade tip have been used. For the Aeronaut propeller a NACA4416 airfoil was used for the root and a MA409 airfoil was used for the outer portions of the propeller. Table A.1 and Table A.2 give an overview of the estimated propeller geometries.

With the determined airfoils, the panel code XFOIL ([91]) was used to generate airfoil lift and drag polars between $\alpha = -30^\circ$ to $\alpha = +30^\circ$. The results were then simplified by the following equations:

$$c_l(\alpha) = cl0 + cla \cdot \alpha \quad (\text{A.1.6})$$

$$c_d(c_l) = cd0 + cd2(c_l - clcd0)^2 \quad (\text{A.1.7})$$

$$cd2 = cd2u \quad \text{if } c_l > clcd0 \quad (\text{A.1.8})$$

$$cd2 = cd2l \quad \text{if } c_l < clcd0 \quad (\text{A.1.9})$$

This method is also used for QProp and can be found in the QProp manual ([79]). When using

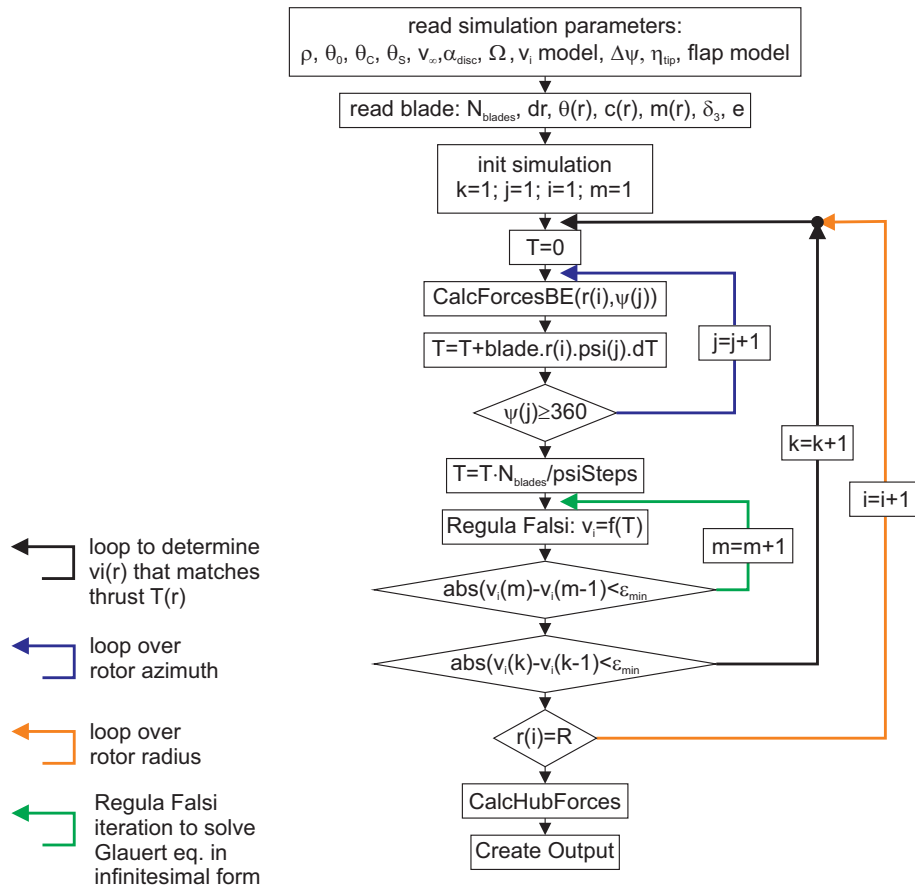


Figure A.9: Flow chart of RotoCalc forward flight setup with $v_i = v_i(r)$.

r/R	chord c	twist θ	rel. thickness t/c	airfoil
0.1	17.50 mm	35°	0.3428	NACA 0034
0.3	27.0 mm	28°	0.1777	NACA 4418
0.5	27.2 mm	16°	0.1349	NACA 4414
0.7	20.8 mm	12°	0.1158	NACA 4411
0.8	16.5 mm	11°	0.109	NACA 4411
0.9	12.8 mm	10°	0.1015	NACA 4411
1.0	9.0 mm	8°	0.1222	NACA 4411

Table A.1: Geometrical parameters for the APC 13x6.5E propeller model.

this simplifications, it is possible to describe an airfoil polar by only six coefficients: $cl_0, cla, cd_0, clcd_0, cd2u, cd2l$, which makes it easier to fine-tune the polars. Furthermore, they make it easy to model the same propeller in QProp, if the results shall be compared.

As described above, RotoCalc will extrapolate angles of attack that are not explicitly defined in the airfoil polar tables but this only makes sense for a small range. For a convenient simulation it is better to provide a full 360° polar without any extrapolations. Different models are used for that purpose in literature. For the current simulations the following equation was used, which is

r/R	chord c	twist θ	rel. thickness t/c	airfoil
0.1	23.90 mm	25°	0.1632	NACA 4416
0.2	31.50 mm	31°	0.0952	MA409
0.3	33.00 mm	25°	0.0909	MA409
0.4	33.30 mm	20°	0.0871	MA409
0.5	32.80 mm	16°	0.0869	MA409
0.6	30.70 mm	13°	0.0879	MA409
0.7	27.50 mm	12°	0.0891	MA409
0.8	23.60 mm	11°	0.0889	MA409
0.9	18.00 mm	9°	0.0944	MA409
1.0	7.00 mm	9°	0.1143	MA409

Table A.2: Geometrical parameters for the Aeronaut CAM Carbon Light 13x6 propeller model. also given in [79] and a plot of similar results can be found in [47]:

$$cl(\alpha) = \cos(\alpha - 45^\circ) \quad (\text{A.1.10})$$

$$cd(\alpha) = 2 \cdot \sin^2(\alpha) \quad (\text{A.1.11})$$

The result of this approach is shown in Figure A.10.

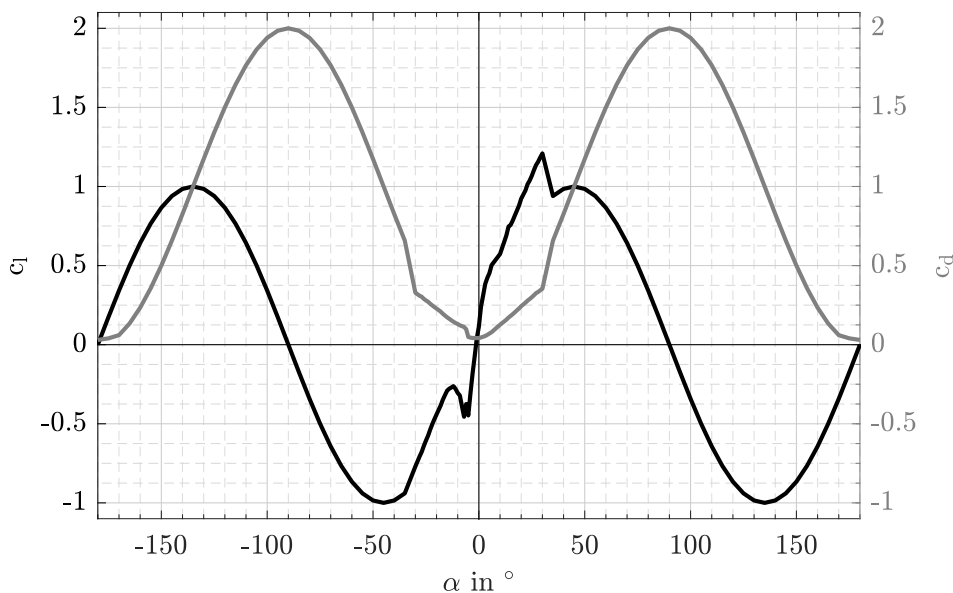


Figure A.10: Polar extension to 360° according to Eq. (A.1.10) for NACA 4418 at $Re = 60K$.

For both propellers a tip loss factor of $\eta_{tip} = 0.95$ was set, which simply means that RotoCalc does not take into account the last 5 % of the blade radius for the calculation of thrust.

The APC propeller was modeled with 96 blade elements and the Aeronaut propeller with 99 blade elements. For both simulations the rotor azimuth was discretized with 72 steps ($\Delta\psi = 5^\circ$). A higher number of blade elements or finer azimuth steps did not change the simulation results.

Fine Tuning of the Simulations

The initial simulations have been carried out without any further adjustments to measurement data. Those initial simulations not only suffer from uncertainties which airfoil is really used for the actual propeller and uncertainties in the geometrical dimensions, especially regarding the blade twist, but also the flow of a rotating propeller can be quite complex. It includes three-dimensional effects, like the effect of centrifugal force on the boundary layer, low Reynolds number separation bubbles as well as additional turbulence introduced to the boundary layer by the rotating propeller. Some observations and a comparison between BE simulations, three-dimensional CFD simulations and an experiment especially for low Re propellers can be found in [92].

Because of this circumstances, without measurement data the initial simulations can only be seen as a first guess, and as a consequence it is quite common for the development of manned helicopters to adjust BE simulations to whirl tower measurements by fine-tuning lift and drag polars.

By manually adjusting the lift and drag polars at three different Reynolds numbers, corresponding to propeller operation at $n = 2000 \text{ RPM}$, $n = 4500 \text{ RPM}$ and $n = 7000 \text{ RPM}$, a very good agreement between simulation and measurement could be achieved for the static propeller operation. It has to be emphasized, that all adjustments have been done only with static case measurements and none of the adjustments directly involved the wind tunnel propeller performance measurements.

A.1.3 Propeller Overview and Static Tests

Before the wind tunnel measurement campaign took place, a total of 20 propellers from seven manufacturers have been purchased and tested on the whirl tower at static operation. In general all propellers performed well and the differences are quite small, so that in most cases the different propeller weights have a larger impact on the flight time than the difference in aerodynamic performance. Regarding an optimal operating condition of a particular propeller, the highest figure of merit measured was $F.o.M. = 0.73$ and the lowest figure of merit was $F.o.M. = 0.64$. The differences at hover thrust ($T_{hover} = 6.13 \text{ N}$) can be larger, because for most of the propellers the optimal F.o.M is reached at higher thrust levels. Consequently, by a bad propeller choice the F.o.M. at hover can fall as low as $F.o.M. = 0.52$.

In general, the tested propellers can be divided into three groups: Wooden propellers, injection molded plastic propellers (often with fiber reinforcements) and CFRP propellers. A general tendency can be clearly seen for the wooden propellers. The best figure of merit measured for a wooden propeller is $F.o.M. = 0.69$ and hence, about 4 % lower than for the best plastic propellers. This issue can be addressed to the lower material strength of the wooden propellers, which makes it necessary to choose thicker airfoils with a lower lift to drag ratio. At $r/R = 0.7$ the Fiala three-bladed 13x6 wooden propeller has a relative airfoil thickness of $t/c = 0.14$ which is significantly thicker than for the APC and Aeronaut propeller described above (see Table A.1 and Table A.2). Consequently the use of wooden propellers cannot be recommended from a performance point of view.

The tested CFRP propeller from Tiger Motor could not outperform the best plastic propellers. Taking the lower weight into account, the use of CFRP propellers still results in a slight improvement of flight time. However, because of the higher price and the higher mechanical sensitivity during transport CFRP propellers have not been included in the selection of possible propeller choices for ANDroMeDA.



Figure A.11: Overview of some of the tested propellers.

Pre-Selection of Propellers for Wind Tunnel Tests and Static Case Simulations

From the static measurements the eight propellers with the best figure of merit at hover thrust have been selected for further measurements at forward flight conditions in the wind tunnel (Table A.3). After the wind tunnel measurements have been completed, the APC 13x6.5E and Aeronaut CAM Carbon Light 13x6 propeller have been identified as the best choice and were modeled in RotoCalc.

propeller	RPM at T_{hov}	Q_{hov}	FoM, hov	FoM, max	$T(FoM., max)$
APC 13x6.5E	4406 min^{-1}	110 Nmm	0.680	0.72	16.32 N
APC 13x8E	4154 min^{-1}	125 Nmm	0.633	0.675	> 18.7 N
APC 13x4.5MR	4681 min^{-1}	107 Nmm	0.658	0.715	> 17.08 N
APC 13x4E	5272 min^{-1}	102 Nmm	0.614	0.69	13.9 N
APC 13x5.5MR	4357 min^{-1}	115 Nmm	0.66	0.728	> 18.6 N
Aeronaut 13x5	4673 min^{-1}	105 Nmm	0.67	0.72	> 14.7 N
Aeronaut 14x6	3755 min^{-1}	121 Nmm	0.674	0.734	> 20.95 N
Aeronaut 13x6	4294 min^{-1}	116 Nmm	0.66	0.709	> 16.4 N

Table A.3: Overview of the eight propellers identified as best suited for ANDroMeDA from static measurements. If $T(FoM., max)$ is denoted with an ">" symbol the maximum F.o.M. could not be reached because of limited motor power.

Figure A.12 illustrates thrust and power at different rotational speeds. The simulations have been fine-tuned, as described above, to achieve a good agreement with static case measurements. Without tuning, the agreement is already quite good for the Aeronaut Propeller and agrees less for the APC propeller. After fine tuning a excellent agreement between simulations and static case measurements can be achieved.

Static Tests of the Coaxial Propeller Setup

Static tests of two APC 13x5.5MR propellers mounted on the coaxial test rig have been conducted, supported by RotoCalc simulations of the isolated rotors. First tests with the two isolated propellers were done to see how big the influence of the motor arm is and if both propellers are able to produce the same thrust. The isolated bottom propeller produces a thrust of $T_{bottom} = 1692 g$ and the isolated upper propeller produces a thrust of $T_{top} = 1750 g$, which indicates that if the propeller inflow is disturbed by the motor arm, it is slightly minimized.

If both propellers are operated together at full thrust, the top propeller is still able to create almost the same thrust and only drops to $T_{top} = 1699 g$. The bottom propeller however, is only able to create $T_{bottom} = 1209 g$, while its RPM does not change much and the motor current is reduced. This indicates, that the bottom propeller RPM is limited by the motor and, if it is operated in the downwash of the top propeller, it can be seen as an isolated axial propeller at forward speed $v_{\infty} = v_{downwash}$.

Consequently, the thrust of the bottom propeller drops about 30 % and hereby reduces the overall thrust by 15 %. The power of the bottom motor is only reduced by 10 %. This experience agrees well with the literature on that subject. In [93] coaxial rotors have been investigated with the help of momentum theory and vortex theory.

To keep the bottom motor fully loaded, a propeller with higher pitch has to be used. To estimate by which amount the bottom pitch has to be increased, RotoCalc simulations have been conducted with an isolated propeller at different axial inflow speeds. A reasonable agreement could be reached at an inflow speed of $v_{\infty} = 10 m/s$ with a thrust reduction of 36 % and a power reduction of 11 %. At this inflow speed a pitch change of $\Delta\beta_0 = 0.9^{\circ}$ is necessary, which corresponds to a change of $\Delta p = 0.45$ ". For most propellers the minimal available step is 2 ", so that it has to be evaluated first, if the motor can handle the higher pitch.

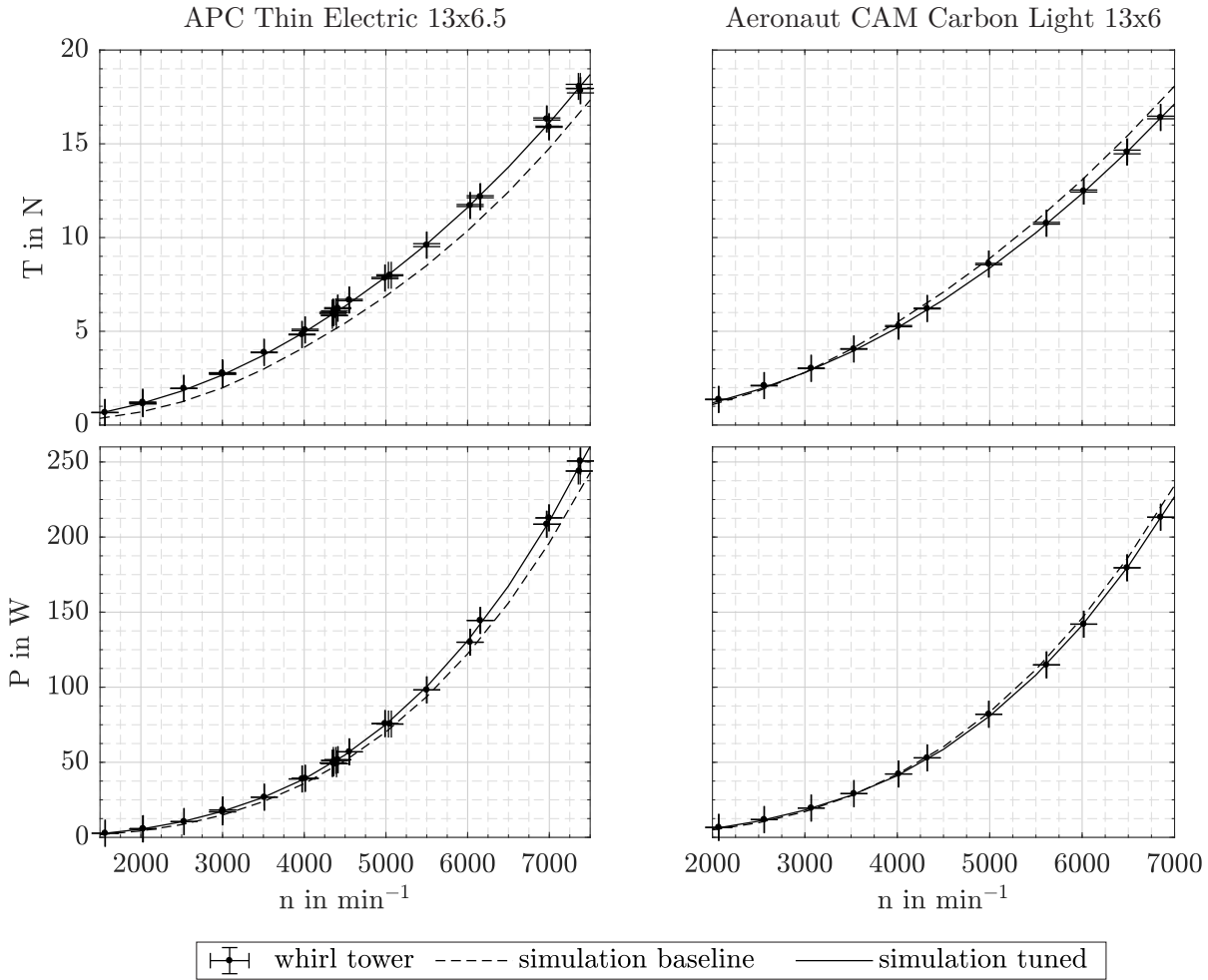


Figure A.12: Static thrust and power of the two simulated propellers at $\rho = 1.14 \text{ kg/m}^3$.

A.1.4 Wind Tunnel Tests of Propellers at Forward Flight Conditions

To evaluate the propeller performance at forward flight conditions, wind tunnel tests have been carried out at the settings listed in Table A.4. To be able to investigate different angles of attack, the whirl tower was tilted, as shown in Figure A.3, and the angle was determined with a precise electronic water scale of type Althen Pro 3600.

Single Propeller Configuration

It could be observed, that from a propeller point of view, the design point of ANDroMeDA is still very close to the static operation. Furthermore, as shown in Figure A.13, at the design operating

α_{disc} in $^\circ$	8	15	22.5	30
V_∞ in m/s	8; 11	8; 11; 15	12; 15; 20	17; 20; 30

Table A.4: Investigated operating conditions in the wind tunnel.

condition even a slightly higher thrust can be achieved with almost the same power, compared to a hovering flight without headwind. This can be explained by the induced power of a rotor in forward flight, as already derived in Eq. (5.8.19). If the mass flow through the rotor disc, given by $\dot{m} = \rho \cdot (\sin(\alpha_{disc}) \cdot v_\infty)$, is increased, the induced velocity will be lowered. This is illustrated in Figure A.14 by solving Eq. (5.7.2) for different operating conditions.

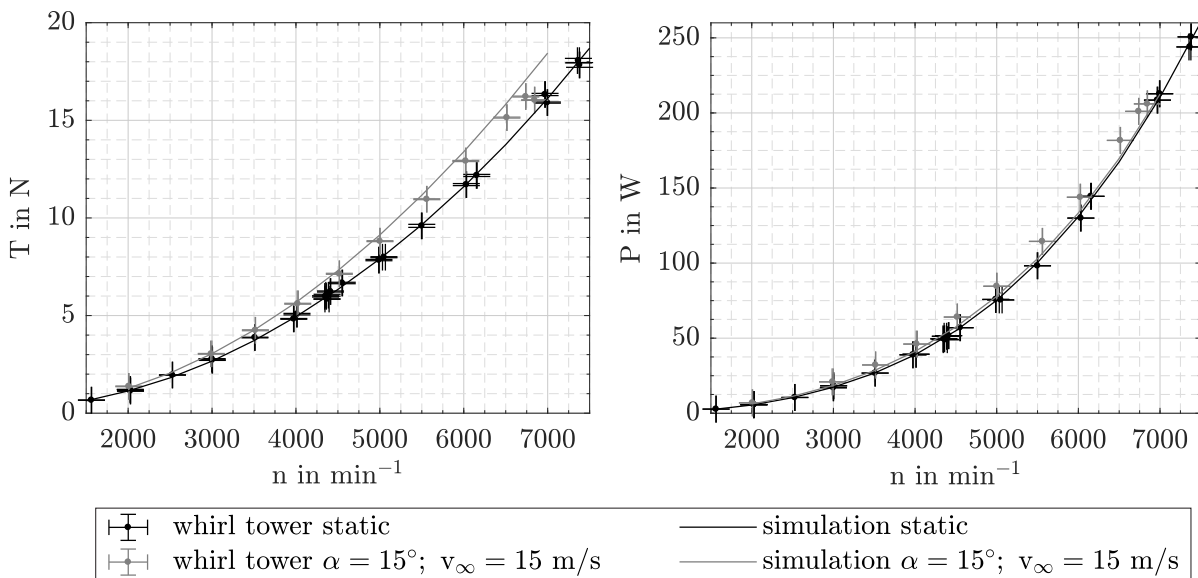


Figure A.13: Thrust and power of the APC thin electric propeller at static operation compared to forward flight at $\rho = 1.16 \text{ kg/m}^3$. Simulations have been done with $v_i = \text{const.}$

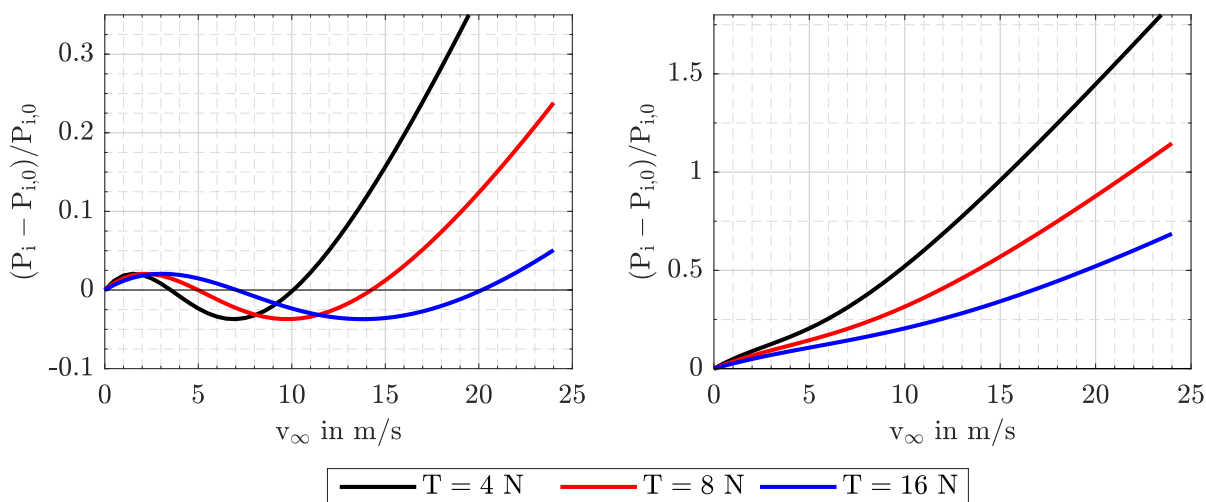


Figure A.14: Induced power P_i of an inclined rotor, calculated with Eq. (5.8.19) and Eq. (5.7.2), compared to the induced power of a hovering rotor $P_{i,0} = P_i(v_\infty = 0)$ at $\alpha_{disc} = 15^\circ$; $\rho = 1.16 \text{ kg/m}^3$ (left) and at $\alpha_{disc} = 30^\circ$; $\rho = 1.16 \text{ kg/m}^3$ (right).

Besides the question, how different propellers will perform at ANDroMeDa’s design point, it was also of interest, how well the propeller performance can be predicted with the help of RoToCalc simulations. Figure A.15 shows the thrust and power of the APC 13x6.5. Two different

operating conditions have been chosen for this example. At $\alpha_{disc} = 8^\circ$ and $v_\infty = 11 \text{ m/s}$ the agreement between simulation and measurement is worst, while at $\alpha_{disc} = 30^\circ$ and $v_\infty = 30 \text{ m/s}$ the agreement is very good.

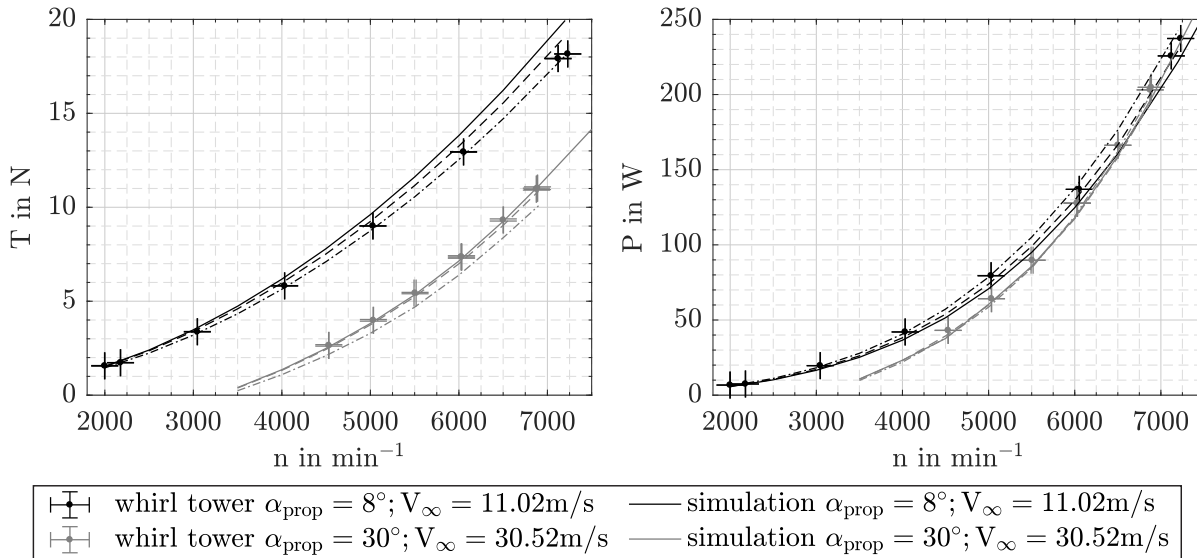


Figure A.15: Agreement between measurements and simulations at two different operating conditions at $\rho = 1.15 \text{ kg/m}^2$. Simulations plotted with a solid line assume a constant v_i . Simulations plotted with a dashed line use $v_i = f(r)$. Simulations plotted with a dash-dot line use $v_i = f(r, \psi)$.

In Figure A.15 the different models of induced velocity, included in the RotoCalc simulations, are also shown. At $\alpha_{disc} = 8^\circ$ and $v_\infty = 11 \text{ m/s}$ the best agreement with measurements can be reached by the use of $v_i = v_i(r, \psi)$, while the model of constant induced velocity over the rotor disc ($v_i = const.$) gives a maximum error of 6 % in thrust and a maximum error of 7 % in power, which is still acceptable for preliminary propeller investigations.

At $\alpha_{disc} = 30^\circ$ and $v_\infty = 30 \text{ m/s}$ the best agreement can be reached with the simple constant induced velocity model ($v_i = const.$). While the use of the complex model ($v_i = v_i(r, \psi)$) seems to over predict the influence of the induced velocity variation, the one-dimensional model ($v_i = v_i(r)$) appears to be a good compromise between the two operating conditions. Another option would be a blend between the simple model ($v_i = const.$) and the two dimensional model ($v_i = v_i(r, \psi)$), depending on the flow through the rotor disc (v_\perp).

For further investigations the use of the simple, constant induced velocity model is preferred to be sure, that no errors are introduced at higher speeds, while the error of 6 % at the design point of ANDroMeDA is still acceptable.

Coaxial Propeller Configuration

Unfortunately, the coaxial test rig suffered from strong vibrations, if operated with the wind tunnel running. In static tests this was not foreseeable, thus, it is assumed that the vibration is induced by varying loads from the advancing and retreating sides of the propellers. Consequently, only very few conclusive measurements could be taken.

The phenomena was investigated with a high speed camera and revealed several Eigenmodes of the test rig design, mostly related to the relatively soft mount of the motors to the load cells. It is

assumed, that for future tests this problem can be eliminated by the use of thicker motor mounts. Because for the actual design of ANDroMeDA the motor mounts are much stiffer no problems are expected. If, however, the coaxial rotor configuration will suffer from strong vibrations in forward flight, as previously mentioned, the rotor layout can be changed to a quadrotor design without changing the frame and tilt mechanisms.

The result of one of the measurements, not contaminated by strong vibrations, is shown in Table A.5. For a realistic operation, a thrust of $T_{top} = 1000 g$ at the top propeller is too high, if the bottom propeller is running at only $T_{bottom} = 650 g$, but this operating condition did not induce severe vibrations, like most of the other operating conditions. The same thrust settings were repeated later for the static operating case and the direct comparison indicates, that the aerodynamic performance of the overall configuration is much better at forward flight conditions, because the inflow of the bottom rotor is less disturbed by the top rotor. This assumption could be confirmed by a flow visualization shown in Figure A.16. However, the aerodynamics of a coaxial

	ESC Signal	Motor Current	RPM
Static Case	+9 %	+75 %	+25 %
$\alpha_{prop} = 15^\circ; V_\infty = 11.88m/s$	+4 %	+20 %	+6 %

Table A.5: Settings for a steady thrust of $T_{bottom} = 650 g$ with the top propeller running at $T_{top} = 1000 g$.

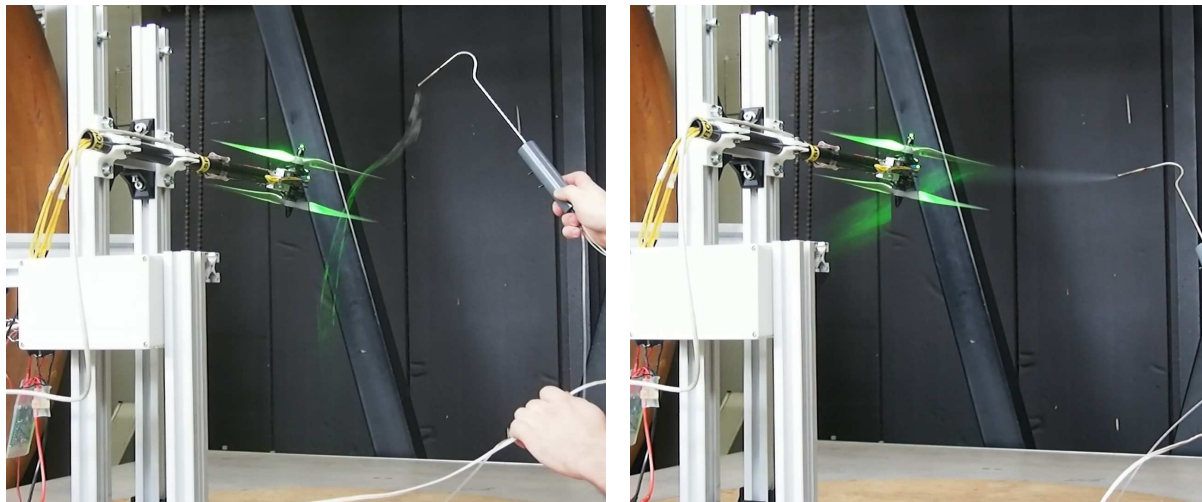


Figure A.16: Smoke visualization of the counter-rotating propeller arrangement at $T_{total} = 12.5N$. Left: Static operation with wind tunnel turned off. Right: $\alpha_{prop} = 15^\circ$ and $v_\infty = 11m/s$.

propeller setup is quite complex and has to be subject of further investigations in the future, if a detailed performance characterization is needed for the operation of ANDroMeDA. With an enforced test rig more operating conditions have to be measured. It appears, that the individual thrust and RPM measurement of top and bottom propeller, combined with the acquisition of the electrical power consumption for both rotors, can be a very useful tool to compare measurements and simulations.

For a full knowledge of the underlying process, it is recommended to combine measurements, CFD simulations with two rotating rotors and BEM simulations. With the combinations of these three methods, it is assumed that in the future a simpler model for the wake of the upper rotor can be derived, which makes it possible to compute thrust and power for both rotors with BEM alone. This would enable a fast performance assessment at forward flight conditions.

A.1.5 Conclusions

During intensive tests and simulations the following conclusions could be drawn regarding the propeller performance for the ANDroMeDA aircraft:

- The investigated propellers have a very similar performance. The F.o.M. varies no more than 5 %, so that often the propeller weight has a higher influence on the flight time than its aerodynamic performance.
- Wooden propellers showed a slightly worse performance which is addressed to the fact that they need a thicker airfoil for static reasons.
- However a wrong propeller choice, which means a propeller that is not well suited for the design point, can cost as much as 20 % in terms of F.o.M.
- The procedure pictured in Figure A.1 proved to result in a good characterization of propeller performance. Consequently, for future changes in the ANDroMeDA configuration it is not necessary to conduct any wind tunnel tests. It is sufficient to take static measurements of a propeller, model it in RotoCalc, tune the simulations to static measurements and simulate its performance at forward flight conditions. The resulting error is expected to be below 10 % while the largest error is expected at low forward speeds where the induced velocity is of the same magnitude as the flow through the rotor disc.
- Several inflow models have been investigated for BEM simulations and have been implemented in the software RotoCalc. The simple constant induced velocity model is expected to be sufficient for most cases and well suited for higher speeds where $v_i \ll v_\infty$.
- The design point of ANDroMeDA, at an inflow speed of $v_\infty = 11 \text{ m/s}$ and an angle of attack between $\alpha_{disc} = 8^\circ$ and $\alpha_{disc} = 15^\circ$, proved to be very close to the static operation of the propeller and for the same thrust the power consumption can be even lower than it is at static operation.
- The aerodynamics of a coaxial rotor setup is quite complex and needs further investigations for a reasonable performance prediction. It could be shown however, that the forward flight condition should be no worse than the static operation, which will be taken as a first approximation for ANDroMeDA.
- The propellers finally chosen for ANDroMeDA are Fiala wooden three bladed propellers of size 14x6 for the top propeller and 14x8 for the bottom propeller. Because of the dynamics of the tilt-rotor concept, only three bladed propellers are acceptable (see Section A.5) and these are the only three bladed propellers with a diameter of 14 inch, available in clockwise and counter-clockwise direction of rotation, at the present time.
- From the tests in this chapter it is known, that an improvement of 5 % to 10 % with well designed plastic propellers, using a thinner airfoil, is possible for ANDroMeDA.

A.2 Modeling Motor/Propeller Dynamics

A.2.1 General Approach

The response time of different motor / ESC / propeller combinations is physically limited by the maximum motor torque and propeller inertia. Applying the conservation of momentum gives:

$$\dot{\Omega} = \frac{M}{I_{prop}} \quad (\text{A.2.1})$$

Where M is the overall torque on the propeller and I_{prop} is the propeller's moment of inertia. For a three bladed wooden Fiala propeller with a diameter of $D_{prop} = 13$ " and a pitch of $p = 8$ " the moment of inertia was estimated by a CAD model of the propeller as $I_{prop} = 2.31 \cdot 10^{-4} \text{ kg m}^2$.

The aerodynamic thrust and torque of a propeller are always proportional to the square of the propeller's rotational speed:

$$T = c_T \cdot \rho \cdot A \cdot (\Omega \cdot R)^2 \quad (\text{A.2.2})$$

$$M_{aero} = c_Q \cdot \rho \cdot A \cdot R \cdot (\Omega \cdot R)^2 \quad (\text{A.2.3})$$

Whirl tower tests at hover thrust and double hover thrust have been used to determine a value of $c_T = 1.60 \cdot 10^{-2}$ and $c_Q = 2.26 \cdot 10^{-3}$ for the 13x8 Fiala propeller. For the dynamics of the combination of motor and propeller the total torque has to be considered:

$$M = M_{motor} + M_{aero} \quad (\text{A.2.4})$$

Writing differential equation Eq. (A.2.1) in the form $\Delta\dot{\Omega} = \Delta M/I_{prop}$ and performing a numerical integration with a small time step Δt , offers the ability to test different models of motor torque. A thrust increase from hover thrust to full thrust (approx. 3.5 times hover thrust) has been investigated with a BULLTEC 30A ESC, which is also used for ANDRoMeDA.

For the initial acceleration phase with a duration of $T_{acceleration} = 0.05 \text{ s}$ a constant peak torque of $M_{motor-peak} = 1.0 \text{ Nm}$ showed a good agreement with the Motor Arris MT-4010 Pro, used for ANDRoMeDA.

After this initial acceleration phase, the motor torque decreases, until it reaches the maximum continuous motor torque, that equals the aerodynamic torque M_{aero} of the propeller at full thrust. The following function has been identified empirically to achieve a agreement with thrust measurements:

$$M_{motor} = M_{motor-peak} - (M_{motor-peak} - M_{motor-full}) \cdot \left(\frac{t}{t_{fall}}\right)^{0.35} \quad (\text{A.2.5})$$

$M_{motor-peak}$ is the motor peak torque for the first acceleration phase, $M_{motor-full}$ is the maximum continuous motor torque and t_{fall} is the time needed for the motor torque to decrease. Figure A.17 shows the modeled torque and the measured torque. It is assumed, that due to the low sampling frequency of the whirl tower of $f_{WT} = 50 \text{ Hz}$, the maximum peak torque cannot be fully captured by the measurement. To be able to model the rotation of the aircraft, described in Section 5.5, or to be able to model other maneuvers an empirical function was derived to model the thrust response as time series:

$$\text{Phase 1 : } T(t) = T_{hov} + a_1 \cdot t \quad (\text{A.2.6})$$

$$\text{Phase 2 : } T(t) = T_{full} - a_2 \cdot (t - t_{rise} - t_{fall})^2 \quad (\text{A.2.7})$$

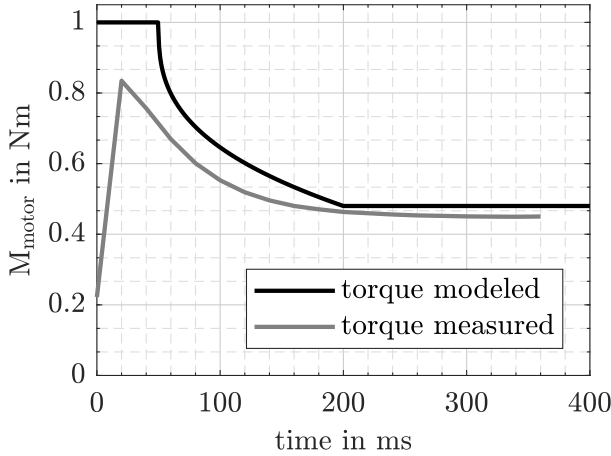


Figure A.17: Modeled torque with $t_{rise} = 0.05$ s, $t_{fall} = 0.15$ s, $M_{motor-peak} = 1.0$ Nm and $M_{motor-full} = 0.48$ Nm.

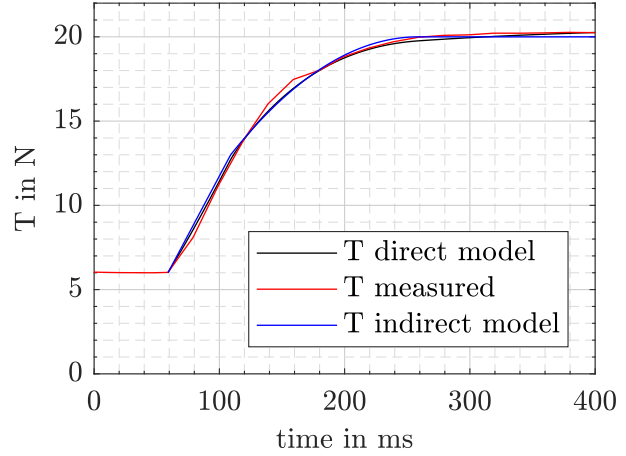


Figure A.18: Thrust modeled indirectly with M_{motor} from Figure A.17 and directly with $T_{full} = 20$ N, $T_{hov} = 60$ N, $a_1 = 140$ N/s, $a_2 = 311$ N/s²

The factor a_1 has to be chosen to model the thrust slope, while a_2 calculates to $a_2 = (T_{full} - T_{hov} - a_1 \cdot t_{rise})/t_{fall}^2$. Figure A.18 gives an overview of the thrust response modeled directly with Eqs. (A.2.6 and A.2.7), the thrust response modeled indirectly by Eqs. (A.2.4 and A.2.5) and the measured thrust response.

As mentioned earlier in Section 5.5, the physical limits of the motor / propeller dynamics are not always met. If a thrust lower than full thrust is commanded, the ESC will not use the maximum motor torque $M_{motor-peak}$.

A.2.2 Dimensional Analysis

A very interesting question that had to be answered during the conceptual design of ANDroMeDA is: "How is the response time of a propulsion system influenced by its propeller diameter?". From experiences with different multirotor aircraft, from propeller diameters of only $D_{prop} = 30$ mm up to propeller diameters of $D_{prop} = 330$ mm, it is obvious that a smaller propeller has a much faster reaction, when its thrust is changed, but how can that be put into numbers?

Eq. (A.2.1) implies that there are two very important quantities responsible for the angular acceleration of a propeller: The maximum motor torque $M_{motor-peak}$ that is available during a step response and the moment of inertia of the propeller. Furthermore, it is important to notice that the necessary RPM change $\Delta\Omega$, for a given thrust change ΔT , is not the same for all rotor sizes.

To estimate the moment of inertia at different propeller sizes, an arbitrary object, made from a homogeneous material, hence having a homogeneous density ρ , is linearly scaled by a factor k in all dimensions. For a propeller this would mean that the propeller diameter is changed by the factor k , while the thickness to chord ratio t/c of the propeller's airfoil remains constant. Mass and moment of inertia, about the z-axis of an arbitrary object, can in general be calculated with:

$$m = \int \rho dV = \rho \cdot \iiint dx dy dz \quad (\text{A.2.8})$$

$$I_{zz} = \int (x^2 + y^2) dm = \rho \int (x^2 + y^2) dV = \rho \iiint (x^2 + y^2) dx dy dz \quad (\text{A.2.9})$$

Introducing the scaling factor k and x', y', z' , for the scaled object, it follows that $x' = k \cdot x$, $y' = k \cdot y$, $z' = k \cdot z$ and $dx' = k \cdot dx$, $dy' = k \cdot dy$, $dz' = k \cdot dz$. Consequently, mass and moment of inertia about the z-axis for an object scaled by k calculates to:

$$\begin{aligned} m' &= \int \rho \, dV' \\ &= \rho \iiint dx' \, dy' \, dz' = \rho \, k^3 \iiint dx \, dy \, dz = k^3 \cdot m \end{aligned} \quad (\text{A.2.10})$$

$$I_{zz'} = \rho \int (x'^2 + y'^2) \, dV' = \rho \, k^5 \int (x^2 + y^2) \, dV = k^5 \cdot I_{zz} \quad (\text{A.2.11})$$

The moment of inertia about the other axes I'_{xx} , I'_{yy} scales equally. Consequently, a propeller upscaled linearly, following Eq. (5.8.16), will have a Moment of Inertia about its rotational axis increased by the fifth power of the scaling factor, if the same homogeneous material is used.

The short term peak torque $M_{motor-peak}$ of an electric brushless motor (BLCD), used for model airplanes or multirotor propulsion, is not easy to identify, because it is not a parameter mentioned in the specifications of any manufacturer. A closer look at data published by a manufacturer of industrial BLCD motors ([94]) revealed a proportional relation between motor mass and peak torque. This tendency could be roughly confirmed, with whirl tower measurements when the step response of two different motors was compared.

The T-Motor MN 5208 with a weight of $m_{motor} = 164 \, g$ was able to achieve a peak torque of $M_{motor-peak} = 1100 \, Nmm$ during step response tests, while the motor finally used for ANDroMeDA-1, the Arris MT4010 Pro 380KV with a weight of $m_{motor} = 94 \, g$, was able to reach a peak torque of $M_{motor-peak} = 800 \, Nmm$.

When two propellers of different diameters are compared, thrust and torque can be expressed by Eqs. (A.2.2 and A.2.3). As mentioned earlier, a propeller scaled according Eq. (5.8.16) will have a constant airfoil thickness to chord ratio t/c and consequently, the aerodynamic efficiency can be expected to remain unaltered, if Reynolds number effects are neglected. This will result in constant aerodynamic coefficients c_T and c_Q .

Eq. (A.2.2) can be rewritten in short as $T = a \cdot \Omega^2$ with $a = c_T \rho \pi R^4$. Using this short form, the change of rotational speed $\Delta\Omega$, necessary to change the thrust from $T = T_0$ to $T = T_1$, can be expressed as:

$$\Delta\Omega = \frac{1}{\sqrt{a}} \cdot \sqrt{T_1 - T_0} \quad (\text{A.2.12})$$

When this is compared to another propeller with a diameter of $D' = k \cdot D$ it yields in:

$$\frac{\Delta\Omega'}{\Delta\Omega} = \sqrt{\frac{a}{a'}} \cdot \sqrt{\frac{T'_1 - T'_0}{T_1 - T_0}} = \left(\frac{R}{R'}\right)^2 \cdot \sqrt{\frac{T'_1 - T'_0}{T_1 - T_0}} = \left(\frac{1}{k}\right)^2 \cdot \sqrt{\frac{T'_1 - T'_0}{T_1 - T_0}} \quad (\text{A.2.13})$$

It follows, that for the same change in thrust, the necessary change of rotational speed is reduced by $1/k^2$, when a larger propeller is used.

Another factor that hasn't been considered yet, is the necessary change of thrust itself. The larger propeller also has to produce a higher thrust, because a smaller number of propellers will be used for the design (compare Table 5.7).

For ANDroMeDA the propeller diameter has been scaled for a constant disc loading $D.L.$, which means that $T'_1 = T_1 \cdot A'/A = T_1 \cdot k^2$ and $T'_0 = T_0 \cdot A'/A = T_0 \cdot k^2$. It follows that:

$$\frac{\Delta\Omega'}{\Delta\Omega} = \frac{1}{k} \quad (\text{A.2.14})$$

Combining all three effects, moment of inertia, motor peak torque and the necessary change of rotational speed in Eq. (A.2.1), leads to the wanted relation. As a simplification, it is assumed, that the peak motor torque $M_{motor-peak}$ is applied constantly for the time of angular acceleration and that the aerodynamic torque M_{aero} can be neglected, because it is small compared to the motor torque ($M_{motor-peak} \gg M_{aero}$). This leads to a response time of:

$$t_{response} = \frac{I_{zz}}{M_{motor-peak}} \cdot \Delta\Omega \quad (\text{A.2.15})$$

If the response times of two rotors having the same disc loading D.L. are compared this results in:

$$\frac{t'_{response}}{t_{response}} = \underbrace{\frac{M_{motor-peak}}{M'_{motor-peak}}}_{\text{Motor}} \cdot \underbrace{k^5}_{\text{Propeller}} \cdot \underbrace{\frac{1}{k^2}}_{\Delta\Omega} \cdot \underbrace{k}_{\text{D.L.}} \quad (\text{A.2.16})$$

On the practical side this means, that the H-4 configuration, compared to the configurations with 8 propellers, has an increased propeller diameter by $k = \sqrt{2}$ and motors, which are allowed to be twice as heavy, and hence should reach twice the peak torque. Consequently, the H-4 configuration is expected to have a lower response time by a factor of $t_{response}(\text{H-4})/t_{response}(\text{H-8}) = 2$.

A numerical simulation, including the aerodynamic torque as well as rise and fall times of the motor torque, as described in the previous section, even showed an increased response time of $t_{response}(\text{H-4})/t_{response}(\text{H-8}) = 2.5$.

A.3 Motor Comparison

After an extensive market survey, four different motors have been chosen that should be, according to manufacturer data, suitable to work with a propeller of 13 to 14 inch diameter. Table A.6 gives an overview of the chosen motors.

Motor	Total weight	$d_{bearings}$	Full thrust	$t_{response}$	P_{hov}
Anti Gravity 4006	71.6 g	12.86 mm	1822 g	0.410 s	83.6 W
DJI E800	110.9 g	16.51 mm	1869 g	0.261 s	79.5 W
Tarrot MT 4006	68.0 g	11.99 mm	1611 g	0.264 s	85.5 W
Arris MT4010PRO	93.9 g	14.64 mm	2053 g	0.252 s	83.5 W

Table A.6: Overview of the four tested motors. All motors have been tested with a Fiala 13x8 three bladed propeller and a BullTEC 40A ESC at $\rho = 1.107 \text{ kg/m}^3$

To determine the total weight of the motors, the weight of the wires has been subtracted by taking specimen of the wires. All motors have been disassembled, as shown in Figure A.19, and the distance of the motor bearings $d_{bearings}$ has been measured. After the tests conducted with tilting propellers (compare chapter A.5) revealed, that even with a three bladed propeller high gyroscopic moments are acting on the motor bearings, a mechanically sound motor design should be selected, which makes the use of very flat configurations (referred to as pancake motors) problematic.

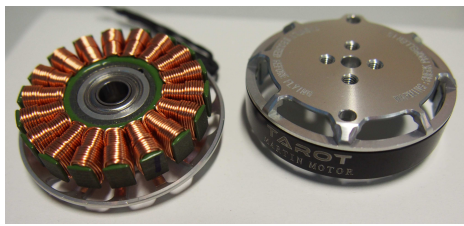
All motors have been tested with a Fiala 13x8 three bladed propeller and a BullTEC 40A ESC in combination with a 6S LiPo battery. The full thrust was interpolated / extrapolated for all motors to match a battery voltage of $v_{batt} = 24.0 \text{ V}$, which corresponds to the first seconds of operation with a fully charged 6S LiPo battery. Response times $t_{response}$ were measured for a step response from hover thrust T_{hov} to full thrust T_{full} . The hover power P_{hov} , listed in Table A.6, is the electrical input power of the corresponding motor at hover thrust, $T_{hov} = 625 \text{ g}$. It should be noted, that this thrust is of course depending on the air density ρ , but since all motors have been tested on the same day at a density of $\rho = 1.107 \text{ kg/m}^3$, the comparison is valid.

To be able to mount the test propeller to the DJI E800 motor, the shaft had to be cut down and the bore of a propeller adapter (tiger motor PA018) had to be enlarged from 4mm to 5mm on a lathe. Normally, the E800 was designed to work only with the proprietary DJI propeller adapters.

From the fact that response times of the Tiger Motor Anti Gravity 4006 are significantly slower than they are with the other motors, and from the fact, that this motor became a lot hotter during operation with the 13x8 propeller, it can be seen that it is operated above its limit and the propeller is too large for that motor. In addition, the low bearing distance makes it a bad choice, even if it is very light weighted.

The Tarrot MT4006, which is also very light, is also a flat design with a low bearing distance and even, if it did not become as hot as the Anti Gravity 4006 and has faster response times, compared to the Anti Gravity 4006, it suffers from deficiencies regarding its maximum thrust.

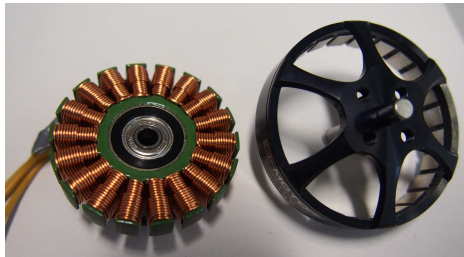
The DJI E800 has clearly the highest efficiency at hovering thrust but is also $\Delta m = 17 \text{ g}$ heavier than the Arris MT4010PRO. Furthermore, the MT4010PRO is the clear winner in terms of maximum thrust and as the only one of the tested motors, it can also be used with larger 14 inch propellers without running too hot. Consequently, the Arris MT4010PRO was selected for ANDroMeDA-1 in combination with 14 inch propellers.



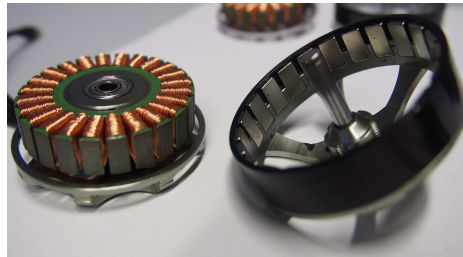
Tarrot MT4006



DJI E800



T-Motor Anti Gravity 4006



Arris MT4010PRO 380KV

Figure A.19: All four motors have been disassembled to inspect their design.

A.4 ESC Comparison

A.4.1 Background

The ESC - electronic speed controller - controls the speed and hence the output power of an electric motor. The phrase ESC reaches back to times when this was often done electro-mechanically with a servo actuator moving a wiper on a potentiometer, because transistors and especially field effect transistors (FETs) were still very expensive.

Until the early 1990s, all electric motors used for remote controlled vehicles have been brushed electric motors, which only needed a DC voltage source to work. The corresponding ESCs used FETs to lower the battery voltage by switching it on and off at very high frequencies, up to several kilohertz and hence, produced a quasi DC voltage, which is lower than the battery output voltage during partial-load operation. The speed of the motor was hereby controlled by the duty cycle of the switching procedure, called pulse width modulation (PWM), which in order controlled the effective output voltage. At full-load operation the battery voltage was directly passed through to the motor.

Despite the lower efficiency, the biggest disadvantage of brushed electric motors is the wear and tear of brushes and collector, caused by friction and sparks during operation. Especially for high power applications in model airplanes, the brushes had to be changed quite often. During the 1990s the first brushless direct current motors (BLDC motors) entered the market. Other than for stepper motors or synchronous permanent magnet motors, the rotating electric field cannot be applied blind, but has to be timed precisely to the present stator position. This process, also referred to as "electronic commutation", was done with the help of position sensors in form of hall sensors or photoelectric sensors in the first BLDC ESC designs. Because the available FETs were still quite big in the 1990s, this first BLDC ESCs were bulky and could easily exceed the dimensions of the motor itself.

In the following years the manufacturers got rid of the position sensors by measuring the so called back-EMF. On a block commutated brushless motor, which means that the voltage of one phase is switched on and off immediately, two of the three phases are supplied with a voltage, while one phase is always switched off, also referred to as "the floating phase". If the current flow on that phase, induced by the coils moving by the motors permanent magnets, is measured, it is possible to get a position feedback and eliminate the sensitive external position sensors. In the beginning often advertised as "sensorless ESC", it is today standard for almost every ESC on the market. The entire circuitry of a brushless ESC is well described in [95] or [96].

Figure A.20 illustrates the basic principle of a sensorless BLDC ESC. With the bridge circuit on the right side, consisting of six transistors TR1 to TR6, the voltage is switched to the motor coils. With four transistors switched on at the same time a current flow can be initiated in six combinations: u-v, v-u, u-w, w-u, vw and wv. The induced voltage on the floating phase is measured by voltage dividers, which are connected to external operational amplifiers (not shown) or directly to the analog-to-digital converter (ADC) of the microprocessor.

During the last two decades, brushless ESCs became smaller, lighter, more reliable and a lot more affordable. While around the year 2000 the ESC could be the most expensive part among the airplane components, today they are inexpensive and available from a large number of brands. The reason for this development is that light and powerful MOSFETS today are available at low prices and also the fabrication of multi-layer circuit boards is mostly done in far-east for a very low price at high unit numbers.

A special development took place during the last five years for ESCs dedicated to multirotor aircraft operation. Some years ago, there was a lack of ESCs capable of multirotor operation,

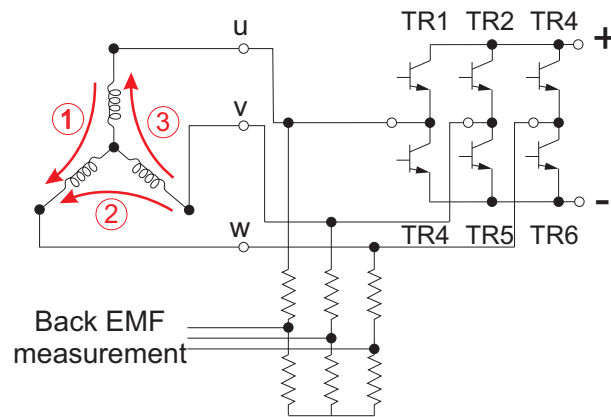


Figure A.20: Principal schematics of a sensorless BLDC speed controller.

because most ESCs introduced large latencies to the propulsion system, which has a negative effect on the flight control algorithm. Hobbyists started to take commercially available ESCs and began to rewrite the firmware running on those ESCs. It turned out, that many available ESCs included suitable hardware for fast speed changes, but they had been limited by the software running on their microprocessor.

When the SWE hexrotor was built in 2013/2014, the standard solution was the so called SimonK firmware, developed by Simon Kirby. Because this firmware became so famous, manufacturers started to use it themselves and officially advertised the ESCs with that firmware. Today, almost all ESCs for multirotor operation are running with the BLHeli firmware, developed by hobbyist Steffen Skaug. The first two versions of this firmware, BLHeli and BLHeli_S are available as open source software. The newest version, BLHeli_32, designed to run on 32 bit ARM processors, is not available as open source anymore.

A.4.2 Test Program

The following aspects have been taken into consideration to compare the different ESCs:

- Full thrust.
- Step response time for a thrust increase from hover thrust T_{hov} to full thrust and from hover thrust to double hover thrust $2 \cdot T_{hov}$.
- Step response time for a thrust decrease from full thrust to hover thrust T_{hov} and from double hover thrust $2 \cdot T_{hov}$ to hover thrust T_{hov} .
- Are there high pitch noises at a certain RPM region? During the previous tests of motors and propellers, conducted with one particular ESC, electromagnetic resonances occurred at a certain RPM. Does this change with different ESCs?
- Temperature of the ESC after 20 minutes of operation at $T = 1.1 \cdot T_{hov}$.
- Efficiency at hover thrust T_{hov} .
- Behaviour during signal loss.

ESC manufacturers often advertise, that their ESCs are able of faster responses than their competitors. Furthermore, the newer generation of ESCs again has shrunk in size and cost and they

are mostly sold for small racing quadrotors. Hence, in the beginning of the test campaign it was not sure if newer, smaller ESCs can be used in combination with large, low RPM motors even if the current rating is suitable. Very little information on that topic can be found online or from vendors.

A.4.3 Tested ESCs

All ESCs selected for testing are rated for operation with a 6S LiPpo battery. Table A.7 shows an overview of the different ESCs.

ESC	Weight	I_{max}	Firmware	Dimensions
DYS XS 30A	9.2 g	30 A	BLHeli_S	32 x 18 x 5.8 mm
BULLTEC BLHeli 30A	27.7 g	30 A	BLHeli	55 x 25 x 9 mm
FlyingFolks 4in1	12.8 g	35 A	BLHeli_32	48 x 45 x 8 mm
DYS ARIA 35A	8.1 g	35 A	BLHeli_32	32 x 16 x 5 mm
Hobbywing XROTOR 40A	31 g	40 A	UNKOWN	32 x 24 x 10 mm
Mikrocopter BLCTRL 3.0	15 g	60 A	UNKOWN	76 x 26 x 10 mm
Holybro Tekko32 4in1	17 g	35 A	BLHeli_32	55 x 40 x 6.4 mm
Hobbywing XROTOR Micro	11 g	40 A	BLHeli_32	32 x 17.9 x 6.2 mm

Table A.7: Overview of the tested ESCs.

The maximum current I_{max} in Table A.7 is the maximum current rating, defined by the manufacturer. The weight was measured "as delivered", means, if the ESC was delivered as bare circuit board it was weighed like that and if it was delivered with heat-sink and wires, it was weighed in this condition.

The BULLTEC BLHeli 30A ESC has been used already in an older version, with SimonK firmware, for the operation of the SWE hexrotor for several years without any problems. As already mentioned in Section B, because of the optical appearance, weight and other specifications it is assumed, that this ESC is also sold as Spider 30A ESC OPTO from the Chinese company Shenzhen ZTW Model Science&Technology Co.,Ltd. Under this label it was, according to the author's knowledge, also operated for many flight hours on several multirotor aircraft for three seasons by an agricultural company without significant problems.

A.4.4 Additional Features

Some ESCs using the BLHeli_32 firmware include a telemetry feature. With an UART data line battery voltage, motor current, ESC temperature and motor RPM can be received from the flight controller. In case of multiple ESCs, using the same BLHeli_32 firmware, all telemetry data lines can be interconnected to one single line, that connects to the flight controller. It is assumed that this is possible because datasets are polled from the flight controller and only one ESC, with the requested ID, answers at the same time. Unfortunately, no documentation for the used UART protocol could be found. The only flight controller software that supports this telemetry feature at the present time is the betafight flight firmware ([97]), which is very popular for fpv racing.

Since betafight is open source, the corresponding code can be analyzed and adapted to the flight controller firmware used for ANDroMeDA in the future. This will eliminate the need for an

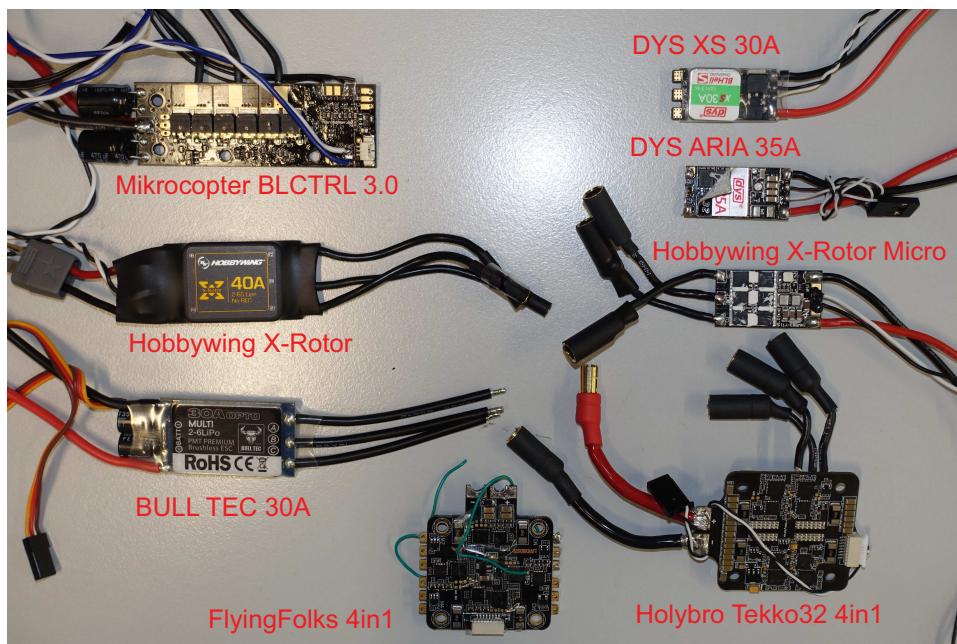


Figure A.21: Overview of all tested ESCs.

additional current sensor and, if properly included in the flight control algorithms, can result in an additional safety and reliability feature for the operation of multiple aircraft. For example ESC over-temperatures or unusual high motor currents or a RPM drop of a single motor can trigger an alarm.

The DYS ARIA 35A does not have a solder pad for the telemetry data line. The FlyingFolks 4in1 ESC does have four separate solder pads for each ESC that have to be wired manually. At the Holybro Tekko32 ESC, a telemetry data line pin for all four ESCs is already included in the 8 pin signal connector. The Hobbywing XROTOR Micro has telemetry data line solder pad.

The so called "4in1" ESCs consist of four ESCs on a single circuit board. They are mostly used for compactly built small FPV racing drones, but would also offer a great benefit for the series production of ANDroMeDA, because one particular "4in1" ESC could be used for the entire front propulsion system and another one for the rear propulsion system. As illustrated in Figure A.22, using a "4in1" ESC instead of four separate ESCs eliminates the need for a power distribution board and furthermore, makes it possible to connect the signal (and additional telemetry) wires of all ESCs with one connector, which in consequence means the entire signal wiring harness can be prepared separately outside the aircraft.

Additionally, the "4in1" ESCs usually include four mounting holes and can be hold in place with nylon screws, rather than being mounted with double-sided tape or zip ties. The only disadvantage is, that in case of a malfunction the entire unit has to be replaced. But considering the relatively low cost, the described advantages and the huge step towards a more professional, clean and production stage like fabrication of ANDroMeDA would absolutely benefit from the use of two "4in1" ESCs, instead of eight separate units. In the current fabrication process four ESCs have to be soldered to the power distribution board all together and all signal wires, which are connected directly to the ESC circuit boards when delivered, have to be extended by soldering. This process is very time consuming. Unfortunately, both of the tested 4in1 ESCs proved to be incompatible with the used motors, as described below. Finding a suitable 4in1 ESC will be subject to further investigations in the future.

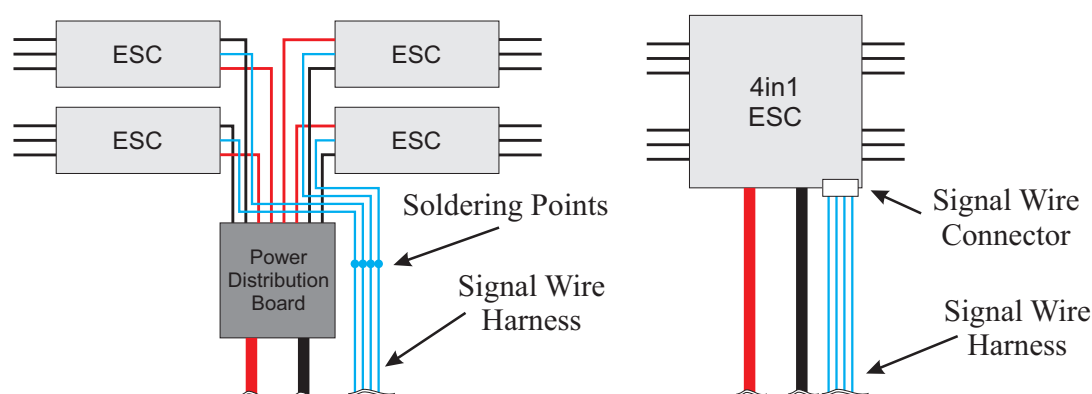


Figure A.22: Wiring schematics of four conventional ESCs compared to a "4in1" ESC.

Almost all ESCs are controlled by an analog input PWM signal with a pulse width between $t_{min} = 1.0 \text{ ms}$ and $t_{max} = 2.0 \text{ ms}$. This signal is based on remote controls used to drive servo actuators. The maximum frequency at which this signal can be sent is about $f = 490 \text{ Hz}$, because at a frequency of $f = 500 \text{ Hz}$ there will be no time left for a pause between the pulses. ESCs with BLHeli firmware implemented newer interpretations of this analog signal called "one shot". Using the one shot protocol, the flight controller can send the analog pulses in an irregular way to sync the timing of sending commands to the ESC with its internal PID main loop. This offers the advantage of less latency between the time a command is calculated by the flight controller and the time it can be actually send to the ESC. The "One Shot" protocol is available at different pulse widths known as "One Shot 42" and "One Shot 125". The newest version of BLHeli firmware also supports a protocol referred to as "D Shot", which sends a digital signal.

Because small FPV racing drones use much smaller motors, combined with much smaller propellers and higher RPMs than large multirotor aircraft, the thrust can be changed a lot faster (compare Section A.2.1), which is highly appreciated by pilots for the very fast and aggressive maneuvers flown with this kind of aircraft. For a larger multirotor aircraft, like ANDroMeDA, it is not expected that other protocols will lead to significant improvements, even if flown at high wind speeds, because the time needed for physical RPM changes at the propulsion system is long, compared to the latencies caused by a thrust signal, sent at $f = 490 \text{ Hz}$.

As the only one of the tested ESCs, the Mikrocopter BLCtrl 3.0 offers the additional possibility to connect it to the flight controller via I2C bus. Since the PX4 flight controller firmware used for the Pixhawk 4 hardware (see Section 7) has not implemented this feature, even if the Pixhawk 4 offers I2C ports, this is not seen as an advantage for the investigated case. In addition, it is also possible to receive telemetry data form the BLCtrl 3.0 on the same I2C connection. But since this is also possible using UART with the BLHeli ESCs, this can be only seen as an advantage over ESCs that do not offer telemetry at all.

A.4.5 Test Results

Full Thrust Comparison

The maximum thrust, that can be reached with a fully charged 6S battery, was compared for all ESCs with the same particular motor specimen, an Arris MT4010PRO, as it will be used for ANDroMeDA-1, and the same particular propeller sepcimen, a Fiala 13x8 three bladed propeller. The measured differences are below 7 %. The Hobbywing X-Rotor ESC reached a maximum

thrust of $T_{full} = 2073 \text{ g}$, while the ESCs with BLHELI_32 firmware had the tendency to produce slightly less thrust. The DYS ARIA 35A reached a maximum of $T_{full} = 1940 \text{ g}$. All values were measured at the same air density of $\rho = 1.09 \text{ kg/m}^3$ at a battery voltage of $U_{batt} = 24.0 \text{ V}$.

Response Times

One very important result of the conducted tests is, that no significant difference in the response times, whether for a step input to accelerate nor for step input to decelerate the propulsion system, could be observed. The results for some of the ESCs are shown in Figure A.23. It can be seen, that the differences are very small and could be also addressed to measurement errors due to the low sampling rate of the whirl tower. The time to increase the thrust from hover thrust $T = T_{hov}$ to full thrust $T = T_{full}$ is always $t = 0.2 \text{ s}$ and the time to decrease the thrust from $T = T_{full}$ to $T = T_{hov}$ is always $t = 0.3 \text{ s}$. Consequently, it is expected that the ESC choice, as long as the ESC is suited for multirotor operation, does not have any impact on the flight characteristics of ANDroMeDA or the handling qualities at higher wind speeds.

It is assumed, that the reason for the almost identical response times is caused by an identical working principal of all BLDC ESCs. As previously shown in Figure 5.15, it makes a big difference, if a small thrust increase $\Delta T \ll T_{full}$ is initiated by a short burst of a full throttle command, followed by a signal corresponding to the target thrust, or if the target thrust is commanded directly. Consequently, it is assumed that by all tested ESCs the value of the input throttle signal is directly transformed into a duty cycle of the output PWM signal, instead of using an internal control loop or acceleration ramp. Furthermore, it is assumed that, if by proper PID tuning, the flight controller is adjusted to overshoot the ESC signal, the relatively slow response time for small thrust changes does not affect the flight characteristics negatively.

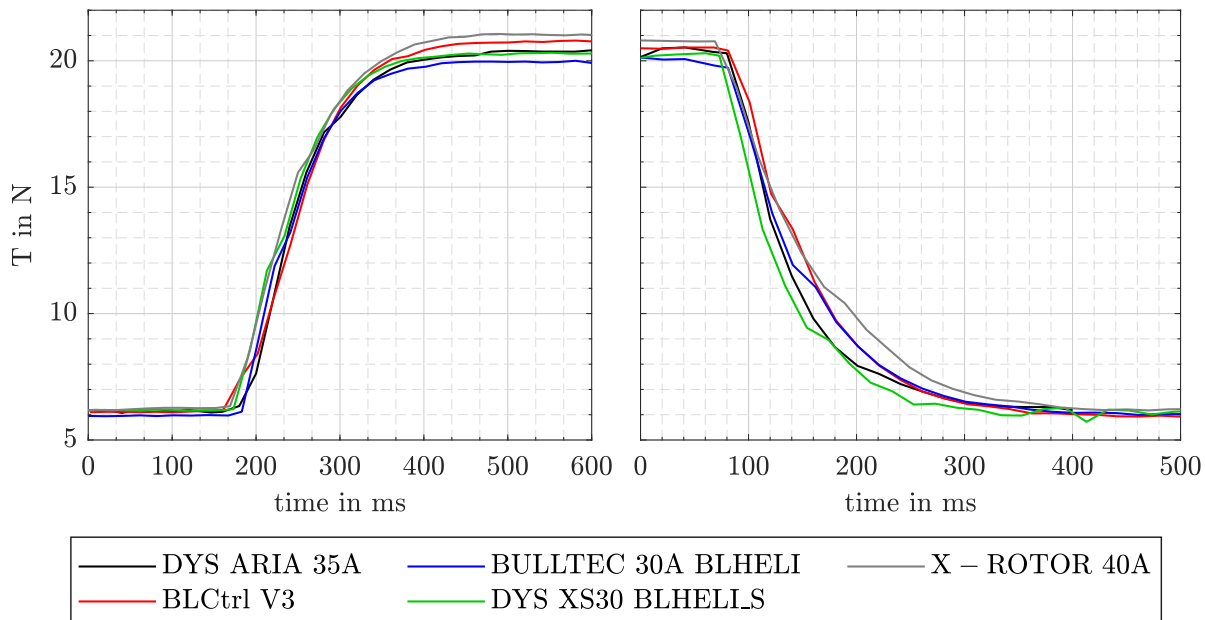


Figure A.23: Response to a sudden increase (left) and decrease (right) of the commanded thrust signal.

Measurements of the current during a step response, show that the Hobbywing X-Rotor ESC exceeds the maximum current drawn by the other ESCs and the DYS Aria seems to be optimized

for a lower current consumption during acceleration, which, however, does not affect its response times.

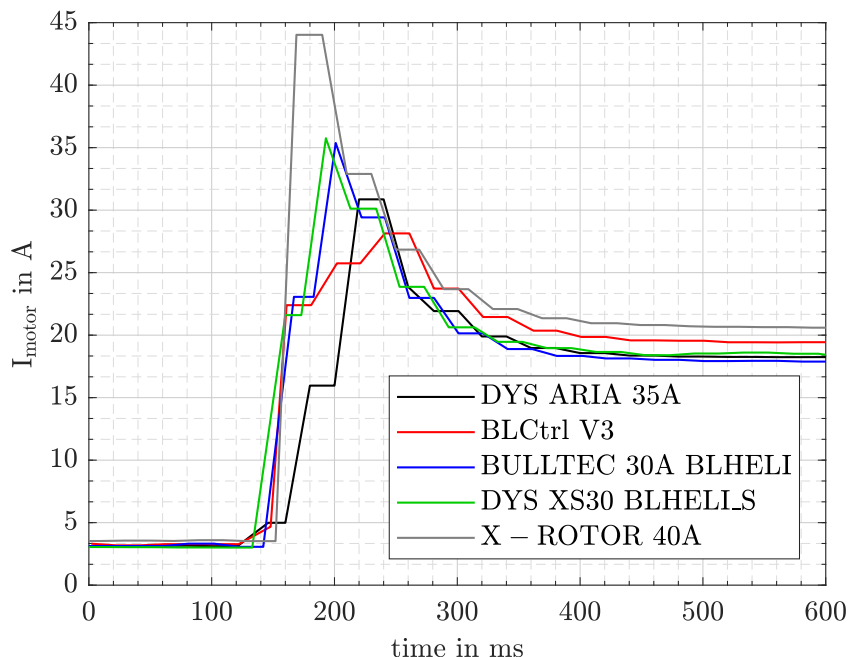


Figure A.24: Motor current during a step response of the different ESCs. Since the whirl tower has a sampling rate of only 50 SPS the true peak current might be higher.

Electromagnetic Resonances

During motor and propeller tests it was already observed, that at certain rotational speeds a very high pitch noise was produced by the motor. A damaged bearing could be excluded, because all motors showed that behaviour. This phenomena could be identified as electromagnetic resonance, which is also visible by an oscillation in the current measurement. With most ESCs resonances could be observed at $n_{motor} = 3000 \text{ min}^{-1}$ and $n_{motor} = 3500 \text{ min}^{-1}$ as well as $n_{motor} = 5800 \text{ min}^{-1}$.

The first version of the BLHELI firmware includes a user parameter, referred to as PWM dither, that is supposed to add a certain amount of randomness to the PWM output voltage and hereby mitigate the resonance. Unfortunately, changing this parameter did only have a small effect. The strongest resonance could be observed with the Hobbywing X-Rotor 40A. With the DYS XS 30 with BLHELI_S firmware, the resonance appeared to be weaker than with the BLHELI firmware used in the BULLTEC 30A ESC. With the DYS ARIA 35A ESC, using the newest BLHELI_32 firmware, the resonances were still noticeable but clearly a lot weaker than with any other ESC, especially when using a PWM output frequency of $f_{PWM} = 48 \text{ kHz}$. This explains why most FPV drone pilots report a "smoother running motor" with BLHELI_32 ESCs.

During an actual flight of a multirotor aircraft, the RPM of the motors is always changing slightly and consequently the electromagnetic resonances are not expected to have a noticeable effect on performance or flying characteristics rather than on the acoustic signature.

Hover Efficiency

The ESC efficiency at hover thrust T_{hov} was not measured directly, since this would introduce additional measurement uncertainties by the involved RPM and torque measurements, necessary to determine the shaft power. Instead the electrical input power was measured at $T = T_{hov}$ and compared between the different ESCs. The differences are small and challenging to measure. Most ESC consumed between $P_{hov} = 77 W$ and $P_{hov} = 82 W$. The only exception is the Hobbywing X-Rotor 40A ESC which had the highest power consumption of $P_{hov} = 87 W$.

Thermal Behaviour

After the test runs at $T = 1.1 \cdot T_{hov}$ for $t = 20 min$ most ESCs reached a temperature of no more than $t_{ESC} = 40^\circ C$ and hence, the thermal behaviour proved to be absolutely uncritical. Also the newer, smaller and lighter ESCs, like the DYS XS30 or DYS ARIA 35A, did not get warmer than the bigger ESCs.

An exception and thereby a clear winner regarding thermal behaviour is the Mikrocopter BLCTRL 3.0, which stayed almost at room temperature during the test, even if no heat sink was mounted. The reason for this is, that 12 strong IRLR 7843 MOSFETs with a maximum continuous drain current of $I_D = 161 A$ are used instead of six MOSFETs. Two MOSFETs are used in parallel for each position of the bridge circuit (compare Figure A.20).

Behaviour in Case of a Signal Loss

The behaviour in case of signal loss is defined by the firmware and hence, can be separated into three groups. All BLHeli ESCs show the same behaviour:

- If an invalid signal is received with a signal PWM pulse length of less than the minimum throttle value for less than $t_{bad-signal} = 160 ms$, it will be treated as minimum throttle signal and the motor will break quickly (compare right side of Figure A.23).
- If an invalid signal is received for a time between $160 ms < t_{bad-signal} > 280 ms$ the last known throttle signal is continued as a failsafe value.
- If an invalid signal is received for a time more than $t_{bad-signal} > 280 ms$ the motor is completely shut down and the ESC needs re-arming, which means that a zero throttle signal has to be send for more than one second to continue operation.

The last point on that list is probably meant as a safety feature, so that in case of a pulled out signal cable during maintenance on ground, the motors will stop spinning. It should be taken into consideration, however, that the signals send from the flight controller to the ESC must not be interrupted during flight under any circumstances.

The Mikrocopter BLCtrl 3.0 is even stricter regarding this safety feature. Even a very short signal loss, longer than $t_{bad-signal} = 90 ms$, will switch of the motor completely and the ESC needs re-arming.

The Hobbywing X-Rotor ESC is quite uncomplicated in such a scenario:

- An invalid signal for as long as $t_{bad-signal} = 600 ms$ will be filtered out completely and the motor will keep spinning at its previous RPM.
- An invalid signal for more than $t_{bad-signal} > 600 ms$ will stop the motor and after a couple of seconds a failure beeping sequence is started, to inform the operator that no valid signal is received at the moment.

- If the signal is recovered after a signal loss, the motor starts spinning immediately without the need for a repeated arming sequence.

Motor Compatibility

Of the four tested ESCs with BLHeli_32 firmware, three appeared to be incompatible with the motors selected for ANDroMeDA. The two tested 4in1 ESCs are built with exactly the same electronic components: MOSFETs QN3109 from UBIQ Semiconductor Corp. ([98]), STM F051K86 Arm Cortex M0 MCU ([99]) and a Fortior FD6288 MOSFET driver IC. The latter is used in almost all investigated ESCs. However, the actual circuit design and geometrical arrangement of the components is different. Both ESCs show the same behaviour: Below $n_{motor} = 2000 \text{ min}^{-1}$, the motor stutters significantly. Above $n_{motor} = 2000 \text{ min}^{-1}$, everything works and even sudden changes in commanded thrust do not result in a loss of motor synchronization. Yet, this behaviour is not acceptable and these ESCs are not well suited for the used motors. Test with various user adjustable firmware settings, like commutation timing and others, did not lead to any improvements in the behaviour.

The Hobbywing XRotor Micro 40A ESC showed the same motor stutter below $n_{motor} = 2000 \text{ min}^{-1}$, but in addition, suffered from serious motor desynchronizations, also at higher RPMs. Different firmware settings minimized the desynchronizations but did not entirely remove them. MOSTFETs and MCU of this ESC could not be identified, because the markings have been removed by the manufacturer.

The fourth tested BLHELI_32 ESC, the DYS ARIA 35A, did not show any problematic behaviour. It is built with IOR H7440 MOSFETs ([100]), a Fortior FD6288 MOSFET driver and an STM F051K66 Arm Cortex M0 MCU ([99]), which is the same as the STM F051K86 but with 32 kByte instead of 64 kByte memory.

The BLHeli firmware development is mostly driven by FPV racing and hence, for the use with small and fast spinning motors. Even, if these motors are operated at the same output power, their electromagnetic behaviour might be different from the larger and slower motors used for ANDroMeDA. Possible reasons why only one of four tested ESCs with BLHELI_32 firmware works with the used motors can only be assumed:

- The firmware of the different ESCs was compiled with different predefined settings, which are not meant to be changed by the end user.
- The measurement of back emf is contaminated by noise, due to the different designs of the ESCs circuit boards. Even the tiny circuit boards include many resistors, diodes, schottky diodes and capacitors which can form filters. Furthermore ground planes on the circuit board might be designed cleaner for the DYS ARIA ESC. Even small differences can have a large impact concerning this issue.
- The ADC (analog digital converter) of the 32Bit Arm MCU used for BLHELI_32 is more sensitive to noise and hence more difficult to handle than the ADC of the 8Bit SiLabs MCU used for BLHELI and BLHELI_S.

From a practical point of view the only possibility to find a suitable ESC with the newest BLHELI_32 firmware, is to purchase more variants and conduct intensive tests. Unfortunately, in many cases the exact same design is sold under various brand names, which makes it even more difficult to find a matching product.

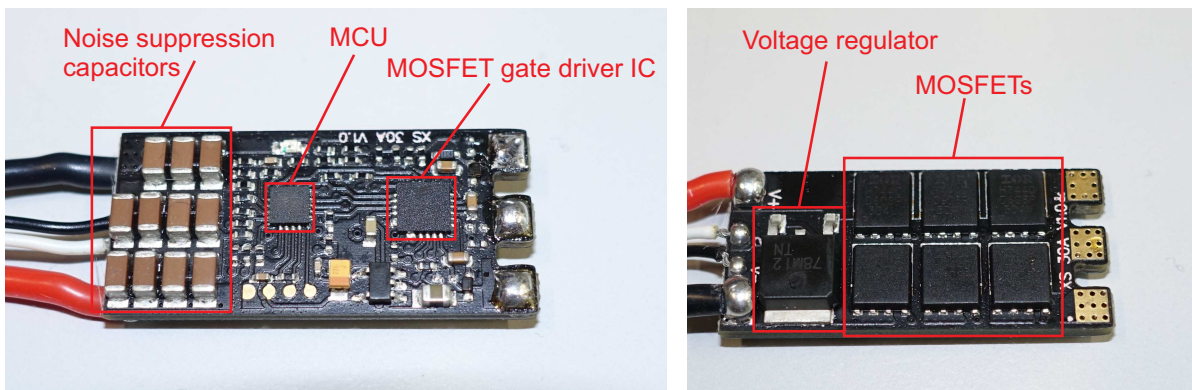


Figure A.25: Main electrical components used for a BLDC ESC at the example of an DYS XS30 ESC. Note that the used 8-Bit MCU is quite small. The 32 Bit MCU used for BLHELI_32 ESCs is slightly larger than the shown MOSFET driver IC.

A.4.6 Additional Observations

The first DYS XS30 ESC tested stopped to work, because of a burnt voltage regulator. This voltage regulator of type 78M12 got hot, when connected to a 6S battery, and caused a high no-load current consumption from the beginning of the tests. To ensure that this is not a design flaw, another XS30 ESC was ordered that did not show the same behaviour. This incident shows how important a careful test of all components is, before assembling the aircraft.

A.4.7 Conclusions

It could be shown, that all ESCs offer a very similar performance regarding maximum thrust and flight time. They are able of producing almost identical response time and hence, it is not expected, that the ESC choice will affect the flight characteristics or PID gains of the flight controller.

However, will the ESC choice have an effect on the mass of the propulsion system and the wiring effort during fabrication. For the first prototype, ANDroMeDA-1, it has been decided to use a BULLTEC 30A OPTO BLHELI ESCs, because it has proved to be reliable during past projects. In addition, every particular ESC and motor will be tested on the whirl tower for 20 minutes before they are installed in the aircraft.

For the future, it would be possible to use more modern and lighter ESCs, as the tests have shown that they can, if compatible, handle the larger motors without problems or thermal issues. A "4in1" ESC can offer a large benefit regarding the fabrication effort, maintenance and weight of the propulsion system. Unfortunately, no compatible "4in1" ESC could be identified so far. For future ANDroMeDA aircraft the tests will continue.

A.5 Tiltrotor Actuator Testing

Because ANDroMeDA will be equipped with tilting propellers, a proper design of the tilting mechanism has to be worked out and a suitable choice of an actuator has to be made. Tilting propellers on a multirotor aircraft are not very common and thus, there are not many experiences available. For smaller racing drones there are three aircraft with tilting propellers commercially available, also developed just recently (see [101], [102] and [103]).

However, the racing tilt drones are much smaller than ANDroMeDA (propeller diameter 4 inches to 6 inches, $MTOW < 1 \text{ kg}$) and all four motor arms are tilted together. In addition, tilting propeller mechanisms can be found at the tail of tricopter configurations, which need it for yaw control but most tricopter designs are also equipped with smaller propellers than the propellers of ANDroMeDA.

Consequently, it is important for the design of ANDroMeDA to conduct initial tests, be able to quantify the forces and moments, caused by propeller tilting, and make sure that the tilting mechanism and tilting actuator will work properly.

A.5.1 Physical Description

The underlying rigid body mechanics for a rotating body that is tilted about a second axis can be described by the following two equations:

$$\mathbf{L} = \mathbf{\Theta} \cdot \boldsymbol{\omega} \quad (\text{A.5.1})$$

$$\frac{d}{dt}\mathbf{L} = \mathbf{M} \quad (\text{A.5.2})$$

Where $\boldsymbol{\omega}$ is the resulting rotation vector, hence the rotor rotation Ω combined with the rotation about the tilt axis ($\dot{\sigma}$), and \mathbf{L} is the vector of angular momentum. It is important to note, that Eqs. (A.5.1 and A.5.2) are only valid in the inertial system.

A fundamental difference between a propeller with two blades, compared to a propeller with three or more blades, can be observed in the equations above. For a two bladed propeller the inertia tensor $\mathbf{\Theta}$ varies periodically over one rotation, while for a propeller with three or more blades the inertia tensor $\mathbf{\Theta}$ is independent of the rotation angle.

This fact can be easily derived, when a two and four bladed propeller are modeled with point masses, as shown in Figure A.26. For a three bladed propeller the derivation is less illustrative but will also lead to a constant inertia ($I_{xx} = \text{const.}$), independent of the propeller position ψ .

To describe the system, three reference frames are introduced: the inertial frame x, y, z , the motor arm frame x'', y'', z'' and the propeller frame x', y', z' . The motor arm frame's y-axis (\mathbf{y}'') is identical to the inertial frame's y-axis (\mathbf{y}) and the motor arm frame is rotated about this axis with the angular rate $\dot{\sigma}$. The propeller frame of reference rotates with the angular rate $\Omega = \dot{\psi}$ about its z-axis, which is also the negative z-axis of the motor arm frame ($\mathbf{z}' = -\mathbf{z}''$).

If a propeller with three or more blades is tilted at a constant tilt rate ($\dot{\sigma} = \text{const.}$), a constant moment about the \mathbf{x}'' axis will establish due to the constantly changing vector of momentum \mathbf{L} (see Eq. (A.5.2)). This is illustrated in Figure A.28 and that moment is known as gyroscopic moment.

If a two bladed propeller is tilted at a constant tilt rate ($\dot{\sigma} = \text{const.}$), in addition to the gyroscopic moment, a moment about the y-axis of the motor arm reference frame (\mathbf{y}'') develops, changing periodically twice per propeller revolution. This can be addressed to the inertia of the two bladed propeller, which changes twice per propeller revolution and is derived graphically in Figure A.29. Since the angular rate of the propeller revolution Ω is a lot faster than the tilt rate $\dot{\sigma}$, the change of tilt angle is not shown in Figure A.29.

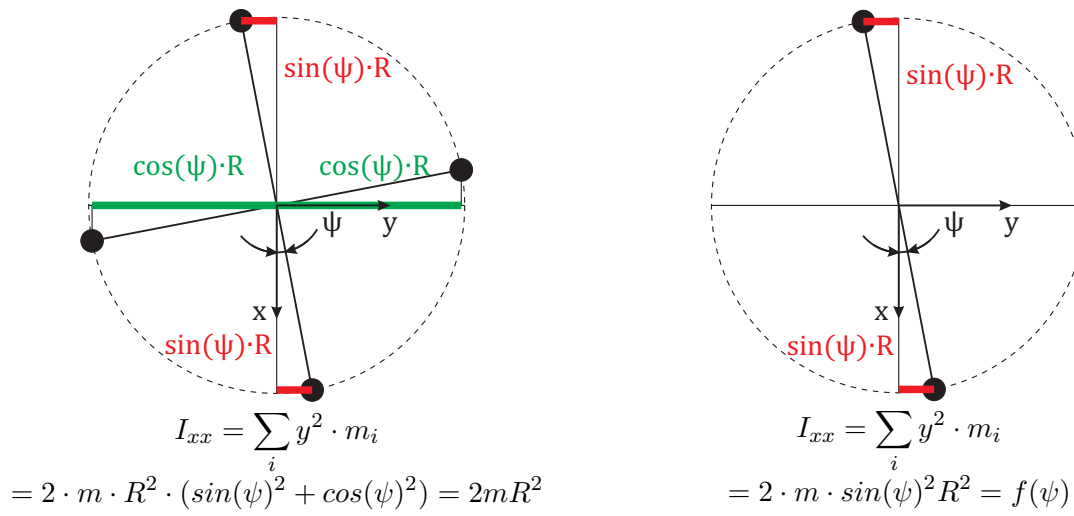


Figure A.26: Moment of inertia about x-axis I_{xx} for a two and four bladed propeller simplified by point masses of mass m .

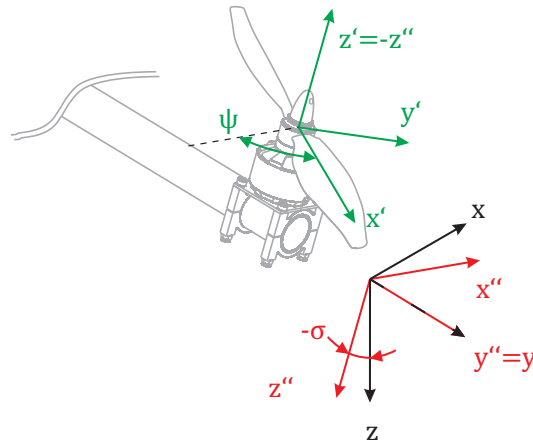


Figure A.27: Coordinate systems to describe the tilt rotor mechanics. The shown motor arm is tilted forward ($\sigma < 0$).

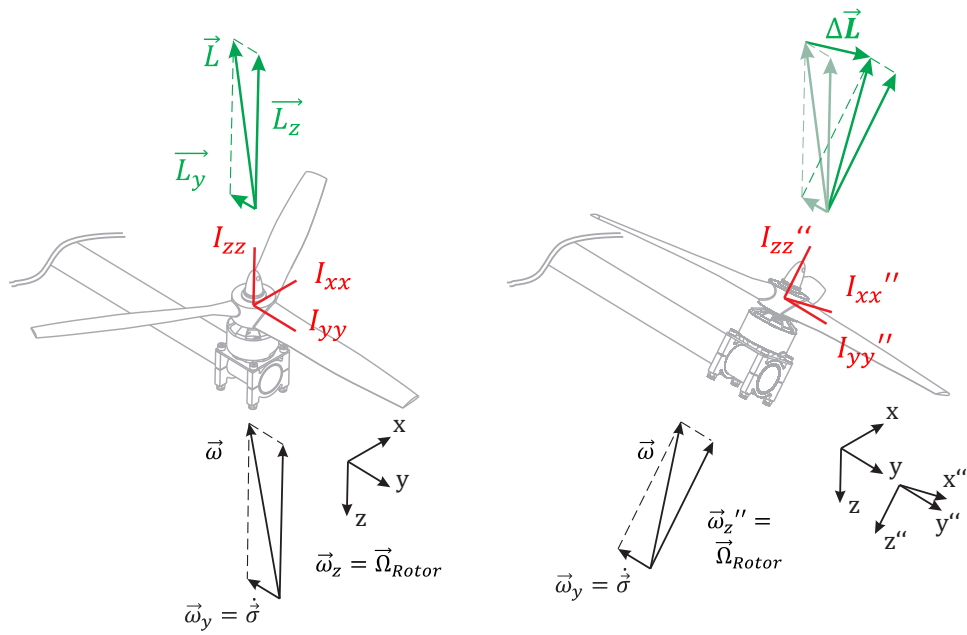


Figure A.28: Gyroscopic moment when a symmetric rotating propeller is tilted.

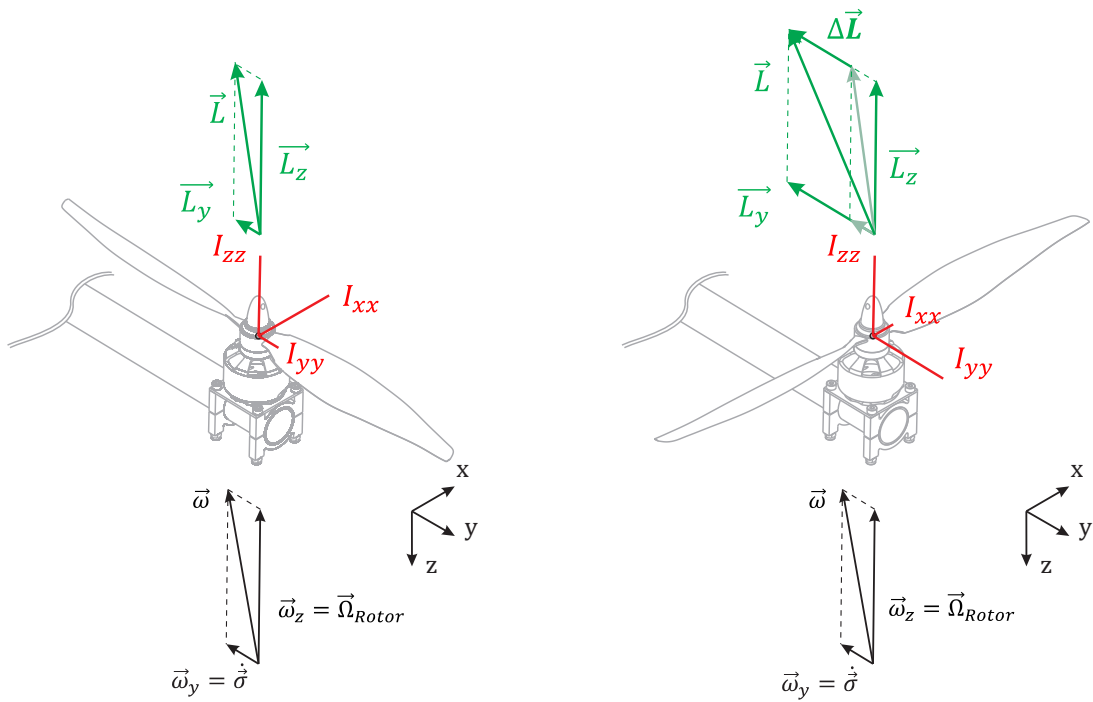


Figure A.29: Periodically changing moment M_y that develops, if a rotating two-bladed propeller is tilted.

A.5.2 Analytical Approach

To be able to solve Eq. (A.5.1), it is necessary to describe the total rotation vector ω . While the propeller rotation can be easily described in the propeller frame of reference: $\omega'_{\text{prop}} = (0 \ 0 \ \Omega)^T$, the motor arm rotation can be described easily in the motor arm frame or the inertial frame of reference: $\omega_{\text{arm}} = (0 \ \dot{\sigma} \ 0)^T$.

First ω_{arm} is converted from the inertial frame of reference to the propeller frame of reference, using the following transformation matrix:

$$\mathbf{T}_{\mathbf{p}-\mathbf{i}} = \begin{bmatrix} -\cos(\psi) \cdot \cos(\sigma) & \sin(\psi) \cdot \cos(\sigma) & -\sin(\sigma) \\ \sin(\psi) & \cos(\psi) & 0 \\ \cos(\psi) \cdot \sin(\sigma) & -\sin(\psi) \cdot \sin(\sigma) & -\cos(\sigma) \end{bmatrix} \quad (\text{A.5.3})$$

The transformation can be derived by a rotation about the z-axis by $\alpha = -\psi$, followed by a rotation about the new y-axis by $\alpha = -\sigma$. In the end, the signs of the first row and the last row are swapped, to change the direction of the x and z-axis.

With the help of this transformation the resulting rotation vector in the propeller frame can be expressed:

$$\omega' = \omega'_{\text{prop}} + \mathbf{T}_{\mathbf{p}-\mathbf{i}}^T \cdot \omega_{\text{arm}} = \begin{bmatrix} \sin(\psi) \cdot \dot{\sigma} \\ \cos(\psi) \cdot \dot{\sigma} \\ \Omega \end{bmatrix} \quad (\text{A.5.4})$$

With the resulting rotation vector available, it is possible to calculate the momentum vector \mathbf{L} in the propeller frame of reference, where the propeller inertia tensor Θ is constant:

$$\mathbf{L}' = \Theta \cdot \omega' \quad (\text{A.5.5})$$

If then the momentum vector is transformed back to the inertial frame of reference, it is also possible to solve Eq. (A.5.2) and calculate the moments that are developed, while a rotating propeller is tilted:

$$\mathbf{M} = \frac{d}{dt} \mathbf{L} = \frac{d}{dt} (\mathbf{T}_{\mathbf{p}-\mathbf{i}} \cdot \mathbf{L}') \quad (\text{A.5.6})$$

With the help of $\mathbf{T}_{\mathbf{p}-\mathbf{i}}$ and a corresponding transformation from the inertial frame to the motor arm frame $\mathbf{T}_{\mathbf{i}-\mathbf{ma}}$ by simple rotation about the y-axis, it is also possible to convert the moment vector gained from Eq. (A.5.6) back to the propeller frame of reference and the motor arm frame of reference. For a simple analytical approach two assumptions are made:

- The propeller rotates with a constant speed $\Omega = 4000 \text{ U/min} = 419 \text{ rad/s}$.
- The tilt movement has a constant tilt rate $\dot{\sigma} = 300^\circ/\text{s} = 5.24 \text{ rad/s}$.

The inertia tensor of a three bladed propeller of type Master Airscrew 13x6 ($m = 62 \text{ g}$) and a two bladed propeller of type Aeronaut CAM Carbon Light 13x6 ($m = 22 \text{ g}$) have been estimated with the help of a uniform density CAD model, drawn to scale according to the dimensions of the two propellers.

The solution for the three-bladed propeller shows, that only a constant gyroscopic moment of $M_{\text{gyroscopic}} = -0.72 \text{ Nm}$ develops and no periodic moments exist. The moments developed by the two bladed propeller on the other hand, shown in Figure A.30, are more complex. The gyroscopic moment is oscillating about its mean value of $\overline{M}_{\text{gyroscopic}} = -0.3 \text{ Nm}$ and in addition, a moment

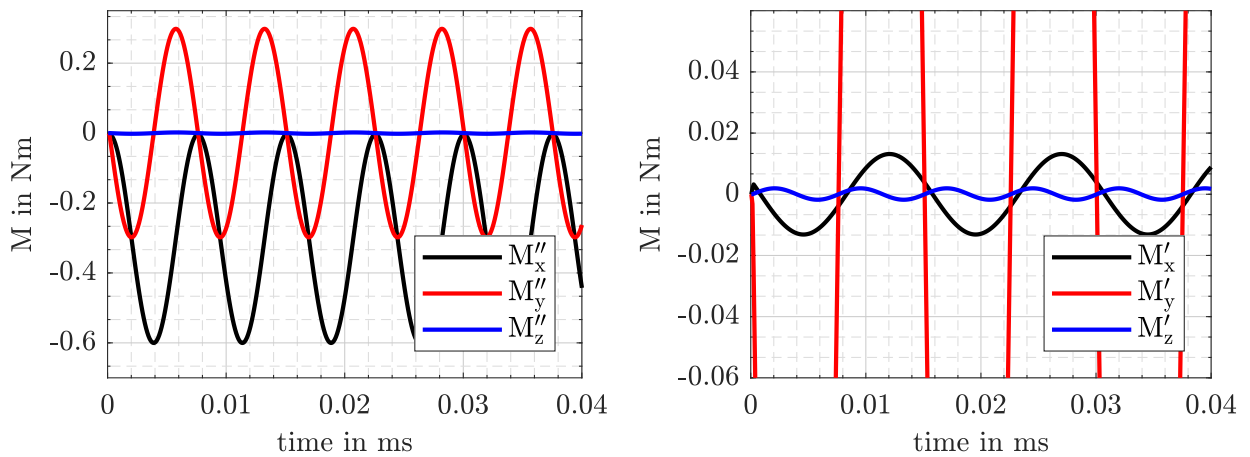


Figure A.30: Moments in the motor arm reference frame (left) and propeller reference frame (right) for a two bladed propeller spinning at $\Omega = 4000 \text{ U/min}$ being tilted at $\dot{\sigma} = 300^\circ/s$.

about the y-axis is oscillating around zero with an amplitude of $\hat{M}_y = 0.3 \text{ Nm}$. This moment will directly load the tilt actuator.

Another interesting fact can be observed in the propeller reference frame of the two bladed propeller (Figure A.30 right). While the largest oscillating moment is M'_y , a small oscillating moment M'_x exists and even a very small moment M'_z is oscillating at $2/rev$ about the rotation axis of the propeller, which in turn means, that the motor torque has to change periodically to maintain a constant propeller RPM, while the propeller it is tilted.

A.5.3 MBS Simulations

To be able to investigate more complex systems, the multi-body-simulation software SIMPACK has been used. Several questions should be answered by that approach:

- What moments will develop, if a coaxial propeller setup (resulting momentum vector $\mathbf{L} = 0$) is tilted ?
- Is it possible to adjust the phase of both propellers of a coaxial two-bladed propeller setup in a way, that no oscillating moments will develop?
- If the front and rear motor arms are designed as end-to-end CFRP tubes, with only one tilt actuator in the middle, do the moments cancel each other out?
- How big will the moment about the y-axis, caused by the acceleration period of the tilting movement be, compared to the other moments?

To answer these questions, several models have been set up. For all simulations the propeller rotation is already present in the beginning, while the tilt motion is accelerated slowly from $t = 0$ s to $t = 0.05$ s. After $t = 0.05$ s the simulations continue with a constant tilt rate of $\dot{\sigma} = 5.24$ rad/s. The most simple scenario is a coaxial propeller configuration with two three-bladed propellers. As expected, only a maximum moment about the y-axis of $M_y = 0.15$ Nm develops during the acceleration phase and after $t = 0.05$ s the joint to the inertial system is completely free of forces, because neither aerodynamic forces nor friction are considered.

For a coaxial configuration with two bladed propellers, the situation changes however. If the forces are averaged, they will always cancel each other out after the system has accelerated to a constant tilt rate. This can be addressed to the resulting vector of angular momentum \mathbf{L} , which is always zero on average. But the moments at the motor mount will always be subjected to strong periodical variations in any case.

With the help of the simulations, it could be observed, that it makes a large difference at what phase the two propellers are spinning. Two completely opposite cases could be provoked, if the propellers are spinning either at a zero phase shift or at a 90° phase shift. The definition of this phase shift is illustrated in Figure A.31.

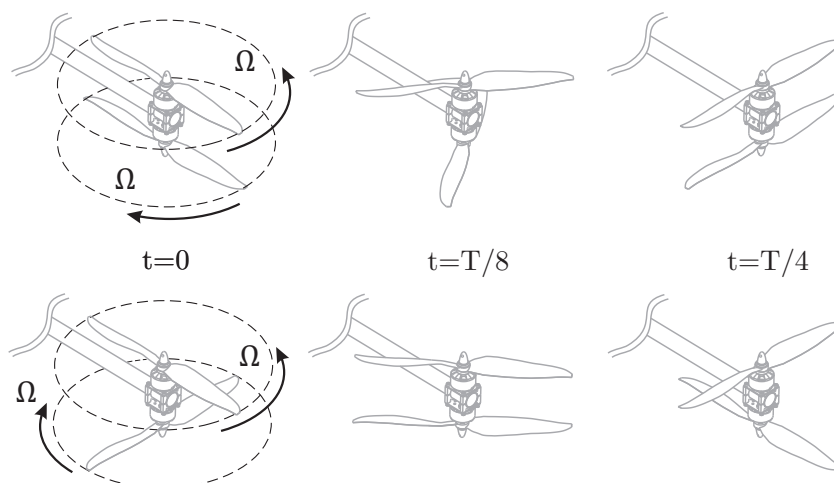


Figure A.31: Definition of the coaxial rotor phase shift, used for SIMPACK simulations: Top: 0° phase shift. Bottom: 90° phase shift

When the propellers spinning at a 0° phase shift, a strong oscillating moment M_y about the y-axis will develop, while the gyroscopic moments M_x'' of both rotors are exactly canceling each other out. If the propellers are spinning at a phase shift of 90° , on the other hand, the oscillating moments about the y-axis M_y are exactly canceling each other out, while the gyroscopic moments of the two propellers result in an oscillating moment about the x-axis in the motor arm reference frame, M_x'' . This case should be favored, to keep the loads on the actuator low. The two scenarios are shown in Figure A.32. It can also be seen, that the oscillating loads on the tilt actuator are by a magnitude larger than the loads during the tilt acceleration period.

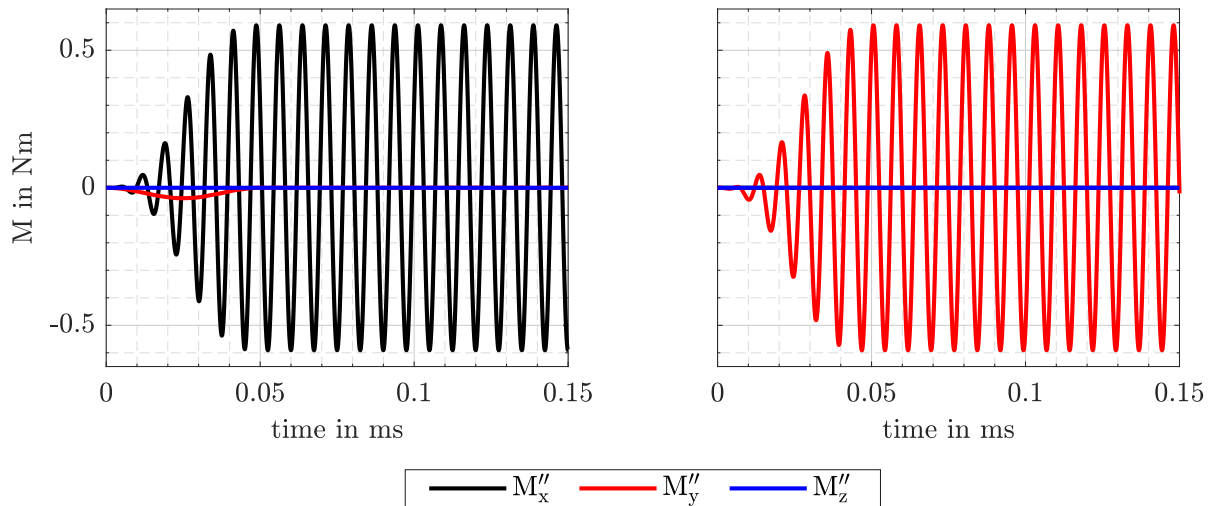


Figure A.32: Moments in the motor arm frame of reference developed by a two bladed coaxial setup. Left: Phase shift of 0° . Right: Phase shift of 90° .

Unfortunately, with two common BLDC motors it is not possible to adjust the phase shift of the propellers. The only way to do this is the use of a gear, with only one motor for both propellers, or the use of some kind of stepper motor. Hence, another simulation was done with two different propeller speeds. This scenario is closer to a real multirotor operation, since the two propellers will never spin at exactly the same RPM and by different RPMs the phase will change continuously, which means that the two propellers are not operating at a specific angle to each other.

The result of this simulation, shown in Figure A.33, illustrates that the moments are slowly changing from M_x'' to M_y'' . Interestingly, this changes need nearly the entire tilt process to take place, even with a relatively large RPM difference of $\Delta n = 100 \text{ min}^{-1}$. For the practical operation of ANDroMeDA, this would mean, that large loads are exerted on the tilt actuator randomly, depending on the current alignment of the two two-bladed propellers during tilting.

To investigate the influence of the CFRP motor arm tube on the system, a model was set up with two two-bladed propellers at the ends of a finite element beam with 16 nodes, shown in Figure A.34. The presence of the flexible motor arm tube increased the moment M_y'' by a factor of eight, while again the phase of the two propellers decides, if there will be a resulting moment M_y'' or not. The real situation, where the motor arm introduces material damping on the system, even if this amount is expected to be not very high for a CFRP tube, is difficult to capture with a MBS simulation without experiments.

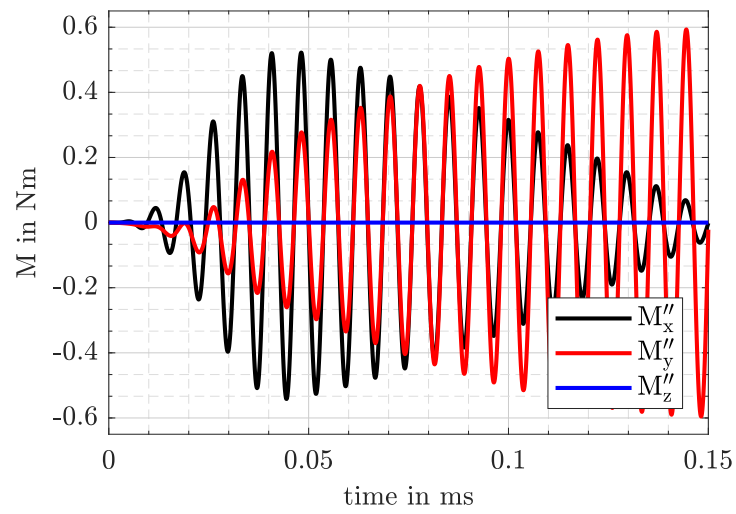


Figure A.33: Moments in the motor arm frame of reference developed by a two bladed coaxial setup with different propeller speeds; $n_{top} = 4000 \text{ min}^{-1}$; $n_{bottom} = 4097 \text{ min}^{-1}$.

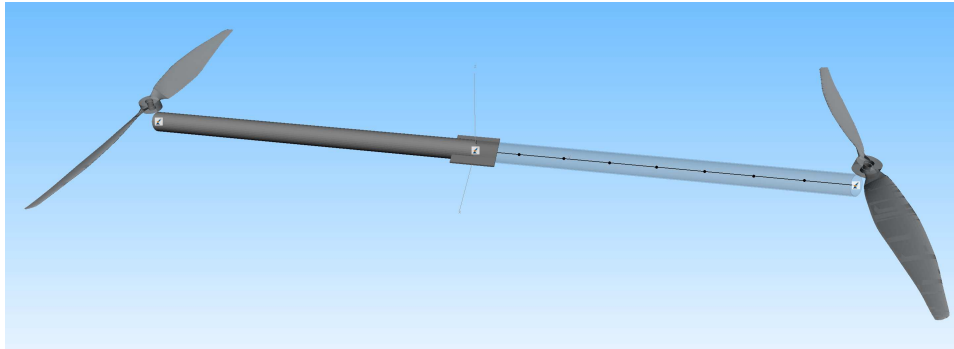


Figure A.34: SIMPACK model for two propellers mounted at the ends of an elastic CFRP tube modeled by eight nodes for each side.

A.5.4 Test Rig

As described above, the simulations could not cover every aspect of the tilting propeller configuration and hence, could not answer all of the open questions. Especially the torque actually applied to the tilt actuator, with a flexible motor arm involved, could not be determined. Furthermore, as well as for the analytical approach, a constant propeller speed and a constant tilt rate was used for the simulations, which cannot be ensured in reality with the propeller driven by a motor and the tilt motion controlled by a tilt actuator at varying loads.

To answer the remaining questions, and finally decide, if it is necessary to use a heavier and aerodynamically inferior three-bladed propeller, and furthermore, to be able to test different tilt actuators under realistic test conditions, a tilt rotor test rig was designed, as shown in Figure A.35.

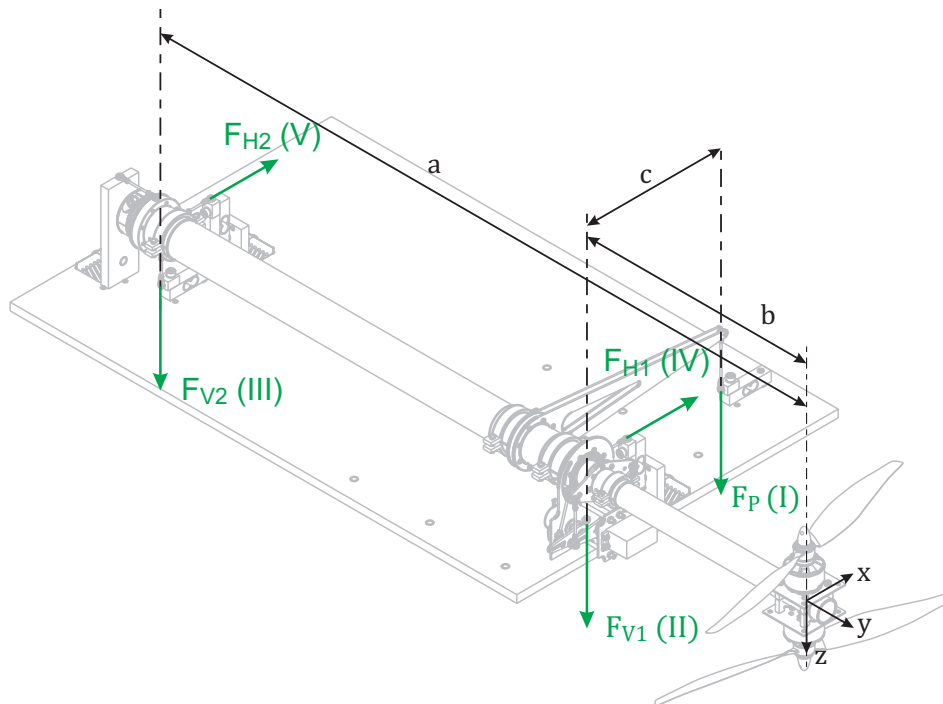


Figure A.35: Tilt rotor test rig designed to measure three moments and two forces: M_x , M_y , M_z , F_x , F_z .

To avoid hysteresis, all five load cells are connected to a large aluminum tube without bearings. Because the attachment was realized with thin steel pins, that can flex, it is made sure that a particular load cell will mostly measure one force or one moment. For example, if the load cell I is removed, the entire apparatus can be tilted around the y-axis, because the supports will flex, but it cannot be moved in any other direction. This type of support is shown in Figure A.36.

The tilt rotor test rig electronics was built with low cost components, using five HX711 load cell amplifiers and four Arduino nano MCUs. Due to the limited number of timers and an inability to read available bytes sent from the USB port, at the exact same time as an interrupt was triggered, it is necessary to use five separate MCUs. This inability was discovered at the whirl tower and in rare cases lead to data loss or garbled motor signals. In addition to the load cells, a tilt angle sensor was realized using a vishay He-351 hall sensor ([104]), and two inductive RPM sensor have been added. A complete schematics of the tilt rotor test rig electronics is given in Figure A.37.

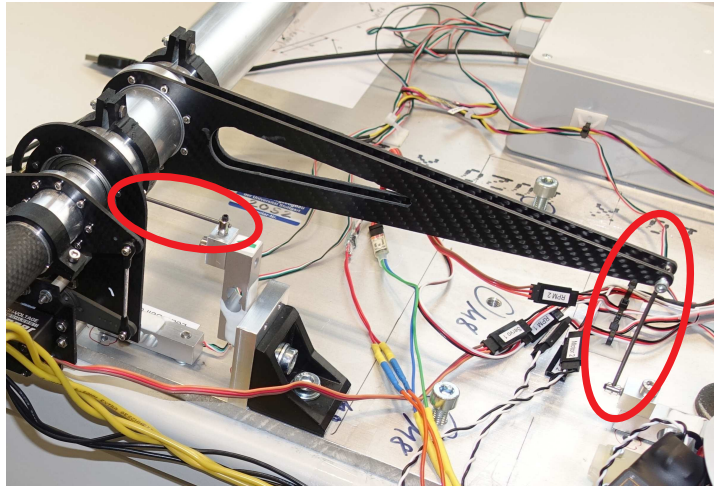


Figure A.36: Semi-flexible connection between load cells and test rig.

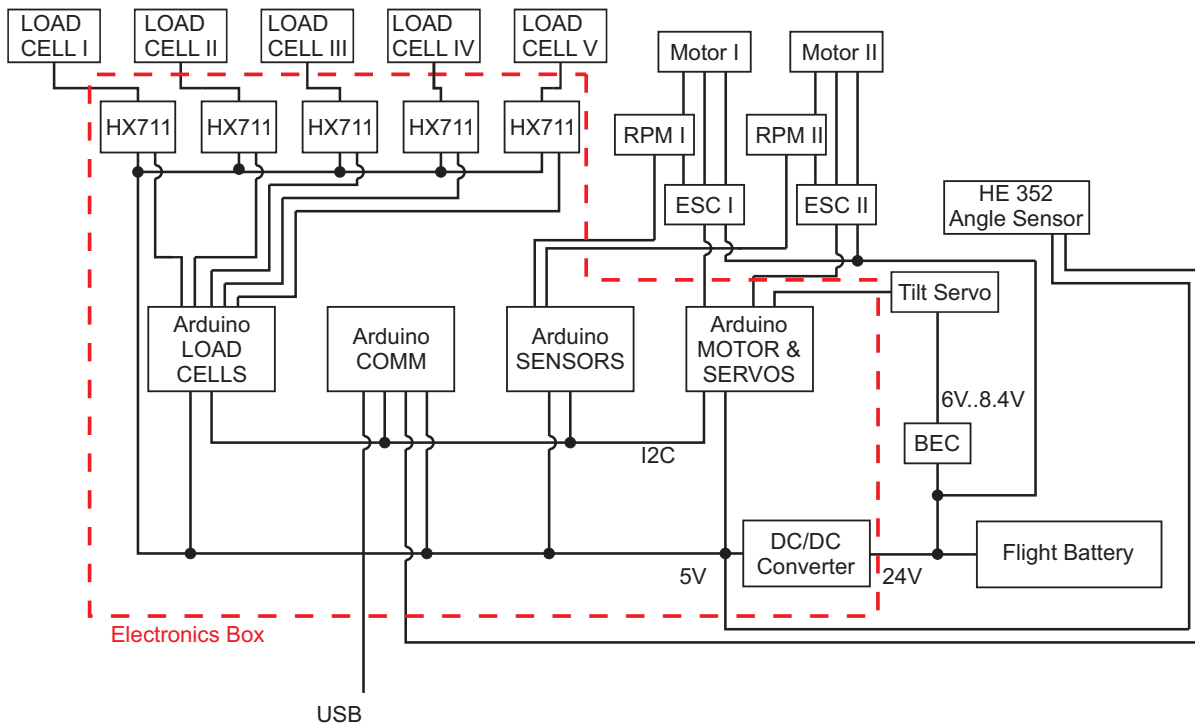


Figure A.37: Schematics of the tilt rotor test rig electronics.

For a five axis force/torque sensor it is very important to perform a proper calibration. In case of the tilt rotor test rig, it was challenging to apply all forces and moments, because of the limited space. Figure A.38 depicts the solution that was finally chosen. A separate calibration rig with multiple pulleys was designed and built. Figure A.39 shows the application of a force $-F_z$. It is hardly possible to build a five axis balance, in a way that one external load will exactly influence one load cell, without any cross-couplings. Consequently, the measurements from all five load cells at a time have to be converted into a corresponding external load. For that purpose a calibration

matrix is used:

$$\mathbf{F} = \mathbf{C} \cdot \mathbf{U} \quad (\text{A.5.7})$$

Where $\mathbf{F} = (F_x \ F_z \ M_x \ M_y \ M_z)^T$ is a vector with the five external loads, \mathbf{C} is the calibration matrix and $\mathbf{U} = (U_I \ U_{II} \ U_{III} \ U_{IV} \ U_V)^T$ a vector with the raw values, received from the load cells, respectively the corresponding HX711 ICs.

To obtain the calibration matrix \mathbf{C} , a very simple approach was chosen as described in [105]. If only one external load F_j is applied once at a time ($F_{i \neq j} = 0$), the j-th column of the inverse calibration matrix can be written as:

$$a_{i,j} = \frac{U_i}{F_j} \quad (\text{A.5.8})$$

After all five separated loads F_j have been applied, all five columns of the matrix \mathbf{C}^{-1} are available and the actual calibration matrix can be obtained by inverting \mathbf{C}^{-1} .

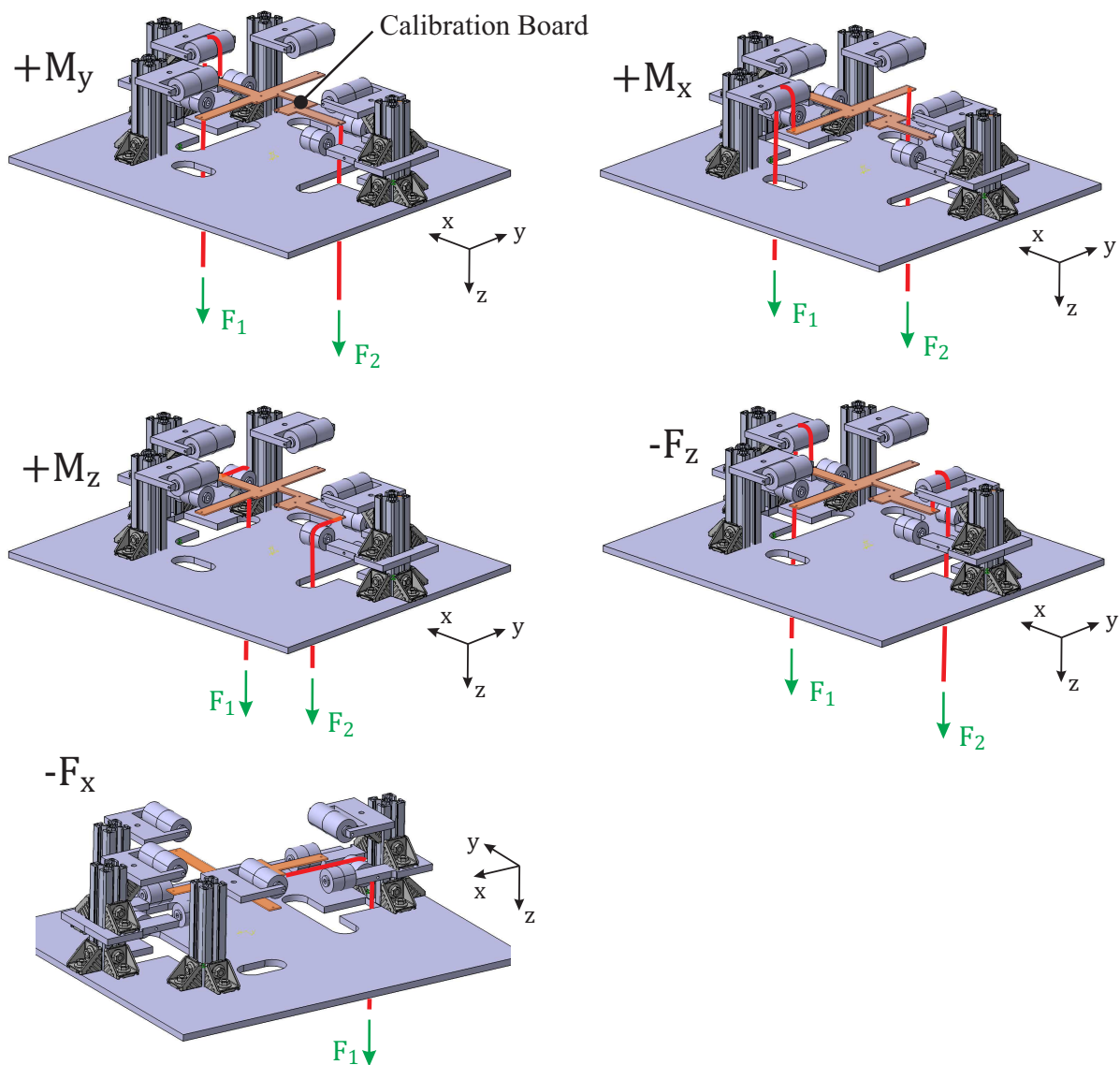


Figure A.38: Calibration procedure.

After the calibration, single load cases have been tested to assure the success of the calibration procedure. The resulting errors have been less than 0.7 % for all load cases, except $M_z = 643.5 \text{ Nmm}$, which caused an error of 1.4 %. A more sophisticated approach, using combined load cases for the calibration, in combination with a least square method will be tested in the future. It should also be mentioned, however, that the tilt rotor test rig was not meant to be a very precise instrument, but to give an overview of the present forces and moments and to visualize the difference between different propeller configurations and investigate the behaviour of different tilt actuators.



Figure A.39: Weights for $-F_z$ calibration applied.

Unfortunately, the HX711 low cost load cell amplifiers are limited to 80 samples/s, which is too slow to capture the oscillating loads caused by propellers spinning at a maximum speed of $f_{prop} = 100 \text{ Hz}$ or more. Consequently, in addition, a Sony RX100 IV digital camera with the capability of taking videos with up to 1000 frames/s was used. With the help of high speed videos, it is possible to see exactly how the propeller is moving.

A.5.5 Measurements and Conclusions

First tests have been conducted with a single propeller and an Align DS615S servo, with a nominal weight of $m_{servo} = 59\text{ g}$, as a tilt actuator, operated at $U_{servo} = 6.0\text{ V}$. Two different propellers have been compared. A two bladed Aeronaut CAM Carbon Light 13x6 which is one of the lightest injection molded plastic propellers on the market, with a weight of $m = 22\text{ g}$, and a Fiala wooden three bladed propeller of size 13x6 with a weight of $m = 44\text{ g}$.

In general both propellers can be tilted quite fast, but with the two bladed propeller a discomfoting noise is present during the tilt movement, while tilting the three bladed propeller seems to be absolutely smooth even if it is twice as heavy. High speed videos revealed, that with the two bladed propeller the entire motor is wobbling, which causes the noise, and the tilt rate $\dot{\sigma}$ is not constant due to the periodically changing moment about the tilt axis. Figure A.40 shows the tilt angle over time for the two bladed propeller, measured optically from a high speed video. Every time the propeller is aligned perpendicular to the motor arm ($\psi = 0^\circ$ or $\psi = 180^\circ$), the tilt movement is slowed down.

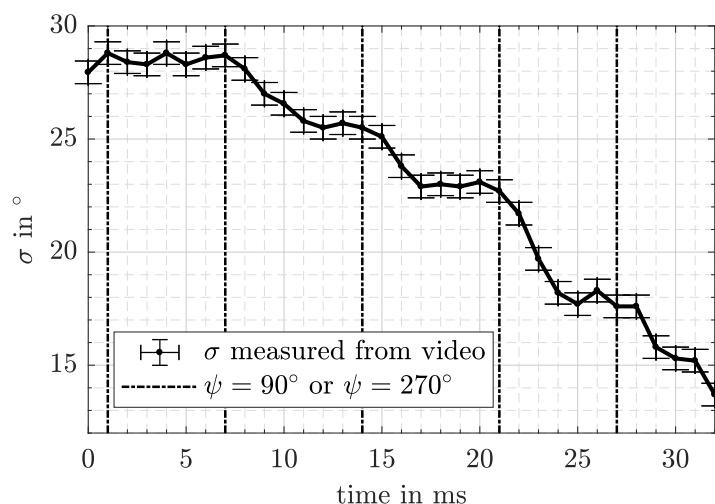


Figure A.40: Tilt movement with a two bladed propeller of type Aeronaut CAM Carbon Light 13x6 measured from high speed video at $f = 1000\text{ frames/s}$.

Because of those highly varying loads on the tilt actuator and the entire structure, it is concluded that three-bladed propellers are absolutely mandatory for a tilt-rotor design, which uses the tilt degree of freedom for flight control where fast response times are needed.

In Figure A.41 a single three-bladed propeller of type Fiala 13x6 is compared to a coaxial configuration with a 14x6 Fiala three-bladed propeller at the top and a 14x8 Fiala three-bladed propeller at the bottom. As expected, with the single propeller configuration a gyroscopic moment can be measured, while this gyroscopic moment is not present with the coaxial propeller set up. Both configurations show an offset of the moment M_x'' if the tilt angle is non-zero. This cannot be explained with the mechanics of a rigid body. It is assumed, that this offset of M_x'' is caused by aerodynamic effects from the propeller wake impinging on the floor and the table where the tilt test rig is mounted.

During the tests, two different model aircraft servo actuators have been tested as tilt actuators: An Align DS615S with a nominal weight of $m_{servo} = 59\text{ g}$ and a Graupner HBS860 with a nominal weight of $m_{servo} = 68\text{ g}$. While the DS615S worked conveniently with single two- and three-bladed propellers, it showed some weak oscillations with two motors mounted and only

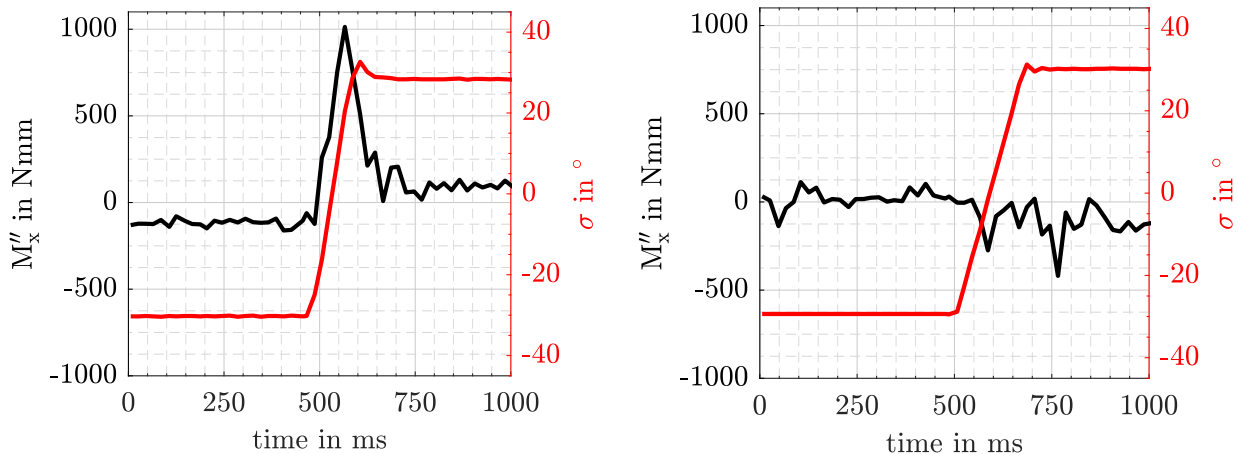


Figure A.41: Measurement of M''_x . Left: Single three bladed propeller. Right: Coaxial configuration with two three bladed propellers.

one Master Airscrew 13x6 three bladed propeller ($m = 62\text{ g}$) operating at the top position. This oscillation was stable and did not cause any damage but proved, that the DS615S is not suitable for the final ANDroMeDA configuration. It is assumed, that the oscillation was caused by backlash in the actuator's gear and the corresponding resonance frequency. The DS615S has noticeably more play than the HBS860.

With the HBS860, the final propulsion system used for ANDroMeDA-1 has been tested extensively at different thrust levels up to full thrust, without encountering any problems. It did not warm up noticeably and seems to handle the load cases without problems. Different supply voltages between $U_{Servo} = 6.0\text{ V}$ and $U_{Servo} = 8.4\text{ V}$ have been tested. At the latter one the servo is faster but does overshoot the target position more. Since the BEC used for ANDroMeDA-1 can be easily adjusted to either $U_{Servo} = 6.0\text{ V}$, $U_{Servo} = 7.2\text{ V}$ or $U_{Servo} = 8.4\text{ V}$, it is possible to make adjustments during the test flights.

Servo actuators for model airplanes and helicopters are available at a large variety on the market and because the specifications given by the manufacturer usually do not include gear backlash or power consumption and since the speeds specified are usually no-load speeds, the potential for further tests is very high. However, because tilt actuator tests are time consuming and some servo actuators are very expensive, no further tests have done so far.

The HBS860 is usually available at only 70 € while some other actuators are priced as high as 250 € (e.g. Futaba BLS 177SV). Experiences in the model helicopter community flying acrobatic helicopters with the HBS860 are very comforting ([106]). Consequently, it will be used for ANDroMeDA-1 and if problems will occur other, higher priced tilt actuators have to be tested.

A.6 Vibration Isolation of Flow Measurement Equipment

A.6.1 Sources of Vibrations

Every rotary wing aircraft, with its many rotating parts, is a natural source of vibration. In addition, a multirotor aircraft introduces a number of propellers rotating at slightly different speeds during maneuvers, which results in beat frequencies.

For a multirotor aircraft, hovering in a calm, windless environment, mostly the rotational frequency of the rotors can cause vibrations. At forward flight conditions or if hovering in a strong headwind, in addition, higher harmonic frequencies come into play. For the three balded propellers, used for ANDroMeDA-1, the third rotor harmonic frequency of $f_{3/rev} = 3 \cdot \Omega_{rotor}$ gets excited by the non-uniform inflow of the rotors. Resulting from the higher dynamic pressure at the advancing blade and the retreating blade being subjected to reverse flow at a radial length of $r/R = \mu$, this is an unavoidable source of vibration and the only way to keep the vibration down, is to keep the advance ratio μ as low as possible, which is contrary to flight performance requirements, because it means to set a high rotational speed.

A.6.2 Influence of Vibrations on the Flow Measurement

As shown with a simple trolley test in calm air (Figure 6.39), it can be demonstrated that the triple hot wire probe is not per se sensitive to vibrations.

However, every vibratory movement of the measurement probe will induce an airflow past it. In an ideal case, this measured airflow can be compensated digitally during post-processing if an inertial measurement unit (IMU) is placed at the same location and the accelerations measured by this IMU are integrated to retrieve its speed. Unfortunately, this ideal case does not exist because this motion compensation will introduce a number of possible errors. First of all, the integration of IMU acceleration will introduce a numerical error. Furthermore, different sampling rates of the flow measurement and the IMU measurement, as well as sensor noise, will increase the error.

Even if it is assumed that this motion compensation procedure with IMU data works flawlessly, there is still another possible error from a fluid dynamic point of view. Similar to the dynamic stall of an airfoil, it is possible that a certain amount of hysteresis is introduced, by a rapidly moving hot wire. This could also be dependent on the oscillation frequency and different resulting Strouhal numbers.

Consequently, a low-vibration measurement probe is strongly preferred over any post-processing vibration compensation techniques and the primary goal is, to allow the tip of the measurement boom to oscillate as little as possible.

A.6.3 Testing Procedure

To excite the measurement boom at different frequencies, a shaker has been designed and built as shown in Figure A.42. This test rig is equipped with two IMUs. One on the moving table and one on the specimen mounted to the table, as for example on the tip of the measurement boom. With the help of these two data sources, a transfer function can be computed, expressing how much of the vibration of the base of the boom is transmitted to the tip. This dimensionless transfer function is also called transmissibility.

In addition, multi body simulations with a flexible beam have been carried out with SIMPACK and MATLAB SimMechanics, to gather a better understanding of the process, and high speed videos with $f = 1000 \text{ frames/s}$ have been taken with a Sony RX100 IV digital camera. The shaker and all testing procedures are described in [107].

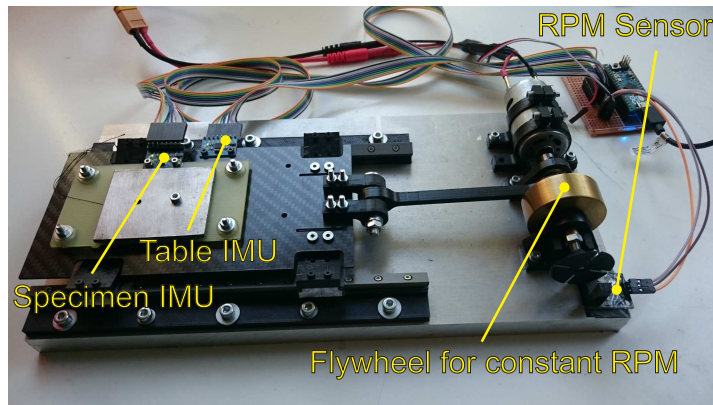


Figure A.42: Shaker table.

A.6.4 Approaches to Isolate the Measurement Probe

The first approach to isolate the measurement boom was designed with rubber dampers, which can be found also on camera gimbal mounts (compare Figure 5.18). This design is shown in Figure A.43. Due to the different in-plane and out-of-plane stiffness of the rubber elements, the initial

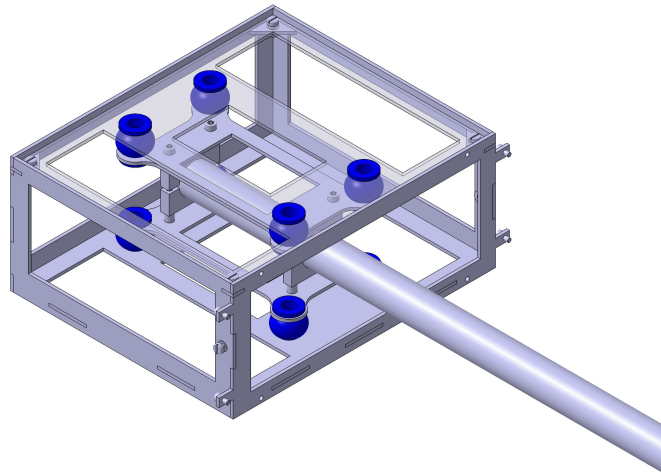


Figure A.43: Initial design: The measurement boom is suspended by eight rubber dampers shown in blue.

design resulted in different eigenfrequencies in the horizontal and vertical plane. Furthermore, both frequencies have been found to be too low and the entire suspension being too soft. A single excitation, as for example a strong single gust or a landing shock, would cause the boom to oscillate heavily. A second approach was realized with silicon dampers of type B1 from the Japanese Taica Corporation, as shown in Figure A.44. The B1 silicon dampers have demonstrated a very high damping rate in isolated tests on the shaker.

Because the first eigenfrequency of the CFRP tube, used as measurement boom, is only between $f_{tube} = 10 \text{ Hz}$ and $f_{tube} = 15 \text{ Hz}$, depending on the weight of the used probe, and thus, much lower than the rotational frequency of the rotors of approximately $f_{rotor} = 50 \text{ Hz}$, a third design was tested with the measurement boom mounted rigidly to the airframe.

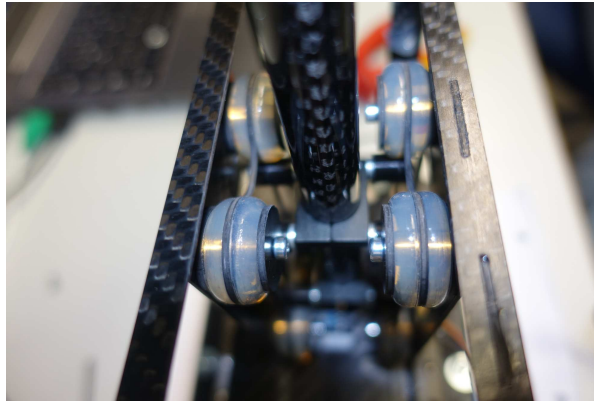


Figure A.44: Measurement boom suspension with eight Taica B1 silicon dampers.

A.6.5 Test Results and Conclusions

To be able to gain the highest level of similarity to the real measurement boom, the dummy boom, used for flight tests and vibration testing, was equipped with an aluminum rod inside the CFRP tube, that represents the masses of the pressure hoses and wiring. This however, introduced additional eigenmodes to the system when the rod started oscillating inside the tube. For further tests it was removed and it was decided, that the hoses and wires will be secured outside the tube at the real measurement boom, because they cannot be secured sufficiently inside the tube.

As already mentioned, the rubber dampers are too soft and will not be used. The CFRP tube has two dominating mode shapes, as illustrated in Figure A.45. To visualize the mode shapes, the two frames from high speed videos with the highest deflections have been taken and the boom position has been marked to derive a drawing.

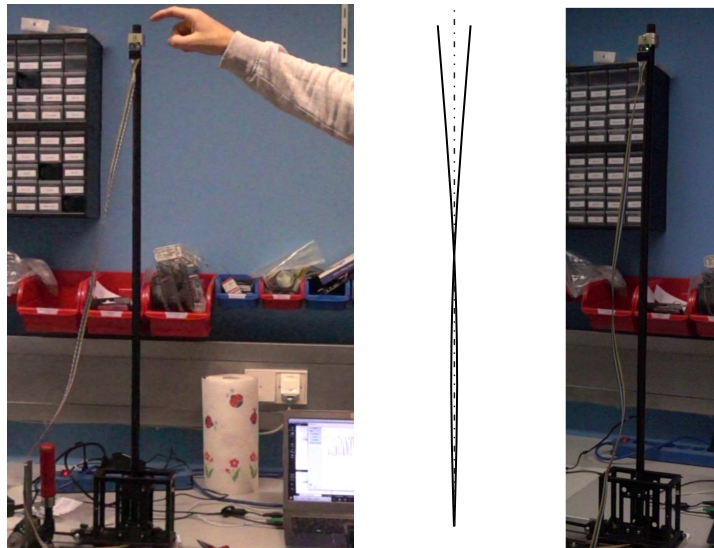


Figure A.45: Modeshapes derived from high speed videos and drawn with deflection upscaled by 300 %. Left: First eigenmode at $f_1 = 10 \text{ Hz}$. Right: Second eigenmode at $f_2 = 95 \text{ Hz}$.

This illustrates, that the highest deflection of the first mode shape is at the tip of the measure-

ment boom. For the second mode shape, the highest deflection occurs a few centimeters below the booms center, while the tip moves only very little.

Tests with the taica B1 silicon dampers revealed, that in general only a slight improvement in terms of a lower transmissibility function could be achieved, while for certain frequency ranges an even higher transmissibility was measured. It is assumed, that more eigenmodes are introduced to the system by more degrees of freedom, which makes the system more complex. Furthermore, it is assumed that the dampers cannot reach their full potential, because they are located far away from the highest deflections. Since the B1 dampers would add an additional weight of $\Delta m_{B1} = 64 \text{ g}$ in total and since the transmissibility is very similar compared to a rigidly mounted boom, it was decided not to use them.

The transmissibility chart of the rigidly mounted boom is shown in Figure A.46. For most frequency ranges the transmissibility is smaller than one, which means vibrations at the tip of the measurement boom are damped. At $f_{rotor} = 50 \text{ Hz}$ the transmissibility is $T = 0.3$ which means that only 30 % of the deflections that are present on the airframe will be transmitted to the probe.

The first eigenfrequency is a lot lower than the rotational frequency of the rotors, and since wind gusts are a phenomena of rather stochastic than periodic nature, the first eigenfrequency is not considered to be a problem. It could be shown, by high speed videos, that an additional resonance at $f_3 = 135 \text{ Hz}$ was present during the tests, because the IMU was mounted eccentrically, which introduced a torsional mode shape. Consequently, this eigenfrequency is not met by the simulation and the increased transmissibility above $f_2 = 95 \text{ Hz}$ (Figure A.46) is also not expected to become a problem during actual measurement flights, because the probe is designed symmetrically (compare Figure 6.29). However, this experience can be taken as an important design guideline for future probe designs. If the center of gravity is not located along the center line of the CFRP tube, translational vibratory movements at the airframe can excite the first torsional eigenfrequency of the CFRP tube.

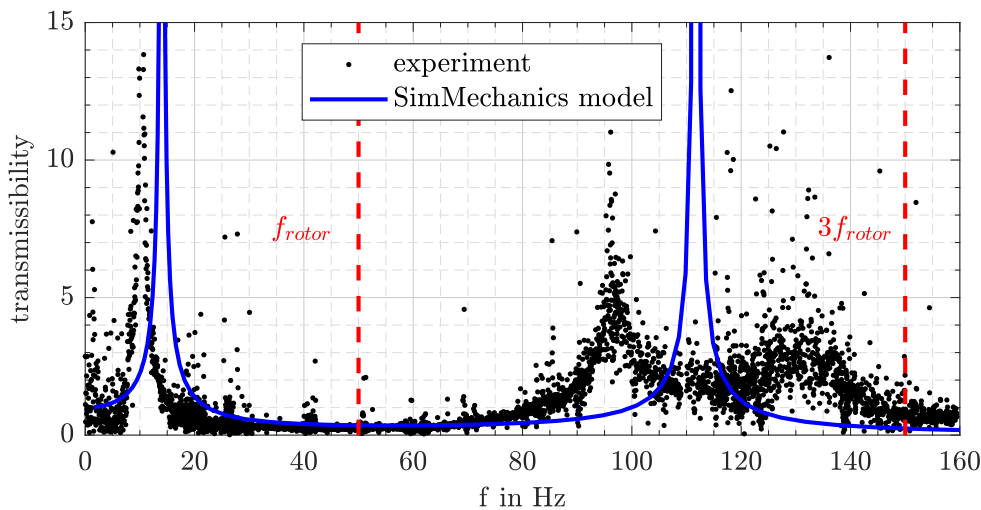


Figure A.46: Transmissibility function of the rigidly mounted measurement boom.

Because the critical second eigenfrequency of $f_2 = 95 \text{ Hz}$ will not be reached by the propellers in flight, other than during a full power climb, which is not needed for conducting measurements, the rigidly mounted measurement boom has been found, to be the most promising design for the first measurement flights. An IMU will be mounted at the tip of the measurement boom to observe all vibrations carefully. If the second eigenfrequency should get excited during measurement flights,

however, a tuned mass damper at the location of the highest tube deflection could be used to overcome this problem, although the feasibility of this solution has to be proven by simulations first.

A.7 Battery Choice

Because a higher voltage will cause smaller losses at wires and connectors it was decided to use a 6S LiPo battery. A battery with six cells can be charged with most available chargers and the number of available ESCs is alot higher than for example for a 8S battery.

No particular battery was chosen until the start of the detailed design phase of the project. Several batteries have been compared in size to design the battery compartment of ANDroMeDA. For the first flight tests, batteries with a capacity between 4000 *mAh* and 10 000 *mAh* have been ordered and will be tested during flight. The former ones can be used as a twin battery pack, since the battery compartment was designed quite large. No prior lab tests or measurements have been conducted because LiPo batteries have become very reliable during the past years. During flight tests it will be decided, which battery is most suitable for the measurement campaigns.

The batteries listed in Table A.8 have been ordered for the flight tests. To calculate the specific energy e_{batt} a voltage of $U_{batt} = 24 V$ has been used for all batteries.

Battery	Capacity	Weight	Dimensions	e_{batt}
ZIPPY Compact 4000mAh 6S 25C	4.0 <i>Ah</i>	557 <i>g</i>	148 x 44 x 40 <i>mm</i>	172 <i>Wh/kg</i>
Turnigy nano-tech 4500mAh 6S 50C	4.5 <i>Ah</i>	687 <i>g</i>	168 x 69 x 44 <i>mm</i>	157 <i>Wh/kg</i>
ZIPPY Compact 6200mAh 6S 40C	6.2 <i>Ah</i>	872 <i>g</i>	158 x 62 x 45 <i>mm</i>	171 <i>Wh/kg</i>
Multistar High Capacity 6S 8000mAh	8.0 <i>Ah</i>	956 <i>g</i>	142 x 63 x 49 <i>mm</i>	201 <i>Wh/kg</i>
Multistar High Capacity 6S 10 000mAh	10.0 <i>Ah</i>	1320 <i>g</i>	170 x 69 x 56 <i>mm</i>	182 <i>Wh/kg</i>

Table A.8: Overview of the ordered batteries to test in flight.

B Mass Estimation

To be able to compare the resulting flight duration of different configurations, their masses have to be known. Because of legal limitations (see Section 1.5) the takeoff weight is fixed to $MTOW = 5 \text{ kg}$ but the maximum battery size that can be carried depends on the empty weight which varies from configuration to configuration.

Knowing only the rotor diameters and rotor distances, the mass estimation during conceptual design is not an easy task. The weights of motors and propellers of the same size can vary from manufacturer to manufacturer and the structural weight of the airframe strongly depends its structural design, which has not been determined at this stage. Therefore, empirical and statistical data from other multirotor aircraft have to be used. It is, however, important to compare the empty weights of the different configurations and to understand, how the differences are linked to the unique features of each configuration.

B.1 Propulsion System

B.1.1 Propeller

If the propeller chord is scaled according to Eq. (5.8.9) this results in a propeller whose entire geometry is scaled linearly and this consequently means, considering a solid object build from a uniform density material, that the propeller mass scales with the third power of the its diameter.

In reality the propeller hub will not be scaled linearly for the most propellers because the shaft diameter does not increase linearly for larger propellers. Figure B.1 shows the masses of different two-bladed propellers suitable for multirotor aircraft operation (e.g. available in clockwise and counterclockwise direction of rotation) manufactured by the company APC. As expected due of the non-linearly scaled propeller hub the mass is less than predicted by a third power scaling law. As shown in Figure B.1 a power law of $m_2 = m_1 \cdot (D_2/D_1)^{2.72}$ fits well.

It can be observed that configurations with larger propellers have a slight disadvantage over the ones with many small propellers because the propeller diameters have been scaled for a constant disc loading hence the second power of the propeller diameter. The propellers chosen for mass estimation are listed in Table B.1. When considering larger propellers a significant amount of weight can be saved if carbon fiber propellers or carbon fiber propeller blades in combination with a metal propeller hub are used. Those items are available from Tarot-RC or T-Motor but have not been included explicitly in the mass estimation due to budget constrains.

No. of propellers	Propeller Type	Propeller weight
$N = 4$	APC 19x8E; APC 19x10E; APC 19x12E	98 g
$N = 6$	APC 16x10E; APC 16x8E	56 g
$N = 8$	APC 13x4E; APC 13x6.5E; APC 13x8E	33 g

Table B.1: Propellers chosen for mass estimation.

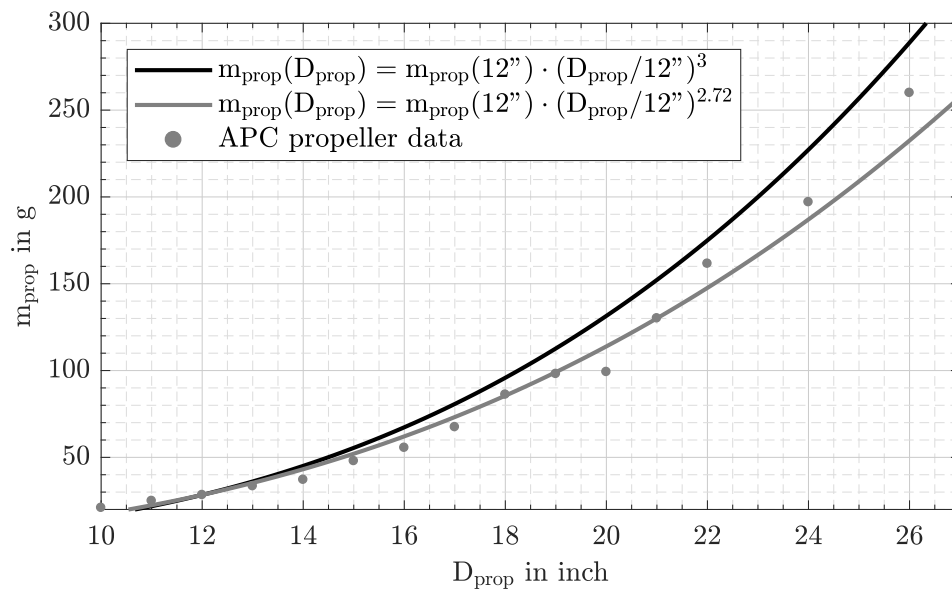


Figure B.1: Propeller weights at different propeller diameters, usually given by the manufacturer in inch.

B.1.2 Motor

Many different brushless electric motors are commercially available for multirotor operation. So called "outrunner" brushless DC motors have become very popular for direct drive propulsion systems especially for multirotor aircraft.

For a brushless motor in the field of model aircraft / UAV it is common to define the parameter k_V , which is a measure for the rotational speed of the motor depending on its operating voltage. Using the parameter k_V leads to the rotational speed of the motor in min^{-1} :

$$n_{no-load} = k_V \cdot U_{batt} \tag{B.1.1}$$

It is important that a battery voltage under load has to be used for Eq. (B.1.1) instead of the nominal voltage (e.g. 3.7 V per cell) and that the rotational speed resulting from Eq. (B.1.1) is a no load speed. A rule of thumb is that the load speed will be about 80 % of the no load speed.

To determine how the motor weight will change with the propeller size, manufacturer data for 68 different motors has been collected. Figure B.2 shows that the scatter of this data is very high but in general motors with a lower k_V also have a higher output power. It is difficult to find a motor with a low k_V value and a low output power.

Figure B.2 shows also that there is no direct tendency for the power to weight ratio to change with the motor size, but there is also high scatter to this data.

In general manufacturer specifications in the model airplane / multirotor sector have to be used carefully, because they have not been validated. Often it is not defined clearly if a given power value is the mechanical output power or the electrical input power and some manufacturers are simply exaggerate their data. In some cases it could be even observed that the specified weight could not be met by the series product available for tests.

Because of the high scatter of data different motors have been selected and the average mass was used instead of using one specific motor. The motors selected for the mass estimation are shown in Table B.2.

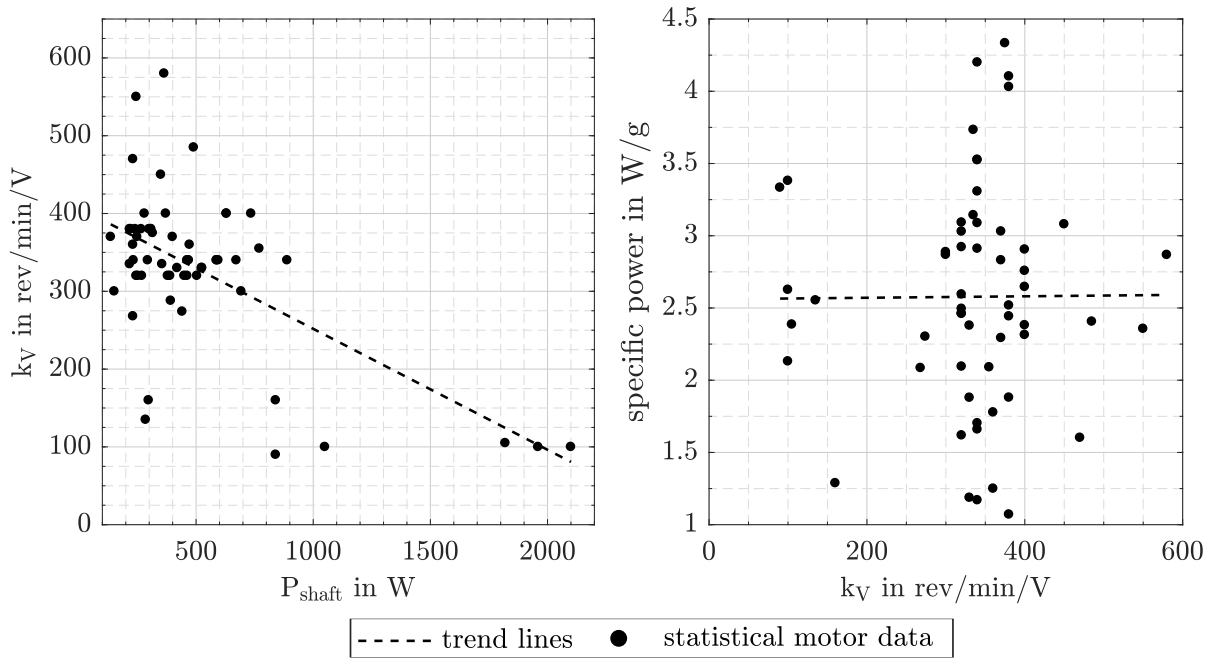


Figure B.2: Statistical data on motor k_v over motor power (left) and specific motor weight over motor k_v (right) collected from several manufacturers.

N propellers	Motor Type	$P_{mech,max}$	Motor k_v	Motor weight
$N = 4$	T-Motor MT3520	693 W	300 min^{-1}/V	205 g
	T-Motor MN5208	595 W	340 min^{-1}/V	145 g
	Multistar Elite 5010	441 W	274 min^{-1}/V	211 g
	Multistar Elite 5008	420 W	320 min^{-1}/V	183 g
	Gartt ML5210	672 W	340 min^{-1}/V	230 g
	Emax MT5210	298 W	160 min^{-1}/V	231 g
				201 g
$N = 6$	T-Motor MN4012	462 W	340 min^{-1}/V	131 g
	T-Motor Antigravity MN4006	266 W	380 min^{-1}/V	70 g
	T-Motor MN5208	595 W	340 min^{-1}/V	145 g
	Xnova MS4812	379 W	320 min^{-1}/V	161 g
	ARRIS 4010 Pro	308 W	380 min^{-1}/V	82.5 g
				118 g
$N = 8$	T-Motor Antigravity MN4006	266 W	380 min^{-1}/V	70 g

Table B.2: Motors chosen for the mass estimation. If the output power was not specified directly a motor efficiency of $\eta_{motor} = 70\%$ has been assumed.

B.1.3 ESCs

The ESCs, electronic speed controllers, for electric brushless DC motors have become lighter every couple of years because of smaller and lighter MOSFETs.

At the same time, most ESCs for multicopter use are operated with the BLHELI firmware (see [108]), which results in a smoother motor operation (compare Section A.4). The new, small, light weight ESCs with BLHeli firmware are usually available at very low cost (often below \$10) from manufacturers from the far-east and are mostly used in small, low cost racing drones.

Because there is not much experience on the use of those tiny ESCs in larger vehicles, BULL TEC 30A ESC, also used for the SWE hexrotor, was used for the mass estimation. This ESC weighs 25 g and is available locally. From visual comparisons it is assumed that this ESC is manufactured by ZTW Technology Co., Ltd. in Shenzhen, China and is originally sold under the name "Spider 30A OPTO ESC".

Previous experiences show that it is not recommended to use ESCs with a lower current capability for the configurations with smaller rotors because high current peaks during maneuvers can occur. Consequently, the overall ESC weight does not scale with the number of rotors. Even if ESCs with higher current capabilities should be used for the quadrotor configuration, the larger ESCs do not scale with the number of rotors. The 40A ESC version of the above mentioned ESC weighs for example $m_{ESC} = 33$ g instead of $m_{ESC} = 25$ g.

The highest weight saving potential is the use of newer, smaller light-weight ESCs and will be tested in the future. For example another ESC from ZTW, sold as "Spider Pro", using smaller MOSFETs weighs only $m_{ESC} = 11$ g instead of $m_{ESC} = 25$ g in the 30 A version.

B.1.4 Wiring

Silicon wires with a cross section of $A_{wire} = 1.5$ mm² and a weight of $m_{wire} = 19$ g/m have been assumed for all configurations. This corresponds to a cross section of approx. 16AWG in the american system and most ESCs and motors of the considered size are factory equipped with such wires. In general for a very light weight design, it would be possible to adjust the wire cross section and use thinner wires for the octorotor configuration than for the quadrotor and hexarotor configuration. But this adds an additional risk, because thinner wires are less robust, especially if they have to withstand the tilt movement of the motor arms. Consequently, thinner wires were not taken into account.

Table B.3 shows the different wire weights for all configurations, using the following equation:

$$m_{wiring} = (19 \text{ g/m} \cdot (y d_{rotor}/2 + x d_{rotor}/2)) \cdot N_{rotors} \quad (\text{B.1.2})$$

Configuration	Weight of propulsion system wiring
H-4	153 g
Y-6	179 g
H-6	226 g
H-8	303 g
H-8 parallel	343 g

Table B.3: Resulting wire weights for the different configurations.

B.1.5 Conclusion

The differences in the propulsion system weight for all the configurations are small. The total weight of the propulsion system is mostly driven by two opposing effects:

On one hand, the configurations with a smaller number of rotors suffer from a non-linear scaling law. For example, one motor for the quadrotor configuration is heavier than two of the motors for the octotorotor configuration and the same applies to the propellers.

On the other hand, the configurations with a larger number of rotors suffer from the multiple use of small parts and wires, whose weight cannot be reduced. For example, all motors need propeller adapters to attach the propellers and every single propulsion unit needs a motor mount and motor mounting screws. The weight of these items are similar for different motor and propeller sizes. Furthermore, for the configurations with a higher number of propellers, the weight of the higher number of ESCs and longer motor wires cannot be reduced to the necessary extent.

As shown in Table B.4, with the assumptions made here, these two lead to only small variations in the total weight of the propulsion system.

Configuration	Overall weight of propulsion system
H-4	1574 g
Y-6	1573 g
H-6	1620 g
H-8	1578 g
H-8 parallel	1618 g

Table B.4: Resulting overall weight of the propulsion system for the different configurations.

B.2 Structure

B.2.1 Airframe

To get a rough estimate of the airframe weight the weight and area of the SWE hexrotor CFRP frame was determined with the help of CAD drawings. This weight was then scaled to the actual frame size for each configuration:

$$m_{frame} = m_{frame,hexa} \cdot \frac{A_{frame}}{A_{frame,hexa}} = m_{frame,hexa} \cdot \frac{l_{frame} \cdot w_{frame}}{A_{frame,hexa}} \quad (\text{B.2.1})$$

Length l_{frame} and width w_{frame} have been taken from the parametric CAD models set up for the overall aerodynamic simulation (compare Figure 5.84). The rotor distances yd_{rotor} and xd_{rotor} in these models have been scaled according to equal control moments (see Section 5.9).

B.2.2 Motor Arms

For all configurations except the H-8 parallel configuration CFRP tubes with an outer diameter of $D_{arm} = 24 \text{ mm}$, an inner diameter of $d_{arm} = 22 \text{ mm}$ and a specific weight of $ms_{arm} = 114 \text{ g/m}$ have been used (see [109]). For the H-8 parallel configuration with its very long motor arms a CFRP tube with an outer diameter of $D_{arm} = 28 \text{ mm}$, an inner diameter of $d_{arm} = 26 \text{ mm}$ and a specific weight of $ms_{arm} = 136 \text{ g/m}$ (see [110]) has been assumed.

B.2.3 Tilt Mechanism

The following components have been included in the weight estimation for each of the tilt mechanisms:

- Two thin section bearings of type INA CSCAA10 which allow the CFRP motor arms to fit inside. The weight according to manufacturer for each of the two bearing is: $m_{bearing} = 10\text{ g}$.
- One tilt servo actuator of type Savox SC-1267SG with a weight of $m_{servo} = 62\text{ g}$.
- The mounts for bearings and motor arms inside the frame are assumed to be similar to the motor mounts and hence were taken into account with $m_{tiltmounts} = 30\text{ g}$.
- Levers and push-pull rods have been considered with $m_{lever} = 15\text{ g}$.
- Miscellaneous items (screws etc.) have been taken into account with $m_{misc} = 10\text{ g}$.

The components above results in $m_{tilt} = 137\text{ g}$ for each tilt mechanism. For all configurations except the H-6 and Y-6 frame two tilt mechanisms have been taken into account which means that differential tilting between left and right hand side is not possible. For the H-6 frame three tilt mechanisms are necessary and for the Y-6 configuration a third tilt mechanism for the tail boom has been included.

B.3 Aerodynamic Cover

The weight of an aerodynamic cover has been roughly accounted for with the following estimation:

$$m_{cover} = m_{scover} \cdot (l_{frame} \cdot w_{frame}) \cdot 1.5 \quad (\text{B.3.1})$$

Where m_{scover} is the specific areal weight of the cover, estimated by $m_{scover} = 600\text{ g/m}^2$. This corresponds to a thin layer of paint, one layer of 50 g m^2 GFRP and one layer of 160 g/m^2 spread tow CFRP and should result in a relatively stiff cover. The factor 1.5 is introduced to account for the three-dimensional shape of the cover. Table B.5 shows the different cover weights.

The main bodies of the different configurations are all of similar size and a cover of the motor arms has not been taken into account. This means, there is not much difference between the configurations except the cover weight of the H-6 configuration with its significantly longer main body.

Configuration	Weight of an aerodynamic cover
H-4	88 g
Y-6	61 g
H-6	128 g
H-8	86 g
H-8 parallel	86 g

Table B.5: Weights estimates of an aerodynamic cover for the different configurations.

B.4 Payload

For all configurations a payload consisting of the following components has been planned:

- Measurement boom: A CFRP tube with $D = 14 \text{ mm}$ and $d = 13 \text{ mm}$ at a specific weight of $m_{sboom} = 31 \text{ g/m}$ will be used as measurement boom. This leads to total weight between $m_{boom} = 36 \text{ g}$ and $m_{boom} = 37 \text{ g}$ for all configurations, because the distance from the front position of the frame to the C.G. is similar for all configurations, resulting in a similar boom length for all configurations.
- Hot wire assembly: The hot wire probes including the necessary mount and everything mounted at the tip of the measurement boom was accounted for with $m_{hot-wire} = 50 \text{ g}$.
- Hot wire battery: A separate battery for the measurement equipment was taken into account with $m_{bat,measure} = 150 \text{ g}$.
- Hot wire electronics: The CTA and data processing electronics was accounted for with $m_{electronics,measure} = 300 \text{ g}$.
- Cables of the measurement electronics: The wiring harness from the tip of the measurement boom to the electronics was estimated as $m_{wiring,measure} = 30 \text{ g}$.
- Separate IMU: To compensate for possible movements of the measurement boom, a separate IMU of type GY512 at the tip of the boom is necessary, estimated at $m_{IMU,measure} = 5 \text{ g}$.

This results in a payload of roughly $m_{payload} = 570 \text{ g}$. Even if the payload is nearly the same for all configurations it is important to include it in the overall mass to achieve a realistic flight time prediction. Less payload will result in a larger flight battery.

B.5 Other Components

B.5.1 Flight Control Systems

For the flight control system and all systems necessary for the operation of ANDroMeDA the following assumptions have been made:

- GPS: $m = 17 \text{ g}$
- BEC: $m = 20 \text{ g}$
- Flight controller: $m = 72 \text{ g}$
- Signal and sensor wiring: $m = 30 \text{ g}$
- Power sensors: $m = 15 \text{ g}$
- Other operational sensors: $m = 20 \text{ g}$
- Power distribution board: $m = 8 \text{ g}$

The used flight controller was estimated with a weight of $m = 72 \text{ g}$ which is twice the weight of the Pixhawk I flight controller.

B.5.2 Miscellaneous

Various other items have been included in different groups of the mass estimation such as:

- Landing gear: $m = 50\text{ g}$
- GPS tower: $m = 8\text{ g}$
- Autopilot mount: $m = 20\text{ g}$
- Measurement boom mount to attach and detach the measurement boom: $m = 40\text{ g}$
- Battery holder: $m = 10\text{ g}$

In addition, a weight of $m_{misc} = 200\text{ g}$ has been included to account for items not considered above.

B.6 Conclusions

Figure B.3 and Table B.6 illustrate the overall weights of all configurations. The differences between the H-4, Y-6 and H-8 coaxial configuration are marginal. The H-6 and H-8 parallel configuration are about 500 g and 400 g heavier.

The H-6 configuration has a higher structural weight resulting from a larger frame and a higher total motor arm length. The third tilt mechanism also adds 137 g to the list. The Y-6 configuration, which has also three tilt mechanisms instead of two, can compensate for the increased weight with a reduced overall motor arm length.

The H-8 parallel configuration carries an additional weight mostly due to the longer and heavier motor arms.

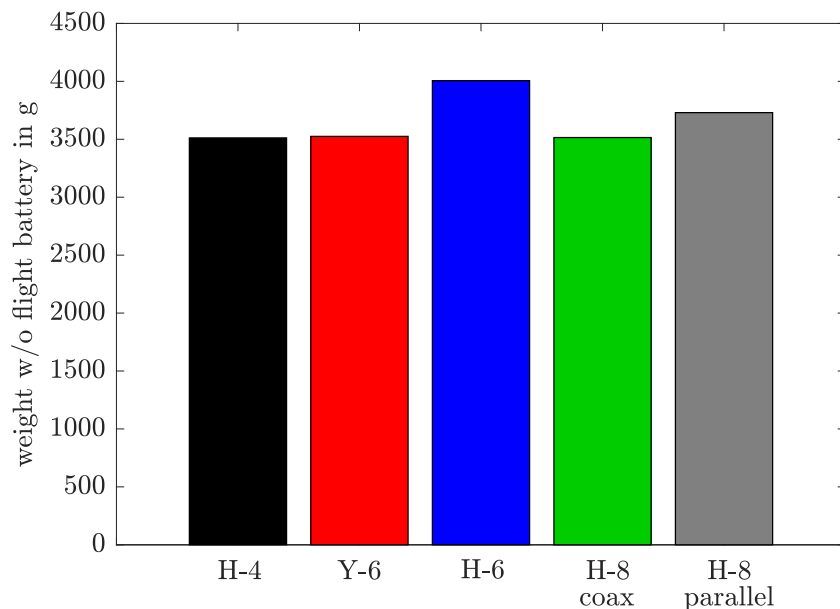


Figure B.3: Comparison of the system empty weight without flight battery for all configurations. The payload is included.

	H-4	Y-6	H-6	H-8	H-8 parallel
Propulsion	1574 <i>g</i>	1573 <i>g</i>	1620 <i>g</i>	1578 <i>g</i>	1618 <i>g</i>
Structure	628 <i>g</i>	527 <i>g</i>	892 <i>g</i>	624 <i>g</i>	799 <i>g</i>
Cover	88 <i>g</i>	61 <i>g</i>	128 <i>g</i>	86 <i>g</i>	86 <i>g</i>
Tilt Mechanisms	274 <i>g</i>	411 <i>g</i>	411 <i>g</i>	274 <i>g</i>	274 <i>g</i>
Payload	571 <i>g</i>	572 <i>g</i>	572 <i>g</i>	571 <i>g</i>	571 <i>g</i>
Flight Control	182 <i>g</i>	182 <i>g</i>	182 <i>g</i>	182 <i>g</i>	182 <i>g</i>
Misc	200 <i>g</i>	200 <i>g</i>	200 <i>g</i>	200 <i>g</i>	200 <i>g</i>
Sum	3512 <i>g</i>	3525 <i>g</i>	4006 <i>g</i>	3516 <i>g</i>	3730 <i>g</i>

Table B.6: Results of the mass estimation for all configurations.

C Flight Mechanical Simulation Model

ANDroMeDA has been included in a Matlab/Simulink model, developed at the Flight Mechanics and Controls Lab at the University of Stuttgart (IFR), that is able to solve the equations of motions for multi-body systems in moving coordinates (tilting rotors), utilizing D'Alembert's principle in the Lagrangian formulation. The flight mechanical model can be used to develop a controller for ANDroMeDA and in addition to evaluate the closed loop flight performance in windy conditions.

C.1 Inertia

The inertia tensors of the motor arms, including propellers and motors, as well as the entire aircraft have derived from the detailed CAD model. Other than a regular multirotor aircraft, ANDroMeDA is not symmetric in the x-direction because of the long measurement boom. Consequently, all components had to be modeled with the correct masses in CAD to determine the C.G. and the resulting battery position. The resulting Inertia tensor of the ANDroMeDA-1 CAD model is:

$$I = \begin{bmatrix} 1.59E + 8 & 6.75E + 5 & -2.36E + 5 \\ 6.72E + 5 & 3.41E + 8 & -4.00E + 4 \\ -2.36E + 5 & -4.01E + 4 & 4.93E + 8 \end{bmatrix} \cdot g \cdot mm^2 \quad (C.1.1)$$

This tensor was determined with a single 6200mAh flight battery and a take-off weight of $TOW = 4.55 \text{ kg}$. Assuming two 4000mAh flight batteries and a take-off weight of $TOW = 5.0 \text{ kg}$ it changes slightly. Compared to the conceptual design the component I_{xx} increased about 30% while the component I_{yy} decreased by 25% and the component I_{zz} decreased by 15%.

C.2 Aerodynamics

The aerodynamic forces have been determined from the overall aerodynamic simulation of the H-4 frame (see Section 5.10). Aerodynamic moments have been neglected since a multirotor is normally symmetric.

The most simple approach is to assume a constant drag coefficient c_D that is independent of the inflow direction. This is an acceptable simplification, if a multirotor aircraft with a nearly symmetric shape has to be modeled, as for example the SWE hexrotor with its huge camera gimbal at the bottom.

For a slim, asymmetric airframe like the ANDroMeDA airframe, this simplification leads to large errors. Consequently, the aerodynamic forces have been modeled with the next higher level of fidelity using linear, quasi-steady aerodynamics in the following formulation:

$$\mathbf{F}_{\text{aero}} = \mathbf{F} \cdot \mathbf{q} = \begin{bmatrix} f_{11} & f_{12} & f_{13} \\ f_{21} & f_{22} & f_{23} \\ f_{31} & f_{32} & f_{33} \end{bmatrix} \cdot \begin{bmatrix} u^2 \\ v^2 \\ w^2 \end{bmatrix} \quad (C.2.1)$$

The coefficients of the matrix \mathbf{F} are dimensional in the form of $c_D \cdot A \cdot \rho/2$. To emphasize the capabilities and limitations of this linear model, it is applied to calculate lift L and drag D resulting from a two dimensional flow past an airfoil:

$$\mathbf{F}_{\text{aero}} = \begin{bmatrix} D \\ L \end{bmatrix} = \begin{bmatrix} f_{11} & f_{12} \\ f_{21} & f_{22} \end{bmatrix} \cdot \begin{bmatrix} u^2 \\ w^2 \end{bmatrix} \quad (\text{C.2.2})$$

For a symmetric airfoil f_{11} is also the no-lift drag coefficient c_{d_0} . Furthermore, in case of a symmetrical airfoil, f_{12} and f_{21} will be zero. The coefficient f_{22} can be used either to model the drag at an angle of attack of $\alpha = 90^\circ$ or to adjust the lift curve slope c_{a_α} to match smaller angles of attack. This leads to the lift coefficient in the form of $c_l(\alpha) = c_{a_\alpha} \cdot \alpha$.

If a non-symmetric airfoil has to be modeled, f_{12} and f_{21} can be used to rotate the no-lift angle of attack to a specific value. Since the flow components can be written as $u = \cos(\alpha) \cdot v_\infty$ and $v = \sin(\alpha) \cdot v_\infty$, lift and drag over the full 360° range of angle of attack will always be of sinusoidal form.

When a real airfoil over the full 360° range of α is considered, there will be a flow separation (stall), leading to a strong decrease of lift at approx. $\alpha = 15^\circ$ to $\alpha = 30^\circ$, a slight recovery in lift until approx. $\alpha = 45^\circ$ and finally the lift will decrease to zero at $\alpha = 90^\circ$ (compare the airfoil modeling for BEM simulations in Section A.1). This phenomena cannot be covered with the linear model.

If such a flow separation occurs and how much the linear drag model deviates from reality, depends strongly on the shape of the airframe. To model non-linear aerodynamics the coefficients of \mathbf{F} have to be expressed as a function of α and β either as a mathematical formulation or in form of a lookup table. In [111] a non-linear, quasi-steady aerodynamic model for multirotor aircraft has been presented, combined with an unsteady aerodynamic model, suitable for highly dynamic maneuvers with fast changes of the inflow direction. In [112] it is shown that the quasi-steady model is already quite accurate.

In case of the ANDroMeDA frame a simulation of the basic H-4 configuration at $\alpha = 0^\circ; \beta = 0^\circ$ at nominal thrust has been used to determine the the coefficient f_{11} . Another simulation at $\alpha = 0^\circ; \beta = 90^\circ$ at nominal thrust has been used for the coefficient f_{22} and finally a third simulation at $\alpha = 90^\circ; \beta = 0^\circ$ at zero thrust has been used to determine the coefficient f_{33} .

Because the rotor downwash is pointing backwards at $\beta = 90^\circ$ (see Figure 5.79), non-zero off-diagonal elements exist in \mathbf{F} . These elements have been neglected, because they are small compared to the main elements. The final aerodynamic coefficient matrix is:

$$\mathbf{F} = \begin{bmatrix} 0.0476 & 0 & 0 \\ 0 & 0.0529 & 0 \\ 0 & 0 & 0.133 \end{bmatrix} \quad (\text{C.2.3})$$

To evaluate the use of the linear model, two additional simulations have been carried out at $\alpha = 0^\circ; \beta = 10^\circ$ and $\alpha = 0^\circ; \beta = 25^\circ$. This test showed an error in the resulting forces of less than 6 %, which is acceptable for the flight simulation.

C.3 Propeller Thrust and Torque

The propeller thrust and torque was modeled by Eqs. (A.2.2 and A.2.3), with factors $\alpha_T = c_T \cdot \rho \cdot A \cdot R^2 = 5.211 \cdot 10^{-5} \text{ N} \cdot \text{s}^2$ and $\alpha_Q = c_Q \cdot \rho \cdot A \cdot R^3 = 13.85 \cdot 10^{-7} \text{ Nm} \cdot \text{s}^2$, according

to whirl tower measurements with Fiala 14x8 propellers. The propeller and motor dynamics has not been modeled, but since the bandwidth of the attitude controller is set low enough to avoid sudden jumps in the commanded RPM, this can be neglected.

C.4 Simulation Results with Changing Wind Speed and Wind Direction

Three extreme wind scenarios, found in Chapter 2, have been entered in the complete simulation chain, including the simplified physical model, described above, and a baseline flight controller, consisting of an attitude controller affecting the propellers rotational speeds and a translational controller directly affecting the tilt angle of the four motor arms.

The results for the IEC gust are shown in Figure C.1 and demonstrate that the maximum

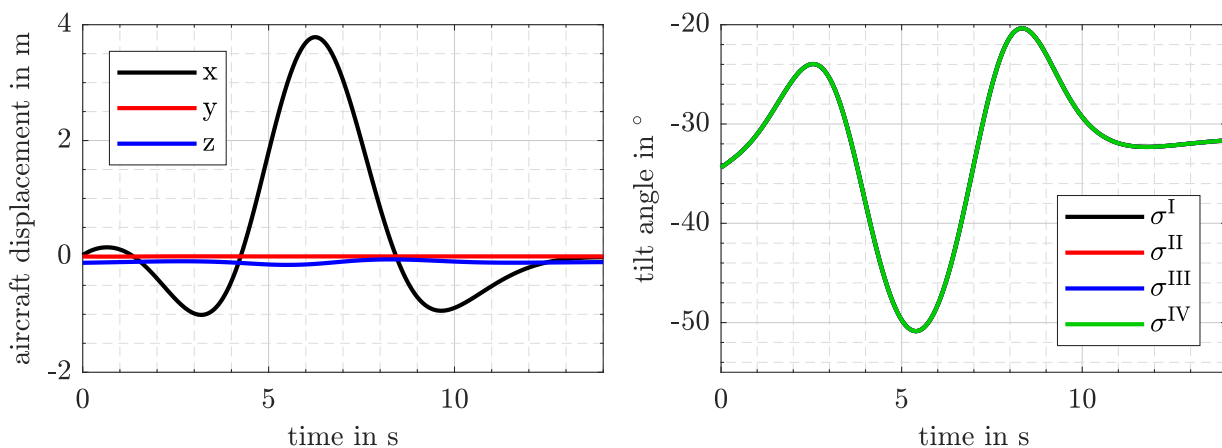


Figure C.1: Simulation results for an IEC gust input described in Chapter 2.

displacement in the longitudinal direction is $\Delta x_{max} = 4 \text{ m}$. Considering the very high wind speeds, this is acceptable but might still seem large. However, it is important to take into consideration that the baseline controller is a velocity controller and not a real position controller, which means that, if it cannot achieve the targeted zero velocity at all times, this will result in a permanent displacement, which will not be corrected after the wind speed decreases again. Also the controller has a relatively low bandwidth, which can be observed by the low tilt actuation speed, which is slower than the maximum tilt actuation speed identified in Section A.5.

On the other hand, this ideal simulation does include many simplifications and cannot regard real-life effects like sensor noise and play in the actuators. Consequently, it is difficult to predict the overall system behaviour with a position controller at real wind disturbances. The actual position keeping performance of ANDroMeDA-1 has to be investigated carefully during test flights. Nevertheless, the simulation is a valuable tool to check physical limitations and reveal problems. For example, from Figure C.1 it can also be seen that the maximum tilt angle is $\sigma = 50^\circ$ for all four motor arms, because of the high wind speed, which is close to the physical tilt limit.

The simulation results with wind speed measurements from the site of Stötten (compare Chapter 2) are shown in Figure C.2. Even if the wind speed time derivative is much larger, the maximum displacement is also about $\Delta x_{max} = 4 \text{ m}$. Since the extreme wind conditions used from the IEC gust and Stötten are one-dimensional, there is no attitude change about the longitudinal axis and no lateral displacement of the aircraft. With the wind measurements from FINO, in three components of the wind vector u, v, w and a maximum lateral wind speed of $v = 3.3 \text{ m/s}$, used as

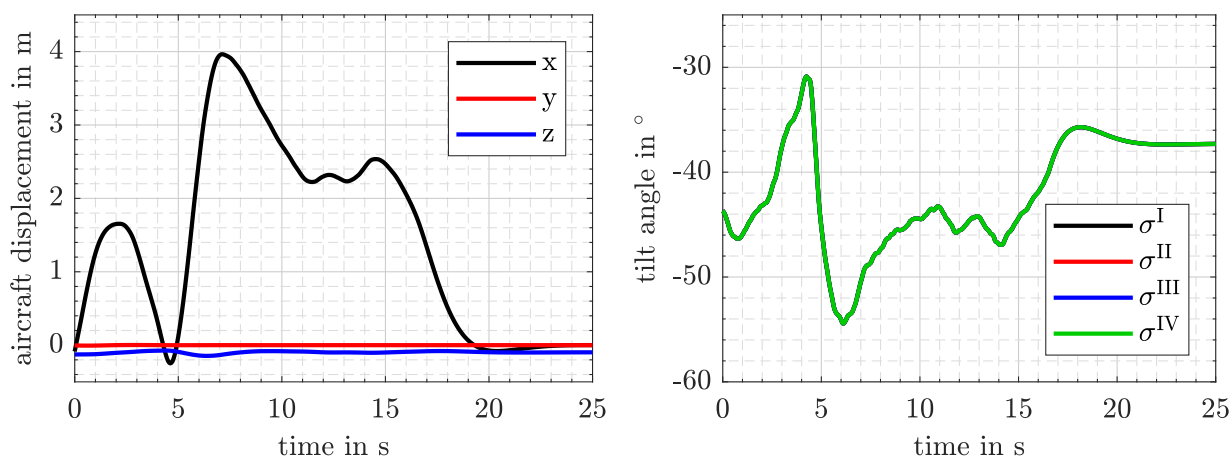


Figure C.2: Simulation results of a wind speed time series input gained from Stötten measurements.

a simulation input, the maximum lateral displacement of the aircraft is less than $\Delta y = 0.08 \text{ m}$, while a bank angle of less than half a degree is needed to compensate for the resulting side force.

D Notch Filter Class

```
#include <px4_defines.h>
#include "NotchFilter.hpp"
#include <cmath>

namespace math
{

void NotchFilter::init(float sample_freq_hz, float center_freq_hz,
float bandwidth_hz, float attenuation_dB)
{
_center_freq = center_freq_hz;
_bandwidth = bandwidth_hz;
_attenuation = attenuation_dB;

if (_center_freq <= 0.0f){
// no filtering
return;
}

float omega = 2.0f * 3.141592653589793f * _center_freq / sample_freq_hz;
float octaves = log2f(_center_freq / (_center_freq - _bandwidth/2)) * 2;
float A = powf(10, -_attenuation/40);
float Q = sqrtf(powf(2, octaves)) / (powf(2,octaves) - 1);
float alpha = sinf(omega) / (2 * Q/A);
_b0 = 1.0f + alpha*A;
_b1 = -2.0f * cosf(omega);
_b2 = 1.0f - alpha*A;
_a0_inv = 1.0f/(1.0f + alpha/A);
_a1 = -2.0f * cosf(omega);
_a2 = 1.0f - alpha/A;

}

float NotchFilter::apply(float sample)
{
if (_center_freq <= 0.0f) {
// no filtering
return sample;
}

// do the filtering
```

```
_ntchsig2 = _ntchsig1;
_ntchsig1 = _ntchsig;
_ntchsig = sample;
float output = (_ntchsig*_b0 + _ntchsig1*_b1 + _ntchsig2*_b2 - _signal1*_a1 -
_signal2*_a2) * _a0_inv;
_signal2 = _signal1;
_signal1 = output;
return output;
}

float NotchFilter::reset(float sample)
{
_ntchsig = 0.0f;
_ntchsig1 = 0.0f;
_ntchsig2 = 0.0f;
_signal1 = 0.0f;
_signal2 = 0.0f;
return apply(sample);
}

} // namespace math
```

Bibliography

- [1] *History of Lidar*, <https://www.zxlidars.com/wind-lidar-history/>, accessed: 2019-01-07.
- [2] T. Mikkelsen, M. Sjöholm, N. Angelou, and J. Mann, ‘3D WindScanner Lidar Measurements of Wind and Turbulence around Wind Turbines, Buildings and Bridges’, *IOP Conference Series: Materials Science and Engineering*, vol. 276, no. 1, p. 012 004, 2017.
- [3] S. Raach, D. Schlipf, F. Haizmann, and P. W. Cheng, ‘Three Dimensional Dynamic Model Based Wind Field Reconstruction from Lidar Data’, *Journal of Physics: Conference Series*, vol. 524, no. 1, p. 012 005, 2014.
- [4] V. Charles F. Woodhouse Clifton Forge, ‘Wind Monitoring Assembly And Method’, U.S. pat. 4,152,933, 1979.
- [5] G. Giebel, U. Schmidt Paulsen, J. Bange, A. La Cour-Harbo, J. Reuder, S. Mayer, A. van der Kroonenberg, and J. Mølgaard, *Autonomous Aerial Sensors for Wind Power Meteorology - A Pre-Project*, English. Danmarks Tekniske Universitet, Risø Nationallaboratoriet for Bæredygtig Energi, 2012.
- [6] *Aerones - tethered heavy-lift drone*, https://www.aerones.com/eng/wind_turbine_maintenance_drone/, accessed: 2019-01-07.
- [7] S. Prudden, A. Fisher, M. Marino, A. Mohamed, S. Watkins, and G. Wild, ‘Measuring wind with Small Unmanned Aircraft Systems’, *Journal of Wind Engineering and Industrial Aerodynamics*, vol. 176, pp. 197–210, 2018.
- [8] V. Berkhout, D. Bergmann, R. Cernusko, M. Durstewitz, and S. Faulstich, *Windenergie Report Deutschland 2016*. Fraunhofer Verlag, May 19, 2017, 116 pp.
- [9] B. Wrenger and J. Cuxart, ‘Evening Transition by a River Sampled Using a Remotely-Piloted Multicopter’, *Boundary-Layer Meteorology*, vol. 165, no. 3, pp. 535–543, Dec. 2017.
- [10] S. Kral, J. Reuder, T. Vihma, I. Suomi, E. O’Connor, R. Kouznetsov, B. Wrenger, A. Rautenberg, G. Urbancic, M. Jonassen, L. Båserud, B. Maronga, S. Mayer, T. Lorenz, A. A. M. Holtslag, G.-J. Steeneveld, A. Seidl, M. Müller, C. Lindenberg, and M. Schygulla, ‘Innovative Strategies for Observations in the Arctic Atmospheric Boundary Layer (ISO-BAR)—The Hailuoto 2017 Campaign’, *Atmosphere*, vol. 9, p. 268, Jul. 2018.
- [11] T. Shimura, M. Inoue, H. Tsujimoto, K. Sasaki, and M. Iguchi, ‘Estimation of wind vector profile using a hexa-rotor unmanned aerial vehicle and its application to meteorological observation up to 1000 m above surface’, *Journal of Atmospheric and Oceanic Technology*, vol. 35, Jun. 2018.
- [12] S. Prudden and S. Watkins, ‘A Flying Anemometer Quadrotor: Part 1’, in *International Micro Air Vehicle Competition and Conference 2016*, Beijing, PR of China, Oct. 2016, pp. 15–21.
- [13] F. Carbajo Fuertes, ‘Innovative Measurement Techniques for Atmospheric Turbulence and Wind Energy’, *Dissertation - École Polytechnique Fédérale de Lausanne*, 2018.

- [14] A. Dobrindt, ‘Verordnung zur Regelung des Betriebs von unbemannten Fluggeräten’, *Bundesgesetzblatt Jahrgang 2017 Teil I Nr. 17*, Apr. 6, 2017.
- [15] A. Turnipseed, D. Anderson, P. D Blanken, W. M Baugh, and R. K Monson, ‘Airflows and Turbulent Flux Measurements in Mountainous Terrain: Part 1. Canopy and Local Effects’, *Agricultural and Forest Meteorology*, vol. 119, pp. 1–21, Oct. 2003.
- [16] E. Johnson, M. Turbe, A. Wu, S. Kannan, and J. Neidhoefer, ‘Flight Test Results of Autonomous Fixed-Wing UAV Transitions to and from Stationary Hover’, English (US), in *Collection of Technical Papers - AIAA Guidance, Navigation, and Control Conference 2006*, vol. 8, Dec. 2006, pp. 5144–5167.
- [17] U. Butter, *Addition to Lecture Manuscript - Flight Mechanics and Flight Control for Helicopters*, Flight Mechanics and Controls Lab - University of Stuttgart, 2010.
- [18] H. Glauert, *A General Theory of the Autogyro*, ser. Reports and memoranda. H.M. Stationery Office, 1928.
- [19] L. P. Yip, ‘Wind-Tunnel Free-Flight Investigation of a 0.15-Scale Model of the F-106B Airplane with Vortex Flaps’, NASA Langley Research Center; Hampton, VA, United States, Tech. Rep., May 1, 1987.
- [20] J. Nowack, ‘Windkanal-Freiflugmessungen zur Bestimmung flugmechanischer Kenngrößen’, Aachen, Techn. Hochsch., Diss., 2010, PhD thesis, RWTH Aachen University, Aachen, 2010, XVII, 162 S. : Ill., graph. Darst.
- [21] J. Milbank, B. Loxton, S. Watkins, and W. H. Melbourne, ‘Replication of Atmospheric Conditions for the Purpose of Testing MAVs MAV Flight Environment Project: Final Report’, RMIT University, Tech. Rep. USAF Project No: AOARD 05-4075, Dec. 23, 2005.
- [22] S. Watkins, M. Abdulrahim, and M. Shortis, ‘Mitigating the Effects of Atmospheric Turbulence: Towards More Useful Micro Air Vehicles’, RMIT University, Tech. Rep., Jul. 18, 2010.
- [23] A. Panta, ‘Qualitative Investigation of the Dynamics of a Leading Edge Control Surfaces for MAV Applications’, in *9th International Micro Air Vehicle Conference and Flight Competition (IMAV 2017)*, Sep. 2017.
- [24] R. Gigacz, A. Mohamed, P. Poksawat, A. Panta, and S. Watkins, ‘Exploring Tandem Wing UAS Designs for Operation in Turbulent Urban Environments’, *International Journal of Micro Air Vehicles*,
- [25] A. Cuerva and A. Sanz-Andrés, ‘On Sonic Anemometer Measurement Theory’, *Journal of Wind Engineering and Industrial Aerodynamics*, vol. 88, no. 1, pp. 25–55, 2000.
- [26] T. Nakai and K. Shimoyama, ‘Ultrasonic Anemometer Angle of Attack Errors under Turbulent Conditions’, *Agricultural and Forest Meteorology*, vol. 162-163, pp. 14–26, 2012.
- [27] S. Franchini, A. Sanz-Andrés, and A. Cuerva, ‘Effect of the Pulse Trajectory on Ultrasonic Fluid Velocity Measurement’, *Experiments in Fluids*, vol. 43, no. 6, pp. 969–978, Dec. 2007.
- [28] M. W. Starnes, ‘The Study of an Acoustic Resonance Anemometer’, PhD thesis, University of London - Imperial College London, 2010.
- [29] K. Bärffuss, F. Pätzold, B. Altstädter, E. Kathe, S. Nowak, L. Bretschneider, U. Bestmann, and A. Lampert, ‘New Setup of the UAS ALADINA for Measuring Boundary Layer Properties, Atmospheric Particles and Solar Radiation’, *Atmosphere*, vol. 9, no. 1, 2018.

-
- [30] N. Wildmann, S. Ravi, and J. Bange, ‘Towards higher Accuracy and better Frequency Response with Standard Multi-Hole Probes in Turbulence Measurement with Remotely Piloted Aircraft (RPA)’, *Atmospheric Measurement Techniques*, vol. 7, no. 4, pp. 1027–1041, 2014.
- [31] K. M. A. Díaz, J. M. F. Oro, and E. B. Marigorta, ‘Direct Calibration Framework of Triple-Hole Pressure Probes for Incompressible Flow’, *Measurement Science and Technology*, vol. 19, no. 7, p. 075 401, 2008.
- [32] S. Prudden, A. Fisher, A. Mohamed, and S. Watkins, ‘An Anemometer for UAS-Based Atmospheric Wind Measurements’, in *17th Australian International Aerospace Congress : AIAC 2017*, 2017.
- [33] C. Lenherr, ‘High Temperature Fast Response Aerodynamic Probe’, PhD thesis, ETH Zurich, 2011.
- [34] G. Koçer, ‘Full-Scale Wind Turbine Flow Field Measurements Using an Instrumented Uninhabited Aerial Vehicle’, en, PhD thesis, ETH Zurich, 2012.
- [35] P. P. Neumann and M. Bartholmai, ‘Real-Time Wind Estimation on a Micro Unmanned Aerial Vehicle using its Inertial Measurement Unit’, *Sensors and Actuators A: Physical*, vol. 235, pp. 300–310, 2015.
- [36] C. Brosy, K. Krampf, M. Zeeman, B. Wolf, W. Junkermann, K. Schäfer, S. Emeis, and H. Kunstmann, ‘Simultaneous Multicopter-Based Air Sampling and Sensing of Meteorological Variables’, *Atmospheric Measurement Techniques*, vol. 10, no. 8, pp. 2773–2784, 2017.
- [37] R. T. Palomaki, N. T. Rose, M. van den Bossche, T. J. Sherman, and S. F. J. De Wekker, ‘Wind Estimation in the Lower Atmosphere Using Multirotor Aircraft’, *Journal of Atmospheric and Oceanic Technology*, vol. 34, no. 5, pp. 1183–1191, 2017.
- [38] J. Moyano Cano, ‘Quadrotor UAV for Wind Profile Characterization’, Master Thesis, Fraunhofer IWES; Institut für Windenergie und Energiesystemtechnik; Kassel, 2013.
- [39] W. Premerlani and P. Bizard, ‘Direction Cosine Matrix IMU: Theory’, *DIY DRONE: USA*, Jan. 2009.
- [40] F. Hoffmann, N. Goddemeier, and T. Bertram, ‘Attitude Estimation and Control of a Quadcopter’, in *2010 IEEE/RSJ International Conference on Intelligent Robots and Systems*, Oct. 2010, pp. 1072–1077.
- [41] S. Wang and Y. Yang, ‘Quadrotor Aircraft Attitude Estimation and Control Based on Kalman Filter’, in *Proceedings of the 31st Chinese Control Conference*, Jul. 2012, pp. 5634–5639.
- [42] M. J. Culter, ‘Design and Control of an Autonomous Variable-Pitch Quadrotor Helicopter’, Master’s thesis, Massachusetts Institute of Technology, 2012.
- [43] B. W. McCormick, *Aerodynamics of V/STOL Flight*. Dover Publications, 1998.
- [44] X. Hafer and G. Sachs, *Senkrechtstarttechnik: Flugmechanik, Aerodynamik, Antriebssysteme (Hochschultext) (German Edition)*. Springer, 1982.
- [45] M. Arnold, P. Cheng, P. Daus, and F. Biskup, ‘Tidal Current Turbine Wake and Park Layout in transient Environments’, in *Proceedings of the ASME 2014 33rd International Conference on Ocean, Offshore and Arctic Engineering, OMAE2014, June 8-13, 2014, San Francisco, California, USA*.

- [46] B. Berry, G. Bowen-Davies, K. Gluesenkamp, Z. Kaler, J. Schmaus, W. Staruk, E. Weiner, and B. Woods, 'Design Optimization of Gamera II: a Human Powered Helicopter', *Annual Forum Proceedings - AHS International*, vol. 1, Jan. 2012.
- [47] S. Wagner, *Lecture Manuscript: Hubschrauber-Aeromechanik*, Institute of Aerodynamics and Gas Dynamics - University of Stuttgart, 2003.
- [48] R. W. Prouty, *Helicopter Performance, Stability, and Control*. Krieger Pub Co., 2001.
- [49] APC, *APC Propeller Performance Data*, <https://www.apcprop.com/technical-information/performance-data/>, accessed: 2019-01-07, Landing Products Inc. 1222 Harter Ave. Woodland, CA 95776, USA, 2019.
- [50] *ANSYS Documentation - CFX 18.0 Modeling Guide*, ANSYS Inc., 2017.
- [51] J. Y. Hwang, M. K. Jung, and O. J. Kwon, 'Numerical Study of Aerodynamic Performance of a Multirotor Unmanned-Aerial-Vehicle Configuration', *Journal of Aircraft*, vol. 52, no. 3, pp. 839–846, Jan. 2019.
- [52] M. M. Zdravkovich and P. W. Bearman, 'Flow Around Circular Cylinders—Volume 1: Fundamentals', *Journal of Fluids Engineering*, vol. 120, no. 1, pp. 216–216, Mar. 1998.
- [53] Hobby King, *HobbyKing Online Shop: Zippy Compact 5000mAh 5S 25C*, https://hobbyking.com/de_de/zippy-compact-5000mah-5s-25c-lipo-pack.html, accessed: 2019-01-07, 2019.
- [54] B. W. McCormick, *Aerodynamics, Aeronautics and Flight Mechanics*. WILEY, 1994.
- [55] C. M. Simoes, *Optimizing a Coaxial Propulsion System to a Quadcopter*, Dept. Engenharia Mecanica, Instituto Superior Tecnico, Lisbon Portugal.
- [56] M. Ramasamy, 'Measurements Comparing Hover Performance of Single, Coaxial, Tandem, and Tilt-Rotor Configurations', in *69th International Forum of the American Helicopter Society*, vol. 4, Jan. 2013, pp. 2439–2461.
- [57] M. W. Mueller and R. D'Andrea, 'Stability and Control of a Quadcopter Despite the Complete Loss of One, Two, or Three Propellers', in *2014 IEEE International Conference on Robotics and Automation (ICRA)*, May 2014, pp. 45–52.
- [58] 'Depron Classic - Technical Data Sheet', Depron (r) International Distributor, Tech. Rep.
- [59] C. G. Lomas, *Fundamentals of Hot-Wire Anemometry*. Cambridge University Press, 1986.
- [60] L. V. King and H. T. Barnes, 'On the Convection of Heat from Small Cylinders in a Stream of Fluid: Determination of the Convection Constants of Small Platinum Wires, with Applications to Hot-Wire Anemometry', *Proceedings of the Royal Society of London A: Mathematical, Physical and Engineering Sciences*, vol. 90, no. 622, pp. 563–570, 1914.
- [61] L. Paulsen, 'Triple Hot-Wire Technique for Simultaneous Measurements of Instantaneous Velocity Components in Turbulent flows', *Journal of Physics E: Scientific Instruments*, vol. 16, no. 6, p. 554, 1983.
- [62] J. O. Hinze, *Turbulence : An Introduction to its Mechanism and Theory*. New York : McGraw-Hill, 1959.
- [63] F. Jorgensen, 'Directional Sensitivity of Wire and Fiber-Film Probes. An Experimental Study.', *DISA Info No. 11*, pp. 31–37, May 1971.
- [64] L. di Mare, T. O. Jelly, and I. J. Day, 'Angular Response of Hot Wire Probes', *Measurement Science and Technology*, vol. 28, no. 3, p. 035303, 2017.

- [65] E. Kit and B. Grits, 'In Situ Calibration of Hot-Film Probes Using a Collocated Sonic Anemometer: Angular Probability Distribution Properties', *Journal of Atmospheric and Oceanic Technology*, vol. 28, no. 1, pp. 104–110, 2011.
- [66] A. Singha and R. Sadr, 'An In-Situ Calibration Technique of a Four-Wire Hot-Wire Anemometer Suitable for Atmospheric Measurement', *Experimental Thermal and Fluid Science*, Apr. 2012.
- [67] T. J. Gieseke and Y. G. Guezennec, 'An Experimental Approach to the Calibration and Use of Triple Hot-Wire Probes', *Experiments in Fluids*, vol. 14, no. 5, pp. 305–315, Apr. 1993.
- [68] J. Andreopoulos, 'Improvements of the Performance of Triple Hot Wire Probes', *Review of Scientific Instruments*, vol. 54, pp. 733–740, Jul. 1983.
- [69] Y. T. Chew and S. M. Ha, 'The Directional Sensitivities of Crossed and Triple Hot-Wire Probes', *Journal of Physics E: Scientific Instruments*, vol. 21, no. 6, p. 613, 1988.
- [70] *Pixhawk 4 - Technical Data Sheet*, Holybro Corporation, Jun. 1, 2018.
- [71] D. Brescianini, M. Hehn, and R. D'Andrea, 'Nonlinear Quadrocopter Attitude Control, Technical Report', Institute for Dynamic Systems and Control (IDSC) ETH Zürich, Tech. Rep., Oct. 10, 2013.
- [72] L. Meier, 'Dynamic robot architecture for robust realtime computer vision', en, PhD thesis, ETH Zurich, Zürich, 2017.
- [73] J. B. Brandt, R. W. Deters, G. Ananda, and M. Selig, (2017-09-22), *UIUC Propeller Database*, University of Illinois at Urbana-Champaign, <http://m-selig.ae.illinois.edu/props/propDB.html>.
- [74] M. Bienek, 'Design and Commissioning of a Propeller/Rotor Test Stand', Bachelor Thesis, SWE - University of Stuttgart, 2016.
- [75] *Micro Load Cell (0-20kg) - CZL635*, <https://www.phidgets.com/?tier=3&catid=9&pcid=7&prodid=225>, accessed: 2019-01-07, Phidgets, 2016.
- [76] *24-Bit Analog-to-Digital Converter(ADC) for Weigh Scales*, HX711, AVIA Semiconductor, Jan. 2015.
- [77] *Model MBA500 - Torque and Thrust Biaxial Sensor - Product Specifications*, FUTEK - Advanced Sensor Technology, Inc., 2019.
- [78] J. Meier, 'Construction and Development of a Test Bench for Measuring the Performance of Coaxial Multicopter Drives', Bachelor Thesis, SWE - University of Stuttgart, 2017.
- [79] M. Drela, *QPROP Formulation*, MIT Department of Aeronautics and Astronautics, Jun. 1, 2006.
- [80] M. Drela and H. Youngren, *XROTOR User Guide*, MIT Department of Aeronautics and Astronautics, Nov. 13, 2003.
- [81] M. Hepperle, *JavaProp Website*, <https://www.mh-aerotoools.de/airfoils/javaprop.htm>, accessed: 2019-01-07.
- [82] J. P. S. Morgado, 'Development of an Open Source Software Tool for Propeller Design in the MAAT Project', PhD thesis, University Beira Interior, Covilhã, Portugal, 2016.
- [83] W. Johnson, 'Rotorcraft Aeromechanics Applications of a Comprehensive Analysis,' Presented at Heli Japan 98', in *AHS International Meeting on Advanced Rotorcraft Technology and Disaster Relief*, 1998.

- [84] W. Johnson, *Helicopter Theory*. Dover Publications Inc., 1994.
- [85] A. R. S. Bramwell, G. T. S. Done, and D. Balmford, *Bramwell's Helicopter Dynamics*. Butterworth-Heinemann, 2001.
- [86] J. G. Leishman, *Principles of Helicopter Aerodynamics (Cambridge Aerospace Series)*. Cambridge University Press, 2016.
- [87] P. M. Goorjian, 'An Invalid Equation in the General Momentum Theory of Actuator Disk', *AIAA Journal Vol. 10, No. 4*, vol. 10, no. 4, pp. 543–544, Apr. 1, 1972.
- [88] A. R. S. Bramwell, *Some Remarks on the Induced Velocity Field of a Lifting Rotor and on Glauert's Formula*, HM Stationary Office, Aeronautical Research Council Current Papers, The City University, London, Oct. 1, 1971.
- [89] R. Gill and R. D'Andrea, 'Propeller thrust and drag in forward flight', in *2017 IEEE Conference on Control Technology and Applications (CCTA)*, Aug. 2017, pp. 73–79.
- [90] K. W. Mangler and H. B. Squire, *The Induced Velocity Field of a Rotor*, HM Stationary Office, A.R.C. Technical Report, Ministry of Supply - Aeronautical Research Council, 1953.
- [91] M. Drela and H. Youngren, *XFOIL 6.9 - User Guide*, MIT Department of Aeronautics and Astronautics, Nov. 30, 2001.
- [92] F. Bohorquez, F. Rankins, J. Baeder, and D. Pines, 'Hover Performance of Rotor Blades at Low Reynolds Numbers for Rotary Wing Micro Air Vehicles. An Experimental and CFD Study', in, ser. Fluid Dynamics and Co-located Conferences, American Institute of Aeronautics and Astronautics, Jan. 2003.
- [93] J. G. Leishman and S. Ananthan, 'Aerodynamic Optimization of a Coaxial Proprotor', *Annual Forum Proceedings-American Helicopter Society*, 62, p. 64, 1 May 9, 2006.
- [94] *Website - Motor Overview*, <http://www.beikimco.com/motor-products/brushless-dc/BLDC-brushless-frameless-parts-kit>, accessed: 2019-01-07, BEIKIMCO - Advanced Magnetics for Motion Control.
- [95] 'Sensorless BLDC Motor Control and BEMF Sampling Methods with ST7MC', STMicroelectronics, Application Note AN1946, 2007, Rev. 2.
- [96] 'Trapezoidal Control of BLDC Motors Using Hall Effect Sensors', Texas Instruments Incorporated, Application Report SPRABQ6, 2013.
- [97] M. Keller, *Betaflight ESC Telemetry - Description on GitHub*, <https://github.com/betaflight/betaflight/wiki/ESC-Telemetry>, accessed: 2019-01-07, 2017.
- [98] 'QN3109M6N N-Channel 30V Fast Switching MOSFET', UBIQ Semiconductor Corp., Datasheet, Rev A.01 D120216P.
- [99] 'STM32F051x4 STM32F051x6 STM32F051x8', STMicroelectronics, Datasheet DocID022265 Rev 7, 2017.
- [100] *HEXFET Power MOSFET IRFH7440PbF*, IRFH7440PBF, Infineon Technologies AG, 2015.
- [101] *Tilt Drone Website*, <https://www.tilt drone.com/>, accessed: 2019-01-07, 2019.
- [102] *Eashine Tilt 180 Drone Website*, https://www.eachine.com/Eachine-Racer-180-FPV-Drone-F3-6DOF-350mW-5_8G-40CH-VTX-1000TVL-CCD-Camera-w-or-I6-Remote-Control-RTF-p-404.html, accessed: 2019-01-07, 2019.
- [103] *Website FoxTech Swift 280 Tilt Drone*, <https://www.foxtechfpv.com/swift-280-tilt-rotor-fpv-quadcopter-pnp.html>, accessed: 2019-01-07, 2019.

-
- [104] ‘Single Turn Bushing Mount Hall Effect Sensor in Size 09’, Vishay Intertechnology, Inc., Datasheet Document Number: 57099, Revision: 27-Mar-15.
- [105] D. Schrand, ‘Cross-talk Compensation Using Matrix Methods’, Sensor Developements Inc., Technical Notes and Articles.
- [106] *RC-Heli Discussion Board*, <https://www.rc-heli.de/board/showthread.php?t=207468>, accessed: 2019-01-07, 2012.
- [107] R. Gleiter, ‘Experimentele Bestimmung des Schwingungsverhaltens der Messinstrumentaufhängung für den Windmesscopter ANDroMeDA’, Master Thesis, SWE - University of Stuttgart, 2018.
- [108] S. Skaug, *Operation Manual for BLHeli SiLabs Rev14.x*, 2017.
- [109] Carbon-Werkge Weißgerber GmbH & Co.KG, *Online shop*, <https://www.carbon-vertrieb.com/>, accessed: 2019-01-07, 2019.
- [110] *Technisches Datenblatt - CFK-Rohr 28/26mm*, Technologie: Prepreg - Wickeltechnik, CG TEC, 2019.
- [111] D. T. Prosser and M. J. Smith, ‘A Physics-Based, Reduced-Order Aerodynamics Model for Bluff Bodies in Unsteady, Arbitrary Motion’, *Journal of the American Helicopter Society*, vol. 60, no. 3, pp. 1–15, Jul. 2015.
- [112] M. J. Smith, J. P. Afman, N. Koukpaizan, and A. Grubb, ‘An Enhanced Prediction Methodology for Rapid Performance and Control Design of Highly Maneuverable UAVs’, in *Proceedings of the 43rd European Rotorcraft Forum*, 2017.

Curriculum Vitae

Contact

Christian Molter
Alexanderstr. 9A
70184 Stuttgart

phone: (07 11) 685 68 241

Mail: christian.molter@rocketmail.com

Born on February 18,1982 in Ludwigsburg

Nationality: German

Education

1992–2002 Abitur - Alfred-Amman-Gymnasium Bönnigheim

2004–2012 Dipl.-Ing. Aerospace Engineering - University of Stuttgart

Work Experience

2006-2012 Several student research assistant positions at the Institute of Aircraft Design and the Institute of Aerodynamics and Gas Dynamics at the University of Stuttgart

2012-2013 Kayser-Threde GmbH, CAD modeling and programming

since 2013 Research assistant at Stuttgart Wind Energy at Institute of Aircraft Design, University of Stuttgart

Languages

German, English

Stuttgart, January 14th 2020